

Complexity

Advanced Topics in Modeling, Bifurcation Analysis, and Control Theory of Complex Systems

Lead Guest Editor: Olfa Boubaker

Guest Editors: Jinde Cao, Sajad Jafari, Christos Volos, Viet-Thanh Pham,
and Zeraouia Elhadj





**Advanced Topics in Modeling,
Bifurcation Analysis, and Control
Theory of Complex Systems**

Complexity

**Advanced Topics in Modeling,
Bifurcation Analysis, and Control
Theory of Complex Systems**

Lead Guest Editor: Olfa Boubaker

Guest Editors: Jinde Cao, Sajad Jafari, Christos Volos,
Viet-Thanh Pham, and Zeraoulia Elhadj



Copyright © 2018 Hindawi. All rights reserved.

This is a special issue published in “Complexity.” All articles are open access articles distributed under the Creative Commons Attribution License, which permits unrestricted use, distribution, and reproduction in any medium, provided the original work is properly cited.

Editorial Board

José Ángel Acosta, Spain
Rodrigo Aldecoa, USA
Juan A. Almendral, Spain
David Arroyo, Spain
Arturo Buscarino, Italy
Guido Caldarelli, Italy
Danilo Comminiello, Italy
Manlio De Domenico, Italy
Pietro De Lellis, Italy
Albert Diaz-Guilera, Spain
Jordi Duch, Spain
Joshua Epstein, USA
Thierry Floquet, France

Mattia Frasca, Italy
Lucia Valentina Gambuzza, Italy
Carlos Gershenson, Mexico
Peter Giesl, UK
Sergio Gómez, Spain
Sigurdur F. Hafstein, Iceland
Giacomo Innocenti, Italy
Jeffrey H. Johnson, UK
Vittorio Loreto, Italy
Didier Maquin, France
Eulalia Martínez, Spain
Ch. P. Monterola, Philippines
Roberto Natella, Italy

Daniela Paolotti, Italy
Luis M. Rocha, USA
Miguel Romance, Spain
Matilde Santos, Spain
Hiroki Sayama, USA
Michele Scarpiniti, Italy
Enzo Pasquale Scilingo, Italy
Samuel Stanton, USA
Roberto Tonelli, Italy
Shahadat Uddin, Australia
Gaetano Valenza, Italy
Dimitri Volchenkov, USA
Christos Volos, Greece

Contents

Advanced Topics in Modeling, Bifurcation Analysis, and Control Theory of Complex Systems

Olfa Boubaker , Sajad Jafari , Christos Volos , Zeraoulia Elhadj, Viet-Thanh Pham ,
and Jinde Cao 

Volume 2018, Article ID 9417479, 3 pages

Multistability Analysis and Function Projective Synchronization in Relay Coupled Oscillators

Ahmad Taher Azar , Ngo Mouelas Adele, Kammogne Soup Tewa Alain , Romanic Kengne ,
and Fotsin Hilaire Bertrand 

Volume 2018, Article ID 3286070, 12 pages

Master-Slave Synchronization of 4D Hyperchaotic Rabinovich Systems

Ke Ding , Christos Volos , Xing Xu, and Bin Du

Volume 2018, Article ID 6520474, 9 pages

Design of Robust Supertwisting Algorithm Based Second-Order Sliding Mode Controller for Nonlinear Systems with Both Matched and Unmatched Uncertainty

Marwa Jouini, Slim Dhahri, and Anis Sellami

Volume 2017, Article ID 1972921, 8 pages

Tracking Control for Mobile Robots Considering the Dynamics of All Their Subsystems: Experimental Implementation

José Rafael García-Sánchez, Ramón Silva-Ortigoza, Salvador Tavera-Mosqueda, Celso Márquez-Sánchez,
Victor Manuel Hernández-Guzmán, Mayra Antonio-Cruz, Gilberto Silva-Ortigoza, and Hind Taud

Volume 2017, Article ID 5318504, 18 pages

Multimedia Security Application of a Ten-Term Chaotic System without Equilibrium

Xiong Wang, Akif Akgul, Sezgin Kacar, and Viet-Thanh Pham

Volume 2017, Article ID 8412093, 10 pages

Dynamic Analysis and Circuit Design of a Novel Hyperchaotic System with Fractional-Order Terms

Abir Lassoued and Olfa Boubaker

Volume 2017, Article ID 3273408, 10 pages

Computer Simulation of Noise Effects of the Neighborhood of Stimulus Threshold for a Mathematical Model of Homeostatic Regulation of Sleep-Wake Cycles

Wuyin Jin, Qian Lin, An Wang, and Chunni Wang

Volume 2017, Article ID 4797545, 7 pages

Mixed Stimulus-Induced Mode Selection in Neural Activity Driven by High and Low Frequency Current under Electromagnetic Radiation

Lulu Lu, Ya Jia, Wangheng Liu, and Lijian Yang

Volume 2017, Article ID 7628537, 11 pages

Nonlinear Complex Dynamics of Carbon Emission Reduction Cournot Game with Bounded Rationality

LiuWei Zhao

Volume 2017, Article ID 8301630, 10 pages

Complexity Dynamic Character Analysis of Retailers Based on the Share of Stochastic Demand and Service

Junhai Ma, Weiya Di, and Hao Ren
Volume 2017, Article ID 1382689, 12 pages

A Novel Clustering Method Based on Quasi-Consensus Motions of Dynamical Multiagent Systems

Ning Cai, Chen Diao, and M. Junaid Khan
Volume 2017, Article ID 4978613, 8 pages

Stabilization of a Network of the FitzHugh–Nagumo Oscillators by Means of a Single Capacitor Based RC Filter Feedback Technique

Elena Adomaitienė, Skaidra Bumelienė, Gytis Mykolaitis, and Arūnas Tamaševičius
Volume 2017, Article ID 4324879, 8 pages

A New Nonlinear Chaotic Complex Model and Its Complex Antilag Synchronization

Emad E. Mahmoud and Fatimah S. Abood
Volume 2017, Article ID 3848953, 13 pages

Study on Triopoly Dynamic Game Model Based on Different Demand Forecast Methods in the Market

Junhai Ma, Lijian Sun, and Xueli Zhan
Volume 2017, Article ID 5434680, 12 pages

Autaptic Modulation of Electrical Activity in a Network of Neuron-Coupled Astrocyte

Shengli Guo, Jun Tang, Jun Ma, and Chunni Wang
Volume 2017, Article ID 4631602, 13 pages

Chaos Control in Fractional Order Smart Grid with Adaptive Sliding Mode Control and Genetically Optimized PID Control and Its FPGA Implementation

Anitha Karthikeyan and Karthikeyan Rajagopal
Volume 2017, Article ID 3815146, 18 pages

Leader-Follower Fixed-Time Group Consensus Control of Multiagent Systems under Directed Topology

Yilun Shang and Yamei Ye
Volume 2017, Article ID 3465076, 9 pages

Centralized and Decentralized Data-Sampling Principles for Outer-Synchronization of Fractional-Order Neural Networks

Jin-E Zhang
Volume 2017, Article ID 6290646, 11 pages

Editorial

Advanced Topics in Modeling, Bifurcation Analysis, and Control Theory of Complex Systems

Olfa Boubaker ¹, **Sajad Jafari** ², **Christos Volos** ³, **Zeraoulia Elhadj**,⁴
Viet-Thanh Pham ⁵, and **Jinde Cao** ⁶

¹National Institute of Applied Sciences and Technology, Tunis, Tunisia

²Amirkabir University of Technology, Tehran, Iran

³University of Thessaloniki, Thessaloniki, Greece

⁴University of Tébessa, Tébessa, Algeria

⁵Hanoi University of Science and Technology, Hanoi, Vietnam

⁶Southeast University, Nanjing, China

Correspondence should be addressed to Olfa Boubaker; olfa.boubaker@insat.rnu.tn

Received 22 November 2017; Accepted 23 November 2017; Published 26 February 2018

Copyright © 2018 Olfa Boubaker et al. This is an open access article distributed under the Creative Commons Attribution License, which permits unrestricted use, distribution, and reproduction in any medium, provided the original work is properly cited.

In the recent years, several complex systems have been investigated in nonlinear theory and have had a huge impact on the scientist researches. Due to the complexity of their design, analysis, and control, innovative insights had emerged in this expanding area.

The purpose of this special issue is to draw attention of the scientific community to recent advances in nonlinear systems theory and their possible applications. The special issue includes several high-quality papers written by leading and emerging specialists in the field. It proposes an array of novel complex models belonging to the class of chaotic/hyperchaotic systems, fractional-order nonlinear systems, game systems, and smart grid and multiagent systems. Stability analyses and bifurcation investigations are also exposed for several models. Advanced control techniques and novel synchronization approaches are moreover suggested. We can quote, in that sense, applications not only related to the technology such as electronics and circuit design, multimedia, networks, and robotics but also related to biomedical and market domains.

More than 37 submissions from 21 countries (Algeria, Cameroon, China, Egypt, Ethiopia, Greece, Honduras, Hong Kong, Iran, Iraq, Lithuania, Mexico, Pakistan, Poland, Saudi Arabia, Spain, Qatar, Thailand, Tunisia, Turkey, USA, and Vietnam) have been received. Among the articles

collected, a large number of high-quality papers existed, which led to 18 published articles with an acceptance rate of 45% (higher than that of the journal). This contribution reflects the strong interest in the considered subject.

Among the published papers in the special issue, three research papers propose novel hyperchaotic/chaotic systems supported by engineering applications and three other papers solve innovative chaos synchronization problems. Three papers propose bifurcation investigations of complex models related to biomedical applications and another three papers present bifurcation analysis and control of game models. Finally, there are two papers focusing on control of multiagent systems, two papers on control of robotic systems in presence of uncertainties, and two papers on control of coupled oscillators by external forcing. A very short description of the addressed topics, in the order of themes cited below, is presented as follows.

In “Dynamic Analysis and Circuit Design of a Novel Hyperchaotic System with Fractional-Order Terms,” by A. Lassoued and O. Boubaker, a novel hyperchaotic system with fractional-order polynomials is designed. Its highly complex dynamics are investigated in terms of equilibrium points, Lyapunov spectrum, and attractor forms and a related electronic circuit is designed.

In “Multimedia Security Application of a Ten-Term Chaotic System without Equilibrium,” by X. Wang et al., a new chaotic system without equilibrium is proposed. The system is realized on an electronic card and applied in multimedia security, such as image encryption and sound steganography.

In “A New Nonlinear Chaotic Complex Model and Its Complex Antilag Synchronization,” by E. E. Mahmoud and F. S. Abood, a new chaotic Lü model with complex factors is covered and a novel antilag synchronization approach is also proposed.

In “Chaos Control in Fractional Order Smart Grid with Adaptive Sliding Mode Control and Genetically Optimized PID Control and Its FPGA Implementation,” by A. Karthikeyan and K. Rajagopal, a specific smart grid system and its nonlinear properties are investigated. The Lyapunov exponents prove the existence of chaos and bifurcation. A related fractional order model is then derived and its bifurcation analysis is also investigated. Two different control methods are finally proposed to suppress the chaotic oscillations.

In “Centralized and Decentralized Data-Sampling Principles for Outer-Synchronization of Fractional-Order Neural Networks,” by J.-E. Zhang, new sufficient criteria for an outer-synchronization of a fractional-order neural networks are derived using centralized and decentralized data-sampling principles.

In “Master-Slave Synchronization of 4D Hyperchaotic Rabinovich Systems,” by K. Ding et al., some original master-slave synchronization criteria are derived for 4D hyperchaotic Rabinovich systems and then extended for 3D chaotic Rabinovich systems.

In “Mixed Stimulus-Induced Mode Selection in Neural Activity Driven by High and Low Frequency Current under Electromagnetic Radiation,” by L. Lu et al., a new Hindmarsh-Rose neuron model with different types of electrical stimulus impended with a high-low frequency current is proposed and deeply analyzed with regard to the transmission of several complex signals.

In “Computer Simulation of Noise Effects of the Neighborhood of Stimulus Threshold for a Mathematical Model of Homeostatic Regulation of Sleep-Wake Cycles,” by W. Jin et al., noise effects on sleep-wake cycles’ neuronal mathematical model determined by the hypocretin/orexin and the local glutamate interneurons spatiotemporal behaviors are analyzed. The conductance and the activation variable of the modulation function are also investigated based on a circadian input skewed in sine function.

In “Autaptic Modulation of Electrical Activity in a Network of Neuron-Coupled Astrocyte,” by S. Guo et al., a simple network is developed for the Hodgkin-Huxley neuron coupled by astrocyte and the autapse and different modes of electrical activities and oscillating behaviors are deeply analyzed.

In “Study on Triopoly Dynamic Game Model Based on Different Demand Forecast Methods in the Market,” by J. Ma et al., a new model of Triopoly game considering inaccurate demand in the market is proposed. Bifurcation dynamics, route to chaos, and basins of attraction are investigated. Finally, a feedback control method is suggested.

In “Complexity Dynamic Character Analysis of Retailers Based on the Share of Stochastic Demand and Service,” by J. Ma et al., a modified price and demand game model based on the stochastic demand and the retailer’s service level is proposed. The bifurcation phenomena as well the chaotic characteristics are shown. Finally, the chaos control of the complex model is achieved.

In “Nonlinear Complex Dynamics of Carbon Emission Reduction Cournot Game with Bounded Rationality,” by L. Zhao, a novel Cournot duopoly game model of carbon emission reduction based on the hypothesis of participant’s bounded rationality is proposed. The dynamic adjustment mechanism of emission reduction for enterprises is analyzed. It is shown that the system can demonstrate chaotic phenomenon. Finally, a delay feedback control is designed to control the system’s complex dynamics.

In “A Novel Clustering Method Based on Quasi-Consensus Motions of Dynamical Multiagent Systems,” by N. Cai et al., a novel approach for clustering based on quasi-consensus of dynamical high-order multiagent systems is suggested and a necessary and sufficient condition for checking the achievement of group consensus is given.

In “Leader-Follower Fixed-Time Group Consensus Control of Multiagent Systems under Directed Topology,” by Y. Shang and Y. Ye, the fixed-time group consensus problem is investigated for a leader-follower network of integrators with directed topology. A nonlinear distributed control protocol, based on local information, is proposed such that the follower agents in each subgroup are able to track their corresponding leaders in a prescribed convergence time regardless of the initial conditions.

In “Design of Robust Supertwisting Algorithm Based Second-Order Sliding Mode Controller for Nonlinear Systems with Both Matched and Unmatched Uncertainty,” by M. Jouini et al., a modified design of the super-twisting controller for nonlinear systems with matched and unmatched uncertainties is proposed. The main contribution resides in adding two terms to the classical design which leads to accelerating the convergence and simultaneously limiting the overshoot and shortening the settling time of the system response.

In “Tracking Control for Mobile Robots Considering the Dynamics of All Their Subsystems: Experimental Implementation,” by J. R. Garcia-Sanchez et al., the trajectory tracking task in a wheeled mobile robot is solved by proposing a three-level hierarchical controller that considers the mathematical model of the mechanical structure, actuators, and power stage. Experimental results show the effectiveness and robustness of the proposed control scheme.

In “Multistability Analysis and Function Projective Synchronization in Relay Coupled Oscillators,” by A. T. Azar et al., regions of stability are discovered in a general class of Genesio-Tesi chaotic oscillators for which attractors and limit cycles are shown and isospike diagrams are also exposed. Finally, finite-time projective synchronization of relay coupled oscillators is displayed.

In “Stabilization of a Network of the FitzHugh–Nagumo Oscillators by Means of a Single Capacitor Based RC Filter Feedback Technique,” by E. Adomaitienė et al., an original control approach for unstable FitzHugh–Nagumo oscillators

is proposed based on analytical, numerical, and also experimental investigations. It is shown that a single capacitor is sufficient to achieve this task if the oscillators are coupled strongly enough.

Acknowledgments

The editors would like to express their thanks to all authors of the special issue for their valuable contributions and to all reviewers for their useful efforts to provide valuable reviews. We expect this special issue to offer a timely view of advanced topics in nonlinear systems, which will grant stimulation for further novel academic researches and innovative applications.

Olfa Boubaker
Sajad Jafari
Christos Volos
Zeraouia Elhadj
Viet-Thanh Pham
Jinde Cao

Research Article

Multistability Analysis and Function Projective Synchronization in Relay Coupled Oscillators

Ahmad Taher Azar ^{1,2}, Ngo Mouelas Adele,³ Kammogne Soup Tewa Alain ³,
Romanic Kengne ^{3,4} and Fotsin Hilaire Bertrand ³

¹Faculty of Computers and Information, Benha University, Benha, Egypt

²School of Engineering and Applied Sciences, Nile University Campus, Sheikh Zayed District, Juhayna Square, 6th of October City, Giza 12588, Egypt

³Laboratoire de Matière Condensée d'Electronique et de Traitement du Signal, Faculty of Science, University of Dschang, P.O. Box 67, Dschang, Cameroon

⁴Research Group on Experimental and Applied Physics for Sustainable Development (EAPhySuD), P.O. Box 412, Dschang, Cameroon

Correspondence should be addressed to Ahmad Taher Azar; ahmad_t.azar@ieee.org

Received 22 July 2017; Revised 1 November 2017; Accepted 9 November 2017; Published 18 January 2018

Academic Editor: Sajad Jafari

Copyright © 2018 Ahmad Taher Azar et al. This is an open access article distributed under the Creative Commons Attribution License, which permits unrestricted use, distribution, and reproduction in any medium, provided the original work is properly cited.

Regions of stability phases discovered in a general class of Genesis–Tesi chaotic oscillators are proposed. In a relatively large region of two-parameter space, the system has coexisting point attractors and limit cycles. The variation of two parameters is used to characterize the multistability by plotting the isospike diagrams for two nonsymmetric initial conditions. The parameters window in which the jerk system exhibits the unusual and striking feature of multiple attractors (e.g., coexistence of six disconnected periodic chaotic attractors and three-point attraction) is investigated. The second aspect of this study presents the synchronization of systems that act as mediators between two dynamical units that, in turn, show function projective synchronization (FPS) with each other. These are the so-called relay systems. In a wide range of operating parameters; this setup leads to synchronization between the outer circuits, while the relaying element remains unsynchronized. The results show that the coupled systems can achieve function projective synchronization in a determined time despite the unpredictability of the scaling function. In the coupling path, the outer dynamical systems show finite-time synchronization of their outputs, that is, displaying the same dynamics at exactly the same moment. Further, this effect is rather general and it has a wide range of applications where sustained oscillations should be retained for proper functioning of the systems.

1. Introduction

Multistability, meaning the coexistence of many different kinds of attractors, is an intrinsic property of many nonlinear dynamical systems and has become very important research topic and received much attention recently [1, 2]. Multistability poses a threat for engineering systems because the system may unpredictably switch into an undesirable state. Multistability exhibits a rich diversity of stable states of a nonlinear dynamical system and makes the system offer a great flexibility. Particularly, when the number of coexisting attractors generating from a dynamical system tends to be infinite, the coexistence of many attractors

depending on the initial condition of a certain state variable is alleged to be extreme multistability [3]. The occurrence of multiple attractors, which implies multiple stability and thus hysteretic dynamics, is one of the most important phenomena encountered in nonlinear dynamical systems. Such type of behavior has been reported in a wide range of systems including electronic circuits [4], laser [5], biological systems [6], Lorenz system [7], Josephson junction [8], and chemical reactions [9]. Multiple attractor bifurcations are said to occur when multiple coexisting attractors are simultaneously created at a bifurcation point [10]. It has been shown earlier that in some cases border collision bifurcations may lead to multiple attractor bifurcations [11].

More recently, Bao and collaborators [12] developed hidden extreme multistability in memristive hyperchaotic system. In that paper, they established a novel memristive hyperchaotic system with no equilibrium based on the newly proposed circuit realization scheme and investigated the phenomenon of extreme multistability with hidden oscillation that reveals the coexistence of infinitely many hidden attractors in the proposed memristive hyperchaotic system. Kengne et al. [13] presented the basic dynamical properties of a simple autonomous jerk system including equilibria and stability, phase portraits, frequency spectra, bifurcation diagrams, and Lyapunov exponent plots. It is shown that the onset of chaos is achieved via the classical period-doubling and symmetry-restoring crisis scenarios. One of the key contributions presented in their work was that the jerk system experiences the striking feature of multiple attractors (e.g., coexistence of four disconnected periodic and chaotic attractors) [13, 14]. It is important to note that the results obtained revealed that there are some unexplored parameters' regions of this circuit where four disconnected nonstatic attractors coexist.

The interaction of two nonlinear systems via a third parameter-matched circuit typically leads to a variety of significant behaviors, among which the most intriguing is probably synchronization (*known usually as relay synchronization*), that is, the coordination of a particular dynamical property of their motion [15]. The interaction between two chaotic systems has been deeply studied during the past decade, focusing on the ability of synchronization even in the presence of noise or delay. In [16], Wagemakers et al. examined the robustness of isochronous synchronization in simple arrays of bidirectionally coupled systems. The results of the study showed experimentally that the relaying unit does not need to be identical to the outer systems which are the ones to be synchronized. Sharma et al. in [17] proposed the dynamics of nonlinear oscillators indirectly coupled through a dynamical environment. The results of the study showed that this form of indirect coupling leads to synchronization and phase-flip transition in periodic as well as chaotic regime of oscillators. The phase-flip transition in the case of relay coupled system was investigated by Sharma et al. in [18]. In that paper, the authors show that, in the absence of time delay, relay coupling through conjugate variables has the same effect as when the interactions involve a time delay. However, this phase-flip transition does not occur abruptly at a certain critical value of the coupling parameter. Relay synchronization (RS) has been used with electronic circuits, as a technique for transmitting and recovering encrypted messages, which can be sent bidirectionally and simultaneously [19]. Apart from its technological applications, RS has also been proposed as a possible mechanism at the basis of isochronous synchronization between distant areas of the brain [20]. Nana and Wofo proposed a theoretical and experimental synchronization of three oscillators coupled as emitter-relay-receiver system [21]. They proposed an experimental setup and showed that it is impossible to achieve a zero synchronization error due to the tolerances of the electrical components. Some demonstrations of chaotic masking of communication as well as selected secure communication lines were observed. Gutiérrez et al. in [22] showed that a generalized synchronization (GS) in relay

systems with instantaneous coupling could be obtained. The authors proved the existence of GS in unidirectional coupled units (drive system \rightarrow response system) by checking the ability of the response system to react identically to different initial conditions of the same driver system, which can be quantified by evaluating the mutual false nearest neighbors or by measuring the conditional Lyapunov exponents. Despite such evidence of RS, there are still open questions of a fundamental nature. The main issue is to characterize properly the relationship established in RS between the dynamics of the relay system and that of the synchronized systems. From the previously mentioned references, the literature needs a strict analysis of the performance of the RS using a scaling function. Besides, the projective synchronization (PS) has been used in the research of secure communication because of the unpredictability of the scaling function which may be a useful element [23]. So the development of the function projective synchronization in relay systems is important challenging research point. This motivates the present study.

The aim of this work is to make some dynamical analysis details of complex systems that can exhibit many major features of the regular and chaotic motion which allows a better understanding of its behavior and providing a generic route of function synchronization in relay coupled jerk oscillators.

The remainder of the paper is organized as follows. In Section 2, the nonlinear system is presented and the dynamical behaviors of the circuit are identified with the help of a numerical two-parameter Lyapunov exponent diagram. The finite-time synchronization issue is formulated in Section 3 in which synchronization and numerical simulations are presented. Finally, conclusions and remarks are given in Section 4.

2. The Model and Its Behavior

2.1. Preliminaries. We consider the following chaotic system:

$$\begin{aligned} \dot{z}_i(t) &= a_i z_{i+1}(t), \quad i = 1, 2, \dots, n-1 \\ &\vdots \\ \dot{z}_n(t) &= f(z(t)), \end{aligned} \tag{1}$$

where $z(t) = (z_1(t), z_2(t), \dots, z_n(t))^T$ is the system state vector, a_i the constants, and $f(z(t))$ the nonlinear smooth function. Actually, through topological transformation, many existing chaotic systems, such as Chen systems, Lorenz systems, Lu systems, can be transformed as in the form of system (1). More recently, a growing interest is in the analysis of the LEs on Lyapunov diagrams, where we associate colors for the largest and the second largest exponent varying simultaneously two system's parameters [24, 25]

Remark 1. In real world, the order of chaotic system (1) usually will not go beyond fourth order. Therefore, the subscripts is less than or equal to 4 (i.e., $i \leq 4$).

If we set $i = 3$, the general class of Genesio–Tesi system is obtained. This system is one of paradigms of chaos since it captures many features of chaotic systems. It includes a

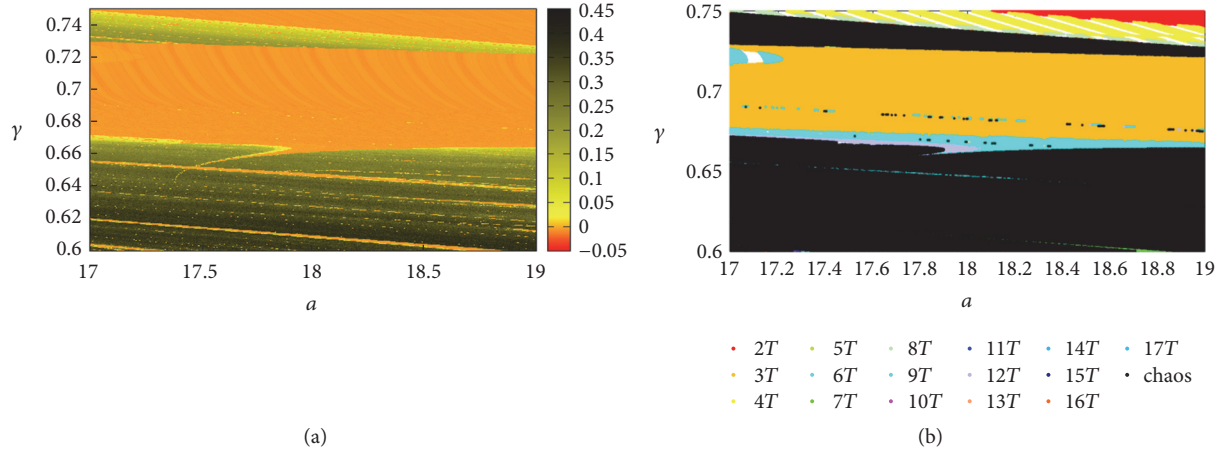


FIGURE 1: Two complementary ways of characterizing the stability of the MO5 circuit in the plan (a, γ) : (a) Lyapunov stability diagram, where the orange shadings mark periodic oscillations and yellow and black denote the chaotic behaviors; (b) isospike diagrams displaying the number of peaks in one period of $x(t)$. These two figures are plotted for the initial conditions $(0.5, 0, 0)$. Regularity, multiperiodicity and “chaos” are represented, respectively, in (b). Each color shows the number of peaks in one period T of $x(t)$.

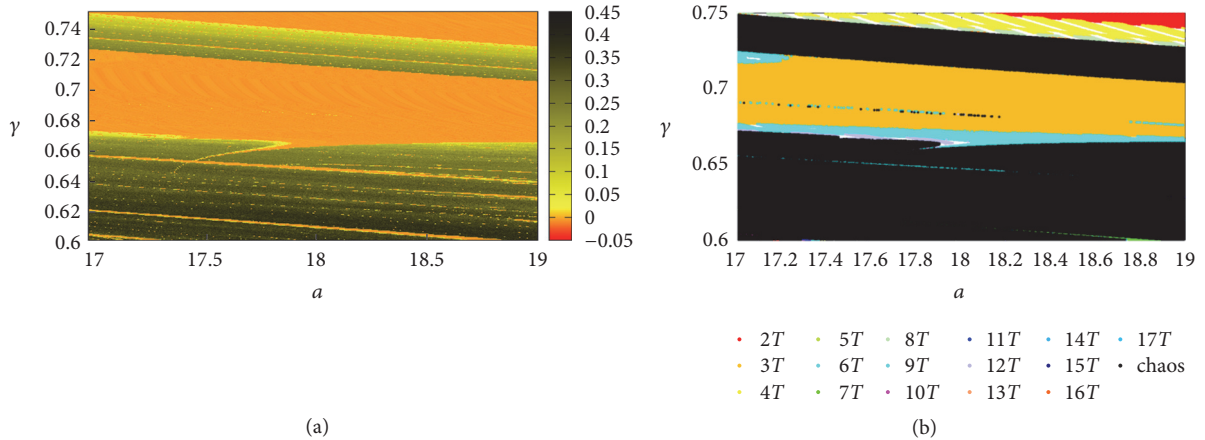


FIGURE 2: In (a) Lyapunov diagram for the (a, γ) plane and in (b) isospike diagram for the same range of parameters as in (a) with the initial conditions set at $(0, 0.5, 0.5)$. These figures have been plotted with the same rank as the parameters in Figure 1.

simple square part and three simple ordinary differential equations that depend on three positive real parameters. Let us consider for this study the simple autonomous jerk system with multiple attractors presented recently by Kengne et al. and described by the following dynamics equations [13, 14]:

$$\begin{aligned} \dot{x}_1 &= x_2, \\ \dot{x}_2 &= ax_3, \\ \dot{x}_3 &= -\gamma x_2 - x_3 + p(x_1), \end{aligned} \quad (2)$$

where a and γ are the positive constants and $p(x_1)$ the polynomial smooth function. For instance, the system is chaotic for the parameters $a = 10$, $\gamma = 0.725$, $p(x_1) = x_1 - x_1^3$. Equation (2) represents a reliable and palpable resource for generating a wide variety of nonlinear phenomena including the multiple stability behavior. This system is capable of displaying many disconnected attractors (for some suitable sets of parameters) depending solely on the choice of initial

conditions [13]. The following section underlines some unexplored parameter’s regions of systems proposed in (2) which shows that many attractors coexist.

2.2. Stability Analysis of the Attractors. This section presents in two complementary ways (described below) phase diagrams characterizing the far-reaching regular organization induced by the set of stable oscillations of the circuit. Although obtained using two very distinct algorithms, the boundaries between chaotic and periodic regions match perfectly by plotting on a fine parameter grid the largest nonzero Lyapunov exponent. Such exponents are familiar indicators that allow one to discriminate chaos (positive exponents) from periodic oscillations (negative exponents). Figures 1 and 2 depict the behavior of MO5 oscillator in the plane (a, γ) for a mesh of 750×750 parameters points. The results are obtained by using the standard fourth-order Runge-Kutta algorithm with fixed time step $h = 5 \times 10^{-3}$. Figures 1 and 2 are obtained by adopting the initial values

as $(0.5, 0, 0)$ and $(0, 0.5, 0.5)$, respectively. As usual the first 5×10^5 integration step disregarded as a transient time is considered to approach the attractor. The discrimination of the solutions and the account of the number of peaks within a period of $x(t)$ are detailed in [25]. Figures 1(a) and 2(a) display the Lyapunov stability diagram, obtained by plotting in two dimensions (in the plane (a, γ)) the largest nonzero Lyapunov exponent for the same parameters. The initial conditions are adopted as $(0.5, 0, 0)$ and $(0, 0.5, 0.5)$, respectively. The orange shadings mark periodic oscillations (negative exponents); the yellow and black colors denote the chaotic behaviors (positive exponent). It is worth noting that the diagrams plotted for the same values of parameters and the different initial conditions should be identical in the case where the circuit depicts no multistability fashion. This aspect is not observed in these two figures. The Lyapunov exponent points out this difference. This method is limited because it can only bring out the regions of coexistence between chaos and regularity, when plotting the isospike diagrams to complete the analysis. Figures 1(b) and 1(c) display the isospike diagrams in the plane (a, γ) for the same values of the parameters for the following initial conditions fixed as $(0.5, 0, 0)$ and $(0, 0.5, 0.5)$, respectively. We use a palette of 17 colors to represent the number of spikes contained in one period of the oscillate state $x(t)$ as indicated by the color dots. Within the parameter range chosen, we obtain 2, 3, 4, 5, 6, 7, 8, 9, 10, 11, 12, 13, 14, 15, 16, and 17 spikes in a single period T of $x(t)$. The black color denotes the chaotic behavior. These two figures are used to study the 2D multistability in MO5 oscillators. They consistency shows all coexistences between the regular and nonregular oscillations.

2.3. Occurrence of Multiple Attractors. Most systems have only one attractor or one single type of attractor. Others may have two different types of coexisting attractors, most likely strange attractors and periodic cycles. It is interesting and striking to see that the simple system reported here has all three different common types of attractors coexisting side by side. Figure 2(a) presents the two-parameter Lyapunov exponent diagrams in the plane for the following initial conditions $(0, 0, 0.5)$. The isospike is presented in Figure 2(b). The same features observed in Figure 1(b) are also observed with additional remarks. For instance, in Figure 1(b) we observe two black bands indicating the chaotic domains. One of these bands corresponds to the high values of γ which borders two distinct periodic structures; the structure of period-3 and period-6 and decreases gradually when the parameter a is monitored, whereas in Figure 2(b) the same band for the different conditions is encircled by two distinct periodic structures, namely, period-3 and period-6 in the three regions; the band here remains solid in its evolution showing the stability of the chaotic attractors. The difference between Figures 1(b) and 2(b) is a fundamental concept resulting from the multistability of attractors. In this work, we presented the multistability zones for the same ranges of variation of the plane (a, γ) .

Previous work [13] reports in some way a detailed dynamical analysis of the system proposed in this work and discovered that the system is capable of displaying *four*

TABLE 1: Coexistence of multiple solutions for suitable values of parameters (a, γ) .

a	γ	Initial conditions	Symmetric coexistence of two attractors	
17.63	0.6714	$(\pm 0.5, 0, 0)$	<i>Period-6</i>	Figure 6(a1)
		$(0, \pm 0.5, \pm 0.5)$	<i>Period-4</i>	Figure 6(a2)
18.16	0.7206	$(\pm 0.5, 0, 0)$	<i>Period-5</i>	Figure 6(b1)
		$(0, \pm 0.5, \pm 0.5)$	<i>Period-3</i>	Figure 6(b2)
18.22	0.6816	$(\pm 0.5, 0, 0)$	<i>Period-3</i>	Figure 6(c1)
		$(0, \pm 0.5, \pm 0.5)$	<i>Period-6</i>	Figure 6(c2)
17.37	0.7401	$(\pm 0.5, 0, 0)$	<i>Chaos</i>	Figure 6(d1)
		$(0, \pm 0.5, \pm 0.5)$	<i>Period-6</i>	Figure 6(d2)
18.03	0.7191	$(\pm 0.5, 0, 0)$	<i>Chaos</i>	Figure 6(e1)
		$(0, \pm 0.5, \pm 0.5)$	<i>Period-3</i>	Figure 6(e2)

disconnected attractors (for some suitable sets of parameters) depending solely on the choice of initial conditions and six disconnected ones using the perturbations method [13–15]. There is a relatively large parameters space of coexisting attractors located on the top of Figure 2(a) where a symmetric pair of point attractors coexists with other attractors. Our analysis shows an additional feature of the coexistence of multiple attractors involving a pair of asymmetric chaotic attractors with a pair of asymmetric periodic ones. Six disconnected attractors with three coexisting equilibrium points attractors are presented instead of four reported in [13] previously mentioned. The three coexisting points obtained, respectively, with the following initial conditions $(-1, 0, 0)$ $(0, 0, 0)$ $(1, 0, 0)$ are an interesting feature of this circuit. We recall that Sprott reported two coexisting equilibriums for a dynamical system with four quadratic nonlinearities to display a butterfly strange attractor. As shown in Figures 3 and 4, the main coexisting regime is a symmetric pair of point attractors coexisting with a symmetric periodic cycle. However, there are several other coexisting regimes as shown in Table 1. Out of well-known dynamics of the chaotic systems encountered in the literature, we present another interesting feature at period-12, two symmetric attractors, conjugated in the phase plan with a nonsymmetric initial condition. Figure 5 displays these dynamics.

The basins of attraction of the different attracting sets provide more information about the coexisting attractors, which are defined as the set of initial conditions whose trajectories converge to the respective attractor. For the following values of the parameters $a = 17.37$ and $\gamma = 0.7401$ where a symmetric pair of point attractors coexists with a symmetric pair of limit cycles in Figure 4(d), the basins in the $x_2 = 0$ (the second coordinate of system (1)) plane are shown in Figure 7. The basins of the two point attractors are indicated by yellow, red, and black, respectively, for the pair of period-3 and period-6 and the pair of chaos. The blue part represents the unbounded solution. The basins have the expected symmetry about the y -axis and a fractal boundary.

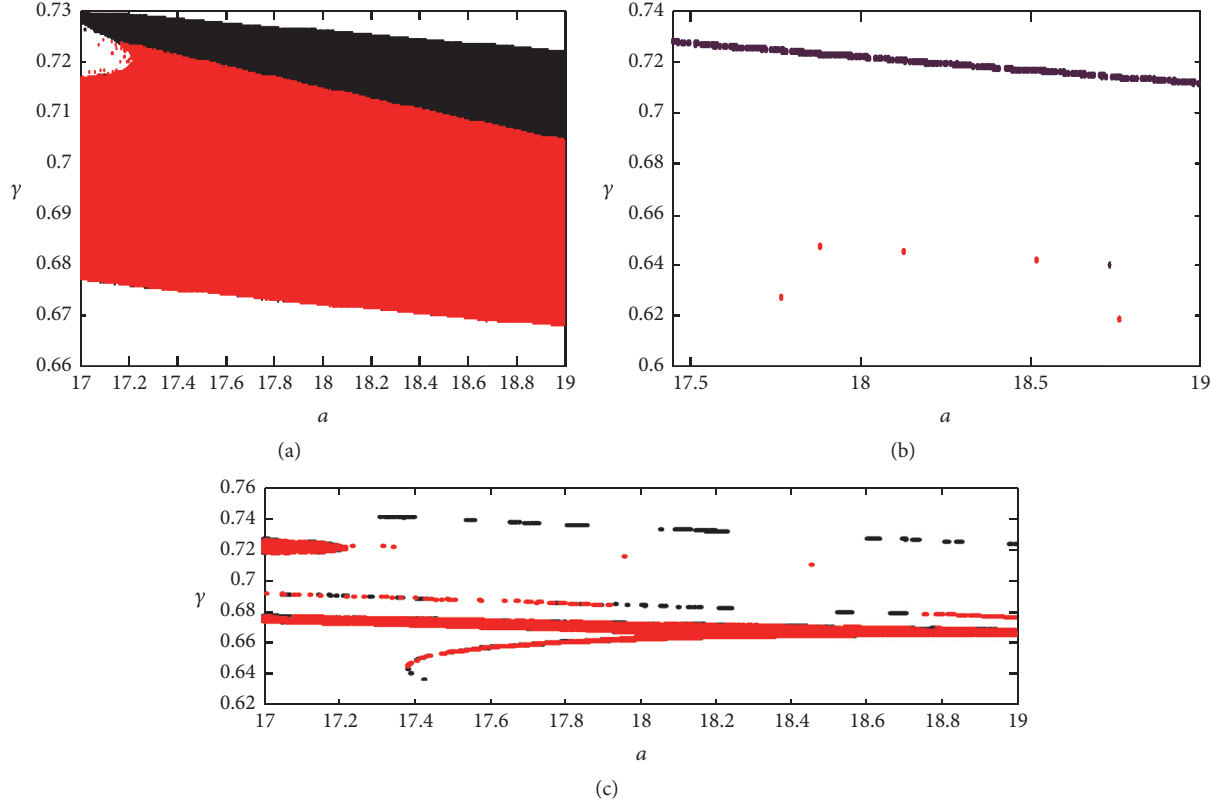


FIGURE 3: Isospike diagram in the (a, γ) panel, the red color codifies the zones with initial conditions $(0.5, 0, 0)$ and the blue color codifies the zones corresponding to initial conditions $(0, 0.5, 0.5)$: (a) 3 peaks in one period of $x(t)$; (b) 5 peaks in one period of; (c) 6 peaks in one period of. The region where the black color is visible is the region of 2D multistability.

3. Function Projective Synchronization in Relay Coupled Oscillators

3.1. Problem Formulation. Now, let us present a theory of the function projective synchronization in relay coupled systems. Our scheme is given as follows: The outer systems noted X and Y are the systems to synchronize while the relay unit is noted by (R) . From this consideration, the outer systems are described as follows:

$$\begin{aligned} \dot{z}_1(t) &= a_1 z_2(t) - \xi(z_1(t), \rho_1(t), m(t)), \\ \dot{z}_i(t) &= a_i z_{i+1}(t), \quad i = 2, \dots, n-1 \\ &\vdots \\ \dot{z}_n(t) &= f(z(t)), \end{aligned} \quad (3)$$

where $z(t)$ represents $X(t) = (x_1(t), x_2(t), \dots, x_n(t))^T$ or $Y(t) = (y_1(t), y_2(t), \dots, y_n(t))^T$. $\xi(z_1(t), \rho_1(t), m(t))$ is the coupling strength function.

The relay system can take the following form:

$$\begin{aligned} \dot{\rho}_i(t) &= a_i \rho_{i+1}(t) + u(t), \quad i = 1, 2, \dots, n-1, \\ \dot{\rho}_n(t) &= f(\rho(t)) + u_n(t), \end{aligned} \quad (4)$$

where $u(t) = [u_1(t), u_2(t), \dots, u_n(t)]^T$ is the controller to be determined.

Definition 2. If there exists a scaling function $m(t)$ satisfying

$$\lim_{t \rightarrow t_0} \|e(t, m(t))\| = 0 \quad \forall e(t_0, m(t_0)) \in R^n \quad (5)$$

then systems (3) and (4) achieve projective synchronization.

Remark 3. Chaos synchronization schemes such as complete synchronization and antisynchronization are special cases of function projective synchronization when $m(t) = 1$ and $m(t) = -1$, respectively.

Taking into account the synchronization between two chaotic systems, take the drive relay as follows:

$$\begin{aligned} \dot{\rho}_1 &= a_1 \rho_2 + u_1, \\ \dot{\rho}_2 &= a_2 \rho_3 + u_2 \\ &\vdots \end{aligned} \quad (6)$$

$$\dot{\rho}_n = \gamma_2 \rho_2 + \gamma_3 \rho_3 + \dots + \gamma_n \rho_n + p(\rho_1) + u_n.$$

Let us define the synchronization errors between our systems as follows:

$$\begin{aligned} e_1 &= x_1 + y_1 - 2m(t) \rho_1, \\ e_2 &= x_2 + y_2 - 2\rho_2 \\ &\vdots \\ e_n &= x_n + y_n - 2\rho_n. \end{aligned} \quad (7)$$

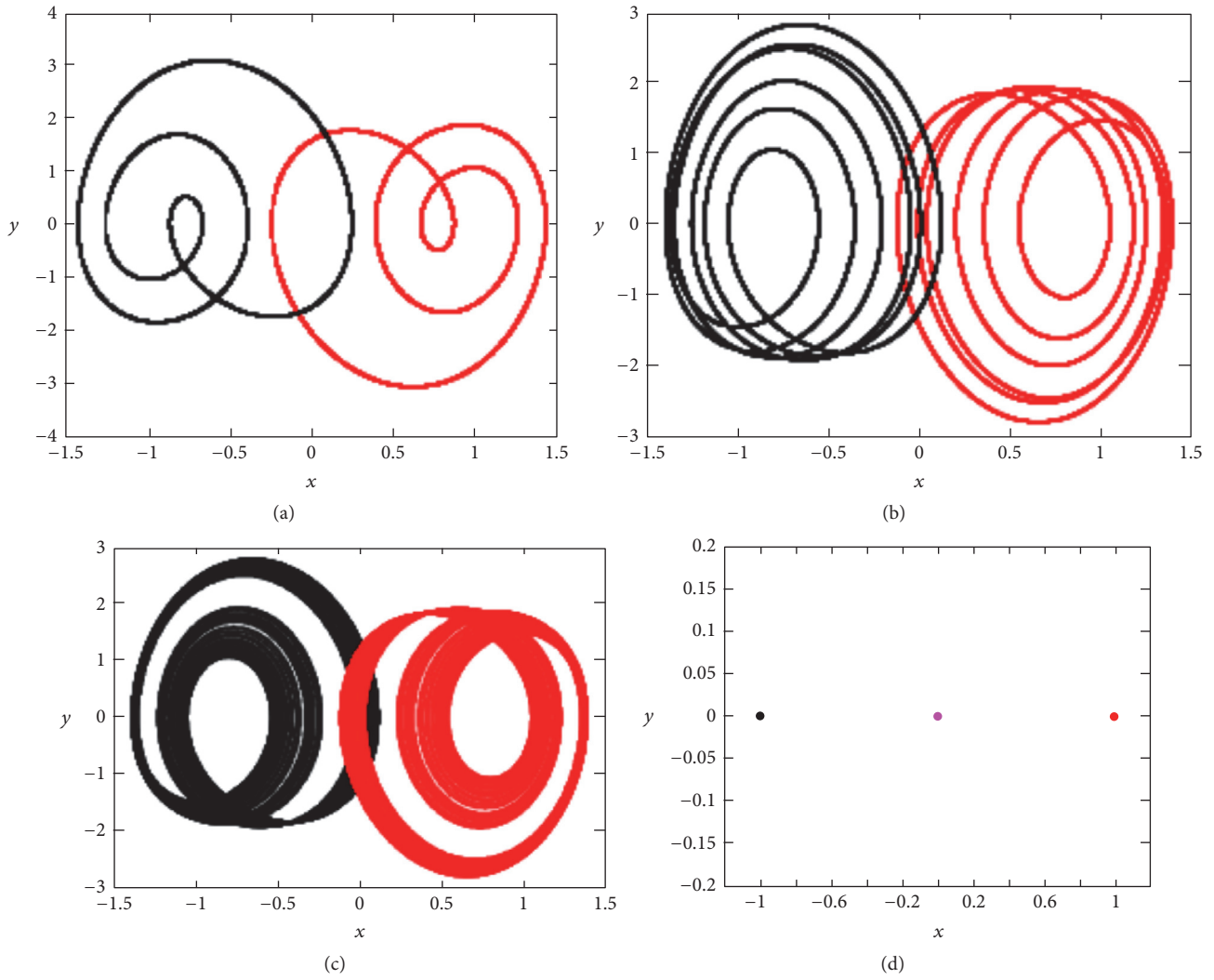


FIGURE 4: Phase portrait of coexisting attractors in the x - y plane: $a = 17.37$, $\gamma = 0.7401$, with the following initial conditions: (a) $(\pm 1, 0, \pm 0.01)$; (b) $(\pm 0.4, 0, \pm 0.6)$; (c) $(\pm 0.58, 0, \pm 0.6)$; (d) $(1, 0, 0)$ for black attraction point, $(0, 0, 0)$ for magenta attraction point, and $(-1, 0, 0)$ for red attraction point (red and black with symmetric initial conditions).

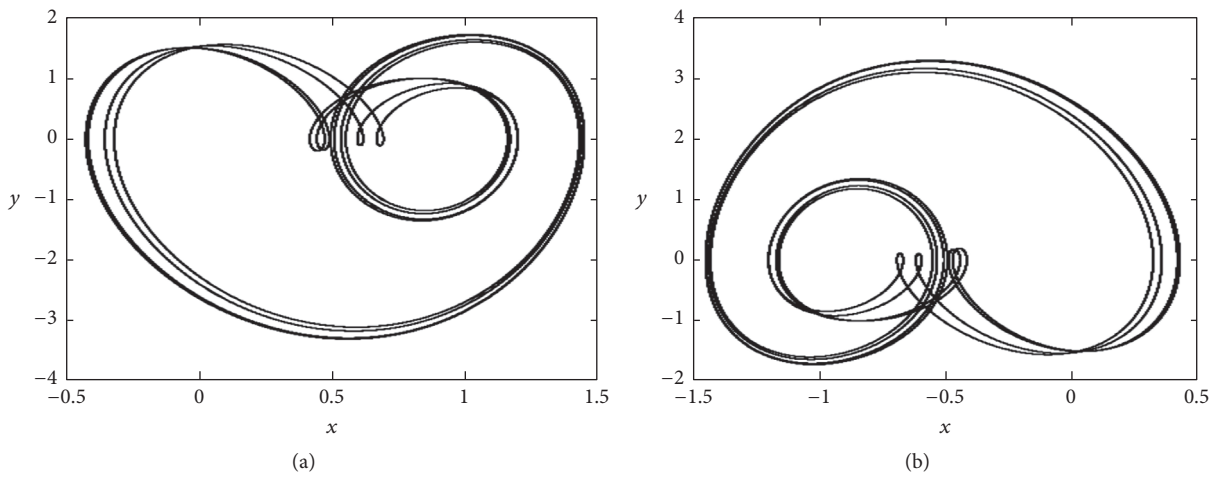


FIGURE 5: (a) Period-12 for $a = 17.7$ and $\gamma = 0.6678$ with initial conditions $(0.5, 0, 0)$. (b) Period-12 for $a = 17.7$ and $\gamma = 0.6678$ with initial conditions $(0, 0.5, 0.5)$.

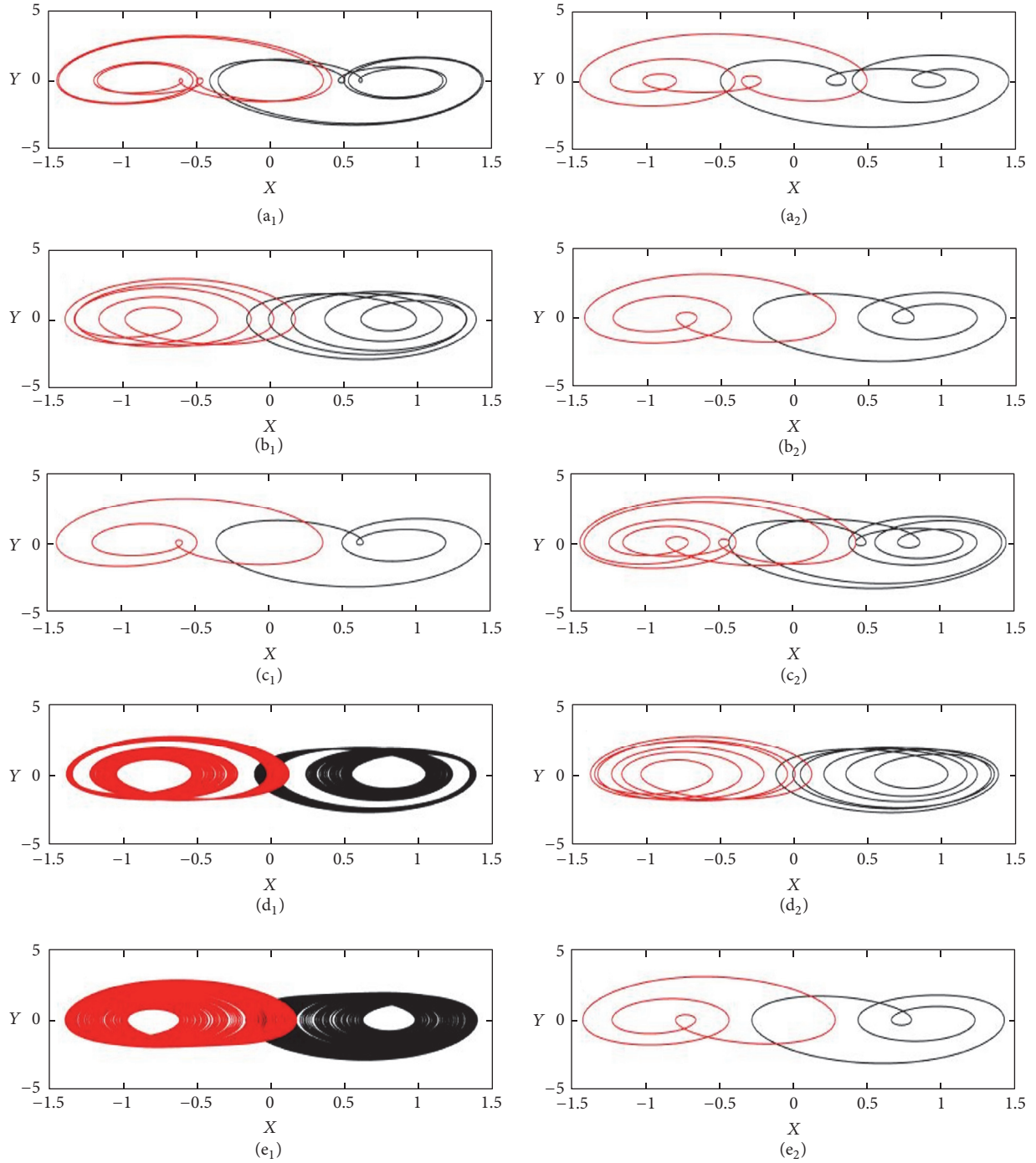


FIGURE 6: Coexistence of four different attractors (a pair of period-3, period-5, and period-6 and a pair of chaotic attractors) for (a), (b), (c), (d), and (e), respectively, represented in Table 1. Notice that attractors are symmetric in pairs.

Considering (7), the dynamics of the errors become

$$\begin{aligned}
 \dot{e}_1 &= \dot{x}_1 + \dot{y}_1 - 2m(t)\dot{\rho}_1 - 2\dot{m}(t)\rho_1, \\
 \dot{e}_2 &= \dot{x}_2 + \dot{y}_2 - 2\dot{\rho}_2 \\
 &\vdots \\
 \dot{e}_n &= \dot{x}_n + \dot{y}_n - 2\dot{\rho}_n.
 \end{aligned} \tag{8}$$

From these equations, we obtain the following error dynamics:

$$\begin{aligned}
 \dot{e}_1 &= -ke_1 + a_1(x_2 + y_2) - 2a_1m(t)\rho_2 - 2\dot{m}(t)\rho_1 \\
 &\quad - 2m(t)u_1, \\
 \dot{e}_2 &= a_2e_3 + 2u_2 \\
 &\vdots
 \end{aligned}$$

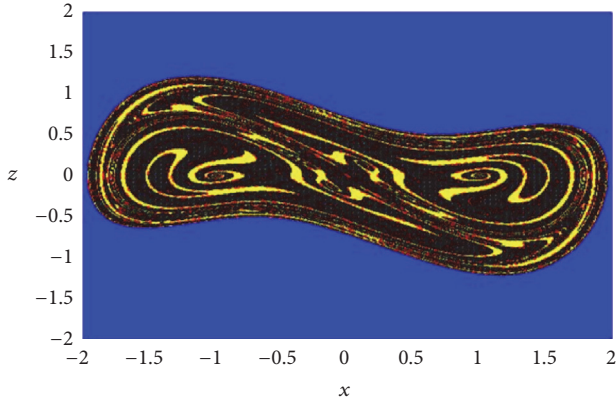


FIGURE 7: Cross-section for $x_2 = 0$ of the basins of the symmetric pair period-3 cycle (yellow), pair of period-6 (red), and the pair of chaotic attractors (black) of system (2) at $a = 17.37$ and $\gamma = 0.7401$. Blue zones correspond to unbounded solutions (color figure online).

$$\begin{aligned} \dot{e}_n &= \gamma_2 e_2 + \gamma_3 e_3 + \cdots + \gamma_n e_n + f(e_1, x_1, \rho_1, y_1, m(t)) \\ &+ 2u_n, \end{aligned} \quad (9)$$

where $f(e_1, x_1, y_1, \rho_1, m(t)) = p(x_1) + p(y_1) - 2p(\rho_1)$.

Let us choose the controllers in the following form:

$$u_1 = \frac{1}{2m(t)} \left(a_1 (x_2 + y_2) - 2a_1 m(t) \rho_2 - 2\dot{m}(t) \rho_1 + \xi |e_1|^{\gamma_0} \text{sign}(e_1) \right), \quad (10a)$$

$$u_n = -\frac{1}{2} (f(0, x_1, \rho_1, y_1, m(t))), \quad (10b)$$

$$u_2 = 0 \quad \vdots \quad (10c)$$

$$u_{(n-1)} = 0.$$

Theorem 4. For the given scaling function matrix $m(t)$, the projective function synchronization in relay coupled oscillators between outer X and outer Y will occur under the relay (6) and the control law (10a), (10b), and (10c).

Proof. In order to prove the stability of the scheme, let us divide the errors dynamics (9) into two subsystems.

Subsystem 1

$$\dot{e}_1 = -ke_1 + a_1 (x_2 + y_2) - 2a_1 m(t) \rho_2 - 2\dot{m}(t) \rho_1 - 2m(t) u_1. \quad (11)$$

Subsystem 2

$$\begin{aligned} \dot{e}_2 &= a_2 e_3 + 2u_2 \\ &\vdots \\ \dot{e}_n &= \gamma_2 e_2 + \gamma_3 e_3 + \cdots + \gamma_n e_n + f(e_1, x_1, \rho_1, y_1, m(t)) \\ &+ 2u_n. \end{aligned} \quad (12)$$

The criterion based on asymptotic stability which states that “if the subsystem (11) is stable under the controller (10a), then the overall stability of the scheme is guaranteed under the controller (10b) and (10c)” was developed as necessary and sufficient condition for the synchronization of the periodic and chaotic systems [25]. On the basis of this criterion, let us seek a suitable Lyapunov function to establish the asymptotic stability of subsystems (11) and (12).

The errors of the scheme become

$$\begin{aligned} \dot{e}_2 &= a_2 e_3 \\ &\vdots \\ \dot{e}_n &= \gamma_2 e_2 + \gamma_3 e_3 + \cdots + \gamma_n e_n + f(e_1, x_1, \rho_1, y_1, m(t)) \\ &- f(0, x_1, \rho_1, y_1, m(t)). \end{aligned} \quad (13)$$

Construct the dynamical Lyapunov function as follows:

$$V = \frac{1}{2} \sum_{i=2}^n e_i^2. \quad (14)$$

Then the time derivative of Lyapunov function V along the trajectory of error system (13) is

$$\begin{aligned} \frac{dV}{dt} &= \dot{e}_2 e_2 + \cdots + \dot{e}_n e_n = \alpha_i \sum_{i=2}^n e_i e_{i+1} + \gamma_n e_n^2 \\ &+ [f(e_1, x_1, \rho_1, y_1, m(t)) - f(0, x_1, \rho_1, y_1, m(t))] \\ &\cdot e_n, \end{aligned} \quad (15)$$

where α_i is a constant depending on the system parameters. Since subsystem (11) is stable and $e_1(t) \rightarrow 0$ then expression (15) becomes

$$\frac{dV}{dt} = \sum_{i=2}^n \alpha_i e_i e_{i+1} + \gamma_n e_n^2 \leq r^2 \sum_{i=2}^n \alpha_i + \gamma_n r^2. \quad (16)$$

The stability is guaranteed if expression (16) is negative. This is possible if $\gamma_n = -\sum_{i=2}^n \alpha_i$ which is consistent with a general class of jerk system [26, 27]. The proof is complete. \square

Definition 5. Consider outer 1 and outer 2 described by systems (4) and (5), respectively. If there exists a constant $t_r = t_r(e(0)) > 0$, such that

$$\lim_{t \rightarrow t_r} \|e(t)\| = 0 \quad (17)$$

and $\|e(t)\| \equiv 0$ when $t \geq t_r$, then the chaos synchronization in relay coupled systems (3) and (4) is achieved in a finite time.

Theorem 6. For any nonzero scaling function $m(t)$, the outer system (3) can synchronize the outer system (4) with relay (6) in a finite time given by

$$t_r = \frac{1}{(1 - \gamma_0) \min(k, \xi)} \ln(1 + |e_1(0)|^{1-\gamma_0}). \quad (18)$$

Proof. Let us choose as a Lyapunov function candidate

$$U = |e_1|. \quad (19)$$

The time derivative of U along the trajectories of the closed-loop system (8) is given by

$$\begin{aligned} \frac{dU}{dt} &= \dot{e}_1 \text{sign}(e_1) \\ &= [-ke_1 - \xi |e_1|^{\gamma_0} \text{sign}(e_1)] \text{sign}(e_1) \\ &= -k |e_1| - \xi |e_1|^{\gamma_0}. \end{aligned} \quad (20)$$

Now, let $\eta = \min(k, \xi)$, then we obtain

$$\frac{dU}{dt} = -\eta [|e_1| + |e_1|^{\gamma_0}] \leq -\eta [U + U^{\gamma_0}]. \quad (21)$$

From (21), we can obtain

$$t_r - t_0 \leq -\frac{1}{\eta} \int_{t_0}^{t_r} \frac{U^{-\gamma_0}}{(1 + U^{1-\gamma_0})} dU. \quad (22)$$

If we suppose that $t_0 = 0$ and $U(t_r) = 0$ since the synchronization is completed, hence

$$t_r \leq \frac{1}{\eta(1 - \gamma_0)} \ln(1 + U^{1-\gamma_0}(t_0)). \quad (23)$$

In addition $U(t_0) = |e_1(0)|$; hence

$$t_r \leq \frac{1}{\eta(1 - \gamma_0)} \ln(1 + |e_1(0)|^{1-\gamma_0}). \quad (24)$$

This proof is complete. \square

Remark 7. The control objective is stated in the mathematical form in (10a), (10b), and (10c). One advantage of this type of controller is that it can be easily constructed through time varying resistors, capacitors, or operational amplifiers and their combinations or using a digital signal processor together with the appropriate converters. The proposed work uses a reduced number of control signals and parameters.

3.2. Numerical Results. In this section, a numerical example and its simulations are presented to demonstrate the effectiveness of the proposed scheme. To illustrate our method, we choose the same circuit where the dynamical analysis is

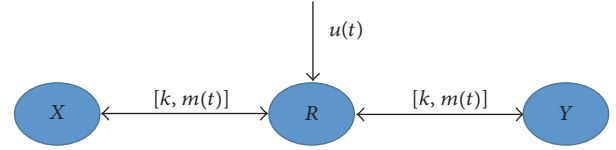


FIGURE 8: Schematic representation of the relay mechanism. Oscillators X and Y are coupled bidirectionally to oscillator R with coupling strength k .

described previously in this work. The dynamic equations of outers is as follows, respectively, for $X(t)$ and $Y(t)$:

$$\begin{aligned} (X) \quad \dot{x}_1 &= x_2 - k(x_1 - m(t)\rho_1), \\ \dot{x}_2 &= ax_3, \\ \dot{x}_3 &= -bx_2 - x_3 + p(x_1), \\ (Y) \quad \dot{y}_1 &= y_2 - k(y_1 - m(t)\rho_1), \\ \dot{y}_2 &= ay_3, \\ \dot{y}_3 &= -by_2 - y_3 + p(y_1), \end{aligned} \quad (25)$$

where a and b are the positive constants and $p(\bullet_1)$ is the polynomial smooth function.

For instance, the system is chaotic for the parameters $a = 10$, $\gamma = 0.725$, $p(\theta_1) = \theta_1 - \theta_1^3$ for any variable θ_1 . $m(t)$ is the scaling function and k is the coupling strength. The impact of k and $m(t)$ on the dynamical behaviors of the entire coupled systems will be investigated later. We set the following parameters: $a = 18.1$ and $\gamma = 0.625$. From (10a), (10b), and (10c) the controllers take the form

$$u_1 = \frac{1}{2m(t)} \left((x_2 + y_2) - 2m(t)\rho_2 - 2m(t)\rho_1 + \xi |e_1|^\gamma \text{sign}(e_1) \right), \quad (26a)$$

$$u_2 = \frac{1}{2} \left(2(m(t) - 1)\rho_1 + (2 - 8m^3(t))\rho_1^3 + 6m(t)x_1y_1\rho_1 \right). \quad (26b)$$

Let us consider the following parameters: $\xi = 0.01$, $k = 2$ and $\eta = 0.01$. The scaling function $m(t)$ is expressed as $m(t) = e_0 + 0.1 \sin(\pi\phi t)$ with e_0 and ϕ the positive constants. Results of our “relay” synchronization in a system of three circadian oscillators are shown in Figure 8. The repressors from the three subsystems are labeled X , R , and Y , respectively. Although each of the oscillators is identical, the initial conditions of the three circuits are different. Whatever the situation of the systems, Wagemakers et al. showed that outer systems can synchronize even if the relay unit has different architecture [16]. There is phase synchrony between the repressor output from oscillators X and Y . If we set the following values of e_0 and ϕ to 0.75 and 0.7, respectively, the attractors of different systems are provided in Figure 9. The diagrams in blue and black represent the outer 1 and outer 2, respectively. The similarity of these graphs is complete. The

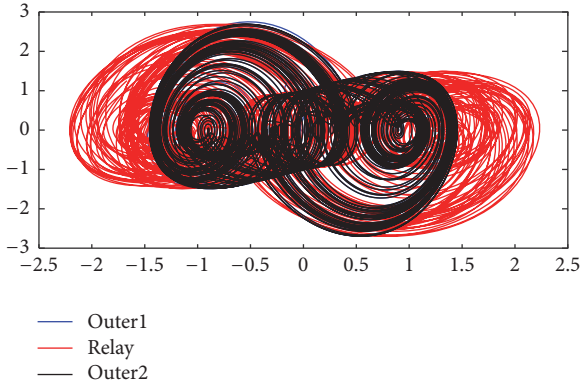


FIGURE 9: Chaotic behavior for $e_0 = 0.75$ $\phi = 0.7$ (blue and black attractors correspond to outer 1 and outer 2, and the third in red represents the relay).

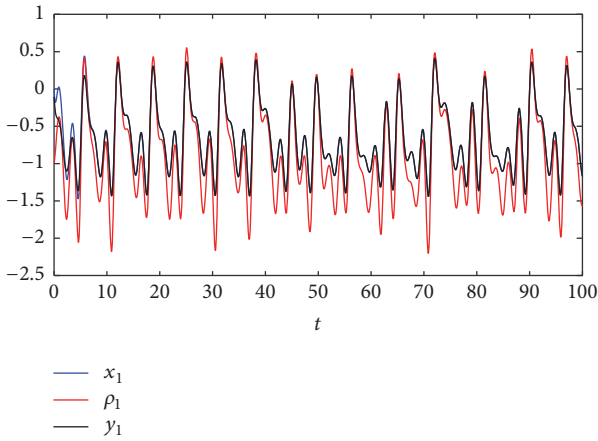


FIGURE 10: Cluster synchronization.

diagram in red displays the relay. The chaotic structure of the relay system renders its manipulation bulky and difficult for an attacker in the practical situations.

One of the major collective coherent behaviors in ensembles of identical and nonidentical chaotic elements is global and cluster synchronization. For complete synchronization we focus on the existence and stability of unique unconditional clusters whose rise does not depend on the origin of the outers. The cluster synchronization is established in relation with the difference between the relay and the outers. Figure 10 presents the diagrams showing the cluster synchronization. Figure 11 displays the global errors of the system given by (7). It is important to observe that the stabilization of the one state leads to other states of the scheme which is consistent with our theory analysis. The errors of synchronization between the outers are provided in Figure 12. From these graphs, we remark that the relay circuit allows finite synchronization and in a short time.

Remark 8. A typical assumption made by most chaotic cryptosystems' designers is that the system's parameters play the role of the key which is not seen as efficient in many secure schemes. In this paper we assume that $m(t)$ plays the role of

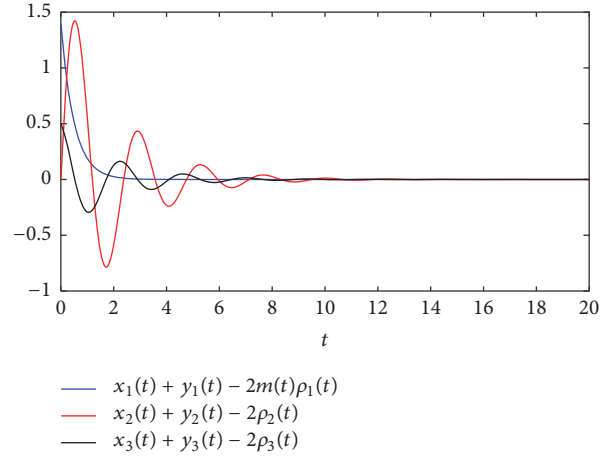


FIGURE 11: The global errors state of synchronization.

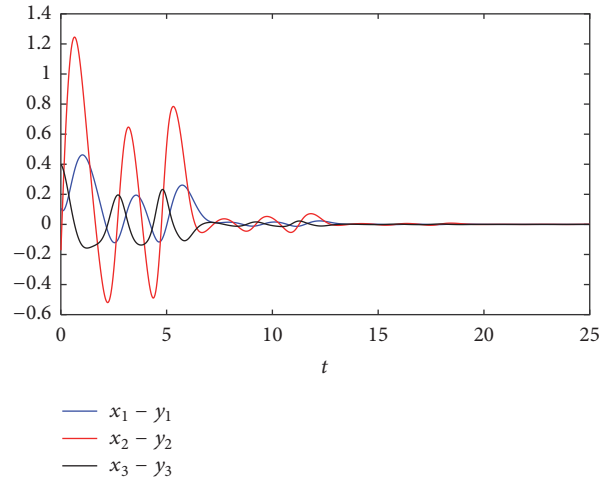


FIGURE 12: Synchronization errors between the outers.

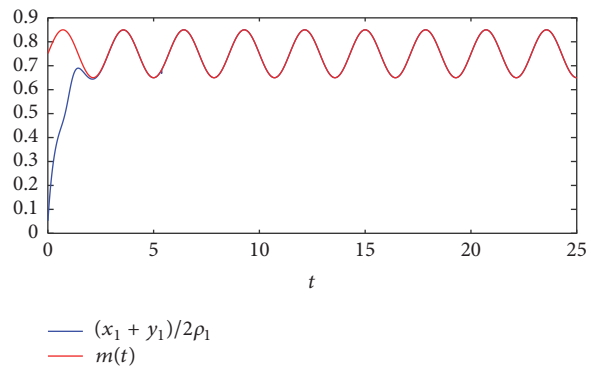
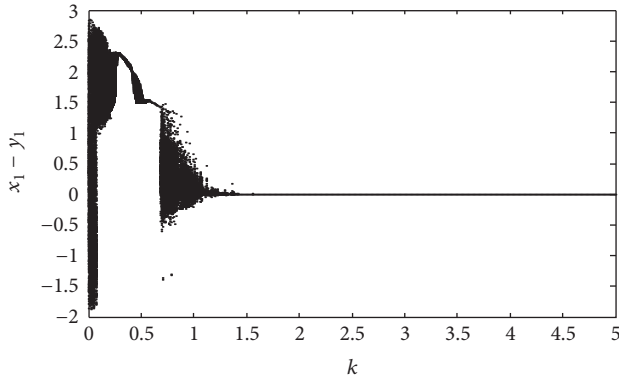
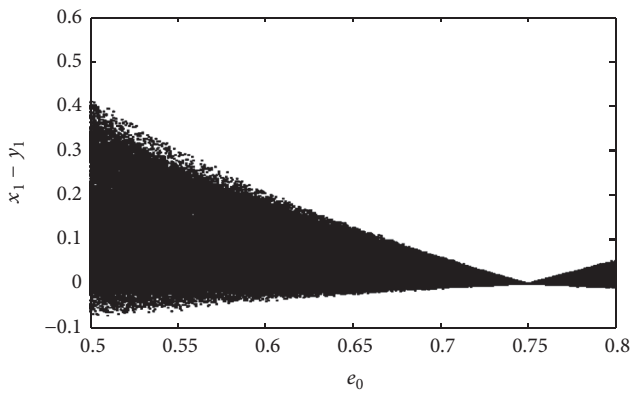
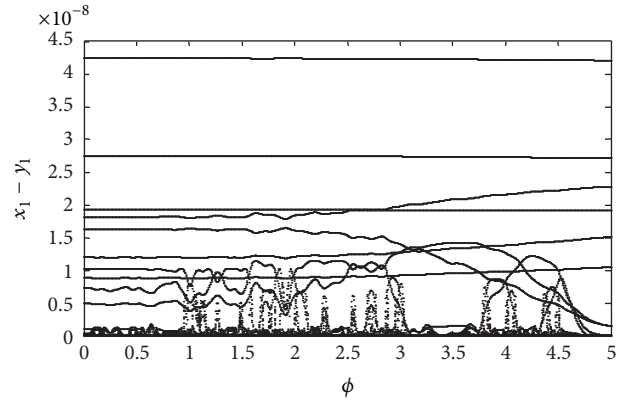


FIGURE 13: Original function (red); retrieved function (blue) for $a = 18.1$ and $\gamma = 0.625$.

the key. From (7) we can derive $e_1(t) = x_1 + y_1 - 2m(t)\rho_1 \rightarrow 0$ as $t \rightarrow t_r$; that is, $(x_1 + y_1)/2\rho_1$ can recover the message signal $m(t)$. Figure 13 depicts the function $m(t)$. The original is plotted in red and the same function is recovered after a short transient behavior.

FIGURE 14: Bifurcation diagram with $k \in [0; 5]$.FIGURE 15: Bifurcation diagram $e_0 \in [0.5, 0.8]$.

3.3. Scaling Function and “Relay” Synchronization. The scheme described above depicts many interesting features. It is possible to analyze a number of situations that are likely to arise when the parameters of the scaling function are monitored. For instance, when chaos synchronization is applied in engineering applications such as in secure communications, the chaos-based synchronization scheme is rather sensitive to attacks. It is necessary to analyze the interactions of the scaling function parameters which is naturally considered as a key and the coupling strength k *vis-à-vis* of the scheme. For small values of the coupling parameter k , the chaotic regime is asynchronous; that is, $X \neq Y$. Transition from asynchronous to synchronous generation occurs through the intermittency of “bubbling” type [28, 29]. Figure 14 shows that the variation of the control parameters allows different behaviors which are periodic or chaotic behavior. One can see that with the increase in k , we move towards the region of periodic synchronous generation. In this context, the optimal value of the coupling which allows the synchronization between the outers is about 1.45. If we vary the values of e_0 and ϕ between the intervals $[0.5, 0.7]$ and $[0, 5]$, respectively, the bifurcation diagrams given on Figures 15 and 16 show a consistent expectation of the function projective synchronization working [30]. One can see that initially the systems are asynchronous. After a while, the symmetry breaking bifurcation occurs when $e_0 = e_{\text{opt}}$. With an increase in e_0

FIGURE 16: Bifurcation diagrams with $\phi \in [0, 5]$.

self-modulation and transition to chaos take place. The errors system remains practically weak when the constant ϕ varies. Note that the knowledge of a set of parameters (k, e_{opt}, ϕ) for unauthorized agent remains a hard test. Their determination is a requirement to detect the synchronization zone which is an excellent agreement with our theoretical predictions.

4. Conclusions and Remarks

In this unexplored regime of the jerk system, new regions of multistability have been found. The complex dynamics of chaotic motions are reported by means of Lyapunov exponent spectrum. By varying the initial conditions, we are also able to detect six coexisting stable attractors and three equilibrium points attractors instead of four encountered in the literature. And on the other hand, we have demonstrated that relay synchronization can be associated with function projective synchronization between the relay unit and the synchronized systems. The mediating role of FPS implies the existence of an invertible function that links the dynamics of the relay system with those of the systems to be synchronized. The key role of FPS is demonstrated by analyzing the bifurcation diagram of the whole system with respect to the parameters of the scaling function $m(t)$. Therefore, our results link the emergence of relay synchronization in instantaneously coupled chaotic systems with the existence of FPS with the relay system and open the possibility of using relay units for secure communications [31]. Comparing our results to those found in the literature [13–21], the isospine diagrams show the overall behavior of the system and the relay unit associated with the unpredictability of the scaling function appears as a fundamental for the feasibility of the reliable secure communications.

Conflicts of Interest

The authors declare that they have no conflicts of interest.

References

- [1] C. Li and J. C. Sprott, “Multistability in the Lorenz system: a broken butterfly,” *International Journal of Bifurcation and Chaos*, vol. 24, no. 10, article 1450131, 2014.

- [2] J. Kengne, Z. N. Tabekoueng, V. K. Tamba, and A. N. Negou, "Periodicity, chaos, and multiple attractors in a memristor-based Shinriki's circuit," *Chaos: An Interdisciplinary Journal of Nonlinear Science*, vol. 25, no. 10, article 103126, 2015.
- [3] C. Hens, S. K. Dana, and U. Feudel, "Extreme multistability: attractor manipulation and robustness," *Chaos: An Interdisciplinary Journal of Nonlinear Science*, vol. 25, no. 5, article 053112, 2015.
- [4] G. M. Maggio, O. De Feo, and M. P. Kennedy, "Nonlinear analysis of the Colpitts oscillator and applications to design," *IEEE Transactions on Circuits and Systems I: Fundamental Theory and Applications*, vol. 46, no. 9, pp. 1118–1130, 1999.
- [5] C. Masoller, "Coexistence of attractors in a laser diode with optical feedback from a large external cavity," *Physical Review A: Atomic, Molecular and Optical Physics*, vol. 50, no. 3, pp. 2569–2578, 1994.
- [6] J. M. Cushing, Henson, and S. M. Blackburn, "Multiple mixed attractors in a competition model," *Journal of Biological Dynamics*, vol. 1, pp. 347–362, 2007.
- [7] C. Li and J. C. Sprott, "Coexisting hidden attractors in a 4-D simplified lorenz system," *International Journal of Bifurcation and Chaos*, vol. 24, no. 3, article 1450034, 2014.
- [8] S. Rajasekar and M. Lakshmanan, "Multiple attractors and their basins of attraction of a long Josephson junction oscillator," *Physics Letters A*, vol. 147, no. 5–6, pp. 264–268, 1990.
- [9] A. Massoudi, M. G. Mahjani, and M. Jafarian, "Multiple attractors in Koper-Gaspard model of electrochemical periodic and chaotic oscillations," *Journal of Electroanalytical Chemistry*, vol. 647, no. 1, pp. 74–86, 2010.
- [10] M. Dutta, H. E. Nusse, J. A. Yorke, and G. Yuan, "Multiple Attractor Bifurcations: A Source of Unpredictability in Piecewise Smooth Systems," *Physical Review Letters*, vol. 83, no. 21, pp. 4281–4284, 1999.
- [11] S. Banerjee, P. Ranjan, and C. Grebogi, "Bifurcations in two-dimensional piecewise smooth maps-theory and applications in switching circuits," *IEEE Transactions on Circuits and Systems I: Fundamental Theory and Applications*, vol. 47, no. 5, pp. 633–643, 2000.
- [12] B. C. Bao, H. Bao, N. Wang, M. Chen, and Q. Xu, "Hidden extreme multistability in memristive hyperchaotic system," *Chaos, Solitons & Fractals*, vol. 94, pp. 102–111, 2017.
- [13] J. Kengne, Z. T. Njitacke, and H. B. Fotsin, "Dynamical analysis of a simple autonomous jerk system with multiple attractors," *Nonlinear Dynamics*, vol. 83, pp. 751–765, 2016.
- [14] A. R. Elsonbaty and A. M. El-Sayed, "Further nonlinear dynamical analysis of simple jerk system with multiple attractors," *Nonlinear Dynamics*, vol. 87, no. 2, pp. 1169–1186, 2017.
- [15] S. Boccaletti, J. Kurths, G. Osipov, D. L. Valladares, and C. S. Zhou, "The synchronization of chaotic systems," *Physics Reports*, vol. 366, no. 1–2, pp. 1–101, 2002.
- [16] A. Wagemakers, J. M. Buldú, and M. A. F. Sanjuán, "Isochronous synchronization in mutually coupled chaotic circuits," *Chaos: An Interdisciplinary Journal of Nonlinear Science*, vol. 17, no. 2, article 023128, 2007.
- [17] A. Sharma, P. R. Sharma, and M. D. Shrimali, "Amplitude death in nonlinear oscillators with indirect coupling," *Physics Letters A*, vol. 376, no. 18, pp. 1562–1566, 2012.
- [18] A. Sharma, M. Dev Shrimali, and S. Kumar Dana, "Phase-flip transition in nonlinear oscillators coupled by dynamic environment," *Chaos: An Interdisciplinary Journal of Nonlinear Science*, vol. 22, no. 2, article 023147, 2012.
- [19] V. Raul, L. G. Leonardo, R. M. Claudio et al., "Dynamical relaying can yield zero time lag neuronal synchrony despite long conduction delays," *Proceedings of the National Academy of Sciences of the United States of America*, vol. 105, no. 44, pp. 17157–17162, 2008.
- [20] A. Wagemakers, J. M. Buldú, and M. A. Sanjuán, "Experimental demonstration of bidirectional chaotic communication by means of isochronal synchronization," *EPL (Europhysics Letters)*, vol. 81, no. 4, article 40005, 2008.
- [21] B. Nana and P. Wofo, "Chaotic masking of communication in an emitter-relay-receiver electronic setup," *Nonlinear Dynamics*, vol. 82, no. 1–2, pp. 899–908, 2015.
- [22] R. Gutiérrez, R. Sevilla-Escoboza, P. Piedrahita et al., "Generalized synchronization in relay systems with instantaneous coupling," *Physical Review E: Statistical, Nonlinear, and Soft Matter Physics*, vol. 88, no. 5, article 052908, 2013.
- [23] S. T. Kammogne and H. B. Fotsin, "Adaptive control for modified projective synchronization-based approach for estimating all parameters of a class of uncertain systems: case of modified colpitts oscillators," *Journal of Chaos*, vol. 2014, Article ID 659647, 13 pages, 2014.
- [24] D. F. Oliveira and E. D. Leonel, "Some dynamical properties of a classical dissipative bouncing ball model with two nonlinearities," *Physica A: Statistical Mechanics and its Applications*, vol. 392, no. 8, pp. 1762–1769, 2013.
- [25] R. A. Freeman and P. V. Kokotovic, *Robust Nonlinear Control Design*, Birkhäuser, Boston, Mass, USA, 1996.
- [26] J. G. Freire and J. A. C. Gallas, "Cyclic organization of stable periodic and chaotic pulsations in Hartley's oscillator," *Chaos, Solitons & Fractals*, vol. 59, pp. 129–134, 2014.
- [27] J. C. Sprott, *Elegant Chaos: Algebraically Simple Chaotic Flows*, World Scientific Publishing, Toh Tuck Link, Singapore, 2010.
- [28] T. Divoux, E. Bertin, V. Vidal, and J.-C. Gémard, "Intermittent outgassing through a non-Newtonian fluid," *Physical Review E: Statistical, Nonlinear, and Soft Matter Physics*, vol. 79, no. 5, article 056204, 2009.
- [29] R. Lakkaraju, F. Toschi, and D. Lohse, "Bubbling reduces intermittency in turbulent thermal convection," *Journal of Fluid Mechanics*, vol. 745, pp. 1–24, 2014.
- [30] A. Boulkroune, A. Bouzeriba, and T. Bouden, "Fuzzy generalized projective synchronization of incommensurate fractional-order chaotic systems," *Neurocomputing*, vol. 173, pp. 606–614, 2016.
- [31] W. Kinzel, A. Englert, and I. Kanter, "On chaos synchronization and secure communication," *Philosophical Transactions. Series A, Mathematical, Physical, and Engineering Sciences*, vol. 368, pp. 379–389, 2010.

Research Article

Master-Slave Synchronization of 4D Hyperchaotic Rabinovich Systems

Ke Ding ^{1,2}, Christos Volos ³, Xing Xu,⁴ and Bin Du¹

¹School of Information Technology, Jiangxi University of Finance and Economics, Nanchang 330013, China

²Jiangxi E-Commerce High Level Engineering Technology Research Centre, Jiangxi University of Finance and Economics, Nanchang 330013, China

³Department of Physics, Aristotle University of Thessaloniki, Thessaloniki, Greece

⁴School of Business Administration, Jiangxi University of Finance and Economics, Nanchang 330013, China

Correspondence should be addressed to Ke Ding; k.ding78@hotmail.com

Received 30 June 2017; Revised 15 September 2017; Accepted 20 September 2017; Published 2 January 2018

Academic Editor: Michele Scarpiniti

Copyright © 2018 Ke Ding et al. This is an open access article distributed under the Creative Commons Attribution License, which permits unrestricted use, distribution, and reproduction in any medium, provided the original work is properly cited.

This paper is concerned with master-slave synchronization of 4D hyperchaotic Rabinovich systems. Compared with some existing papers, this paper has two contributions. The first contribution is that the nonlinear terms of error systems remained which inherit nonlinear features from master and slave 4D hyperchaotic Rabinovich systems, rather than discarding nonlinear features of original hyperchaotic Rabinovich systems and eliminating those nonlinear terms to derive linear error systems as the control methods in some existing papers. The second contribution is that the synchronization criteria of this paper are global rather than local synchronization results in some existing papers. In addition, those synchronization criteria and control methods for 4D hyperchaotic Rabinovich systems are extended to investigate the synchronization of 3D chaotic Rabinovich systems. The effectiveness of synchronization criteria is illustrated by three simulation examples.

1. Introduction

The classic hyperchaotic Rabinovich system was a system of 3D differential equations which was used to describe the plasma oscillation [1]. In [2], a 4D hyperchaotic Rabinovich system was introduced, which has been seen in wide applications in plasma oscillation, security communication, image encryption, and cell kinetics; see, for example, [2–4].

There exist various dynamical behaviors of 4D hyperchaotic Rabinovich systems. Synchronization is the typical dynamical behavior of chaotic systems [1, 5–31]. Master-slave synchronization of Rabinovich systems has been observed and attracted many researches' interests. In [32], some local synchronization criteria were derived for 3D Rabinovich systems by using linear feedback control and Routh-Hurwitz criteria. In [4, 13, 32], some synchronization criteria were derived for 3D or 4D Rabinovich systems by the control which eliminated all the nonlinear terms of the error system. However, the Rabinovich systems are nonlinear systems in which the nonlinear terms play an important role in the dynamical evolution of trajectories. The linear error systems

can be derived by the control method of eliminating nonlinear terms in error systems. Thus, how to design controllers to remain nonlinear terms in error systems and how to use those controllers to derive global synchronization criteria are the main motivations of this paper.

In this paper, a master-slave scheme for 4D hyperchaotic Rabinovich systems is constructed. Some global master-slave synchronization criteria for 4D hyperchaotic Rabinovich systems are derived by using the designed controllers. The nonlinear features of error systems remained. Those control methods and synchronization criteria for 4D Rabinovich systems can be used to derive synchronization criteria for 3D Rabinovich systems. Three examples are used to illustrate the effectiveness of our results.

2. Preliminaries

Consider the following 4D Rabinovich system as a master system:

$$\begin{aligned}\dot{x}_1(t) &= -ax_1(t) + hx_2(t) + x_2(t)x_3(t), \\ \dot{x}_2(t) &= hx_1(t) - bx_2(t) - x_1(t)x_3(t) + x_4(t),\end{aligned}$$

$$\begin{aligned}
\dot{x}_3(t) &= -dx_3(t) + x_1(t)x_2(t), \\
\dot{x}_4(t) &= -cx_4(t), \\
x_1(0) &= x_{1_0}, \\
x_2(0) &= x_{2_0}, \\
x_3(0) &= x_{3_0}, \\
x_4(0) &= x_{4_0},
\end{aligned} \tag{1}$$

where $(x_1(t), x_2(t), x_3(t), x_4(t))^T \in \mathbb{R}^4$ is the state variable and a, b, c, d , and h are four positive constants. When $h = 6.75, a = 4, b = 1, c = 2$, and $d = 1$, a hyperchaotic attractor can be observed [2].

Because the trajectories of a hyperchaotic system are bounded [2], one can assume that there exists a positive constant l such that

$$|x_2(t)| \leq l, \quad \forall t \geq 0, \tag{2}$$

where the bound l can be derived by observing the trajectory $x_2(t)$ of 4D master system when Matlab is used to plot the trajectory $x_2(t)$ of master system.

One can construct the following slave scheme associated with system (1):

$$\begin{aligned}
\dot{y}_1(t) &= -ay_1(t) + hy_2(t) + y_2(t)y_3(t) + u_1(t), \\
\dot{y}_2(t) &= hy_1(t) - by_2(t) + y_4(t) - y_1(t)y_3(t) \\
&\quad + u_2(t), \\
\dot{y}_3(t) &= -dy_3(t) + y_1(t)y_2(t) + u_3(t), \\
\dot{y}_4(t) &= -cy_4(t) + u_4(t), \\
y_1(0) &= y_{1_0}, \\
y_2(0) &= y_{2_0}, \\
y_3(0) &= y_{3_0}, \\
y_4(0) &= y_{4_0},
\end{aligned} \tag{3}$$

where $(y_1(t), y_2(t), y_3(t), y_4(t))^T \in \mathbb{R}^4$ is the state variable of slave system and $u_1(t), u_2(t), u_3(t)$, and $u_4(t)$ are the external controls.

Let $e_i(t) = x_i(t) - y_i(t)$ for $i = 1, 2, 3, 4$. Then, one can construct the following error system for schemes (1) and (3):

$$\begin{aligned}
\dot{e}_1(t) &= -ae_1(t) + he_2(t) \\
&\quad + (x_2(t)x_3(t) - y_2(t)y_3(t)) - u_1(t), \\
\dot{e}_2(t) &= he_1(t) - be_2(t) + e_4(t) \\
&\quad - (x_1(t)x_3(t) - y_1(t)y_3(t)) - u_2(t),
\end{aligned}$$

$$\begin{aligned}
\dot{e}_3(t) &= -de_3(t) + (x_1(t)x_2(t) - y_1(t)y_2(t)) \\
&\quad - u_3(t), \\
\dot{e}_4(t) &= -ce_4(t) - u_4(t), \\
e_1(0) &= x_{1_0} - y_{1_0}, \\
e_2(0) &= x_{2_0} - y_{2_0}, \\
e_3(0) &= x_{3_0} - y_{3_0}, \\
e_4(0) &= x_{4_0} - y_{4_0}.
\end{aligned} \tag{4}$$

In this paper, we design $u_1(t) = k_1e_1(t) + k_4y_2^2(t)e_1(t)$, $u_2(t) = k_2e_2(t)$, $u_3(t) = k_3e_3(t)$, and $u_4(t) = k_5e_4(t)$. Then, the error system described by (4) can be rewritten as

$$\begin{aligned}
\dot{e}_1(t) &= -(a + k_1 + k_4y_2^2(t))e_1(t) + he_2(t) \\
&\quad + (x_2(t)x_3(t) - y_2(t)y_3(t)), \\
\dot{e}_2(t) &= he_1(t) - (b + k_2)e_2(t) + e_4(t) \\
&\quad - (x_1(t)x_3(t) - y_1(t)y_3(t)), \\
\dot{e}_3(t) &= -(d + k_3)e_3(t) \\
&\quad + (x_1(t)x_2(t) - y_1(t)y_2(t)), \\
\dot{e}_4(t) &= -ce_4(t) - k_5e_4(t), \\
e_1(0) &= x_{1_0} - y_{1_0}, \\
e_2(0) &= x_{2_0} - y_{2_0}, \\
e_3(0) &= x_{3_0} - y_{3_0}, \\
e_4(0) &= x_{4_0} - y_{4_0}.
\end{aligned} \tag{5}$$

The main purpose of this paper is to design k_1, k_2, k_3, k_4 , and k_5 to guarantee the global stability of the error system described by (5).

3. Main Results: Synchronization Criteria

3.1. Synchronization Criteria for 4D Hyperchaotic Rabinovich Systems. Now, we give some synchronization results for two 4D hyperchaotic Rabinovich systems described by (1) and (3).

Theorem 1. *If $k_5 > 0$ and k_1, k_2, k_3 , and k_4 satisfy*

$$\begin{aligned}
k_4 &> \frac{1}{4(d + k_3)}, \\
(a + k_1) &> \frac{l^2}{4(d + k_3)} + \frac{h^2}{(b + k_2)}, \\
l^2 &< 4\frac{d + k_3}{k_4} \left(k_4 - \frac{1}{4(d + k_3)} \right) \left(a + k_1 - \frac{h^2}{b + k_2} \right),
\end{aligned} \tag{6}$$

then two 4D hyperchaotic Rabinovich systems described by (1) and (3) achieve global synchronization.

Proof. One can construct Lyapunov function

$$V(t) = \frac{e_1^2(t) + e_2^2(t) + e_3^2(t) + e_4^2(t)/c}{2}. \quad (7)$$

Calculating the derivative of $V(t)$ along with (5) gives

$$\begin{aligned} \dot{V}(t) &= -\left(a + k_1 + k_4 y_2^2(t)\right) e_1^2(t) + 2h e_1(t) e_2(t) \\ &\quad - (b + k_2) e_2^2(t) - (d + k_3) e_3^2(t) \\ &\quad + 2(x_2(t) + y_2(t)) e_1(t) e_3(t) - \frac{k_4}{c} e_4^2(t) \\ &\leq -\left(\frac{h}{\sqrt{b+k_2}} e_1(t) - \sqrt{b+k_2} e_2(t)\right)^2 \\ &\quad + \frac{h^2}{b+k_2} e_1^2(t) \\ &\quad - \left(\frac{x_2(t) + y_2(t)}{2\sqrt{d+k_3}} e_1(t) - \sqrt{d+k_3} e_3(t)\right)^2 \\ &\quad + \frac{(x_2(t) + y_2(t))^2}{4(d+k_3)} e_1^2(t) - \frac{k_5}{c} e_4^2(t) \\ &\quad - (a + k_1 + k_4 y_2^2(t)) e_1^2(t). \end{aligned} \quad (8)$$

It is easy to see that

$$\frac{h^2}{b+k_2} + \frac{(x_2(t) + y_2(t))^2}{4(d+k_3)} < a + k_1 + k_4 y_2^2(t) \quad (9)$$

and $e_i(t) \neq 0$ for $i = 1, 2, 3, 4$ can ensure $\dot{V}(t) < 0$.

The inequality described by (9) can be rearranged as

$$\tilde{A} y_2^2(t) + \tilde{B} y_2(t) + \tilde{C} > 0 \quad (10)$$

with

$$\begin{aligned} \tilde{A} &= k_4 - \frac{1}{4(d+k_3)}, \\ \tilde{B} &= -\frac{x_2(t)}{2(d+k_3)}, \\ \tilde{C} &= -\frac{x_2^2(t)}{4(d+k_3)} - \frac{h^2}{(b+k_2)} + (a+k_1). \end{aligned} \quad (11)$$

Solving (10), one can have

$$\begin{aligned} \tilde{A} &> 0, \\ \tilde{C} &> 0, \\ \tilde{B}^2 - 4\tilde{A}\tilde{C} &< 0; \end{aligned} \quad (12)$$

that is,

$$\begin{aligned} k_4 &> \frac{1}{4(d+k_3)}, \\ (a+k_1) &> \frac{x_2^2(t)}{4(d+k_3)} + \frac{h^2}{(b+k_2)}, \\ x_2^2(t) &< 4 \frac{d+k_3}{k_4} \left(k_4 - \frac{1}{4(d+k_3)}\right) \left(a+k_1 - \frac{h^2}{b+k_2}\right). \end{aligned} \quad (13)$$

Due to the bound l of trajectory $x_2(t)$ in (2), one can get

$$\begin{aligned} (a+k_1) &> \frac{l^2}{4(d+k_3)} + \frac{h^2}{(b+k_2)}, \\ l^2 &< 4 \frac{d+k_3}{k_4} \left(k_4 - \frac{1}{4(d+k_3)}\right) \left(a+k_1 - \frac{h^2}{b+k_2}\right). \end{aligned} \quad (14)$$

By virtue of LaSalle Invariant principle, one can derive that the trajectories of (5) will be convergent to the largest invariant set in $dV(t)/dt = 0$ when $t \rightarrow \infty$. One can also obtain that $\dot{V}(t) < 0$ for all $e_i(t) \neq 0$, $i = 1, 2, 3, 4$, which means the stability of the error system described by (5), that is, the synchronization of two hyperchaotic systems described by (1) and (3). This completes the proof. \square

Remark 2. In [32], some synchronization criteria were derived for 3D Rabinovich systems by using linear feedback control and Routh-Hurwitz criteria. But those results were local, rather than global. The synchronization criterion in Theorem 1 of this paper is global, which is one contribution of this paper.

Remark 3. Rabinovich systems are nonlinear dynamical systems, in which nonlinear terms play an important role in the evolution of trajectories. In [13], some synchronization criteria were derived for 4D Rabinovich systems by the control which eliminated all the nonlinear terms of the error system. In [4, 32], some synchronization criteria were obtained for 3D Rabinovich systems by using the sliding mode controls which also eliminated the nonlinear terms of the error system. Although the linear error systems can be easily obtained after the nonlinear terms of error systems were eliminated and synchronization criteria for linear error systems can also be easily derived, the nonlinear features in the original 4D hyperchaotic systems were discarded. It should be pointed out that the synchronization criterion in Theorem 1 of this paper is global and the nonlinear terms of error systems remained which inherit the nonlinear features from master and slave 4D hyperchaotic Rabinovich systems by the control methods in this paper, which are the main contributions of this paper.

If $k_1 = 0$, one can have the following corollary.

Corollary 4. If $k_5 > 0$, $k_1 = 0$, and k_2, k_3, k_4 satisfy

$$\begin{aligned} k_4 &> \frac{1}{4(d+k_3)}, \\ a &> \frac{l^2}{4(d+k_3)} + \frac{h^2}{(b+k_2)}, \\ l^2 &< 4 \frac{d+k_3}{k_4} \left(k_4 - \frac{1}{4(d+k_3)} \right) \left(a - \frac{h^2}{b+k_2} \right), \end{aligned} \quad (15)$$

then two 4D hyperchaotic Rabinovich systems described by (1) and (3) achieve global synchronization.

If $k_2 = 0$, one can derive the following corollary.

Corollary 5. If $k_5 > 0$, $k_2 = 0$, and k_1, k_3, k_4 satisfy

$$\begin{aligned} k_4 &> \frac{1}{4(d+k_3)}, \\ (a+k_1) &> \frac{l^2}{4(d+k_3)} + \frac{h^2}{b}, \\ l^2 &< 4 \frac{d+k_3}{k_4} \left(k_4 - \frac{1}{4(d+k_3)} \right) \left(a+k_1 - \frac{h^2}{b} \right), \end{aligned} \quad (16)$$

then two 4D hyperchaotic Rabinovich systems described by (1) and (3) achieve global synchronization.

If $k_3 = 0$, one can obtain the following corollary.

Corollary 6. If $k_5 > 0$, $k_3 = 0$, and k_1, k_2, k_4 satisfy

$$\begin{aligned} k_4 &> \frac{1}{4d}, \\ (a+k_1) &> \frac{l^2}{4d} + \frac{h^2}{b+k_2}, \\ l^2 &< 4 \frac{d}{k_4} \left(k_4 - \frac{1}{4d} \right) \left(a+k_1 - \frac{h^2}{b+k_2} \right), \end{aligned} \quad (17)$$

then two 4D hyperchaotic Rabinovich systems described by (1) and (3) achieve global synchronization.

If $k_1 = k_2 = k_3 = 0$, one can have the following corollary.

Corollary 7. If $a > l^2/4d + h^2/b$, $k_5 > 0$, $k_1 = k_2 = k_3 = 0$, and k_4 satisfies

$$\begin{aligned} \frac{1}{4d} &< k_4, \\ l^2 &< 4 \frac{d}{k_4} \left(k_4 - \frac{1}{4d} \right) \left(a - \frac{h^2}{b} \right), \end{aligned} \quad (18)$$

then two 4D hyperchaotic Rabinovich systems described by (1) and (3) achieve global synchronization.

Remark 8. Corollary 7 is easier to be used than Theorem 1 and Corollaries 4, 5, and 6. But Corollary 7 is more conservative than those results.

3.2. An Application to Synchronization of 3D Chaotic Rabinovich Systems. Consider the following 3D Rabinovich system as a master system:

$$\begin{aligned} \dot{x}_1(t) &= -ax_1(t) + hx_2(t) + x_2(t)x_3(t), \\ \dot{x}_2(t) &= hx_1(t) - bx_2(t) - x_1(t)x_3(t), \\ \dot{x}_3(t) &= -dx_3(t) + x_1(t)x_2(t), \\ x_1(0) &= x_{1_0}, \\ x_2(0) &= x_{2_0}, \\ x_3(0) &= x_{3_0}, \end{aligned} \quad (19)$$

where $(x_1(t), x_2(t), x_3(t))^T \in \mathbb{R}^3$ is the state variable and a, b, d, h are four positive constants. As the bound in (2), one can assume that there exists a constant l such that

$$|x_2(t)| \leq l, \quad \forall t \geq 0. \quad (20)$$

One can construct the following slave scheme associated with system (19):

$$\begin{aligned} \dot{y}_1(t) &= -ay_1(t) + hy_2(t) + y_2(t)y_3(t) + u_1(t), \\ \dot{y}_2(t) &= hy_1(t) - by_2(t) - y_1(t)y_3(t) + u_2(t), \\ \dot{y}_3(t) &= -dy_3(t) + y_1(t)y_2(t) + u_3(t), \\ y_1(0) &= y_{1_0}, \\ y_2(0) &= y_{2_0}, \\ y_3(0) &= y_{3_0}, \end{aligned} \quad (21)$$

where $(y_1(t), y_2(t), y_3(t))^T \in \mathbb{R}^3$ is the state variable of slave system and $u_1(t), u_2(t),$ and $u_3(t)$ are the external controls.

Let $e_i(t) = x_i(t) - y_i(t)$ for $i = 1, 2, 3$. Then, one may construct the following error system for schemes (19) and (21):

$$\begin{aligned} \dot{e}_1(t) &= -ae_1(t) + he_2(t) \\ &\quad + (x_2(t)x_3(t) - y_2(t)y_3(t)) - u_1(t), \\ \dot{e}_2(t) &= he_1(t) - be_2(t) \\ &\quad - (x_1(t)x_3(t) - y_1(t)y_3(t)) - u_2(t), \\ \dot{e}_3(t) &= -de_3(t) + (x_1(t)x_2(t) - y_1(t)y_2(t)) \\ &\quad - u_3(t), \\ e_1(0) &= x_{1_0} - y_{1_0}, \\ e_2(0) &= x_{2_0} - y_{2_0}, \\ e_3(0) &= x_{3_0} - y_{3_0}. \end{aligned} \quad (22)$$

In this paper, we choose $u_1(t) = k_1 e_1(t) + k_4 y_2(t)^2 e_1(t)$, $u_2(t) = k_2 e_2(t)$, and $u_3(t) = k_3 e_3(t)$. Thus, the 3D error system described by (22) can be rewritten as

$$\begin{aligned}
\dot{e}_1(t) &= -(a + k_1 + k_4) e_1(t) + h e_2(t) \\
&\quad + (x_2(t) x_3(t) - y_2(t) y_3(t)), \\
\dot{e}_2(t) &= h e_1(t) - (b + k_2) e_2(t) \\
&\quad - (x_1(t) x_3(t) - y_1(t) y_3(t)), \\
\dot{e}_3(t) &= -(d + k_3) e_3(t) \\
&\quad + (x_1(t) x_2(t) - y_1(t) y_2(t)), \\
e_1(0) &= x_{1_0} - y_{1_0}, \\
e_2(0) &= x_{2_0} - y_{2_0}, \\
e_3(0) &= x_{3_0} - y_{3_0}.
\end{aligned} \tag{23}$$

Constructing the Lyapunov function

$$V(t) = \frac{e_1^2(t) + e_2^2(t) + e_3^2(t)}{2} \tag{24}$$

and using the similar method in Theorem 1, one can have the following synchronization for 3D chaotic Rabinovich systems.

Theorem 9. *If k_1, k_2, k_3, k_4 satisfy*

$$\begin{aligned}
k_4 &> \frac{1}{4(d + k_3)}, \\
(a + k_1) &> \frac{l^2}{4(d + k_3)} + \frac{h^2}{(b + k_2)}, \\
l^2 &< 4 \frac{d + k_3}{k_4} \left(k_4 - \frac{1}{4(d + k_3)} \right) \left(a + k_1 - \frac{h^2}{b + k_2} \right),
\end{aligned} \tag{25}$$

then two 3D chaotic Rabinovich systems described by (19) and (21) achieve global synchronization.

4. Three Illustrated Examples

Example 10. Consider the 4D hyperchaotic Rabinovich system described by (1) with $h = 6.75$, $a = 4$, $b = 1$, $c = 2$, and $d = 1$. The initial condition is $x_1(0) = 0.1$, $x_2(0) = 0.1$, $x_3(0) = 0$, $x_4(0) = 0$. Figures 1 and 2 demonstrate attractors of (1), in which the bound of $x_2(t)$ is 6.7, that is, $|x_2(t)| \leq 6.7, \forall t \geq 0$.

Then, one can study slave Rabinovich system described by (3). The initial condition is $y_1(0) = 0.1$, $y_2(0) = 0.1$, $y_3(0) = -0.05$, and $y_4(0) = 0.1$. Defining $e_i(t) = x_i(t) - y_i(t)$ for $i = 1, 2, 3, 4$, one can derive error system (5), where the initial condition is $e_1(0) = x_1(0) - y_1(0) = 0$, $e_2(0) = x_2(0) - y_2(0) = 0$, $e_3(0) = x_3(0) - y_3(0) = 0.05$, and

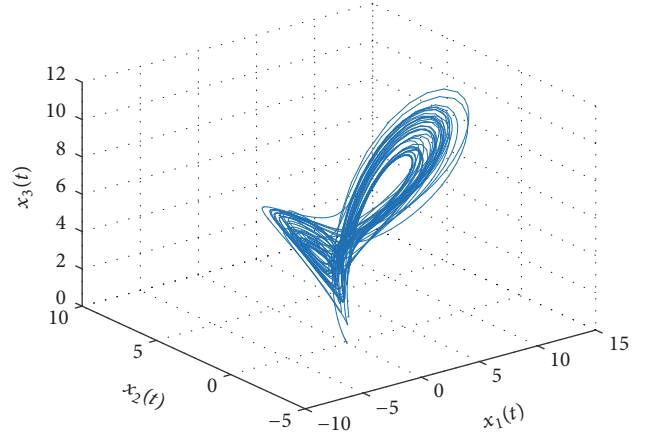


FIGURE 1: The attractor of (1) with $h = 6.75$, $a = 4$, $b = 1$, $c = 2$, and $d = 1$.

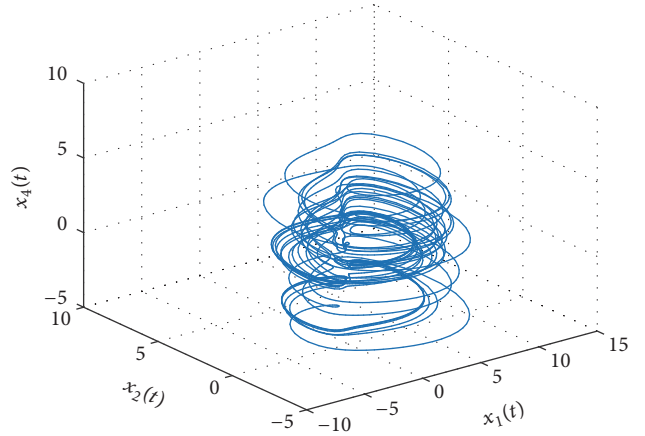


FIGURE 2: The attractor of (1) with $h = 6.75$, $a = 4$, $b = 1$, $c = 2$, and $d = 1$.

$e_4(0) = x_4(0) - y_4(0) = -0.1$. By using Theorem 1, one can derive

$$\begin{aligned}
k_4 &> \frac{1}{4(1 + k_3)}, \\
(4 + k_1) &> \frac{6.7^2}{4(1 + k_3)} + \frac{6.75^2}{(1 + k_2)}, \\
6.7^2 &< 4 \frac{1 + k_3}{k_4} \left(k_4 - \frac{1}{4(1 + k_3)} \right) \left(4 + k_1 - \frac{6.75^2}{1 + k_2} \right).
\end{aligned} \tag{26}$$

If we choose $k_1 = 0.1$, $k_2 = 21.78125$, $k_3 = 4.61125$, and $k_5 = 1$, then $k_4 > 0.9356$. We choose $k_4 = 0.94$. Figure 3 illustrates the trajectories $e_1(t)$, $e_2(t)$, $e_3(t)$, and $e_4(t)$ for error system (5), which can clearly demonstrate the synchronization of hyperchaotic systems (1) and (3).

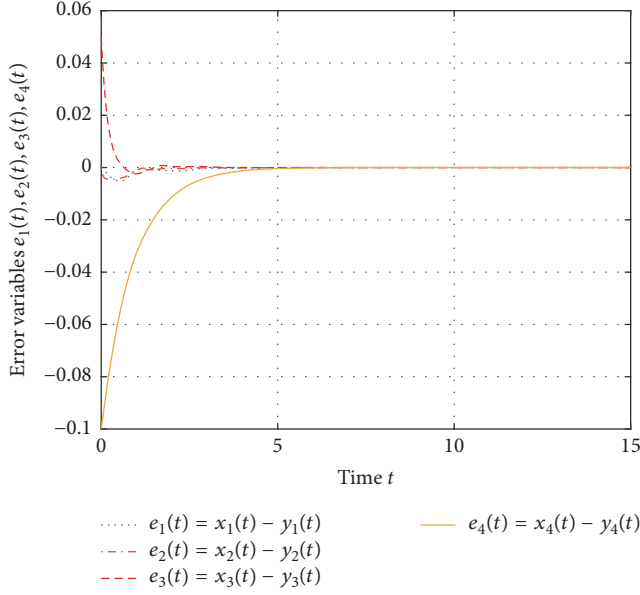


FIGURE 3: The trajectories of (5) with $k_1 = 0.1$, $k_2 = 21.78125$, $k_3 = 4.61125$, $k_4 = 0.94$, and $k_5 = 1$.

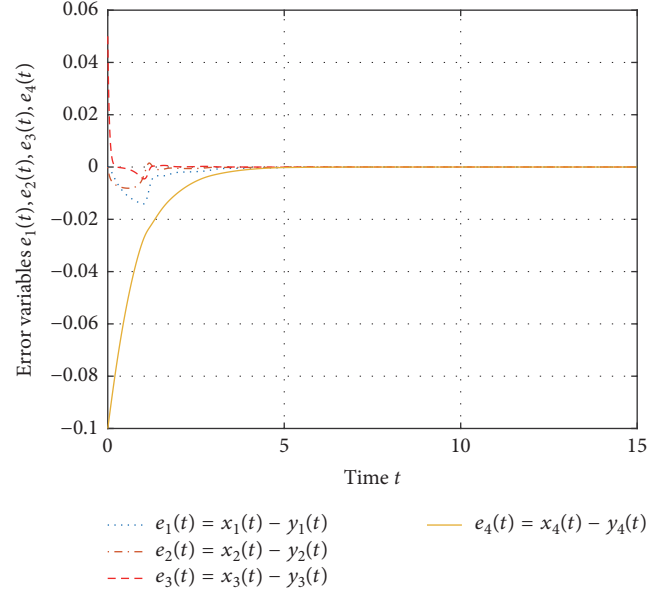


FIGURE 4: The trajectories of (5) with $k_1 = 0$, $k_2 = 14.1875$, $k_3 = 21.445$, $k_4 = 0.03$, and $k_5 = 1$.

If $k_1 = 0$ in (26), one can derive that

$$\begin{aligned}
 k_4 &> \frac{1}{4(1+k_3)}, \\
 4 &> \frac{6.7^2}{4(1+k_3)} + \frac{6.75^2}{(1+k_2)}, \\
 6.7^2 &< 4 \frac{1+k_3}{k_4} \left(k_4 - \frac{1}{4(1+k_3)} \right) \left(4 - \frac{6.75^2}{1+k_2} \right).
 \end{aligned} \tag{27}$$

After setting $k_2 = 14.1875$, $k_3 = 21.445$, and $k_5 = 1$, one can derive $k_4 > 1/44.89$ by Corollary 4. We choose $k_4 = 0.03$. Figure 4 reveals the trajectories $e_1(t)$, $e_2(t)$, $e_3(t)$, and $e_4(t)$ for error system (5), which can clearly illustrate the synchronization of hyperchaotic systems (1) and (3).

If $k_2 = 0$ in (26), one can obtain that

$$\begin{aligned}
 k_4 &> \frac{1}{4(1+k_3)}, \\
 (4+k_1) &> \frac{6.7^2}{4(1+k_3)} + 6.75^2, \\
 6.7^2 &< 4 \frac{1+k_3}{k_4} \left(k_4 - \frac{1}{4(1+k_3)} \right) \left(4+k_1 - 6.75^2 \right).
 \end{aligned} \tag{28}$$

Setting $k_1 = 43$, $k_3 = 10.2225$, and $k_5 = 1$, one can derive $k_4 > 0.07$ by Corollary 5. We choose $k_4 = 0.08$. Figure 5 gives the trajectories $e_1(t)$, $e_2(t)$, $e_3(t)$, and $e_4(t)$ for error system (5), which can clearly reveal the synchronization of hyperchaotic systems (1) and (3).

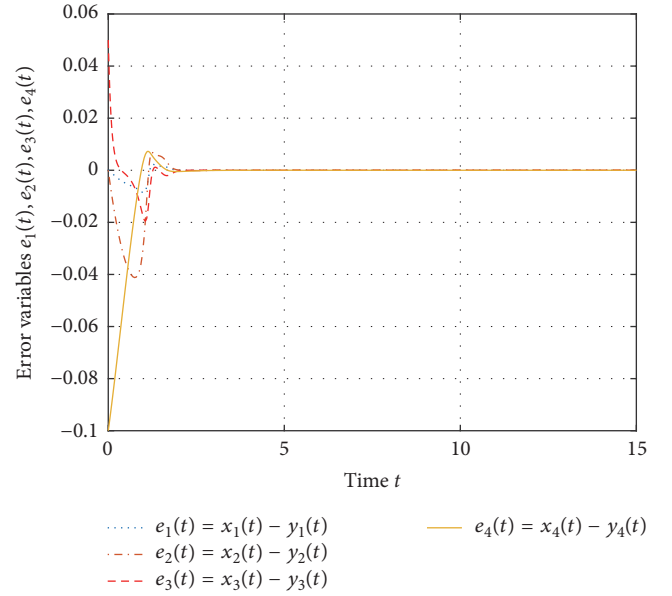


FIGURE 5: The trajectories of (5) with $k_1 = 43$, $k_2 = 0$, $k_3 = 10.2225$, $k_4 = 0.08$, and $k_5 = 1$.

If $k_3 = 0$ in (26), one can have

$$\begin{aligned}
 k_4 &> \frac{1}{4}, \\
 (4+k_1) &> \frac{6.7^2}{4} + \frac{6.75^2}{(1+k_2)}, \\
 6.7^2 &< 4 \frac{1}{k_4} \left(k_4 - \frac{1}{4} \right) \left(4+k_1 - \frac{6.75^2}{1+k_2} \right).
 \end{aligned} \tag{29}$$

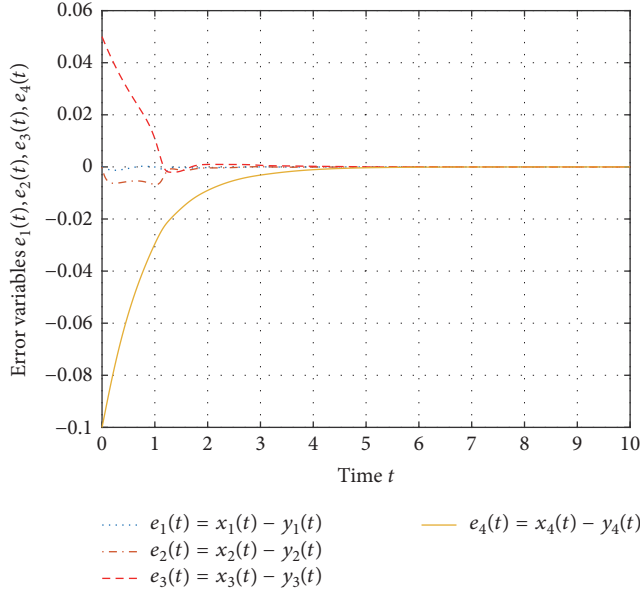


FIGURE 6: The trajectories of (5) with $k_1 = 19.2225$, $k_2 = 14.1875$, $k_3 = 0$, $k_4 = 3.86$, and $k_5 = 1$.

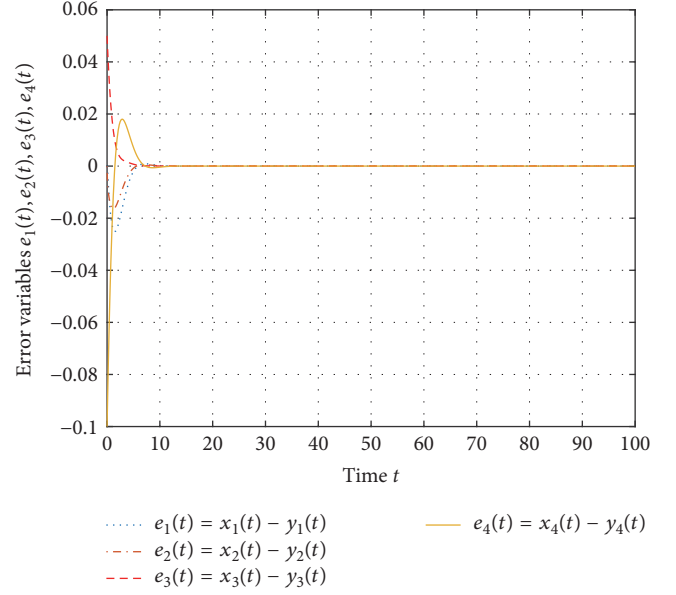


FIGURE 8: The trajectories of (5) with $k_1 = k_2 = k_3 = 0$, $k_4 = 0.26$, and $k_5 = 1$.

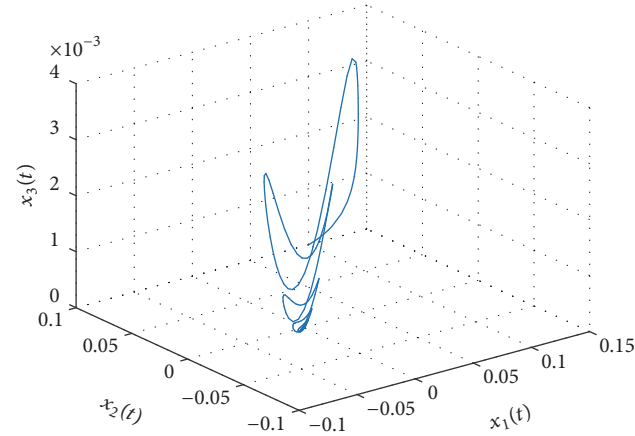


FIGURE 7: The trajectories of (19) with $h = 6.75$, $a = 4.3$, $b = 10.8$, $c = 2$, and $d = 1$.

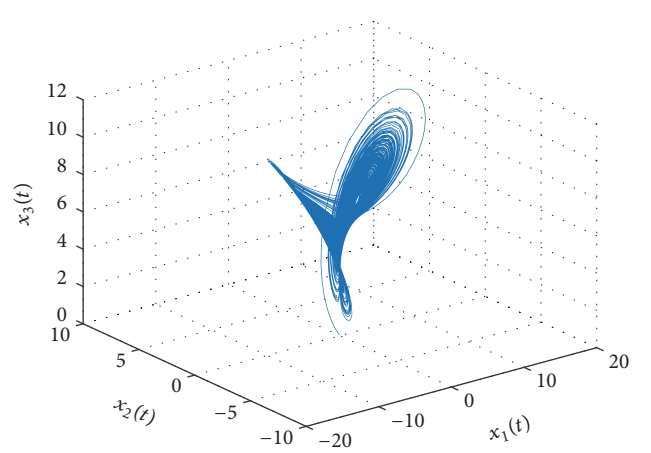


FIGURE 9: The trajectories of (19) with $h = 6.75$, $a = 4$, $b = 1$, and $d = 1$.

Setting $k_1 = 19.2225$, $k_2 = 14.1875$, and $k_5 = 1$, one can derive $k_4 > 3.85$ by Corollary 6. We choose $k_4 = 3.86$. Figure 6 gives the trajectories $e_1(t)$, $e_2(t)$, $e_3(t)$, $e_4(t)$ for error system (5), which can clearly reveal the synchronization of hyperchaotic systems (1) and (3).

Remark 11. It is easy to see that Corollary 7 fails to make any conclusion because $4 < 6.7^2/4 + 6.75^2$ when $k_1 = k_2 = k_3 = 0$.

Example 12. Consider the 4D Rabinovich systems and the error system described by (1), (3), and (5) with $h = 6.75$, $a = 4.3$, $b = 10.8$, $c = 2$, and $d = 1$, respectively, where the initial conditions are the same as those in Example 10. Figure 7 implies that $|x_2(t)| \leq 0.1$ for $t \geq 0$. From Corollary 7, one can have $a = 4.3 > 0.1^2/4 + 6.75^2/10.8 = 4.213$, $k_4 > 0.2581$. We can choose $k_1 = k_2 = k_3 = 0$, $k_4 = 0.26$, and

$k_5 = 1$. Figure 8 provides the trajectories $e_1(t)$, $e_2(t)$, $e_3(t)$, and $e_4(t)$ for error system (5), which can clearly illustrate the synchronization of Rabinovich systems (1) and (3).

Example 13. Consider the 3D hyperchaotic Rabinovich systems and the error system described by (19), (21), and (23) with $h = 6.75$, $a = 4$, $b = 1$, and $d = 1$, respectively, where the initial conditions are $x_1(0) = 0.1$, $x_2(0) = 0.1$, $x_3(0) = 0$, $y_1(0) = 0.1$, $y_2(0) = 0.1$, $y_3(0) = -0.05$, $e_1(0) = x_1(0) - y_1(0) = 0$, $e_2(0) = x_2(0) - y_2(0) = 0$, and $e_3(0) = x_3(0) - y_3(0) = 0.05$. Figure 9 implies that $|x_2(t)| \leq 6.1$ for $t \geq 0$.

Setting $k_1 = 14.1875$ and $k_2 = k_3 = 0$, one can have $k_4 > 0.26$ by Theorem 9. We can choose $k_1 = 14.1875$, $k_2 = k_3 = 0$, and $k_4 = 0.3$. Figure 10 gives the trajectories $e_1(t)$, $e_2(t)$,

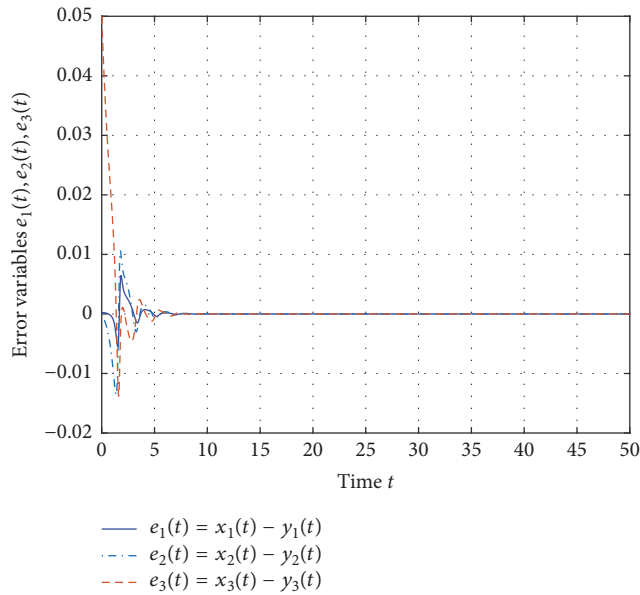


FIGURE 10: The trajectories of (23) with $k_1 = 14.1875$, $k_2 = k_3 = 0$, and $k_4 = 0.3$.

and $e_3(t)$ for error system (23), which can clearly illustrate the synchronization of chaotic systems (19) and (21).

5. Conclusions and Future Works

We have derived some global synchronization criteria for 4D hyperchaotic Rabinovich systems. We have kept the nonlinear terms of error systems. Those control methods and synchronization criteria for 4D hyperchaotic Rabinovich systems can be used to study the synchronization of 3D chaotic Rabinovich systems. We have used three examples to demonstrate the effectiveness our derived results. In this paper, we only consider the state feedback control. Our future research focus is to design the time-delayed controllers.

Conflicts of Interest

The authors declare that there are no conflicts of interest regarding the publication of this paper.

Acknowledgments

This paper is partially supported by the National Natural Science Foundation of China under Grant 61561023, the Key Project of Youth Science Fund of Jiangxi China under Grant 20133ACB21009, the Project of Science and Technology Fund of Jiangxi Education Department of China under Grant GJJ160429, and the Project of Jiangxi E-Commerce High Level Engineering Technology Research Centre.

References

[1] A. S. Pikovski, M. I. Rabinovich, and V. Y. Trakhtengerts, "Onset of stochasticity in decay confinement of parametric instability," *Soviet Physics JETP*, vol. 47, no. 4, pp. 715–719, 1978.

[2] Y. Liu, Q. Yang, and G. Pang, "A hyperchaotic system from the Rabinovich system," *Journal of Computational and Applied Mathematics*, vol. 234, no. 1, pp. 101–113, 2010.

[3] S. Emiroglu and Y. Uyaroglu, "Control of Rabinovich chaotic system based on passive control," *Scientific Research and Essays*, vol. 5, no. 21, pp. 3298–3305, 2010.

[4] U. E. Kocamaz, Y. Uyaroglu, and H. Kizmaz, "Control of Rabinovich chaotic system using sliding mode control," *International Journal of Adaptive Control and Signal Processing*, vol. 28, no. 12, pp. 1413–1421, 2014.

[5] K. Ding and Q.-L. Han, "Master-slave synchronization criteria for chaotic Hindmarsh-Rose neurons using linear feedback control," *Complexity*, vol. 21, no. 5, pp. 319–327, 2016.

[6] K. Ding and Q.-L. Han, "Synchronization of two coupled Hindmarsh-Rose neurons," *Kybernetika*, vol. 51, no. 5, pp. 784–799, 2015.

[7] K. Ding and Q.-L. Han, "Master-slave synchronization criteria for horizontal platform systems using time delay feedback control," *Journal of Sound and Vibration*, vol. 330, no. 11, pp. 2419–2436, 2011.

[8] Z. Elhadj and J. C. Sprott, "A rigorous determination of the overall period in the structure of a chaotic attractor," *International Journal of Bifurcation and Chaos*, vol. 23, no. 3, Article ID 1350046, 4 pages, 2013.

[9] Z. Elhadj and J. C. Sprott, "Simplest 3D continuous-time quadratic systems as candidates for generating multiscroll chaotic attractors," *International Journal of Bifurcation and Chaos*, vol. 23, no. 7, Article ID 1350120, 6 pages, 2013.

[10] Q.-L. Han, "Absolute stability of time-delay systems with sector-bounded nonlinearity," *Automatica*, vol. 41, no. 12, pp. 2171–2176, 2005.

[11] Q.-L. Han, "On designing time-varying delay feedback controllers for master-slave synchronization of Lur'e systems," *IEEE Transactions on Circuits and Systems I: Regular Papers*, vol. 54, no. 7, pp. 1573–1583, 2007.

[12] Q.-L. Han, Y. Liu, and F. Yang, "Optimal Communication Network-Based H_∞Quantized Control with Packet Dropouts for a Class of Discrete-Time Neural Networks with Distributed Time Delay," *IEEE Transactions on Neural Networks and Learning Systems*, vol. 27, no. 2, pp. 426–434, 2016.

[13] J. M. He and F. Q. Chen, "A new fractional order hyperchaotic Rabinovich system and its dynamical behaviors," *International Journal of Non-Linear Mechanics*, vol. 95, pp. 73–81, 2017.

[14] W. L. He and J. D. Cao, "Exponential synchronization of hybrid coupled networks with delayed coupling," *IEEE Transactions on Neural Networks and Learning Systems*, vol. 21, no. 4, pp. 571–583, 2010.

[15] S. Jafari, S. M. R. H. Golpayegani, A. H. Jafari, and S. Gharibzadeh, "Letter to the editor: Some remarks on chaotic systems," *International Journal of General Systems*, vol. 41, no. 3, pp. 329–330, 2012.

[16] S. Jafari, V.-T. Pham, and T. Kapitaniak, "Multiscroll chaotic sea obtained from a simple 3D system without equilibrium," *International Journal of Bifurcation and Chaos*, vol. 26, no. 2, Article ID 1650031, 7 pages, 2016.

[17] Y. Liu, Z. Wang, J. Liang, and X. Liu, "Synchronization and state estimation for discrete-time complex networks with distributed delays," *IEEE Transactions on Systems, Man, and Cybernetics, Part B*, vol. 38, no. 5, pp. 1314–1325, 2008.

[18] Y. Liu, Z. Wang, J. Liang, and X. Liu, "Stability and synchronization of discrete-time Markovian jumping neural networks

- with mixed mode-dependent time delays,” *IEEE Transactions on Neural Networks and Learning Systems*, vol. 20, no. 7, pp. 1102–1116, 2009.
- [19] Y. Liu, Z. Wang, J. Liang, and X. Liu, “Synchronization of coupled neutral-type neural networks with jumping-mode-dependent discrete and unbounded distributed delays,” *IEEE Transactions on Systems, Man, and Cybernetics, Part B: Cybernetics*, vol. 43, pp. 102–114, 2013.
- [20] Q. Lu, S.-R. Liu, X.-G. Xie, and J. Wang, “Decision making and finite-time motion control for a group of robots,” *IEEE Transactions on Cybernetics*, vol. 43, no. 2, pp. 738–750, 2013.
- [21] H. Mehdi and O. Boubaker, “PSO-Lyapunov motion/force control of robot arms with model uncertainties,” *Robotica*, vol. 34, no. 3, pp. 634–651, 2016.
- [22] H. Mkaouer and O. Boubaker, “Robust control of a class of chaotic and hyperchaotic driven systems,” *Pramana—Journal of Physics*, vol. 88, no. 1, article no. 9, 2017.
- [23] V.-T. Pham, S. Jafari, X. Wang, and J. Ma, “A chaotic system with different shapes of equilibria,” *International Journal of Bifurcation and Chaos*, vol. 26, no. 4, Article ID 1650069, 1650069, 5 pages, 2016.
- [24] V.-T. Pham, S. Jafari, and T. Kapitaniak, “Constructing a chaotic system with an infinite number of equilibrium points,” *International Journal of Bifurcation and Chaos*, vol. 26, no. 13, Article ID 1650225, 1650225, 7 pages, 2016.
- [25] M. Scarpiniti, D. Comminiello, G. Scarano, R. Parisi, and A. Uncini, “Steady-state performance of spline adaptive filters,” *IEEE Transactions on Signal Processing*, vol. 64, no. 4, pp. 816–828, 2016.
- [26] M. Scarpiniti, D. Comminiello, R. Parisi, and A. Uncini, “Novel cascade spline architectures for the identification of nonlinear systems,” *IEEE Transactions on Circuits and Systems I: Regular Papers*, vol. 62, no. 7, pp. 1825–1835, 2015.
- [27] S. Scardapane, D. Comminiello, M. Scarpiniti, and A. Uncini, “Online sequential extreme learning machine with kernels,” *IEEE Transactions on Neural Networks and Learning Systems*, vol. 26, no. 9, pp. 2214–2220, 2015.
- [28] C. Volos, I. Kyprianidis, I. Stouboulos, and S. Vaidyanathan, “Design of a chaotic random bit generator using a Duffing-van der Pol system,” *International Journal of System Dynamics Applications*, vol. 5, no. 3, 18 pages, 2016.
- [29] F. Yang and Y. Li, “Set-membership fuzzy filtering for nonlinear discrete-time systems,” *IEEE Transactions on Systems, Man, and Cybernetics, Part B: Cybernetics*, vol. 40, no. 1, pp. 116–124, 2010.
- [30] F. Yang and Q.-L. Han, “ H_∞ control for networked systems with multiple packet dropouts,” *Information Sciences*, vol. 252, pp. 106–117, 2013.
- [31] J. Chen, F. Yang, and Q.-L. Han, “Model-free predictive H ∞ control for grid-connected solar power generation systems,” *IEEE Transactions on Control Systems Technology*, vol. 22, no. 5, pp. 2039–2047, 2014.
- [32] U. E. Kocamaz, Y. Uyaroglu, and H. Kizmaz, “Controlling hyperchaotic Rabinovich system with single state controllers: Comparison of linear feedback, sliding mode, and passive control methods,” *Optik - International Journal for Light and Electron Optics*, vol. 130, pp. 914–921, 2017.

Research Article

Design of Robust Supertwisting Algorithm Based Second-Order Sliding Mode Controller for Nonlinear Systems with Both Matched and Unmatched Uncertainty

Marwa Jouini, Slim Dhahri, and Anis Sellami

Laboratory of Engineering of Industrial System and Renewable Energy (LISIER), Higher National Engineering School of Tunis (ENSIT), 5 Avenue Taha Hussein, BP 56, Bab Menara, 1008 Tunis, Tunisia

Correspondence should be addressed to Marwa Jouini; marwajouini7@gmail.com

Received 4 August 2017; Revised 8 November 2017; Accepted 22 November 2017; Published 13 December 2017

Academic Editor: Olfa Boubaker

Copyright © 2017 Marwa Jouini et al. This is an open access article distributed under the Creative Commons Attribution License, which permits unrestricted use, distribution, and reproduction in any medium, provided the original work is properly cited.

This paper proposes a robust supertwisting algorithm (STA) design for nonlinear systems where both matched and unmatched uncertainties are considered. The main contributions reside primarily to conceive a novel structure of STA, in order to ensure the desired performance of the uncertain nonlinear system. The modified algorithm is formed of double closed-loop feedback, in which two linear terms are added to the classical STA. In addition, an integral sliding mode switching surface is proposed to construct the attractiveness and reachability of sliding mode. Sufficient conditions are derived to guarantee the exact differentiation stability in finite time based on Lyapunov function theory. Finally, a comparative study for a variable-length pendulum system illustrates the robustness and the effectiveness of the proposed approach compared to other STA schemes.

1. Introduction

Sliding Mode Control (SMC) strategy is considered an effective methodology for control uncertain systems. This strategy gives a major objective in control system design to attain stability in the presence of uncertainties [1–5]. The design of the SMC systems mainly consists of two steps: the choice of the sliding mode switching surface and the design of the sliding mode controller. Moreover, SMC has believed significant amount of interest due to several advantages, such that fast convergence, high robustness, and invariance to certain internal system parameter variations and its implementation are easy [5–9]. On the other hand, the worst disadvantage of the SMC methodology is the chattering phenomenon. Thus, to reduce this problem of the chattering effect, numerous techniques are proposed in literature [10–13]; one of them is the supertwisting algorithm (STA) method. The STA has become the prototype of Second-Order Sliding Mode Control (SOSMC) algorithm, which has the capability of system robust stabilization, finite time convergence to the sliding surface, and chattering reduction even in the presence of uncertainties [14–16]. Also, it is able to enforce that the system

states converge to the sliding variable [17, 18]. Nevertheless, the more disadvantage in the supertwisting algorithm is difficulty of designing the gains of the signum function, which leads a very slow convergence and slowly setting time response [14]. In this context, several works have been presented recently proving the stability of the STA using Lyapunov theory and presenting an easy synthesis method of these gains [18]. In addition, great effort has been devoted to enhance the convergence and the robustness of the traditional STA. We can quote some methods: paper [19] proposes the addition of a new term in the classical STA, which leads to improved convergence. In [18, 20], the regulation mechanism has been modified by adding a linear term of the sliding variable to the traditional STA. To this end, the aforementioned methods can be only improving the speed convergence of the sliding variable in zero, but they lead a large overshoot of the system response.

In this paper we focus on developing a new modified structure of STA with bounded uncertainty in order to limit the overshoot and shorten the settling time of the system response. This new structure has double closed-loop feedback terms. The first one consists of an outer loop negative

feedback to accelerate the sliding variable to close to zero and the second feedback is a correction term about an auxiliary variable to reduce the overshoot. Compared with the existing results, the main contributions of this paper are highlighted as follows:

- (i) Apply the proposed method for an uncertain nonlinear system, considering two types of uncertainties such as matched and unmatched.
- (ii) An integral sliding surface is designed to construct the reachability of the sliding mode.
- (iii) A variable-length pendulum system is included to illustrate the applicability of the proposed STA and a comparative study is established with other STA schemes.

The rest of this paper is organized as follows: Section 2 describes the mathematical system description and the problem formulation. The proposed approach is detailed in Section 3. In Section 4, the proving of reaching condition using the Lyapunov function is given. Simulation results are presented in Section 5, and conclusion remarks are in Section 6.

2. Mathematical System Description and Problem Formulation

Consider a second-order uncertain nonlinear system described by the state equation:

$$\begin{aligned} \dot{x}_1(t) &= x_2(t), \\ \dot{x}_2(t) &= f(t, x) + \Delta f(t, x) \\ &\quad + [g(t, x) + \Delta g(t, x)] u(t), \\ y(t) &= x_1(t), \end{aligned} \quad (1)$$

where $x_1(t)$, $x_2(t)$ are the state variables of the system, $x(t) = [x_1(t), x_2(t)]^T \in \mathbb{R}^2$ is the state vector, $u(t) \in \mathbb{R}$ is the input signal control, and $y(t)$ denotes the output vector. $f(t, x)$ and $g(t, x)$ represent the nonlinear dynamic function and the nonlinear control function, respectively. $\Delta f(t, x)$ and $\Delta g(t, x)$ are the corresponding unknown uncertainties of nonlinear vector which can be regarded as satisfying the following assumptions.

Assumption 1. The matched uncertainty $\Delta g(t, x)$ is assumed to be bounded by the unknown scalar $\zeta > 0$ such that

$$\|\Delta g(t, x)\| \leq \zeta. \quad (2)$$

Assumption 2. There exists an unknown nonnegative nonlinear function $\gamma(t, x)$ such that the unmatched uncertainty $\Delta f(t, x)$ is bounded as

$$\|\Delta f(t, x)\| \leq \gamma(t, x). \quad (3)$$

The main objective of this paper is to design a control input signal for the nonlinear uncertain system (1), which satisfies assumptions (2) and (3), such that the sliding variable $\sigma(t)$ converges to zero in finite time.

Let us consider the classical STA with matched uncertainty used for the design of second-order sliding mode controller [18, 19]:

$$\begin{aligned} \dot{\sigma}(t) &= -\lambda_1 |\sigma(t)|^{1/2} \text{sign}(\sigma(t)) + v(t), \\ \dot{v}(t) &= -\lambda_3 \text{sign}(\sigma(t)) + \Theta(t), \end{aligned} \quad (4)$$

where $\sigma(t)$ and $v(t)$ are, respectively, the sliding variable and the auxiliary variable, λ_1 and λ_3 are some positive constants, and the uncertainty $\Theta(t)$ can be expressed as follows:

$$\Theta(t) = k(t) \text{sign}(\sigma(t)), \quad (5)$$

where $k(t)$ is the amplitude of uncertainty. Its value should satisfy the following inequalities:

$$\begin{aligned} 0 &\leq k(t) \leq M, \\ |\dot{k}(t)| &\leq N, \end{aligned} \quad (6)$$

where M and N are positive constants.

In order to accelerate the convergence of the sliding variable $\sigma(t)$ to zero, the gain of signum function (λ_1, λ_3) must have large values. On the other hand, the values of λ_1 and λ_3 should be as small as possible to reduce the chattering phenomenon [19]. To avoid the conflict, many researches [18, 20, 21] propose the following STA system:

$$\begin{aligned} \dot{\sigma}(t) &= -\lambda_1 |\sigma(t)|^{1/2} \text{sign}(\sigma(t)) - \lambda_2 \sigma(t) + v(t) \\ \dot{v}(t) &= -\lambda_3 \text{sign}(\sigma(t)) - \lambda_4 \sigma(t) + \Theta(t), \end{aligned} \quad (7)$$

where λ_2 and λ_4 are positive constants.

The modified structure (7) is used to obtain a faster convergence of $\sigma(t)$. However, if the absolute value of $\dot{v}(t)$ increased, then v increased also; consequently this produces a long setting time and overshoot of sliding variable. To solve this problem, we propose a novel modified STA in the next section.

3. Proposed Approach

The objective of this paper is to ameliorate the structure of supertwisting algorithm in order to improve the convergence of sliding variable. However, the proposed method includes a new structure to limit the absolute value of $v(t)$ defined in (7), in which a negative feedback term about $v(t)$ to $\dot{v}(t)$ is added. The new modified algorithm with double closed-loop feedback can be formulated as follows:

$$\begin{aligned} \dot{\sigma}(t) &= -\lambda_1 |\sigma(t)|^{1/2} \text{sign}(\sigma(t)) - \lambda_2 \sigma(t) + v(t) \\ \dot{v}(t) &= -\lambda_3 \text{sign}(\sigma(t)) - \lambda_4 v(t) + \Theta(t), \end{aligned} \quad (8)$$

where λ_1 , λ_2 , λ_3 , λ_4 are positive constants. The parameters of the novel modified STA can be selected according to the matched uncertainty (5). λ_1 and λ_3 can be fitted to reduce the chattering phenomenon and λ_2 and λ_4 can be adjusted to guarantee the convergence of the sliding variable $\sigma(t)$. Using relation (8) and the initial conditions ($\sigma(0) > 0$, $v(0) = 0$,

$\Theta(0) = 0$), we can calculate the regulation mechanism as follows:

$$v(t) = -\frac{\lambda_3}{\lambda_4} (1 - e^{-\lambda_4 t}). \quad (9)$$

From (8) and (9), we can note that the overshoot of the sliding variable can be reduced by $-\lambda_4 v(t)$ and the linear correction term $-\lambda_2 \sigma(t)$ makes the system faster. Indeed, the performance advantages of the new structure of ST are achieved.

3.1. Stability Analysis of the Novel Structure of STA. In this section, the task is to determinate sufficient conditions to ensure the robustness of the modified algorithm with matched uncertainty (5). Relation (8) can be driven as a mathematical model:

$$\begin{aligned} \dot{X}_1(t) &= -\lambda_1 |X_1(t)|^{1/2} \text{sign}(X_1(t)) - \lambda_2 X_1(t) \\ &\quad + X_2(t), \\ \dot{X}_2(t) &= -\lambda_3 \text{sign}(X_1(t)) - \lambda_4 X_2(t) \\ &\quad + k(t) \text{sign}(X_1(t)), \end{aligned} \quad (10)$$

where $\begin{bmatrix} \sigma(t) \\ v(t) \end{bmatrix} = \begin{bmatrix} X_1(t) \\ X_2(t) \end{bmatrix}$.

To facilitate further development, we take $z = \begin{bmatrix} z_1 \\ z_2 \end{bmatrix} = \begin{bmatrix} |X_1(t)|^{1/2} \text{sign}(X_1(t)) \\ X_2(t) \end{bmatrix}$.

The derivative of the vector z using (10) is given by

$$\dot{z} = \frac{1}{|z_1|} Az + \frac{1}{|z_1|} \begin{bmatrix} 0 \\ k(t) z_1 \end{bmatrix} = \frac{1}{|z_1|} Qz, \quad (11)$$

where

$$\begin{aligned} |z_1| &= |X_1|^{1/2}, \\ A &= \begin{bmatrix} -\frac{\lambda_1}{2} - \frac{\lambda_2}{2} |z_1| & \frac{1}{2} \\ -\lambda_3 & -\lambda_4 |z_1| \end{bmatrix}, \\ Q &= \begin{bmatrix} -\frac{\lambda_1}{2} - \frac{\lambda_2}{2} |z_1| & \frac{1}{2} \\ -\lambda_3 + k(t) & -\lambda_4 |z_1| \end{bmatrix}. \end{aligned} \quad (12)$$

Using the fact that $\lambda_1, \lambda_2, \lambda_3$, and λ_4 are positive scalars, then the matrix A is Hurwitz.

Choose $\lambda_1 = a\lambda_3$ and $\lambda_2 = b\lambda_4$, where $a > 0$ and $b > 0$. The stability of the novel modified STA can be designed according to the following theorem.

Theorem 3. Consider the new modified STA (8) with the matched uncertainty (5). If the parameters $\lambda_1, \lambda_2, \lambda_3$, and λ_4 are positive constants, then the sliding mode of system (1) will be built in finite time; that is, the sliding variable will converge to the sliding surface in finite time.

Proof. Propose the following candidate Lyapunov function with respect to the vector z :

$$V(z) = z^T Pz, \quad (13)$$

where P is a symmetric positive definite matrix as

$$P = \begin{bmatrix} \frac{\lambda_4}{\lambda_2} + \left(\frac{2\lambda_3}{\lambda_1}\right)^2 & -\frac{2\lambda_3}{\lambda_1} \\ -\frac{2\lambda_3}{\lambda_1} & 1 \end{bmatrix} = \begin{bmatrix} b + \left(\frac{2}{a}\right)^2 & -\frac{2}{a} \\ -\frac{2}{a} & 1 \end{bmatrix}. \quad (14)$$

It is easy to show that the Lyapunov function (13) can be bounded from both sides [17] by

$$\alpha_{\min}\{P\} \|z\|^2 \leq V(z) \leq \alpha_{\max}\{P\} \|z\|^2, \quad (15)$$

where α_{\min} and α_{\max} are, respectively, the minimum and maximum eigenvalues of P and $\|z\|^2$ is the Euclidean norm of z .

Using relation (15), it results that

$$\|z\|^2 \geq \frac{V(z)}{\alpha_{\max}\{P\}}, \quad (16)$$

$$\|z\|^2 \leq \frac{V(z)}{\alpha_{\min}\{P\}}. \quad (17)$$

According to (17), it turns out that

$$|z_1| \leq \|z\| \leq \frac{V^{1/2}(z)}{\alpha_{\min}^{1/2}\{P\}}. \quad (18)$$

The time derivative of $V(z)$ can be calculated as follows:

$$\begin{aligned} \dot{V}(z) &= z^T P \dot{z} + \dot{z}^T Pz = z^T P \frac{1}{|z_1|} Qz + \frac{1}{|z_1|} Q^T z^T Pz \\ &= \frac{1}{|z_1|} z^T [PQ + Q^T P] z = -z^T Gz, \end{aligned} \quad (19)$$

where

$$G = \begin{bmatrix} \left(\frac{4b}{a^2} + b^2\right) \lambda_4 + \frac{ab\lambda_3}{|z_1|} + \frac{4k(t)}{a|z_1|} & -\frac{(2+b)\lambda_4}{a} - \frac{2}{a^2|z_1|} - \frac{b}{2|z_1|} - \frac{k(t)}{|z_1|} \\ -\frac{(2+b)\lambda_4}{a} - \frac{2}{a^2|z_1|} - \frac{b}{2|z_1|} - \frac{k(t)}{|z_1|} & 2\lambda_4 + \frac{2}{a|z_1|} \end{bmatrix}. \quad (20)$$

To guarantee $\dot{V}(z)$ is negative definite, (19) can be handled as follows:

$$\dot{V}(z) = -z^T G_1 z - \frac{1}{|z_1|} z^T G_2 z \quad (21)$$

with

$$G_1 = \begin{bmatrix} \left(\frac{4b}{a^2} + b^2 \right) \lambda_4 & -\frac{(2+b)\lambda_4}{a} \\ -\frac{(2+b)\lambda_4}{a} & 2\lambda_4 \end{bmatrix}, \quad (22)$$

$$G_2 = \begin{bmatrix} \left(ab\lambda_3 + \frac{4k(t)}{a} \right) & -\left(\frac{2}{a^2} + \frac{b}{2} + k(t) \right) \\ -\left(\frac{2}{a^2} + \frac{b}{2} + k(t) \right) & \frac{2}{a} \end{bmatrix},$$

where G_1 and G_2 are symmetrical matrices.

The time derivative of $V(z)$ is bounded as follows:

$$\begin{aligned} \dot{V}(z) &\leq -\alpha_{\min}\{G_1\} \|z\|^2 - \frac{1}{|z_1|} \alpha_{\min}\{G_2\} \|z\|^2 \\ &\leq -\left(\alpha_{\min}\{G_1\} + \frac{1}{|z_1|} \alpha_{\min}\{G_2\} \right) \|z\|^2, \end{aligned} \quad (23)$$

where $\alpha_{\min}\{G_1\}, \{G_2\}$ are, respectively, the minimum eigenvalue of G_1 and G_2 .

Using (16)–(18), the inequality (23) can be expressed as follows:

$$\begin{aligned} \dot{V}(z) &\leq -\frac{\alpha_{\min}\{G_1\}}{\alpha_{\max}\{P\}} V(z) \\ &\quad = -\beta_1 V(z) \\ &\quad - \frac{\alpha_{\min}^{1/2}\{P\} \alpha_{\min}\{G_2\}}{\alpha_{\max}\{P\}} V^{1/2}(z), \end{aligned} \quad (24)$$

where β_1 and β_2 are positive constants.

Hence, the time derivative of $V(z)$ is bounded as follows:

$$\dot{V}(z) \leq -\beta_1 V(z) - \beta_2 V^{1/2}(z). \quad (25)$$

Equation (25) shows that the derivative of the Lyapunov function is negative definite ($\dot{V}(z) \leq 0$). We can conclude that the new modified STA (8) with matched uncertainty (5) converges to zero in finite time. \square

3.2. Comparative Study. A comparative analysis has been made to compare the convergence performances between the different structures of supertwisting algorithm: the classical STA, the modified STA (MSTA) (see references [18–21]), and the novel modified STA. In order to obtain smaller amplitude chattering, the parameters λ_1 and λ_3 should be adjusted as small as possible, and the parameters λ_2 and λ_4 are selected to guarantee the convergence of the sliding variable. These parameters are chosen as $\lambda_1 = 0.5$, $\lambda_2 = 2$, $\lambda_3 = 0.6$, and

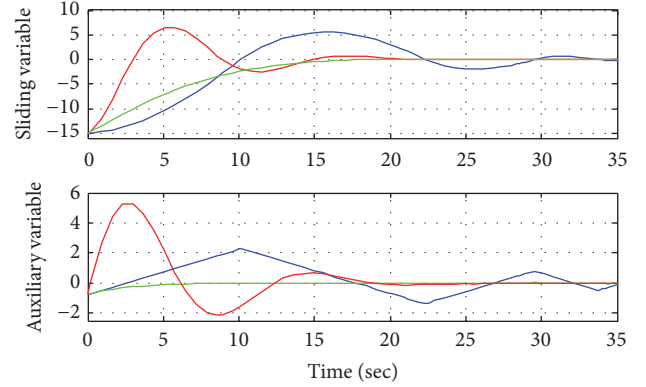


FIGURE 1: Dynamic of the sliding variable and the auxiliary variable with different structures of STA (blue line: the classical STA, red line: the modified STA, and green line the novel modified STA).

TABLE 1: The performances of the different structures of STA.

Structure	Overshoot	Settling time
Classical STA	5.5%	33.8 s
Modified STA	6.52%	19 s
Novel modified STA	1.1%	18 s

$\lambda_4 = 2$. Figure 1 shows the dynamic of the sliding variable and the auxiliary variable with the following initial conditions: $\sigma(0) = -15$ and $\nu(0) = -0.75$.

It can be observed in Figure 1 and Table 1 that a faster speed of the sliding variable approaching zero is obtained in modified STA and the novel modified STA, as they add the same linear correction term $-\lambda_2\sigma(t)$ compared to classical STA. Moreover, by the effect of the linear feedback term $-\lambda_4\nu(t)$ added in the novel modified structure, the sliding variable $\sigma(t)$ obtains small overshoot (1.1%). Thus, the new structure of STA proposed achieves the best convergence performances in terms of settling time and overshoot.

4. Sliding Mode Reachability

To reduce the steady error, an integral term of tracking error is introduced, which makes up the integral sliding surface [22, 23] as follows:

$$\sigma(t) = \dot{e}(t) + k_1 e(t) + k_2 \int_0^t e(\tau) d\tau, \quad (26)$$

where $e(t) = y(t) - y_{\text{ref}}(t) = x_1(t) - x_{\text{ref}}(t)$ is the tracking error, $y_{\text{ref}}(t)$ denotes the reference trajectory, and k_1 and k_2 are positive constants.

The time derivative of (26) yields that

$$\begin{aligned} \dot{\sigma}(t) &= \ddot{e}(t) + k_1 \dot{e}(t) + k_2 e(t) \\ &= (\ddot{x}_2(t) - \ddot{x}_{\text{ref}}(t)) + k_1 (\dot{x}_2(t) - \dot{x}_{\text{ref}}(t)) \\ &\quad + k_2 (x_1(t) - x_{\text{ref}}(t)). \end{aligned} \quad (27)$$

Using (1), the above equation can be rewritten as

$$\begin{aligned} \dot{\sigma}(t) = & (f(t, x) + \Delta f(t, x) \\ & + (g(t, x) + \Delta g(t, x))u(t) - \ddot{x}_{\text{ref}}(t)) + k_1(x_2(t) \\ & - \dot{x}_{\text{ref}}(t)) + k_2(x_1(t) - x_{\text{ref}}(t)). \end{aligned} \quad (28)$$

Substituting (8) into (28), the control law is given by

$$\begin{aligned} u(t) = & (g(t, x) + \Delta g(t, x))^{-1} [-f(t, x) - \Delta f(t, x) \\ & + \ddot{x}_{\text{ref}}(t) - k_1(x_2(t) - \dot{x}_{\text{ref}}(t)) \\ & - k_2(x_1(t) - x_{\text{ref}}(t)) - \lambda_1 |\sigma(t)|^{1/2} \text{sign}(\sigma(t)) \\ & - \lambda_2 \sigma(t) + v(t)]. \end{aligned} \quad (29)$$

Theorem 4. Consider a dynamic uncertain second-order system (1) subject both matched and unmatched uncertainties. If the sliding mode surface is selected as (26) and the control input is designed as (29); then, the states variables converge to the trajectories signal and the sliding variable will reach the sliding surface $\sigma(t) = 0$ in finite time.

Proof. Consider the Lyapunov function as follows:

$$V(\sigma, t) = \frac{1}{2} \sigma(t)^2. \quad (30)$$

To ensure that the sliding mode is reached in finite time, the derivative of $V(\sigma, t)$ with respect to time must be negative definite.

Take the time derivative of Lyapunov function $V(\sigma, t)$ as follows:

$$\dot{V}(\sigma, t) = \sigma(t) \dot{\sigma}(t). \quad (31)$$

Substituting (28) into (31), we can obtain

$$\begin{aligned} \dot{V}(\sigma, t) = & \sigma(t) [(f(t, x) + \Delta f(t, x) \\ & + (g(t, x) + \Delta g(t, x))u(t) - \ddot{x}_{\text{ref}}(t)) + k_1(x_2(t) \\ & - \dot{x}_{\text{ref}}(t)) + k_2(x_1(t) - x_{\text{ref}}(t))]. \end{aligned} \quad (32)$$

Substituting equation (29) into (32), it results that

$$\begin{aligned} \dot{V}(\sigma, t) = & \sigma(t) [(g(t, x) + \Delta g(t, x))^{-1} \\ & \cdot (-\lambda_1 |\sigma(t)|^{1/2} \text{sign}(\sigma(t)) - \lambda_2 \sigma(t) + v(t))]. \end{aligned} \quad (33)$$

Using (2) and (9), (33) can be calculated as

$$\begin{aligned} \dot{V}(\sigma, t) \leq & - [(|g(t, x) + \zeta|)^{-1}] \left[\left(\lambda_1 |\sigma(t)|^{3/2} \right. \right. \\ & \left. \left. + \lambda_2 |\sigma(t)|^2 - |\sigma(t)| \frac{\lambda_3}{\lambda_4} (1 - e^{-\lambda_4 t}) \right) \right] \leq - |\sigma(t)| \\ & \cdot (|g(t, x) + \zeta|)^{-1} \left[\lambda_1 |\sigma(t)|^{1/2} + \lambda_2 |\sigma(t)| + \frac{\lambda_3}{\lambda_4} (1 \right. \\ & \left. - e^{-\lambda_4 t}) \right] \end{aligned} \quad (34)$$

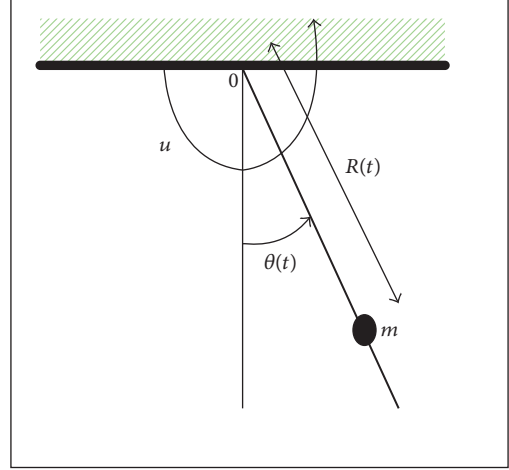


FIGURE 2: Pendulum system.

TABLE 2: Parameters values of the pendulum system.

Notations	Significance	Values
m	The mass	1 kg
g	The acceleration gravity	9.81 m/s ²
R	The distance from $o \rightarrow m$	$0.8 + 0.1 \sin 8t + 0.3 \cos 4t$
θ_{ref}	The reference trajectory	$0.5 \sin 0.5t + 0.5 \cos t$

and then $\dot{V}(\sigma, t)$ can be rewritten as

$$\dot{V}(\sigma, t) \leq -\eta |\sigma(t)|, \quad (35)$$

where $\eta = (|g(t, x) + \zeta|)^{-1} (\lambda_1 |\sigma(t)|^{1/2} + \lambda_2 |\sigma(t)| + (\lambda_3/\lambda_4)(1 - e^{-\lambda_4 t}))$. It is clear from (35) that if $\eta > 0$, then $\dot{V}(\sigma, t)$ is negative definite.

Therefore, we conclude that the sliding mode can be reached in finite time $\sigma(t) = 0$ and the control law as defined in (29) would guarantee that $x(t) \rightarrow x_{\text{ref}}(t)$ when $t \rightarrow \infty$. \square

5. Simulation Results and Discussions

In this section, the effectiveness of our developed algorithm will be illustrated using a pendulum system example. We compare our results with those obtained by other existing methods such as classical and modified STA (MSTA). The pendulum system is driven by an engine installed on the top side, which is called control torque u (see Figure 2) [24]. Thus, the task is tracking some function $\theta_{\text{ref}}(t)$ in real time by the oscillation angle $\theta(t)$ of the rod.

The dynamic equation of the pendulum system is expressed by

$$\ddot{\theta}(t) = -2 \frac{\dot{R}}{R} \dot{\theta}(t) - \frac{g}{R} \sin(\theta(t)) + \frac{1}{mR^2} u(t). \quad (36)$$

The parameters of this system are presented in Table 2.

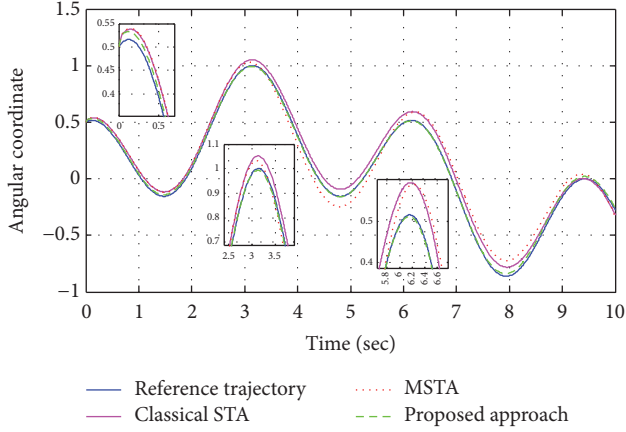


FIGURE 3: The response $x_1(t)$ of the system with matched and unmatched uncertainties.

We consider $x_1(t) = \theta(t)$ and $x_2(t) = \dot{\theta}(t)$; the state space of the pendulum system can be described by

$$\begin{aligned} \dot{x}_1(t) &= x_2(t), \\ \dot{x}_2(t) &= -2\frac{\dot{R}}{R}x_2(t) - \frac{g}{R}\sin(x_1(t)) + \Delta f(t, x) \\ &\quad + \left(\frac{1}{mR^2} + \Delta g(t, x)\right)u(t), \\ y(t) &= x_1(t). \end{aligned} \quad (37)$$

The unmatched and matched uncertainties are chosen by the following equations:

$$\begin{aligned} \Delta f(x, t) &= 0.1 \cos 3t^2 + x_1^2(t) \sin(0.5x_1(t)) \\ &\quad + 0.2 \cos(2x_2^2(t)) + x_2^2(t), \\ \Delta g(t, x) &= 0.1 \cos(2x_1(t)). \end{aligned} \quad (38)$$

According to Assumptions 1 and 2, it can be verified that $\gamma(t, x) = 0.3 + \|x\|^2$ and $\zeta = 0.1$. The bounded uncertainty of the supertwisting algorithm can be selected as $\Theta(t) = (0.1 \sin(2\pi t)) \text{sign}(\sigma(t))$.

In the simulation, the initial values for the state system (37) are selected as $x_1(0) = 0.5$ and $x_2(0) = 1$ and the following parameters are used as $k_1 = 0.2$, $k_2 = 0.01$, $\lambda_1 = 25$, $\lambda_2 = 8$, $\lambda_3 = 2$, and $\lambda_4 = 1$.

Figures 3 and 4 show, respectively, the system state variables $x_1(t)$ and $x_2(t)$ of the pendulum system with both matched and unmatched uncertainties using different approaches. It is easy to see that the angular coordinate and the angular velocity of the system for the three methods converge to desired trajectories without chattering phenomenon despite the presence of uncertainties. For comparison, we can note that the performance results of our proposed method are better than what is reported in [18] and [21].

However, the results of Figures 5 and 6 show that the proposed structure of STA outperform the MSTA. Indeed,

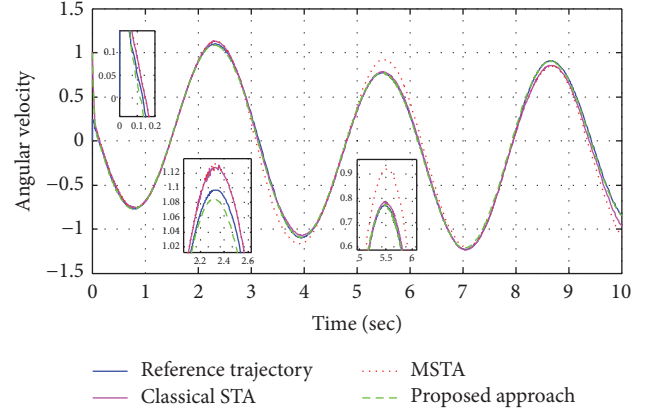


FIGURE 4: The response $x_2(t)$ of the system with matched and unmatched uncertainties.

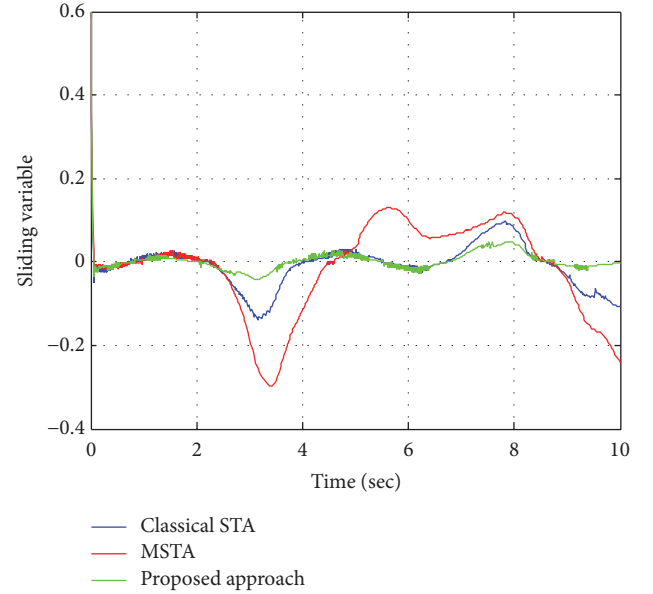


FIGURE 5: Sliding variable $\sigma(t)$.

Figure 5 illustrates the evolution responses of the sliding variable for the different structures of supertwisting algorithm. We can note the novel modified STA given a faster convergence of sliding variable and smallest tracking error (Figure 6) compared to other results obtained by especially using the classical and modified STA [18–21]. A similar analysis can be seen in Table 3. The performance indexes of different methods listed in this table confirm that the novel modified STA has a faster settling time and shorting overshoot. This indicates that the proposed approach is more resistant to uncertainties.

The time evolution of the control signals shown in Figure 7 clearly demonstrates that the case of using the novel structure is producing small vibrations. In addition, the superiority of the new modified STA is shown in Table 4. Consequently, the proposed control method has good performance qualities for the nonlinear model of pendulum

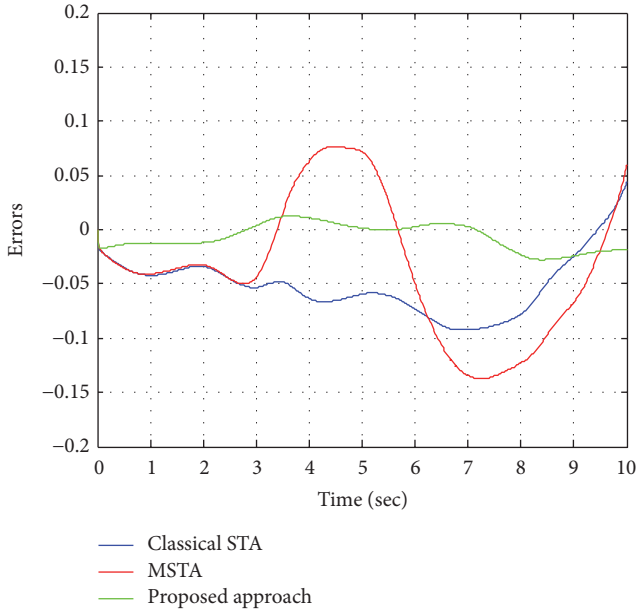
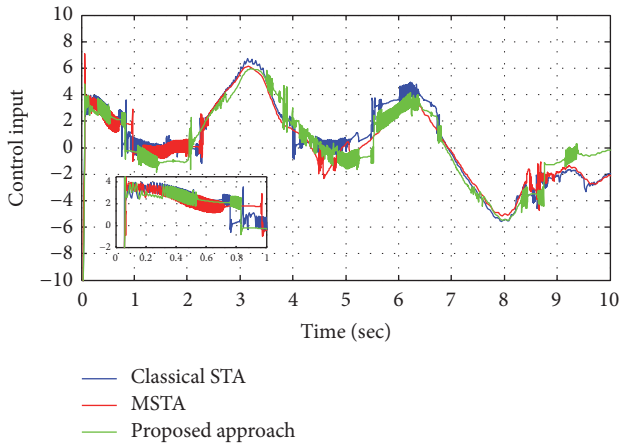
FIGURE 6: Tracking error $e(t)$.FIGURE 7: Control inputs $u(t)$ for pendulum system.

TABLE 3: Comparison performances of the super-twisting algorithm.

Supertwisting algorithm	Overshoot	Settling time
Classical [18]	$D_\sigma = 1.4\%$	$t_{r,\sigma} = 0.8$ sec
	$D_{x_1} = 10\%$	$t_{r,x_1} = 2$ sec
	$D_{x_2} = 30\%$	$t_{r,x_2} = 0.18$ sec
Modified [18–21]	$D_\sigma = 1.12\%$	$t_{r,\sigma} = 0.78$ sec
	$D_{x_1} = 6\%$	$t_{r,x_1} = 0.8$ sec
	$D_{x_2} = 26\%$	$t_{r,x_2} = 0.18$ sec
Proposed approach	$D_\sigma = 0.8\%$	$t_{r,\sigma} = 0.75$ sec
	$D_{x_1} = 2\%$	$t_{r,x_1} = 0.5$ sec
	$D_{x_2} = 10\%$	$t_{r,x_2} = 0.15$ sec

system in the presence of matched and unmatched uncertainties.

TABLE 4: Control effort measures for different structures of STA.

Control input under	Classical STA	Modified STA	Novel modified STA
$\ u\ $	26.41	26.53	26.00

6. Conclusion

In this paper, a new structure of supertwisting algorithm is proposed and applied to an uncertain nonlinear system subject to matched and unmatched uncertainties. The main idea consists of adding two closed-loop feedback terms to the traditional supertwisting with bounded uncertainty in order to ameliorate the performances of the system response. Theoretical analysis is achieved to guarantee the stability using the Lyapunov function. Therefore, a comparative study demonstrates that the proposed approach can improve the convergence of the sliding variable and makes the system faster despite the presence of uncertainties. The proposed approach shows favorable results compared with the methods reported in the literature.

Conflicts of Interest

There are no any conflicts of interest related to this paper.

References

- [1] A. Levant, “Sliding order and sliding accuracy in sliding mode control,” *International Journal of Control*, vol. 58, no. 6, pp. 1247–1263, 1993.
- [2] X. Zhang, “Integral sliding mode control for non-linear systems with mismatched uncertainty based on quadratic sliding mode,” *The Journal of Engineering*, p. 6, 2015.
- [3] J. Huang, Z.-H. Guan, T. Matsuno, T. Fukuda, and K. Sekiyama, “Sliding-mode velocity control of mobile-wheeled inverted-pendulum systems,” *IEEE Transactions on Robotics*, vol. 26, no. 4, pp. 750–758, 2010.
- [4] F. S. Ahmed, S. Laghrouche, and M. El Bagdouri, “Second-order sliding mode based output-feedback control of an engine air path actuator in presence of uncertainties,” in *Proceedings of the 1st Conference on Control and Fault-Tolerant Systems (SysTol’10)*, pp. 50–56, Nice, France, October 2010.
- [5] Y. Niu, Z. Wang, and X. Wang, “Robust sliding mode design for uncertain stochastic systems based on H_∞ control method,” *Optimal Control Applications and Methods*, vol. 31, no. 2, pp. 93–104, 2010.
- [6] A. H. Alqahtani and V. I. Utkin, “Self-optimization of photovoltaic system power generation based on sliding mode control,” in *Proceedings of the 38th Annual Conference on IEEE Industrial Electronics Society (IECON’12)*, pp. 3468–3474, IEEE, Montreal, Canada, October 2012.
- [7] H. Fukushima, K. Muro, and F. Matsuno, “Sliding-mode control for transformation to an inverted pendulum mode of a mobile robot with wheel-arms,” *IEEE Transactions on Industrial Electronics*, vol. 62, no. 7, pp. 4257–4266, 2015.
- [8] S. Wajdi, S. Anis, and G. Garcia, “Robust sliding mode control approach for systems affected by unmatched uncertainties using H_∞ with pole clustering constraints,” *Optimal Control Applications and Methods*, vol. 36, no. 6, pp. 919–935, 2015.

- [9] K. Xing, J. Huang, J. He, Y. Wang, Q. Xu, and J. Wu, "Sliding mode tracking for actuators comprising pneumatic muscle and torsion spring," *Transactions of the Institute of Measurement and Control*, vol. 34, no. 2-3, pp. 255–277, 2012.
- [10] Y. Feng, F. Han, and X. Yu, "Chattering free full-order sliding-mode control," *Automatica*, vol. 50, no. 4, pp. 1310–1314, 2014.
- [11] J. X. Xu, Z. Q. Guo, and T. H. Lee, "Design and implementation of integral sliding-mode control on an underactuated two-wheeled mobile robot," *IEEE Transactions on Industrial Electronics*, vol. 61, no. 7, pp. 3671–3681, 2014.
- [12] H. Lee and V. I. Utkin, "Chattering suppression methods in sliding mode control systems," *Annual Reviews in Control*, vol. 31, no. 2, pp. 179–188, 2007.
- [13] S. Kamal, A. Chalanga, J. Moreno, L. Fridman, and B. Bandyopadhyay, "Higher order super-twisting algorithm," in *Proceedings of the 13th International Workshop on Variable Structure Systems (VSS)*, pp. 1–5, Nantes, France, June 2014.
- [14] S. Kuntanapreeda, "Super-twisting sliding-mode traction control of vehicles with tractive force observer," *Control Engineering Practice*, vol. 38, pp. 26–36, 2015.
- [15] M. Jouini, S. Dhahri, N. Amara, and A. Sellami, "Second order and classical sliding mode control of a MAXPID system: a comparison performance," in *Proceedings of the 15th International Conference on Sciences and Techniques of Automatic Control and Computer Engineering (STA '14)*, pp. 936–941, Hammamet, Tunisia, December 2014.
- [16] L. Derafa, A. Benallegue, and L. Fridman, "Super twisting control algorithm for the attitude tracking of a four rotors UAV," *Journal of The Franklin Institute*, vol. 349, no. 2, pp. 685–699, 2012.
- [17] J. A. Moreno and M. Osorio, "Strict Lyapunov functions for the super-twisting algorithm," *IEEE Transactions on Automatic Control*, vol. 57, no. 4, pp. 1035–1040, 2012.
- [18] J. A. Moreno, "On strict Lyapunov functions for some non-homogeneous super-twisting algorithms," *Journal of The Franklin Institute*, vol. 351, no. 4, pp. 1902–1919, 2014.
- [19] V. I. Utkin and A. S. Poznyak, "Adaptive sliding mode control with application to super-twist algorithm: equivalent control method," *Automatica*, vol. 49, no. 1, pp. 39–47, 2013.
- [20] J. A. Moreno and M. Osorio, "A Lyapunov approach to second-order sliding mode controllers and observers," in *Proceedings of the 47th IEEE Conference on Decision and Control (CDC '08)*, pp. 2856–2861, Cancun, Mexico, December 2008.
- [21] I. Nagesh and C. Edwards, "A multivariable super-twisting sliding mode approach," *Automatica*, vol. 50, no. 3, pp. 984–988, 2014.
- [22] D. Liu, W. Guo, and W. Wang, "Second-order sliding mode tracking control for the piezoelectric actuator with hysteretic nonlinearity," *Journal of Mechanical Science and Technology*, vol. 27, no. 1, pp. 199–205, 2013.
- [23] X. Zheng, X. Jian, D. Wenzheng, and C. Hongjie, "Nonlinear integral sliding mode control for a second order nonlinear system," *Journal of Control Science and Engineering*, vol. 2015, Article ID 218198, pp. 1–7, 2015.
- [24] A. Levant, "Principles of 2-sliding mode design," *Automatica*, vol. 43, no. 4, pp. 576–586, 2007.

Research Article

Tracking Control for Mobile Robots Considering the Dynamics of All Their Subsystems: Experimental Implementation

José Rafael García-Sánchez,¹ Ramón Silva-Ortigoza,¹ Salvador Tavera-Mosqueda,¹
Celso Márquez-Sánchez,¹ Víctor Manuel Hernández-Guzmán,² Mayra Antonio-Cruz,¹
Gilberto Silva-Ortigoza,³ and Hind Taud¹

¹Área de Mecatrónica, CIDETEC, Instituto Politécnico Nacional, Unidad Profesional Adolfo López Mateos,
07700 Ciudad de México, Mexico

²Facultad de Ingeniería, Universidad Autónoma de Querétaro, 76150 Querétaro, QRO, Mexico

³Facultad de Ciencias Físico Matemáticas, Benemérita Universidad Autónoma de Puebla, 72570 Puebla, PUE, Mexico

Correspondence should be addressed to Ramón Silva-Ortigoza; rsilvao@ipn.mx

Received 20 June 2017; Revised 2 September 2017; Accepted 19 September 2017; Published 7 December 2017

Academic Editor: Jinde Cao

Copyright © 2017 José Rafael García-Sánchez et al. This is an open access article distributed under the Creative Commons Attribution License, which permits unrestricted use, distribution, and reproduction in any medium, provided the original work is properly cited.

The trajectory tracking task in a wheeled mobile robot (WMR) is solved by proposing a three-level hierarchical controller that considers the mathematical model of the *mechanical structure* (differential drive WMR), *actuators* (DC motors), and *power stage* (DC/DC Buck power converters). The highest hierarchical level is a kinematic control for the mechanical structure; the medium level includes two controllers based on differential flatness for the actuators; and the lowest hierarchical level consists of two average controllers also based on differential flatness for the power stage. In order to experimentally validate the feasibility of the proposed control scheme, the hierarchical controller is implemented via a Σ - Δ -modulator in a differential drive WMR prototype that we have built. Such an implementation is achieved by using MATLAB-Simulink and the real-time interface ControlDesk together with a DS1104 board. The experimental results show the effectiveness and robustness of the proposed control scheme.

1. Introduction

In recent years, wheeled mobile robots (WMRs) have been widely studied [1–3]. As a matter of fact, diverse applications of WMRs have been reported in many fields like handling explosives or radioactive materials/waste, planetary and maritime exploration, mining and petrochemical industry, medicine, agriculture, home, and entertainment, among others [4–7]. On one hand, control of WMRs is not an easy task since their models are nonlinear and are subject to nonholonomic constraints [8, 9]. Despite these difficulties, significant advances have been achieved in the design of controllers solving several problems associated with a WMR:

regulation, path following, obstacle avoidance, and trajectory tracking.

Nevertheless, to the best of the authors' knowledge, any of the control schemes reported with experiments until now have not taken into account the full dynamics of the three subsystems composing, in general, a WMR, that is, (a) *mechanical structure*, (b) *actuators*, and (c) *power stage*. This is because most controllers solving the aforementioned problems have been designed by only taking into account the kinematic/dynamic model of the WMR mechanical structure and just few others have been designed by taking into account the actuators mathematical model. This means that importance of the power stage has been neglected. However, it is stated in [10] that taking into account the power stage

dynamics in the design of control algorithms for mechatronic systems leads to important improvements. Moreover, not only dynamics of the power stage but also, if required, dynamics associated with the electric power generation should be considered. This is, by itself, an important current research topic [11–19].

One of the main reasons why dynamics associated with power stage and electric power generation are not considered when designing controllers for WMRs is that the resulting mathematical model becomes more complex and, hence, design of the control algorithm also becomes more complex. However, consideration of dynamics associated with these subsystems could lead to new research areas where the power electronics would play an important role with regard to the storage, distribution, and transformation of electrical energy [20–28]. Some approximations in this direction are presented in [29, 30], where dynamics associated with actuators, power stage, and electric power generation are considered in mechatronic systems.

The remainder of this paper is organized as follows. Previous works on trajectory tracking for WMRs are reviewed in Section 2, while a discussion on such a literature and contribution of the present paper are given in Section 3. In Section 4, design of a three-level hierarchical controller that solves the trajectory tracking task in a WMR is presented. Some experimental results obtained when controlling a WMR prototype that we have built are shown in Section 5. Finally, conclusions are given in Section 6.

2. Literature Review

With the purpose of underlining contribution of the present paper, an exhaustive review of the more relevant literature on trajectory tracking in differential drive WMRs is presented below. Two main approaches related to the mechanical structure have been proposed: (i) design based on the WMR kinematic model and (ii) design based on the WMR dynamic model. Thus, the state-of-the-art review is based on whether or not dynamics associated with the other two WMR subsystems, that is, the actuators and the power stage, are taken into account.

2.1. Considering Only the Mechanical Structure. This subsection describes previous works related to the trajectory tracking task, where the mathematical model, either kinematic or dynamic, of only the mechanical structure of a differential drive WMR is employed.

2.1.1. Kinematic Model. Papers that take into account the kinematic model of a differential drive WMR when designing control algorithms are considered here. Kanayama et al. [31] proposed a stable tracking control strategy to determine the linear and rotational velocities of a vehicle. They have also shown through numerical simulations that their controller is still effective when there are small disturbances. Samson and Ait-Abderrahim [32] introduced a feedback controller designed on the basis of a virtual reference for position and orientation. Murray and Sastry [33] reported a methodology

to represent a WMR in chained form. They have also succeeded to track a preestablished trajectory by using sinusoids as control inputs. A robust controller based on sliding modes was proposed by Chacal and Sira-Ramírez [34], where the system differential flatness property is used and stochastic perturbation signals are considered. Walsh et al. [35] designed an exponentially stable control law. Jiang and Nijmeijer [36] introduced two controllers based on backstepping, a local one and a global one. Both controllers achieve exponential convergence. Kim and Oh [37] developed a modified input-output linearization controller for nonsquare systems, where the three state variables are considered as outputs. Jiang and Nijmeijer [38] focused on a recursive technique to solve the trajectory tracking and path following tasks when the system is represented in a chained form. This was carried out through a coordinate transformation. Dixon et al. [39] implemented a differentiable kinematic control law that uses a damped dynamic oscillator, which achieves the exponential convergence of the tracking and regulation errors to a neighborhood of the origin. Another work introduced by Dixon et al. [40] dealt with a differentiable kinematic control law that allows simultaneously solving the trajectory tracking and regulation problems, exponentially for the first one and asymptotically for the second one. Additionally, Dixon et al. [41] elaborated a variable structure-like tracking controller that is robust under parametric uncertainty, also with exponential convergence of the tracking and regulation errors to the origin. In [42], Lee et al. solved the trajectory tracking and regulation problems via a backstepping control. By using polar coordinates, Chwa [43] designed a pair of discontinuous controllers to asymptotically stabilize the trajectory tracking errors in position and in the heading direction. Thus, the trajectory tracking and stabilization problems were solved. Klančar and Škrjanc [44] proposed a model-predictive trajectory tracking control, where the linearized tracking error dynamics is used to predict the behavior of a WMR. Another solution of the trajectory tracking task was carried out by Tsai et al. [45], where a robust visual tracking control to track a dynamic moving object was considered. Lee et al. [46] carried out a sliding mode control by using an RFID sensor space to estimate the position of a WMR. Recently, Scaglia et al. [47] suggested a linear interpolation based methodology to design control algorithms. It is assumed that the evolution of the system can be approximated by a linear interpolation. Hence, the tracking errors can be reduced by decreasing the sampling time. Cheng et al. [48] suggested a feedback control law via Lyapunov's direct method and backstepping, achieving global asymptotic stability. Lastly, Chwa [49] studied a fuzzy adaptive tracking controller by considering the slippage between the wheels and the surface. Other relevant papers concerning the controller design by using only the kinematic model of the mechanical structure are [50–59].

2.1.2. Dynamic Model. One of the first papers where the dynamic model of a WMR was taken into account for the design of a controller was by d'Andréa-Novel et al. [60], who obtained the WMR dynamic model through the Euler-Lagrange formulation. In addition, they introduced a control law based on static state feedback. Fierro and Lewis [61]

elaborated a kinematic/torque control law using backstepping to solve the trajectory tracking, path following, and stabilization problems. Yang and Kim [62] suggested a sliding mode controller, which is robust to bounded external disturbances. Dong et al. [63] developed an adaptive robust controller that does not require exactly knowing the WMR physical parameters. Dixon et al. [64] dealt with a visual servoing controller that adapts to the parametric uncertainty associated with the camera and with the mechanical parameters of the WMR dynamic model. Likewise, Pourboghrat and Karlsson [65] elaborated a robust adaptive controller to solve the trajectory tracking and stabilization problems. Dong and Kuhnert [66] focused on the design of an adaptive neural network control that is robust to parametric uncertainty. Chen et al. [67] proposed a kinematic control to generate the desired velocity profiles for the wheels. They also formulated an adaptive sliding mode controller that allows the real velocities to reach the desired ones. Solea et al. [68] presented a robust sliding mode controller when there are external disturbances and parametric uncertainty in the WMR. Recently, Cao et al. [69] developed an adaptive kinematic controller (based on the backstepping method) and a dynamic adaptive controller. The latter allows reaching the desired velocity profiles imposed by the former. Shojaei et al. [70] designed a control algorithm, robust under parametric and nonparametric uncertainty, which combines an inverse dynamics control and an adaptive robust PID control. Finally, other contributions that employ the dynamic model only of the WMR mechanical structure in the control design can be found in [71–80].

2.2. Considering the Mechanical Structure and Actuators. It has not been common to take into account the dynamics of the actuators in research related to WMRs. However, it is important to highlight that the exclusion of this dynamics can cause degradation in the performance of a robot [81] and even can produce system instability [82–84]. Few papers have incorporated such dynamics into the control algorithms when the kinematic or dynamic model of the WMR is considered. This subsection reviews the research that has employed the mathematical model of both the mechanical structure and the actuators in the trajectory tracking control design for differential drive WMRs.

2.2.1. Kinematic Model. By considering both the mechanical structure and the actuators, Espinosa et al. [85] designed an adaptive optimal controller in the drive control loop and an optimal-fuzzy control for the trajectory tracking task for a wheelchair when there are obstacles in the workspace. Silva-Ortigoza et al. [86] designed a two-stage controller where the first stage corresponds to a control based on input-output linearization for the mechanical structure and the second stage refers to a controller based on differential flatness for the actuators. Recently, Zuo et al. [87] described a control strategy that integrates a kinematic control and an adaptive wavelet neural network, which is robust to disturbances. Lastly, Silva-Ortigoza et al. [88] proposed a robust hierarchical

controller where the high-level control is based on input-output linearization for the mechanical structure and the low-level control is based on a PI control for the actuators.

2.2.2. Dynamic Model. Taking into account both the dynamic model of the mechanical structure and the mathematical model of the actuators during the control design stage for the WMR is not easy, since control design becomes more complex. However, it allows designing controllers that solve the trajectory tracking problem more effectively. This can be observed when the WMR is moving at high speeds or when its mass is variable [89]. Motivated by these facts, Anupoju et al. [90] designed three adaptive controllers, the first one for the kinematic model of the mechanical structure, the second one for the dynamic model of that same mechanical structure, and the third one for the actuators. Das and Kar [91] formulated an adaptive fuzzy logic-based controller. Hou et al. [92] proposed a robust adaptive controller via backstepping and a fuzzy logic approach. More recently, Luo et al. [93] elaborated an adaptive neural network dynamic surface controller based on a disturbance observer, where uncertain parameters were taken into account. Lastly, other contributions that take into account the dynamic model of the mechanical structure and the dynamics of the actuators in the control design are reported in [94–103].

2.3. Considering the Mechanical Structure, Actuators, and Power Stage. Few controllers have considered the mathematical models of the three subsystems that compose a WMR. In such controllers, only the kinematic model of the WMR has been used.

2.3.1. Kinematic Model. Ortigoza et al. in [104] presented a trajectory tracking controller by considering an input-output linearization-based controller for the mechanical structure, a controller based on differential flatness for the actuators, and a sliding mode plus PI controller for the power stage. In [105], Sánchez et al. proposed a kinematic controller for the WMR, a controller based on differential flatness for the actuators, and a differential flatness-based controller for the power stage. Controllers reported in [104, 105] were tested only via numerical simulations.

3. Discussion and Contribution

After carrying out the review of the literature associated with design of controllers for the trajectory tracking task in differential drive WMRs, it was found that, generally, this task has been solved in three directions: (a) by only using the kinematic or dynamic model of the mechanical structure [31–80], (b) by employing the kinematic/dynamic model of the mechanical structure along with the dynamics of the actuators [85–103], and (c) by considering the kinematic model of the mechanical structure along with the dynamics of the actuators and power stage [104, 105]. In the last direction, contributions that have carried out interesting efforts are [106–114]. However, those papers only focus on the design of the power stage without considering the other dynamics.

Motivated by the aforementioned ideas, the hierarchical control approach in mobile robotics (see [86, 104, 105, 115]), and use of DC/DC converter-DC motor systems (see [116, 117]), the purpose of the present paper is threefold. First, it aims, to introduce a three-level hierarchical controller that considers dynamics of the three subsystems that compose a WMR to solve, in a more complete way, the trajectory tracking task. Second, it aims, to experimentally validate the proposed controller by implementing it in a WMR prototype that we have built, where the experimental results show the effectiveness and robustness of the designed hierarchical controller. Third, it aims, to experimentally compare to results associated with a controller that neglects dynamics of the power stage. After an assessment of the results, it is observed that the performance of the WMR with the hierarchical controller is better than, or at least similar to, the one achieved with the control that neglects the dynamics of the power stage.

4. Hierarchical Trajectory Tracking Control via Σ - Δ -Modulator Considering the Dynamics of All the WMR Subsystems

A hierarchical trajectory tracking controller for a differential drive WMR is presented in this section, which is designed by considering dynamics of all of the subsystems that integrate a WMR. The system under study is shown in Figure 1, where the three subsystems can be seen, that is, mechanical structure (differential drive WMR), actuators (DC motors), and power stage (DC/DC Buck power converters). In such a figure, and in the remainder of this paper, the parameters, components, and variables associated with the right Buck converter-DC motor and left Buck converter-DC motor are distinguished by the subscripts r and l , respectively. The design of the hierarchical controller is carried out as follows:

- (1) At the highest hierarchical level, a kinematic controller for the mechanical structure delivers the desired DC motor angular velocities ω_r and ω_l . If velocities of wheels reach these values, then the WMR tracks the desired trajectory; that is, $(x, y, \varphi) \rightarrow (x^*, y^*, \varphi^*)$.
- (2) At the medium level, two flatness-based controllers deliver ϑ_r and ϑ_l , the desired voltage profiles that the Buck converters output voltages have to track. If these desired voltages are reached, then the angular velocities of the DC motors track the desired angular velocity profiles; that is, $(\omega_r, \omega_l) \rightarrow (\omega_r, \omega_l)$.
- (3) At the lowest level, two flatness-based average controllers deliver u_{av_r} and u_{av_l} which ensure that the Buck converters output voltages track the desired voltage profiles; that is, $(v_r, v_l) \rightarrow (\vartheta_r, \vartheta_l)$.

In order to accomplish the trajectory tracking task for the WMR, the controllers designed in (1)–(3) are interconnected using a hierarchical approach. The switched implementation of the resulting controller is performed at the Buck converters by using the Σ - Δ -modulator [118].

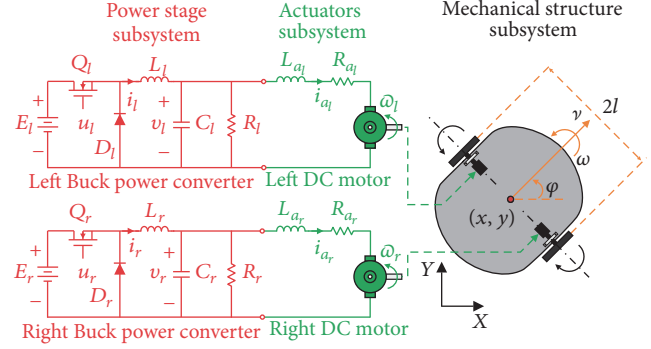


FIGURE 1: WMR complete system.

4.1. Control at the Highest Hierarchical Level: Mechanical Structure. In this subsection, a kinematic controller that solves the trajectory tracking task in a WMR is presented.

The kinematic model of a differential drive WMR, which moves without slipping on the XY plane, is given by [119]

$$\begin{aligned} \dot{x} &= \nu \cos \varphi, \\ \dot{y} &= \nu \sin \varphi, \\ \dot{\varphi} &= \omega, \end{aligned} \quad (1)$$

with the inputs

$$\begin{pmatrix} \nu \\ \omega \end{pmatrix} = \begin{pmatrix} \frac{r}{2} & \frac{r}{2} \\ \frac{r}{2l} & -\frac{r}{2l} \end{pmatrix} \begin{pmatrix} \omega_r \\ \omega_l \end{pmatrix}, \quad (2)$$

where (x, y) is the position of the midpoint of the axis which joins the wheels and φ is the orientation of the WMR. Also, r is radius of the driving wheels and $2l$ is distance between them, while ω_r and ω_l are the right and left angular velocities of the wheels, respectively. Lastly, ν is the straight line velocity and ω is the angular velocity, both of the WMR (see Figure 1). In these equations, and in the remainder of this paper, the derivative with respect to time t will be denoted by a “dot” or by d/dt .

The control objective is tracking of the following reference robot:

$$\begin{aligned} \dot{x}^* &= \nu^* \cos \varphi^*, \\ \dot{y}^* &= \nu^* \sin \varphi^*, \\ \dot{\varphi}^* &= \omega^*, \end{aligned} \quad (3)$$

where (x^*, y^*) and φ^* represent the pose and orientation, respectively, of the reference robot, whereas ν^* and ω^* are its reference inputs. Thus, in accordance with [98], the following error signals are defined:

$$\begin{pmatrix} e_1 \\ e_2 \\ e_3 \end{pmatrix} = \begin{pmatrix} K_2 \cos \varphi & K_2 \sin \varphi & 0 \\ -K_2 \sin \varphi & K_2 \cos \varphi & \alpha \\ 0 & 0 & 1 \end{pmatrix} \begin{pmatrix} x^* - x \\ y^* - y \\ \varphi^* - \varphi \end{pmatrix}, \quad (4)$$

with K_2 and α being positive constants. In (4), the matrix is globally nonsingular because its determinant is equal to K_2^2 . The time derivative of (4) is given as

$$\begin{pmatrix} \dot{e}_1 \\ \dot{e}_2 \\ \dot{e}_3 \end{pmatrix} = \begin{pmatrix} -K_2 & e_2 - \alpha e_3 \\ 0 & -e_1 - \alpha \\ 0 & -1 \end{pmatrix} \begin{pmatrix} \nu \\ \omega \end{pmatrix} + \begin{pmatrix} \nu^* K_2 \cos e_3 \\ K_2 \nu^* \sin e_3 + \alpha \omega^* \\ \omega^* \end{pmatrix}, \quad (5)$$

where (1) and (3) have been used. The following control inputs have been retaken from [71]:

$$\begin{aligned} \nu &= \nu^* \cos e_3 + K_1 e_1, \\ \omega &= \omega^* + \nu^* K_2 e_2 + K_3 \sin e_3, \end{aligned} \quad (6)$$

with K_1 and K_3 being positive constants. In [98], the following positive function was defined:

$$V(e_1, e_2, e_3) = \frac{1}{2}e_1^2 + \frac{1}{2}e_2^2 + (1 - \cos e_3). \quad (7)$$

Through the analysis of its time derivative, \dot{V} , along trajectories (5), when (6) are considered as control inputs, it was shown that the error dynamics (5) is asymptotically stable; that is, $(e_1, e_2, e_3) = (0, 0, 0)$, since matrix in (4) is nonsingular. This fact implies that system (1) in closed loop with (6) achieves that $(x, y, \varphi) \rightarrow (x^*, y^*, \varphi^*)$ when $t \rightarrow \infty$. Likewise, according to the stability analysis carried out in [98], it was shown that $\alpha = 1/K_3$ and ν^* must be greater than 0.

Lastly, by substituting (6) in (2), after some mathematical manipulation, the controls are transformed into the right and left angular velocities to be used as inputs. That is,

$$\omega_r = \frac{\nu^* (\cos e_3 + lK_2 e_2) + l(\omega^* + K_3 \sin e_3) + K_1 e_1}{r}, \quad (8)$$

$$\omega_l = \frac{\nu^* (\cos e_3 - lK_2 e_2) - l(\omega^* + K_3 \sin e_3) + K_1 e_1}{r}. \quad (9)$$

4.2. Control at the Medium Level: Actuators. The objective of this subsection is to design a controller ensuring that the actual angular velocities of the DC motors $(\bar{\omega}_r, \bar{\omega}_l)$ track the desired angular velocity profiles imposed by the WMR kinematic control (ω_r, ω_l) ; that is, $(\bar{\omega}_r, \bar{\omega}_l) \rightarrow (\omega_r, \omega_l)$.

The mathematical model of a DC motor expressed in terms of the angular velocity [119], $\bar{\omega}$, is given by

$$\begin{aligned} L_a \frac{di_a}{dt} &= \vartheta - R_a i_a - k_e \bar{\omega}, \\ J \frac{d\bar{\omega}}{dt} &= -b\bar{\omega} + k_m i_a, \end{aligned} \quad (10)$$

where ϑ is the input voltage of the motor, i_a is the armature current, k_e is the counterelectromotive force constant, k_m is

the motor torque constant, L_a is the armature inductance, R_a is the armature resistance, J is the moment of inertia of the rotor and motor load, and b is the viscous friction coefficient of the motor.

Since the aforementioned parameters are required for control design and manufacturer does not provide them, in this paper such parameters are obtained via the experimental characterization of the DC motor. For such an aim, a first-order approximation of (10) is considered by assuming that armature inductance may be neglected [120]. That is,

$$\frac{d\bar{\omega}}{dt} = -\mu\bar{\omega} + \gamma\vartheta, \quad (11)$$

where

$$\mu = \frac{1}{\tau}, \quad (12)$$

$$\gamma = \frac{K}{\tau},$$

$$\tau = \frac{JR_a}{bR_a + k_e k_m}, \quad (13)$$

$$K = \frac{k_m}{bR_a + k_e k_m}.$$

In order to get the numerical values of the parameters τ and K , an experimental characterization must be done. The corresponding values of τ and K associated with the right motor characterization are

$$\begin{aligned} \tau_r &= 98 \times 10^{-3}, \\ K_r &= 540 \times 10^{-3}, \end{aligned} \quad (14)$$

and for the left motor

$$\begin{aligned} \tau_l &= 98 \times 10^{-3}, \\ K_l &= 590 \times 10^{-3}. \end{aligned} \quad (15)$$

In this manner, using (11), (12), (14), and (15), the first-order dynamic models of the DC motors are given by

$$\frac{d\bar{\omega}_r}{dt} = -10.2\bar{\omega}_r + 5.5\vartheta_r, \quad (16)$$

for the right motor and

$$\frac{d\bar{\omega}_l}{dt} = -10.2\bar{\omega}_l + 6\vartheta_l, \quad (17)$$

for the left motor.

On the other hand, with the intention to achieve $(\bar{\omega}_r, \bar{\omega}_l) \rightarrow (\omega_r, \omega_l)$, a differential flatness-based control [119, 121, 122] is proposed for the first-order linear system (11). To this end, the dynamics (11) is rewritten in terms of the flat output $F_1 = \bar{\omega}$, as

$$\vartheta = \frac{\dot{F}_1 + \mu F_1}{\gamma}. \quad (18)$$

If the control input ϑ is chosen as

$$\vartheta = \frac{\delta + \mu F_1}{\gamma} \quad (19)$$

and it is replaced in (18), then the tracking problem related to the angular velocity of the DC motor is reduced to control the following system:

$$\dot{F}_1 = \delta, \quad (20)$$

where δ is an auxiliary control. In order to ensure that $F_1 \rightarrow F_1^*$ when $t \rightarrow \infty$, a proper selection for δ is

$$\delta = \dot{F}_1^* - k_p (F_1 - F_1^*) - k_i \int_0^t (F_1 - F_1^*) d\sigma, \quad (21)$$

with F_1^* being the desired angular velocity, that is, either ω_r or ω_l for the right or the left motor, respectively, and (k_p, k_i) positive constants. Once (21) is replaced in (20), the tracking error is defined as $e_m = F_1 - F_1^*$, and the derivative with respect to time of the resulting expression is calculated. Then, the following tracking error dynamics is obtained:

$$\ddot{e}_m + k_p \dot{e}_m + k_i e_m = 0, \quad (22)$$

whose characteristic polynomial is

$$p_{c_1}(s) = s^2 + k_p s + k_i. \quad (23)$$

By equating (23) with a Hurwitz polynomial defined by

$$p_{d_1}(s) = s^2 + 2\xi_1 \omega_{n_1} s + \omega_{n_1}^2, \quad (24)$$

where $(\xi_1, \omega_{n_1}) > 0$, not only is $F_1 \rightarrow F_1^*$ achieved, but also the gains k_p and k_i are found. That is,

$$\begin{aligned} k_p &= 2\xi_1 \omega_{n_1}, \\ k_i &= \omega_{n_1}^2. \end{aligned} \quad (25)$$

4.3. Control at the Lowest Hierarchical Level: Power Stage. The purpose of this subsection is to propose a controller that allows the actual output voltages of the Buck converters (v_r, v_l) to track the desired voltage profiles $(\vartheta_r, \vartheta_l)$ imposed by controllers of the DC motors; that is, $(v_r, v_l) \rightarrow (\vartheta_r, \vartheta_l)$.

According to [118], the average dynamics of a Buck converter are given as

$$\begin{aligned} L \frac{di}{dt} &= -v + E u_{av}, \\ C \frac{dv}{dt} &= i - \frac{v}{R}, \end{aligned} \quad (26)$$

where i is electric current through the inductor L , v is the output voltage of the converter associated with the capacitor C , R is the load resistance, and E is voltage of the converter power supply. Variable u_{av} represents the switch position, which is an average signal that satisfies $u_{av} \in [0, 1]$. It is important to mention that the switched model of the Buck converter is

obtained when u_{av} is replaced by u in (26), with u being a signal that takes values in the discrete set $\{0, 1\}$.

In order to design a differential flatness-based controller for the converter [119, 123–125], the dynamics (26) is represented in terms of the flat output $F_2 = v$, as follows:

$$u_{av} = \frac{LC}{E} \ddot{F}_2 + \frac{L}{RE} \dot{F}_2 + \frac{1}{E} F_2, \quad (27)$$

with the suitable definition of u_{av} , given by

$$u_{av} = \frac{LC}{E} \eta + \frac{L}{RE} \dot{F}_2 + \frac{1}{E} F_2. \quad (28)$$

After replacing (28) in (27), the tracking problem, associated with the output voltage of the Buck converter, is reduced to control the system given by

$$\ddot{F}_2 = \eta. \quad (29)$$

In order to achieve that $F_2 \rightarrow F_2^*$ when $t \rightarrow \infty$, with F_2^* being the desired voltage profile at the converter output, that is, either ϑ_r or ϑ_l for the right or left Buck converters, respectively, a convenient proposal of η is

$$\begin{aligned} \eta &= \ddot{F}_2^* - \beta_2 (\dot{F}_2 - \dot{F}_2^*) - \beta_1 (F_2 - F_2^*) \\ &\quad - \beta_0 \int_0^t (F_2 - F_2^*) d\sigma. \end{aligned} \quad (30)$$

When (30) is substituted into (29) and after defining the tracking error as $e_c = F_2 - F_2^*$, the following tracking error dynamics is obtained:

$$\ddot{e}_c + \beta_2 \dot{e}_c + \beta_1 e_c + \beta_0 e_c = 0, \quad (31)$$

whose characteristic polynomial is

$$p_{c_2}(s) = s^3 + \beta_2 s^2 + \beta_1 s + \beta_0, \quad (32)$$

which is forced to be stable by equating it with a Hurwitz polynomial to achieve $F_2 \rightarrow F_2^*$, defined by

$$p_{d_2}(s) = (s + a_2) (s^2 + 2\xi_2 \omega_{n_2} s + \omega_{n_2}^2), \quad (33)$$

with $a_2 > 0$, $\xi_2 > 0$, and $\omega_{n_2} > 0$. Hence, the gains β_2 , β_1 , and β_0 are determined by

$$\begin{aligned} \beta_2 &= a_2 + 2\xi_2 \omega_{n_2}, \\ \beta_1 &= 2\xi_2 \omega_{n_2} a_2 + \omega_{n_2}^2, \\ \beta_0 &= a_2 \omega_{n_2}^2. \end{aligned} \quad (34)$$

4.4. Hierarchical Tracking Control. In this subsection, controllers designed in Sections 4.1, 4.2, and 4.3 are integrated using a hierarchical approach (see [86, 104, 105, 115–117]) to solve the trajectory tracking task for a differential drive WMR when dynamics associated with each one of subsystems composing the WMR are considered (see Figure 1).

Using the kinematic models associated with a differential drive WMR (1) and a reference robot (3), it was found that

velocity profiles ω_r and ω_l , ensuring $(x, y, \varphi) \rightarrow (x^*, y^*, \varphi^*)$, are given by (8) and (9), respectively. On the other hand, profiles of voltages ϑ_r and ϑ_l that applied to DC motors ensure $(\bar{\omega}_r, \bar{\omega}_l) \rightarrow (\omega_r, \omega_l)$ are given, according to (19) and (21), as

$$\vartheta_r = \frac{\delta_r + \mu_r \bar{\omega}_r}{\gamma_r}, \quad (35)$$

$$\vartheta_l = \frac{\delta_l + \mu_l \bar{\omega}_l}{\gamma_l}, \quad (36)$$

with the auxiliary controls δ_r and δ_l defined by

$$\delta_r = \dot{\bar{\omega}}_r^* - k_{p_r} (\bar{\omega}_r - \bar{\omega}_r^*) - k_{i_r} \int_0^t (\bar{\omega}_r - \bar{\omega}_r^*) d\sigma, \quad (37)$$

$$\delta_l = \dot{\bar{\omega}}_l^* - k_{p_l} (\bar{\omega}_l - \bar{\omega}_l^*) - k_{i_l} \int_0^t (\bar{\omega}_l - \bar{\omega}_l^*) d\sigma, \quad (38)$$

where

$$(\bar{\omega}_r^*, \bar{\omega}_l^*) = (\omega_r, \omega_l). \quad (39)$$

Likewise, since each DC motor is driven by a Buck converter, it is found from (28) and (30) that the actual voltages at the converters outputs are ensured to converge to their desire profiles; that is, $(v_r, v_l) \rightarrow (\vartheta_r, \vartheta_l)$, if the converter transistors are commuted according to u_{av_r} and u_{av_l} , which are given as

$$u_{av_r} = \frac{L_r C_r}{E_r} \eta_r + \frac{L_r}{R_r E_r} \dot{v}_r + \frac{1}{E_r} v_r, \quad (40)$$

$$u_{av_l} = \frac{L_l C_l}{E_l} \eta_l + \frac{L_l}{R_l E_l} \dot{v}_l + \frac{1}{E_l} v_l, \quad (41)$$

with the auxiliary controls η_r and η_l defined by

$$\eta_r = \ddot{v}_r^* - \beta_{2_r} (\dot{v}_r - \dot{v}_r^*) - \beta_{1_r} (v_r - v_r^*) - \beta_{0_r} \int_0^t (v_r - v_r^*) d\sigma, \quad (42)$$

$$\eta_l = \ddot{v}_l^* - \beta_{2_l} (\dot{v}_l - \dot{v}_l^*) - \beta_{1_l} (v_l - v_l^*) - \beta_{0_l} \int_0^t (v_l - v_l^*) d\sigma, \quad (43)$$

where

$$(v_r^*, v_l^*) = (\vartheta_r, \vartheta_l). \quad (44)$$

Finally, since controllers (40) and (41) have been designed on the basis of average models of the Buck converters, the corresponding switched implementations, u_r and u_l , are achieved using a Σ - Δ -modulator [118]. Hence, both signals u_r and u_l only take values in the discrete set $\{0, 1\}$. Thus,

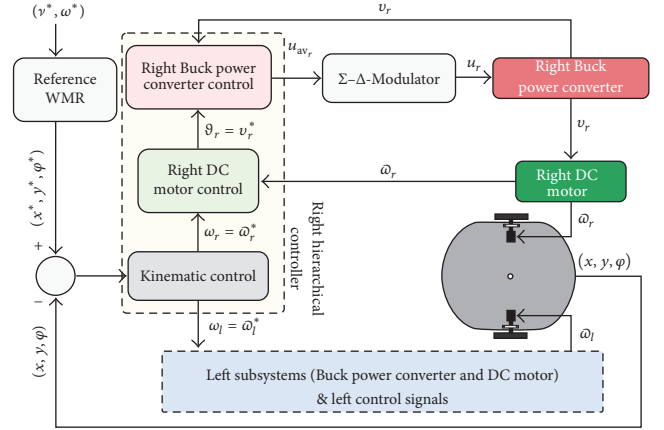


FIGURE 2: Block diagram of the hierarchical controller along with the WMR.

synthesis of the average controllers (40) and (41) via a Σ - Δ -modulator is given as

$$u_r = \frac{1}{2} [1 + \text{sign}(e_r)], \quad (45)$$

$$\dot{e}_r = u_{av_r} - u_r,$$

$$u_l = \frac{1}{2} [1 + \text{sign}(e_l)], \quad (46)$$

$$\dot{e}_l = u_{av_l} - u_l.$$

In summary, the switched controllers (45)-(46) ensure that $(v_r, v_l) \rightarrow (\vartheta_r, \vartheta_l)$, so that $(\bar{\omega}_r, \bar{\omega}_l) \rightarrow (\omega_r, \omega_l)$. In consequence, the control objective for the WMR is attained; that is, $(x, y, \varphi) \rightarrow (x^*, y^*, \varphi^*)$. The integration of the hierarchical controller is shown in the block diagram presented in Figure 2.

5. Experimental Results

In this section, some experiments are presented intended to evaluate performance achieved by the hierarchical controller that has been designed. Controller (8)-(9), (35)-(36), and (45)-(46) has been tested on the WMR prototype shown in Figure 3. This prototype has, as power stage, two DC/DC Buck power converters. Controller reported in [98] is also tested for comparison purposes. Since controller in [98] is designed without taking into account the power stage dynamics, another WMR prototype is employed, which possesses H-bridges instead of DC/DC Buck power converters. See Figure 4.

5.1. Experimental Results of the Hierarchical Controller.

Implementation of the hierarchical controller was carried out in the differential drive WMR prototype shown in Figure 3, which was designed and built at the Mechatronics Laboratory of CIDETEC-IPN.

The WMR prototype shown in Figure 3 is 0.39 m in length, 0.36 m in width, and 0.35 m in height, and its total

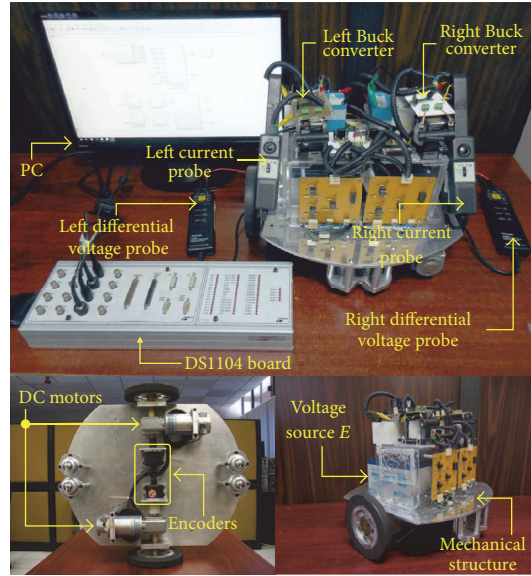


FIGURE 3: A differential drive WMR prototype with a power stage composed by DC/DC Buck power converters.

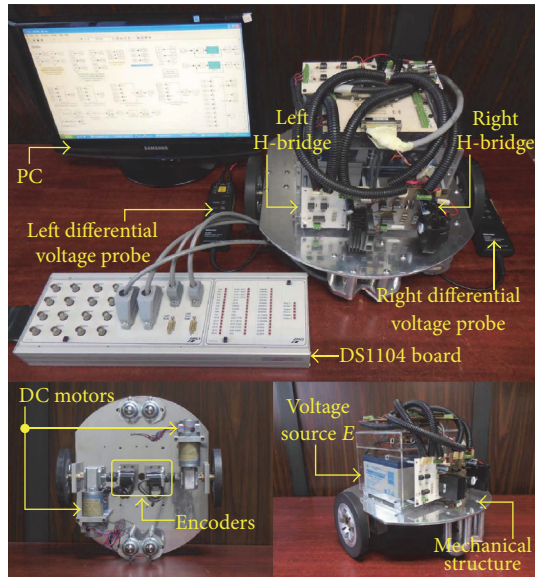


FIGURE 4: A differential drive WMR prototype with a power stage composed by H-bridges.

mass is 19 kg. Parameters related to the wheels used in controls (8) and (9) are given by

$$\begin{aligned} r &= 0.075 \text{ m}, \\ 2l &= 0.40 \text{ m}. \end{aligned} \quad (47)$$

Both wheels of the prototype are actuated by brushed DC motors GNM3150+G2.6 (24 V, 55 W) which are provided with a 20:1 gearbox, whose angular velocities are measured

via Autonics E50S8-1000 incremental encoders. Parameters associated with DC motors, used in (35) and (36), are

$$\begin{aligned} \mu_r &= 10.2, \\ \gamma_r &= 5.5, \\ \mu_l &= 10.2, \\ \gamma_l &= 6. \end{aligned} \quad (48)$$

Likewise, each motor is driven by a DC/DC Buck power converter, whose voltages (v_r, v_l) and currents (i_r, i_l) are measured by Tektronix P5200A voltage probes and Tektronix A622 current probes, respectively. Parameters associated with Buck converters, used in switched controls (45), are

$$\begin{aligned} L_r &= 10.129 \times 10^{-3} \text{ H}, \\ L_l &= 10.6 \times 10^{-3} \text{ H}, \\ C_r = C_l &= 220 \times 10^{-6} \text{ F}, \\ R_r = R_l &= 100 \Omega, \\ E_r = E_l &= 28 \text{ V}. \end{aligned} \quad (49)$$

Figure 3 also shows connections of the WMR prototype to the DS1104 board, Matlab-Simulink, and ControlDesk.

On the other hand, gains of the high-level controller (8) and (9) were selected as

$$\begin{aligned} K_1 &= 3, \\ K_2 &= 5, \\ K_3 &= 3, \end{aligned} \quad (50)$$

while gains associated with the medium-level controllers (35) and (36) were obtained by selecting their parameters as follows:

$$\begin{aligned}\xi_{1_r} &= \xi_{1_l} = 0.75, \\ \omega_{n_{1_r}} &= \omega_{n_{1_l}} = 20.\end{aligned}\quad (51)$$

Lastly, gains of the low-level controllers (45) were proposed by choosing the following parameters:

$$\begin{aligned}a_{2_r} &= a_{2_l} = 180, \\ \xi_{2_r} &= \xi_{2_l} = 100, \\ \omega_{n_{2_r}} &= \omega_{n_{2_l}} = 200.\end{aligned}\quad (52)$$

The desired trajectory that is imposed on the WMR is generated from the reference velocities v^* and ω^* determined by the following Bézier polynomials:

$$\begin{aligned}p_v(t) &= \bar{v}(t_i) + [\bar{v}(t_f) - \bar{v}(t_i)] \psi(t, t_i, t_f), \\ p_\omega(t) &= \bar{\omega}(t_i) + [\bar{\omega}(t_f) - \bar{\omega}(t_i)] \psi(t, t_i, t_f),\end{aligned}\quad (53)$$

where t_i and t_f are the initial and final times of the given trajectory. Pairs $[\bar{v}(t_i), \bar{v}(t_f)]$ and $[\bar{\omega}(t_i), \bar{\omega}(t_f)]$ represent the constant linear and angular velocities which are joined smoothly through p_v and p_ω , respectively, over the time interval $[t_i, t_f]$. Function $\psi(t, t_i, t_f)$ is a polynomial given by

$$\begin{aligned}\psi(t, t_i, t_f) &= \left(\frac{t - t_i}{t_f - t_i} \right)^3 \\ &\times \left[10 - 15 \left(\frac{t - t_i}{t_f - t_i} \right) + 6 \left(\frac{t - t_i}{t_f - t_i} \right)^2 \right].\end{aligned}\quad (54)$$

The reference velocities v^* and ω^* were generated using (53) according to Table 1. Thus, by using (3), the trajectory to be tracked by the WMR in the XY plane, that is, (x^*, y^*, φ^*) , is depicted in subfigures (a) and (b) associated with Figures 5–9.

Figure 5 shows performance achieved under the variations given in Table 2 for the loads of the Buck converters. Figure 6 presents results when the abrupt variations defined in Table 3 are considered for the power supplies. Lastly, Figure 7 depicts results when the abrupt changes presented in Table 4 are considered for the inductances-capacitances of the Buck converters.

According to experimental results in Figures 5–7, the control objective is successfully achieved; that is, $(x, y, \varphi) \rightarrow (x^*, y^*, \varphi^*)$. Furthermore, it can also be seen that the hierarchical controller is robust with respect to abrupt variations in the system parameters.

5.2. Experimental Results When the Power Stage Dynamics Is Neglected. The experimental implementation of controller reported in [98] is carried out in this section. The aim is to

TABLE 1: Desired trajectory defined by Bézier polynomials.

$0 \leq t < 0.4$:	$v^* = p_v(t);$ $\bar{v}_i(t_i = 0) = 0.1;$ $\bar{v}_f(t_f = 0.4) = 0.7;$	$\omega^* = 0;$
$0.4 \leq t < 1.3$:	$v^* = 0.7;$	$\omega^* = 0;$
$1.3 \leq t < 1.8$:	$v^* = p_v(t);$ $\bar{v}_i(t_i = 1.3) = 0.7;$ $\bar{v}_f(t_f = 1.8) = 0.5;$	$\omega^* = p_\omega(t);$ $\bar{\omega}_i(t_i = 1.3) = 0;$ $\bar{\omega}_f(t_f = 1.8) = 1.8;$
$1.8 \leq t < 3.5$:	$v^* = 0.5;$	$\omega^* = 1.8;$
$3.5 \leq t < 4.5$:	$v^* = p_v(t);$ $\bar{v}_i(t_i = 3.5) = 0.5;$ $\bar{v}_f(t_f = 4.5) = 0.4;$	$\omega^* = p_\omega(t);$ $\bar{\omega}_i(t_i = 3.5) = 1.8;$ $\bar{\omega}_f(t_f = 4.5) = -1.8;$
$4.5 \leq t < 5.5$:	$v^* = 0.4;$	$\omega^* = -1.8;$
$5.5 \leq t < 5.8$:	$v^* = p_v(t);$ $\bar{v}_i(t_i = 5.5) = 0.4;$ $\bar{v}_f(t_f = 5.8) = 0.3;$	$\omega^* = p_\omega(t);$ $\bar{\omega}_i(t_i = 5.5) = -1.8;$ $\bar{\omega}_f(t_f = 5.8) = -0.75;$
$5.8 \leq t \leq 6$:	$v^* = p_v(t);$ $\bar{v}_i(t_i = 5.8) = 0.3;$ $\bar{v}_f(t_f = 6) = 0.2;$	$\omega^* = p_\omega(t);$ $\bar{\omega}_i(t_i = 5.8) = -0.75;$ $\bar{\omega}_f(t_f = 6) = -0.25.$

TABLE 2: Abrupt changes in R_r and R_l .

R_{m_r}	R_{m_l}	Time interval
R_r	R_l	$t < 1$ s
9% R_r	9% R_l	$1 \text{ s} \leq t < 3$ s
R_r	R_l	$3 \text{ s} \leq t < 5$ s
9% R_r	9% R_l	$5 \text{ s} \leq t$

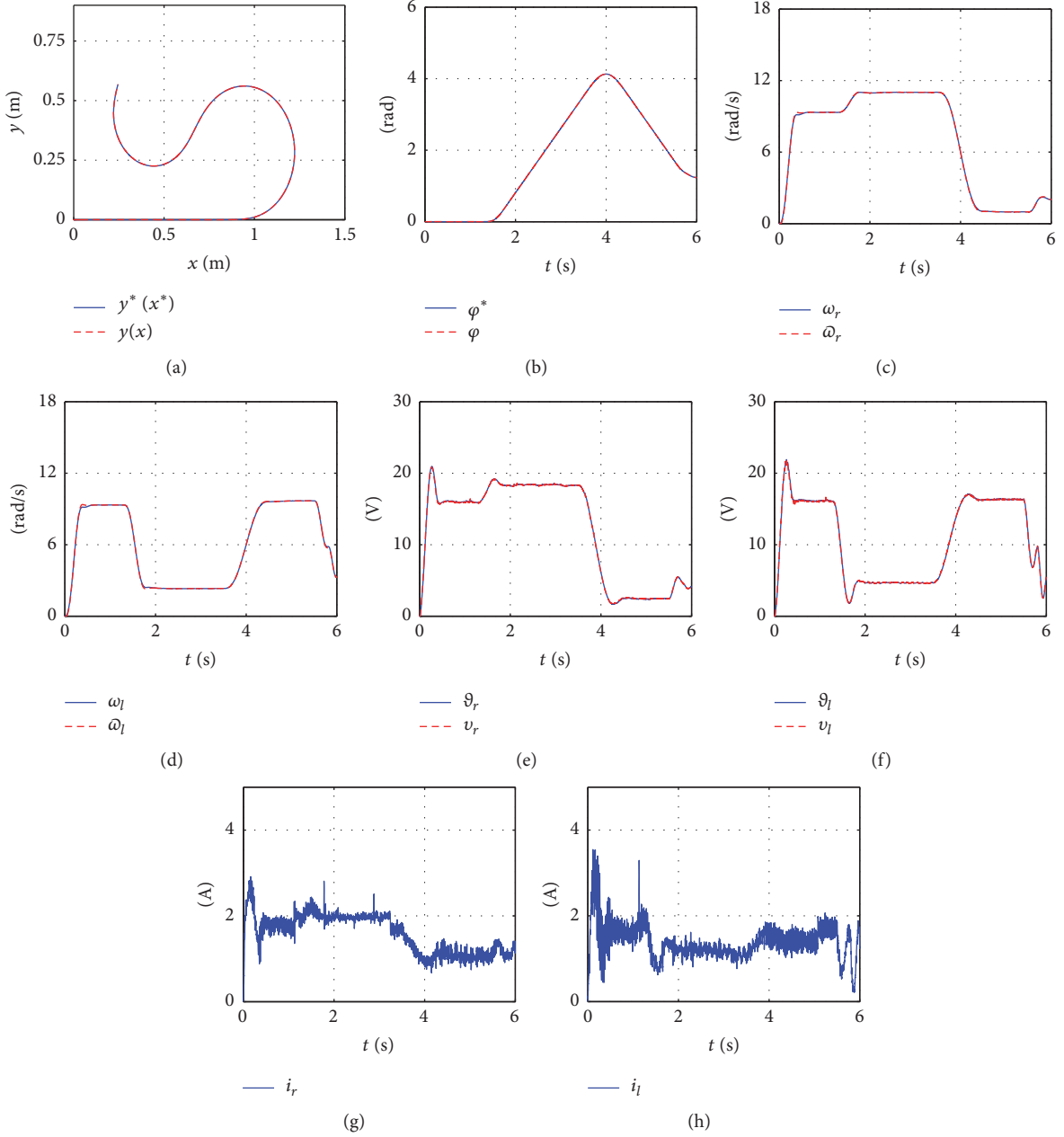
TABLE 3: Abrupt changes in E_r and E_l .

E_{m_r}	E_{m_l}	Time interval
E_r	E_l	$t < 1$ s
75% E_r	75% E_l	$1 \text{ s} \leq t < 3$ s
E_r	E_l	$3 \text{ s} \leq t < 5$ s
75% E_r	75% E_l	$5 \text{ s} \leq t$

TABLE 4: Abrupt changes in L_r, C_r, L_l , and C_l .

L_{m_r}	C_{m_r}	L_{m_l}	C_{m_l}	Time interval
L_r	C_r	L_l	C_l	$t < 1$ s
32% L_r	33% C_r	37% L_l	33% C_l	$1 \text{ s} \leq t < 3$ s
L_r	C_r	L_l	C_l	$3 \text{ s} \leq t < 5$ s
32% L_r	33% C_r	37% L_l	33% C_l	$5 \text{ s} \leq t$

show that performance achieved with the hierarchical controller introduced in the present paper is better than, or at least similar to, performance achieved with controllers that do not consider the dynamics of the power stage [31–103]. For such an aim, the differential drive WMR prototype depicted in Figure 4 was employed. It is stressed that power stage of this prototype is composed by H-bridges instead of Buck converters. The physical characteristics of this WMR prototype are similar to those of the WMR prototype shown in Figure 3. Controller gains as well as trajectory to be tracked by the WMR prototype shown in Figure 4 are the same as those used in Section 5.1.

FIGURE 5: Experimental results when uncertainties exist in R_r and R_l .TABLE 5: Abrupt changes in E_r and E_l .

E_{m_r}	E_{m_l}	Time interval
E_r	E_l	$t < 1$ s
87.5% E_r	87.5% E_l	$1 \text{ s} \leq t < 3$ s
E_r	E_l	$3 \text{ s} \leq t < 5$ s
87.5% E_r	87.5% E_l	$5 \text{ s} \leq t$

When the power supplies are subject to variations defined in Table 3, the WMR shown in Figure 4 behaves as shown in Figure 8. When the abrupt variations defined in Table 5 are

considered now for the power supplies, the WMR behaves as depicted in Figure 9. As observed in Figure 8, controller fails when solving the trajectory tracking task if variations in power supplies are large enough (see Table 3). However, if the variations are much smaller (see Table 5), the control successfully solves such a task; that is, $(x, y, \varphi) \rightarrow (x^*, y^*, \varphi^*)$. See Figure 9.

6. Conclusions

A hierarchical controller solving the trajectory tracking task in a differential drive WMR has been introduced in this paper.

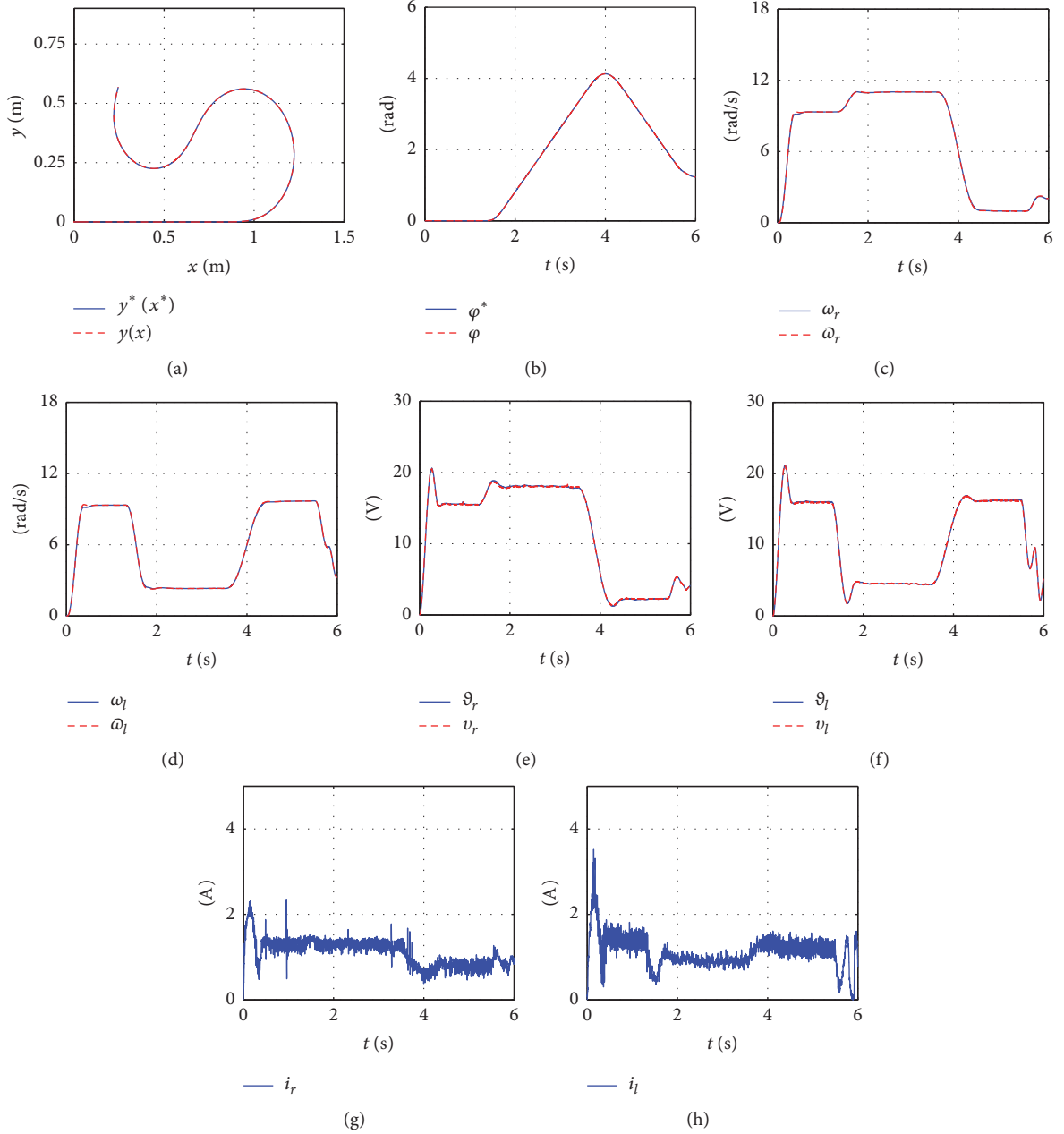


FIGURE 6: Experimental results when uncertainties exist in E_r and E_l .

This control scheme is composed by a kinematic controller at the highest hierarchical level intended for the mechanical structure. Two differential flatness-based controllers are designed at the medium level intended for the WMR actuators (DC motors). Two average differential flatness-based controllers are employed at the lowest hierarchical level intended for the power stage (Buck power converters). Hence, this is the first time that a trajectory tracking controller is designed for WMRs by taking into account the power stage dynamics during the design stage.

The closed-loop switched practical implementation was performed via Σ - Δ -modulation in a differential drive WMR that was designed and built for such an aim. The experimental results confirm that the control objective is achieved; that

is, $(x, y, \varphi) \rightarrow (x^*, y^*, \varphi^*)$, even when large, abrupt, and simultaneous changes appear in the system parameters. Additionally, the proposed controller was compared experimentally to a control scheme that neglects the power stage dynamics. According to experimental results, the proposal in the present paper achieves better performances.

Although the control objective is shown above to be achieved, the solution presented here only considers the unidirectional trajectory tracking task. Concerning this task, it is shown in [126] that this does not necessarily imply that robot is limited when tracking complex trajectories.

Future research will be focused on solving other control problems, such as obstacle avoidance and path-following, by using a similar approach to the one presented in this work. It

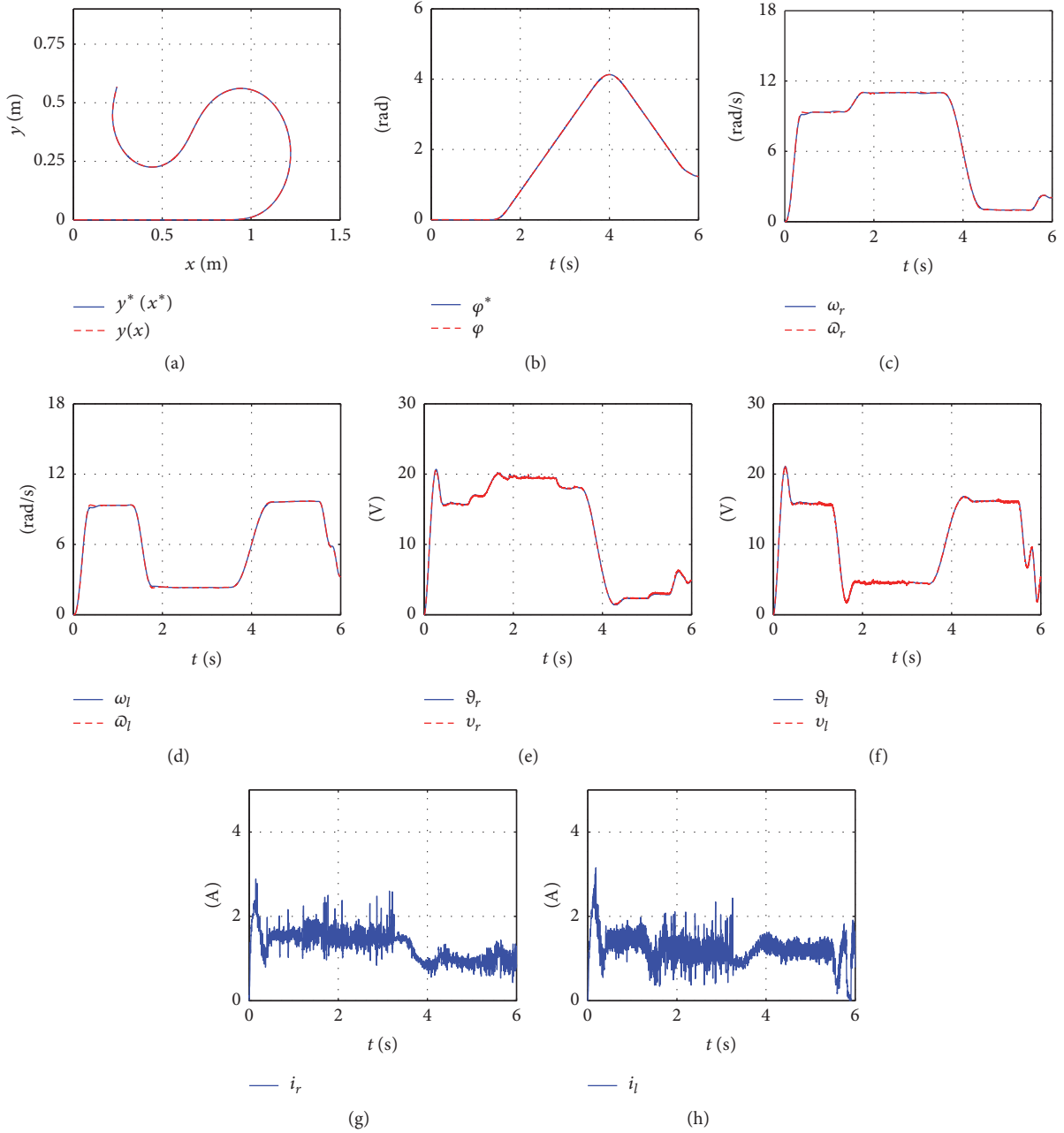


FIGURE 7: Experimental results when abrupt changes associated with L_r , C_r , L_l , and C_l appear.

would be convenient, however, that the robot power stage be redesigned in order to perform bidirectional trajectory tracking [127–129].

It is worth mentioning that recent important contributions on WMRs reported in the literature within the past few months do not take into account dynamics of the three subsystems composing a WMR (see [130–150]). In this respect, consideration of such dynamics in the design of controllers may lead to new research areas where power electronics would play a very important role.

Conflicts of Interest

The authors declare that the research was conducted in the absence of any commercial, financial, or personal relationships that could be construed as potential conflicts of interest.

Acknowledgments

This work was supported by Secretaría de Investigación y Posgrado del Instituto Politécnico Nacional, México. The work

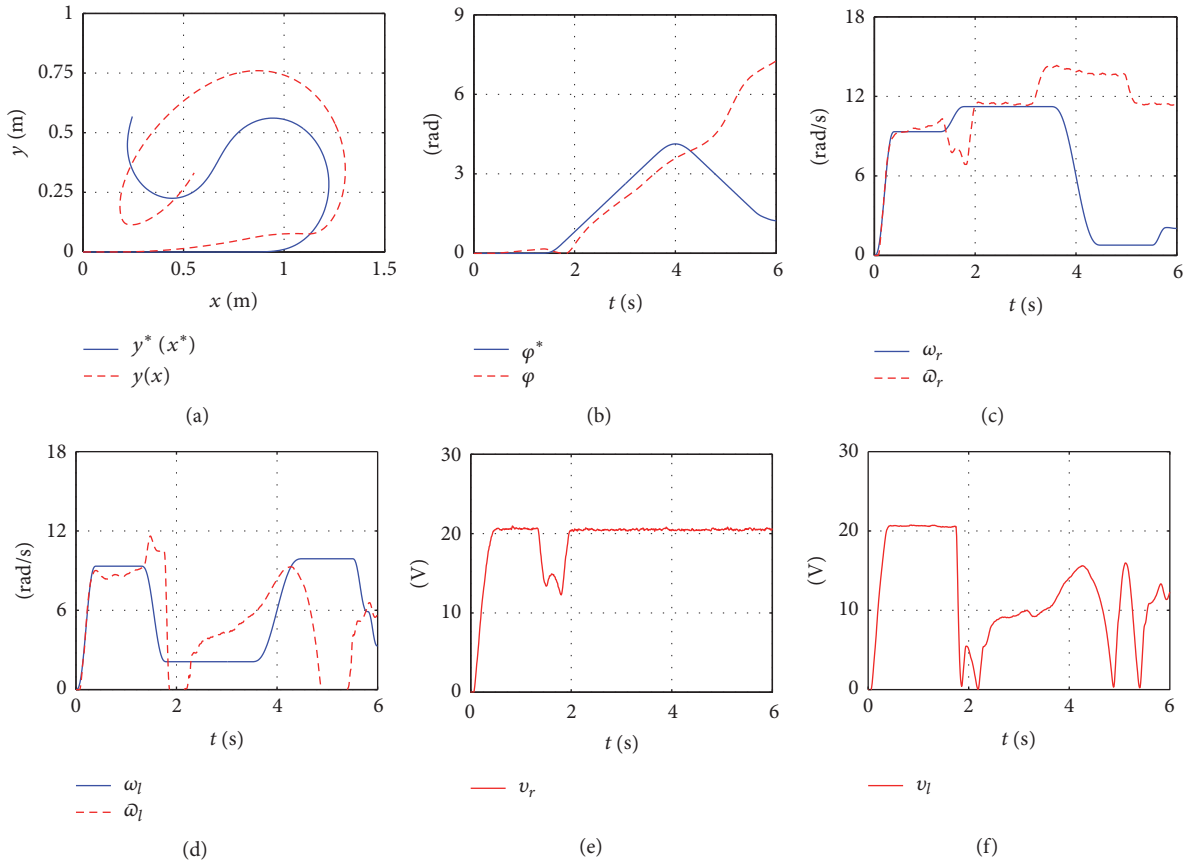


FIGURE 8: Control objective is not accomplished when abrupt changes in Table 3, that is, associated with E , appear.

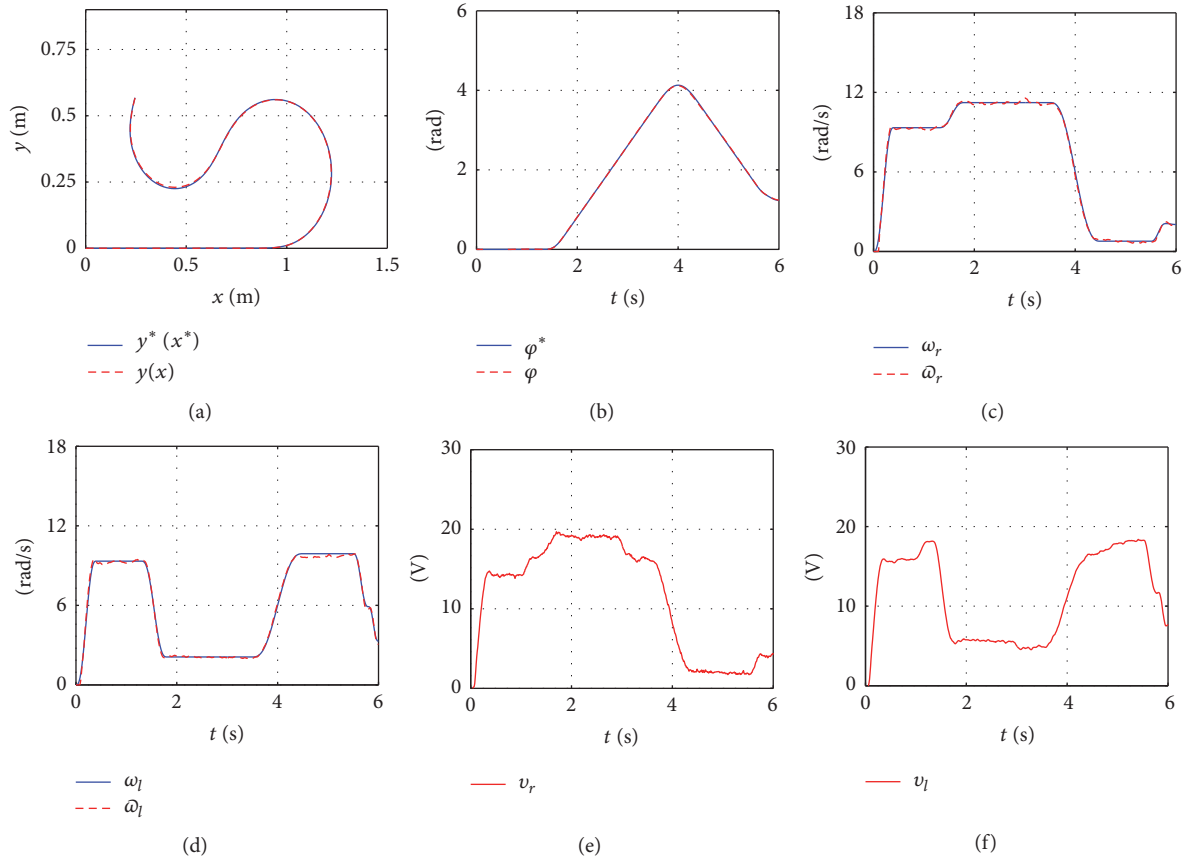


FIGURE 9: Control objective is accomplished when abrupt changes associated with E are small (see Tables 3 and 5).

of José Rafael García-Sánchez, Salvador Tavera-Mosqueda, Celso Márquez-Sánchez, and Mayra Antonio-Cruz was supported by CONACYT-México, and BEIFI scholarships. Ramón Silva-Ortigoza and Hind Taud acknowledge financial support from the IPN programs EDI and SIBE and from SNI-México. Lastly, Victor Manuel Hernández-Guzmán and Gilberto Silva-Ortigoza acknowledge SNI-México, for financial support.

References

- [1] R. Siegwart and I. R. Nourbakhsh, *Introduction to Autonomous Mobile Robots*, MIT Press, Cambridge, MA, USA, 2004.
- [2] F. Fahimi, *Autonomous Robots: Modeling, Path Planning, and Control*, Springer-Verlag, NY, USA, 2009.
- [3] R. Silva-Ortigoza, M. Marcelino-Aranda, G. Silva-Ortigoza et al., "Wheeled mobile robots: a review," *IEEE Latin America Transactions*, vol. 10, no. 6, pp. 2209–2217, 2012.
- [4] G. Bekey and J. Yuh, "The status of robotics," *IEEE Robotics and Automation Magazine*, vol. 15, no. 1, pp. 80–86, 2008.
- [5] B. Siciliano and O. Khatib, Eds., *Handbook of Robotics*, Springer-Verlag, Berlin, Heidelberg, DE, 2008.
- [6] A. Harris and J. M. Conrad, "Survey of popular robotics simulators, frameworks, and toolkits," in *Proceedings of the IEEE SoutheastCon 2011 - Building Global Engineers*, pp. 243–249, Nashville, TN, USA, 2011.
- [7] K. Yoshida and S. Tadokoro, Eds., *Field and Service Robotics*, Springer-Verlag, NY, USA, 2014.
- [8] A. M. Bloch, M. Reyhanoglu, and N. H. McClamroch, "Control and stabilization of nonholonomic dynamic systems," *IEEE Transactions on Automatic Control*, vol. 37, no. 11, pp. 1746–1757, 1992.
- [9] I. Kolmanovsky and N. H. McClamroch, "Developments in nonholonomic control problems," *IEEE Control Systems Magazine*, vol. 15, no. 6, pp. 20–36, 1995.
- [10] K. Erenturk, "Hybrid control of a mechatronic system: fuzzy logic and grey system modeling approach," *IEEE/ASME Transactions on Mechatronics*, vol. 12, no. 6, pp. 703–710, 2007.
- [11] S. R. Bull, "Renewable energy today and tomorrow," *Proceedings of the IEEE*, vol. 89, no. 8, pp. 1216–1226, 2001.
- [12] A. B. Stambouli and E. Traversa, "Fuel cells, an alternative to standard sources of energy," *Renewable & Sustainable Energy Reviews*, vol. 6, no. 3, pp. 295–304, 2002.
- [13] S. Rahman, "Green power: what is it and where can we find it?" *IEEE Power & Energy Magazine*, vol. 1, no. 1, pp. 30–37, 2003.
- [14] Z. L. Wang and J. Song, "Piezoelectric nanogenerators based on zinc oxide nanowire arrays," *Science*, vol. 312, no. 5771, pp. 242–246, 2006.
- [15] F. Blaabjerg and K. Ma, "Future on power electronics for wind turbine systems," *IEEE Journal of Emerging and Selected Topics in Power Electronics*, vol. 1, no. 3, pp. 139–152, 2013.
- [16] O. Abedinia, A. Ghasemi, and N. Ojaroudi, "Improved time varying inertia weight PSO for solved economic load dispatch with subsidies and wind power effects," *Complexity*, vol. 21, no. 4, pp. 40–49, 2014.
- [17] J. Widén, N. Carpman, V. Castellucci et al., "Variability assessment and forecasting of renewables: A review for solar, wind, wave and tidal resources," *Renewable & Sustainable Energy Reviews*, vol. 44, pp. 356–375, 2015.
- [18] S. Sivakumar, M. J. Sathik, P. S. Manoj, and G. Sundararajan, "An assessment on performance of DC-DC converters for renewable energy applications," *Renewable & Sustainable Energy Reviews*, vol. 58, pp. 1475–1485, 2016.
- [19] T. M. Pinho, J. P. Coelho, G. Veiga, A. P. Moreira, and J. Boaventura-Cunha, "A multilayer model predictive control methodology applied to a biomass supply chain operational level," *Complexity*, Article ID 5402896, 10 pages, 2017.
- [20] B. K. Bose, "Energy, environment, and advances in power electronics," *IEEE Transactions on Power Electronics*, vol. 15, no. 4, pp. 688–701, 2000.
- [21] F. Blaabjerg, Z. Chen, and S. B. Kjaer, "Power electronics as efficient interface in dispersed power generation systems," *IEEE Transactions on Power Electronics*, vol. 19, no. 5, pp. 1184–1194, 2004.
- [22] J. M. Carrasco, L. G. Franquelo, J. T. Bialasiewicz et al., "Power electronic systems for the grid integration of renewable energy sources: a survey," *IEEE Transactions on Industrial Electronics*, vol. 53, no. 4, pp. 1002–1016, 2006.
- [23] A. Emadi, Y. J. Lee, and K. Rajashekara, "Power electronics and motor drives in electric, hybrid electric, and plug-in hybrid electric vehicles," *IEEE Transactions on Industrial Electronics*, vol. 55, no. 6, pp. 2237–2245, 2008.
- [24] S. Vazquez, S. M. Lukic, E. Galván, L. G. Franquelo, and J. M. Carrasco, "Energy storage systems for transport and grid applications," *IEEE Transactions on Industrial Electronics*, vol. 57, no. 12, pp. 3881–3895, 2010.
- [25] J. D. van Wyk and F. C. Lee, "On a future for power electronics," *IEEE Journal of Emerging and Selected Topics in Power Electronics*, vol. 1, no. 2, pp. 59–72, 2013.
- [26] J. Hu, J. Cao, and T. Yong, "Multi-level dispatch control architecture for power systems with demand-side resources," *IET Generation, Transmission & Distribution*, vol. 9, no. 16, pp. 2799–2810, 2015.
- [27] O. Abedinia and N. Amjadi, "Net demand prediction for power systems by a new neural network-based forecasting engine," *Complexity*, vol. 21, no. S2, pp. 296–308, 2016.
- [28] J. Hu, M. Z. Q. Chen, J. Cao, and J. M. Guerrero, "Coordinated active power dispatch for a microgrid via distributed lambda iteration," *IEEE Journal on Emerging and Selected Topics in Circuits and Systems*, vol. 7, no. 2, pp. 250–261, 2017.
- [29] M. Godoy Simões, N. Franceschetti, and J. Adamowski, "Drive system control and energy management of a solar powered electric vehicle," in *Proceedings of the APEC '98 Thirteenth Annual Applied Power Electronics Conference and Exposition*, pp. 49–55, Anaheim, CA, USA, 1998.
- [30] S. A. KH. Mozaffari Niapour, S. Danyali, M. B. B. Sharifian, and M. R. Feyzi, "Brushless DC motor drives supplied by PV power system based on Z-source inverter and FL-IC MPPT controller," *Energy Conversion and Management*, vol. 52, no. 8-9, pp. 3043–3059, 2011.
- [31] Y. Kanayama, Y. Kimura, F. Miyazaki, and T. Noguchi, "A stable tracking control method for an autonomous mobile robot," in *Proceedings of the IEEE International Conference on Robotics and Automation*, pp. 384–389, Cincinnati, OH, USA, 1990.
- [32] C. Samson and K. Ait-Abderrahim, "Feedback control of a non-holonomic wheeled cart in cartesian space," in *Proceedings of IEEE the International Conference on Robotics and Automation 1991*, pp. 1136–1141, Sacramento, CA, USA, 1991.
- [33] R. M. Murray and S. S. Sastry, "Nonholonomic motion planning: steering using sinusoids," *IEEE Transactions on Automatic Control*, vol. 38, no. 5, pp. 700–716, 1993.

- [34] J. Chacal B. and H. Sira-Ramírez, “On the sliding mode control of wheeled mobile robots,” in *Proceedings of the IEEE International Conference on Systems, Man and Cybernetics*, pp. 1938–1943, San Antonio, TX, USA, 1994.
- [35] G. Walsh, D. Tilbury, S. Sastry, R. Murray, and J. P. Laumond, “Stabilization of trajectories for systems with nonholonomic constraints,” *IEEE Transactions on Automatic Control*, vol. 39, no. 1, pp. 216–222, 1994.
- [36] Z.-P. Jiang and H. Nijmeijer, “Tracking control of mobile robots: a case study in backstepping,” *Automatica*, vol. 33, no. 7, pp. 1393–1399, 1997.
- [37] D.-H. Kim and J.-H. Oh, “Tracking control of a two-wheeled mobile robot using input-output linearization,” *Control Engineering Practice*, vol. 7, no. 3, pp. 369–373, 1999.
- [38] Z.-P. Jiang and H. Nijmeijer, “A recursive technique for tracking control of nonholonomic systems in chained form,” *IEEE Transactions on Automatic Control*, vol. 44, no. 2, pp. 265–279, 1999.
- [39] W. E. Dixon, D. M. Dawson, E. Zergeroglu, and F. Zhang, “Robust tracking and regulation control for mobile robots,” *International Journal of Robust and Nonlinear Control*, vol. 10, no. 4, pp. 199–216, 2000.
- [40] W. E. Dixon, D. M. Dawson, F. Zhang, and E. Zergeroglu, “Global exponential tracking control of a mobile robot system via a PE condition,” *IEEE Transactions on Systems, Man, and Cybernetics, Part B: Cybernetics*, vol. 30, no. 1, pp. 129–142, 2000.
- [41] W. E. Dixon, D. M. Dawson, and E. Zergeroglu, “Tracking and regulation control of a mobile robot system with kinematic disturbances: a variable structure-like approach,” *Journal of Dynamic Systems, Measurement, and Control*, vol. 122, no. 4, pp. 616–623, 2000.
- [42] T.-C. Lee, K.-T. Song, C.-H. Lee, and C.-C. Teng, “Tracking control of unicycle-modeled mobile robots using a saturation feedback controller,” *IEEE Transactions on Control Systems Technology*, vol. 9, no. 2, pp. 305–318, 2001.
- [43] D. Chwa, “Sliding-mode tracking control of nonholonomic wheeled mobile robots in polar coordinates,” *IEEE Transactions on Control Systems Technology*, vol. 12, no. 4, pp. 637–644, 2004.
- [44] G. Klančar and I. Škrjanc, “Tracking-error model-based predictive control for mobile robots in real time,” *Robotics and Autonomous Systems*, vol. 55, no. 6, pp. 460–469, 2007.
- [45] C.-Y. Tsai, K.-T. Song, X. Dutoit, H. Van Brussel, and M. Nuttin, “Robust visual tracking control system of a mobile robot based on a dual-Jacobian visual interaction model,” *Robotics and Autonomous Systems*, vol. 57, no. 6-7, pp. 652–664, 2009.
- [46] J. H. Lee, C. Lin, H. Lim, and J. M. Lee, “Sliding mode control for trajectory tracking of mobile robot in the RFID sensor space,” *International Journal of Control, Automation, and Systems*, vol. 7, no. 3, pp. 429–435, 2009.
- [47] G. Scaglia, A. Rosales, L. Quintero, V. Mut, and R. Agarwal, “A linear-interpolation-based controller design for trajectory tracking of mobile robots,” *Control Engineering Practice*, vol. 18, no. 3, pp. 318–329, 2010.
- [48] L. Cheng, L. Cao, H.-Y. Wu, Q.-M. Zhu, W.-X. Xu, and L. Liu, “Trajectory tracking control of nonholonomic mobile robots by backstepping,” in *Proceedings of the 2011 International Conference on Modelling, Identification and Control*, pp. 134–139, Shanghai, China, 2011.
- [49] D. Chwa, “Fuzzy adaptive tracking control of wheeled mobile robots with state-dependent kinematic and dynamic disturbances,” *IEEE Transactions on Fuzzy Systems*, vol. 20, no. 3, pp. 587–593, 2012.
- [50] C. Canudas de Wit and O. J. Sordalen, “Exponential stabilization of mobile robots with nonholonomic constraints,” *IEEE Transactions on Automatic Control*, vol. 37, no. 11, pp. 1791–1797, 1992.
- [51] G. Oriolo, A. De Luca, and M. Vendittelli, “WMR control via dynamic feedback linearization: Design, implementation, and experimental validation,” *IEEE Transactions on Control Systems Technology*, vol. 10, no. 6, pp. 835–852, 2002.
- [52] S. Sun, “Designing approach on trajectory-tracking control of mobile robot,” *Robotics and Computer-Integrated Manufacturing*, vol. 21, no. 1, pp. 81–85, 2005.
- [53] D. Gu and H. Hu, “Receding horizon tracking control of wheeled mobile robots,” *IEEE Transactions on Control Systems Technology*, vol. 14, no. 4, pp. 743–749, 2006.
- [54] M. Defoort, T. Floquet, A. Kökösy, and W. Perruquetti, “Sliding-mode formation control for cooperative autonomous mobile robots,” *IEEE Transactions on Industrial Electronics*, vol. 55, no. 11, pp. 3944–3953, 2008.
- [55] R.-J. Wai and C.-M. Liu, “Design of dynamic petri recurrent fuzzy neural network and its application to path-tracking control of nonholonomic mobile robot,” *IEEE Transactions on Industrial Electronics*, vol. 56, no. 7, pp. 2667–2683, 2009.
- [56] J. Wang, Z. Lu, W. Chen, and X. Wu, “An adaptive trajectory tracking control of wheeled mobile robots,” in *Proceedings of the 2011 6th IEEE Conference on Industrial Electronics and Applications, ICIEA 2011*, pp. 1156–1160, Beijing, China, 2011.
- [57] S. Blažič, “A novel trajectory-tracking control law for wheeled mobile robots,” *Robotics and Autonomous Systems*, vol. 59, no. 11, pp. 1001–1007, 2011.
- [58] M. H. Amoozgar and Y. M. Zhang, “Trajectory tracking of wheeled mobile robots: a kinematical approach,” in *Proceedings of the 2012 8th IEEE/ASME International Conference on Mechatronic and Embedded Systems and Applications, MESA 2012*, pp. 275–280, Suzhou, China, 2012.
- [59] S. Blažič, “On periodic control laws for mobile robots,” *IEEE Transactions on Industrial Electronics*, vol. 61, no. 7, pp. 3660–3670, 2014.
- [60] B. d’Andréa-Novel, G. Bastin, and G. Campion, “Modelling and control of non-holonomic wheeled mobile robots,” in *Proceedings of the 1991 IEEE International Conference on Robotics and Automation*, pp. 1130–1135, Sacramento, CA, USA, 1991.
- [61] R. Fierro and F. Lewis, “Control of a nonholonomic mobile robot: backstepping kinematics into dynamics,” in *Proceedings of the 1995 34th IEEE Conference on Decision and Control*, pp. 3805–3810, New Orleans, LA, USA, 1995.
- [62] J.-M. Yang and J.-H. Kim, “Sliding mode control for trajectory tracking of nonholonomic wheeled mobile robots,” *IEEE Transactions on Robotics and Automation*, vol. 15, no. 3, pp. 578–587, 1999.
- [63] W. Dong, W. L. Xu, and W. Huo, “Trajectory tracking control of dynamic non-holonomic systems with unknown dynamics,” *International Journal of Robust and Nonlinear Control*, vol. 9, no. 13, pp. 905–922, 1999.
- [64] W. E. Dixon, D. M. Dawson, E. Zergeroglu, and A. Behal, “Adaptive tracking control of a wheeled mobile robot via an uncalibrated camera system,” *IEEE Transactions on Systems, Man, and Cybernetics, Part B: Cybernetics*, vol. 31, no. 3, pp. 341–352, 2001.
- [65] F. Pourboghraat and M. P. Karlsson, “Adaptive control of dynamic mobile robots with nonholonomic constraints,” *Computers and Electrical Engineering*, vol. 28, no. 4, pp. 241–253, 2002.

- [66] W. Dong and K.-D. Kuhnert, "Robust adaptive control of nonholonomic mobile robot with parameter and nonparameter uncertainties," *IEEE Transactions on Robotics*, vol. 21, no. 2, pp. 261–266, 2005.
- [67] C.-Y. Chen, T.-H. S. Li, Y.-C. Yeh, and C.-C. Chang, "Design and implementation of an adaptive sliding-mode dynamic controller for wheeled mobile robots," *Mechatronics*, vol. 19, no. 2, pp. 156–166, 2009.
- [68] R. Solea, A. Filipescu, and U. Nunes, "Sliding-mode control for trajectory-tracking of a wheeled mobile robot in presence of uncertainties," in *Proceedings of the 7th Asian Control Conference*, pp. 1701–1706, Hong Kong, China, 2009.
- [69] Z. Cao, Y. Zhao, and Q. Wu, "Adaptive trajectory tracking control for a nonholonomic mobile robot," *Chinese Journal of Mechanical Engineering*, vol. 24, no. 4, pp. 546–552, 2011.
- [70] K. Shojaei, A. M. Shahri, and B. Tabibian, "Design and implementation of an inverse dynamics controller for uncertain nonholonomic robotic systems," *Journal of Intelligent & Robotic Systems*, vol. 71, no. 1, pp. 65–83, 2013.
- [71] T. Fukao, H. Nakagawa, and N. Adachi, "Adaptive tracking control of a nonholonomic mobile robot," *IEEE Transactions on Robotics and Automation*, vol. 16, no. 5, pp. 609–615, 2000.
- [72] C. de Sousa Jr., E. M. Hemerly, and R. K. H. Galvão, "Adaptive control for mobile robot using wavelet networks," *IEEE Transactions on Systems, Man, and Cybernetics, Part B: Cybernetics*, vol. 32, no. 4, pp. 493–504, 2002.
- [73] W. E. Dixon, M. S. de Queiroz, D. M. Dawson, and T. J. Flynn, "Adaptive tracking and regulation of a wheeled mobile robot with controller/update law modularity," *IEEE Transactions on Control Systems Technology*, vol. 12, no. 1, pp. 138–147, 2004.
- [74] K. Morioka, J.-H. Lee, and H. Hashimoto, "Human-following mobile robot in a distributed intelligent sensor network," *IEEE Transactions on Industrial Electronics*, vol. 51, no. 1, pp. 229–237, 2004.
- [75] T.-J. Ren, T.-C. Chen, and C.-J. Chen, "Motion control for a two-wheeled vehicle using a self-tuning PID controller," *Control Engineering Practice*, vol. 16, no. 3, pp. 365–375, 2008.
- [76] F. N. Martins, W. C. Celeste, R. Carelli, M. Sarcinelli-Filho, and T. F. Bastos-Filho, "An adaptive dynamic controller for autonomous mobile robot trajectory tracking," *Control Engineering Practice*, vol. 16, no. 11, pp. 1354–1363, 2008.
- [77] B. S. Park, S. J. Yoo, J. B. Park, and Y. H. Choi, "Adaptive neural sliding mode control of nonholonomic wheeled mobile robots with model uncertainty," *IEEE Transactions on Control Systems Technology*, vol. 17, no. 1, pp. 207–214, 2009.
- [78] D. Chwa, "Tracking control of differential-drive wheeled mobile robots using a backstepping-like feedback linearization," *IEEE Transactions on Systems, Man, and Cybernetics, Part A: Systems and Humans*, vol. 40, no. 6, pp. 1285–1295, 2010.
- [79] H.-S. Kang, Y.-T. Kim, C.-H. Hyun, and M. Park, "Generalized extended state observer approach to robust tracking control for wheeled mobile robot with skidding and slipping," *International Journal of Advanced Robotic Systems*, vol. 10, no. 3, pp. 1–10, 2013.
- [80] J. Huang, C. Wen, W. Wang, and Z.-P. Jiang, "Adaptive output feedback tracking control of a nonholonomic mobile robot," *Automatica*, vol. 50, no. 3, pp. 821–831, 2014.
- [81] C. Aguilar-Avelar and J. Moreno-Valenzuela, "A MRAC principle for a single-link electrically driven robot with parameter uncertainties," *Complexity*, Article ID 9296012, 13 pages, 2017.
- [82] M. C. Good, L. M. Sweet, and K. L. Strobel, "Dynamic models for control system design of integrated robot and drive systems," *Journal of Dynamic Systems, Measurement, and Control*, vol. 107, no. 1, pp. 53–59, 1985.
- [83] T. Tarn, A. K. Bejczy, X. Yun, and Z. Li, "Effect of motor dynamics on nonlinear feedback robot arm control," *IEEE Transactions on Robotics and Automation*, vol. 7, no. 1, pp. 114–122, 1991.
- [84] C.-L. Hwang, "Comparison of path tracking control of a car-like mobile robot with and without motor dynamics," *IEEE/ASME Transactions on Mechatronics*, vol. 21, no. 4, pp. 1801–1811, 2016.
- [85] F. Espinosa, E. López, R. Mateos, M. Mazo, and R. García, "Advanced and intelligent control techniques applied to the drive control and path tracking systems on a robotic wheelchair," *Autonomous Robots*, vol. 11, no. 2, pp. 137–148, 2001.
- [86] R. Silva-Ortigoza, G. Silva-Ortigoza, V. M. Hernández-Guzmán, V. R. Barrientos-Sotelo, J. M. Albarrán-Jiménez, and V. M. Silva-García, "Trajectory tracking in a mobile robot without using velocity measurements for control of wheels," *IEEE Latin America Transactions*, vol. 6, no. 7, pp. 598–607, 2008.
- [87] Y. Zuo, Y. Wang, X. Liu et al., "Neural network robust control for a nonholonomic mobile robot including actuator dynamics," *International Journal of Innovative Computing, Information and Control*, vol. 6, no. 8, pp. 3437–3449, 2010.
- [88] R. Silva-Ortigoza, C. Márquez-Sánchez, M. Marcelino-Aranda et al., "Construction of a WMR for trajectory tracking control: Experimental results," *The Scientific World Journal*, vol. 2013, Article ID 723645, 2013.
- [89] L. M. Sweet and M. C. Good, "Redefinition of the robot motion-control problem," *IEEE Control Systems Magazine*, vol. 5, no. 3, pp. 18–25, 1985.
- [90] C. M. Anupoju, C.-Y. Su, and M. Oya, "Adaptive motion tracking control of uncertain nonholonomic mechanical systems including actuator dynamics," *IEEE Proceedings - Control Theory and Applications*, vol. 152, no. 5, pp. 575–580, 2005.
- [91] T. Das and I. N. Kar, "Design and implementation of an adaptive fuzzy logic-based controller for wheeled mobile robots," *IEEE Transactions on Control Systems Technology*, vol. 14, no. 3, pp. 501–510, 2006.
- [92] Z.-G. Hou, A.-M. Zou, L. Cheng, and M. Tan, "Adaptive control of an electrically driven nonholonomic mobile robot via backstepping and fuzzy approach," *IEEE Transactions on Control Systems Technology*, vol. 17, no. 4, pp. 803–815, 2009.
- [93] S. Luo, S. Wu, Z. Liu, and H. Guan, "Wheeled mobile robot RBFNN dynamic surface control based on disturbance observer," *ISRN Applied Mathematics*, vol. 2014, Article ID 634936, 9 pages, 2014.
- [94] K. Kozłowski and J. Majchrzak, "A backstepping approach to control a nonholonomic mobile robot," in *Proceedings of the IEEE International Conference on Robotics and Automation 2002*, pp. 3972–3977, Washington D.C., USA, 2002.
- [95] T. Das, I. N. Kar, and S. Chaudhury, "Simple neuron-based adaptive controller for a nonholonomic mobile robot including actuator dynamics," *Neurocomputing*, vol. 69, no. 16–18, pp. 2140–2151, 2006.
- [96] N. A. Martins, D. W. Bertol, E. R. de Pieri, E. B. Castelan, and M. M. Dias, "Neural dynamic control of a nonholonomic mobile robot incorporating the actuator dynamics," in *Proceedings of the 2008 International Conference on Computational Intelligence for Modelling Control and Automation, CIMCA 2008*, pp. 563–568, Vienna, Austria, 2008.
- [97] B. S. Park, S. J. Yoo, J. B. Park, and Y. H. Choi, "Adaptive tracking control of nonholonomic mobile robots considering actuator

- dynamics: Dynamic surface design approach,” in *Proceedings of the 2009 American Control Conference, ACC 2009*, pp. 3860–3865, St. Louis, MO, USA, 2009.
- [98] J. L. Avendaño-Juárez, V. M. Hernández-Guzmán, and R. Silva-Ortigoza, “Velocity and current inner loops in a wheeled mobile robot,” *Advanced Robotics*, vol. 24, no. 8-9, pp. 1385–1404, 2010.
- [99] B. S. Park, S. J. Yoo, J. B. Park, and Y. H. Choi, “A simple adaptive control approach for trajectory tracking of electrically driven nonholonomic mobile robots,” *IEEE Transactions on Control Systems Technology*, vol. 18, no. 5, pp. 1199–1206, 2010.
- [100] I. Zohar, A. Ailon, and R. Rabinovici, “Mobile robot characterized by dynamic and kinematic equations and actuator dynamics: trajectory tracking and related application,” *Robotics and Autonomous Systems*, vol. 59, no. 6, pp. 343–353, 2011.
- [101] K. Shojaei and A. M. Shahri, “Output feedback tracking control of uncertain non-holonomic wheeled mobile robots: a dynamic surface control approach,” *IET Control Theory & Applications*, vol. 6, no. 2, pp. 216–228, 2012.
- [102] C.-L. Hwang and H.-M. Wu, “Trajectory tracking of a mobile robot with frictions and uncertainties using hierarchical sliding-mode under-actuated control,” *IET Control Theory & Applications*, vol. 7, no. 7, pp. 952–965, 2013.
- [103] J. Taheri-Kalani and M. J. Khosrowjerdi, “Adaptive trajectory tracking control of wheeled mobile robots with disturbance observer,” *International Journal of Adaptive Control and Signal Processing*, vol. 28, no. 1, pp. 14–27, 2014.
- [104] R. Silva-Ortigoza, J. R. García-Sánchez, V. M. Hernández-Guzmán, C. Márquez-Sánchez, and M. Marcelino-Aranda, “Trajectory tracking control for a differential drive wheeled mobile robot considering the dynamics related to the actuators and power stage,” *IEEE Latin America Transactions*, vol. 14, no. 2, pp. 657–664, 2016, <http://www.ewh.ieee.org/reg/9/etrans/esp/publicaciones.php>.
- [105] J. R. García-Sánchez, S. Tavera-Mosqueda, R. Silva-Ortigoza, M. Antonio-Cruz, G. Silva-Ortigoza, and J. de J. Rubio, “Assessment of an average tracking controller that considers all the subsystems involved in a WMR: implementation via PWM or sigma-delta modulation,” *IEEE Latin America Transactions*, vol. 14, no. 3, pp. 1093–1102, 2016.
- [106] E. Montané, P. Miribel-Catalá, J. López-Sánchez, M. Puig-Vidal, S. Bota, and J. Samitier, “High-voltage smart power integrated circuits to drive piezoceramic actuators for microrobotic applications,” *IEE Proceedings - Circuits, Devices and Systems*, vol. 148, no. 6, pp. 343–347, 2001.
- [107] M. Karpelson, G.-Y. Wei, and R. J. Wood, “A review of actuation and power electronics options for flapping-wing robotic insects,” in *Proceedings of the 2008 IEEE International Conference on Robotics and Automation, ICRA 2008*, pp. 779–786, Pasadena, CA, USA, 2008.
- [108] M. G. Tina, C. Ventura, P. Arena, L. Patané, D. A. Grasso, and M. Pollino, “Design considerations about a photovoltaic power system to supply a mobile robot,” in *Proceedings of the 2010 IEEE International Symposium on Industrial Electronics, ISIE 2010*, pp. 1829–1834, Bari, Italy, 2010.
- [109] M. Karpelson, J. P. Whitney, G.-Y. Wei, and R. J. Wood, “Design and fabrication of ultralight high-voltage power circuits for flapping-wing robotic insects,” in *Proceedings of the 26th Annual IEEE Applied Power Electronics Conference and Exposition, APEC 2011*, pp. 2070–2077, Fort Worth, TX, USA, 2011.
- [110] A. Azidehak, M. Hoshyari, and M. Ahmad Sharbafi, “Design and implementation of minimal components brushless DC motor driver for mobile robots,” in *Proceedings of the 2011 IEEE International Conference on Mechatronics, ICM 2011*, pp. 642–647, Istanbul, Turkey, 2011.
- [111] M. Karpelson, G.-Y. Wei, and R. J. Wood, “Driving high voltage piezoelectric actuators in microrobotic applications,” *Sensors and Actuators A: Physical*, vol. 176, pp. 78–89, 2012.
- [112] C. Chen, Y. Tang, H. Wang, and Y. Wang, “A review of fabrication options and power electronics for flapping-wing robotic insects,” *International Journal of Advanced Robotic Systems*, vol. 10, no. 3, pp. 1–12, 2013.
- [113] Y. Tang, C. Chen, A. Khaligh, I. Penskiy, and S. Bergbreiter, “An ultracompact dual-stage converter for driving electrostatic actuators in mobile microrobots,” *IEEE Transactions on Power Electronics*, vol. 29, no. 6, pp. 2991–3000, 2014.
- [114] Y. Tang and A. Khaligh, “Bidirectional resonant DC-DC step-up converters for driving high-voltage actuators in mobile microrobots,” *IEEE Transactions on Power Electronics*, vol. 31, no. 1, pp. 340–352, 2016.
- [115] A. W. Divelbiss and J. T. Wen, “Trajectory tracking control of a car-trailer system,” *IEEE Transactions on Control Systems Technology*, vol. 5, no. 3, pp. 269–278, 1997.
- [116] R. Silva-Ortigoza, C. Márquez-Sánchez, F. Carrizosa-Corral, M. Antonio-Cruz, J. M. Alba-Martínez, and G. Saldaña-González, “Hierarchical velocity control based on differential flatness for a DC/DC Buck converter-DC motor system,” *Mathematical Problems in Engineering*, vol. 2014, Article ID 912815, 12 pages, 2014.
- [117] R. Silva-Ortigoza, V. Hernández-Guzmán, M. Antonio-Cruz, and D. Muñoz-Carrillo, “DC/DC Buck power converter as a smooth starter for a DC motor based on a hierarchical control,” *IEEE Transactions on Power Electronics*, vol. 30, no. 2, pp. 1076–1084, 2015.
- [118] H. Sira-Ramírez and R. Silva-Ortigoza, *Control Design Techniques in Power Electronics Devices*, Springer-Verlag, London, UK, 2006.
- [119] H. Sira-Ramírez and S. K. Agrawal, *Differentially Flat Systems*, Marcel Dekker, New York, NY, USA, 2004.
- [120] R. Toukhtarian, A. Sanjab, and S. Saab, “On the model order reduction of a direct current motor,” *International Journal of Electrical Engineering Education*, vol. 52, no. 1, pp. 52–70, 2015.
- [121] M. Fliess, H. Sira-Ramírez, and R. Marquez, “Regulation of nonminimum phase outputs: a flatness based approach,” in *Perspectives in Control*, D. Normand-Cyrot, Ed., Springer-Verlag, London, UK, 1998.
- [122] N. Faiz, S. K. Agrawal, and R. M. Murray, “Trajectory planning of differentially flat systems with dynamics and inequalities,” *Journal of Guidance, Control, and Dynamics*, vol. 24, no. 2, pp. 219–227, 2001.
- [123] E. Song, A. F. Lynch, and V. Dinavahi, “Experimental validation of nonlinear control for a voltage source converter,” *IEEE Transactions on Control Systems Technology*, vol. 17, no. 5, pp. 1135–1144, 2009.
- [124] P. Thounthong and S. Pierfederici, “A new control law based on the differential flatness principle for multiphase interleaved DC-DC converter,” *IEEE Transactions on Circuits and Systems II: Express Briefs*, vol. 57, no. 11, pp. 903–907, 2010.
- [125] M. Pahlevaninezhad, P. Das, J. Drobniak, P. K. Jain, and A. Bakhshai, “A new control approach based on the differential flatness theory for an AC/DC converter used in electric vehicles,” *IEEE Transactions on Power Electronics*, vol. 27, no. 4, pp. 2085–2103, 2012.

- [126] C. Márquez-Sánchez, J. R. García-Sánchez, C. Y. Sosa-Cervantes et al., "Trajectory generation for wheeled mobile robots via Bézier polynomials," *IEEE Latin America Transactions*, vol. 14, no. 11, pp. 4482–4490, 2016.
- [127] R. Silva-Ortigoza, J. N. Alba-Juárez, J. R. García-Sánchez, M. Antonio-Cruz, V. M. Hernández-Guzmán, and H. Taud, "Modeling and experimental validation of a bidirectional DC/DC Buck power electronic converter–DC motor system," *IEEE Latin America Transactions*, vol. 15, no. 6, pp. 1043–1051, 2017.
- [128] R. Silva-Ortigoza, J. N. Alba-Juárez, J. R. García-Sánchez, V. M. Hernández-Guzmán, C. Y. Sosa-Cervantes, and H. Taud, "A sensorless passivity-based control for the DC/DC Buck converter–inverter–DC motor system," *IEEE Latin America Transactions*, vol. 14, no. 10, pp. 4227–4234, 2016.
- [129] E. Hernández-Márquez, R. Silva-Ortigoza, J. R. García-Sánchez, V. H. García-Rodríguez, and J. N. Alba-Juárez, "A new "DC/DC Buck-Boost converter–DC motor" system: Modeling and experimental validation," *IEEE Latin America Transactions*, vol. 15, no. 11, pp. 2043–2049, 2017, <http://www.ewh.ieee.org/reg/9/etrans/esp/publicaciones.php>.
- [130] Z. Li, C. Yang, C.-Y. Su, J. Deng, and W. Zhang, "Vision-based model predictive control for steering of a nonholonomic mobile robot," *IEEE Transactions on Control Systems Technology*, vol. 24, no. 2, pp. 553–564, 2016.
- [131] H. Yang, X. Fan, P. Shi, and C. Hua, "Nonlinear control for tracking and obstacle avoidance of a wheeled mobile robot with nonholonomic constraint," *IEEE Transactions on Control Systems Technology*, vol. 24, no. 2, pp. 741–746, 2016.
- [132] R. D. Cruz-Morales, M. Velasco-Villa, R. Castro-Linares, and E. R. Palacios-Hernandez, "Leader-follower formation for non-holonomic mobile robots: Discrete-time approach," *International Journal of Advanced Robotic Systems*, vol. 13, no. 2, pp. 1–12, 2016.
- [133] K. J. Kaliński and M. Mazur, "Optimal control of 2-wheeled mobile robot at energy performance index," *Mechanical Systems and Signal Processing*, vol. 70–71, pp. 373–386, 2016.
- [134] N.-B. Hoang and H.-J. Kang, "Neural network-based adaptive tracking control of mobile robots in the presence of wheel slip and external disturbance force," *Neurocomputing*, vol. 188, pp. 12–22, 2016.
- [135] C.-L. Hwang and W.-L. Fang, "Global fuzzy adaptive hierarchical path tracking control of a mobile robot with experimental validation," *IEEE Transactions on Fuzzy Systems*, vol. 24, no. 3, pp. 724–740, 2016.
- [136] I.-H. Li, Y.-H. Chien, W.-Y. Wang, and Y.-F. Kao, "Hybrid intelligent algorithm for indoor path planning and trajectory-tracking control of wheeled mobile robot," *International Journal of Fuzzy Systems*, vol. 18, no. 4, pp. 595–608, 2016.
- [137] E. Vos, A. J. van der Schaft, and J. M. Scherpen, "Formation control and velocity tracking for a group of nonholonomic wheeled robots," *IEEE Transactions on Automatic Control*, vol. 61, no. 9, pp. 2702–2707, 2016.
- [138] Z. Peng, G. Wen, S. Yang, and A. Rahmani, "Distributed consensus-based formation control for nonholonomic wheeled mobile robots using adaptive neural network," *Nonlinear Dynamics*, vol. 86, no. 1, pp. 605–622, 2016.
- [139] K. R. Simba, N. Uchiyama, and S. Sano, "Real-time smooth trajectory generation for nonholonomic mobile robots using Bézier curves," *Robotics and Computer-Integrated Manufacturing*, vol. 41, pp. 31–42, 2016.
- [140] H. Xiao, Z. Li, C. Yang et al., "Robust stabilization of a wheeled mobile robot using model predictive control based on neurodynamics optimization," *IEEE Transactions on Industrial Electronics*, vol. 64, no. 1, pp. 505–516, 2017.
- [141] M. Seder, M. Baotić, and I. Petrović, "Receding horizon control for convergent navigation of a differential drive mobile robot," *IEEE Transactions on Control Systems Technology*, vol. 25, no. 2, pp. 653–660, 2017.
- [142] S. Yang, Y. Cao, Z. Peng, G. Wen, and K. Guo, "Distributed formation control of nonholonomic autonomous vehicle via RBF neural network," *Mechanical Systems and Signal Processing*, vol. 87, part B, pp. 81–95, 2017.
- [143] M. Chen, "Disturbance attenuation tracking control for wheeled mobile robots with skidding and slipping," *IEEE Transactions on Industrial Electronics*, vol. 64, no. 4, pp. 3359–3368, 2017.
- [144] H. Wang, D. Guo, X. Liang, W. Chen, G. Hu, and K. K. Leang, "Adaptive vision-based leader-follower formation control of mobile robots," *IEEE Transactions on Industrial Electronics*, vol. 64, no. 4, pp. 2893–2902, 2017.
- [145] H. Ashrafioun, S. Nersesov, and G. Clayton, "Trajectory tracking control of planar underactuated vehicles," *IEEE Transactions on Automatic Control*, vol. 62, no. 4, pp. 1959–1965, 2017.
- [146] K. Y. Lui, H. Cho, C. Ha, and D. Lee, "First-person view semi-autonomous teleoperation of cooperative wheeled mobile robots with visuo-haptic feedback," *International Journal of Robotics Research*, vol. 36, no. 5–7, pp. 840–860, 2017.
- [147] B. Mu, J. Chen, Y. Shi, and Y. Chang, "Design and implementation of nonuniform sampling cooperative control on a group of two-wheeled mobile robots," *IEEE Transactions on Industrial Electronics*, vol. 64, no. 6, pp. 5035–5044, 2017.
- [148] N. Lashkari, M. Biglarbegian, and S. X. Yang, "Development of a new robust controller with velocity estimator for docked mobile robots: theory and experiments," *IEEE/ASME Transactions on Mechatronics*, vol. 22, no. 3, pp. 1287–1298, 2017.
- [149] C.-H. Sun, Y.-J. Chen, Y.-T. Wang, and S.-K. Huang, "Sequentially switched fuzzy-model-based control for wheeled mobile robot with visual odometry," *Applied Mathematical Modelling: Simulation and Computation for Engineering and Environmental Systems*, vol. 47, pp. 765–776, 2017.
- [150] B. S. Park and S. J. Yoo, "A low-complexity tracker design for uncertain nonholonomic wheeled mobile robots with time-varying input delay at nonlinear dynamic level," *Nonlinear Dynamics*, vol. 89, no. 3, pp. 1705–1717, 2017.

Research Article

Multimedia Security Application of a Ten-Term Chaotic System without Equilibrium

Xiong Wang,¹ Akif Akgul,² Sezgin Kacar,² and Viet-Thanh Pham³

¹*Institute for Advanced Study, Shenzhen University, Shenzhen, Guangdong 518060, China*

²*Department of Electrical and Electronics Engineering, Faculty of Technology, Sakarya University, Serdivan, Turkey*

³*Modeling Evolutionary Algorithms Simulation and Artificial Intelligent, Faculty of Electrical & Electronics Engineering, Ton Duc Thang University, Ho Chi Minh City, Vietnam*

Correspondence should be addressed to Viet-Thanh Pham; phamvietthanh@tdt.edu.vn

Received 19 July 2017; Revised 4 October 2017; Accepted 31 October 2017; Published 15 November 2017

Academic Editor: Dimitri Volchenkov

Copyright © 2017 Xiong Wang et al. This is an open access article distributed under the Creative Commons Attribution License, which permits unrestricted use, distribution, and reproduction in any medium, provided the original work is properly cited.

A system without equilibrium has been proposed in this work. Although there is an absence of equilibrium points, the system displays chaos, which has been confirmed by phase portraits and Lyapunov exponents. The system is realized on an electronic card, which exhibits chaotic signals. Furthermore, chaotic property of the system is applied in multimedia security such as image encryption and sound steganography.

1. Introduction

Recently, there is an increased interest in multimedia communication, which is vital in various areas ranging from entertainment industries, economics, and medical applications to militaries [1, 2]. Several attempts have been made to provide confidentiality, identity, and integrity. A considerable amount of studies about multimedia security has been introduced, for example, data encryption, steganographic messages, watermarking, or multimedia authentication [1–6].

Extensive researches have shown that the use of chaos for multimedia communication is a potential application [7–11]. Because of the similar characteristics between chaotic systems and cryptographic primitives, chaotic cryptography is a major area of interest [12]. Liu et al. presented the audio encryption scheme with confusion and diffusion [13]. They based on a multiscroll chaotic system and one-time keys [13]. By using complex hyperchaotic systems, color image encryption was proposed [14]. Chaos maps with Markov properties were applied to construct a new encryption algorithm [15]. In addition, Ghebleh and Kanso introduced a robust chaos scheme to image steganography [16]. In order to generate message authentication codes, suitability of chaos functions was studied in [17].

In this work, we study a ten-term chaotic system without equilibrium and its multimedia security application. The chaotic attractors in this system are “hidden attractors” because the basin of attraction for a hidden attractor is not connected with any unstable fixed point [18–21]. It is noted that the concept of hidden attractors has been suggested in connection with the occurrence of unpredictable attractors in multistable systems [21]. Researchers have shown that multistability is connected with the occurrence of unpredictable attractors [21–30]. Recently, hidden attractor has been investigated in numerous systems such as Chua system [19], drilling system [31], Lorenz-like system [32], Goodwin oscillator [33], electromechanical systems [34], two-dimensional maps [35], phase-locked loop circuits [36], and Rabinovich–Fabrikant system [37].

2. A System without Equilibrium and Its Implementation

2.1. A System without Equilibrium. Chaotic systems without equilibrium attract have been attracting a lot of interest [38–42]. When mentioning a chaotic system without equilibrium, it means that there is no real equilibrium in such a system.

In this work, we study a general three-dimensional form described by

$$\begin{aligned}\dot{x} &= a_1 y, \\ \dot{y} &= a_2 x + a_3 y + a_4 z + a_5 xz, \\ \dot{z} &= a_6 x + a_7 z + a_8 xy + a_9 xz + a_{10},\end{aligned}\quad (1)$$

in which a_i ($i = 1, \dots, 10$) are parameters and $a_i \neq 0$.

We can solve the following three equations to find the system's equilibrium:

$$\begin{aligned}a_1 y &= 0, \\ a_2 x + a_3 y + a_4 z + a_5 xz &= 0, \\ a_6 x + a_7 z + a_8 xy + a_9 xz + a_{10} &= 0.\end{aligned}\quad (2)$$

From (2), we have

$$Ax^2 + Bx + C = 0, \quad (3)$$

in which

$$\begin{aligned}A &= a_2 a_5 a_9 - a_5^2 a_6, \\ B &= a_2 a_5 a_7 - a_4 a_5 a_6 - a_5^2 a_{10}, \\ C &= -a_4 a_5 a_{10},\end{aligned}\quad (4)$$

for

$$a_5 a_7 - a_4 a_9 \neq 0. \quad (5)$$

As a result, there is no equilibrium in general form (1) for

$$\Delta = B^2 - 4AC < 0. \quad (6)$$

Based on conditions (5) and (6) and $a_i \neq 0$, we have applied a search procedure [40] to find the set of parameters for which general form (1) does not have equilibrium. A set of parameters has been found as follows:

$$\begin{aligned}a_1 &= a, \\ a_2 &= a_7 = a_8 = -1, \\ a_3 &= b, \\ a_4 &= c, \\ a_5 &= a_6 = a_{10} = 1, \\ a_9 &= d,\end{aligned}\quad (7)$$

where $a, b, c, d > 0$. General form (1) is rewritten by

$$\begin{aligned}\dot{x} &= ay, \\ \dot{y} &= -x + by + cz + xz, \\ \dot{z} &= x - z - xy + dxz + 1.\end{aligned}\quad (8)$$

It is simple to see that system (8) has no equilibrium for $a = 2$, $b = 0.1$, $c = 2.5$, and $d = 0.3$. However, it displays

chaos as shown in Figure 1. In this case, calculated Lyapunov exponents of the system are illustrated in Figure 2. Lyapunov exponents are $L_1 = 0.2563$, $L_2 = 0$, and $L_3 = -0.5762$ for $t = 10,000$. Positive Lyapunov exponent $L_1 = 0.2563$ verifies the chaotic behavior of system (8). Attractors of system (8) are hidden attractors according the introduced definition in [21]. It is noted that the hidden attractors are observed in systems without equilibria, with no unstable fixed points or with one stable fixed point [21].

2.2. Electronic Circuit Implementation of the Chaotic System without Equilibrium. Electronic implementation of a chaotic model is useful for confirming the model's feasibility as well as realizing applications [43–45]. The main aim of this section is to design a circuit to realize the system without equilibrium by using electronic elements [46–51]. The chaotic system must be rescaled for electronic circuit implementation. The amplitude values of system (x , y , and z) are in the interval of $(-80, 60)$. They are higher than the interval of $(-15, 15)$ which are electronic materials limitations. For scale process, let $X/2 = x$, $Y/6 = y$, and $Z = z/4$ and then adjust the original state variables x , y , z instead of the variables X , Y , Z . As a result, the scaled system finally becomes of the following form:

$$\begin{aligned}\dot{X} &= 3aY, \\ \dot{Y} &= -\frac{1}{3}X + bY + \frac{2}{3}cZ + \frac{4}{3}XZ, \\ \dot{Z} &= \frac{1}{2}X - Z - 3XY + 2dXZ + \frac{1}{4}.\end{aligned}\quad (9)$$

An electronic circuit is designed for the scaled system as shown in Figure 3.

As can be seen in Figure 3, we selected $C1 = C2 = C3 = 1 \text{ nF}$, $R1 = 66 \text{ k}\Omega$, $R2 = R3 = R8 = R9 = R15 = R16 = 100 \text{ k}\Omega$, $R4 = 1200 \text{ k}\Omega$, $R5 = 4000 \text{ k}\Omega$, $R6 = 240 \text{ k}\Omega$, $R7 = 30 \text{ k}\Omega$, $R10 = 800 \text{ k}\Omega$, $R11 = 400 \text{ k}\Omega$, $R12 = 24000 \text{ k}\Omega$, $R13 = 67 \text{ k}\Omega$, and $R14 = 14 \text{ k}\Omega$. The scaled chaotic system was done on the electronic card (see Figure 4). All phase portraits on the oscilloscope are shown in Figure 5, which illustrate the feasibility of the system.

3. Image Encryption and Sound Steganography Applications of the System without Equilibrium

After considering the circuit implementation of the system, in this section, image encryption and hiding of encrypted image data in a sound file have been implemented to show that the no-equilibrium chaotic system can be used in multimedia security applications. In order to realize these applications, firstly random number generator design has been done.

3.1. Random Number Generator (RNG) Design. One of the most basic structures used in chaos-based encryption and steganography applications is RNG. In this study, before the security applications, a RNG design has been implemented

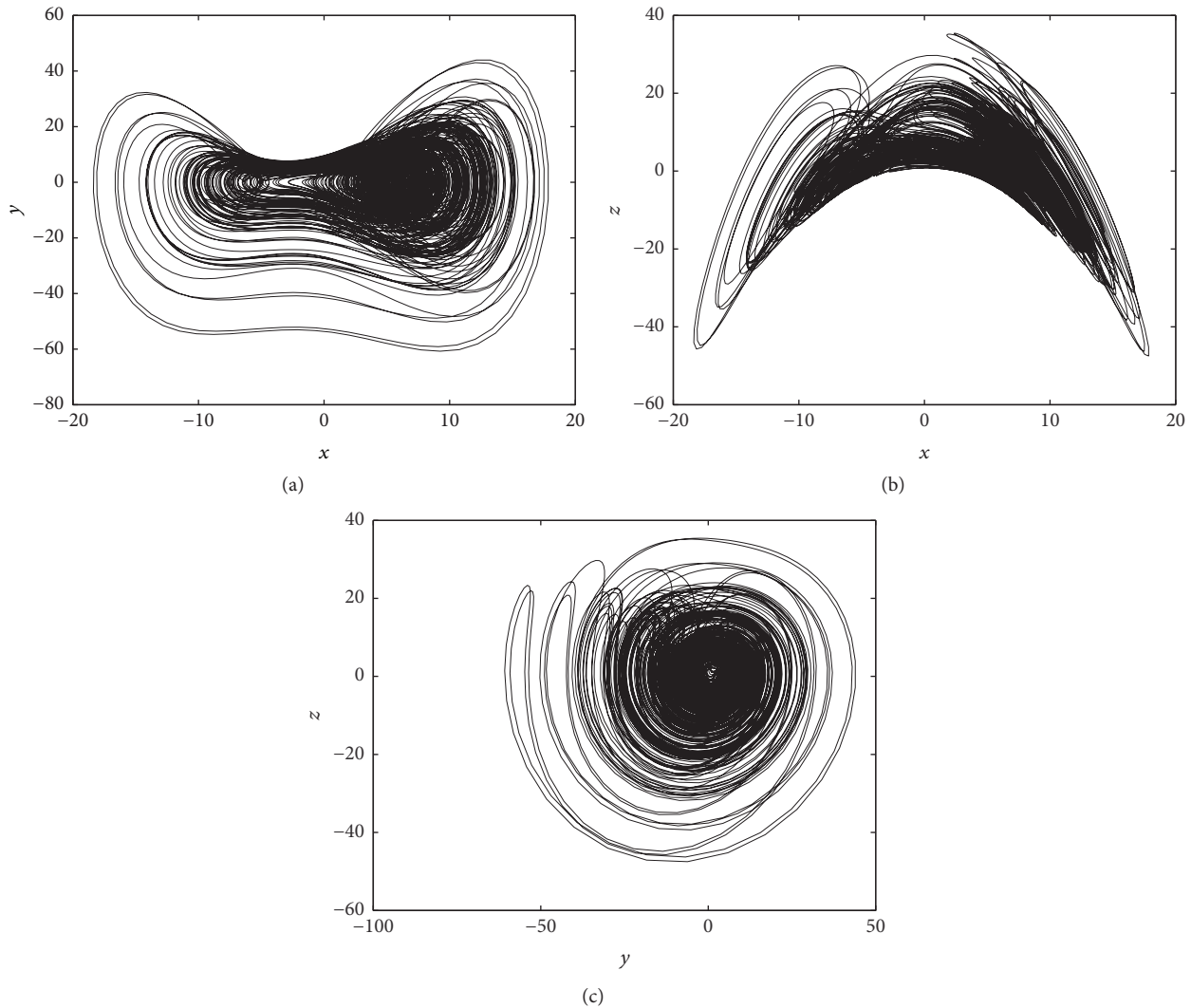


FIGURE 1: Projections of attractors without equilibrium in (a) $x - y$ plane, (b) $x - z$ plane, and (c) $y - z$ plane for $a = 2$, $b = 0.1$, $c = 2.5$, and $d = 0.3$ and initial conditions $(x(0), y(0), z(0)) = (1, 1, 1)$. The attractor of system (8) is “hidden” according to the definition introduced in [21].

for use in these applications. In RNG design, $\text{mod}(256)$ operation has been performed by taking 13, 14, and 15 digits after the point of state variables obtained by using Runge–Kutta 4 (RK4) algorithm. In this case, 8 bits of each state variable are obtained in each iteration of the RK4 algorithm. Finally, each 8-bit sequence obtained from 3 state variables (x, y, z) has been XORed at each iteration to obtain a random bit sequence of RNG. In Table 1, the statistical NIST-800-22 test results of the random number sequence of 1,000,000 bits obtained from the designed RNG are shown.

The statistical NIST-800-22 test is known as the internationally accepted best random test. The NIST test is a comprehensive test consisting of 15 different tests. In order to be able to speak of a complete randomness, obtained P values from the all of 15 tests must be provided with the condition of $1 > P \text{ value} > 0.01$. When the values in Table 1 are examined,

it is seen that the RNG based on the new system is successful in all tests.

3.2. Image Encryption Application. In this application, image encryption is performed using RNG obtained in Section 3.1. In the application 128×128 pixel size image with gray scale (“pepper”) is used. All pixels of the original image have converted to binary and all binary bits have been subjected to XOR processing with a random bit sequence obtained from the RNG to perform encryption. The decryption process is also performed by applying the reverse of the encryption process. Figure 6 shows the original, encrypted, and decrypted images. As seen in the figure, the encrypted image is not understood. So, the encryption is visually very successful. Correlation, histogram, entropy, and differential attack analyses were also performed to analyze the performance of the

TABLE 1: NIST-800-22 test results of the new chaotic system based RNG.

Statistical tests	P value	Result
Frequency (Monobit) Test	0,4556674150378	Successful
Block-Frequency Test	0,312738896039824	Successful
Cumulative-Sums Test	0,5441395972238	Successful
Runs Test	0,117478755093071	Successful
Longest-Run Test	0,88635602631487	Successful
Binary Matrix Rank Test	0,594206193094231	Successful
Discrete Fourier Transform Test	0,783086624373691	Successful
Nonoverlapping Templates Test	0,0586441453317821	Successful
Overlapping Templates Test	0,868314176679646	Successful
Maurer's Universal Statistical Test	0,349319372138117	Successful
Approximate Entropy Test	0,0419351614775444	Successful
Random-Excursions Test ($x = -4$)	0,746783846542712	Successful
Random-Excursions Variant Test ($x = -9$)	0,810174242469133	Successful
Serial Test-1	0,366073450623053	Successful
Serial Test-2	0,333453364381209	Successful
Linear-Complexity Test	0,992656091838689	Successful

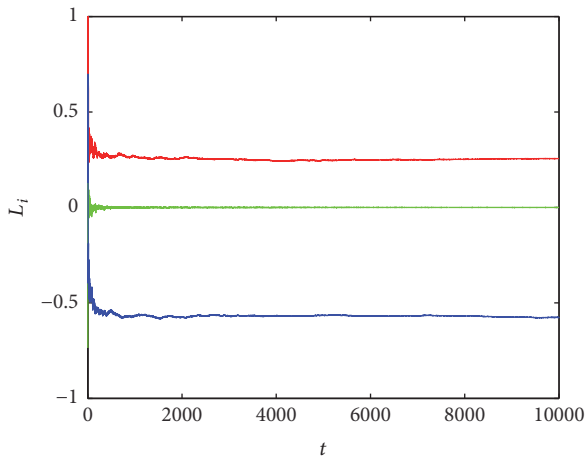


FIGURE 2: Lyapunov exponents of system without equilibrium (8) for $a = 2$, $b = 0.1$, $c = 2.5$, and $d = 0.3$ and initial conditions $(x(0), y(0), z(0)) = (1, 1, 1)$: L_1 (red), L_2 (green), and L_3 (blue). Positive value of Lyapunov exponent L_1 indicates chaos of system (8).

encryption. Figures 7 and 8 show correlation distributions and histogram graphs. In these graphs, it is seen that encryption process provides a very homogeneous distribution. The homogeneity of the encrypted image distributions shows the encryption is good. In addition, we have implemented some existing image encryption methods to compare with our encryption method (see Tables 2 and 3). The entropy, correlation, and differential attack (NPCR and UACI) results and encryption time show the good performance of the proposed image encryption method.

3.3. Sound Steganography Application. In this section, the 128×128 encrypted picture obtained in Section 3.2 has

TABLE 2: Security analysis result and comparisons (256×256 “pepper” image).

	Entropy	Correlation	NPCR	UACI
This work	7.9972	0.0042	99.9802	30.0634
Ref. [52]	7.9560	0.5210	99.6289	31.8345
Ref. [53]	7.9972	0.0520	99.6109	12.7548
Ref. [54]	7.9820	0.0052	99.5773	34.1402
Ref. [55]	7.9958	0.0068	99.6170	25.125
Ref. [56]	7.9991	0.0082	99.028	33.10
Ref. [57]	7.998	0.0071	99.50	33.39

TABLE 3: Encryption time and comparisons (256×256 “pepper” image).

	Encryption time (s)
This work	0.4865
Ref. [52]	1.6734
Ref. [58]	3.704
Ref. [59]	0.712
Ref. [60]	5.6544
Ref. [61]	0.5630

been hidden in the original sound as in Figure 9. In this hiding process, firstly, the pixel values of the encrypted picture are converted into binary numbers. Secondly, the float values obtained from the sound data are converted to 32-bit binary numbers. Finally, all the bits belonging to the encrypted image are hidden by placing them in the LSB bits of the 32-bit binary numbers of the selected sound data using the RNG obtained in Section 3.1. As a result, the sound data in which the encrypted image is hidden is shown in Figure 9. There is no visual difference

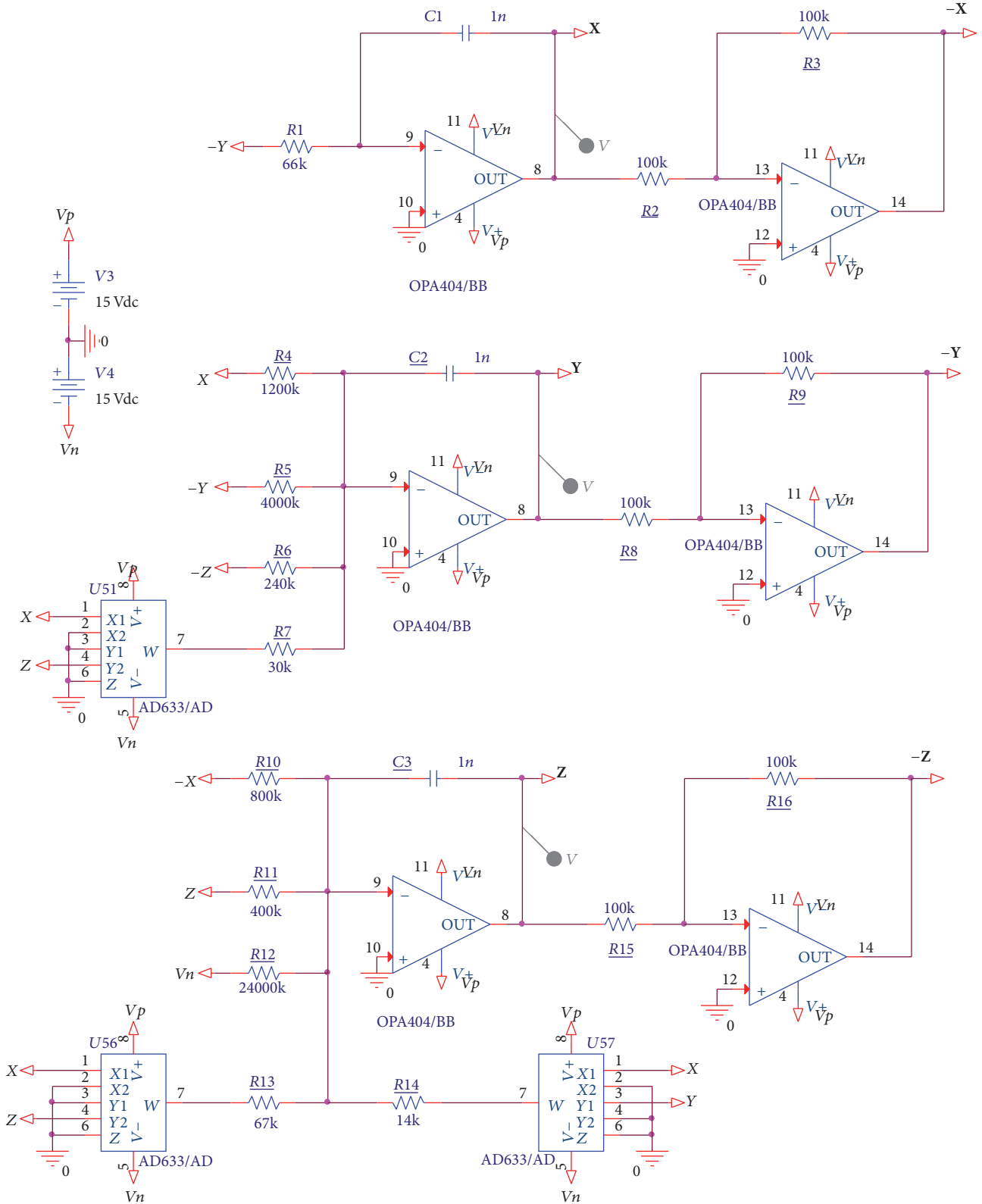


FIGURE 3: The circuit schematic of the scaled system.

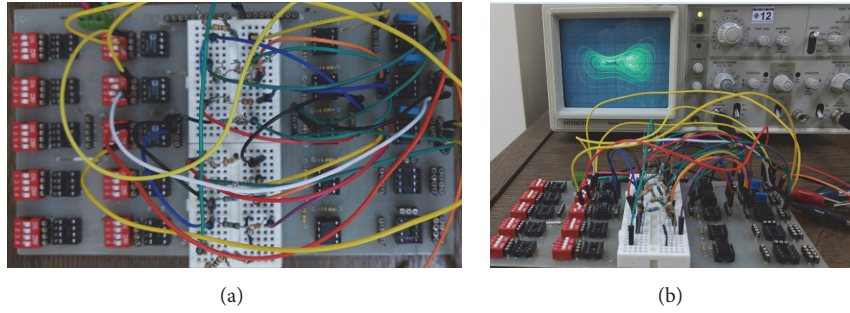


FIGURE 4: The experimental circuit of the scaled chaotic system.

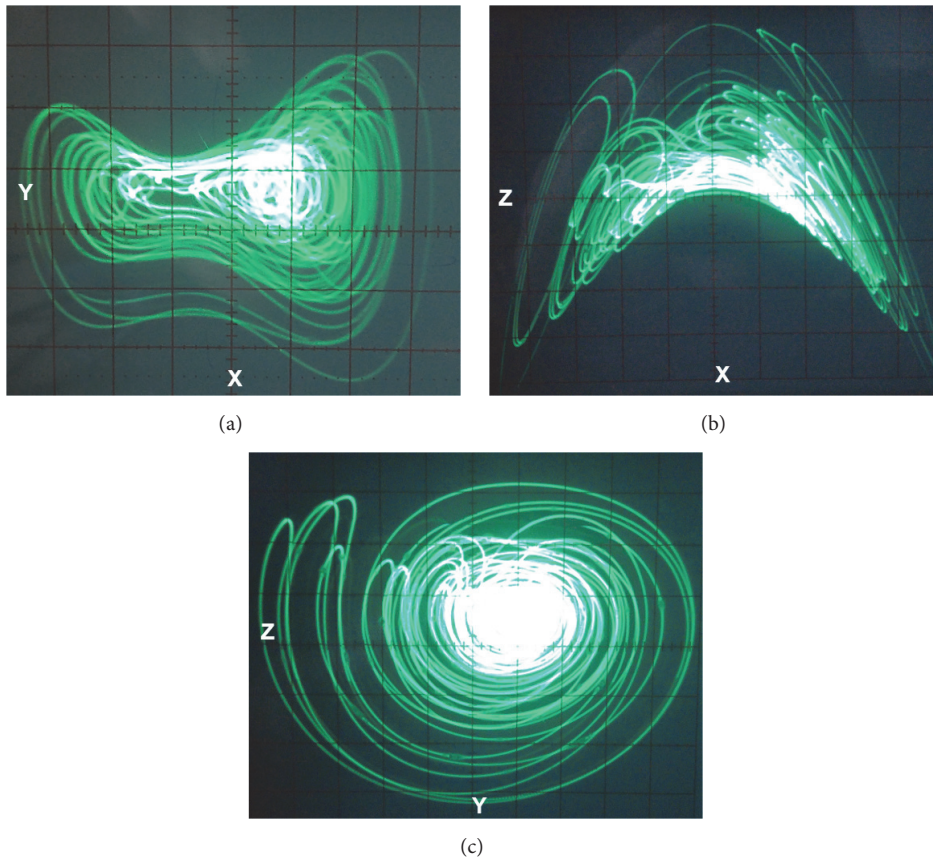


FIGURE 5: All phase portraits of the scaled chaotic system on the oscilloscope: (a) $X - Y$ plane, (b) $X - Z$ plane, and (c) $Y - Z$ plane.

between the original and embedded sound data seen in Figure 9. This shows that the steganography application has a good performance. Since it is not enough that there is no difference visually between the original and embedded sounds, analyses of correlation, histogram, entropy, mean square error (MSE), maximum absolute error (MAXERR), and the energy ratio (L2RAT) were also performed. As seen in Figures 10 and 11, correlation distributions and histograms of the original and embedded sounds are the same. In addition, the results of the analyses in Table 4 indicate that there is no difference between the original and embedded sounds. This means that the sound steganography application based on the chaotic system without equilibrium has a good performance.

TABLE 4: Security analysis of the steganography process.

Analysis	Original sound	Embedded sound
Correlation	0.9994	0.9994
Entropy	13.4926	13.4926
MSE		0
MAXERR		0
L2RAT		1

4. Conclusions

This paper introduces a 3D system without equilibrium, which exhibits chaotic behavior. The system includes ten

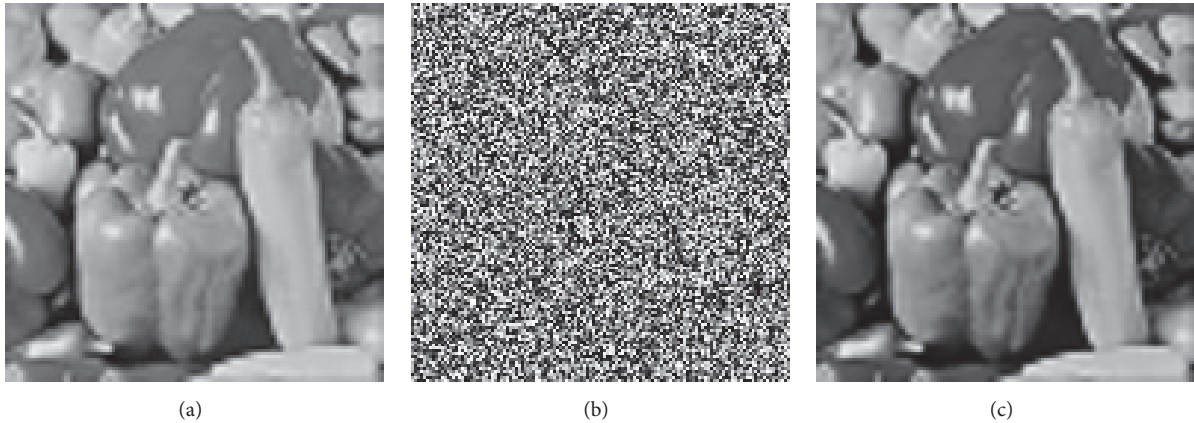


FIGURE 6: Original, encrypted, and decrypted images.

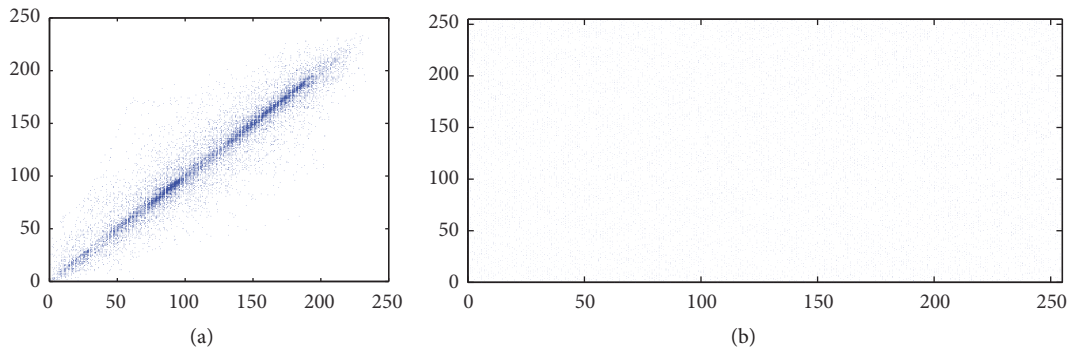


FIGURE 7: Correlation distributions of original and encrypted images.

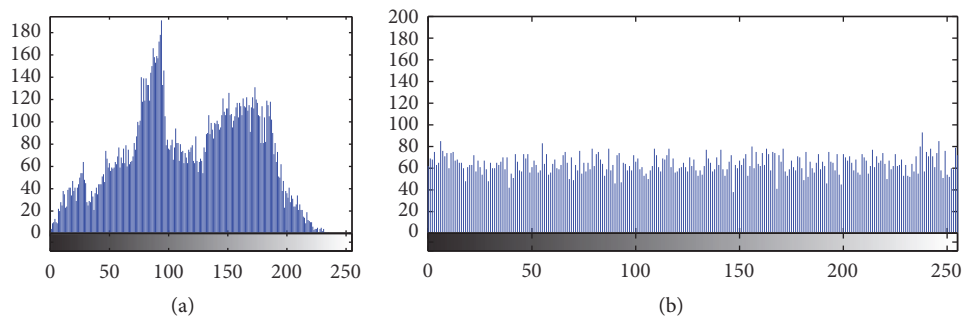


FIGURE 8: Histograms of original and encrypted images.

terms and has been implemented easily by an electronic circuit. The findings of this work add to a growing list of systems with hidden attractors. This work enhances our understanding of practical applications using systems with hidden attractors. We have used the system without equilibrium for image encryption and sound steganography. According to our knowledge, this is the first time that the 128 kbit data can be encrypted and hidden in sound files. Therefore the findings of this work have important implications for future practice. Other chaotic systems without equilibrium will be discovered in our future researches.

Conflicts of Interest

The authors declare that there are no conflicts of interest regarding the publication of this paper.

Acknowledgments

The authors acknowledge Professor GuanRong Chen, Department of Electronic Engineering, City University of Hong Kong, for suggesting many helpful references. The author Xiong Wang was supported by the National Natural

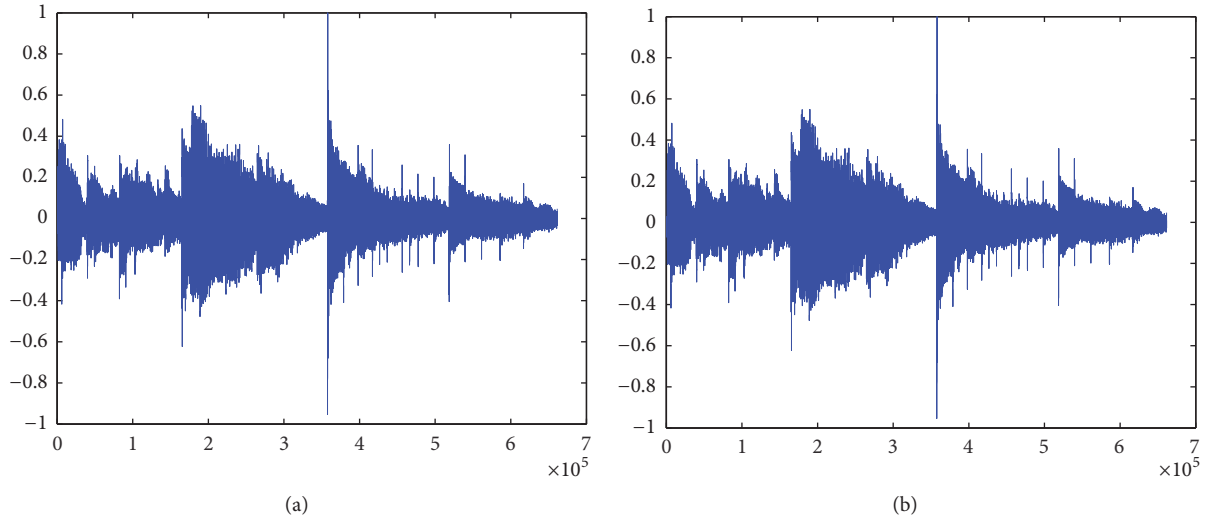


FIGURE 9: Original and embedded sound.

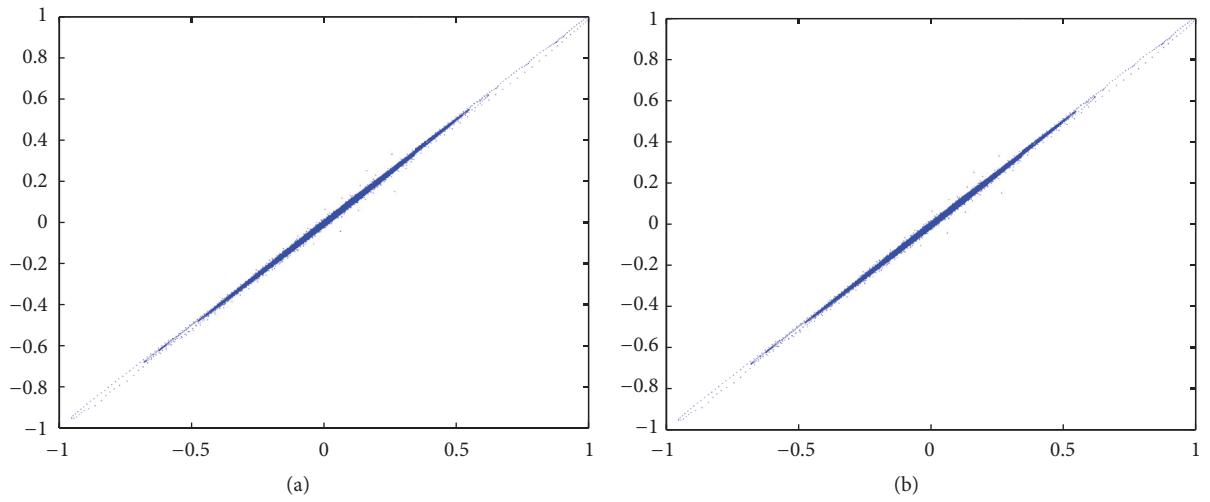


FIGURE 10: Correlation distributions of original and embedded sounds.

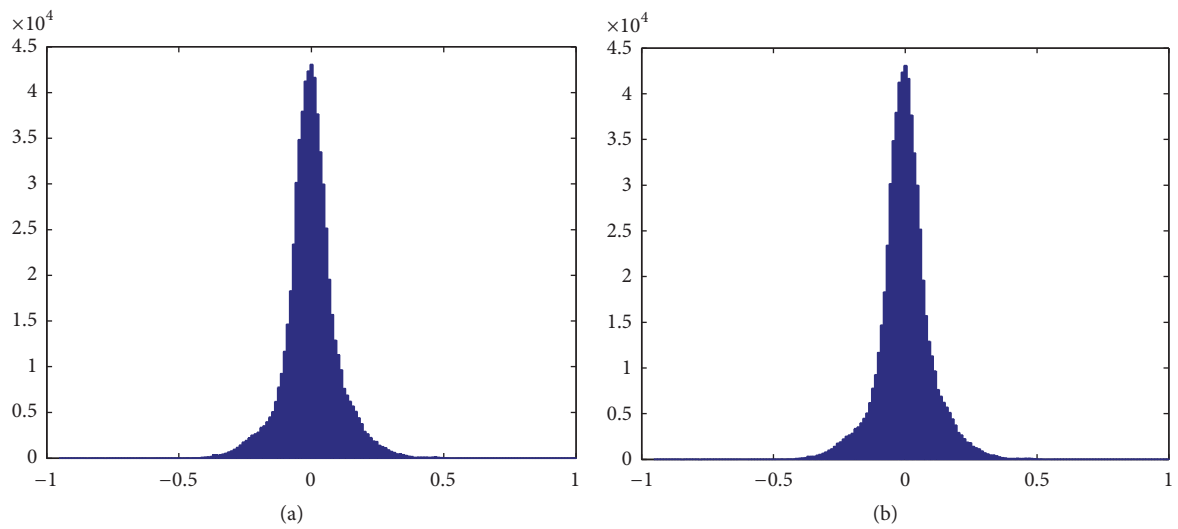


FIGURE 11: Histograms of original and embedded sounds.

Science Foundation of China (no. 61601306) and Shenzhen Overseas High Level Talent Peacock Project Fund (no. 20150215145C).

References

- [1] F. Y. Shih, *Multimedia Security: Watermarking, Steganography, and Forensics*, CRC Press, Boca Raton, Fla, USA, 2013.
- [2] A. E. Hassanien, M. M. Fouad, A. A. Manaf, M. Zamani, R. Ahmad, and J. Kacprzyk, *Multimedia Forensics and Security Foundations, Innovations, and Applications*, Springer, Berlin, Germany, 2017.
- [3] N. Dey and V. Santhi, *Intelligent Techniques in Signal Processing for Multimedia Security*, Springer, Berlin, Germany, 2017.
- [4] I. J. Cox, J. Kilian, F. T. Leighton, and T. Shamoon, "Secure spread spectrum watermarking for multimedia," *IEEE Transactions on Image Processing*, vol. 6, no. 12, pp. 1673–1687, 1997.
- [5] M. U. Celik, G. Sharma, E. Saber, and A. M. Tekalp, "Hierarchical watermarking for secure image authentication with localization," *IEEE Transactions on Image Processing*, vol. 11, no. 6, pp. 585–595, 2002.
- [6] J. Eggers and B. Girod, *Informed Watermarking*, Kluwer Academic, 2002, Kluwer Academic, Dordrecht, The Netherlands, 2002.
- [7] M. S. Baptista, "Cryptography with chaos," *Physics Letters A*, vol. 240, no. 1-2, pp. 50–54, 1998.
- [8] K.-W. Wong, "A combined chaotic cryptographic and hashing scheme," *Physics Letters. A*, vol. 307, no. 5-6, pp. 292–298, 2003.
- [9] Z. Dawei, C. Guanrong, and L. Wenbo, "A chaos-based robust wavelet-domain watermarking algorithm," *Chaos, Solitons & Fractals*, vol. 22, no. 1, pp. 47–54, 2004.
- [10] Y.-T. Wu and F. Y. Shih, "Digital watermarking based on chaotic map and reference register," *Pattern Recognition*, vol. 40, no. 12, pp. 3753–3763, 2007.
- [11] D. Zhao, G. Chen, and W. Liu, "Image scrambling encryption algorithm of pixel bit based on chaos map," *Pattern Recognition Letters*, vol. 31, no. 5, pp. 347–354, 2010.
- [12] G. Alvarez and S. Li, "Some basic cryptographic requirements for chaos-based cryptosystems," *International Journal of Bifurcation and Chaos in Applied Sciences and Engineering*, vol. 16, no. 8, pp. 2129–2151, 2006.
- [13] H. Liu, A. Kadir, and Y. Li, "Audio encryption scheme by confusion and diffusion based on multi-scroll chaotic system and one-time keys," *Optik - International Journal for Light and Electron Optics*, vol. 127, no. 19, pp. 7431–7438, 2016.
- [14] H. Liu, A. Kadir, and Y. Li, "Asymmetric color pathological image encryption scheme based on complex hyper chaotic system," *Optik*, vol. 127, no. 15, pp. 5812–5819, 2016.
- [15] Q. Liu, P.-Y. Li, M.-C. Zhang, Y.-X. Sui, and H.-J. Yang, "A novel image encryption algorithm based on chaos maps with Markov properties," *Communications in Nonlinear Science and Numerical Simulation*, vol. 20, no. 2, pp. 506–515, 2015.
- [16] M. Ghebleh and A. Kanso, "A robust chaotic algorithm for digital image steganography," *Communications in Nonlinear Science and Numerical Simulation*, vol. 19, no. 6, pp. 1898–1907, 2014.
- [17] G. Arumugam, V. Lakshmi Praba, and S. Radhakrishnan, "Study of chaos functions for their suitability in generating Message Authentication Codes," *Applied Soft Computing Journal*, vol. 7, no. 3, pp. 1064–1071, 2007.
- [18] G. A. Leonov, N. V. Kuznetsov, and V. I. Vagaitsev, "Localization of hidden Chua's attractors," *Physics Letters A*, vol. 375, no. 23, pp. 2230–2233, 2011.
- [19] G. A. Leonov, N. V. Kuznetsov, and V. I. Vagaitsev, "Hidden attractor in smooth Chua systems," *Physica D: Nonlinear Phenomena*, vol. 241, no. 18, pp. 1482–1486, 2012.
- [20] G. A. Leonov and N. V. Kuznetsov, "Hidden attractors in dynamical systems: from hidden oscillations in hilbert-kolmogorov, Aizerman, and Kalman problems to hidden chaotic attractor in chua circuits," *International Journal of Bifurcation and Chaos*, vol. 23, no. 1, Article ID 1330002, 2013.
- [21] D. Dudkowski, S. Jafari, T. Kapitaniak, N. V. Kuznetsov, G. A. Leonov, and A. Prasad, "Hidden attractors in dynamical systems," *Physics Reports*, vol. 637, pp. 1–50, 2016.
- [22] T. Kapitaniak, "Generating strange nonchaotic trajectories," *Physical Review E*, vol. 47, no. 2, pp. 1408–1410, 1993.
- [23] B. Blazejczyk-Okolewska and T. Kapitaniak, "Dynamics of impact oscillator with dry friction," *Chaos, Solitons & Fractals*, vol. 7, no. 9, pp. 1455–1459, 1996.
- [24] B. Blazejczyk-Okolewska and T. Kapitaniak, "Co-existing attractors of impact oscillator," *Chaos, Solitons & Fractals*, vol. 9, no. 8, pp. 1439–1443, 1998.
- [25] S. Kraut and U. Feudel, "Multistability, noise, and attractor hopping: the crucial role of chaotic saddles," *Physical Review E: Statistical, Nonlinear, and Soft Matter Physics*, vol. 66, no. 1, Article ID 015207, pp. 015207/1–015207/4, 2002.
- [26] S. L. T. de Souza, A. M. Batista, I. L. Caldas, R. L. Viana, and T. Kapitaniak, "Noise-induced basin hopping in a vibro-impact system," *Chaos, Solitons and Fractals*, vol. 32, no. 2, pp. 758–767, 2007.
- [27] U. Feudel, "Complex dynamics in multistable systems," *International Journal of Bifurcation and Chaos in Applied Sciences and Engineering*, vol. 18, no. 6, pp. 1607–1626, 2008.
- [28] M. D. Shrimali, A. Prasad, R. Ramaswamy, and U. Feudel, "The nature of attractor basins in multistable systems," *International Journal of Bifurcation and Chaos*, vol. 18, no. 6, pp. 1675–1688, 2008.
- [29] A. Chudzik, P. Perlikowski, A. Stefanski, and T. Kapitaniak, "Multistability and rare attractors in van der Pol-Duffing oscillator," *International Journal of Bifurcation and Chaos in Applied Sciences and Engineering*, vol. 21, no. 7, pp. 1907–1912, 2011.
- [30] A. N. Pisarchik and U. Feudel, "Control of multistability," *Physics Reports*, vol. 540, no. 4, pp. 167–218, 2014.
- [31] G. A. Leonov, N. V. Kuznetsov, M. A. Kiseleva, E. P. Solovyeva, and A. M. Zaretskiy, "Hidden oscillations in mathematical model of drilling system actuated by induction motor with a wound rotor," *Nonlinear Dynamics*, vol. 77, no. 1-2, pp. 277–288, 2014.
- [32] G. A. Leonov, N. V. Kuznetsov, and T. N. Mokaev, "Hidden attractor and homoclinic orbit in Lorenz-like system describing convective fluid motion in rotating cavity," *Communications in Nonlinear Science and Numerical Simulation*, vol. 28, no. 1-3, pp. 166–174, 2015.
- [33] Z. T. Zhusubaliyev, E. Mosekilde, A. N. Churilov, and A. Medvedev, "Multistability and hidden attractors in an impulsive Goodwin oscillator with time delay," *European Physical Journal: Special Topics*, vol. 224, no. 8, pp. 1519–1539, 2015.
- [34] M. A. Kiseleva, N. V. Kuznetsov, and G. A. Leonov, "Hidden attractors in electromechanical systems with and without equilibria," *IFAC-PapersOnLine*, vol. 49, no. 14, pp. 51–55, 2016.

- [35] H. Jiang, Y. Liu, Z. Wei, and L. Zhang, "Hidden chaotic attractors in a class of two-dimensional maps," *Nonlinear Dynamics*, vol. 85, no. 4, pp. 2719–2727, 2016.
- [36] N. V. Kuznetsov, G. A. Leonov, M. V. Yuldashev, and R. V. Yuldashev, "Hidden attractors in dynamical models of phase-locked loop circuits: limitations of simulation in MATLAB and SPICE," *Communications in Nonlinear Science and Numerical Simulation*, vol. 51, pp. 39–49, 2017.
- [37] M.-F. Danca, N. Kuznetsov, and G. Chen, "Unusual dynamics and hidden attractors of the Rabinovich–Fabrikant system," *Nonlinear Dynamics*, vol. 88, no. 1, pp. 791–805, 2017.
- [38] Z. Wei, "Dynamical behaviors of a chaotic system with no equilibria," *Physics Letters. A*, vol. 376, no. 2, pp. 102–108, 2011.
- [39] Z. Wang, S. Cang, E. O. Ochola, and Y. Sun, "A hyperchaotic system without equilibrium," *Nonlinear Dynamics*, vol. 69, no. 1–2, pp. 531–537, 2012.
- [40] S. Jafari, J. C. Sprott, and S. Hashemi Golpayegani, "Elementary quadratic chaotic flows with no equilibria," *Physics Letters A*, vol. 377, no. 9, pp. 699–702, 2013.
- [41] X. Wang and G. Chen, "Constructing a chaotic system with any number of equilibria," *Nonlinear Dynamics*, vol. 71, no. 3, pp. 429–436, 2013.
- [42] Z. Wei, R. Wang, and A. Liu, "A new finding of the existence of hidden hyperchaotic attractors with no equilibria," *Mathematics and Computers in Simulation*, vol. 100, pp. 13–23, 2014.
- [43] C. K. Volos, I. M. Kyprianidis, and I. N. Stouboulos, "A chaotic path planning generator for autonomous mobile robots," *Robotics and Autonomous Systems*, vol. 60, no. 4, pp. 651–656, 2012.
- [44] S. Bouali, A. Buscarino, L. Fortuna, M. Frasca, and L. V. Gambuzza, "Emulating complex business cycles by using an electronic analogue," *Nonlinear Analysis: Real World Applications*, vol. 13, no. 6, pp. 2459–2465, 2012.
- [45] C. K. Volos, I. M. Kyprianidis, and I. N. Stouboulos, "Image encryption process based on chaotic synchronization phenomena," *Signal Processing*, vol. 93, no. 5, pp. 1328–1340, 2013.
- [46] A. Buscarino, L. Fortuna, M. Frasca, and G. Sciuto, "Design of time-delay chaotic electronic circuits," *IEEE Transactions on Circuits and Systems I: Regular Papers*, vol. 58, no. 8, pp. 1888–1896, 2011.
- [47] W.-J. Zhou, Z.-P. Wang, M.-W. Wu, W.-H. Zheng, and J.-F. Weng, "Dynamics analysis and circuit implementation of a new three-dimensional chaotic system," *Optik*, vol. 126, no. 7–8, Article ID 55317, pp. 765–768, 2015.
- [48] Q. Lai and L. Wang, "Chaos, bifurcation, coexisting attractors and circuit design of a three-dimensional continuous autonomous system," *Optik*, vol. 127, no. 13, pp. 5400–5406, 2016.
- [49] A. Akgul, I. Moroz, I. Pehlivan, and S. Vaidyanathan, "A new four-scroll chaotic attractor and its engineering applications," *Optik - International Journal for Light and Electron Optics*, vol. 127, no. 13, pp. 5491–5499, 2016.
- [50] A. Akgul, S. Hussain, and I. Pehlivan, "A new three-dimensional chaotic system, its dynamical analysis and electronic circuit applications," *Optik*, vol. 127, no. 18, pp. 7062–7071, 2016.
- [51] B. Bao, T. Jiang, Q. Xu, M. Chen, H. Wu, and Y. Hu, "Coexisting infinitely many attractors in active band-pass filter-based memristive circuit," *Nonlinear Dynamics*, vol. 86, no. 3, pp. 1711–1723, 2016.
- [52] Ü. Çavuşoğlu, S. Kaçar, I. Pehlivan, and A. Zengin, "Secure image encryption algorithm design using a novel chaos based S-Box," *Chaos, Solitons and Fractals*, vol. 95, pp. 92–101, 2017.
- [53] O. M. Al-Hazaimeh, N. Alhindawi, S. M. A. Hayajneh, and A. Almomani, "HANON chaotic map - based new digital image encryption algorithm," *MAGNT Research Report*, vol. 2, pp. 261–266, 2014.
- [54] H. M. Al-Naijar, "Digital image encryption algorithm based on a linear independence scheme and the logistic map," in *Proceedings of the International Arab Conference on Information Technology (ACIT '11)*, pp. 215–219, 2011.
- [55] H. Al-Naijar and N. Al-Rousan, "Data hiding in encrypted image based on multi-chaotic approach," *International Journal of Scientific and Engineering Research*, vol. 4, pp. 1–5, 2013.
- [56] R. Enayatifar, A. H. Abdullah, and I. F. Isnin, "Chaos-based image encryption using a hybrid genetic algorithm and a DNA sequence," *Optics and Lasers in Engineering*, vol. 56, no. 5, pp. 83–93, 2014.
- [57] R. Enayatifar, H. J. Sadaei, A. H. Abdullah, M. Lee, and I. F. Isnin, "A novel chaotic based image encryption using a hybrid model of deoxyribonucleic acid and cellular automata," *Optics and Lasers in Engineering*, vol. 71, pp. 33–41, 2015.
- [58] S. Lian, J. Sun, and Z. Wang, "A block cipher based on a suitable use of the chaotic standard map," *Chaos, Solitons & Fractals*, vol. 26, no. 1, pp. 117–129, 2005.
- [59] K. Wong, B. S. Kwok, and W. Law, "A fast image encryption scheme based on chaotic standard map," *Physics Letters, Section A: General, Atomic and Solid State Physics*, vol. 372, no. 15, pp. 2645–2652, 2008.
- [60] Y. Wu, G. Yang, H. Jin, and J. P. Noonan, "Image encryption using the two-dimensional logistic chaotic map," *Journal of Electronic Imaging*, vol. 21, no. 1, Article ID 013014, 2012.
- [61] X. Liao, S. Lai, and Q. Zhou, "A novel image encryption algorithm based on self-adaptive wave transmission," *Signal Processing*, vol. 90, no. 9, pp. 2714–2722, 2010.

Research Article

Dynamic Analysis and Circuit Design of a Novel Hyperchaotic System with Fractional-Order Terms

Abir Lassoued and Olfa Boubaker

National Institute of Applied Sciences and Technology (INSAT), Centre Urbain Nord, BP 676, 1080 Tunis Cedex, Tunisia

Correspondence should be addressed to Abir Lassoued; lassoued.abir5@gmail.com

Received 28 June 2017; Revised 19 September 2017; Accepted 1 October 2017; Published 26 October 2017

Academic Editor: Dimitri Volchenkov

Copyright © 2017 Abir Lassoued and Olfa Boubaker. This is an open access article distributed under the Creative Commons Attribution License, which permits unrestricted use, distribution, and reproduction in any medium, provided the original work is properly cited.

A novel hyperchaotic system with fractional-order (FO) terms is designed. Its highly complex dynamics are investigated in terms of equilibrium points, Lyapunov spectrum, and attractor forms. It will be shown that the proposed system exhibits larger Lyapunov exponents than related hyperchaotic systems. Finally, to enhance its potential application, a related circuit is designed by using the MultiSIM Software. Simulation results verify the effectiveness of the suggested circuit.

1. Introduction

Hyperchaos was discovered by Rössler in 1979 [1] and the first hyperchaotic circuit was implemented by Matsumoto in 1986 [2]. In these last years, hyperchaotic systems have gained the interest of the scientific community and new systems and circuits are proposed [3–8]. This great interest can be explained by the aptitude of hyperchaotic systems to generate complex dynamics characterized by more than one positive Lyapunov exponent and attractors deployed in multiple directions. In practical applications and particularly in secure communication, chaotic synchronization has been explored by using electronic circuits, namely, Duffing circuit [9], Chua circuit [10], and Rössler circuit [11]. However, for hyperchaotic circuits, many challenging problems are still pending due to their complex behaviors.

On the other hand, several researches have attempted to construct chaotic and hyperchaotic models with simple algebraic structures highly recommended for circuit design. The most famous chaotic one is the Jerk system proposed by Sprott, in 1994 [12, 13], which contains simple nonlinear terms. However, it is well known that most systems contain conventional nonlinear terms like piecewise linear functions [14–17], integer order polynomials [8, 18], sine functions [19], time delayed functions [20], and switching functions [21]. In this framework, fractional-order polynomials could be used

to build complex chaotic behaviors and, to the best of our knowledge, they have not been harnessed until now.

The purpose of this paper is to build a novel hyperchaotic system with more complex dynamics than those proposed by related works. Expecting that the PWNL function with FO terms gives us more complex chaotic properties than the piecewise linear one, this PWNL function is constructed from absolute functions and FO polynomials. To enhance the potential application of the proposed system, its related circuit is designed afterwards with MultiSIM Software.

The rest of this paper is structured as follows. In Section 2, the mathematical model of the hyperchaotic system is proposed and its basic properties are presented. In Section 3, the dynamic analysis of the novel system is investigated by pointing out its elementary characteristics such as the Lyapunov exponents, the attractor forms, and the equilibrium points. In Section 4, the oscillator circuit of the hyperchaotic system is designed afterwards.

2. Mathematical Model and Basic Properties

Let consider the mathematical model of the novel hyperchaotic system with FO terms expressed by the following differential equations:

$$\dot{x} = y,$$

$$\dot{y} = z,$$

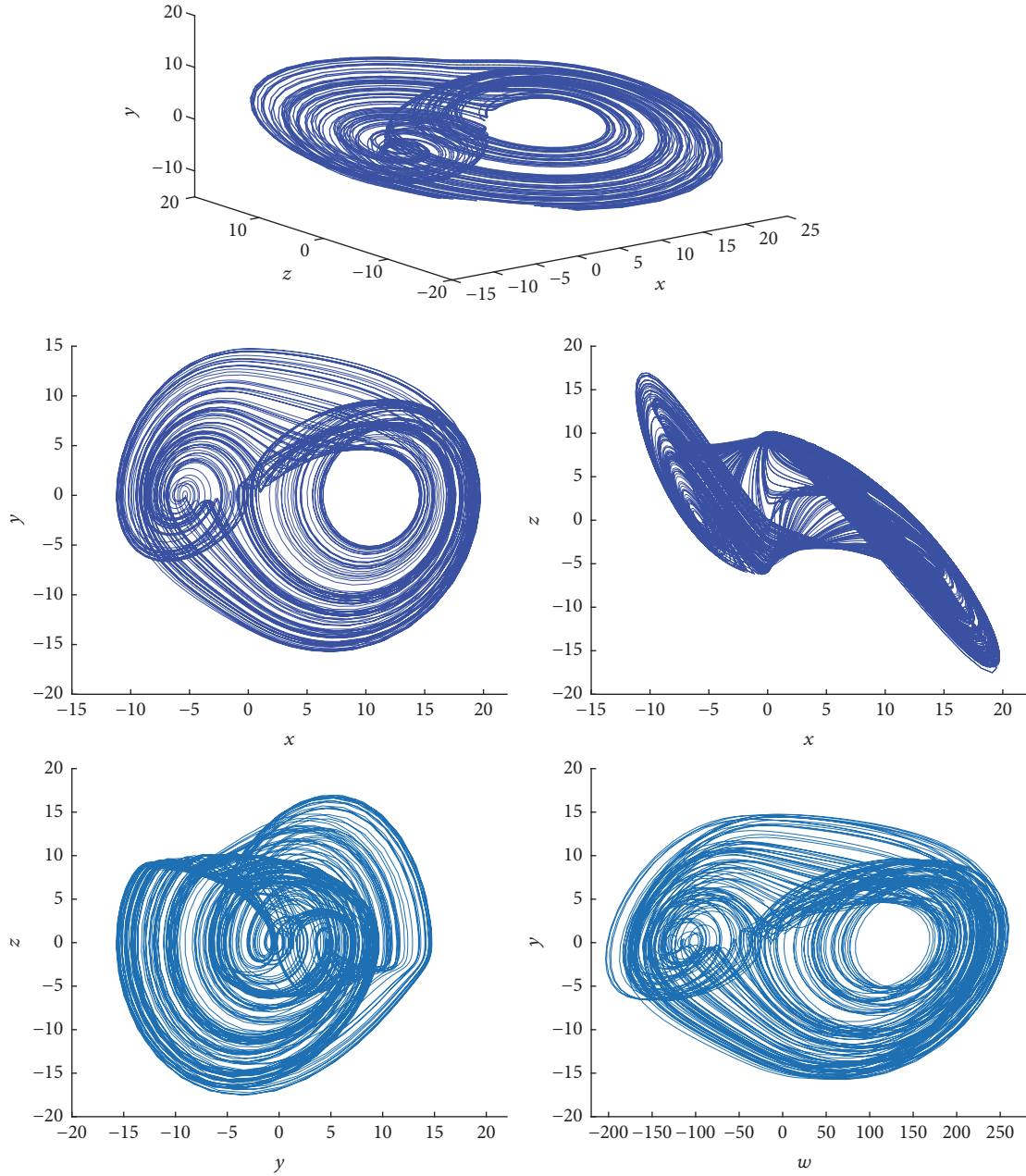


FIGURE 1: Projections of the attractor related to the hyperchaotic system (1) onto the spaces (x, y, z) , (x, y) , (x, z) , (y, z) , and (w, y) .

$$\begin{aligned} \dot{z} &= -az - by + G(x) \\ \dot{w} &= ky - hw + G(x), \end{aligned} \quad (1)$$

with $G(x)$ being a nonlinear function defined as

$$G(x) = -cx^2 + d|x|x + m|x|^r x^{-1}, \quad 1 < r < 2, \quad (2)$$

where (a, b, c, d, h, k, m, r) are the system's parameters and (x, y, z, w) are the state variables. r is a fractional number satisfying $1 < r < 2$. Since $r \neq 1$, $|x|^r x^{-1}$ will never be an indeterminate form. The nonlinear function $G(x)$ can be written as follows:

$$G(x) = \begin{cases} (-c - d)x^2 - m(-x)^{r-1}, & \text{if } x < 0, \\ 0, & \text{if } x = 0, \\ (-c + d)x^2 + mx^{r-1}, & \text{if } x > 0. \end{cases} \quad (3)$$

System (1) can exhibit chaotic behavior if the general condition of dissipativity is satisfied such as

$$\frac{\partial \dot{x}}{\partial x} + \frac{\partial \dot{y}}{\partial y} + \frac{\partial \dot{z}}{\partial z} + \frac{\partial \dot{w}}{\partial w} = -a - h < 0. \quad (4)$$

As long as $a + h > 0$, system (1) is dissipative and it converges to an attractor. Thus, when the parameters (a, b, c, d, m, r, h, k) are equal to $(0.93, 1.11, -0.11, -0.21, 6.26, 1.32, 0.001, 14)$ and the initial condition is equal to $(1, 1, 1, 1)$, system (1) generates a strange attractor displayed in Figure 1. This attractor has

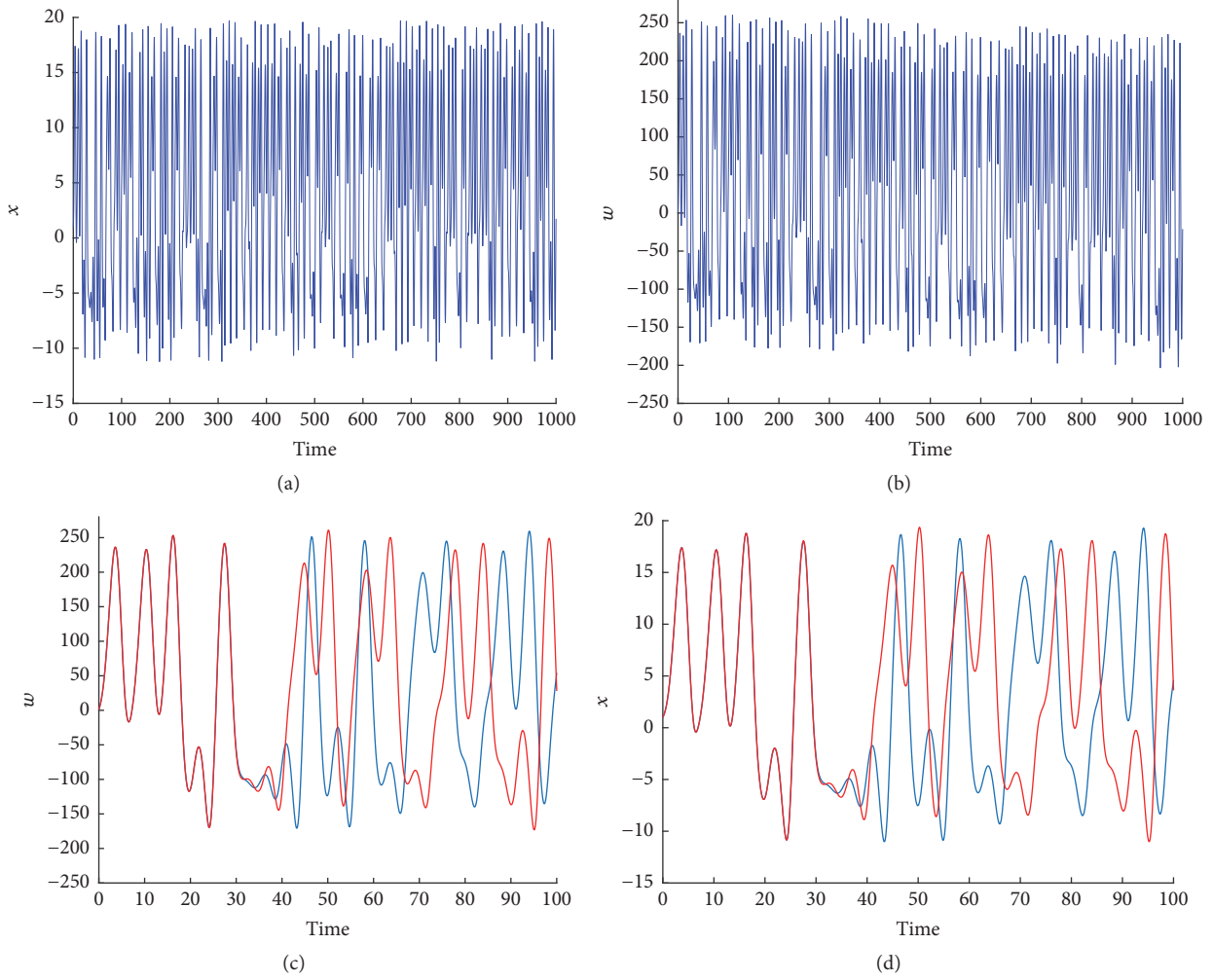


FIGURE 2: Time series and sensitive dependence on initial conditions $(1, 1, 1)$ (blue) and $(1.001, 1, 1)$ (red): (a) and (d) variable x ; (b) and (c) variable w .

an asymmetrical form with respect to all the principal axes characterized by two scrolls of different sizes.

The time series of the state variables x and w are described in Figures 2(a) and 2(b). These signals represent the chaotification rates of each variable. On the other hand, system (1) is sensitive to initial conditions as shown in Figures 2(c) and 2(d). Note that the variation range of the variable w is extended within $[-250, 200]$, unlike the other variables. This point must be considered in practical applications.

3. Dynamic Analysis

3.1. Equilibrium and Stability. The equilibrium points of system (1) are obtained by solving these equations:

$$\begin{aligned} y &= z = w = 0, \\ -cx^2 + d|x|x + m|x|^r x^{-1} &= 0. \end{aligned} \quad (5)$$

Proposition 1. (i) If $x = 0$, then $w = 0$ and the origin $H_1 = (0, 0, 0, 0)$ is the first equilibrium of system (1).

(ii) If $x > 0$, then $w = 0$ and $H_2 = (((c-d)/m)^{1/\alpha}, 0, 0, 0)$ is an equilibrium of system (2) where $\alpha = r - 3$.

(iii) If $x < 0$, then $w = 0$ and $H_3 = ((-(-c-d)/m)^{1/\alpha}, 0, 0, 0)$ is an equilibrium of system (2) where $\alpha = r - 3$.

Proof. Case (i) is obvious.

For case (ii), we should solve the following equation: $-c + d + mx^{r-3} = 0$ which admits the solution $x^\alpha = (c-d)/m$ with $\alpha = r - 3$. The roots of this equation are given by [22]

$$x = \left| \frac{(c-d)}{m} \right|^{1/\alpha} e^{(j\theta_1 \pm 2n\pi)/\alpha} \quad (6)$$

with $n \in \mathbb{N}$, θ_1 being the phase of x^α , and α being a fractional number. Notice that the term $(c-d)/m$ is positive when $c = -0.11$, $d = -0.21$, and $m = 6.26$. Then, θ_1 is equal to zero and we have $x = ((c-d)/m)^{1/\alpha}$.

For case (iii), we should solve the following equation: $-c - d - m(-x)^{r-3} = 0$ which admits the solution $(-x)^\alpha = X^\alpha = (-c-d)/m$ with $\alpha = r - 3$. The roots of this equation are given by [22]

$$X = \left| \frac{(-c-d)}{m} \right|^{1/\alpha} e^{(j\theta_2 \pm 2n\pi)/\alpha} \quad (7)$$

TABLE 1: Stability analysis of system (1).

Equilibrium point	Jacobian matrix	Corresponding eigenvalues	Stability analysis
H_1	$\begin{pmatrix} 0 & 1 & 0 & 0 \\ 0 & 0 & 1 & 0 \\ 0 & -b & -a & 0 \\ 0 & k & 0 & -h \end{pmatrix}$	$\begin{aligned} \lambda_1 &= 0 \\ \lambda_2 &= -0.001 \\ \lambda_3 &= -0.465 + 0.945i \\ \lambda_4 &= -0.465 - 0.945i \end{aligned}$	Stable point
H_2	$\begin{pmatrix} 0 & 1 & 0 & 0 \\ 0 & 0 & 1 & 0 \\ \Delta_1 & -b & -a & 0 \\ \Delta_1 & k & 0 & -h \end{pmatrix}$ $\Delta_1 = 2dx - 2cx + (r-1)mx^{r-2}$	$\begin{aligned} \lambda_1 &= -0.001 \\ \lambda_2 &= -1.273 \\ \lambda_3 &= 0.171 + 1.232i \\ \lambda_4 &= 0.171 - 1.232i \end{aligned}$	Unstable point
H_3	$\begin{pmatrix} 0 & 1 & 0 & 0 \\ 0 & 0 & 1 & 0 \\ \Delta_2 & -b & -a & 0 \\ \Delta_2 & k & 0 & -h \end{pmatrix}$ $\Delta_2 = -2dx - 2cx - (r-1)mx^{r-2}$	$\begin{aligned} \lambda_1 &= -0.001 \\ \lambda_2 &= -2.297 \\ \lambda_3 &= 0.683 + 1.945i \\ \lambda_4 &= 0.683 - 1.945i \end{aligned}$	Unstable point

with $n \in \mathbb{N}$, θ_2 being the phase of x^α , and α being a fractional number. Notice that the term $(-c-d)/m$ is positive when $c = -0.11$, $d = -0.21$, and $m = 6.26$. Then, θ_2 is equal to zero and we have $x = (-(-c-d)/m)^{1/\alpha}$.

When the parameters (a, b, c, d, m, r, h, k) are equal to $(0.93, 1.11, -0.11, -0.21, 6.26, 1.32, 0.001, 14)$, system (1) admits three equilibrium points: $H_1 = (0, 0, 0, 0)$, $H_2 = (11.73, 0, 0, 0)$, and $H_3 = (-5.87, 0, 0, 0)$. For the stability analysis, Table 1 gives the Jacobian matrix J and its corresponding eigenvalues calculated for each equilibrium point. \square

3.2. Lyapunov Exponents Analysis. System (1) exhibits four Lyapunov exponents (LEs). These LEs are esteemed using the Wolf algorithm [23], as shown in Figure 3 as

$$\begin{aligned} \text{LE}_1 &= 0.232, \\ \text{LE}_2 &= 0.020, \\ \text{LE}_3 &= 0, \\ \text{LE}_4 &= -1.169. \end{aligned} \quad (8)$$

Since the LE spectrum has two positive Lyapunov exponents; thus system (1) is hyperchaotic. λ_1 is the largest positive one. This exponent increases the expansion degree of the attractor in the phase space.

In addition, the corresponding Kaplan-Yorke dimension is

$$D_L = 3 + \frac{(\lambda_1 + \lambda_2 + \lambda_3)}{|\lambda_4|} = 3.19. \quad (9)$$

3.3. Routes to Chaos. System (1) can display periodic orbits, chaos, and hyperchaos attractors under different conditions. In fact, when the parameter m varies and the parameters (a, b, c, d, r, h, k) are fixed, two Hopf bifurcations are detected as shown in Figure 4. These bifurcations are denoted H in the bifurcation diagram and they appear when $m = 0.99$ and $m = 2.11$, respectively. Each Hopf point is characterized by a

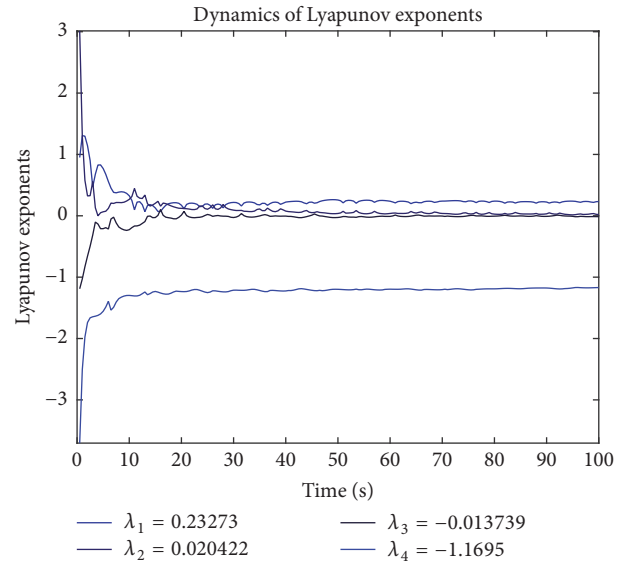


FIGURE 3: The Lyapunov exponent spectrum of the hyperchaotic system (1).

first Lyapunov coefficient (FLC). A positive FLC indicates the existence of a supercritical Hopf bifurcation, whereas a negative one indicates a subcritical Hopf bifurcation. In system (1), the two points obtained are supercritical Hopf bifurcations. This type of bifurcation indicates that the evolution to chaotic behavior is possible.

In addition, as the parameter of bifurcation m increases, system (1) undergoes the following routes:

- (i) If $-1 \leq m \leq 0.3$, then system (1) exhibits periodic orbit. Figure 5(a) shows this regular attractor with $m = -0.5$.
- (ii) If $0.3 < m \leq 2.1$, then system (1) converges to a fixed point as shown in Figure 5(b).

TABLE 2: The LEs of some typical attractors of system (1).

m	LE_1	LE_2	LE_3	LE_4	Attractor
3.6	0	0	-0.42	0.8	Periodic orbit
3.8	0.05	0	-0.01	-0.92	Chaotic attractor
6	0.18	0.007	0	-1.10	Hyperchaotic attractor
6.5	0.17	0.01	0	-1.16	Hyperchaotic attractor

TABLE 3: Comparative analysis with related hyperchaotic systems.

Hyperchaotic system	Lyapunov exponents	Kaplan-Yorke dimension
Proposed hyperchaotic system	$LE_1 = 0.231$	$D_{KY} = 3.19$
	$LE_2 = 0.020$	
	$LE_3 = 0$	
	$LE_4 = -1.169$	
Piecewise linear hyperchaotic circuit [25]	$LE_1 = 0.064$	$D_{KY} = 3.089$
	$LE_2 = 0.033$	
	$LE_3 = 0$	
	$LE_4 = -1.098$	
Hyperchaotic hyperjerk system [26]	$LE_1 = 0.142$	$D_{KY} = 3.134$
	$LE_2 = 0.046$	
	$LE_3 = 0$	
	$LE_4 = -1.396$	

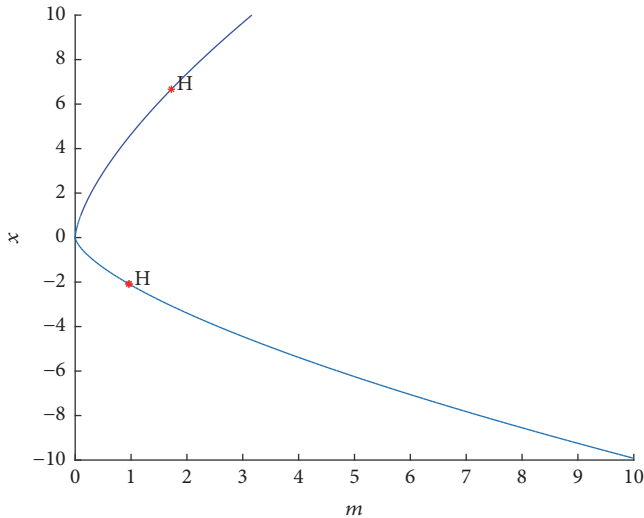


FIGURE 4: Hopf bifurcations.

- (iii) If $2.1 < m \leq 3.8$, then another periodic orbit is obtained as shown in Figure 5(c) with $m = 1$.
- (iv) If $3.8 < m \leq 5.5$, system (1) exhibits chaotic attractor. Figure 5(d) shows this strange attractor with $m = 4.5$.
- (v) If $5.5 < m < 7$, then system (1) exhibits hyperchaotic attractor. Figure 5(e) shows this strange attractor with $m = 6$.

Some typical attractors are tabulated in Table 2 according to the parameter m .

3.4. Comparative Analysis. Referring to the survey paper [24], the first Lyapunov exponent can be one of the comparative criteria between hyperchaotic systems. Table 3 presents

a comparative analysis between system (1) and two related ones, recently proposed in literature. Such a choice is based on the fact that, identical to system (1), the first comparative example contains linear piecewise functions whereas the second one is based on the jerk equation. Based on Table 3, it is clear that system (1) exhibits more complex dynamics. Thus, this confirms the highlight potential applications of noninteger order terms with respect to classical nonlinear terms.

4. Circuit Design

It is obvious that hardware implementation of chaotic systems is an interesting task in engineering applications, namely, for secure communications and random bits generation. Therefore, the aim of this section is to design an analog circuit that can build hyperchaotic behaviors according to system (1).

4.1. Design of the Analog Circuit with MultiSIM. For the circuit implementation, we choose the particular case study when the system parameter r is fixed to 1.5. Thus, the proposed system will be defined by the following model:

$$\begin{aligned}
 \dot{x} &= y, \\
 \dot{y} &= z, \\
 \dot{z} &= -az - by - cx^2 + d|x|x + m\sqrt{|x|}\text{sgn}(x) \\
 \dot{w} &= ky - hw - cx^2 + d|x|x + m\sqrt{|x|}\text{sgn}(x),
 \end{aligned} \tag{10}$$

where the system parameters (a, b, c, d, m, h, k) are equal to $(1, 1, -0.11, -0.21, 5, 0.01, 14)$. System (10) exhibits four LEs such as

$$LE_1 = 0.18,$$

$$LE_2 = 0.04,$$

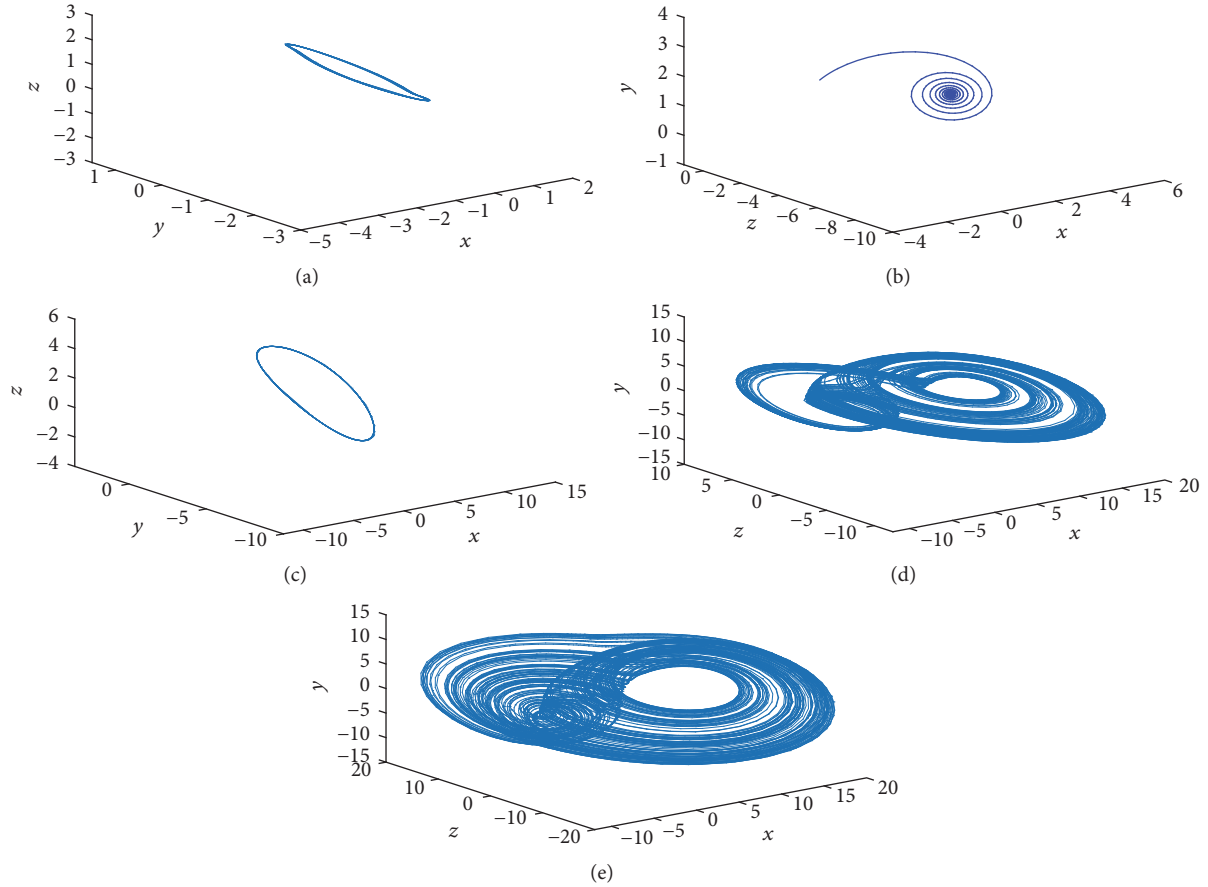


FIGURE 5: Different attractors forms exhibited by system (1) when parameter m varies.

$$\begin{aligned} LE_3 &= 0, \\ LE_4 &= -1.2. \end{aligned} \quad (11)$$

Despite the observation of the obtained phase portraits of system (10), we deduce that the maximum value of the signal w can reach the level of 250. Thus, 250 V is a sufficiently high voltage for the common components used in the proposed circuit. Therefore, a linear transformation for system (10) is necessary to decrease the amplitude of the state variables. Letting $u = x/2$, $v = y/2$, $g = z/2$, and $f = w/160$ and then setting the original state variables x , y , z , and w instead of the variable u , v , g , and f , the adjusted system becomes the following one:

$$\begin{aligned} \dot{x} &= y, \\ \dot{y} &= z, \\ \dot{z} &= az - by - 2cx^2 + 2d|x|x + \frac{m}{\sqrt{2}}\sqrt{|x|}\text{sgn}(x) \\ \dot{w} &= ky - 80hw - 2cx^2 + 2d|x|x + \frac{m}{\sqrt{2}}\sqrt{|x|}\text{sgn}(x). \end{aligned} \quad (12)$$

The amplitude of the state variables of system (10) has decreased as shown in Figure 6. Moreover, the two systems (10) and (12) are equivalent since the linear transformation does not change the physical properties of nonlinear systems.

To design the hyperchaotic circuit of system (12), only common electronic components are used such as resistors, capacitors, diodes, multipliers, and operational amplifiers. In fact, the nonlinear terms of system (12) should be designed first, namely, the quadratic term, the absolute function, the sign function, and the square root function. The quadratic term is implemented with the analog multiplier. The square root element is designed with two operational amplifiers as only active elements [27]. The analog circuit of the square root element is provided in Figure 7.

For the theoretical study and based on [27], the second voltage source in Figure 7 should be fixed to 2.878 V. However, in experimentation applications, we have obtained the root square function by using a stabilized voltage equal to 2.9 V as shown in Figure 8. This figure describes two voltages; the first one is a positive source signal and the second one is the output signal of the square root circuit. Based on these results, the observed maximum voltages are equal to 720 mV and 900 mV ($\approx \sqrt{0.72} = 0.88$), respectively. Thus, the square root function is correctly obtained with 2.9 V. In addition, based on MultiSIM results and experimental simulations, if the source voltage is included in [2.7 V, 3 V] then system (12) generates strange attractors. To avoid making this paper more cumbersome, details on experiments and experimental results will be soon presented in future works, confirming the MultiSIM results.

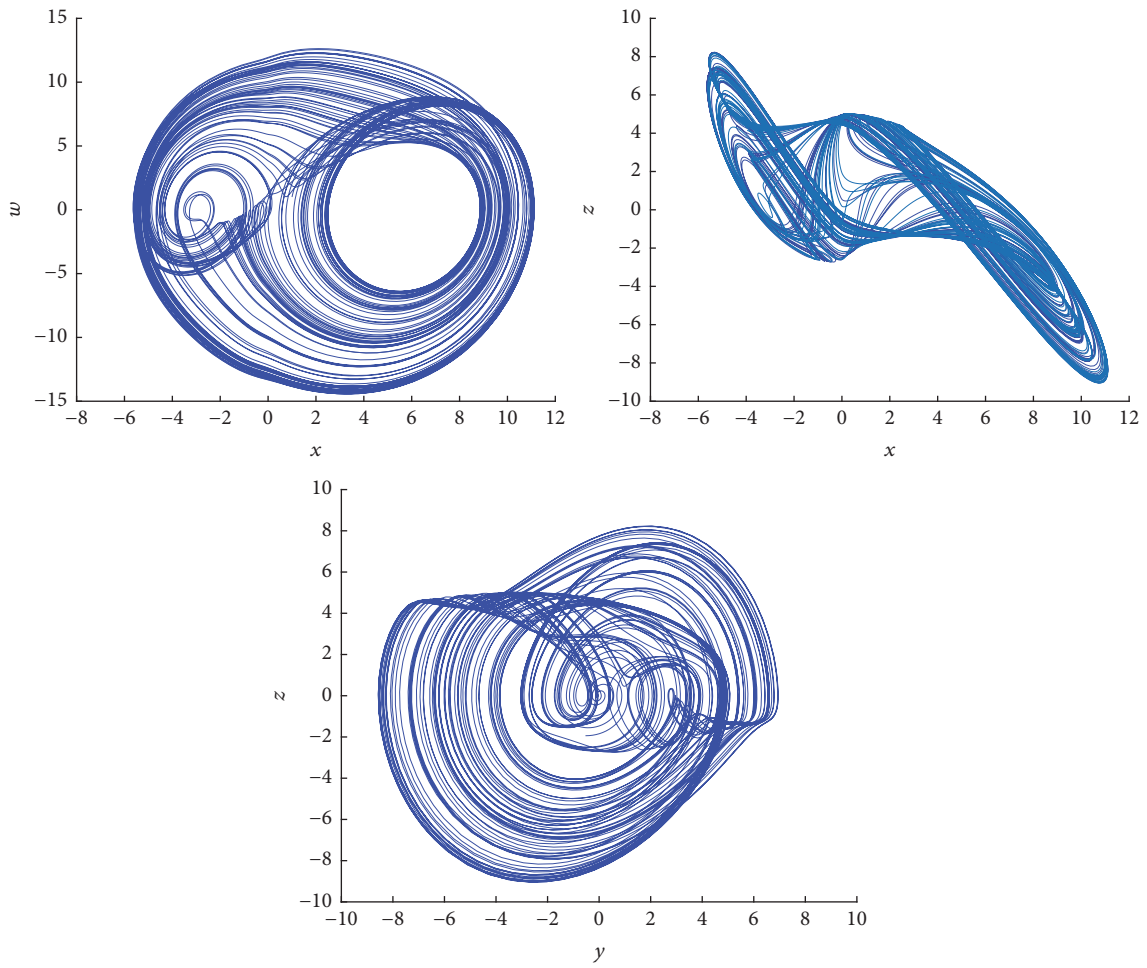


FIGURE 6: Projections of the attractor related to the adjusted hyperchaotic system (12) onto the spaces (x, w) , (x, z) , and (y, z) .

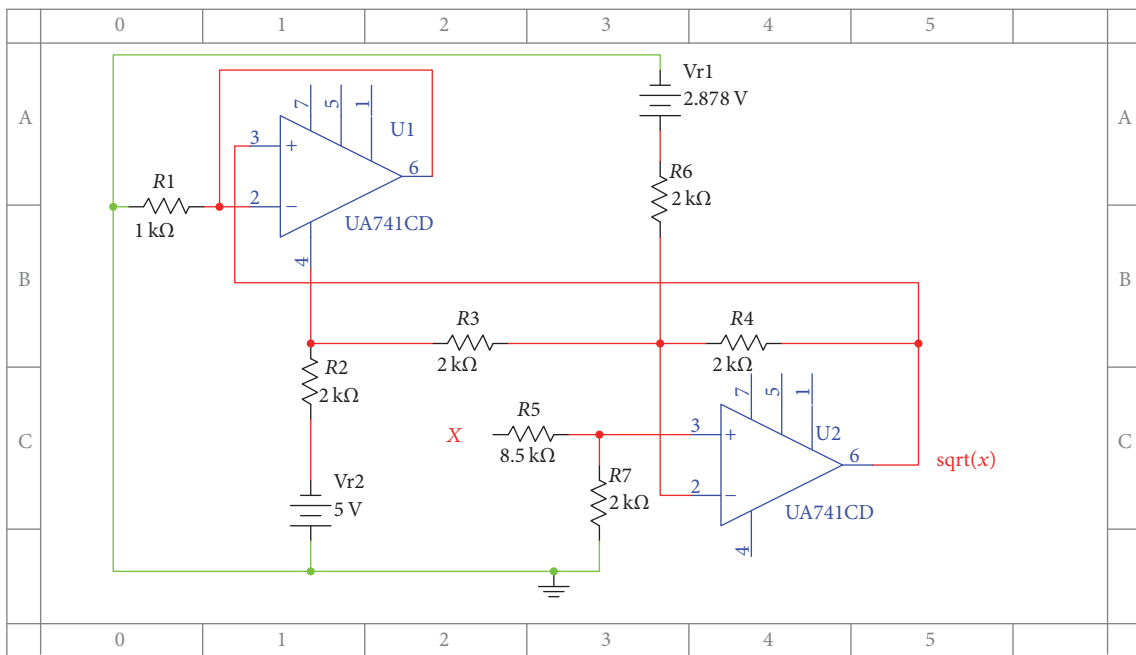


FIGURE 7: Circuit design of the square root function with MultiSIM.

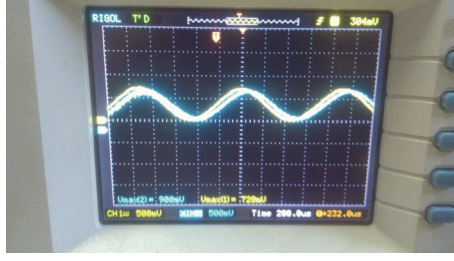


FIGURE 8: Experimental results of the square root function.

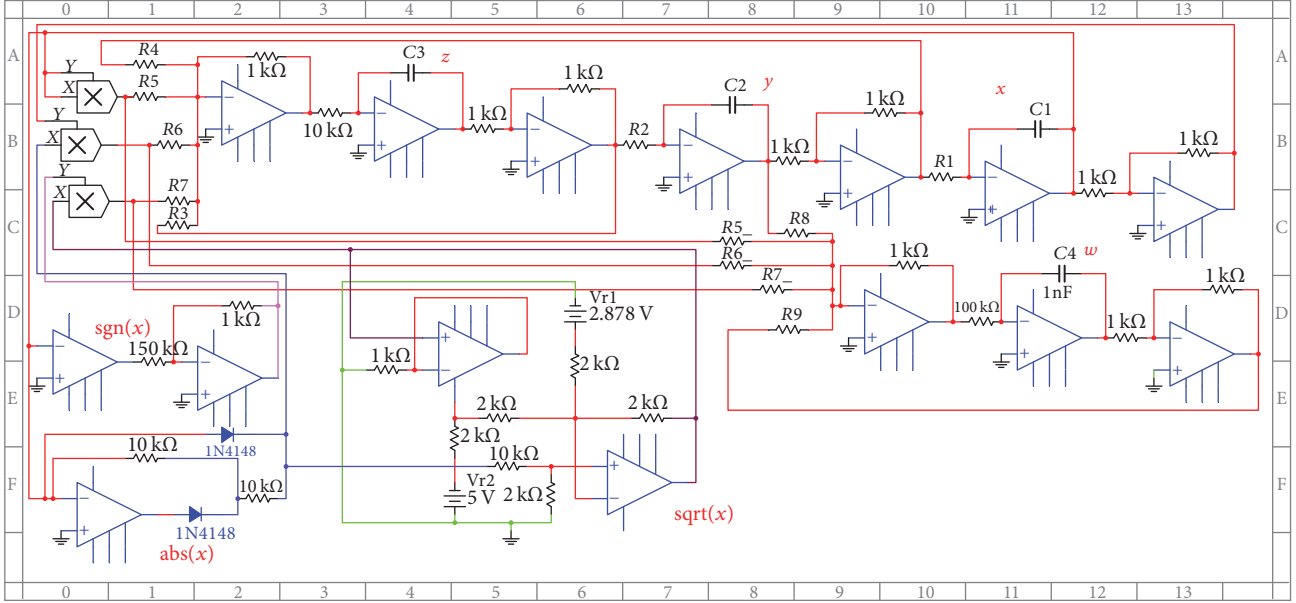


FIGURE 9: Circuit design of the hyperchaotic system with MultiSIM.

The corresponding circuit equation of the hyperchaotic system can be described as

$$\begin{aligned} \dot{x} &= \frac{1}{R_1 C_1} y, \\ \dot{y} &= \frac{1}{R_2 C_2} z, \\ \dot{z} &= -\frac{1}{R_3 C_3} z - \frac{1}{R_4 C_3} y + \frac{1}{R_5 C_3} x^2 - \frac{1}{R_6 C_3} |x| x \\ &\quad + \frac{1}{R_7 C_3} \sqrt{|x|} \operatorname{sgn}(x) \end{aligned} \quad (13)$$

$$\begin{aligned} \dot{w} &= -\frac{1}{R_8 C_4} y - \frac{1}{R_9 C_4} w + \frac{1}{R_5 C_4} x^2 - \frac{1}{R_6 C_4} |x| x \\ &\quad + \frac{1}{R_7 C_4} \sqrt{|x|} \operatorname{sgn}(x). \end{aligned}$$

According to system (12) and (13) and design considerations, we fixed the values of the resistances and the capacitors as

$$\begin{aligned} C_1 &= C_2 = C_3 = 1 \text{ nF}, \\ C_4 &= 0.1 \text{ nF}, \end{aligned}$$

$$\begin{aligned} R_1 &= R_2 = 100 \text{ k}\Omega, \\ R_3 &= R_4 = 10 \text{ k}\Omega, \\ R_5 &= 4.554 \text{ k}\Omega, \\ R_6 &= 2.5 \text{ k}\Omega, \\ R_7 &= 0.2 \text{ k}\Omega, \\ R_8 &= 7 \text{ k}\Omega, \\ R_9 &= 1.25 \text{ k}\Omega. \end{aligned} \quad (14)$$

Finally, the obtained circuit diagram, designed with MultiSIM Software, is provided in Figure 9 where the multiplier is AD633 and the operator amplifier is UA741.

4.2. Simulation Results. For the oscillator circuit, all active devices (UA741 and AD633) are powered by ± 15 V. Several design considerations were taken into account to prevent degrading the hyperchaotic behavior such as the adjustment of the resistors and the capacitors for the integration operations.

The oscilloscope traces of the proposed circuit are shown in Figure 10. Comparing the different hyperchaotic attractors shown in Figures 6 and 10, a good qualitative agreement

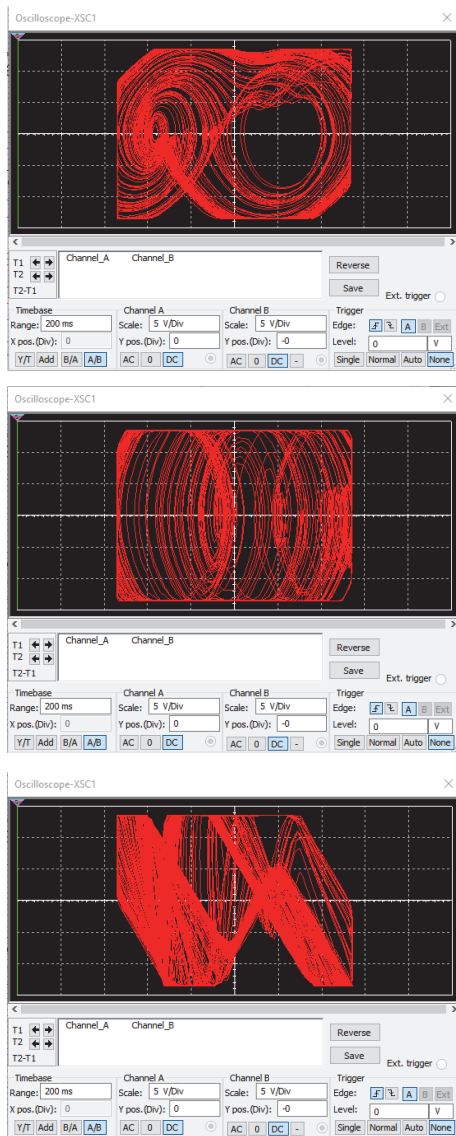


FIGURE 10: Simulation results of the hyperchaotic system with MultiSIM Software.

between the numerical simulations with Matlab and the electrical simulations with MultiSIM Software is observed. In fact, for MultiSIM Software, we have obtained the same attractors forms as those obtained by Matlab simulations. However, in these last attractors, some saturation effects are detected due to the operational amplifiers responses. To avoid making this paper more cumbersome, details on experiments and experimental results will be presented in future works, where saturation effects of amplifiers will be deeply analyzed.

5. Conclusions

In this paper, a novel hyperchaotic system is proposed by considering fractional-order polynomials. Analytical and numerical results show that this system exhibits more complex behaviors than those proposed by related works. Moreover, its analog circuit is designed and simulated with MultiSIM Software. In future works, experimental realization of

the hyperchaotic circuit will be proposed and the saturation effects induced by the operational amplifiers will be analyzed. Thereafter, the proposed circuit will be considered for secure image encryption and decryption applications.

Conflicts of Interest

The authors declare that there are no conflicts of interest regarding the publication of this paper.

References

- [1] O. E. Rossler, "An equation for hyperchaos," *Physics Letters A*, vol. 71, no. 2-3, pp. 155–157, 1979.
- [2] T. Matsumoto, L. Chua, and K. Kobayashi, "Hyperchaos: laboratory experiment and numerical confirmation," *IEEE Transactions on Circuits and Systems*, vol. 33, no. 11, pp. 1143–1147, 1986.
- [3] C.-L. Li, J.-B. Xiong, and W. Li, "A new hyperchaotic system and its generalized synchronization," *Optik-International Journal for Light and Electron Optics*, vol. 125, no. 1, pp. 575–579, 2014.
- [4] Z. Wei, R. Wang, and A. Liu, "A new finding of the existence of hidden hyperchaotic attractors with no equilibria," *Mathematics and Computers in Simulation*, vol. 100, pp. 13–23, 2014.
- [5] K. Rajagopal, L. Guessas, S. Vaidyanathan, A. Karthikeyan, and A. Srinivasan, "Dynamical analysis and FPGA implementation of a novel hyperchaotic system and its synchronization using adaptive sliding mode control and genetically optimized PID control," *Mathematical Problems in Engineering*, vol. 2017, Article ID 7307452, 14 pages, 2017.
- [6] Y. Feng, Z. Wei, U. E. Kocamaz, A. Akgül, and I. Moroz, "Synchronization and electronic circuit application of hidden hyperchaos in a four-dimensional self-exciting homopolar disc dynamo without equilibria," *Complexity*, vol. 2017, Article ID 7101927, 11 pages, 2017.
- [7] Z. Wei and W. Zhang, "Hidden hyperchaotic attractors in a modified lorenz-stenflo system with only one stable equilibrium," *International Journal of Bifurcation and Chaos*, vol. 24, no. 10, article 1450127, 2014.
- [8] A. T. Azar, C. Volos, N. A. Gerodimos et al., "A novel chaotic system without equilibrium: Dynamics, synchronization, and circuit realization," *Complexity*, vol. 2017, Article ID 7871467, 11 pages, 2017.
- [9] A. E. Matouk, "Chaos, feedback control and synchronization of a fractional-order modified autonomous Van der Pol-Duffing circuit," *Communications in Nonlinear Science and Numerical Simulation*, vol. 16, no. 2, pp. 975–986, 2011.
- [10] M. Mamat, W. S. Mada Sanjaya, and D. S. Maulana, "Numerical simulation chaotic synchronization of Chua circuit and its application for secure communication," *Applied Mathematical Sciences*, vol. 7, no. 1-4, pp. 1–10, 2013.
- [11] T. L. Carroll, "A simple circuit for demonstrating regular and synchronized chaos," *American Journal of Physics*, vol. 63, no. 4, pp. 377–379, 1995.
- [12] J. C. Sprott, "Some simple chaotic flows," *Physical Review E: Statistical, Nonlinear, and Soft Matter Physics*, vol. 50, no. 2, part A, pp. R647–R650, 1994.
- [13] H. P. Gottlieb, "What is the simplest jerk function that gives chaos?" *American Journal of Physics*, vol. 64, no. 5, article 525, 1996.
- [14] J. C. Sprott, "A new class of chaotic circuit," *Physics Letters A*, vol. 266, no. 1, pp. 19–23, 2000.

- [15] E. Campos-Cantón, “Chaotic attractors based on unstable dissipative systems via third-order differential equation,” *International Journal of Modern Physics C*, vol. 27, no. 1, 2016.
- [16] R. J. Escalante-González, E. Campos-Cantón, and M. Nicol, “Generation of multi-scroll attractors without equilibria via piecewise linear systems,” *Chaos: An Interdisciplinary Journal of Nonlinear Science*, vol. 27, no. 5, article 053109, 2017.
- [17] R. J. Escalante-González and E. Campos-Cantón, “Generation of chaotic attractors without equilibria via piecewise linear systems,” *International Journal of Modern Physics C*, vol. 28, no. 1, article 1750008, 2017.
- [18] V. Patidar and K. K. Sud, “Bifurcation and chaos in simple jerk dynamical systems,” *Pramana—Journal of Physics*, vol. 64, no. 1, pp. 75–93, 2005.
- [19] S. Vaidyanathan, C. Volos, V.-T. Pham, K. Madhavan, and B. A. Idowu, “Adaptive backstepping control, synchronization and circuit simulation of a 3-D novel jerk chaotic system with two hyperbolic sinusoidal nonlinearities,” *Archives of Control Sciences*, vol. 24, no. 3, pp. 375–403, 2014.
- [20] Z. Wei, V.-T. Pham, T. Kapitaniak, and Z. Wang, “Bifurcation analysis and circuit realization for multiple-delayed wangchen system with hidden chaotic attractors,” *Nonlinear Dynamics*, vol. 85, no. 3, pp. 1635–1650, 2016.
- [21] P. Li, T. Zheng, C. Li, X. Wang, and W. Hu, “A unique jerk system with hidden chaotic oscillation,” *Nonlinear Dynamics*, vol. 86, no. 1, pp. 197–203, 2016.
- [22] A. G. Radwan, A. M. Soliman, A. S. Elwakil, and A. Sedeek, “On the stability of linear systems with fractional-order elements,” *Chaos, Solitons & Fractals*, vol. 40, no. 5, pp. 2317–2328, 2009.
- [23] A. Wolf, J. B. Swift, H. L. Swinney, and J. A. Vastano, “Determining Lyapunov exponents from a time series,” *Physica D: Nonlinear Phenomena*, vol. 16, no. 3, pp. 285–317, 1985.
- [24] A. Lassoued and O. Boubaker, “On new chaotic and hyperchaotic systems: a literature survey,” *Lithuanian Association of Nonlinear Analysts. Nonlinear Analysis: Modelling and Control*, vol. 21, no. 6, pp. 770–789, 2016.
- [25] C. Li, J. C. Sprott, W. Thio, and H. Zhu, “A new piecewise linear hyperchaotic circuit,” *IEEE Transactions on Circuits and Systems II: Express Briefs*, vol. 61, no. 12, pp. 977–981, 2014.
- [26] S. Vaidyanathan, “Analysis, adaptive control and synchronization of a novel 4-D hyperchaotic hyperjerk system via backstepping control method,” *Archives of Control Sciences*, vol. 26, no. 3, pp. 311–338, 2016.
- [27] T. Kamsri, P. Julsereewong, and V. Riewruja, “Simple square-root extractor using op amps,” in *Proceedings of the 2008 International Conference on Control, Automation and Systems, ICCAS 2008*, pp. 1812–1815, October 2008.

Research Article

Computer Simulation of Noise Effects of the Neighborhood of Stimulus Threshold for a Mathematical Model of Homeostatic Regulation of Sleep-Wake Cycles

Wuyin Jin,¹ Qian Lin,² An Wang,¹ and Chunni Wang³

¹School of Mechanical & Electrical Engineering, Lanzhou University of Technology, Lanzhou 730050, China

²Editorial Department of Journal of Lanzhou University of Technology, Lanzhou University of Technology, Lanzhou 730050, China

³Department of Physics, Lanzhou University of Technology, Lanzhou 730050, China

Correspondence should be addressed to Wuyin Jin; wuyinjin@hotmail.com

Received 4 July 2017; Accepted 13 September 2017; Published 22 October 2017

Academic Editor: Sajad Jafari

Copyright © 2017 Wuyin Jin et al. This is an open access article distributed under the Creative Commons Attribution License, which permits unrestricted use, distribution, and reproduction in any medium, provided the original work is properly cited.

The noise effects on a homeostatic regulation of sleep-wake cycles' neuronal mathematical model determined by the hypocretin/orexin and the local glutamate interneurons spatiotemporal behaviors are studied within the neighborhood of stimulus threshold in this work; the neuronal noise added to the stimulus, the conductance, and the activation variable of the modulation function are investigated, respectively, based on a circadian input skewed in sine function. The computer simulation results suggested that the increased amplitude of external current input will lead to the fact that awakening time is advanced but the sleepy time remains the same; for the bigger conductance and modulation noise, the regulatory mechanism of the model sometimes will be collapsed and the coupled two neurons of the model show very irregular activities; the falling asleep or wake transform appears at nondeterminate time.

1. Introduction

Noise not only is a problem for neurons, but also can be a solution in information processing. Several strategies have been adopted to use noise in this fashion; for example, stochastic resonance is a process by which the ability of threshold-like systems to detect and transmit weak signals can be enhanced by the presence of a certain level of noise [1]. Neural noise is a general term that designates random influences on the transmembrane voltage of single neurons and by extension of the firing activity of neural networks. This noise can influence the transmission and integration of signals from other neurons and alter the firing activity of neurons in isolation [2–4], and there are some significant effects near bifurcation points [5, 6], the weak neural noise, that seem to be less relevant when the neurons operate in spike generating regime for a suprathreshold; however, the situation is completely different in the neighborhood of threshold where noise can induce significant changes in the impulse patterns; furthermore, in the central neural system,

the neurons often work in the neighborhood of threshold, but neurons are heterogeneous and noise is inevitable [7]. Sleep is essential for the maintenance of the brain and the body, yet many features of sleep are poorly understood and mathematical models are an important tool for probing proposed biological mechanisms; in addition, noise is an inevitable factor in real neuronal systems, which plays an important role in spatiotemporal dynamics of neuronal networks, for nearly a century of study; some regulation nonlinear sleep models about circadian [8], diversity-induced resonance [9], temporal dynamics [10], physiological substrates [11, 12], and more have been proposed to investigate the neural regulatory mechanism for sleep-wake cycle; however, sleep and its underlying processes still hold many mysteries; it remains unclear how identified brain regions interact to bring about the different stages of sleep and wakefulness, how the timing of sleep depends on the length of time spent awake and work load, and how pathologies associated with sleep, such as narcolepsy, arise [13]. As we all know, there are homeostatic formation mechanism and biological function

between connection neurons [14, 15]; in this work, we study the spatiotemporal behaviors of noise effects in the neighborhood of stimulus threshold for a mathematical model of homeostatic regulation of sleep-wake cycles proposed by Postnova et al. [16]. The effects of neuronal noise added to the stimulus, the conductance, and the modulation function are investigated, respectively, based on a circadian input skewed in sine function proposed by Daan et al. [17].

2. Model and Input

The mathematical model of regulation sleep-wake cycles employed in this work is suggested by Postnova et al., the homeostatic regulation process in this model is determined by the neuropeptide hypocretin/orexin (Hcrt/ox), and the Hcrt/ox neurons are silent during sleep and active during wakefulness depending on reciprocal excitatory synaptic connections with local glutamate (Glu) interneurons. The model formed by two simplified Hodgkin-Huxley type neurons that are connected via Glu synapses, one of which additionally contains Hcrt/ox as the functionally relevant cotransmitter (see Figure 1 of [16]); particularly, they proposed a novel modulation function for the synaptic efficacy to regulate Hcrt/ox neuronal firing and silent state [16], and the important role of the orexin also is studied by Rempé et al. [13]. The mathematical model of regulation of sleep-wake cycles is given in the following form [16]; the membrane of two coupled neurons is given by

$$C \frac{dV_{\text{Glu}}}{dt} = -I_{\text{Glu}} - I_{\text{NaGlu}} - I_{\text{KGlu}} - I_{\text{sysHcrt/Orx}}, \quad (1)$$

$$C \frac{dV_{\text{Hcrt/Orx}}}{dt} = -I_{\text{Hcrt/Orx}} - I_{\text{NaHcrt/Orx}} - I_{\text{KHcrt/Orx}} - I_{\text{sysGlu}} + I_{\text{ext}}, \quad (2)$$

where the leak, sodium, and potassium currents are described by

$$\begin{aligned} I_n &= g_n (V_n - E_n), \\ I_{\text{Na}_n} &= g_{\text{Na}} \alpha_{\text{Na}_n} (V_n - E_{\text{Na}}), \\ I_{\text{K}_n} &= g_{\text{K}} \alpha_{\text{K}_n} (V_n - E_{\text{K}}); \end{aligned} \quad (3)$$

here, n refers to Hcrt/ox and Glu, respectively. The sodium current is considered to be activated instantaneously; the potassium current is activated with a time delay

$$\frac{da_{\text{K}_n}}{dt} = \frac{a_{\text{K}_n\infty} - a_{\text{K}_n}}{\tau_{\text{K}}}, \quad (4)$$

$$a_{\text{K}_n\infty} = \frac{1}{1 + \exp(-s_{\text{K}}(V_n - V_{0\text{K}}))}, \quad (5)$$

$$a_{\text{Na}} = a_{\text{Na}\infty} = \frac{1}{1 + \exp(-s_{\text{Na}}(V_n - V_{0\text{Na}}))}. \quad (6)$$

And the transmembrane currents

$$I_{\text{syn gl}_u} = g_{\text{gl}_u} a_{\text{gl}_u} (V_{\text{Hcrt/Orx}} - E_{\text{syn}}), \quad (7)$$

with

$$\begin{aligned} \frac{da_{\text{gl}_u}}{dt} &= \frac{a_{\text{gl}_u\infty} - a_{\text{gl}_u}}{\tau_{\text{gl}_u}}, \\ a_{\text{gl}_u\infty} &= \frac{1}{1 + \exp(-s_{\text{syn}}(V_{\text{Glu}} - V_{\text{spike}}))}, \end{aligned} \quad (8)$$

$$I_{\text{synHcrt/orx}} = I_{\text{gl}_u(\text{Hcrt/Orx})} + I_{\text{Hcrt/Orx}},$$

$$I_{\text{gl}_u(\text{Hcrt/Orx})} = g_{\text{gl}_u(\text{Hcrt/Orx})} a_{\text{gl}_u(\text{Hcrt/Orx})} (V_{\text{Glu}} - E_{\text{syn}}),$$

$$I_{\text{Hcrt/Orx}} = g_{\text{gl}_u(\text{Hcrt/Orx})} a_{\text{Hcrt/Orx}} (V_{\text{Glu}} - E_{\text{syn}}),$$

which are modelled by

$$\begin{aligned} \frac{da_{\text{gl}_u(\text{Hcrt/Orx})}}{dt} &= \frac{a_{\text{Hcrt/Orx}\infty} - a_{\text{gl}_u(\text{Hcrt/Orx})}}{\tau_{\text{Glu}}}, \\ \frac{da_{\text{Hcrt/Orx}}}{dt} &= \frac{Ma_{\text{Hcrt/Orx}\infty} - a_{\text{Hcrt/Orx}}}{\tau_{\text{Hcrt/Orx}}}, \end{aligned} \quad (9)$$

$$a_{\text{Hcrt/Orx}\infty} = \frac{1}{1 + \exp(-s_{\text{syn}}(V_{\text{Hcrt/Orx}} - V_{\text{spike}}))},$$

with a homeostatic function defined by

$$\frac{dM}{dt} = \frac{M_{\text{max}} - M}{\tau_{\text{increase}}} - \frac{Ma_{\text{Hcrt/Orx}\infty}}{\tau_{\text{decrease}}}. \quad (10)$$

All the parameters' meaning and value of (1)–(10) are in detail described in [16], as well as their supplements.

The external current input is applied to the Hcrt/ox neuron as a circadian input proposed in [17], which is defined by skewed sine function; an additional phase shift φ is added to be consistent with day and night

$$\begin{aligned} I_{\text{ext}} &= A [0.97 \sin(\omega t - \varphi) + 0.22 \sin(2\omega t - \varphi) \\ &\quad + 0.07 \sin(3\omega t - \varphi) + 0.03 \sin(4\omega t - \varphi) \\ &\quad + 0.001 \sin(5\omega t - \varphi) + 1], \end{aligned} \quad (11)$$

where A is a parameter for scaling the amplitude of the stimulus, ω is the angular frequency of the one-day-night circadian current, and $\varphi = \pi/3$ is an additional phase shift in this work.

3. Computer Simulation of Noise Effects of Regulation of Sleep-Wake Cycles

3.1. Regulation of Sleep-Wake Cycles of the Deterministic Model. As an illustration for the mathematical model of homeostatic regulation of sleep-wake cycles, the coupled Hcrt/ox and Glu of sleep-wake cycles activities are shown in Figures 1(b) and 1(c), respectively, under one typical amplitude of external current input $A = 1.0 \mu\text{A}/\text{cm}^2$ (shown in Figure 1(a)); these neuronal activities are ongoing with regulation function M (shown in Figure 1(d)). Seen from Figure 1, the presynaptic Hcrt/ox neuron induces firing (waking

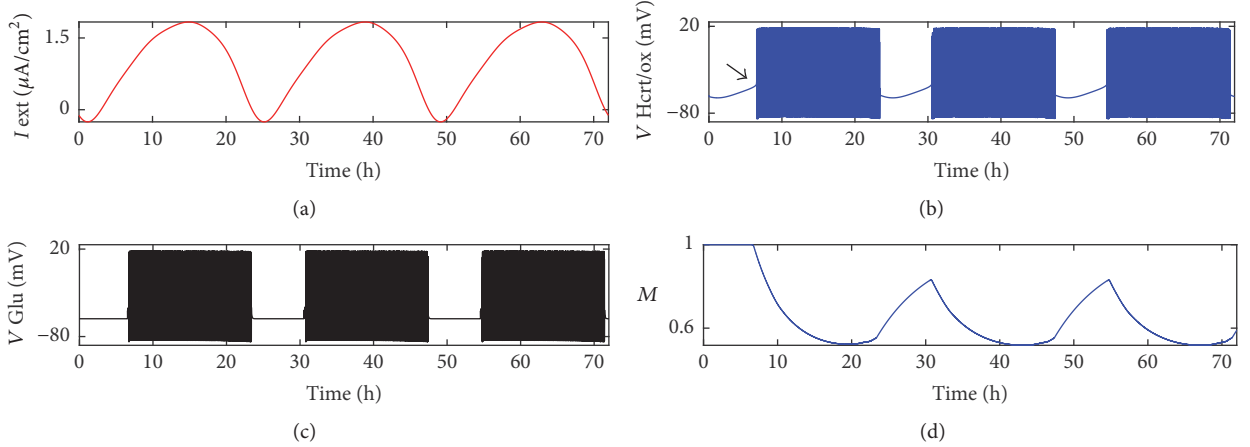


FIGURE 1: An illustration of the mathematical model of homeostatic regulation of sleep-wake cycles, the coupled Hcrt/ox (b), and Glu (c) of sleep-wake cycles activities, respectively, under one typical amplitude of external current input $A = 1.0 \mu\text{A}/\text{cm}^2$ (a), and the variety of regulation function M (d). Moreover, the increased amplitude of external current input will advance wake time but slightly change sleepy time.

up) almost at half past six (marked by an arrow in Figure 1(b)) in the morning and recovers to the silence (falling asleep) at half past twenty-three at midnight; these results are consistent with physiological time. The postsynaptic spikes appear with a certain delay because Hcrt/ox postsynaptic potentials need time for sufficient superposition that activates neuron. The regulation function M declines with beginning spike and recovers when also the presynaptic firing is switched off.

One more interesting result we got in this work is that the increased amplitude of external current input will lead to awakening time being advanced; for example, the awakening time will be advanced from half past six to half past three in the morning while the amplitude A of external current input increased from $1.0 \mu\text{A}/\text{cm}^2$ to $12 \mu\text{A}/\text{cm}^2$, but the sleepy time still stays at half past twenty-three at midnight; this phenomenon may be like the fact that the older people's sleep becomes less and less.

3.2. Effects of Noise on Regulation of Sleep-Wake Cycles. Based on research of deterministic regulation of sleep-wake cycles model, we found that, to excite the coupled Hcrt/ox and Glu of the sleep-wake cycles model neuron, the external stimulus current amplitude must be greater than $0.465 \mu\text{A}/\text{cm}^2$; therefore, in this section, the amplitude of external current input is set to $A = 0.46 \mu\text{A}/\text{cm}^2$ as a stimulus threshold only can excite Hcrt/ox neuron in short duration, but the Glu neuron just displays the subthreshold activity shown in Figure 2(a).

And, an additive Gaussian white noise is added to current, conductance, and regulation function, respectively, to compare study significant differences in the regulation process; here, the Gaussian white noise ξ is calculated according to

$$\xi = \left[\left(-\frac{4D}{\Delta t} \right) \ln(a) \right]^{1/2} \cos(2\pi b), \quad (12)$$

where Δt is the time step of the integrator and $a, b \in [0, 1]$ are uniformly distributed random numbers. The noise intensity is adjusted by the parameter D .

3.2.1. Effects of Current Noise. When the amplitude of external current input locates within subthreshold regime, the regulation of sleep-wake cycles function cannot work normally; for example, $A = 0.46 \mu\text{A}/\text{cm}^2$, as subthreshold external input can only excite Hcrt/ox neuron in short duration one time a day in the noonday, as shown in Figure 2(a), but the Glu neuron just displays the subthreshold activity without any fire; all of these results in the regulation function M generate small vibration, which could be found in the bottom line of Figure 2(a).

With the additional noise defined in (12), being added to the right of (2) as current noise, the model produces general regulated activation while the value of noise intensity (D) is greater than a certain value even if the amplitude of external current input locates within subthreshold regime, as an example, when $A = 0.46 \mu\text{A}/\text{cm}^2$ and $D \geq 0.007$, for the other smaller intensity noise in neighborhood, leading to the seemingly random regulation process (as shown in Figure 2(b), where $D = 0.006$); occasionally, the model shows a sudden and terrible change; it could be seen in Figure 2(c) with same noise intensity $D = 0.006$ too; the Glu neuron does not respond (fire) to Hcrt/ox neuron on the third cycle, which looks like falling ill.

3.2.2. Effects of Conductance Noise. For an evaluation of the efficacy of noise in the different conductance, we firstly have examined the noise effects on the slow repolarizing variable of two coupled neurons (Hcrt/ox and Glu); two different noises with the same intensity as defined in (12) are added to the right of (4) at the same time; the amplitude of external current input is still set to $A = 0.46 \mu\text{A}/\text{cm}^2$ as subthreshold stimulus. The simulation results demonstrate that both of the neurons of sleep-wake cycle model are excited (wakefulness) all the time without sleep when noise intensity $D > 0.00002$, seeming to be losing sleep.

While $D \in [0.0000001, 0.00001]$, the model generates similar regulation process; especially when D is close to

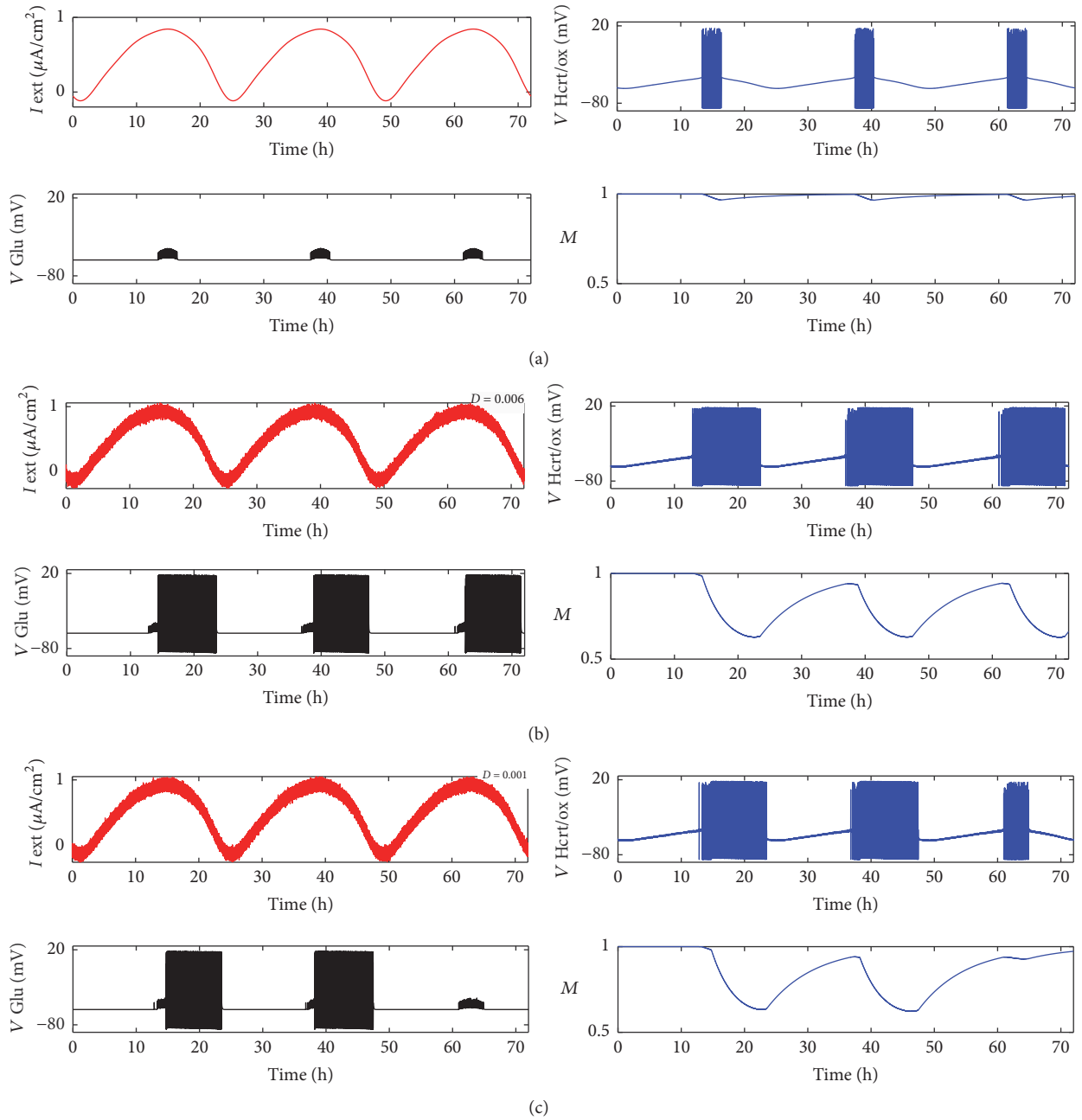


FIGURE 2: In subthreshold regime, the amplitude of external current input is set to $A = 0.46 \mu A/cm^2$ to the deterministic regulation of sleep-wake cycles model stimulus which only can excite Hcrt/ox neuron, but the Glu neuron just displays the subthreshold activities (a), but, after an additive Gaussian white noise is added to current, leading to the seemingly random regulation process, it sometimes shows similar regulation function (b) (where the noise intensity $D = 0.006$); occasionally, the model shows a sudden and terrible change (c) (where $D = 0.006$ too).

0.00001, the coupled two neurons can wake up (fire) about half past six in the morning and become silent (sleepy) about half past twenty-two at midnight, shown in Figure 3(a), which are similar to those in Figure 1. But, with the decreasing noise intensity from 0.00001 to 0.0000001, the wake time will be delayed more and more with the decrease of intensity changing from about six o'clock in the morning to two o'clock

in the noonday; however, the sleepy time almost does not change, staying at about half past twenty-two at midnight.

For the case of continued decrease of noise strength below 0.0000001, the similar regulation function will be broken like behavior in Figure 2(c).

Moreover, the effects of individual noise also have been examined separately; for the same strength noise, the Hcrt/ox

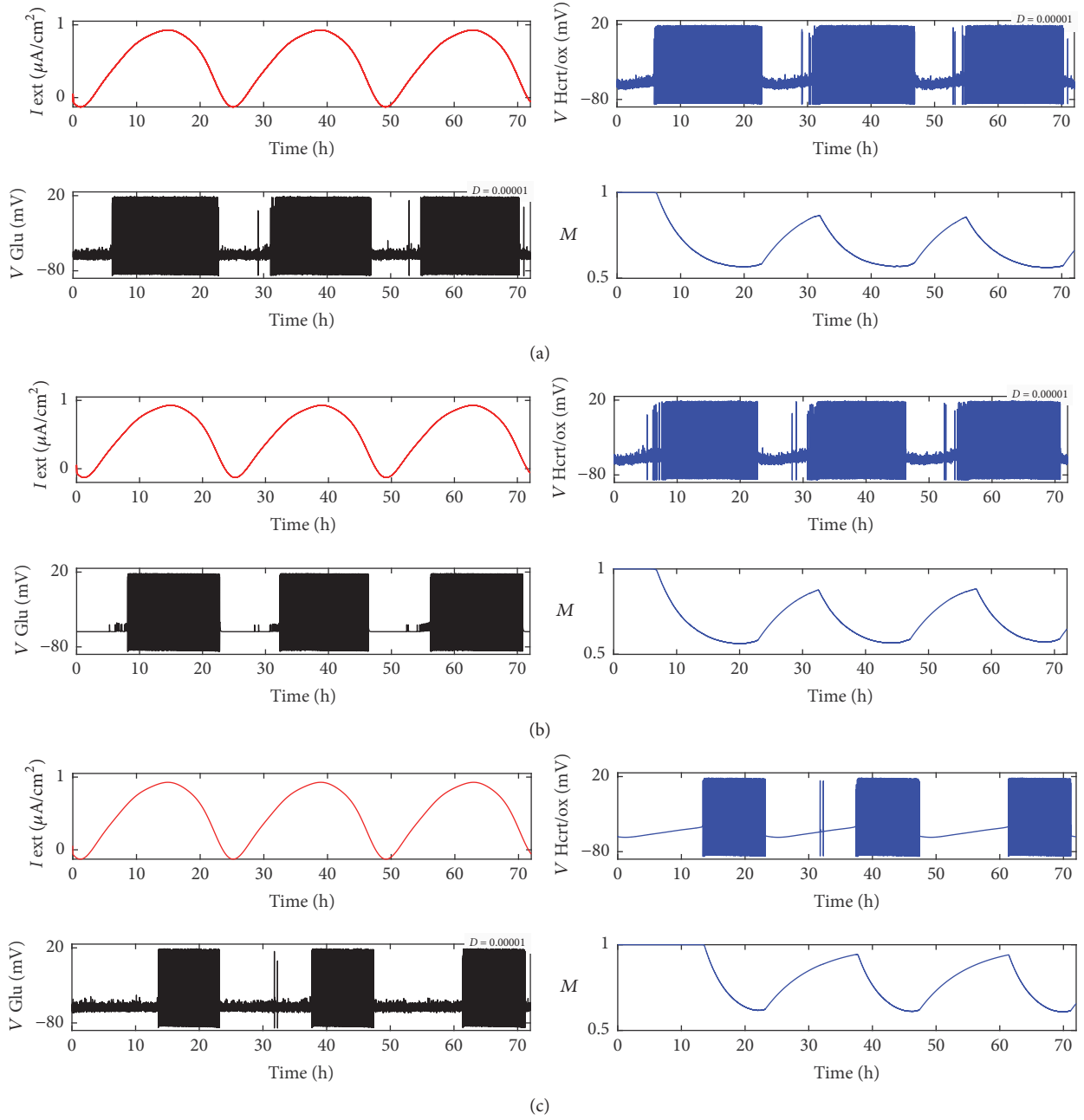


FIGURE 3: Effects of conductance noise. With the amplitude of external current input still being set to $A = 0.46 \mu\text{A}/\text{cm}^2$ as subthreshold stimulus, the proper noise added to the slow repolarizing variable of two coupled Hcrt/ox and Glu neuron can produce the similar regulation function (a). For the individual noise, the Hcrt/ox neuron's conductance noise generates more significant effect on the regulation function (b) than the Glu neuron (c). Furthermore, the neurons of sleep-wake cycle model are excited all the time without sleep when noise intensity $D > 0.00002$.

neuron conductance noise generates more significant effect on the regulation function than the Glu neuron, which could be found in Figures 3(b) and 3(c).

3.2.3. Effects of the Modulation Function. To demonstrate the effects of noise modulation function, the same amplitude of external current input $A = 0.46 \mu\text{A}/\text{cm}^2$ is chosen as subthreshold stimulus; through the study of different noise, we found that the regulation process of modulation function

almost does not change under the weak noise, as shown in Figure 4(a) for $D = 0.000000001$; the neurons' activity mainly depends on the external current input. For the bigger strength of noise, the function of regulation will lose its effectiveness (see Figure 4(b) for $D = 0.0000001$) with increasing noise intensity, even damaging the function of the neurons themselves, as an example shown in Figure 4(c) for $D = 0.01$; the value (M) of the modulation function randomly changes from -40 to 20 , obviously different from

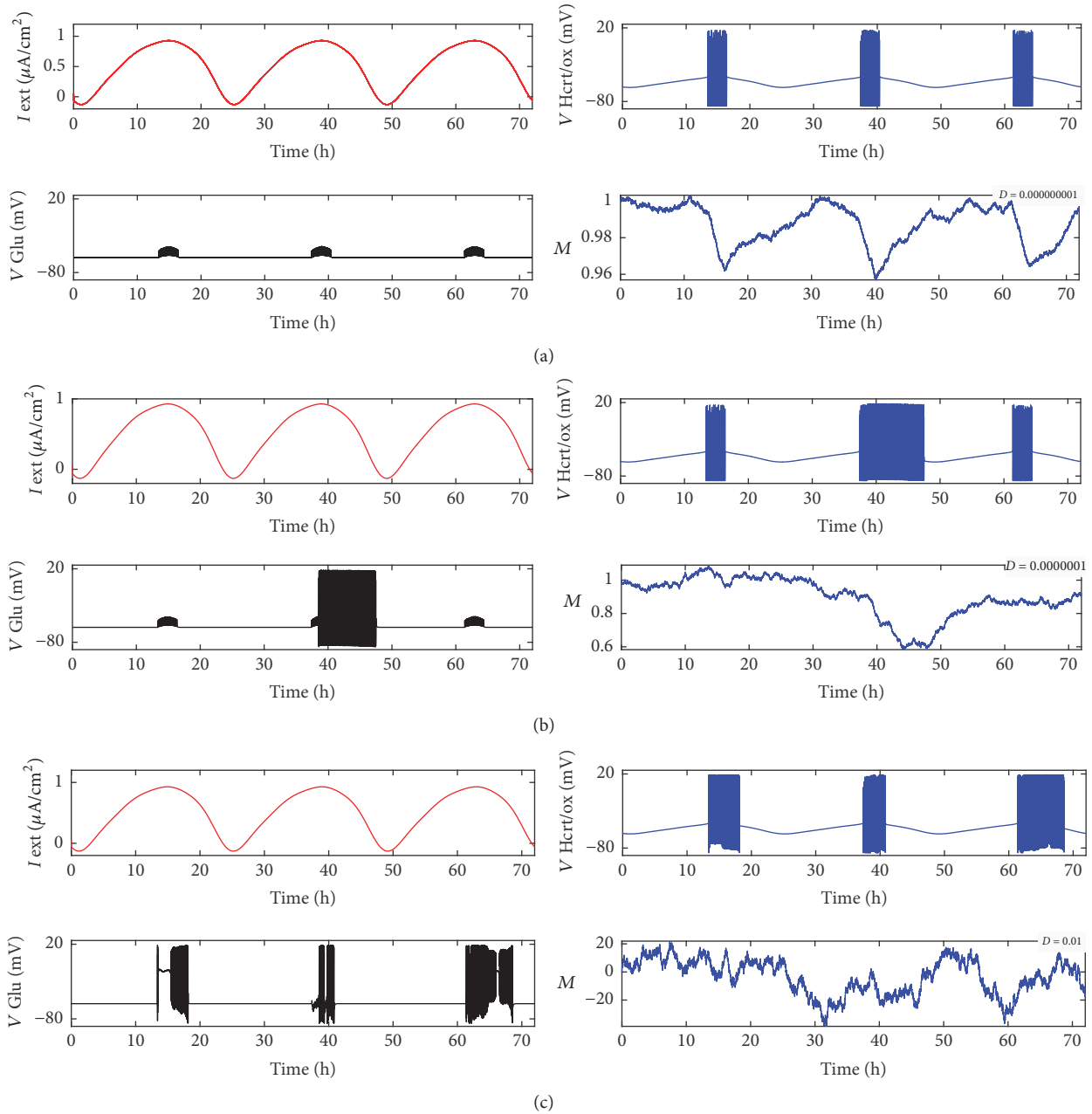


FIGURE 4: With the same subthreshold amplitude of external current input $A = 0.46 \mu\text{A}/\text{cm}^2$, the small noise intensity of the modulation function has weak effect on the regulation process, as shown in (a) for $D = 0.000000001$, but, for the bigger strength of noise, the function of regulation will lose its effectiveness ((b) for $D = 0.0000001$), even damaging the function of the neurons themselves; the value of the modulation function becomes very bigger and randomly changes within $-40 \sim 20$ (c), all of which means that homeostatic regulation function of sleep-wake cycles is more sensitive to noise.

normal (see Figure 1), and the Glu neuron is depolarized for a long duration, meaning that it is dead from the biological point of view.

4. Conclusions

The positive and negative function of noise in the neighborhood of stimulus threshold for a mathematical model of homeostatic regulation of sleep-wake cycles are studied

based on a circadian input; the noise is added to the stimulus, the conductance, and the modulation function; the results illustrated that the weak current, conductance, and variable of regulation function noise have significant influence on the transitions between sleep and wakefulness, the bigger amplitude of external current will advance wake time but slightly change sleepy time, and the weak conductance and modulation noise generate seemingly regulation process, but, for the strong noise, the regulation function will lose its

effectiveness and even damage the function of the neurons themselves.

Conflicts of Interest

The authors declare that they have no conflicts of interest.

Acknowledgments

The authors are grateful for the support of the National Natural Science Foundation of China under Grant nos. 11372122 and 11072099.

References

- [1] A. A. Faisal, L. P. J. Selen, and D. M. Wolpert, "Noise in the nervous system," *Nature Reviews Neuroscience*, vol. 9, no. 4, pp. 292–303, 2008.
- [2] A. Longtin, "Neuronal noise," *Scholarpedia*, vol. 8, no. 9, p. 1618, 2007.
- [3] G. Wang, W. Jin, and C. Hu, "The complete synchronization of Morris-Lecar neurons influenced by noise," *Nonlinear Dynamics*, vol. 73, no. 3, pp. 1715–1719, 2013.
- [4] G. Wang, W. Jin, and A. Wang, "Synchronous firing patterns and transitions in small-world neuronal network," *Nonlinear Dynamics*, vol. 81, no. 3, pp. 1453–1458, 2015.
- [5] B. Jia and H. G. Gu, "Dynamics and physiological roles of stochastic firing patterns near bifurcation points," *International Journal of Bifurcation & Chaos*, vol. 27, no. 7, Article ID 1750113, 2017.
- [6] H. Gu, Z. Zhao, B. Jia, and S. Chen, "Dynamics of on-off neural firing patterns and stochastic effects near a sub-critical Hopf bifurcation," *PLoS ONE*, vol. 10, no. 4, Article ID e0121028, 2015.
- [7] S. Postnova, C. Finke, W. Jin, H. Schneider, and H. A. Braun, "A computational study of the interdependencies between neuronal impulse pattern, noise effects and synchronization," *Journal of Physiology-Paris*, vol. 104, no. 3-4, pp. 176–189, 2010.
- [8] S. Postnova, S. W. Lockley, and P. A. Robinson, "Sleep propensity under forced desynchrony in a model of arousal state dynamics," *Journal of Biological Rhythms*, vol. 31, no. 5, pp. 498–508, 2016.
- [9] M. Patriarca, S. Postnova, H. A. Braun, E. Hernández-García, and R. Toral, "Diversity and noise effects in a model of homeostatic regulation of the sleep-wake cycle," *PLoS Computational Biology*, vol. 8, no. 8, Article ID e1002650, e1002650, 17 pages, 2012.
- [10] P. McCauley, L. V. Kalachev, D. J. Mollicone, S. Banks, D. F. Dinges, and H. P. A. Van Dongen, "Dynamic circadian modulation in a biomathematical model for the effects of sleep and sleep loss on waking neurobehavioral performance," *SLEEP*, vol. 36, no. 12, pp. 1987–1997, 2013.
- [11] M. Fleshner, V. Booth, D. B. Forger, and C. G. Diniz Behn, "Circadian regulation of sleep-wake behaviour in nocturnal rats requires multiple signals from suprachiasmatic nucleus," *Philosophical Transactions of the Royal Society A: Mathematical, Physical & Engineering Sciences*, vol. 369, no. 1952, pp. 3855–3883, 2011.
- [12] S. Sorooshyari, R. Huerta, and L. De Lecea, "A framework for quantitative modeling of neural circuits involved in sleep-to-wake transition," *Frontiers in Neurology*, vol. 6, article no. 32, 2015.
- [13] M. J. Rempe, J. Best, and D. Terman, "A mathematical model of the sleep/wake cycle," *Journal of Mathematical Biology*, vol. 60, no. 5, pp. 615–644, 2010.
- [14] C. Wang, S. Guo, and Y. Xu, "Formation of autapse connected to neuron and its biological function," *Complexity*, vol. 2017, Article ID 5436737, 9 pages, 2017.
- [15] M. S. Goldman, "Memory without Feedback in a Neural Network," *Neuron*, vol. 61, no. 4, pp. 621–634, 2009.
- [16] S. Postnova, K. Voigt, and H. A. Braun, "A mathematical model of homeostatic regulation of sleep-wake cycles by hypocretin/orexin," *Journal of Biological Rhythms*, vol. 24, no. 6, pp. 523–535, 2009.
- [17] S. Daan, D. G. Beersma, and A. A. Borbély, "Timing of human sleep: recovery process gated by a circadian pacemaker," *American Journal of Physiology-Endocrinology and Metabolism*, vol. 246, no. 2, pp. R161–R183, 1984.

Research Article

Mixed Stimulus-Induced Mode Selection in Neural Activity Driven by High and Low Frequency Current under Electromagnetic Radiation

Lulu Lu,¹ Ya Jia,¹ Wangheng Liu,² and Lijian Yang¹

¹*Institute of Biophysics and Department of Physics, Central China Normal University, Wuhan 430079, China*

²*School of Electrical and Electronic Engineering, Wuhan Polytechnic University, Wuhan 430023, China*

Correspondence should be addressed to Ya Jia; jiay@mail.ccnu.edu.cn

Received 2 August 2017; Revised 15 September 2017; Accepted 27 September 2017; Published 19 October 2017

Academic Editor: Zeraouia Elhadj

Copyright © 2017 Lulu Lu et al. This is an open access article distributed under the Creative Commons Attribution License, which permits unrestricted use, distribution, and reproduction in any medium, provided the original work is properly cited.

The electrical activities of neurons are dependent on the complex electrophysiological condition in neuronal system, the three-variable Hindmarsh-Rose (HR) neuron model is improved to describe the dynamical behaviors of neuronal activities with electromagnetic induction being considered, and the mode transition of electrical activities in neuron is detected when external electromagnetic radiation is imposed on the neuron. In this paper, different types of electrical stimulus impended with a high-low frequency current are imposed on new HR neuron model, and mixed stimulus-induced mode selection in neural activity is discussed in detail. It is found that mode selection of electrical activities stimulated by high-low frequency current, which also changes the excitability of neuron, can be triggered owing to adding the Gaussian white noise. Meanwhile, the mode selection of the neuron electrical activity is much dependent on the amplitude B of the high frequency current under the same noise intensity, and the high frequency response is selected preferentially by applying appropriate parameters and noise intensity. Our results provide insights into the transmission of complex signals in nerve system, which is valuable in engineering prospective applications such as information encoding.

1. Introduction

Dynamic behaviors of neurons are significant to acquaintance with signal exchange in the brain or even with related diseases; as a result, preceding works have been investigated [1–9]; based on this, several models are established to study mode selection of neurons. The external forcing current and other bifurcation parameters [10–26] are used to investigate the transition between modes of electrical activities and dynamical response because the excitability of neuron can be changed by external electric stimuli effectively. For example, Wang et al. [10, 11] studied the fact that neuron electrical activities can be modulated by an external electric field and the responses of three classes of Morris-Lecar neurons to sinusoidal inputs and synaptic pulse-like stimuli. Lv et al. [12] investigated mode transition of electrical activity in a neuron under magnetic flow effect. Wang et al. [13] discussed the possible electric response in biological neurons

under electric stimulus. Ciszak and Bellesi [14] considered a network of coupled neurons in which the strength of the interactions is modulated by synaptic long term potentiation and depression. Tang et al. [15] confirmed that the membrane potential of a neuron depends on the changes of transmembrane current, opening/closing of ion channels, and even the regulation induced by astrocyte in a network composed of neuron bridged by astrocyte, and a review for dynamics in neuron and neuronal network [16, 17] was also provided for possible guide. Zhang et al. [18] suggested that the HR system may give an effective response to external stimulus by adjusting its intrinsic parameter, and this transition mode confirmed self-adaption of neuron. Djeundam et al. [19] analyzed the bifurcations occurring in the 3D HR model with and without random signal.

Indeed, the relevant topics about neurodynamics and neuronal network have been investigated widely by the known neuron models [20–29]. For example, Jun et al.

[20] investigated dynamic characteristics of the fractional-order Hindmarsh-Rose (HR) neuronal model, and the results showed possible differences in dynamic characteristic between the fractional-order HR neuronal model and an integer-ordered model. Guo et al. [21] found that both excitatory and electrical autapses increase the occurrence of burst firing, thus reducing neuronal firing regularity. It is also found that a time delay could decrease and suppress the chaotic state in the case of inhibitory chemical self-connections with a proper autaptic intensity [22–24]. Yi et al. [25] constructed the fact that neuron can exhibit different spiking patterns, even chaotic behaviors, depending on the values of stimulus frequencies. Baptista et al. [27] studied the combined action of chemical and electrical synapses in small networks of HR neurons.

It is thought that real neuron activities are complex and the oscillatory behaviors depend on the energy supply; as a result, the calculation and estimation of general energy are very important in dynamical systems. For example, the Hamilton energy function [28] of generic dynamical system is investigated to observe the emergence of action potential and mode transition in electrical activities. Yamada and Kashimori [29] found that the learning of face stimuli makes the functional connections between these inferior temporal networks. Ma et al. [30–32] investigated the death and breakup of spiral wave in the neuronal network. With the deepening of research development, more and more achievements are observed [33–37]. Pinto et al. [33] analyzed transitions between synchrony and asynchrony in both slow oscillations and fast spikes by adding artificial electrical coupling. Gu et al. [34] confirmed the on-off firing pattern as noise-induced stochastic firing pattern near a subcritical Hopf bifurcation point. Yilmaz et al. [36, 37] explained the effects of an autapse localized pacemaker activity across a Newman–Watts small-world network consisting of stochastic Hodgkin–Huxley neurons.

As it can be known, the relevant experiments of the neuron electrical activity play a vital role in achieving biological functions of the nervous system [38–43]. The latest researches described the complex bifurcations related to real experiments and HR neuron model; the experimental results [38, 39] demonstrate the dynamics of a neuronal transition from chaotic bursting to chaotic spiking in the nervous system, which agree with published findings in theoretical neuronal models [40, 41]. In addition, it is found that the firing, spike frequency, and instantaneous spike frequency observed in the experiment were simulated and explained using HH models. References [42, 43] illustrate the dynamics of different firing patterns and the frequency and temporal coding mechanisms of aortic baroreceptor.

Neuron can be thought as an effective signal processor and different external stimuli are encoded to give possible outputs and response; thus signal can be propagated in the nerve systems. In most of the previous works, specific external stimulus is often used. In fact, neurons can receive many signal inputs synchronously via multiple channels; as mentioned in [44], a low frequency (LF) signal and a high frequency (HF) forcing simultaneously confirmed that neuron gave response sensitively to intensity compared with

angular frequency completely, and the energy dependence on external forcing was also discussed. The potential mechanism is that stronger stimulus can input enough energy to induce mode transition while angular frequency can cause slight modulation on firing rhythm at fixed intensity. Besides the mode selection and transition in electrical activities, coherence resonance is also interesting by applying appropriate forcing and changing membrane temperature [45, 46]. Electromagnetic induction and radiation are important phenomenon in excitable media because external electromagnetic field can cause polarization and magnetization in molecular level. Up to now, many nonlinear electric devices such as negative resistor and memristor [47–49] can be used to design oscillatory circuit and some circuits could be effective in reproducing electrical activities in neurons. But, the most important aspect could be that potential mechanism and application should be considered in physical view. For example, electromagnetic induction on neuron generates induction current and excitability of neuron is changed [50], and external electromagnetic radiation could further induce multiple mode response in electrical activities of neuron.

The high-low frequency signal is widely applied in the nonlinear system, which amount to two periodic forces. Such two-frequency periodic forces are often used in many different fields, including commutation technologies, where information carriers are usually HF signal modulated by LF signal that encodes the data. The application of high-low frequency signals is pervasive in neural systems; for example, bursting neurons exhibit two widely different time scales; two frequency signals correspond to different signal input channels in the neuron. In addition, HF stimulation is playing an important role in biological phenomena, such as increased drug uptake by brain cells, resonantly enhanced biodegradation of microorganisms, and ultrasonic irradiation of two different frequency signals which has been seen to enhance cavitation yield.

In this paper, different types of electrical stimulus impended with a high-low frequency current are imposed on HR neuron model, and the mixed stimulus-induced mode selection in neural activity is discussed; thus the excitability of neuron is time-varying. It is found that the mode transition in electrical activity can be investigated by adding the Gaussian white noise. Meanwhile, it might be significant to explain the phenomenon of signal transmission in neurons when other signal types are imposed simultaneously.

2. Model and Scheme

According to the Maxwell electromagnetic induction theorem, the influence of dynamic behavior on the electrical activity of each neuron can be attributed to the bioelectricity within the nervous system (e.g., fluctuation of ion concentration between the inside and outside of the cell). Therefore, in this improved HR neuron model [50], the fluctuation of electromagnetic radiation is established, and the influence of magnetic flux is considered during the emergence of collective electrical activities and signals propagation among

a large set of neurons. The dynamical equations for the new neuron model are described as follows:

$$\begin{aligned} \frac{dx}{dt} &= y - ax^3 + bx^2 - z - k_1\rho(\varphi)x + I_{\text{ext}}, \\ \frac{dy}{dt} &= c - dx^2 - y, \\ \frac{dz}{dt} &= r[s(x + 1.6) - z], \\ \frac{d\varphi}{dt} &= kx - k_2\varphi, \end{aligned} \quad (1)$$

where x , y , z , and φ describe the membrane potential, the slow current associated with recovery variable, the adaption current, and the magnetic flux across the membrane of neuron, respectively. The parameters are selected as $a = 1$, $b = 3$, $c = 1$, $d = 5$, $r = 0.006$, and $s = 4$. The external forcing current I_{ext} is the direct current when $I_{\text{ext}} = I$, and I_{ext} is the high-low frequency current when $I_{\text{ext}} = I + A \cos(\omega t) + B \cos(N\omega t)$. kx and $k_2\varphi$ describe the membrane potential-induced changes on magnet flux and the leakage of magnet flux, respectively. The term $k_1\rho(\varphi)x$ is the feedback current on the membrane potential induced by electromagnetic induction, where k_1 is the feedback gain. The physical unit is verified as follows:

$$i' = \frac{dq(\varphi)}{dt} = \frac{dq(\varphi)}{d\varphi} \frac{d\varphi}{dt} = \rho(\varphi)V = k_1\rho(\varphi)x, \quad (2)$$

where V is the induced voltage and has the same physical units as variable x , and the dependence of electric charge on magnet flux defined by the memory conductance is

$$\rho(\varphi) = \frac{dq(\varphi)}{d\varphi} = \alpha + 3\beta\varphi^2, \quad (3)$$

where α , β are parameters and q is the charge across the memristor. The $\rho(\varphi)$ is the memory conductance of a magnetic flux-controlled memristor [47, 48], which is used to describe the coupling between magnetic flux and membrane potential of neurons. In fact, induction current can be triggered and fed back to membrane potential via the memristor coupling, and the excitability of neuron can be decreased. With this improved model, many phenomena of electrical activity in the neuron are investigated under the electromagnetic induction. Compared with the previous models, our new model holds more variable parameters and presents more complex dynamical behaviors by analyzing the bifurcation of interspike interval (ISI).

3. Results and Discussion

In the numerical studies, the parameters are selected as $k = 0.9$, $k_1 = 0.4$, $k_2 = 0.5$, $\alpha = 0.4$, and $\beta = 0.02$, the fourth-order Runge–Kutta algorithm is used, the time step is set as 0.001, the transient period for calculating is 1500 time units, and the initial values for (x, y, z, φ) are set as $(0.1, 0.2, 0.1, 0)$.

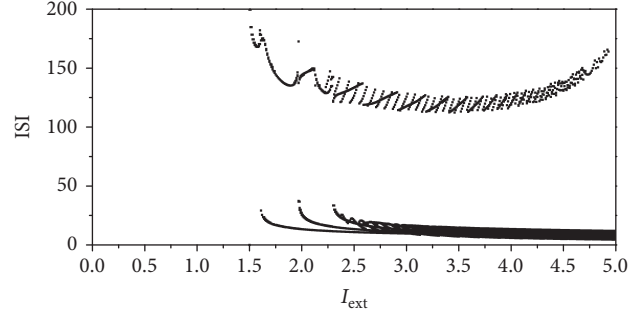


FIGURE 1: Bifurcation diagram with the increasing of external direct current I_{ext} .

3.1. Neuron Electrical Activities Stimulated by External Direct Current. In statistical view, the interspike interval is a measure of the order in electrical activity of neuron. The bifurcation diagram of ISI (i.e., the interspike interval) is plotted with the increasing of external direct current $I_{\text{ext}} = I$, and numerical results are presented by Figure 1.

Although the excitability and response in electrical activities are changed by induction current equation (2), Figure 1 shows that the interspike interval of neuron is not detected since the electric activity of neuron is quiescent state when the external direct current I_{ext} is increased from 0 to 1.5. However, it is also shown that there are multiple modes in electrical activities of neuron when the external direct current I_{ext} is increased from 1.5 to 5.0.

Under different external direct current I_{ext} , the sampled time series of electrical activities of neuron are shown by Figure 2, which can explore the dynamical properties of electrical activities of neuron. It is also found that the quiescent, spiking, bursting, and periodical states can be observed by selecting appropriate external direct current I_{ext} .

3.2. Neuron Electrical Activities Stimulated by High-Low Frequency Current. When the periodical type of external high-low frequency current $I_{\text{ext}} = I + A \cos(\omega t) + B \cos(N\omega t)$ is considered, for simplicity, we set $I = 0$; the term $A \cos(\omega t)$ is external low frequency (LF) signal with amplitude A , and the term $B \cos(N\omega t)$ is high frequency (HF) modulation with amplitude B , whose angular frequency is N times that of the low frequency signal, $N \gg 1$. Then the change of bifurcation diagram of ISI is calculated with different parameters, and the results are shown in Figure 3.

Figure 3 confirmed that the parameters of external high-low frequency current (i.e., B , ω , N) play a crucial role in the varieties of electrical activities when electromagnetic induction φ is considered. Comparing the ISI diagram of the three different parameters, the mode in electrical activities of neuron is much dependent on the parameter ω ; this underlying mechanism might be that the low frequency signal is more important. Figure 3(a) shows that appropriate large amplitude B is effective in making the electrical activities appear in the continuous bursting state. It is found that the bursting electrical activities can be transformed into spiking state and quiescent state (when ω value ranges from 0.17 to 0.2, the ISI value is zero) by increasing the parameter ω value as shown

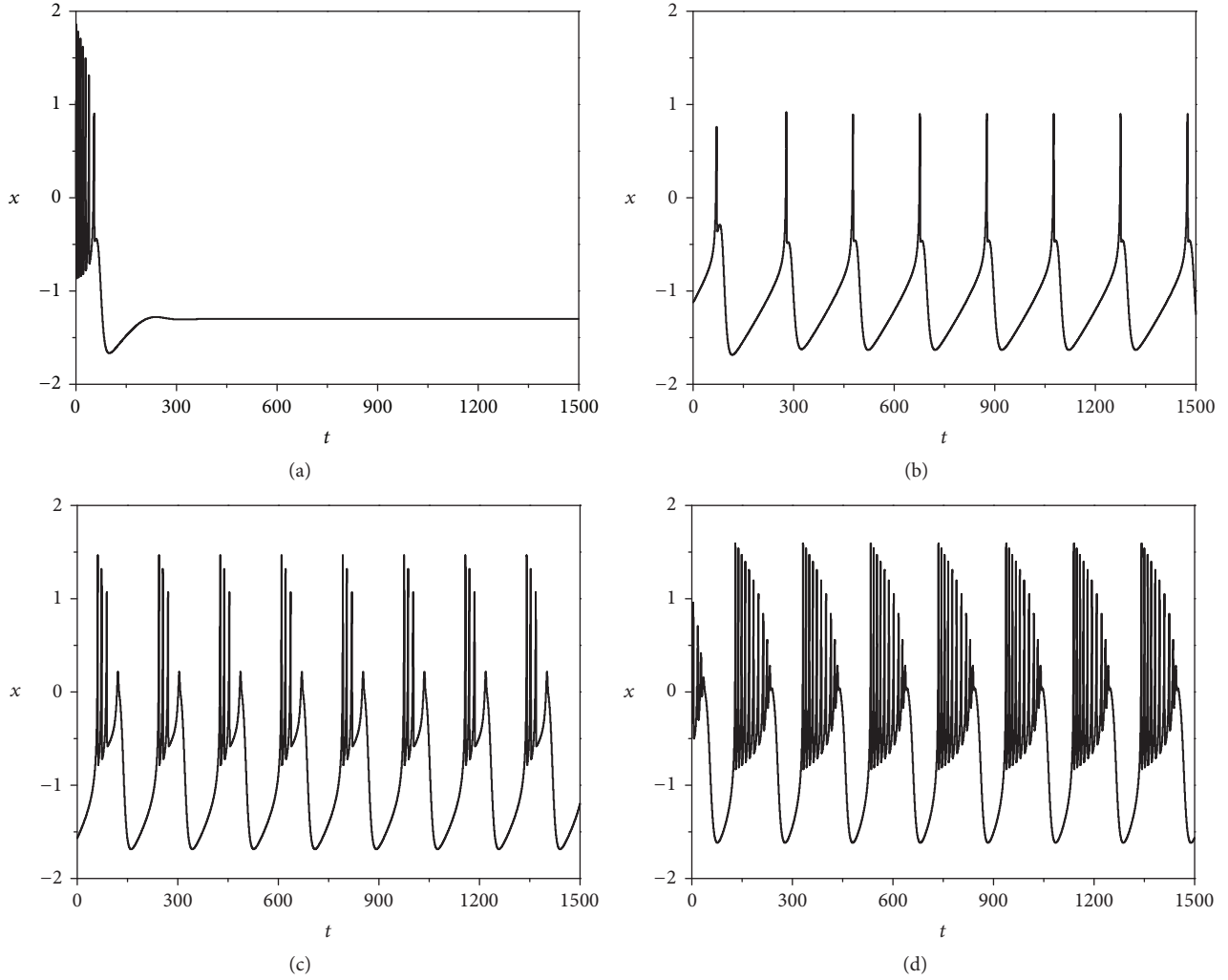


FIGURE 2: Sampled time series of membrane potential under different external direct current I_{ext} . (a) $I_{\text{ext}} = 1.0$. (b) $I_{\text{ext}} = 1.5$. (c) $I_{\text{ext}} = 2.3$. (d) $I_{\text{ext}} = 3.5$.

in Figure 3(b). The mode transformation by changing the parameter N in neuron also can be observed in Figure 3(c).

With the increasing of amplitude value B of HF, Figures 4(a)–4(d) show that the electrical activities of neuron can transform the spiking state into the double bursting state. With the increasing of frequency ω , Figures 4(e)–4(h) make it apparent that, for small values of the high-low frequency ω , the electrical activity of the neuron is found in a spiking state. After increasing the frequency ω of the high-low frequency current beyond some threshold value, the mode in electrical activities of neuron undergoes a transition from the spiking state to the bursting one. However, if we further increase ω , the electrical activity of neuron goes back to the spiking state. That is, the mode in electrical activities of neuron undergoes a succession of two transitions (spiking state \rightarrow bursting state \rightarrow spiking state). In addition, with the increasing of the parameter N of HF, Figures 4(i)–4(l) confirm that the electrical activity has not been changed and the bursting state is maintained. This is consistent with the bifurcation diagram for ISI in Figure 3.

3.3. Electrical Activities Stimulated by Direct Current and Gaussian White Noise. It is obviously known that noise can change the dynamical properties in electrical activities of neurons; therefore, noise is imposed on the neuron to detect the possible mode transition in electrical activities; here we insert the noise into the electromagnet flux term of system (1); it reads

$$\begin{aligned}
 \frac{dx}{dt} &= y - ax^3 + bx^2 - z + I_{\text{ext}} - k_1\rho(\varphi)x, \\
 \frac{dy}{dt} &= c - dx^2 - y, \\
 \frac{dz}{dt} &= r[s(x + 1.6) - z], \\
 \frac{d\varphi}{dt} &= kx - k_2\varphi + \xi(t),
 \end{aligned} \tag{4}$$

where $\xi(t)$ is Gaussian white noise, which represents the effect of external field or electromagnetic radiation-induced

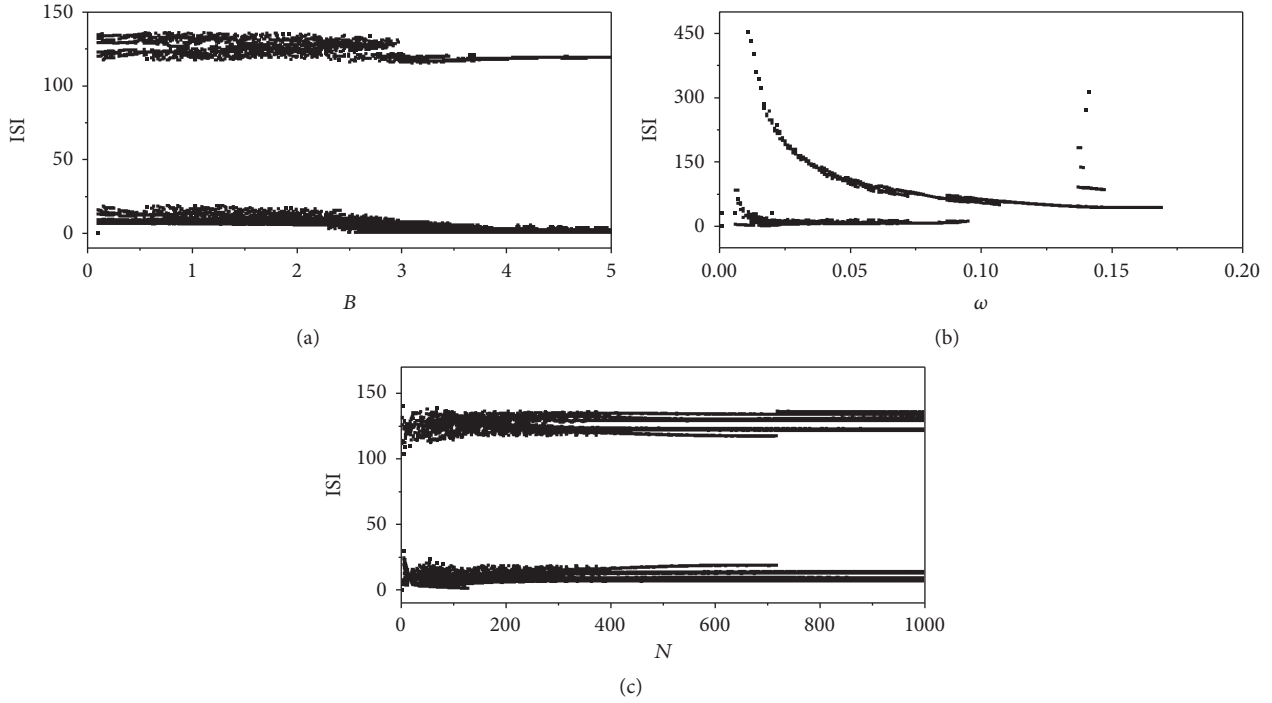


FIGURE 3: Bifurcation diagram with the increasing of different parameters. (a) $A = 1.6$, $\omega = 0.04$, and $N = 200$. (b) $A = 1.6$, $B = 1.6$, and $N = 200$. (c) $A = 1.6$, $B = 1.6$, and $\omega = 0.04$.

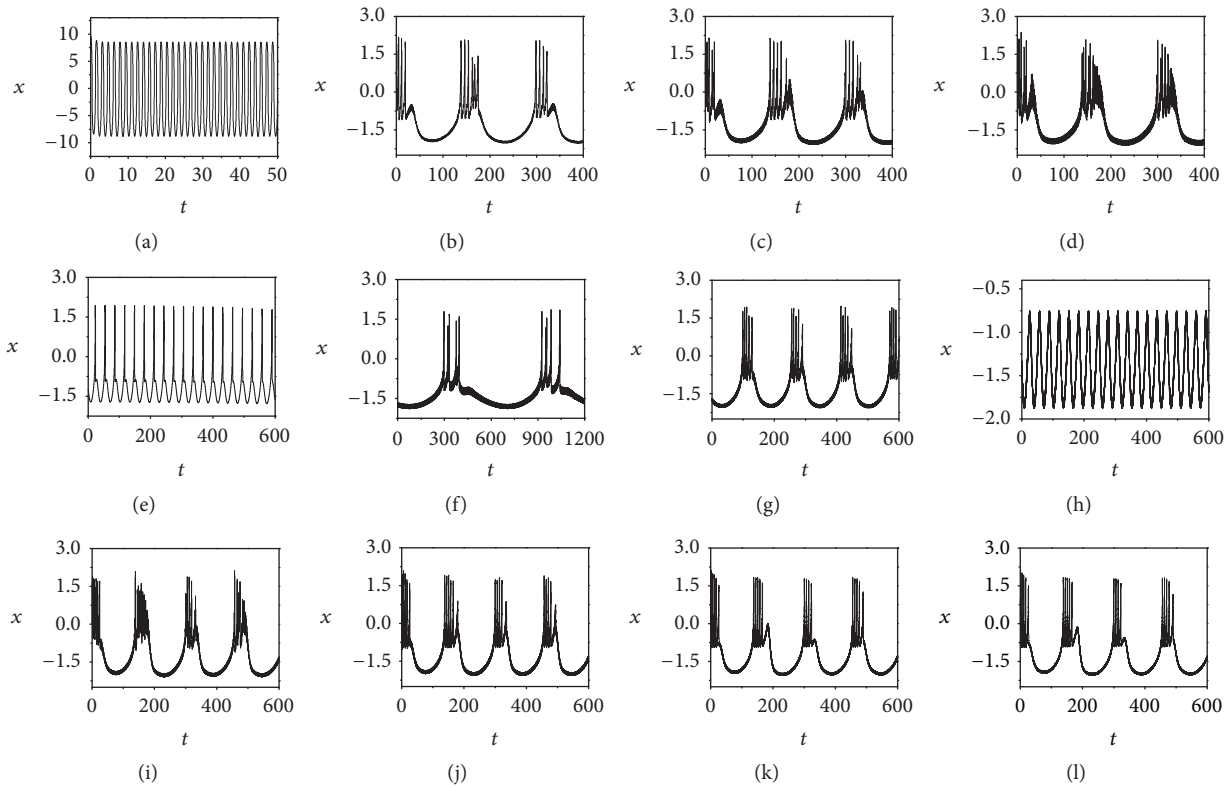


FIGURE 4: Sampled time series of membrane potential under different parameters. In the first layer, $A = 1.6$, $\omega = 0.04$, $N = 200$, (a) $B = 0.1$, (b) $B = 0.9$, (c) $B = 1.9$, and (d) $B = 2.5$. In the second layer, $A = B = 1.6$, $N = 200$, (e) $\omega = 0.001$, (f) $\omega = 0.01$, (g) $\omega = 0.04$, and (h) $\omega = 0.2$. In the last layer, $A = B = 1.6$, $\omega = 0.04$, (i) $N = 100$, (j) $N = 300$, (k) $N = 700$, and (l) $N = 900$. The external high-low frequency current is set as $I_{\text{ext}} = A \cos(\omega t) + B \cos(N\omega t)$.

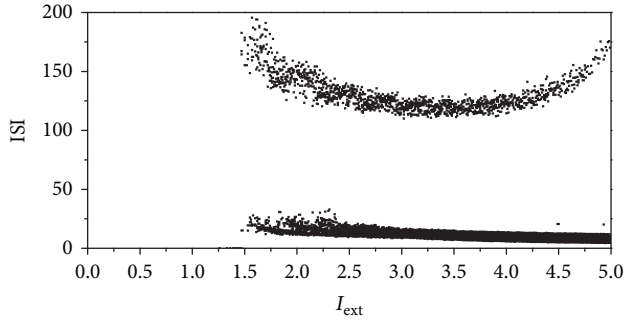


FIGURE 5: Bifurcation diagram with the increasing of external direct current I_{ext} . $D = 0.2$.

magnet flux on the membrane; its statistical properties can be defined as $\langle \xi(t) \rangle = 0$, $\langle \xi(t)\xi(t') \rangle = 2D\delta(t - t')$, and D is the noise intensity.

When the external direct current $I_{\text{ext}} = I$ is considered, the bifurcation analysis is carried at fixed noise intensity $D = 0.2$ of Gaussian white noise with the increasing of external direct current I_{ext} . Figure 5 shows that when the external direct current is in the range 0~1.4, the electrical activity is in the quiescent state, and the interspike interval (ISI) value is zero. When the external direct current is in the range 1.4~5.0, the results of Figure 5 show that the mode of electrical activity of the neuron can be transformed and the bursting state can be reached when the small direct current is imposed under the Gaussian white noise.

The sample time series for membrane potential are calculated under different external direct currents in Figure 6. When the direct current is 1.40, the electrical activity appears in the bursting state. Figures 6(a)–6(d) confirm that the different states (quiescent state, spiking state, and bursting state) can be observed by appending the Gaussian white noise.

3.4. Electrical Activities Stimulated by High-Low Frequency Current and Gaussian White Noise. When the periodical type of high-low frequency current $I_{\text{ext}} = I + A \cos(\omega t) + B \cos(N\omega t)$ is considered (for simplicity, here we set $I = 0$), Figure 7 shows the mode transformation of the neuron with the increase of the high-low frequency current parameters under the noise intensity $D = 0.2$ of Gaussian white noise. In the first layer of panel in Figure 7(a), there are interspike intervals with the creasing of HF amplitudes, in the second layer in Figure 7(b), there is ISI with differential frequency of high-low frequency current, and in the third layer in Figure 7(c), there is ISI with different parameter N of the HF current.

Comparing the factors in Figure 7(a) with the distribution in Figure 3(a), it is interesting that they have a huge differentiation in the profile. Figures 7(a) and 3(a) show that a certain diversity of the neuronal electrical activity is observed when noise intensity is fixed, and the electrical activities can be effectively suppressed by increasing the amplitude B of HF. The mode transition of the neuronal electrical activity is transformed from bursting state to spiking state

and high frequency response of electrical activity is selected preferentially when the Gaussian white noise is imposed.

Comparing Figure 7(b) with Figure 3(b), it is found that ISI of neuronal electrical activity become small with the frequency ω of high-low frequency current increases. Bursting state can be triggered and high frequency response of electrical activity is selected preferentially when high-low frequency current and the Gaussian white noise are imposed. Figures 7(c) and 3(c) show that the large transformations of electrical activities cannot be triggered with the increasing of HF current parameter N . Although the mode selection in neuron electrical activity is not much dependent on parameter N of HF current, the mode in electrical activities of neuron is much dependent on the parameters (i.e., B , ω , N). Furthermore, the relevant time series of membrane potential are provided with the increasing of different parameters (i.e., B , ω , N) in Figure 8.

It is confirmed that the bursting state of neuronal electrical activity can be changed into different mode by applying an appropriate intensity of the Gaussian white noise in Figures 8(a)–8(d). With the increasing of the amplitude B of HF current, the time series of electrical activity become more intensive. Figures 8(e)–8(h) and 8(i)–8(l) show that the transformation of the neuronal electrical activity is not obvious with the increasing of the high frequency signal parameters when high-low frequency current and the Gaussian white noise are imposed; this is consistent with the bifurcation diagram for ISI in Figure 7.

Figure 9(a) is the time series of membrane potential when $A = 1.6$, $\omega = 0.04$, $N = 200$, and $B = 7.2$, and its magnification is shown in Figure 9(b). In order to observe the electrical activity of the neuron distinctly, the Fast Fourier Transform (FFT) is performed by the Origin software, and Fourier analysis converts a signal from its original domain (sampled time series) to the power spectrum in the frequency domain. The power spectra can be calculated by manipulating the FFT in Figure 9(c). We analyzed the results of intensive oscillations; the frequency of high peak distribution and low peak distribution (the frequency value is about 1.25) is between the external HF frequency value (about 0.04) and the external LF frequency value (about 8.0). It means that the electrical activity of the neuron is affected by the signal of high-low frequency current. Meanwhile, according to the frequency value of the above results, the mode selection in electrical activities of neuron might be more dependent on the low frequency current. Figure 9(c) shows that when the variation of power occurs around zero frequency, it signifies cluster discharge in neuron electrical activity, and when variation of power occurs around frequency 1.3, it illustrates that the electrical activities of neuron are of uniform period; this is consistent with the results in Figure 8.

Furthermore, the bifurcation diagrams are plotted with the increasing of the noise intensity D in Figure 10. It can be seen that the mode transformation of the neuron electrical activity by changing amplitude B of HF current or the frequency ω of high-low frequency current is more obvious than that of changing parameter N under the different noise intensities. The effect of noise intensity is not obvious when high-low frequency current and the Gaussian white noise are

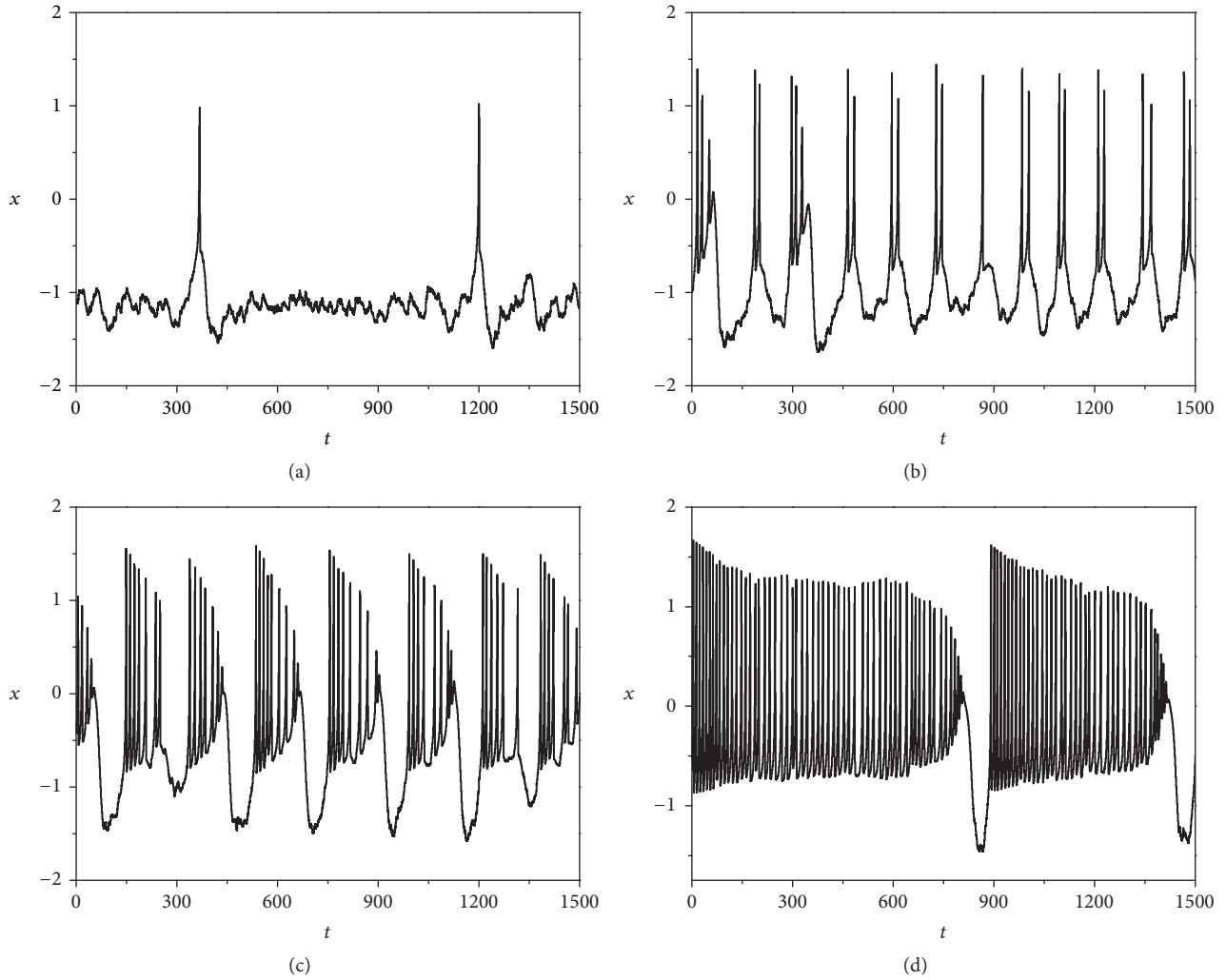


FIGURE 6: Sampled time series of membrane potential under different external direct current I_{ext} , $D = 0.2$. (a) $I_{\text{ext}} = 1.5$. (b) $I_{\text{ext}} = 2.3$. (c) $I_{\text{ext}} = 3.5$. (d) $I_{\text{ext}} = 4.5$.

imposed. Figures 10(a) and 10(b) shows that, with increasing of amplitude B , the double bursting state of electrical activity is developed into the spiking state. However, as shown in both Figures 10(b) and 10(c), by changing the frequency ω , the double state of electrical activity is converted into the triple bursting state, and with alternation in parameter N in Figures 10(a) and 10(d), the mode transformation of electrical activity is not obvious.

4. Conclusions

In this paper, different types of electrical stimulus impended with a high-low frequency current are imposed on new HR neuron model, and mixed stimulus-induced mode selection in neuron electrical activity is discussed in detail. Based on the improved HR neuron model, the dynamics of electrical activities of neuron is investigated by using the bifurcation analysis and the time series analysis. The effect of the high-low frequency current and the Gaussian white noise is also

considered. It is found that the influence by the amplitude B of the HF current in electrical activity of the neuron is larger than that of the other parameters (i.e., ω , N) under the same noise intensity, and the high frequency response is selected preferentially by applying appropriate parameters and noise intensity. The underlying mechanism can be related to the induction current of high-low frequency signal.

5. Open Problems

In this previous investigations, mixed stimulus-induced mode selection in neuron electrical activity driven by high-low frequency current is discussed under the electromagnetic radiation. Therefore, it is interesting to investigate the phase shift between two periodic signals and the energy change between the different states in further works. Vibrational resonance within the whole parameter plane could be considered to get an insight into the transmission of LF signal in the excitable neuron system. In addition, the Fourier coefficient

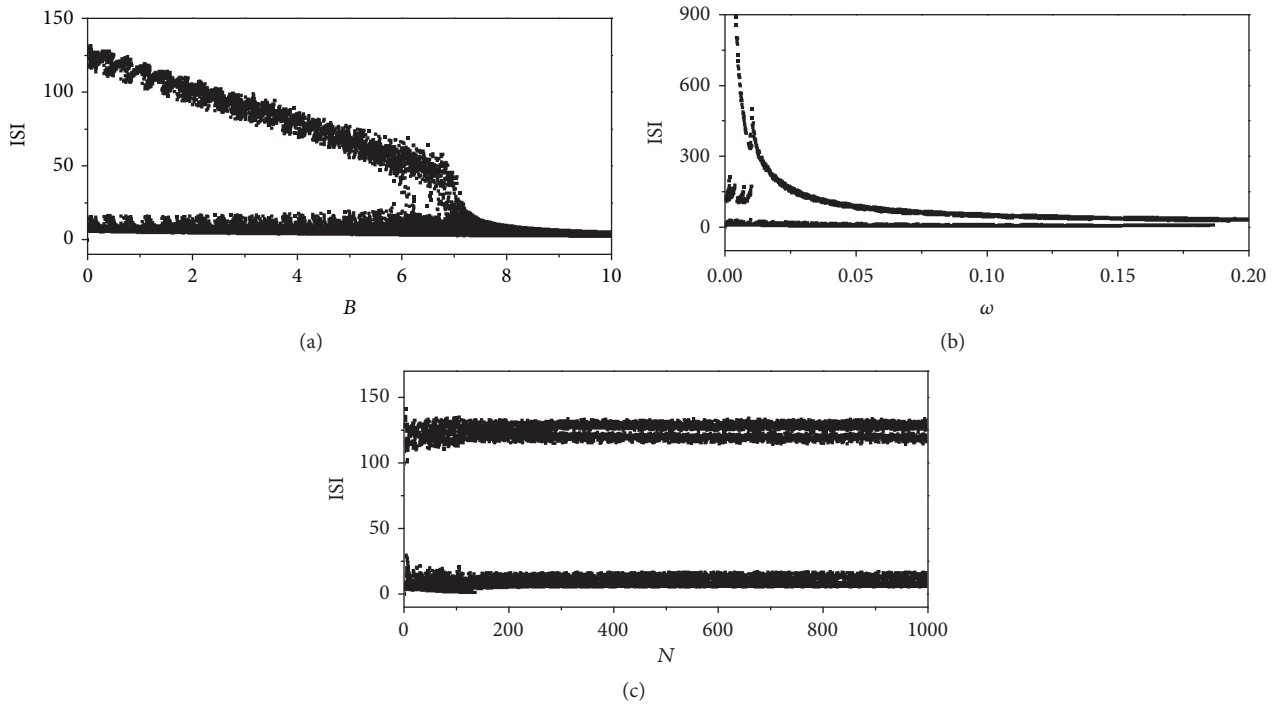


FIGURE 7: Bifurcation diagram with the increasing of different parameters. $D = 0.2$. (a) $A = 1.6$, $\omega = 0.04$, and $N = 200$. (b) $A = 1.6$, $B = 1.6$, and $N = 200$. (c) $A = 1.6$, $B = 1.6$, and $\omega = 0.04$.

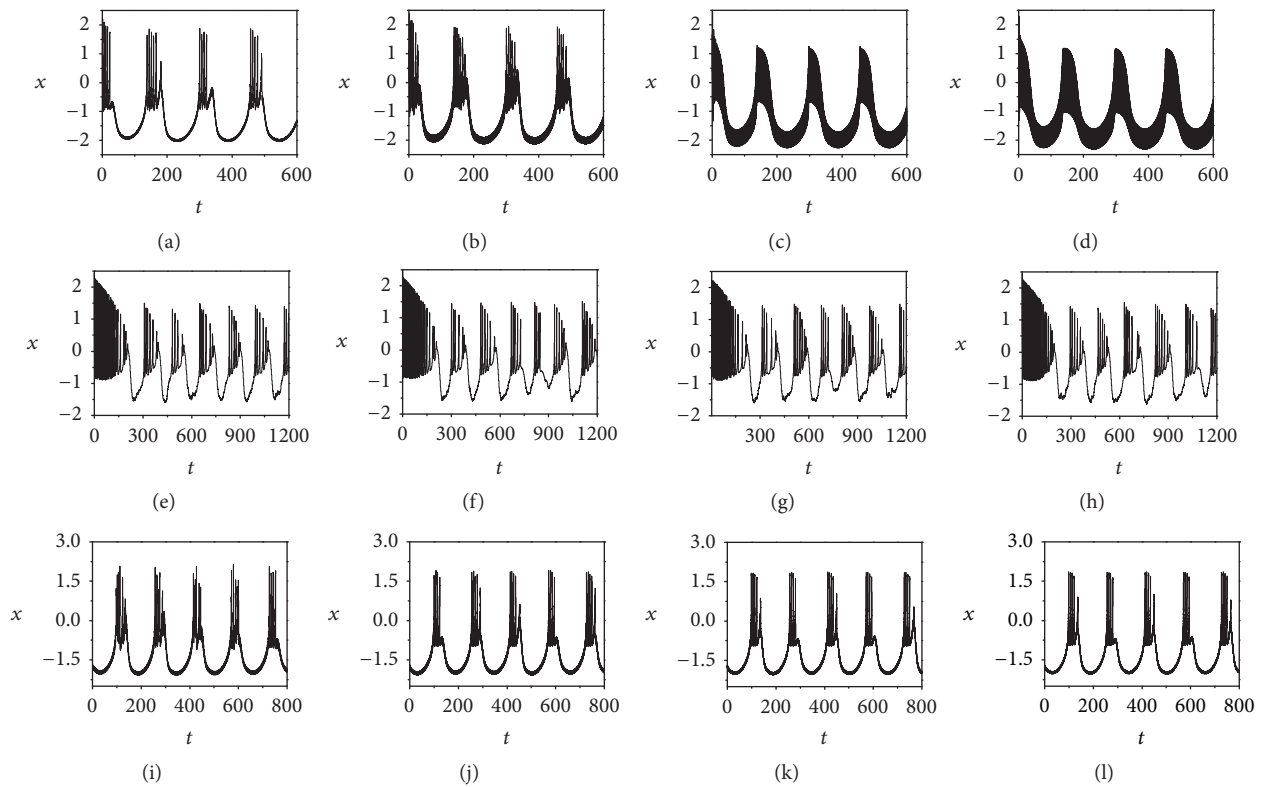


FIGURE 8: Sampled time series of membrane potential under different parameters. In the first layer, $A = 1.6$, $\omega = 0.04$, $N = 200$, (a) $B = 0.9$, (b) $B = 3.0$, (c) $B = 7.2$, and (d) $B = 9.0$. In the second layer, $A = 1.6$, $B = 1.6$, $N = 200$, (e) $\omega = 0.001$, (f) $\omega = 0.01$, (g) $\omega = 0.04$, and (h) $\omega = 0.2$. In the last layer, $A = 1.6$, $B = 1.6$, $\omega = 0.04$, (i) $N = 100$, (j) $N = 300$, (k) $N = 700$, and (l) $N = 900$. The Gaussian white noise intensity $D = 0.2$, and the external high-low frequency current is set as $I_{\text{ext}} = A \cos(\omega t) + B \cos(N\omega t)$.

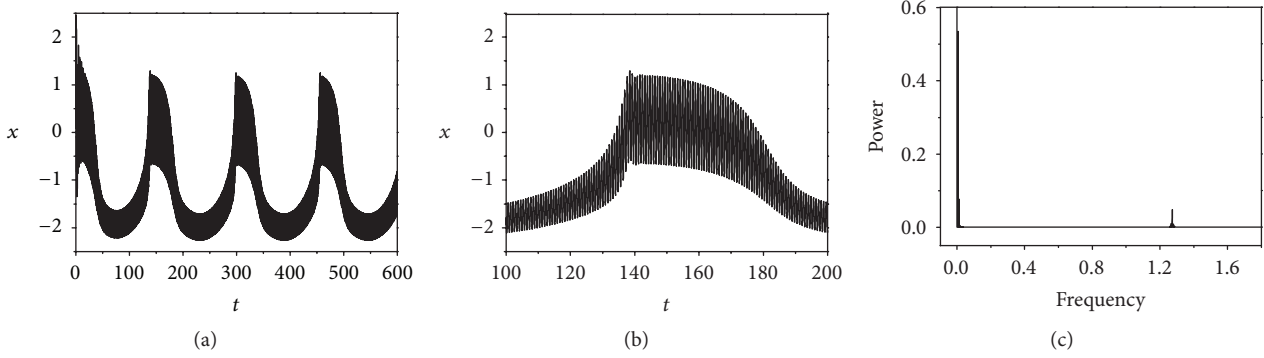


FIGURE 9: Sampled time series of membrane potential and power spectrum of electrical activity.

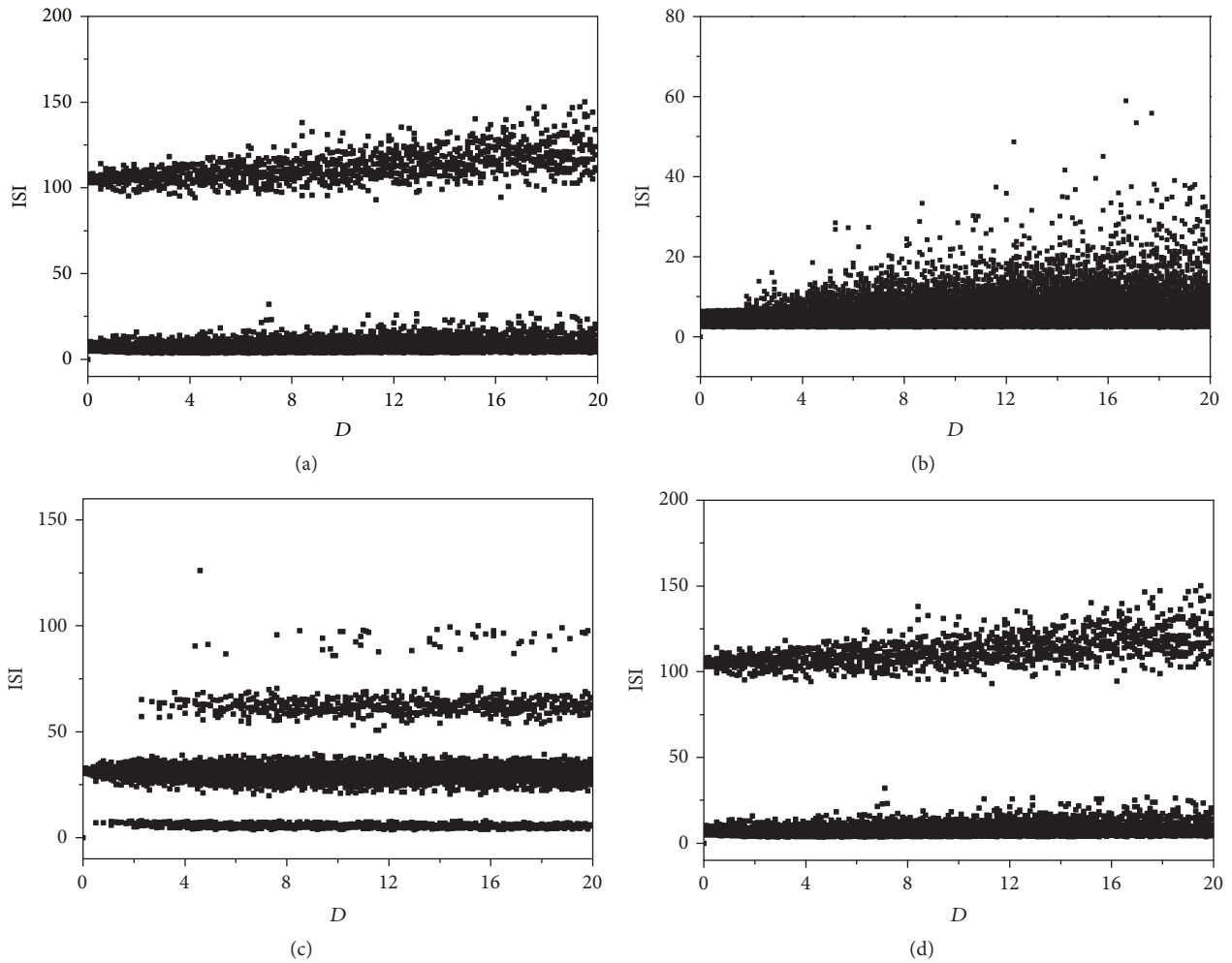


FIGURE 10: Bifurcation diagrams with the increasing of noise intensity D . (a) $A = 1.6$, $B = 1.6$, $\omega = 0.04$, and $N = 50$. (b) $A = 1.6$, $B = 9.0$, $\omega = 0.04$, and $N = 50$. (c) $A = 1.6$, $B = 1.6$, $\omega = 0.2$, and $N = 50$. (d) $A = 1.6$, $B = 1.6$, $\omega = 0.04$, and $N = 300$.

Q and power spectrum could be introduced for evaluating the response of the system to the input LF signal. As it is known that the neuron network plays a significant role in the neuron system, therefore, the neuron network state transformation of different neuron models driving by the different external signals might be investigated under the electromagnetic field;

the coherent resonance of the coupling neuron network is expected to be observed.

Conflicts of Interest

The authors declare that they have no conflicts of interest.

Acknowledgments

The authors gratefully thank Professor Jun Ma from Lanzhou University of Technology for the constructive suggestions. This work was supported by the National Natural Science Foundation of China, under Grant nos. 11775091 and 11474117.

References

- [1] A. L. Hodgkin and A. F. Huxley, "The dual effect of membrane potential on sodium conductance in the giant axon of Loligo," *The Journal of Physiology*, vol. 116, no. 4, pp. 497–506, 1952.
- [2] R. Fitzhugh, "Impulses and physiological states in theoretical models," *Biophysical Journal*, vol. 1, pp. 445–466, 1961.
- [3] G. B. Ermentrout and D. H. Terman, *Mathematical Foundations of Neuroscience*, Springer Science & Business Media, New York, NY, USA, 2010.
- [4] C. Morris and H. Lecar, "Voltage oscillations in the barnacle giant muscle fiber," *Biophysical Journal*, vol. 35, no. 1, pp. 193–213, 1981.
- [5] J. L. Hindmarsh and R. M. Rose, "A model of the nerve impulse using two first-order differential equations," *Nature*, vol. 296, no. 5853, pp. 162–164, 1982.
- [6] J. L. Hindmarsh and R. M. Rose, "A model of neuronal bursting using three coupled first order differential equations," *Proceedings of the Royal Society of London B: Biological Sciences*, vol. 221, no. 1222, pp. 87–102, 1984.
- [7] T. R. Chay, "Chaos in a three-variable model of an excitable cell," *Physica D: Nonlinear Phenomena*, vol. 16, no. 2, pp. 233–242, 1985.
- [8] L. Li, H. Gu, M. Yang, Z. Liu, and W. Ren, "A series of bifurcation scenarios in the firing pattern transitions in an experimental neural pacemaker," *International Journal of Bifurcation and Chaos*, vol. 14, no. 5, pp. 1813–1817, 2004.
- [9] Z. Yang and Q. Lu, "Transitions from bursting to spiking due to depolarizing current in the Chay neuronal model," *Communications in Nonlinear Science and Numerical Simulation*, vol. 12, no. 3, pp. 357–365, 2007.
- [10] H. Wang, L. Wang, L. Yu, and Y. Chen, "Response of Morris-Lecar neurons to various stimuli," *Physical Review E: Statistical, Nonlinear, and Soft Matter Physics*, vol. 83, no. 2, Article ID 021915, 2011.
- [11] H. Wang and Y. Chen, "Spatiotemporal activities of neural network exposed to external electric fields," *Nonlinear Dynamics*, vol. 85, no. 2, pp. 881–891, 2016.
- [12] M. Lv, C. Wang, G. Ren, J. Ma, and X. Song, "Model of electrical activity in a neuron under magnetic flow effect," *Nonlinear Dynamics*, vol. 85, no. 3, pp. 1479–1490, 2016.
- [13] H. Wang, Y. Chen, and Y. Chen, "First-spike latency in Hodgkin's three classes of neurons," *Journal of Theoretical Biology*, vol. 328, pp. 19–25, 2013.
- [14] M. Ciszak and M. Bellesi, "Synaptic plasticity modulates autonomous transitions between waking and sleep states: Insights from a Morris-Lecar model," *Chaos: An Interdisciplinary Journal of Nonlinear Science*, vol. 21, no. 4, Article ID 043119, 2011.
- [15] J. Tang, J.-M. Luo, and J. Ma, "Information transmission in a neuron-astrocyte coupled model," *PLoS ONE*, vol. 8, no. 11, Article ID e80324, 2013.
- [16] J. Ma and J. Tang, "A review for dynamics in neuron and neuronal network," *Nonlinear Dynamics*, vol. 89, no. 3, pp. 1569–1578, 2017.
- [17] J. Ma and J. Tang, "A review for dynamics of collective behaviors of network of neurons," *Science China Technological Sciences*, vol. 58, no. 12, pp. 2038–2045, 2015.
- [18] J. Zhang, C. Wang, M. Wang, and S. Huang, "Firing patterns transition induced by system size in coupled Hindmarsh-Rose neural system," *Neurocomputing*, vol. 74, no. 17, pp. 2961–2966, 2011.
- [19] S. R. D. Djeundam, R. Yamapi, T. C. Kofane, and M. A. Aziz-Alaoui, "Deterministic and stochastic bifurcations in the Hindmarsh-Rose neuronal model," *Chaos*, vol. 23, no. 3, p. 033125, 2013.
- [20] D. Jun, Z. Guang-Jun, X. Yong, Y. Hong, and W. Jue, "Dynamic behavior analysis of fractional-order Hindmarsh-Rose neuronal model," *Cognitive Neurodynamics*, vol. 8, no. 2, pp. 167–175, 2014.
- [21] D. Guo, S. Wu, M. Chen et al., "Regulation of Irregular Neuronal Firing by Autaptic Transmission," *Scientific Reports*, vol. 6, Article ID 26096, 2016.
- [22] J. Tang, J. Zhang, J. Ma, G. Y. Zhang, and X. Q. Yang, "Astrocyte calcium wave induces seizure-like behavior in neuron network," *Science China Technological Sciences*, vol. 60, pp. 1011–1018, 2016.
- [23] J. Ma, X. Song, J. Tang, and C. Wang, "Wave emitting and propagation induced by autapse in a forward feedback neuronal network," *Neurocomputing*, vol. 167, pp. 378–389, 2015.
- [24] H. Wang, J. Ma, Y. Chen, and Y. Chen, "Effect of an autapse on the firing pattern transition in a bursting neuron," *Communications in Nonlinear Science and Numerical Simulation*, vol. 19, no. 9, pp. 3242–3254, 2014.
- [25] G.-S. Yi, J. Wang, C.-X. Han, B. Deng, and X.-L. Wei, "Spiking patterns of a minimal neuron to ELF sinusoidal electric field," *Applied Mathematical Modelling*, vol. 36, no. 8, pp. 3673–3684, 2012.
- [26] Y. Li, G. Schmid, P. Hänggi, and L. Schimansky-Geier, "Spontaneous spiking in an autaptic Hodgkin-Huxley setup," *Physical Review E: Statistical, Nonlinear, and Soft Matter Physics*, vol. 82, no. 6, Article ID 061907, 2010.
- [27] M. S. Baptista, F. M. Moukam Kakmeni, and C. Grebogi, "Combined effect of chemical and electrical synapses in Hindmarsh-Rose neural networks on synchronization and the rate of information," *Physical Review E: Statistical, Nonlinear, and Soft Matter Physics*, vol. 82, no. 3, Article ID 036203, 12 pages, 2010.
- [28] C. N. Wang, Y. Wang, and J. Ma, "Calculation of Hamilton energy function of dynamical system by using Helmholtz theorem," *Acta Physica Sinica*, vol. 65, no. 24, Article ID 240501, 2016.
- [29] Y. Yamada and Y. Kashimori, "Neural mechanism of dynamic responses of neurons in inferior temporal cortex in face perception," *Cognitive Neurodynamics*, vol. 7, no. 1, pp. 23–38, 2013.
- [30] J. Ma, Y. Xu, G. Ren, and C. Wang, "Prediction for breakup of spiral wave in a regular neuronal network," *Nonlinear Dynamics*, vol. 84, no. 2, pp. 497–509, 2016.
- [31] J. Ma, L. Huang, J. Tang, H.-P. Ying, and W.-Y. Jin, "Spiral wave death, breakup induced by ion channel poisoning on regular Hodgkin-Huxley neuronal networks," *Communications in Nonlinear Science and Numerical Simulation*, vol. 17, no. 11, pp. 4281–4293, 2012.
- [32] J. Ma, L. Huang, H. P. Ying, and Z. S. Pu, "Detecting the breakup of spiral waves in small-world networks of neurons due to channel block," *Chinese Science Bulletin*, vol. 57, no. 17, pp. 2094–2101, 2012.

- [33] R. D. Pinto, P. Varona, A. R. Volkovskii, A. Szücs, H. D. Abarbanel, and M. I. Rabinovich, "Synchronous behavior of two coupled electronic neurons," *Physical Review E: Statistical, Nonlinear, and Soft Matter Physics*, vol. 62, no. 2, pp. 2644–2656, 2000.
- [34] H. Gu, Z. Zhao, B. Jia, and S. Chen, "Dynamics of on-off neural firing patterns and stochastic effects near a sub-critical Hopf bifurcation," *PLoS ONE*, vol. 10, no. 4, Article ID e0121028, 2015.
- [35] N. Korkmaz, İ. Öztürk, and R. Kılıç, "The investigation of chemical coupling in a HR neuron model with reconfigurable implementations," *Nonlinear Dynamics*, vol. 86, no. 3, pp. 1841–1854, 2016.
- [36] E. Yilmaz, V. Baysal, M. Ozer, and M. Perc, "Autaptic pacemaker mediated propagation of weak rhythmic activity across small-world neuronal networks," *Physica A: Statistical Mechanics and its Applications*, vol. 444, pp. 538–546, 2016.
- [37] E. Yilmaz, M. Ozer, V. Baysal, and M. Perc, "Autapse-induced multiple coherence resonance in single neurons and neuronal networks," *Scientific Reports*, vol. 6, Article ID 30914, 2016.
- [38] H. Gu, "Experimental observation of transition from chaotic bursting to chaotic spiking in a neural pacemaker," *Chaos: An Interdisciplinary Journal of Nonlinear Science*, vol. 23, no. 2, Article ID 023126, 2013.
- [39] H. G. Gu, B. B. Pan, G. R. Chen, and L. X. Duan, "Biological experimental demonstration of bifurcations from bursting to spiking predicted by theoretical models," *Nonlinear Dynamics*, vol. 78, no. 1, pp. 391–407, 2014.
- [40] B. Jia, H. Gu, and L. Xue, "A basic bifurcation structure from bursting to spiking of injured nerve fibers in a two-dimensional parameter space," *Cognitive Neurodynamics*, vol. 11, no. 2, pp. 189–200, 2017.
- [41] Z. Zhao and H. Gu, "Transitions between classes of neuronal excitability and bifurcations induced by autapse," *Scientific Reports*, vol. 7, p. 6760, 2017.
- [42] H. G. Gu and B. B. Pan, "A four-dimensional neuronal model to describe the complex nonlinear dynamics observed in the firing patterns of a sciatic nerve chronic constriction injury model," *Nonlinear Dynamics*, vol. 81, no. 4, pp. 2107–2126, 2015.
- [43] H. Gu and B. Pan, "Identification of neural firing patterns, frequency and temporal coding mechanisms in individual aortic baroreceptors," *Frontiers in Computational Neuroscience*, vol. 9, no. AUGUST, article no. 108, 2015.
- [44] Y. Wang, C. Wang, G. Ren, J. Tang, and W. Jin, "Energy dependence on modes of electric activities of neuron driven by multi-channel signals," *Nonlinear Dynamics*, vol. 89, no. 3, pp. 1967–1987, 2017.
- [45] L. Yang, W. Liu, M. Yi et al., "Vibrational resonance induced by transition of phase-locking modes in excitable systems," *Physical Review E: Statistical, Nonlinear, and Soft Matter Physics*, vol. 86, no. 1, Article ID 016209, 2012.
- [46] L. Yang and Y. Jia, "Effects of patch temperature on spontaneous action potential train due to channel fluctuations: Coherence resonance," *BioSystems*, vol. 81, no. 3, pp. 267–280, 2005.
- [47] B. C. Bao, Z. Liu, and J. P. Xu, "Steady periodic memristor oscillator with transient chaotic behaviours," *IEEE Electronics Letters*, vol. 46, no. 3, pp. 228–230, 2010.
- [48] B. Muthuswamy, "Implementing memristor based chaotic circuits," *International Journal of Bifurcation and Chaos*, vol. 20, no. 5, pp. 1335–1350, 2010.
- [49] G. Ren, Y. Xu, and C. Wang, "Synchronization behavior of coupled neuron circuits composed of memristors," *Nonlinear Dynamics*, vol. 88, no. 2, pp. 893–901, 2017.
- [50] M. Lv and J. Ma, "Multiple modes of electrical activities in a new neuron model under electromagnetic radiation," *Neurocomputing*, vol. 205, pp. 375–381, 2016.

Research Article

Nonlinear Complex Dynamics of Carbon Emission Reduction Cournot Game with Bounded Rationality

LiuWei Zhao

Computational Experiment Center for Social Science, School of Management, Jiangsu University, Zhenjiang, Jiangsu 212013, China

Correspondence should be addressed to LiuWei Zhao; 136901672@qq.com

Received 8 July 2017; Revised 14 August 2017; Accepted 10 September 2017; Published 12 October 2017

Academic Editor: Viet-Thanh Pham

Copyright © 2017 LiuWei Zhao. This is an open access article distributed under the Creative Commons Attribution License, which permits unrestricted use, distribution, and reproduction in any medium, provided the original work is properly cited.

Based on the hypothesis of participant's bounded rationality, our study formulated a novel Cournot duopoly game model of carbon emission reduction and, subsequently, analyzed the dynamic adjustment mechanism of emission reduction for enterprises. The existence and stability of the equilibrium solution of game are further discussed by the nonlinear dynamics theory. Our findings revealed that the parameters have key significance on the dynamic properties of the system. However, when the adjustment speed gets too large, the system loses the original stability and vividly demonstrates complex chaos phenomenon. Higher market prices in carbon trading have an outstanding impact on the stability of the system, which easily leads to system instability. Our study further controlled the chaos behavior of the power system by the delay feedback control. The results of the numerical analysis depict that the unstable behavior of the dynamic system can be controlled efficiently and quickly, in the quest to restore back a stable and orderly market. Our novel method is proved to have provided decision makers with effective solution to market instability.

1. Introduction

Massive economic growth has resulted in severe environmental issues such as environmental pollution and global climate warming. There is, therefore, huge concerns arising from the United Nations Framework Convention on Climate Change (UNFCCC) and various countries, to develop a series of related policies and regulations to curb these environmental menaces. Carbon emission trading (carbon trading for short) is one of the key market mechanism approaches used to reduce global greenhouse, thus carbon dioxide emission reduction. On 9 May 1992, an environmental treaty on the issue of climate change was negotiated and passed by international governments and the United Nations Framework Convention. In December 1997 in Tokyo, Japan, the "Kyoto Protocol" was issued. The Kyoto Protocol launched a market mechanism as a new solution to the problems of greenhouse gas emission reduction with a focus on the reduction of carbon dioxide since carbon emission has been the principal greenhouse gas. This entails trading carbon as a commodity: emitting carbon dioxide beyond the limits generates a potential cost; and conversely, those who are within a defined scope hold a potential value.

Despite the fact that China is a developing country and not subject to stricter obligation of reducing emissions under the Kyoto Protocol, this global climate changes and the carbon trading in developed countries around the world has brought tremendous changes in China. Consequently, China is playing an active role in the establishment of carbon trading pilots in larger cities, such as Beijing, Shanghai, and other provinces and cities. China has already initiated such pilot projects and far advanced in its implementation. The main participants in the carbon trading market are the industrial enterprises. This carbon trading impacts on enterprises' production processes, technology, profits, and other critical aspects. Therefore, it is of great significance to study and analyze the influence of carbon trading on the production, decision-making, and profits of the enterprise, which would provide sufficient theoretical basis for the perfection and implementation of the right carbon trading policy.

The main concerns about carbon emissions trading can be categorized into three aspects: firstly, the initial allocation of carbon emissions rights [1, 2]; secondly, the price of carbon emissions trading [3]; and thirdly the economic benefits arising from carbon emissions trading [4]. With regard to

the development of carbon emissions trading, the industry structure of the enterprises has a great impact on the carbon trading. For instance, in the oligopolistic industry market, the carbon trading price is more susceptible to the impact of enterprises' transactions, in consequence, making the carbon emissions trading prices deviate from the market's equilibrium price. Therefore, the research on the game behavior of carbon emissions trading in oligopoly market has become a vital problem that needs to be solved urgently.

The two classical models in the theory of oligopoly are those of Cournot [5, 6] and Bertrand [7, 8]. In Cournot's model, the firms choose to compete on output quantity, and in Bertrand's model, they choose to compete on price. Both models can be interpreted as static games where decisions are made simultaneously and where each firm maximizes its own profit, in a context of perfect and complete information [9, 10]. This paper introduces carbon emission trading in the classic Cournot output game framework and formulates a novel Cournot duopoly game model of carbon emission reduction based on the hypothesis of participant's bounded rationality. The dynamic adjustment mechanism of emission reduction is also analyzed in this paper. According to the hypothesis that the market inverse demand function and the cost function are linear functions and the participants have bounded rationality, our study constructs the nonlinear dynamic Cournot game model to analyze the local stability of the Nash equilibrium. The stability of the boundary equilibrium for the four-dimensional dynamical system is further analyzed based on the stability of the discrete system. Consequently, the parameters conditions of interior equilibrium and stability are obtained according to Schur-Cohn criterion. Based on the analysis of all equilibrium's stability of the nonlinear investment game system, our study adopts the numerical simulation results to analyze the influence of the model parameters on the stability and complexity of the dynamic system. The chaos behavior of the system is effectively controlled by the delayed feedback control method.

This article is organized as follows: in Section 2, the model is established based on the hypothesis of bounded rationality. In Section 3, we discuss the existence and local stability of the equilibrium points in the system. In Section 4, we demonstrate the dynamic features of this system with numerical simulations, including bifurcation diagram, phase portrait, and sensitive dependence on initial conditions. In Section 5, delayed feedback control is utilized to stabilize the chaotic behaviors of the system.

2. Model Hypotheses and Establishment

Our study assumes that the two production enterprises develop and produce homogeneous products. Each enterprise's action strategy is to choose the amount of investment in emission reduction during various periods and meet the requirements: two participating companies develop the corresponding emission reduction investment strategy in the discrete timeline. The $K_i(t-1)$ reflects the company's capital stock in the period of the $t-1$, $x_i(t)$ for its single-stage carbon emission reduction in the period of t , and emission reduction cost coefficient is β_i ($\beta > 0$), so the enterprise's single-stage

emission reduction investment is $\beta_i x_i(t)$. Due to the existence of a certain amount of capital depreciation, investment capital stock $K_i(t-1)$ flows into the next economic period, and it remains $\theta K_i(t-1)$, among which θ ($0 < \theta < 1$) stands for the residual ratio. Thus, we can reach that the relational expression in the adjacent two periods of investment capital stock of enterprise i is

$$K_i(t) = \theta K_i(t-1) + \beta_i x_i(t), \quad i = 1, 2. \quad (1)$$

For each particular enterprise's products amount in a certain period of time, production potential is determined by the accumulation amount of corporate investment capital in the period $K_i(t)$. Our study utilizes a linear form $q_i(t) = B_i K_i(t)$ to represent [11], among which positive constant B_i denotes the technological level of enterprises for innovative production on emerging products. Thus, we can reach that $q_i(t) = B_i(\theta K_i(t-1) + \beta_i x_i(t))$, $i = 1, 2$.

Our study assumes that the sales price of this kind of products on the market is a linear inverse demand function $p(t) = a - bQ(t)$, $a, b > 0$, and $Q(t) = q_1(t) + q_2(t)$ represents the sum of the two firms' supply in the market. At the same time, the firm's linear production cost function $C_i(q_i(t)) = c_i q_i(t)$ ($i = 1, 2$), marginal costs c_1 and c_2 are positive numbers.

The relationship between the amount of carbon dioxide produced by the enterprise during the production process and its production $q_i(t)$ is expressed as a linear relationship in the form of $k_i q_i(t)$. k_i ($k_i > 0$) is the coefficient of carbon dioxide produced by the enterprise i . Therefore, the enterprise's total carbon emission is $k_i q_i(t) - x_i(t)$ in the single period of t . Each enterprise in the t period has a certain quota of carbon emissions rights- $y_i(t)$, and the enterprise's carbon emissions trading volume is $y_i(t) - (k_i q_i(t) - x_i(t))$, and the market price of carbon trading is P . If $y_i(t) - (k_i q_i(t) - x_i(t)) > 0$, it means that the company sells the remaining carbon emissions; on the other hand, if the company needs to buy the lacking carbon emissions, $y_i(t) - (k_i q_i(t) - x_i(t)) = -(y_j(t) - (k_j q_j(t) - x_j(t)))$.

Based on the above assumptions about the function relationship among the variables, the profit of the enterprise i in the period t is calculated as follows:

$$\begin{aligned} \pi_i(x_1(t), x_2(t)) &= q_i(t)(p(t) - c_i) - \beta_i x_i(t) \\ &+ P(y_i(t) - (k_i q_i(t) - x_i(t))), \quad (2) \end{aligned}$$

$$i = 1, 2.$$

The specific expression of each variable is substituted into (2) and reaches first partial derivative about $x_i(t)$ on $\pi_i(x_1(t), x_2(t))$, and the marginal profits of the two enterprises are

$$\begin{aligned} \varphi_1(t) &= \frac{\partial \pi_1(x_1(t), x_2(t))}{\partial x_1(t)} = P \\ &+ \beta_1 \begin{pmatrix} -bB_1B_2(\theta K_2(t-1) + \beta_2 x_2(t)) + aB_1 - c_1B_1 \\ -Pk_1B_1 - 1 - 2bB_1^2(\theta K_1(t-1) + \beta_1 x_1(t)) \end{pmatrix}, \quad (3a) \end{aligned}$$

$$\varphi_2(t) = \frac{\partial \pi_2(x_1(t), x_2(t))}{\partial x_2(t)} = P + \beta_2 \begin{pmatrix} -bB_1B_2(\theta K_1(t-1) + \beta_1 x_1(t)) + aB_2 - c_2B_2 \\ -Pk_2B_2 - 1 - 2bB_2^2(\theta K_2(t-1) + \beta_2 x_2(t)) \end{pmatrix}. \quad (3b)$$

In reality, due to the asymmetry of market information and the constraints of their own conditions, enterprises can generally reach only limited degree of rationality in the decision-making and cannot make a complete control on the future market demand; therefore, the two production enterprises will rely on their own local knowledge about the marginal profits to adjust the emission reduction strategies during the next period. In other words, if the business observes the positive marginal profit in the current period, then it will increase emission reduction in the period of $t + 1$ and vice versa. As a result, the enterprise's dynamic adjustment mechanism can be expressed as

$$x_i(t+1) = x_i(t) + \alpha_i(x_i(t))\varphi_i(t), \quad i = 1, 2, \quad (4)$$

where $\alpha_i(x_i(t))$ is a positive adjustment function and reflects the company's adjustment range of emission reduction based on the marginal profits. Our study considers the form of the adjustment function in linear form as $\alpha_i(x_i(t)) = \alpha_i x_i(t)$, the coefficient $\alpha_i > 0$ when the enterprise adjusts the rate of emission reduction strategy according to the marginal profit signal. Thus, (4) is

$$x_i(t+1) = x_i(t) + \alpha_i x_i(t)\varphi_i(t), \quad i = 1, 2. \quad (5)$$

By connecting (1), (3a), (3b), and (5), in order to obtain the same expression by replacing $K_i(t-1)$ with $I_i(t)$, as shown from (6), we obtained a four-dimensional discrete dynamical model by replacing $K_i(t-1)$ with $I_i(t)$ as follows:

$$\begin{aligned} x_1(t+1) &= x_1(t) + \alpha_1 x_1(t) \left[P + \beta_1 \begin{pmatrix} -bB_1B_2(\theta I_2(t) + \beta_2 x_2(t)) + aB_1 - c_1B_1 \\ -Pk_1B_1 - 1 - 2bB_1^2(\theta I_1(t) + \beta_1 x_1(t)) \end{pmatrix} \right] \\ x_2(t+1) &= x_2(t) + \alpha_2 x_2(t) \left[P + \beta_2 \begin{pmatrix} -bB_1B_2(\theta I_1(t) + \beta_1 x_1(t)) + aB_2 - c_2B_2 \\ -Pk_2B_2 - 1 - 2bB_2^2(\theta I_2(t) + \beta_2 x_2(t)) \end{pmatrix} \right] \\ I_1(t+1) &= \theta I_1(t) + \beta_1 x_1(t) \\ I_2(t+1) &= \theta I_2(t) + \beta_2 x_2(t). \end{aligned} \quad (6)$$

The discrete dynamical system (6) is based on the assumption that the market inverse demand function and the production cost function are all linear forms, describing the competition model of the emission reduction strategy between the two production enterprises. The game participants with bounded rational expectation will adjust the emission reduction strategy in different periods according to the marginal profits.

3. Analysis of Equilibrium Point's Stability

In the dynamical system (6), let $x_i(t+1) = x_i(t)$ and $I_i(t+1) = I_i(t)$ ($i = 1, 2$); we then get

$$\begin{aligned} x_1(t) &\left[P + \beta_1 \begin{pmatrix} -bB_1B_2(\theta I_2(t) + \beta_2 x_2(t)) + aB_1 - c_1B_1 \\ -Pk_1B_1 - 1 - 2bB_1^2(\theta I_1(t) + \beta_1 x_1(t)) \end{pmatrix} \right] \\ &= 0 \\ x_2(t) &\left[P + \beta_2 \begin{pmatrix} -bB_1B_2(\theta I_1(t) + \beta_1 x_1(t)) + aB_2 - c_2B_2 \\ -Pk_2B_2 - 1 - 2bB_2^2(\theta I_2(t) + \beta_2 x_2(t)) \end{pmatrix} \right] \\ &= 0 \\ \frac{(1-\theta)}{\beta_1} I_1(t) &= x_1(t) \\ \frac{(1-\theta)}{\beta_2} I_2(t) &= x_2(t). \end{aligned} \quad (7)$$

In solving (7), we obtained the four equilibrium points of the dynamical system (6) as follows:

$$\begin{aligned} E_0 &= (0, 0, 0, 0), \\ E_1 &= \left(\frac{(1-\theta)(P - \beta_1 + B_1\beta_1(a - c_1 - Pk_1))}{2bB_1^2\beta_1^2}, 0, \frac{P - \beta_1 + B_1\beta_1(a - c_1 - Pk_1)}{2bB_1^2\beta_1}, 0 \right), \\ E_2 &= \left(0, \frac{(1-\theta)(P - \beta_2 + B_2\beta_2(a - c_2 - Pk_2))}{2bB_2^2\beta_2^2}, 0, \frac{P - \beta_2 + B_2\beta_2(a - c_2 - Pk_2)}{2bB_2^2\beta_2} \right), \\ E^* &= \left(\frac{(1-\theta)W_1}{3bB_1^2\beta_1^2B_2\beta_2}, \frac{(1-\theta)W_2}{3bB_1B_2^2\beta_1\beta_2^2}, \frac{W_1}{3bB_1^2B_2\beta_1\beta_2}, \frac{W_2}{3bB_1B_2^2\beta_1\beta_2} \right), \end{aligned} \quad (8)$$

where $W_1 = 2B_2(P - \beta_1)\beta_2 + B_1\beta_1(\beta_2(1 + B_2(a - 2c_1 + c_2 - 2Pk_1 + Pk_2)) - P)$, $W_2 = B_1\beta_1(2P + (B_2(a + c_1 - 2c_2 + Pk_1 - 2Pk_2) - 2)\beta_2) - B_2(P - \beta_1)\beta_2$.

Easy to know, E_0 , E_1 , and E_2 are the boundary equilibrium points; E^* is the only interior point equilibrium. Since the real economic significance of the system equilibrium point is taken into account, only the case when the equilibrium point is nonnegative is discussed. According to the assumption that the parameters b , β_1 , β_2 , B_1 , B_2 , and θ are positive parameters, so parameters need to meet the following conditions when E_1 , E_2 , and E^* are greater than zero:

$$\begin{aligned}
P - \beta_1 + B_1\beta_1(a - c_1 - Pk_1) &> 0, \\
P - \beta_2 + B_2\beta_2(a - c_2 - Pk_2) &> 0, \\
W_1 &> 0, \\
W_2 &> 0.
\end{aligned} \tag{9}$$

In the following analysis, the nonnegative condition (9) is assumed to be true.

3.1. Boundary Equilibrium Point Stability. To discuss the stability of the equilibrium points (x_1, x_2, I_1, I_2) of the dynamical system (6), we first calculated the corresponding Jacobian matrix:

$$J(x_1, x_2, I_1, I_2) = \begin{pmatrix} 1 - \alpha_1 M_1 & -bB_1 B_2 x_1 \alpha_1 \beta_1 \beta_2 & -2b\theta B_1^2 x_1 \alpha_1 \beta_1 & -b\theta B_1 B_2 x_1 \alpha_1 \beta_1 \\ -bB_1 B_2 x_2 \alpha_2 \beta_1 \beta_2 & 1 - \alpha_2 M_2 & -b\theta B_1 B_2 x_2 \alpha_2 \beta_2 & -2b\theta B_2^2 x_2 \alpha_2 \beta_2 \\ \beta_1 & 0 & \theta & 0 \\ 0 & \beta_2 & 0 & \theta \end{pmatrix}, \tag{10}$$

where $M_1 = \beta_1 + 2bB_1^2\beta_1(\theta I_1 + 2x_1\beta_1) - P - B_1\beta_1(a - c_1 - Pk_1 - bB_2(\theta I_2 + x_2\beta_2))$, $M_2 = \beta_2 + 2bB_2^2\beta_2(\theta I_2 + 2x_2\beta_2) - B_2\beta_2(a - c_2 - Pk_2 - bB_1(\theta I_1 + x_1\beta_1)) - P$.

According to the Schur-Cohn stability criterion [12], when all the eigenvalues of the characteristic polynomial corresponding to the Jacobian matrix (10) are in the unit circle on the complex plane, that is, the modulus of any

eigenvalue is less than 1, the equilibrium point (x_1, x_2, I_1, I_2) is asymptotically stable.

Proposition 1. *Boundary equilibrium point is unstable.*

Proof. Substituting $E_0 = (0, 0, 0, 0)$ into the general formula (10) of the system Jacobian matrix, the Jacobi matrix of system (6) at the equilibrium point is expressed as follows:

$$J(E_0) = \begin{pmatrix} 1 + \alpha_1 \begin{pmatrix} B_1(a - c_1)\beta_1 - \beta_1 \\ +P(1 - B_1k_1\beta_1) \end{pmatrix} & 0 & 0 & 0 \\ 0 & 1 + \alpha_2 \begin{pmatrix} +B_2(a - c_2)\beta_2 - \beta_2 \\ +P(1 - B_2k_2\beta_2) \end{pmatrix} & 0 & 0 \\ \beta_1 & 0 & \theta & 0 \\ 0 & \beta_2 & 0 & \theta \end{pmatrix}. \tag{11}$$

We can reach four characteristic roots by calculation, namely,

$$\begin{aligned}
\lambda_1 &= \lambda_2 = \theta, \\
\lambda_3 &= 1 + \alpha_1 (B_1(a - c_1)\beta_1 - \beta_1 + P(1 - B_1k_1\beta_1)), \\
\lambda_4 &= 1 + \alpha_2 (B_2(a - c_2)\beta_2 - \beta_2 + P(1 - B_2k_2\beta_2)).
\end{aligned} \tag{12}$$

From the nonnegative condition (9) of the equilibrium point and the adjustment coefficient $\alpha_i > 0$, the latter two characteristic roots both satisfy $|\lambda_{3,4}| > 1$. Therefore, the equilibrium point is unstable. \square

Proposition 2. *E_1 and E_2 are unstable equilibrium points.*

Proof. Jacobian matrix (10) in the specific form at the boundary equilibrium point is

$$J(E_1) = \begin{pmatrix} 1 + \alpha_1(1 - \theta)H_1 & \frac{(1 - \theta)B_2\alpha_1 H_1\beta_2}{2B_1\beta_1} & \frac{(1 - \theta)\theta\alpha_1 H_1}{\beta_1} & \frac{(1 - \theta)\theta B_2\alpha_1 H_1}{2B_1\beta_1} \\ 0 & 1 + \frac{\alpha_2 W_2}{2B_1\beta_1} & 0 & 0 \\ \beta_1 & 0 & \theta & 0 \\ 0 & \beta_2 & 0 & \theta \end{pmatrix}, \tag{13}$$

where $H_1 = (1 - B_1(a - c_1 - Pk_1))\beta_1 - P$.

By calculating the eigenvalue of the Jacobian matrix $J(E_1)$, $\lambda_1 = \theta$, $\lambda_2 = 1 + \alpha_2 W_2 / 2B_1 \beta_1$, $\lambda_{3,4} = (1/2)(H_2 \pm \sqrt{H_2^2 - 4\theta})$, where $H_2 = 1 + \theta + (1 - \theta)\alpha_1((1 - B_1(a - c_1 - Pk_1))\beta_1 - P)$.

From the previous parameters that $B_1, \alpha_2 > 0$, $\lambda_2 > 1$ can be pushed by the inequality equation (9). Thus, according to discrete dynamical system's equilibrium point stability determination conditions in the second chapter, we can

know that E_1 is unstable boundary equilibrium. Similarly, the border equilibrium E_2 is also unstable. \square

3.2. Interior Point Equilibrium Stability. This section focuses on the stability of interior point equilibrium E^* . The Jacobian matrix (10) of interior point equilibrium E^* is expressed as follows:

$$J(E^*) = \begin{pmatrix} 1 - \frac{2(1-\theta)\alpha_1 W_1}{3B_2\beta_2} & -\frac{(1-\theta)\alpha_1 W_1}{3B_1\beta_1} & \frac{2(1-\theta)\theta\alpha_1 W_1}{3B_2\beta_1\beta_2} & -\frac{(1-\theta)\theta\alpha_1 W_1}{3B_1\beta_1\beta_2} \\ -\frac{(1-\theta)\alpha_2 W_2}{3B_2\beta_2} & 1 - \frac{2(1-\theta)\alpha_2 W_2}{3B_1\beta_1} & -\frac{(1-\theta)\theta\alpha_2 W_2}{3B_2\beta_1\beta_2} & \frac{2(1-\theta)\theta\alpha_2 W_2}{3B_1\beta_1\beta_2} \\ \beta_1 & 0 & \theta & 0 \\ 0 & \beta_2 & 0 & \theta \end{pmatrix}. \quad (14)$$

The characteristic polynomial of the matrix $J(E^*)$ is given as $P(\lambda)$, and $P(\lambda) = \lambda^4 + p_1\lambda^3 + p_2\lambda^2 + p_3\lambda + p_4$, and the polynomial coefficients by the numerical calculation are as follows:

$$p_1 = -2 \left(1 + \theta - \frac{(1-\theta)}{3} \left(\frac{W_2\alpha_2}{3B_1\beta_1} + \frac{W_1\alpha_1}{B_2\beta_2} \right) \right),$$

$$p_2 = \frac{\left(\frac{(-1+\theta)W_1\alpha_1(2(1+3\theta)B_1\beta_1 - (1-\theta)W_2\alpha_2)}{+B_2(3(1+4\theta+\theta^2)B_1\beta_1 - 2(1+2\theta-3\theta^2)W_2\alpha_2)} \right)}{3B_1B_2\beta_1\beta_2},$$

$$p_3 = -\frac{2\theta \left(\frac{3B_2\beta_2((2\theta^2-3+\theta)W_2\alpha_2 + 3(1+\theta)B_1\beta_1)}{-(1-\theta)W_1\alpha_1(3(3+2\theta)B_1\beta_1 - 8(1-\theta)W_2\alpha_2)} \right)}{9B_1B_2\beta_1\beta_2},$$

$$p_4 = \theta^2.$$

(15)

From the Schur-Cohn stability criterion [12], if there is an associated characteristic polynomial $P(\lambda)$, that is, all eigenvalues of the Jacobian matrix $J(E^*)$ are located in the unit circle on the complex plane, then the coefficients of the polynomial need to satisfy the conditions in the Schur-Cohn stability criteria at the same time. The system parameters are added to it and simplified:

$$P(1) = 1 + p_1 + p_2 + p_3 + p_4 = \frac{\alpha_1\alpha_2(\theta-1)^2 W_1 W_2}{3B_1B_2\beta_1\beta_2} > 0,$$

$$P(-1) = 1 - p_1 + p_2 - p_3 + p_4 = \frac{\left[B_1B_2\beta_1\beta_2 \left(\frac{4(1+\theta)(3(1+\theta)-N_1)}{-(1-\theta)\alpha_1(P-\beta_1)(8(1+\theta)-N_2)} \right) + \left(\frac{2(1-\theta)B_2^2\alpha_2(2(1+\theta)-(1-\theta)\alpha_1(P-\beta_1))}{(P-\beta_1)\beta_2^2 + B_1^2\beta_1N_3(4(1+\theta)-N_1)} \right) \right]}{3B_1B_2\beta_1\beta_2} > 0, \quad (16)$$

$$1 \pm p_4 = 1 \pm \theta^2 > 0,$$

where $N_1 = (1 - \theta)\alpha_2(2P + (B_2(a + c_1 - 2c_2 + Pk_1 - 2Pk_2) - 2)\beta_2)$, $N_2 = (1 - \theta)\alpha_2(5P + (B_2(a + 4c_1 - 5c_2 + 4Pk_1 - 5Pk_2) - 5)\beta_2)$, $N_3 = (1 - \theta)\alpha_1(P - (1 + B_2(a - 2c_1 + c_2 - 2Pk_1 + Pk_2))\beta_2)$.

From the positive and negative assumptions of the system parameters and inequality (9), we can learn that the stability conditions $P(1) > 0$ and $1 \pm p_4 > 0$ are tenable for sure. Therefore, the sufficient conditions for the asymptotic stability of the internal point equalization E^* of the dynamical system (6) are classified as follows.

When $P(-1) = 1 - p_1 + p_2 - p_3 + p_4 > 0$ and $|M_3^\pm| > 0$,

$$p_1 + p_3 < 1 + p_2 + p_4$$

$$p_2 - p_2p_4 + p_4 - p_4^3 - p_1p_3 + p_1^2p_4$$

$$< \left| 1 - p_4^2 + p_2p_4 - p_2p_4^2 + p_1p_3p_4 - p_3^2 \right|.$$

(17)

All the eigenvalues of $J(E^*)$ satisfy the $|\lambda_i| < 1$ ($i = 1, 2, 3, 4$), so that the equilibrium point E^* is stable when the condition (17) is satisfied. From the above equilibrium point analysis, we can see that the stability of the known equilibrium points is dependent on the value of the system parameters.

4. Numerical Simulation

In order to intuitively analyze the dynamic behavior of model (6), we used the numerical simulation to visually describe the dynamic evolution process of the discrete dynamical system

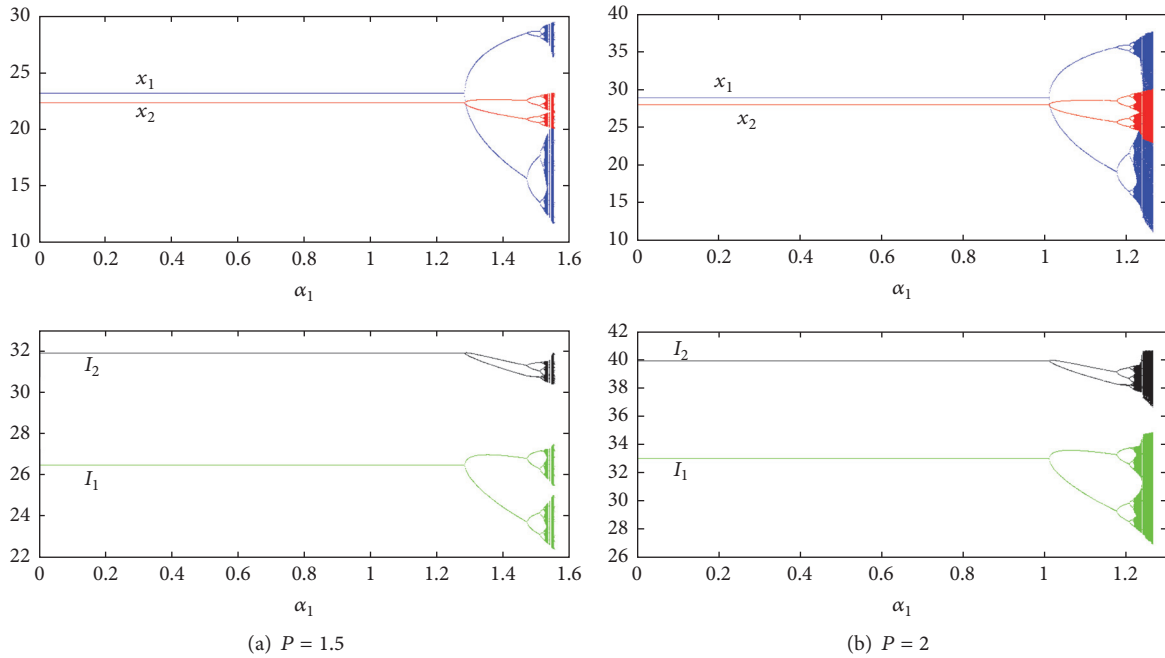


FIGURE 1: Bifurcation diagrams for system (6) with respect to the adjustment rate α_1 .

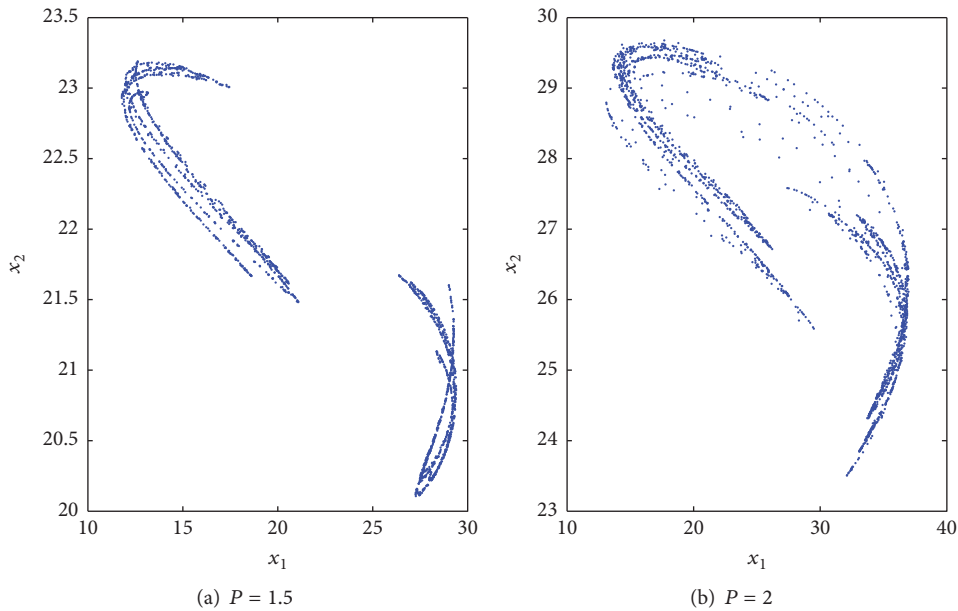


FIGURE 2: Phase portraits for Figure 1 with various values of P and α_1 .

(6) with the change of the model parameters, focusing on the market price of carbon trading P and adjusting speed α 's influence on the dynamic nature of the system. Our study assumes that the parameters are taken as follows: $a = 5$, $b = 1$, $\beta_1 = 0.4$, $\beta_2 = 0.5$, $k_1 = 0.4$, $k_2 = 0.6$, $B_1 = 0.6$, $B_2 = 0.8$, $c_1 = 0.3$, $c_2 = 0.5$, $\theta = 0.35$.

Fixed enterprise 2's strategy adjustment speed is $\alpha_2 = 0.3$. Figure 1 shows the bifurcation diagram of system (6) with enterprise 1 adjusting the speed α_1 , and the carbon trading

market price is P , and P is 1.5 and 2, respectively. It is easy to see that, in Figures 1(a) and 1(b), with the value α_1 increase, the system from the internal equalization changes period doubling bifurcation and eventually enters the chaotic state. Figure 1 not only shows the different paths of chaos in the system, but also shows that the larger the market price of carbon trading P is, the earlier the state variable enters into the chaotic state, and the system has the stronger instability. Figure 2 gives a more detailed description

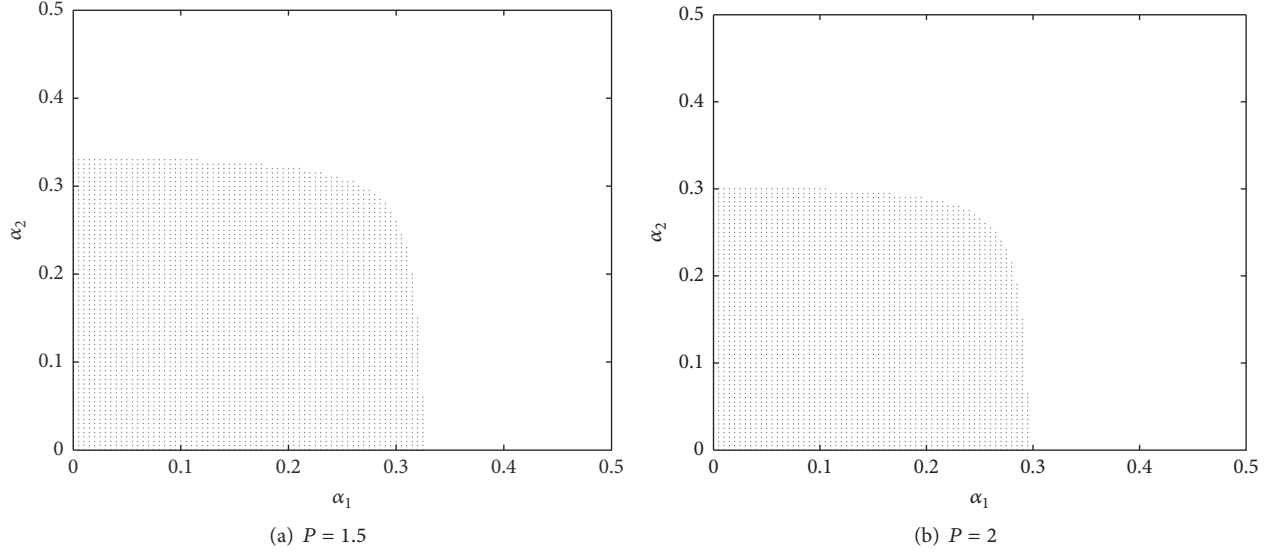


FIGURE 3: The stability region of dynamic system (6) in (α_1, α_2) -plane.

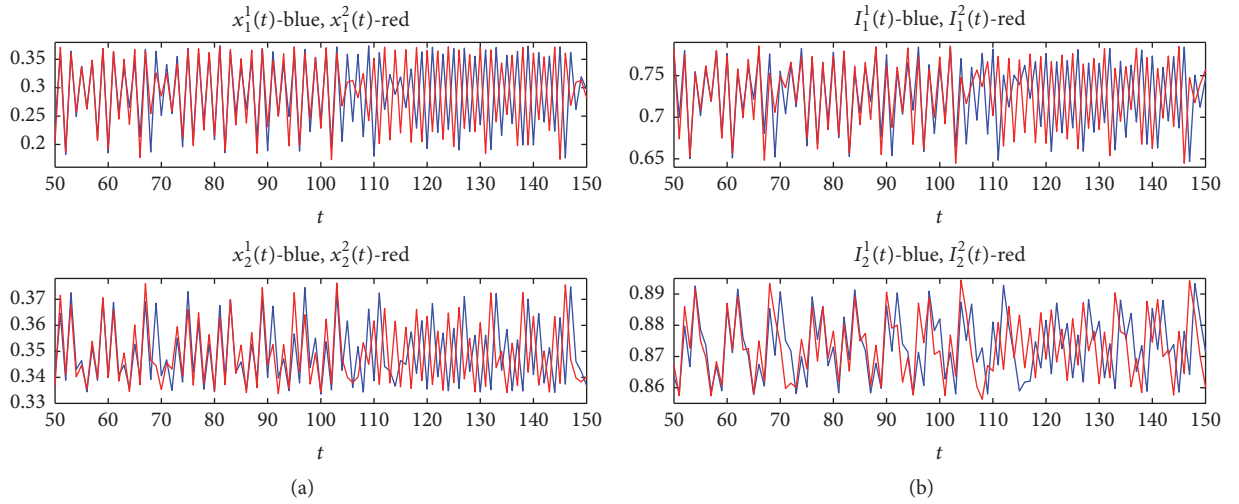


FIGURE 4: Sensitivity of the dynamic system (6) to initial conditions when losing stability.

of the system orbit's change, which is a two-dimensional phase diagram corresponding to the values of the orbit in the different states in Figure 1.

Figure 3 clearly validates this conclusion by calculating the equilibrium point stability condition (17) through the program and plotting the stable region of the system on the plane (α_1, α_2) . Comparing the two subgraphs of Figure 3, it can be seen that the increase of P leads to the decrease in the stability of system (6), and the dynamic evolution of the system becomes more unstable.

We selected the adjustment coefficient $\alpha_1 = 1.23$ of the system in the chaotic state of Figure 1(b). The initial values of the system are $(x_1(0), x_2(0), I_1(0), I_2(0)) = (0.2, 0.2, 0.2, 0.2)$

and $(0.20001, 0.2, 0.2, 0.2)$, and the evolution diagram of the system state variables with the time is plotted. The partial image is shown in Figure 4. As the number of iterations increases, the same state variable is gradually separated under the influence of two initial conditions and subsequently conducts motion according to the respective orbit; thus, system (6) has sensitive dependence on the initial condition.

In order to highlight the effect of the market price of carbon trading on the stability of the orbital motion of the dynamical system (6), the bifurcation results of the system with different adjustment coefficients α_1 are depicted in Figure 5. Figure 5 shows the doubling cycle bifurcation phenomenon. From Figure 5, the system becomes more

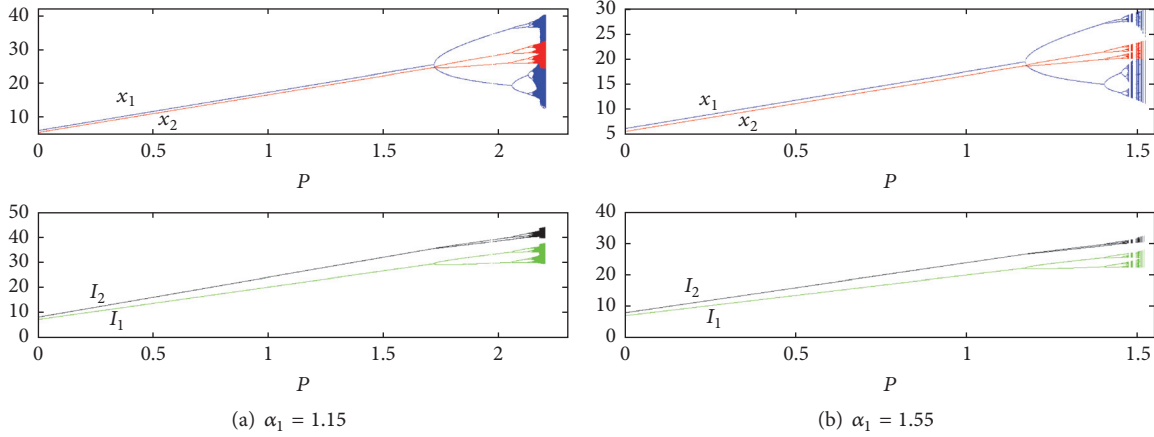


FIGURE 5: Bifurcation diagram for dynamic system (6) with respect to the residual rate P .

unstable with the increase of P . This suggests that increases in carbon trading's market prices lead to the increase of carbon stocks on the market, hence, facilitating environmental protectionism mechanisms which are environmentally beneficial. Companies are also actively working for energy-saving and emission reduction. When the price continues to rise, it results in the increase of inventories in the market. However, beyond a certain extent, the carbon stocks create market's oversupply, hence influencing the stability of the market. Although, from an economic point of view, this phenomenon is in line with the laws of the market, this phenomenon depicts clearly an undesirable infinite loop under the harmonious development and environmental protection as it fails to achieve the desired environmental protection.

5. Chaos Control

From the numerical simulation results of the evolution process in system (6), it can be seen that the adjustment speed and the marketing price of carbon trading have a great influence on the stability of the system. The chaotic behavior of the dynamical system (6) is controlled by the delayed feedback control method, so that the system can be restored to the stable motion state.

Adding the feedback control item $K(x_1(t) - x_1(t+1))$ to system (6) and simplifying the system, we obtained the following form of controlled dynamical system:

$$\begin{aligned}
 x_1(t+1) &= x_1(t) + \frac{\alpha_1}{1+K} x_1(t) \left[P \right. \\
 &\quad \left. + \beta_1 \begin{pmatrix} -bB_1B_2(\theta I_2(t) + \beta_2 x_2(t)) + aB_1 - c_1B_1 \\ -Pk_1B_1 - 1 - 2bB_1^2(\theta I_1(t) + \beta_1 x_1(t)) \end{pmatrix} \right] \\
 x_2(t+1) &= x_2(t) + \alpha_2 x_2(t) \left[P \right. \\
 &\quad \left. + \beta_2 \begin{pmatrix} -bB_1B_2(\theta I_1(t) + \beta_1 x_1(t)) + aB_2 - c_2B_2 \\ -Pk_2B_2 - 1 - 2bB_2^2(\theta I_2(t) + \beta_2 x_2(t)) \end{pmatrix} \right] \\
 I_1(t+1) &= \theta I_1(t) + \beta_1 x_1(t) \\
 I_2(t+1) &= \theta I_2(t) + \beta_2 x_2(t).
 \end{aligned} \tag{18}$$

The stability of the controlled system (18) is analyzed. It is easy to know that the controlled system has the same equilibrium point as the discrete dynamical system (6). The Jacobian matrix corresponding to the controlled system (18) is

$$J(x_1, x_2, I_1, I_2) = \begin{pmatrix} 1 - \frac{\alpha_1 M_1}{1+K} & \frac{-bB_1B_2x_1\alpha_1\beta_1\beta_2}{1+K} & \frac{-2b\theta B_1^2x_1\alpha_1\beta_1}{1+K} & \frac{-b\theta B_1B_2x_1\alpha_1\beta_1}{K+1} \\ -bB_1B_2x_2\alpha_2\beta_1\beta_2 & 1 - \alpha_2 M_2 & -b\theta B_1B_2x_2\alpha_2\beta_2 & -2b\theta B_2^2x_2\alpha_2\beta_2 \\ \beta_1 & 0 & \theta & 0 \\ 0 & \beta_2 & 0 & \theta \end{pmatrix}. \tag{19}$$

As shown in Figure 1(b), when the adjustment coefficient is about 1.21, system (6) enters the chaotic state. The

expression of the Jacobian matrix (19) in the interior point equalization E^* is given under the original parameter value:

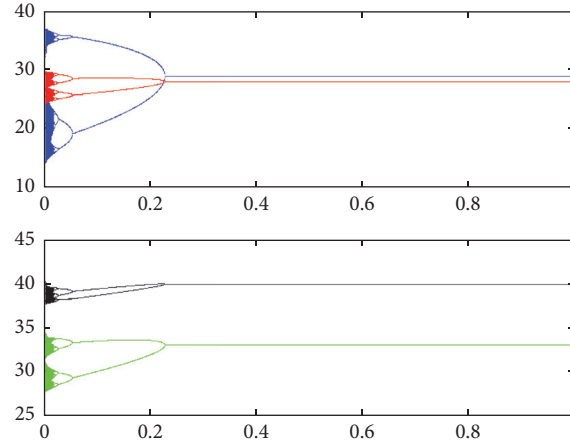


FIGURE 6: Bifurcation diagram of system (18) with respect to the controlling factor k .

$$J = \begin{pmatrix} 1 - \frac{1.37453}{1+K} & -\frac{0.68728}{1+K} & -\frac{1.20272}{1+K} & \frac{0.48109}{1+K} \\ -0.1261 & 0.7478 & -0.11034 & -0.17654 \\ 0.4 & 0 & 0.35 & 0 \\ 0 & 0.5 & 0 & 0.35 \end{pmatrix}. \quad (20)$$

Our study sets the characteristic polynomial of the matrix (20) as $P(\lambda) = \lambda^4 + u_1\lambda^3 + u_2\lambda^2 + u_3\lambda + u_4$, and when the coefficients of the matrix satisfy the Schur-Cohn criterion, then

$$\begin{aligned} &|1 + u_2 + u_4| > u_1 + u_3 \\ &1 \pm u_4 > 0 \\ &\left|1 - u_4^2 + u_2u_4 - u_2u_4^2 + u_1u_3u_4 - u_3^2\right| \\ &> u_2 - u_2u_4 + u_4 - u_4^3 - u_1u_3 + u_1^2u_4. \end{aligned} \quad (21)$$

The characteristic root of matrix (18) is located within the unit circle on the complex plane, and it can be seen that the internal equilibrium point of the controlled system (18) is stable under the settled parameter values, and the chaotic motion of system (6) can also be adjusted to the expected stable orbit, and it can consequently reach the value range of feedback gain intensity.

The effectiveness of control on the chaos of the discrete dynamical system (6) is reached by numerical simulation. Figure 6 shows that if we add the feedback control term $K(x_1(t) - x_1(t+1))$ into the dynamic iterative equation on the emission reduction of the controlled system (6), the unstable orbit can be controlled as long as the feedback gain intensity K is greater than 0.231. The process that chaotic behaviors of the controlled system under the different gain intensities evolve from the initial value to the stable orbit is expressed in Figure 7. By comparison, the time the state variable

reaches stable state in Figure 7(b) is shorter than that in Figure 7(a). The carbon trading market also gets stabilized more quickly.

6. Conclusion

Based on the hypothesis of participant's bounded rationality, our study formulated a novel Cournot duopoly game model of carbon emission reduction and subsequently analyzed the dynamic adjustment mechanism of emission reduction of the participating enterprises. The main idea in our model is that each firm's decision is to choose its carbon emission in each period according to the marginal profit observed from the previous period. We have established a corresponding dynamics of players' carbon emission adjustment and done a detailed dynamic analysis for it. There are three boundary equilibriums and a unique interior equilibrium in this system. By analyzing the stability of each equilibrium point of the discrete dynamical model system, the conditions of the asymptotic equilibrium of the interior point were obtained according to the Schur-Cohn stability criterion. Furthermore, the numerical simulation model of this paper intuitively shows the dynamic evolution process and the complexity of the system. The simulation results revealed that the parameters influence the dynamic properties of the system. It is observed that the equilibrium of the system may lose stability via different bifurcations, either flip bifurcation or Neimark-Sacker bifurcation. Moreover, when the adjustment speed gets too high, the system is likely to lose the original stability and even show complex chaos easily. Higher carbon trading market prices affect the stability of the system and may lead to system instability. Finally, the delay control method has been proved to effectively control the system in the quest to restore back a stable and an equilibrium market.

Conflicts of Interest

The author declares that they have no conflicts of interest.

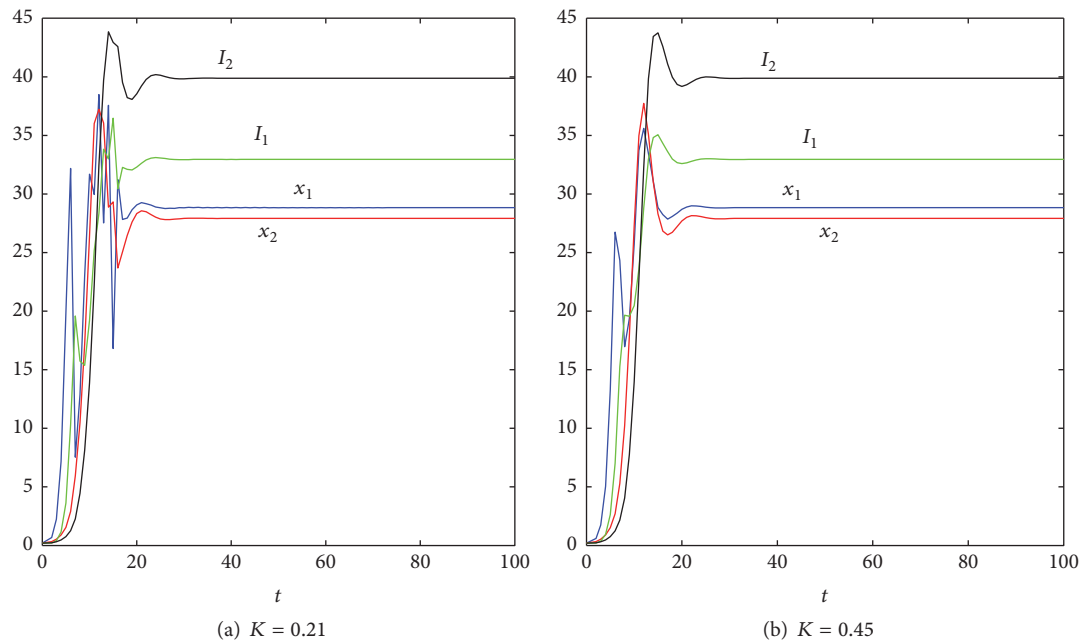


FIGURE 7: The evolution path of system (18) at different gain intensities.

Acknowledgments

This work is supported by the National Nature Science Foundation of China (nos. 71171099, 71471076, and 71701090), China Scholarship Council under Grant 20123227110011, and Postgraduate Research & Practice Innovation Program of Jiangsu Province (KYCX17_1743).

References

- [1] C. Wenyong and W. U. Zongxin, "Carbon emission permit allocation and trading," *Journal of Tsinghua University (Science and Technology)*, vol. 38, no. 12, pp. 15–18, 1998.
- [2] L. H. Goulder, M. A. C. Hafstead, and M. Dworsky, "Impacts of alternative emissions allowance allocation methods under a federal cap-and-trade program," *Journal of Environmental Economics and Management*, vol. 60, no. 3, pp. 161–181, 2010.
- [3] C. Xiao-hong and W. Zhi-yun, "Empirical Research on Price Impact Factor of Carbon Emission Exchange," *Evidence from EU ETS. Systems Engineering*, vol. 30, no. 2, pp. 53–60, 2012.
- [4] M. Kara, S. Syri, A. Lehtilä et al., "The impacts of EU CO2 emissions trading on electricity markets and electricity consumers in Finland," *Energy Economics*, vol. 30, no. 2, pp. 193–211, 2008.
- [5] A. Cournot, *The American Mathematical Monthly*, Mathematical Association of America, Washington, DC, USA, 1928.
- [6] F. Tramontana, A. A. Elsadany, B. Xin, and H. N. Agiza, "Local stability of the Cournot solution with increasing heterogeneous competitors," *Nonlinear Analysis: Real World Applications*, vol. 26, pp. 150–160, 2015.
- [7] J. Bertrand, "Révue de la Théorie Mathématique de la Richesse Sociale et des Recherches sur les Principes Mathématiques de la Théorie des Richesses," *Journal des Savants*, pp. 499–508, 1883.
- [8] E. Ahmed, A. A. Elsadany, and T. Puu, "On Bertrand duopoly game with differentiated goods," *Applied Mathematics and Computation*, vol. 251, pp. 169–179, 2015.
- [9] A. A. Elsadany, H. N. Agiza, and E. M. Elabbasy, "Complex dynamics and chaos control of heterogeneous quadropoly game," *Applied Mathematics and Computation*, vol. 219, no. 24, pp. 11110–11118, 2013.
- [10] J. n. Andaluz and G. Jarne, "On the dynamics of economic games based on product differentiation," *Mathematics and Computers in Simulation*, vol. 113, pp. 16–27, 2015.
- [11] Z. Ding, Q. Li, S. Jiang, and X. Wang, "Dynamics in a Cournot investment game with heterogeneous players," *Applied Mathematics and Computation*, vol. 256, pp. 939–950, 2015.
- [12] X. X. Liao, *The stability of power system theory and application*, National defence industry press, Beijing, China, 2000.

Research Article

Complexity Dynamic Character Analysis of Retailers Based on the Share of Stochastic Demand and Service

Junhai Ma, Weiya Di, and Hao Ren

College of Management and Economics, Tianjin University, Tianjin 300072, China

Correspondence should be addressed to Weiya Di; weiyd140612@126.com and Hao Ren; hren20161028@126.com

Received 27 March 2017; Revised 12 May 2017; Accepted 22 May 2017; Published 24 September 2017

Academic Editor: Sajad Jafari

Copyright © 2017 Junhai Ma et al. This is an open access article distributed under the Creative Commons Attribution License, which permits unrestricted use, distribution, and reproduction in any medium, provided the original work is properly cited.

Apart from the price fluctuation, the retailers' service level becomes another key factor that affects the market demand. This paper depicts a modified price and demand game model based on the stochastic demand and the retailer's service level which influences the market demand decided by customers' preference, while the market demand is stochastic in this model. We explore how the price adjustment speed affects the stability of the supply chain system with respect to service level and stochastic demand. The dynamic behavior of the system is researched by simulation and the stability domain and the bifurcation phenomenon are shown clearly. The largest Lyapunov exponent and the chaotic attractor are also given to confirm the chaotic characteristic of the system. The simulation results indicate that relatively small price adjustment speed may maintain the system at stable state. With the price adjustment speed gradually increasing, the price system gets unstable and finally becomes chaotic. This chaotic phenomenon will perturb the product market and this phenomenon should be controlled to keep the system stay in the stable region. So the chaos control is done and the chaos can be controlled completely. The conclusion makes significant contribution to the system referring to the price fluctuation based on the service level and stochastic demand.

1. Introduction

Bertrand duopoly model is frequently used when the competitive behaviors are discussed in proper research. Hence, the dynamic behaviors of the whole supply chain system have already been probed. However, the retail service level plays an important role in influencing the retail price which indirectly changes the dynamic behaviors of the whole supply chain system that contains one supplier and two retailers.

The two retailers are duopoly in the product market. Xiao and Yang [1] established a price-service competition model with the circumstance whereby the demand is uncertainty in two competing supply chains considering the risk sensitivity. The outcome showed the higher service investment efficiency of one retailer may lead to lower optimal price and service level of his rival. Yan and Pei [2] focused on the retail service in a dual-channel supply chain, while the result suggested that the improved retail services enhanced the supply chain performance effectively in a dual-channel supply chain. Hall et al. [3] engaged in the dynamic retail price and ordering decisions in the category management setting,

and this research found brand's own price and the cross-price effect had an effect on the brand-by-brand market. Ghosh and Mitra [4] examined the different and opposite results to the ones obtained from a similar comparison in the standard setting through comparing the Bertrand and Cournot model in mixed markets with public and private enterprises considering maximum welfare and maximum profit separately.

C. H. Tremblay and V. J. Tremblay [5] introduced a Cournot-Bertrand duopoly model in a Cournot-type firm and a Bertrand-type firm based on the degree of product differentiation. The Cournot-Bertrand equilibrium was calculated and the analysis of the equilibrium was also conducted. Sieke et al. [6] investigated the service level based supply contracts including flat penalty contract and unit penalty contract in a coordinated supply chain. The optimal values of the contract parameters were decided and service level measures were connected to traditional service level measures. Ma and Zhang [7] analyzed the property of three oligarchs which have different rationalities in insurance market based on the price game model and variable feedback

control method. Naimzada and Tramontana [8] studied the liner demand and cost functions with product differentiation, and a dynamic model was established to probe into the stability properties in the mixed Cournot-Bertrand duopoly model. Elsadany [9] developed a triopoly game to indicate the characteristic of a dynamic Cournot game through three bounded rational players. Jha and Shanker [10] introduced the circumstance where a supplier produced products and supplied them to a set of buyers. The lead time can be reduced with an added cash cost and a service level constraint was also included in the research. Wang and Ma [11] centered on the limited information in a Cournot-Bertrand mixed duopoly game model. The bounded rational principles were used to help the two firms make management decisions. He discussed the Nash equilibrium point and the local stability of the game. Mahmoodi and Eshghi [12] added the price competition and the stochastic demand into the duopoly supply chains; the effect of price and the uncertainty demand on the system were discussed.

Ahmed et al. [13] pointed out that the gradient adjustment mechanism of price was applied in a dynamic Bertrand duopoly in which the goods were differentiated. Kawabata and Takarada [14] probed into the effect of free trade agreements on the welfare in Bertrand and Cournot competition model under differentiated products. Brianzoni et al. [15] studied the mathematical properties and dynamics of a Bertrand duopoly with horizontal differentiated products and nonlinear costs, and the new evidence has been offered. Liu and Wang [16] investigated the quality control game that discussed the different risk attitudes affecting quality control game of supply chain especially in logistics service supply chain, instead of considering one member's risk attitude and ignoring the combination of two members' risk attitudes. Fang and Shou [17] managed supply uncertainty under supply chain Cournot competition between two supply chains consisting of a retailer and an exclusive supplier, respectively.

Esmailzadeh and Talezadeh [18] conducted the optimal pricing decisions for two complementary products in a two-echelon supply chain under different market powers with game theory approaches. Ma and Guo [19] examined the impacts of information on the dynamical price game in two Bertrand game models, whereby the player obtains information of his rival before making decisions. Q.-H. Li and B. Li [20] designed the dual-channel supply chain; thus channel competition became inevitable. Hence, value-added services provided by retailers were considered. Equilibrium problems regarding retail services and fairness concerns were analyzed. Protopappa-Sieke et al. [21] developed the optimal two-period inventory allocation policies under multiple service level contracts in view of the fact that optimal inventory allocation had a significant impact on profits in the retail industry. How a manufacturer responds to a service level contract was analyzed as considering to minimize the expected costs.

The structure of the paper is as follows. Firstly, the basic Bertrand duopoly model considering the service level and stochastic demand is established in Section 2. Secondly, the analysis of the model mentioned in the above section has been conducted in Section 3. Then, we simulate the stability

domain and the dynamical behaviors, and the related discussions have been made in Section 4. Lastly, the conclusion will be given in Section 5.

2. Demand Model

Since oligopoly game model has already been researched in previous literature, while the oligopoly situation has been discussed, we consider that the other retailer comes into the monopoly market. Due to the entrance of the other retailer, exclusive monopoly was broken. What is more, the marketing competition is more vehement. Retailer's demand is influenced by the other retailer's price. In addition to retail price, we also consider that the market demand is associated with the service level of themselves and the competitors. Meanwhile, we assume the products that two retailers sell are homogeneous. Hence, the demand function of the two retailers is shown as follows:

$$\begin{aligned} d_1 &= a_1 - b_1 p_1 + b_2 p_2 + k_1 v_1 - k_2 v_2, \\ d_2 &= a_2 - b_1 p_2 + b_2 p_1 + k_1 v_2 - k_2 v_1, \end{aligned} \quad (1)$$

where k_i ($i = 1, 2$) shows the ratio of customers buying the product, which represents the service discrepancy level of the products. b_i ($i = 1, 2$) represents the price sensitive coefficient, which expresses the degree of market demand influenced by the price of their products and competition's product price. Due to the difference of the price and service level between two products, customers will make their own choice according to the price and service level. We must be clear that the higher the service level of the products is, the more the consumers will choose to buy the products in condition of the same price level facing the homogeneous product.

In the expression above, we find that the market demand is affected by both retail price and the service level. The higher service level will bring about the larger cost. The cost of service level is shown in

$$c_i = \eta_i \frac{v_i^2}{2}, \quad i = 1, 2. \quad (2)$$

In (2), v_i means the service level of two retailers. η_i is the influence coefficient, which is used to signify the influence degree of the service level to cost.

While the product market is complex and stochastic, the final demand of the customers is uncertain. We set the demand as stochastic variable a_i , whereby the stochastic demand is the sum of the fixed demand $a_{i,0}$ and the potential stochastic part with market uncertainty e , that is, $a_i = a_{i,0} + e$. And the expectation and variance of e are 0 and r , respectively. We assume that retailers can predict the stochastic demand of their products. Retailers can help to make decisions with the market information forecast, when facing the uncertain factors in the product market. The forecast value of the stochastic demand is f , and f is composed with stochastic variable a_i and the error term ε , that is, $f_i = a_i + \varepsilon$. The expectation and variance of ε are 0 and s ,

separately. We have to point out that e and s are independent. Just like the former research that in Li [22], we know

$$E(a_i f) = \frac{s_i}{r_i + s_i} a_{i,0} + \frac{r_i}{r_i + s_i} f_i, \quad (3)$$

$$E((f - a_{i,0})^2) = r + s.$$

The profit function of the manufacturer is depicted in (4). In this equation, w represents the wholesale prices that manufacturer sells the products to retailer:

$$\pi_m = (d_1 + d_2) w. \quad (4)$$

The retailers' operating goal is to maximize profits. The retailer's profit function is shown as follows:

$$\pi_{R,i} = (p_i - w - c_i) d_i, \quad i = 1, 2. \quad (5)$$

When retailers and manufacturer in the market share the information, the expected profits decision models of manufacturer and retailers are shown as follows, respectively:

$$\begin{aligned} \max E(\pi_m^{is}) &= (d_1 + d_2) w, \\ \max E(\pi_{R,1}^{is}) &= [(p_1 - w - c_1) f_1 d_1], \\ \max E(\pi_{R,2}^{is}) &= [(p_2 - w - c_2) f_2 d_2]. \end{aligned} \quad (6)$$

We can deduce the marginal profits of two retailers through calculating the first-order partial derivative of (6):

$$\begin{aligned} \frac{\partial E(\pi_{R,1}^{NI})}{\partial p_1} &= (1 - g_1) a_{0,1} + g_1 f_1 - 2b_1 p_1 + b_2 p_2 \\ &\quad + k_1 v_1 - k_2 v_2 + b_1 w + b_1 \eta_1 \frac{v_1^2}{2}, \\ \frac{\partial E(\pi_{R,2}^{NI})}{\partial p_2} &= (1 - g_2) a_{0,2} + g_2 f_2 - 2b_1 p_2 + b_2 p_1 \\ &\quad + k_1 v_2 - k_2 v_1 + b_1 w + b_1 \eta_2 \frac{v_2^2}{2}. \end{aligned} \quad (7)$$

For the sake of simplicity, we make $g_i = r_i / (r_i + s_i)$ ($i = 1, 2$) in (7).

2.1. Optimal Decision. If there is only one retailer in the market, the retailer regards profit maximization as the goal to give the optimal decision in the circumstance of discrete game. When there are two retailers in the market, the optimal decision of retailer 1 is influenced by retailer 2. Meanwhile, retailer 2 optimal decision is also affected by retailer 1 decision. Hence, we assume the information in the market can be shared between two retailers; that is, the optimal decisions of two retailers are known to each other. When the marginal profits reduce to zero, we have the optimal decision for retailers. The retail price and the service level are the decision variables.

For retailer 1, we calculate the first-order derivative of its profit. When the marginal profit gets to zero, the optimal retail price and optimal service level will be derived in equation. The detailed process is as follows:

$$\begin{aligned} \frac{\partial E(\pi_{R,1}^{NI})}{\partial p_1} &= 0, \\ \frac{\partial E(\pi_{R,1}^{NI})}{\partial V_1} &= 0, \end{aligned} \quad (8)$$

$$\begin{aligned} p_1^{is} &= \frac{1}{2b_1} \left((1 - g_1) a_{0,1} + g_1 f_1 + b_2 p_2 - k_2 v_2 + b_1 w \right. \\ &\quad \left. + \frac{3k_1^2}{2\eta_1 b_1} \right), \\ v_1^{is} &= \frac{k_1}{b_1 \eta_1}. \end{aligned} \quad (9)$$

Analogously, the optimal decision of retailer 2 will be conducted. Equation (10) has the same meaning as (8). The optimal decision of retailer 2 is expressed in (11):

$$\begin{aligned} \frac{\partial E(\pi_{R,2}^{NI})}{\partial p_2} &= 0, \\ \frac{\partial E(\pi_{R,2}^{NI})}{\partial V_2} &= 0, \end{aligned} \quad (10)$$

$$\begin{aligned} p_2^{is} &= \frac{1}{2b_1} \left((1 - g_2) a_{0,2} + g_2 f_2 + b_2 p_1 - k_2 v_1 + b_1 w \right. \\ &\quad \left. + \frac{3k_1^2}{2\eta_2 b_1} \right), \\ v_2^{is} &= \frac{k_1}{b_1 \eta_2}. \end{aligned} \quad (11)$$

When two retailers make their own optimal decision, we may further find the second derivatives of the retail prices and service level are less than zero. Therefore, the optimal decision of the system will be derived, which means the system has the equilibrium point: $p_1^*, p_2^*, v_1^*, v_2^*$. The calculation will be expressed as follows:

$$\begin{aligned} \frac{\partial^2 E(\pi_{R,1}^{NI})}{\partial^2 p_1} &< 0, \\ \frac{\partial^2 E(\pi_{R,1}^{NI})}{\partial^2 V_1} &< 0, \\ \frac{\partial^2 E(\pi_{R,2}^{NI})}{\partial^2 p_2} &< 0, \\ \frac{\partial^2 E(\pi_{R,2}^{NI})}{\partial^2 V_2} &< 0. \end{aligned} \quad (12)$$

Through jointing (9) and (11), the optimal solution of the system will be solved:

$$\begin{aligned} p_1^* &= \frac{2b_1}{4b_1^2 - b_2^2} \left(R_1 + \frac{b_2}{2b_1} R_2 + \frac{b_2}{2b_1} B + A \right), \\ p_2^* &= \frac{2b_1}{4b_1^2 - b_2^2} \left(R_2 + \frac{b_2}{2b_1} R_1 + \frac{b_2}{2b_1} A + B \right), \\ v_1^* &= \frac{k_1}{b_1 \eta_1}, \\ v_2^* &= \frac{k_1}{b_1 \eta_2}. \end{aligned} \quad (13)$$

In (13), we have $R_1 = (1 - g_1)a_{0,1} + g_1 f_1$, $R_2 = (1 - g_2)a_{0,2} + g_2 f_2$, $A = b_1 w + k_1(3k_1 \eta_2 - k_2 \eta_1)/b_1 \eta_1 \eta_2$, $B = b_1 w + k_1(3k_1 \eta_1 - k_2 \eta_2)/b_1 \eta_1 \eta_2$.

2.2. The Complex Dynamics of the System. Due to the complexity of the product market, the competition between enterprises in the market is increasingly fierce. Retailers do not know the perfect information of the market, while the market is complex and customers' demands are uncertain. In addition, the more the transactions are, the greater the uncertainty will be, the more incomplete the information will be. Hence, the market demand cannot be forecasted accurately. The bounded rationality expectations solve this problem faultlessly. The retail price of next period will be decided according to the retail price in this period and the marginal profits, which makes up the discrete dynamic system of the product market.

$$\begin{aligned} p_1(t+1) &= p_1(t) + \theta_1 p_1(t) \left((1 - g_1) a_{0,1} + g_1 f_1 \right. \\ &\quad \left. - 2b_1 p_1 + b_2 p_2 + k_1 v_1 - k_2 v_2 + b_1 w + b_1 \eta_1 \frac{v_1^2}{2} \right), \\ p_2(t+1) &= p_2(t) + \theta_2 p_2(t) \left((1 - g_2) a_{0,2} + g_2 f_2 \right. \\ &\quad \left. - 2b_1 p_2 + b_2 p_1 + k_1 v_2 - k_2 v_1 + b_1 w + b_1 \eta_2 \frac{v_2^2}{2} \right). \end{aligned} \quad (14)$$

In the equation above, θ_i ($i = 1, 2$) is the price adjustment speed of retailer i , and the price adjustment speed is positive, which is set to make sure that retail price of next period is practically significant. When the marginal profit takes positive value, the retail price of next period will increase. However, when the marginal profit takes negative value, the retail price of next period will decrease.

The system (14) is nonlinear; the system is running under constant interference. When the system is disturbed, whether it can maintain a predetermined trajectory, the stability of the system becomes the primary question to study. What is different from the linear system is that the nonlinear system has multiple equilibriums. We obtain four equilibriums of system (14): $E_0(0, 0)$, $E_1(0, (R_2 + B)/2b_1)$, $E_2((R_1 + A)/2b_1, 0)$,

$E^*((2b_1/(4b_1^2 - b_2^2))(R_1 + (b_2/2b_1)R_2 + (b_2/2b_1)B + A), (2b_1/(4b_1^2 - b_2^2))(R_2 + (b_2/2b_1)R_1 + (b_2/2b_1)A + B))$.

We may find that E_0, E_1, E_2 are boundary points, and E^* is within the system. We guess that E^* is the unique Nash equilibrium. In order to verify the guess and analyze the stability of the system, we calculate the Jacobian matrix of system (14):

$$J(E) = \begin{pmatrix} J_{11} & J_{12} \\ J_{21} & J_{22} \end{pmatrix}. \quad (15)$$

In the equation above,

$$\begin{aligned} J_{11} &= 1 + \theta_1 R_1 + \theta_1 b_2 p_2 + \theta_1 A - 4\theta_1 b_1 p_1, \\ J_{12} &= \theta_1 b_2 p_1, \\ J_{21} &= \theta_2 b_2 p_2, \\ J_{22} &= 1 + \theta_2 R_2 + \theta_1 b_2 p_1 + \theta_2 B - 4\theta_2 b_1 p_1. \end{aligned} \quad (16)$$

E^* is the unique Nash equilibrium; the best profit of the system can be obtained when the best decision is in E^* . We all know that when the margin profit is more than zero, the retailers will adjust their retail prices, until the margin profit goes up to zero. At this time, the system reaches to equilibrium state. Retailers will not change their own retail price any more, and the equilibrium state will be maintained by these two game players. Therefore, among all the equilibrium points, only the Nash equilibrium E^* has practical significance. Then, this part will explore the local stability of the Nash equilibrium by using the Jacobian matrix and the July criterion.

The characteristic polynomial of the Jacobian matrix takes the following form:

$$F(\lambda) = \lambda^2 - (J_{11} + J_{22})\lambda - (J_{11}J_{22} - J_{12}J_{21}). \quad (17)$$

In order to guarantee that the Nash equilibrium is local stability, $J_{i,j}$ ($i, j = 1, 2$) must satisfy the following limitations:

$$\begin{aligned} -(J_{11} + J_{22}) + (J_{11}J_{22} - J_{12}J_{21}) + 1 &> 0, \\ (J_{11} + J_{22}) + (J_{11}J_{22} - J_{12}J_{21}) + 1 &> 0, \\ J_{11}J_{22} - J_{12}J_{21} &< 1, \\ J_{11} + J_{22} &> 0. \end{aligned} \quad (18)$$

Due to the fact that limitations are so complex, the process to solve inequality (18) is very complicated. If the Nash equilibrium satisfies inequality (18), we may insure that Nash equilibrium is locally stable. We will probe into the dynamic characteristic of the system through numerical simulation in next section.

3. Dynamic Characteristics of the System

In consideration of the complexity of system (14), the numerical simulation method will be employed in this paper as this method has been widely used in most of the literatures.

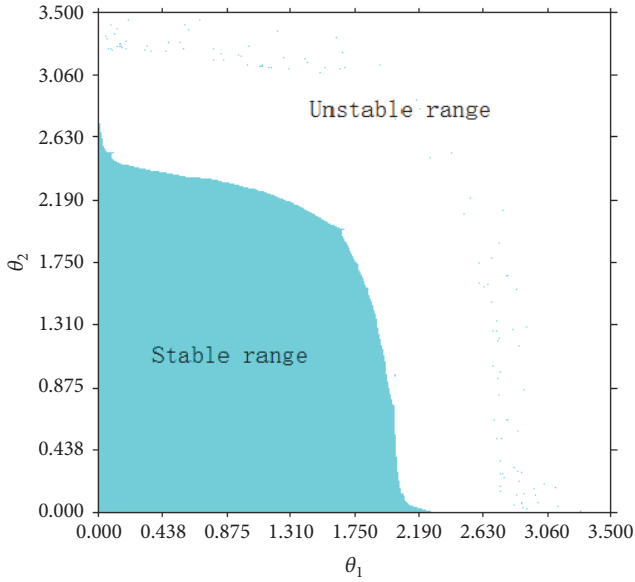


FIGURE 1: The stable range of system (14).

The stable region, bifurcation, and chaos will be investigated; meanwhile, the largest Lyapunov exponent, entropy, chaotic attractor, and the time domain response will be discussed to verify the dynamic characteristics of this system. At last, the sensitivity of initial value will be analyzed. We take the parameter values as follows: $g_1 = 0.7$, $g_2 = 0.6$, $a_{0,1} = 0.5$, $a_{0,2} = 0.55$, $f_1 = 0.6$, $f_2 = 0.65$, $b_1 = 1$, $b_2 = 0.5$, $k_1 = 1.1$, $k_2 = 1.2$, $v_1 = 0.7$, $v_2 = 0.6$, $w = 0.1$, $\eta_1 = 0.2$, $\eta_2 = 0.3$.

3.1. The Stable Region. The decision variables of the system are retail prices of two retailers. As retail prices obtain different values, the system will change to either the stable range or the unstable range. Figure 1 depicts the stable region of the system with blue range and the unstable of the system with white region. When employed values are in the blue range, the system will tend to the equilibrium state after iteration period by period. Then the system will stay at the Nash equilibrium state unless some factors outside break the equilibrium state.

3.2. The Bifurcation and Chaos Behavior. The fixed point is stable when all the eigenvalues of the Jacobian are in the unit circle. When θ_1 and θ_2 satisfy the critical value, the system appears as saddle point. If one characteristic root $\lambda_2 = -1$ and all the other eigenvalues are within the unit circle, the fixed point will be unstable and produce period-doubling bifurcation. From Figure 2, we can see that system (14) will appear as period-doubling bifurcation.

We discuss the bifurcation and chaos behaviors of the system in this section with parameter basin plots and the bifurcation diagram. We set the initial values of the system as $p_1(0) = 0.25$ and $p_2(0) = 0.2$, which represent the retail price of two retailers at the first moment.

Figure 3 describes the parameter basin plots of system (14) with respect to the price adjustment speeds θ_1 and θ_2 .

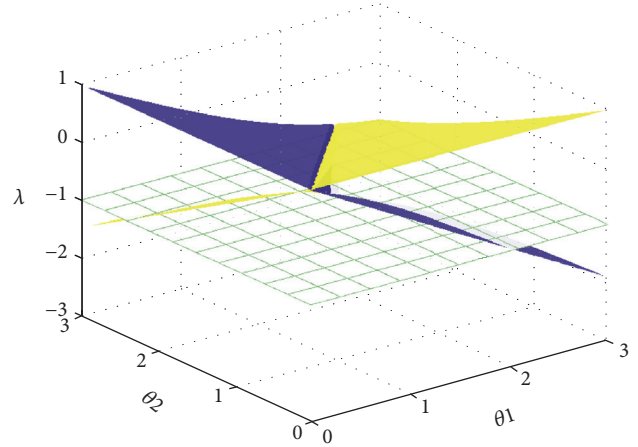


FIGURE 2: The characteristic root of system (14).

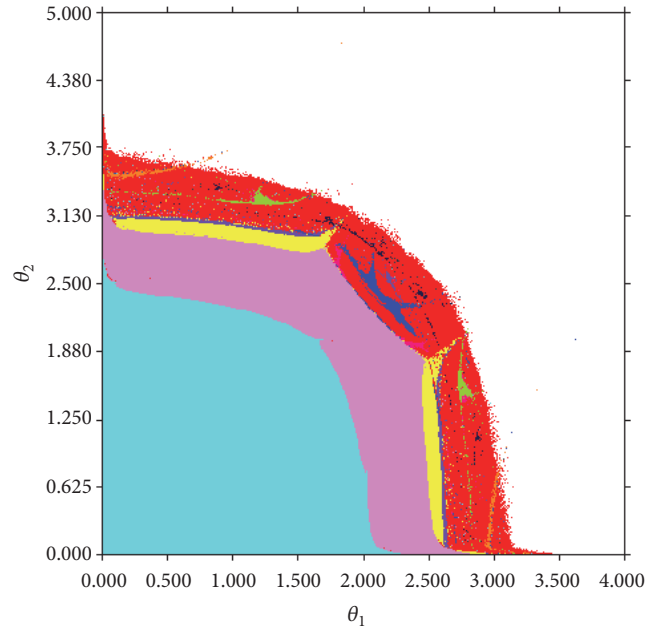


FIGURE 3: The parameter basin plots of system (14).

Different colors in this figure represent the stable region, stable cycles of periods, and chaotic states separately: the light blue range is the stable region, pink range means the stable cycles of period 2, orange range is the stable cycles of period 3, yellow range is the stable cycles of period 4, green range is the stable cycles of period 5, dark blue range is the stable cycles of period 6, cyan range is the stable cycles of period 7, purple range is the stable cycles of period 8, red range represents chaos, and white means divergence. If the retail prices are in the white region, one of the retailers is outside the product market, and the market will be oligopolistic market. Through the observation of Figure 3, we find pink, yellow, dark blue, and purple constitute the road from even period cycles to chaos, the road being called the flip bifurcation in discrete dynamical system; meanwhile, orange, green, and cyan constitute the road from odd period cycles to chaos.

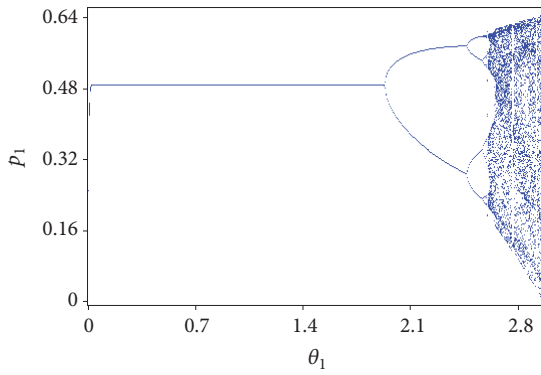
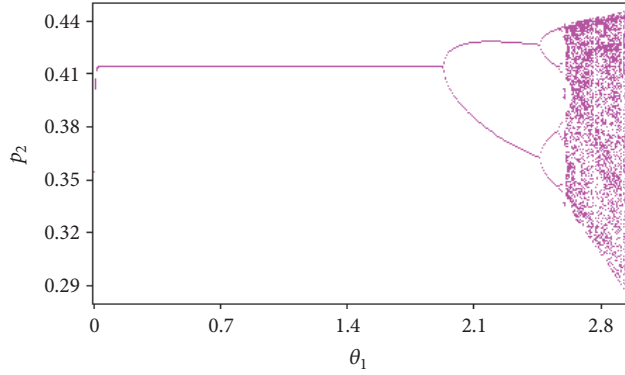
(a) Bifurcation diagram of p_1 with respect to θ_1 when $\theta_2 = 1.2$ (b) Bifurcation diagram of p_2 with respect to θ_1 when $\theta_2 = 1.2$

FIGURE 4

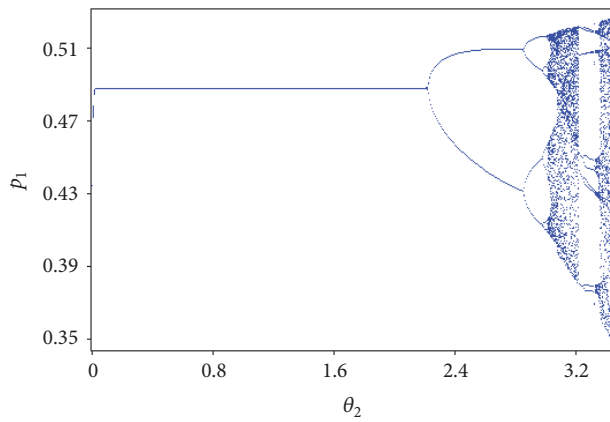
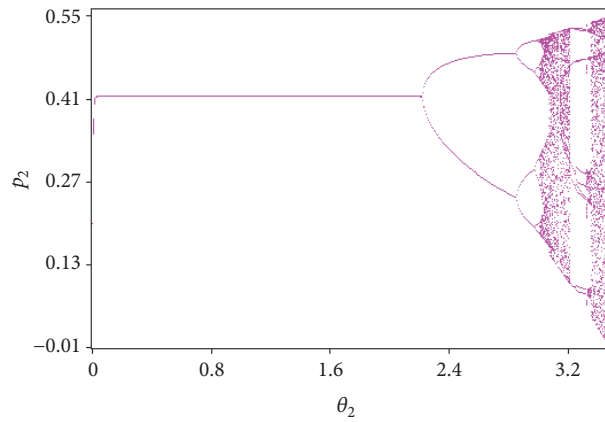
(a) Bifurcation diagram of p_1 with respect to θ_2 when $\theta_1 = 1.2$ (b) Bifurcation diagram of p_2 with respect to θ_2 when $\theta_1 = 1.2$

FIGURE 5

By observing this figure, we may find the retail price changes from the stable region to the even period cycles and next it gets to chaotic region. This phenomenon is the flip bifurcation, whereby the retailers adjust their own retail price, the system will go from the even period cycles to the chaotic region directly.

Figures 4(a) and 4(b) give the bifurcation diagram of retail prices with respect to θ_1 when $\theta_2 = 1.2$. This figure can explain the complex dynamic behavior of the system more intuitively, whereby one of the price adjustment speeds is fixed and the other adjustment speed changes within a certain range. This paper investigates the adjustment speed of retailers' prices firstly by keeping θ_2 fixed at 1.2 and θ_1 varying from zero to 3. In Figure 4(a), retailer 1's retail price is stable at 0.49 as θ_1 vary from zero to 1.95. Just at this time, the system begins the first bifurcation, while the system runs into stable cycles of period 2. As θ_1 increases to 2.47, the system gets to stable cycles of period 4. When θ_1 gets the value of 2.58, retail 1's price goes into stable cycles of period 8. After that, the system falls into a chaotic state.

Figure 4(b) depicts the bifurcation diagram of p_2 with respect to θ_1 when $\theta_2 = 1.2$. The bifurcation points of this figure are completely the same as the bifurcation points in Figure 4(a). However, what is different from Figure 4(a) is the

value of retail price. Retailer 2's retail price is stable at 0.415 as θ_1 vary from zero to 1.95. Next, p_2 gets to cycles of periods 2, 4, and 8 in sequence. In the end, p_2 also falls into chaos.

Figures 5(a) and 5(b) describe the bifurcation behavior of retail prices when θ_2 increases gradually and θ_1 keeps the fixed value 1.2, which is the same as Figure 4; this shows the complex dynamic behavior of retail price considering the price adjustment speed of retailer 2 varying from zero to 3.5. In Figure 5(a), as θ_2 is small and less than 2.22; the retail price of retailer 1 keeps a fixed number of 0.488. After that, the retail price falls into the stable cycles of period 2; when θ_2 increases to 2.85, the retail price falls into the stable cycles of period 4; then when θ_2 goes to 2.98, the retail price falls into the stable cycles of period 8; and so forth. After the system passes through multiple iterations, it will turn into chaos, which will not be expected to appear.

Analogously, the complex dynamic behavior of retail price 2 considering the price adjustment speed of retailer 2 varying from zero to 3.5 will be shown in Figure 5(b). Firstly, retailer price 2 is stable at 0.414 when θ_2 is at $[0, 2.22]$. Then the system turns into bifurcation and chaos state orderly. It is worth noting that the stable price of retailer 2 is less than that of retailer 1, which means retailer 2 may possess more market share. This phenomenon is not conducive to retailer 1. And

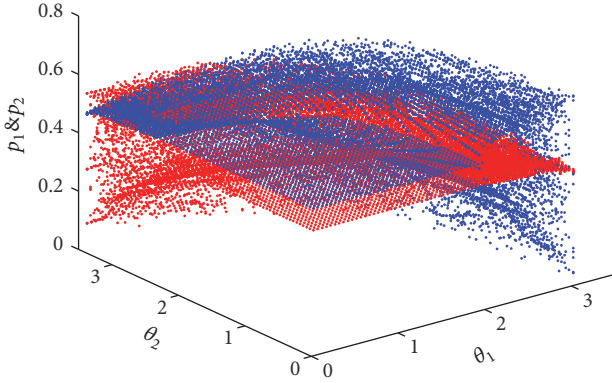


FIGURE 6: 3D bifurcation diagram of p_1 and p_2 .

retailer 1 must take measures to decrease its own retail price to win more market demand.

Through the analysis of Figures 4 and 5, we find that relatively small price adjustment speed may maintain the system at stable state. Figure 6 shows the stability of the system from a three-dimensional perspective. With the price adjustment speed gradually increasing, the price system gets unstable and finally becomes chaotic. Hence, from the point of view of management, the retailer should choose a relatively reasonable adjustment speed to alter the retail price in each decision unit.

3.3. The Largest Lyapunov Exponent. The largest Lyapunov exponent (LLE) is another way to make clear the complex dynamic characteristics of the system. And the LLE represents the extreme sensitivity to initial value of the system vividly that two of the same initial value generated in the trajectory separate according to index methods with the passage of time. As we want to judge whether the chaotic phenomenon exists in the system, we just need to observe the LLE intuitively. If the LLE is more than zero, it means that the differences of the initial value increase with exponential form after periods of iteration; that is, the system falls into chaotic region. On the contrary, if the LLE is less than zero, it means that the system is in stable state, while the system is not initially sensitive and keeps a fixed value all the time. When the LLE equals zero, the system is periodic and quasi-periodic. The expression of LLE is as follows:

$$\lambda = \lim_{n \rightarrow \infty} \frac{1}{n} \sum_{n=0}^{n-1} \ln \left| \frac{df(x_n, \mu)}{dx} \right|. \quad (19)$$

We used MATLAB to simulate Figures 7(a) and 7(b). Figures 7(a) and 7(b) explore the LLE with the increase of price adjustment speed. The system acts out the complex dynamic behavior as the price adjustment speed changes. In Figure 7(a), when θ_1 is in $[0, 1.95]$, the LLE is less than zero and the system is in stable state; while θ_1 is in $[1.95, 2.6]$, the LLE is equal to zero and the system is in bifurcation region; when θ_1 is more than 2.6, the LLE is more than zero and the system is in chaotic region. Figure 7(b) shows the LLE with respect to θ_2 , and it has the same changing process with θ_1 . Figure 7

accounts for the state of the dynamic system more intuitively; meanwhile, the bifurcation point and the chaos point in Figure 7 are in consistent with the bifurcation diagrams.

3.4. The Entropy. Entropy is an important quantity to characterize chaotic systems. In different types of dynamic systems, the entropy values are different. Entropy values can be used to distinguish between regular motion, chaotic motion, and random motion. In the random motion system, the entropy is unbounded; in the regular motion system, the entropy is zero; in the chaotic motion system, the entropy is greater than zero. The greater the entropy, the greater the rate of loss of information, the greater the degree of chaos in the system, or the more complex the system.

It can be seen from Figure 8 that as the system progressively enters chaos, the entropy of the system increases rapidly from zero. The law of change is also the same as the change of bifurcation and maximum Lyapunov exponent.

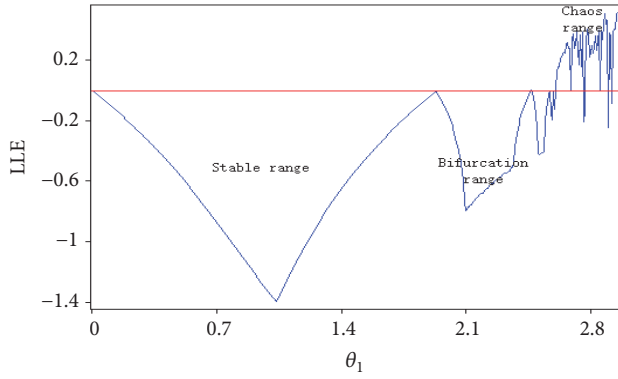
3.5. The Chaotic Attractor. The chaotic attractor investigates the chaotic characteristics of the system and the chaotic attractors will be given in Figures 9(a), 9(b), and 9(c), while the price adjustment speeds are in stable region and chaotic region, respectively. Strange attractor is the joint action's product of overall stability and local instability. All the movement outside the attractor will finally converge to the chaotic attractor. Meanwhile the movement inside the attractor is instable. If the attractor is a fixed point, the system is in stable state. On the contrary, when the attractor is not a fixed point and period cycle, the system is in chaos.

In Figure 9(a), we judged on the parameter basin plots, bifurcation diagram, the largest Lyapunov exponent, and entropy of system; when θ_1 and θ_2 equal 1.2, they are all in stable states, and at this moment the attractor is a fixed point.

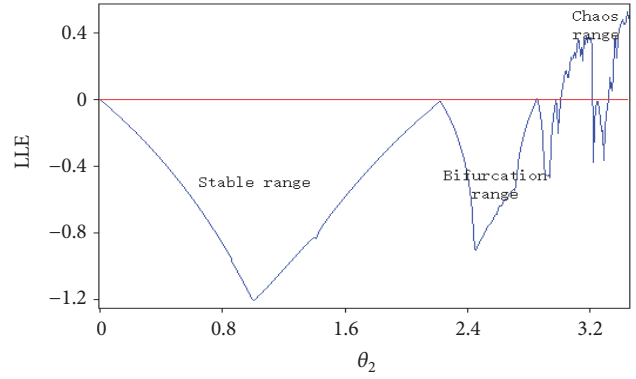
From the parameter basin plots, bifurcation diagram, the largest Lyapunov exponent, and entropy of system, we may see that the systems are in chaotic states while $\theta_1 = 2.8$, $\theta_2 = 1.2$ and $\theta_1 = 1.2$, $\theta_2 = 3.2$. Hence, the attractors expand to a big area, and the system begins to do limit movement in Figures 9(b) and 9(c). Then the attractors turn into chaotic attractors. Just now, the system becomes complex and the dynamic characteristics of the system are more obviously.

3.6. Time Domain Response. The time domain response depicts the changing process of the price data with the increase of time, which is arranged by the whole time index. There are different shapes for the time domain response. Figures 10(a), 10(b), and 10(c) describe the time domain responses of the system when the price adjustment speeds are in stable region and chaotic region, respectively. In Figure 10, blue line represents the retail price of retailer 1, and red line represents the retailer price of retailer 2.

In Figure 10(a), θ_1 and θ_2 equal 1.2. The price adjustment speeds are all in stable states. Then the two retail price fix at the equilibrium point E^* (0.488, 0.414), and two retail price will not change as the time changes. It is the same as Figure 9; we set $\theta_1 = 2.8$, $\theta_2 = 1.2$, and $\theta_1 = 1.2$, $\theta_2 = 3.2$ in Figures 10(b) and 10(c). In Figure 10(b), while θ_1 is in stable region and

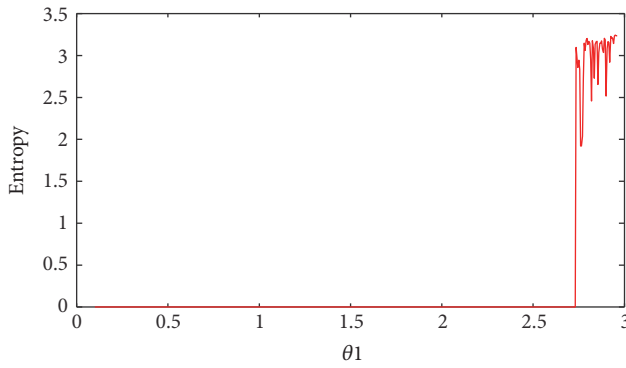


(a) The largest Lyapunov exponent of system with respect to θ_1 when $\theta_2 = 1.2$

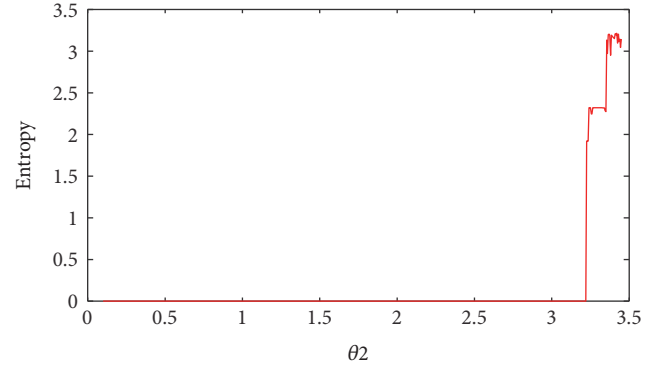


(b) The largest Lyapunov exponent of system with respect to θ_2 when $\theta_1 = 1.2$

FIGURE 7



(a) The entropy of system with respect to θ_1 when $\theta_2 = 1.2$



(b) The entropy of system with respect to θ_2 when $\theta_1 = 1.2$

FIGURE 8

θ_2 is in chaotic area, the fluctuation of blue line is obviously big compared to that of the red line, and the red line just tends to the value 0.36. Uniformly in Figure 10(c), the fluctuation of blue line is obviously small compared to that of the red line, and the blue line just tends to the value 0.45 as θ_2 is in stable region and θ_1 is in chaotic region. This phenomenon shows that when the price adjustment speed is in stable state, the time domain response is smooth. On the contrary, the time domain response will be in big fluctuation while the price adjustment speed is in chaotic state.

4. Chaos Control

With the findings of sections above, we come to the conclusion that if the adjustment speeds of the retail prices are in chaotic region, the system will be complex, and the manager cannot make decision in time that phenomenon is not expected to appear in the product market. Therefore, we should take measure to expand the stable region and control the chaos further. *From the management point of view, the market is sharply fluctuating while the adjustment speeds of the retail prices expand from the stable region to chaotic region; hence the adjustment speeds of the retail prices must be in stable region so as to keep the market smooth. Then the chaos control method becomes necessary.*

Here, we employ the widely used control method, that is, parameter adjustment control method to control the chaotic phenomenon. Ma and Li [23] adopted this kind of method to control the complex dynamic behavior of the pricing game models in a risk-averse supply chain, and the chaos has been controlled perfectly. Hence, we also adopt parameter adjustment control method so as to solve this problem in this section. The manager may control the chaotic behavior through introducing the control parameter u , and we set $u = 0.6$ as Ma et al. [24] have conducted the chaos control with setting the control parameter as 0.6. The other parameters employ the values set in the sections above. After that, the stable range and the bifurcation diagram will be given to account for the state of the system. With the parameter adjustment control, the system will be

$$\begin{aligned}
 p_1(t+1) = & (1-u) \left(p_1(t) + \theta_1 p_1(t) \left((1-g_1) a_{0,1} \right. \right. \\
 & + g_1 f_1 - 2b_1 p_1 + b_2 p_2 + k_1 v_1 - k_2 v_2 + b_1 w \\
 & \left. \left. + b_1 \eta_1 \frac{v_1^2}{2} \right) \right) + u p_1(t),
 \end{aligned}$$

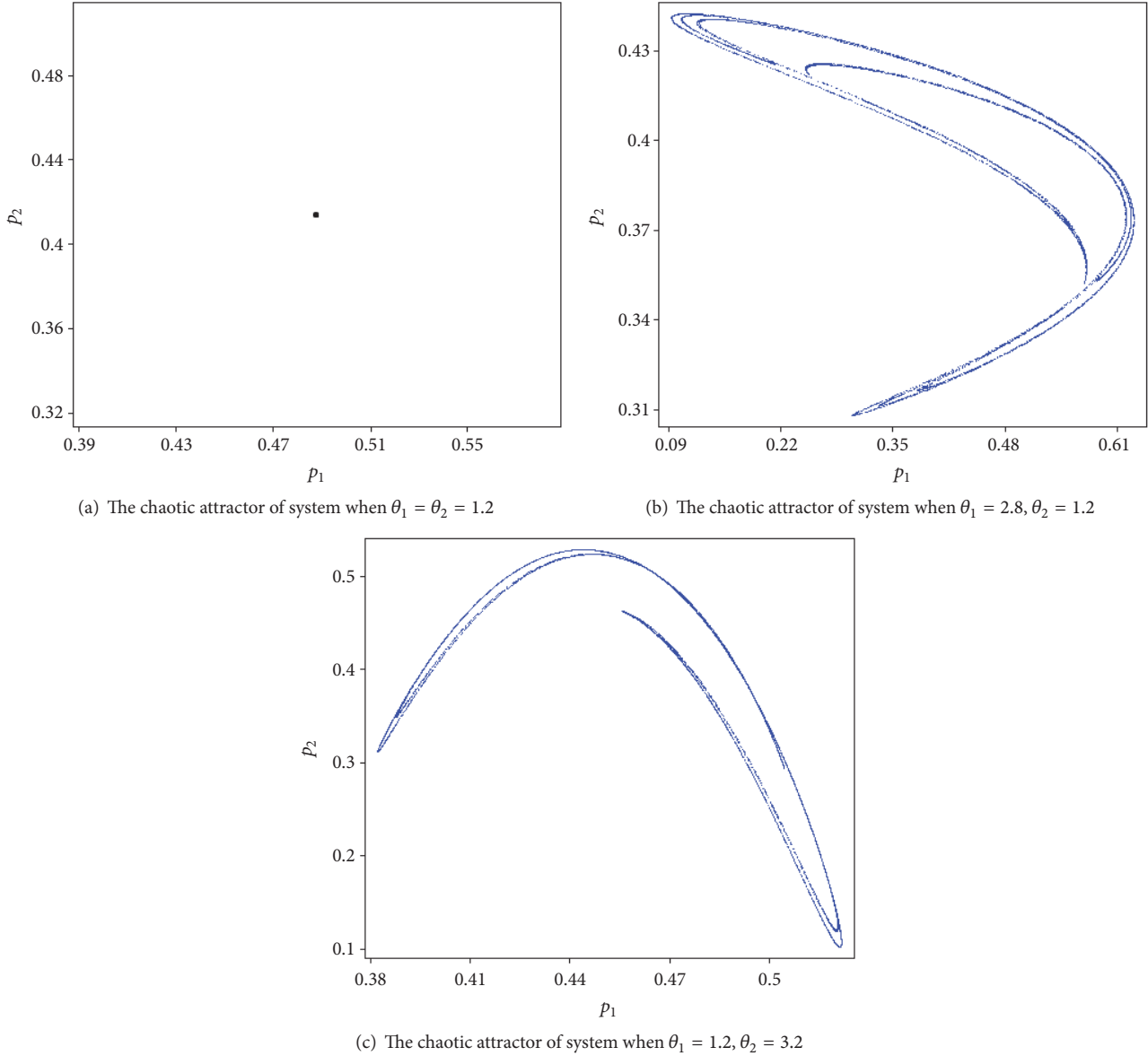


FIGURE 9

$$\begin{aligned}
 p_2(t+1) = & (1-u) \left(p_2(t) + \theta_2 p_2(t) \left((1-g_2) a_{0,2} \right. \right. \\
 & + g_2 f_2 - 2b_1 p_2 + b_2 p_1 + k_1 v_2 - k_2 v_1 + b_1 w \\
 & \left. \left. + b_1 \eta_2 \frac{v_2^2}{2} \right) \right) + u p_2(t).
 \end{aligned}
 \tag{20}$$

Figure 11 depicts the stable region after having been controlled by the control parameter. Compared to the stable region of system (14), the stable region of system (20) increases obviously, which means a relative large price adjustment speed will not make the system run into chaos. This is helpful for managers to adjust the retail price with a more range.

The complex dynamic behavior of system (20) has been investigated in Figures 12 and 13. The first bifurcation point of the system is big compared to that before controlling, the value of which is 5, and it is bigger than value (1.95) of first bifurcation point in system (14) in Figure 9 depicting the bifurcation diagram of p with respect to θ_1 when $\theta_2 = 1.2$. Figure 10 shows the bifurcation diagram of p with respect to θ_2 when $\theta_1 = 1.2$. It is similar to the phenomenon in Figure 12 that the first bifurcation point of the system is big compared to that before controlling. The first bifurcation point expands to 5.92 that the stable region of system (20) is enlarged. Hence, the managers will make decisions relatively simple.

Bifurcation diagram of p when the control parameter u varies from 0 to 1 is given in Figure 14. When u takes the value of zero, system (20) will be the same as system (14), and then the system is chaotic. With the increase of u , the

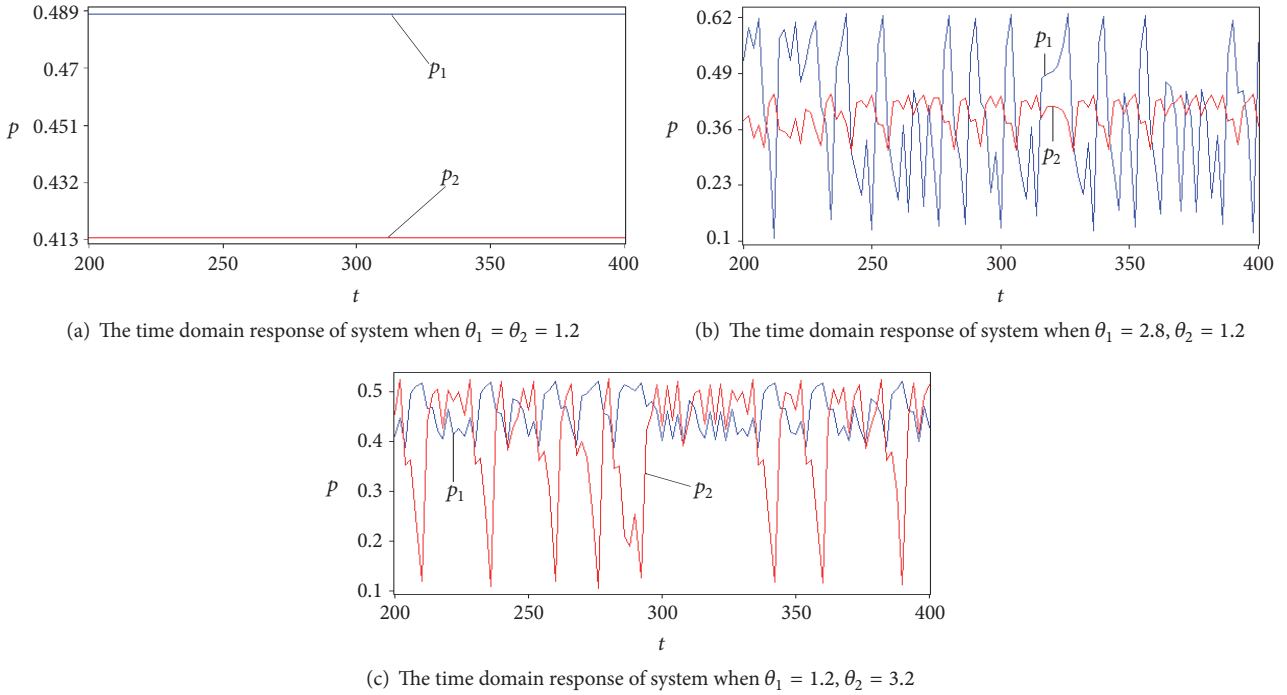


FIGURE 10

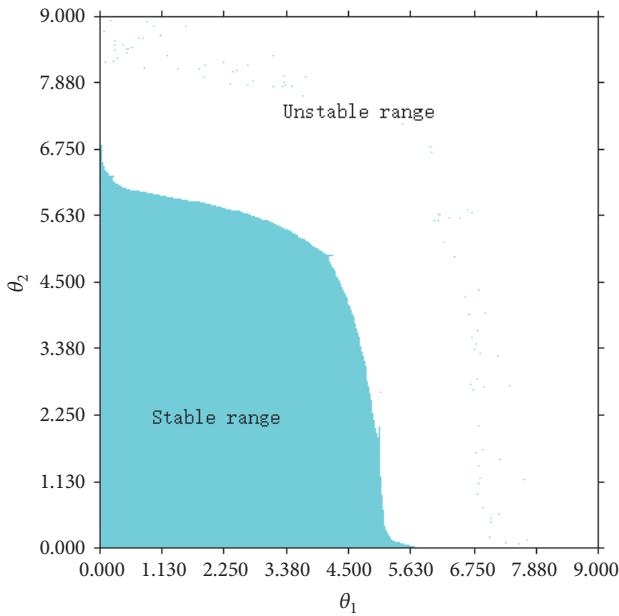


FIGURE 11: The stable range of system (20).

system changes from the chaotic region to the bifurcation region and finally falls into the stable region, which means the chaos behavior has been controlled completely.

5. Conclusion

Previous researches have explored the price fluctuation with price and demand game model in the supply chain

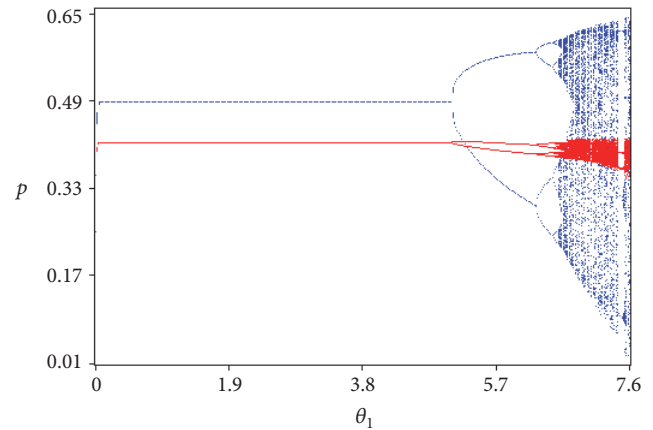


FIGURE 12: Bifurcation diagram of p with respect to θ_1 when $\theta_2 = 1.2$.

management. However the retailers' service level has not been involved in the basic demand model. This paper depicts a modified Bertrand duopoly model based on the stochastic demand and the retailer's service level which influences the market demand decided by customers' preference, while the market demand is stochastic in this model. How the price adjustment speed affects the stability of the supply chain system with respect to service level and stochastic demand has been studied in this paper. The dynamic behavior of the system is researched by simulation and the stability domain and the bifurcation phenomenon are shown clearly. The largest Lyapunov exponent, the chaotic attractor, and the time series are also given to confirm the chaotic characteristic of the system.

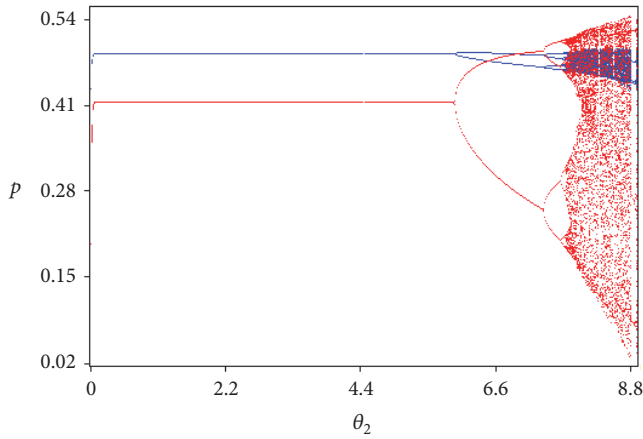


FIGURE 13: Bifurcation diagram of p with respect to θ_2 when $\theta_1 = 1.2$.

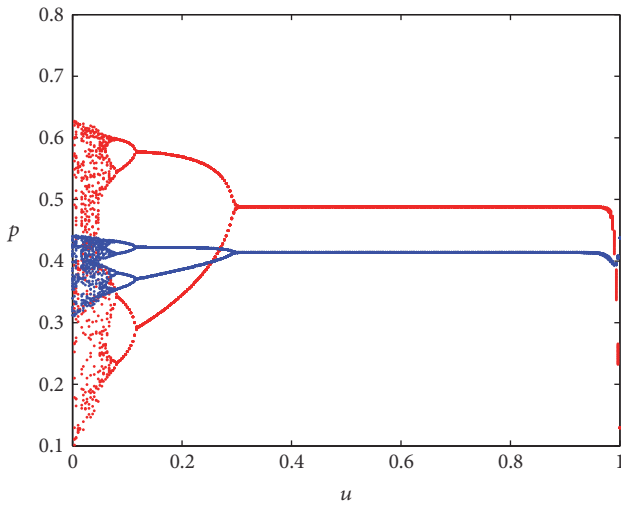


FIGURE 14: Bifurcation diagram of p when u varies from 0 to 1.

We come to the conclusion that (1) with the price adjustment speed gradually increasing, the price system gets unstable and finally becomes chaotic; (2) a relatively small price adjustment speed may maintain the system at stable state; (3) chaos can be controlled completely with the parameter control method. This chaotic phenomenon will perturb the product market. Hence, the conclusion makes significant contribution to the system, referring to the price fluctuation based on the service level and stochastic demand.

In spite of the contribution that this paper has offered to the managers, some limitations still exist in this paper. Firstly, the supply chain only contains two retailers; in order for this study to be more close to the reality and be used in more scales of enterprises, we may study the dynamic game behavior in the three-oligarch product market. Secondly, this paper only does the numerical simulation, while there are no real data to support the conclusion of the paper. Hence, some real data should be collected to identify the conclusion.

Conflicts of Interest

The authors declare no conflicts of interest.

Authors' Contributions

Weiya Di and Junhai Ma built the supply chain model; Junhai Ma provided economic interpretation; Weiya Di carried out numerical simulation; Hao Ren performed mathematical derivation; the authors wrote this research manuscript together. All authors have read and approved the final manuscript.

Acknowledgments

The research was supported by the National Natural Science Foundation of China (71571131).

References

- [1] T. Xiao and D. Yang, "Price and service competition of supply chains with risk-averse retailers under demand uncertainty," *International Journal of Production Economics*, vol. 114, no. 1, pp. 187–200, 2008.
- [2] R. Yan and Z. Pei, "Retail services and firm profit in a dual-channel market," *Journal of Retailing and Consumer Services*, vol. 16, no. 4, pp. 306–314, 2009.
- [3] J. M. Hall, P. K. Kopalle, and A. Krishna, "Retailer Dynamic Pricing and Ordering Decisions: Category Management versus Brand-by-Brand Approaches," *Journal of Retailing*, vol. 86, no. 2, pp. 172–183, 2010.
- [4] A. Ghosh and M. Mitra, "Comparing Bertrand and Cournot in mixed markets," *Economics Letters*, vol. 109, no. 2, pp. 72–74, 2010.
- [5] C. H. Tremblay and V. J. Tremblay, "The Cournot-Bertrand model and the degree of product differentiation," *Economics Letters*, vol. 111, no. 3, pp. 233–235, 2011.
- [6] M. A. Sieke, R. W. Seifert, and U. W. Thonemann, "Designing service level contracts for supply chain coordination," *Production and Operations Management*, vol. 21, no. 4, pp. 698–714, 2012.
- [7] J. Ma and J. Zhang, "Price game and chaos control among three oligarchs with different rationalities in property insurance market," *Chaos. An Interdisciplinary Journal of Nonlinear Science*, vol. 22, no. 4, Article ID 043120, 043120, 13 pages, 2012.
- [8] A. K. Naimzada and F. Tramontana, "Dynamic properties of a Cournot-Bertrand duopoly game with differentiated products," *Economic Modelling*, vol. 29, no. 4, pp. 1436–1439, 2012.
- [9] A. A. Elsadany, "Competition analysis of a triopoly game with bounded rationality," *Chaos, Solitons and Fractals*, vol. 45, no. 11, pp. 1343–1348, 2012.
- [10] J. K. Jha and K. Shanker, "Single-vendor multi-buyer integrated production-inventory model with controllable lead time and service level constraints," *Applied Mathematical Modelling. Simulation and Computation for Engineering and Environmental Systems*, vol. 37, no. 4, pp. 1753–1767, 2013.
- [11] H. Wang and J. Ma, "Complexity analysis of a cournot-bertrand duopoly game model with limited information," *Discrete Dynamics in Nature and Society*, vol. 2013, Article ID 287371, 2013.

- [12] A. Mahmoodi and K. Eshghi, "Price competition in duopoly supply chains with stochastic demand," *Journal of Manufacturing Systems*, vol. 33, no. 4, pp. 604–612, 2014.
- [13] E. Ahmed, A. A. Elsadany, and T. Puu, "On Bertrand duopoly game with differentiated goods," *Applied Mathematics and Computation*, vol. 251, pp. 169–179, 2015.
- [14] Y. Kawabata and Y. Takarada, "Welfare implications of free trade agreements under Bertrand and Cournot competition with product differentiation," *International Economics*, vol. 142, pp. 4–14, 2015.
- [15] S. Brianzoni, L. Gori, and E. Michetti, "Dynamics of a Bertrand duopoly with differentiated products and nonlinear costs: Analysis, comparisons and new evidences," *Chaos, Solitons and Fractals*, vol. 79, pp. 191–203, 2015.
- [16] W. Liu and Y. Wang, "Quality control game model in logistics service supply chain based on different combinations of risk attitude," *International Journal of Production Economics*, vol. 161, pp. 181–191, 2015.
- [17] Y. Fang and B. Shou, "Managing supply uncertainty under supply chain Cournot competition," *European Journal of Operational Research*, vol. 243, no. 1, pp. 156–176, 2015.
- [18] A. Esmailzadeh and A. A. Taleizadeh, "Pricing in a two-echelon supply chain with different market powers: Game theory approaches," *Journal of Industrial Engineering International*, vol. 12, no. 1, pp. 119–135, 2016.
- [19] J. Ma and Z. Guo, "The influence of information on the stability of a dynamic Bertrand game," *Communications in Nonlinear Science and Numerical Simulation*, vol. 30, no. 1-3, pp. 32–44, 2016.
- [20] Q.-H. Li and B. Li, "Dual-channel supply chain equilibrium problems regarding retail services and fairness concerns," *Applied Mathematical Modelling. Simulation and Computation for Engineering and Environmental Systems*, vol. 40, no. 15-16, pp. 7349–7367, 2016.
- [21] M. Protopappa-Sieke, M. A. Sieke, and U. W. Thonemann, "Optimal two-period inventory allocation under multiple service level contracts," *European Journal of Operational Research*, vol. 252, no. 1, pp. 145–155, 2016.
- [22] L. Li, "Information sharing in a supply chain with horizontal competition," *Management Science*, vol. 48, no. 9, pp. 1196–1212, 2002.
- [23] J. Ma and Q. Li, "The complex dynamics of Bertrand-Stackelberg pricing models in a risk-averse supply chain," *Discrete Dynamics in Nature and Society*, vol. 2014, Article ID 749769, 14 pages, 2014.
- [24] J. Ma, X. Ma, and W. Lou, "Analysis of the Complexity Entropy and Chaos Control of the Bullwhip Effect Considering Price of Evolutionary Game between Two Retailers," *Entropy*, vol. 18, no. 11, p. 416, 2016.

Research Article

A Novel Clustering Method Based on Quasi-Consensus Motions of Dynamical Multiagent Systems

Ning Cai,^{1,2} Chen Diao,^{1,2} and M. Junaid Khan³

¹College of Electrical Engineering, Northwest Minzu University, Lanzhou, China

²Key Laboratory of National Language Intelligent Processing, Gansu Province, China

³National University of Sciences and Technology, Islamabad, Pakistan

Correspondence should be addressed to Ning Cai; caining91@tsinghua.org.cn

Received 18 February 2017; Accepted 26 March 2017; Published 13 September 2017

Academic Editor: Zeraouia Elhadj

Copyright © 2017 Ning Cai et al. This is an open access article distributed under the Creative Commons Attribution License, which permits unrestricted use, distribution, and reproduction in any medium, provided the original work is properly cited.

This paper presents a novel approach for clustering, which is based on quasi-consensus of dynamical linear high-order multiagent systems. The graph topology is associated with a selected multiagent system, with each agent corresponding to one vertex. In order to reveal the cluster structure, the agents belonging to a similar cluster are expected to aggregate together. To establish the theoretical foundation, a necessary and sufficient condition is given to check the achievement of group consensus. Two numerical instances are furnished to illustrate the results of our approach.

1. Introduction

With a rapid increase in the scale of massive data and information, the probing of potential knowledge in big data, such as data structures and certain unknown correlations, has been attracting more and more scholars. As an essential technique of data mining, clustering has been widely applied in various practical fields, such as linguistics [1], bone microarchitecture analysis [2], community detection [3], wind power prediction [4], image segmentation [5, 6], and even genome expression study [7].

Clustering is about assigning certain set of data points into different clusters, for the purpose of highlighting the similitude of data points being organized in the same cluster, while simultaneously reflecting the distinctions between different clusters [8]. In the past decades, diverse clustering algorithms and criteria have been developed adequately, for example, normalized cut [6] and min-max cut [9] algorithms, the graph partitioning algorithms [10], the algorithms based on optimization of modularity functions [11], and the spectral clustering algorithms [12].

In addition to the abovementioned literature, some clustering algorithms have also been presented which are built on the study of certain dynamical behaviors of networks,

for example, the random walk algorithms and the network synchronization algorithms. Random walk implies shifting along a random route, with each step to a new nearest vertex. By random walk algorithms [13], the clustering structure of a given network topology could be probed with the aid of generated random walk flows. Conversely, the network synchronization algorithm stands from another perspective [14], which considers coordinating different signals among vertices. Typically certain Kuramoto vibrator is employed, such that synchronization of vibrations could be achieved within the same group.

In this research article, a novel method for clustering is presented, which is rooted upon observation to the motions of dynamical multiagent systems. Concretely speaking, for the purpose of discerning the different affiliations of vertices in a given network, the selected dynamical multiagent system should be linked with the concerned network topology, and there should be a one-to-one correspondence between each pair of dynamical agent and vertex. The agents keep on moving inside a common space, either physical or abstract. Those corresponding to the vertices that are affiliated with any specific cluster should aggregate as time elapses. Finally, the clustering structure would be uncovered automatically, according to the formation of agent positions.

Analogical topics as discussed above are usually referred to as group consensus in the field of control theory. Yu and Wang earlier were concerned with this phenomenon in [15]. Hu et al. discussed group consensus for two classes of dynamical multiagent systems, respectively, which are systems with hybrid protocols (there is discontinuous transfer of information between nearest groups [16]) and systems with distinct groups comprising different types of agents [17]. To achieve group synchronization of the coupled vibrators, Su et al. considered both the adaptive pinning control strategy [18] and the case with multiple leaders [19]. Xie et al. [20] addressed the group consensus problem of first-order systems. Other recent relevant studies include [21–23].

The novelty of the current work compared with the aforementioned results in the literature lies in several perspectives. As far as we know, in the existing researches, the expected clustering formation is prescribed in advance, paying primary attention to synthesis of specific information transfer protocol for each group, so that the agents assigned to the group could ultimately aggregate. In contrast, in the framework of the current paper, the cluster distribution should completely be determined by the topology of network itself, without the need of any prerequisite knowledge beforehand. In this regard, the advantage of the current work is explicit, especially in its potential practicability.

Besides introducing a novel method for clustering, a major contribution of this paper is proposing a criterion for checking whether or not a high-order LTI (Linear Time-Invariant) multiagent system can reach group consensus, which generalizes the existing well-known necessary and sufficient condition for consensus achievement [24–28]. In fact, the existing condition on consensus is a particular instance of the condition for group consensus presented here.

In addition to the above, the current paper provides an exemplification of the usage of unstable dynamical systems, whereas, in contrast, unstable systems are conventionally regarded as being insignificant in control theory.

Theoretical studies on dynamical multiagent systems have already been extensive in the area of control theory, especially on the consensus problem. However, the application instances corresponding to these theories that can well support them are still scarce. Our exploration attempts to introduce a practical scenario from the field of data analysis, under a motivation to facilitate applying, verifying, or enriching certain relevant researches.

The remaining part of the current paper holds the following organization. The preliminaries and model formulation are introduced in Section 2. In Section 3, the clustering method is expounded in detail, based on theoretical analysis on condition for group consensus. Section 4 exemplifies the technique by two simulation cases. Finally, this paper is concluded in Section 5.

2. Model Formulation and Preliminaries

The topology of the network for clustering can be expressed by $G = G(V, E)$, with V being the vertex set and E the weighted edge set. The G is assumed to be a graph of

m th order, being undirected and connected. The ultimate objective of clustering is to assign the m elements of V into divergent affiliations, in accordance with the topology of G .

For such a purpose, a procedure rooted in observing the motions of dynamical multiagent systems is put forward, to figure out the clustering formation automatically. The procedure is composed of the following two fundamental steps.

Step 1. Define a dynamical multiagent system as follows and attach with it the network topology concerned, with each agent associated with one particular vertex.

$$\dot{x}_i = h(t, x_i) + \sum_{j=1}^m w_{1j} f(t, x_j, x_i) \quad (i = 1, 2, \dots, m), \quad (1)$$

where $x_i(t) \in \Theta$ ($i = 1, 2, \dots, m$) expresses the state of agent i which is moving in a normed state space Θ , $w_{ij} \in R^+$ is the weight indicating the strength of communication link between vertices i and j , and the functions $h(\cdot)$ and $f(\cdot)$ express the self-dynamics and the dynamical interagent information transfer protocol, respectively.

Step 2. Determine appropriate initial values $x_i(0) \in \Theta$ ($i = 1, 2, \dots, m$) and then let the dynamical system operate autonomously.

As time elapses, group consensus or quasi-consensus would manifest, as long as the overall setup of both the structure and parameters of dynamical multiagent system (1) is feasibly configured. Finally, a clustering result can be concluded via observing the setup formed by the agent states within the state space.

The definition below formulates the concept of group consensus discussed in this paper.

Definition 1. For the dynamical multiagent system (1), if

$$\lim_{t \rightarrow \infty} \|x_i(t) - x_j(t)\| = 0 \quad (2)$$

then agents i and j reach an *agreement*. For a vertex set $V_l \subset V$, if $\forall i, j \in V_l$, the agents i and j reach an agreement, and then system (1) reaches a *consensus* in V_l . If consensus is reached in each $V_1, V_2, \dots, V_l, \dots, V_\beta$, respectively, with

$$V_1 \cup V_2 \cup \dots \cup V_l \cup \dots \cup V_\beta = V \quad (3)$$

then the entire dynamical system reaches a *group consensus*.

Remark 2. The assumption that the graph is both undirected and connected is merely due to practical requirements of clustering and is not due to any technical limitations. This can be understood through later discussions.

3. Group Consensus of Dynamical Linear Time-Invariant Systems

In this section, the detail of the clustering process is elaborated by employing high-order LTI multiagent systems, which are described as

$$\dot{x}_i = Ax_i + F \sum_{j=1}^m w_{ij} (x_j - x_i) \quad (i = 1, 2, \dots, m), \quad (4)$$

where $x_i(t) = [x_{i1}(t) \ x_{i2}(t) \ \dots \ x_{in}(t)]^T \in \mathbb{R}^n$ ($i = 1, 2, \dots, m$) expresses the state vector of agent i and matrices $A, F \in \mathbb{R}^{n \times n}$ express the LTI self-dynamics of the agents and the information transfer protocol between nearest agents, respectively. The technique for successfully acquiring a rational clustering result depends on appropriately selecting values of the pair of matrices A and F .

To this end, some previous results on consensus are reviewed first.

Lemma 3 (see [28]). *For the dynamical LTI high-order system (4), if it reaches consensus, then, as $t \rightarrow \infty$, the motion of any agent is regulated by the equation $\dot{\xi} = A\xi$.*

Lemma 4 (see [29]). *The Laplacian matrix L of a directed graph G has exactly one zero eigenvalue $\lambda_1 = 0$ iff G includes a spanning tree, with the corresponding eigenvector $\phi = [1 \ 1 \ \dots \ 1]^T$. Besides, all the remaining eigenvalues $\lambda_2, \dots, \lambda_m$ have positive real parts.*

Corollary 5. *The Laplacian matrix L of an undirected graph G has exactly a single zero eigenvalue $\lambda_1 = 0$ iff G is connected, with the associated eigenvector $\phi = [1 \ 1 \ \dots \ 1]^T$. Besides, all the remaining eigenvalues $\lambda_2, \dots, \lambda_m \in \mathbb{R}^+$.*

Lemma 6 (see [28]). *For the dynamical multiagent system (4) with $\lambda_1 = 0, \lambda_2, \dots, \lambda_m$ as the eigenvalues of the Laplacian matrix of the directed graph G , if A is not Hurwitz then the system reaches consensus iff*

- (1) the graph topology G includes a spanning tree;
- (2) all the matrices $A - \lambda_i F$ ($i \in \{1, 2, \dots, m\}$ $\lambda_i \neq 0$) are Hurwitz.

Lemma 3 implies that if a certain subset of agents reaches a consensus, then the overall motion of this subset will ultimately be dominated by the matrix A . As long as A is Hurwitz, the motions of distinct consentaneous subsets would independently converge to the origin of state space, even without any exchange of information. Consequently, in order to differentiate agents between distinct affiliations, matrix A should not be Hurwitz. Actually, it is preferable for A to be unstable to avoid the possibility of critical stability, such that distinct clusters would mutually diverge.

Theorem 7. *Consider the dynamical system (4). Suppose that the spectrum of Laplacian matrix of the directed graph with spanning tree is*

$$\{\lambda_1 = 0, \lambda_2, \dots, \lambda_m\} \quad (5)$$

with the series of matrices

$$A, A - \lambda_2 F, \dots, A - \lambda_{\alpha-1} F \quad (6)$$

being not Hurwitz and

$$A - \lambda_\alpha F, A - \lambda_{\alpha+1} F, \dots, A - \lambda_m F \quad (7)$$

being Hurwitz. The pair of agents i and $i + 1$ (or m and 1 , if $i = m$) reaches agreement iff the i th row ψ_i^T of the product $\Psi = TQ$ possesses the configuration:

$$\psi_i^T = \begin{bmatrix} * & 0 & \dots & 0 & * & \dots & * \\ (1) & (2) & & (\alpha-1) & (\alpha) & & (m) \end{bmatrix}, \quad (8)$$

where $T \in \mathbb{R}^{m \times m}$ represents any feasible solution of the matrix equation

$$TL = \Phi = \begin{bmatrix} 1 & -1 & & & & & \\ & 1 & -1 & & & & \\ & & \dots & \dots & & & \\ & & & & 1 & -1 & \\ -1 & 0 & \dots & \dots & & & 1 \end{bmatrix}, \quad (9)$$

$Q \in \mathbb{R}^{m \times m}$ represents the nonsingular matrix that transforms the Laplacian matrix into the similar Jordan canonical form

$$Q^{-1}LQ = J = \begin{bmatrix} 0 & & & & & \\ & \lambda_2 & * & & & \\ & & \lambda_3 & \ddots & & \\ & & & \ddots & * & \\ & & & & & \lambda_m \end{bmatrix}, \quad (10)$$

and “*” denotes any arbitrary value.

Proof. If the stack vector of the states of agents is defined as

$$x^T = [x_1^T \ x_2^T \ \dots \ x_m^T]^T \quad (11)$$

then the system dynamics can be described by

$$\dot{x} = (I_m \otimes A - L \otimes F)x. \quad (12)$$

Let $\tilde{x} = (Q^{-1} \otimes I_n)x$; then (12) can be transformed into

$$\dot{\tilde{x}} = (I_m \otimes A - J \otimes F)\tilde{x} \quad (13)$$

which is equivalent to

$$\begin{bmatrix} \dot{\tilde{x}}_1 \\ \dot{\tilde{x}}_2 \\ \vdots \\ \dot{\tilde{x}}_\alpha \\ \vdots \\ \dot{\tilde{x}}_m \end{bmatrix} = \begin{bmatrix} A & & & & & \\ & A - \lambda_2 F & \Omega & & & \\ & & \ddots & \ddots & & \\ & & & A - \lambda_{\alpha-1} F & \Omega & \\ & & & & A - \lambda_\alpha F & \ddots \\ & & & & & \ddots & \Omega \\ & & & & & & A - \lambda_m F \end{bmatrix} \begin{bmatrix} \tilde{x}_1 \\ \tilde{x}_2 \\ \vdots \\ \tilde{x}_\alpha \\ \vdots \\ \tilde{x}_m \end{bmatrix}, \quad (14)$$

where “ Ω ” denotes an indefinite matrix that may be either F or zero. Define the auxiliary vectors

$$\eta_i = \sum_{j=1}^m w_{ij} (x_i - x_j) \quad (i = 1, 2, \dots, m) \quad (15)$$

and the stacked form as

$$\eta = [\eta_1^T \ \eta_2^T \ \dots \ \eta_m^T]^T. \quad (16)$$

It is evident that $\eta = (L \otimes I_n)x$ and

$$(T \otimes I_n)\eta = (TL \otimes I_n)x. \quad (17)$$

Substituting (9) into the above equation yields

$$(TL \otimes I_n)x = (\Phi \otimes I_n)x. \quad (18)$$

It follows that

$$\begin{aligned} (\Phi \otimes I_n)x &= (TL \otimes I_n)x = (TL \otimes I_n)(Q \otimes I_n)\tilde{x} \\ &= (TQJQ^{-1} \otimes I_n)(Q \otimes I_n)\tilde{x} \\ &= (TQJ \otimes I_n)\tilde{x} = (TQ \otimes I_n)(J \otimes I_n)\tilde{x}. \end{aligned} \quad (19)$$

According to (14), $\dot{\tilde{x}}_m = (A - \lambda_m F)\tilde{x}_m$; thus $\lim_{t \rightarrow \infty} \tilde{x}_m(t) = 0$ because $A - \lambda_m F$ is Hurwitz. Also, $\dot{\tilde{x}}_{m-1} = (A - \lambda_{m-1} F)\tilde{x}_{m-1} + \Omega\tilde{x}_m$ holds, leading to $\lim_{t \rightarrow \infty} \tilde{x}_{m-1}(t) = 0$, because $A - \lambda_{m-1} F$ is Hurwitz and $\lim_{t \rightarrow \infty} \tilde{x}_m(t) = 0$. A similar analysis can be recursively conducted till \tilde{x}_α is derived. As a result, it can be concluded that

$$\begin{aligned} \lim_{t \rightarrow \infty} \tilde{x}_1(t) &= * \\ \lim_{t \rightarrow \infty} \tilde{x}_2(t) &= * \\ &\vdots \\ \lim_{t \rightarrow \infty} \tilde{x}_{\alpha-1}(t) &= * \\ \lim_{t \rightarrow \infty} \tilde{x}_\alpha(t) &= 0 \\ &\vdots \\ \lim_{t \rightarrow \infty} \tilde{x}_m(t) &= 0. \end{aligned} \quad (20)$$

Due to the structure of J and the fact that $\lambda_1 = 0$, the limits of the first n entries of vector $(J \otimes I_n)\tilde{x}$ are zero and the limits of the entries indexed by $n+1$ to $n(\alpha-1)$ are indefinite, while the limits of the remaining entries are all zero. In other words,

$$\begin{aligned} \lim_{t \rightarrow \infty} (J \otimes I_n)\tilde{x} \\ = \begin{bmatrix} 0 & \dots & 0 & * & \dots & * & 0 & \dots & 0 \end{bmatrix}^T. \end{aligned} \quad (21)$$

Equation (19) can be rewritten as

$$(\Phi \otimes I_n)x = (\Psi \otimes I_n)(J \otimes I_n)\tilde{x}. \quad (22)$$

According to the structure of Φ , the fact that agents i and $i+1$ ($i = 1, 2, \dots, m-1$) reach an agreement implies that the entries in the left side of (22) indexed from $(i-1)n+1$ to ni tend to approach zero. That is to say,

$$\lim_{t \rightarrow \infty} (\psi_i^T \otimes I_n)(J \otimes I_n)\tilde{x} = 0. \quad (23)$$

If $\psi_i^T = \begin{bmatrix} * & 0 & \dots & 0 & * & \dots & * \\ (1) & (2) & & (\alpha-1) & (\alpha) & & (m) \end{bmatrix}$, then (23) is true because of the structure of (21). Conversely, if $\lim_{t \rightarrow \infty} (\psi_i^T \otimes I_n)(J \otimes I_n)\tilde{x} = 0$, by noticing the fact that agreements are independent of the initial states and concerning the structure of (21), one can conclude that

$$\psi_i^T = \begin{bmatrix} * & 0 & \dots & 0 & * & \dots & * \\ (1) & (2) & & (\alpha-1) & (\alpha) & & (m) \end{bmatrix}. \quad (24)$$

Remark 8. Theorem 7 can verify the agreement between any two agents, since the index assignment is trivial for a network. With this theorem, an overall portrait of the group consensus can be easily derived.

Remark 9. For the sake of the clustering application, only the undirected graph should be concerned. However, Theorem 7 is more generalized since it addresses the systems with graphs that could have directed arcs.

Remark 10. Matrix T can be figured out by solving the matrix equation (9) as

$$T = \Phi L^\dagger \quad (25)$$

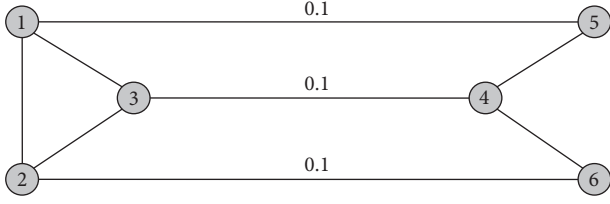


FIGURE 1: Instance with group consensus. Default edge weight is 1.

with L^\dagger expressing a Moore-Penrose inverse [30] of the singular Laplacian matrix L . Besides, matrix Q is constituted by the generalized eigenvectors of L . Therefore, it is simple to compute the matrix product $\Psi = TQ$.

Remark 11. Both the matrices T and Q are derived from the Laplacian matrix. Thus, if only the value of α is definite, the clustering result merely depends on the topology of graph.

Remark 12. Theorem 7 is a bridge connecting the concept of consensus with the diverse nonconsensus cases. The smaller the value of α , the higher the degree of freedom that matrix Ψ would possess, for the sake of ensuring agreement. Here are two extremes: if $\alpha = 2$, then the overall system reaches a consensus, whatever the value of Ψ is; oppositely, if all the matrices $A - \lambda_i F$ ($i \in \{1, 2, \dots, m\}$) are not Hurwitz, then there should be no agreement at all. Actually, the existing well-known criterion for checking the consensus [24–28] (summarized as Lemma 6 here) can be regarded as a particular case or corollary of Theorem 7 when $\alpha = 2$.

4. Simulations on Clustering

This section will exemplify the presented technique of clustering by two simple and typical simulation instances.

Example 1. Consider a graph in Figure 1.

The weighted adjacency matrix is

$$W = \begin{bmatrix} 0 & 1 & 1 & 0 & 0.1 & 0 \\ 1 & 0 & 1 & 0 & 0 & 0.1 \\ 1 & 1 & 0 & 0.1 & 0 & 0 \\ 0 & 0 & 0.1 & 0 & 1 & 1 \\ 0.1 & 0 & 0 & 1 & 0 & 0 \\ 0 & 0.1 & 0 & 1 & 0 & 0 \end{bmatrix} \quad (26)$$

with the associated Laplacian matrix

$$L = \begin{bmatrix} 2.1 & -1 & -1 & 0 & -0.1 & 0 \\ -1 & 2.1 & -1 & 0 & 0 & -0.1 \\ -1 & -1 & 2.1 & -0.1 & 0 & 0 \\ 0 & 0 & -0.1 & 2.1 & -1 & -1 \\ -0.1 & 0 & 0 & -1 & 1.1 & 0 \\ 0 & -0.1 & 0 & -1 & 0 & 1.1 \end{bmatrix} \quad (27)$$

and spectrum $\{0, 0.2, 1.095, 3, 3.105, 3.2\}$. Set the corresponding multiagent system as

$$A = \begin{bmatrix} 0.25 & 1 \\ -1 & 0.25 \end{bmatrix}, \quad (28)$$

$$F = \begin{bmatrix} 0 & -1 \\ 0.5 & 1 \end{bmatrix}.$$

In this instance, $A - \lambda_1 F$ and $A - \lambda_2 F$ are unstable and $A - \lambda_3 F, \dots, A - \lambda_6 F$ are Hurwitz. Therefore, $\alpha = 3$. It yields that

$$T = \begin{bmatrix} 0.324 & -0.324 & 0 & 0 & 0.029 & -0.029 \\ 0 & 0.323 & -0.323 & -0.010 & -0.01 & 0.02 \\ 1.563 & 1.563 & 1.875 & -1.875 & -1.562 & -1.563 \\ -0.020 & 0.01 & 0.010 & 0.323 & -0.617 & 0.294 \\ 0.029 & -0.029 & 0 & 0 & 0.912 & -0.912 \\ -1.895 & -1.542 & -1.563 & 1.566 & 1.248 & 2.189 \end{bmatrix}, \quad (29)$$

$$Q = \begin{bmatrix} 0.408 & -0.408 & 0.035 & -0.289 & -0.706 & 0.289 \\ 0.408 & -0.408 & -0.035 & -0.289 & 0.706 & 0.289 \\ 0.408 & -0.408 & 0 & 0.577 & 0 & -0.577 \\ 0.408 & 0.408 & 0 & 0.577 & 0 & 0.577 \\ 0.408 & 0.408 & 0.706 & -0.289 & 0.035 & -0.289 \\ 0.408 & 0.408 & -0.706 & -0.289 & -0.035 & -0.289 \end{bmatrix}.$$

Consequently,

$$\Psi = TQ = \begin{bmatrix} 0 & 0 & 0.064 & 0 & -0.455 & 0 \\ 0 & 0 & -0.032 & -0.289 & 0.227 & 0.271 \\ 0 & -4.083 & 0 & 0 & 0 & -0.361 \\ 0 & 0 & -0.645 & 0.289 & -0.011 & 0.271 \\ 0 & 0 & 1.290 & 0 & 0.023 & 0 \\ 0 & 4.083 & -0.677 & 0 & 0.216 & -0.180 \end{bmatrix}. \quad (30)$$

Based on Theorem 7, it is explicitly known that agents 1~3 reach a consensus; meanwhile agents 4~6 reach another consensus. As a result, a clustering formation is clearly exhibited. The motions of agents in the 2-dimensional state space are illustrated in Figure 2.

Example 2. In the second example, consider the graph illustrated in Figure 3.

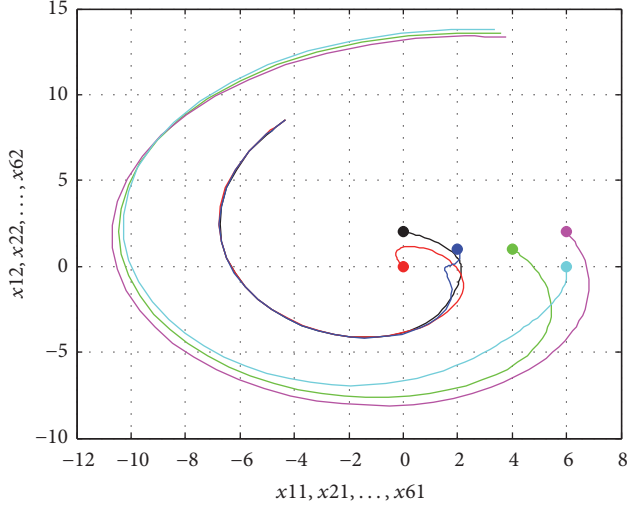


FIGURE 2: Group consensus motions with $t \in [0, 5]$. Thick dots denote starting positions.

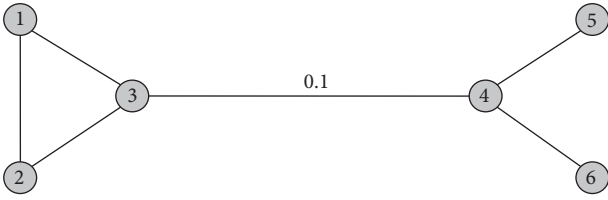


FIGURE 3: Second graph where default edge weight is 1.

The adjacency matrix is

$$W = \begin{bmatrix} 0 & 1 & 1 & 0 & 0 & 0 \\ 1 & 0 & 1 & 0 & 0 & 0 \\ 1 & 1 & 0 & 0.1 & 0 & 0 \\ 0 & 0 & 0.1 & 0 & 1 & 1 \\ 0 & 0 & 0 & 1 & 0 & 0 \\ 0 & 0 & 0 & 1 & 0 & 0 \end{bmatrix} \quad (31)$$

and the Laplacian matrix is

$$L = \begin{bmatrix} 2 & -1 & -1 & 0 & 0 & 0 \\ -1 & 2 & -1 & 0 & 0 & 0 \\ -1 & -1 & 2.1 & -0.1 & 0 & 0 \\ 0 & 0 & -0.1 & 2.1 & -1 & -1 \\ 0 & 0 & 0 & -1 & 1 & 0 \\ 0 & 0 & 0 & -1 & 0 & 1 \end{bmatrix} \quad (32)$$

with the spectrum $\{0, 0.0638, 1, 3, 3, 3.1362\}$. Let the associated agents be LTI second-order systems with

$$A = \begin{bmatrix} 0.25 & 2 \\ -2 & 0.25 \end{bmatrix}, \quad (33)$$

$$F = \begin{bmatrix} 0.5 & -1 \\ 4 & 0.5 \end{bmatrix}.$$

In this case, $A - \lambda_1 F$, $A - \lambda_2 F$ are unstable, whereas $A - \lambda_3 F, \dots, A - \lambda_6 F$ are Hurwitz. Still, $\alpha = 3$. It can be easily derived that

$$T = \begin{bmatrix} 0.333 & -0.333 & 0 & 0 & 0 & 0 \\ 0.167 & 0.5 & -0.167 & -0.167 & -0.167 & -0.167 \\ 5 & 5 & 5 & -5 & -5 & -5 \\ -0.167 & -0.167 & -0.167 & -0.167 & -0.833 & -0.167 \\ 0 & 0 & 0 & 0 & 1 & -1 \\ -5.667 & -5.333 & -5 & 5 & 5 & 6 \end{bmatrix}, \quad (34)$$

Q

$$= \begin{bmatrix} 0.408 & 0.417 & 0 & 0.289 & 0.707 & -0.276 \\ 0.408 & 0.417 & 0 & 0.289 & -0.707 & -0.276 \\ 0.408 & 0.390 & 0 & -0.577 & 0 & 0.590 \\ 0.408 & -0.390 & 0 & -0.577 & 0 & -0.590 \\ 0.408 & -0.417 & -0.707 & 0.289 & 0 & 0.276 \\ 0.408 & -0.417 & 0.707 & 0.289 & 0 & 0.276 \end{bmatrix}.$$

As a result

$$\Psi = TQ = \begin{bmatrix} 0 & 0 & 0 & 0 & 0.471 & 0 \\ 0 & 0.417 & 0 & 0.289 & -0.236 & 0.276 \\ 0 & 12.242 & 0 & 0 & 0 & 0.376 \\ 0 & 0.417 & 0.707 & -0.289 & 0 & -0.276 \\ 0 & 0 & -1.414 & 0 & 0 & 0 \\ 0 & -13.076 & 0.707 & 0 & -0.236 & 0.176 \end{bmatrix}. \quad (35)$$

According to Theorem 7, only two pairs of agents can achieve agreement, respectively, which are agents 1 and 2 and agents 5 and 6. The state trajectories obtained from the experiment are shown in Figure 4.

Although not all agents could achieve a precise group consensus in this case, from Figure 4, the six agents can still be differentiated as two distinct clusters, practically, because the speed of divergence between the two clusters is much faster than the speed of divergence of the agents inside any cluster, in a certain time span. The variation of difference between the states of agents 2 and 3 is illustrated in Figure 5, which is $x_{22}(t) - x_{32}(t)$.

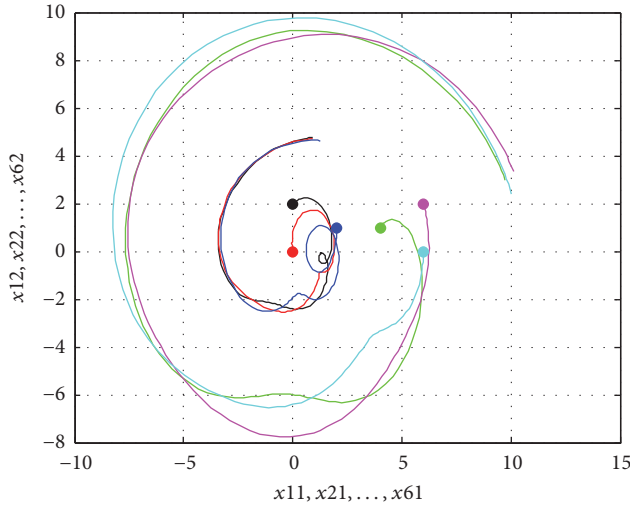


FIGURE 4: Quasi-consentaneous state trajectories of Example 2 with $t \in [0, 3]$. Thick dots denote starting positions.

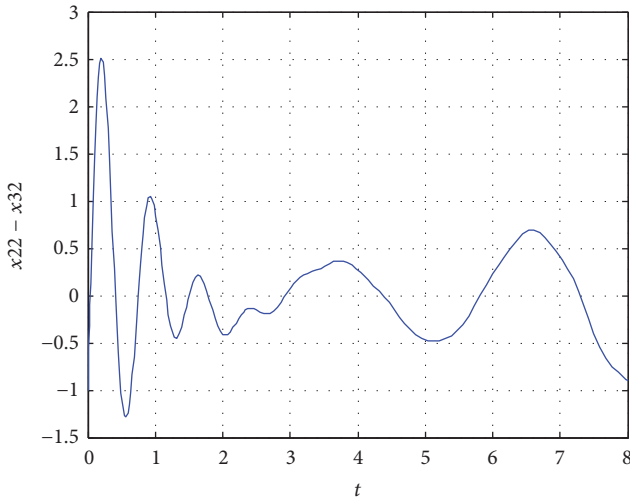


FIGURE 5: Variation of difference between states of agents 2 and 3.

From Figure 5, one can clearly sense that the vicissitude of the difference between agent 3 and the other agents in the same cluster is sophisticated, including two phases: before $t = 3$, there is a tendency of agreement; however, afterwards, the tendency turns into a departure. This can be intuitively explained via a comparison with Example 1.

Let us inspect the dynamical equation of agent 3; that is,

$$\dot{x}_3 = Ax_3 + F \sum_{j \in V_1} w_{3j} (x_j - x_3) + F \sum_{j \in V_2} w_{3j} (x_j - x_3). \quad (36)$$

The vector field is composed of three components as shown above: the autonomous force, the interactive force from the nearest neighbors of the same cluster, and the interactive force from the other cluster. During the first phase of Example 2, the effect of the third component is relatively weak, because of the small value of w_{43} ; thus the states of agents belonging to the same cluster, that is, 1, 2, and 3,

tend to achieve a consensus; however, as time elapses and the distance between the two clusters increases, the effect of the third component also keeps on increasing and ultimately it overwhelms the diminished second component and tears agent 3 away from its nearest neighbors 1 and 2. By contrast, in Example 1, a precise group consensus can be reached because the interactive force from the third component is balanced upon every agent.

5. Conclusion

A novel method for clustering is introduced in the current paper, based on group consensus or quasi-consensus of the motions of dynamical systems. For the sake of categorizing the vertex set into disparate clusters, a specific dynamical multiagent system is attached to the graph addressed, with each vertex associated with an agent. If the dynamical system is appropriately configured, then the agents affiliated with the similar cluster should gradually assemble together in their common state space; meanwhile the different clusters diverge away mutually. In addition to the method of clustering, a primary contribution is the presentation of a criterion for checking whether or not a group consensus could be reached by high-order linear multiagent systems, which is a necessary and sufficient condition generalizing the previous well-known condition of consensus. In fact, the scope of possible utility of the condition for group consensus is broader, beyond the clustering scenario being dealt with here. Two typical simulation instances are exhibited to exemplify the process of clustering method. As to the potential future extensions, there are several explicit major directions: (1) the method can be utilized to handle various real-world applications such as image segmentation, electrocardiosignal analysis, and classification of natural languages; (2) a further exploration toward the mechanism of group consensus or quasi-consensus could be conducted, and a more straightforward correlation between group consensus and the topological characteristics of networks might be obtained; (3) the patterns of diverse nonconsensus motions can be studied in depth.

Conflicts of Interest

The authors declare that there are no conflicts of interest regarding the publication of this paper.

Acknowledgments

This work is supported by National Natural Science Foundation (NNSF) of China (Grants 61374054 and 61263002), by Fundamental Research Funds for the Central Universities (Grants 31920160003 and 31920170141), and by Program for Young Talents of State Ethnic Affairs Commission (SEAC) of China (Grant 2013-3-21).

References

- [1] A. Cangelosi and D. Parisi, Eds., *Simulating the Evolution of Language*, Springer, London, UK, 2002.

- [2] M. H. Edwards, D. E. Robinson, K. A. Ward et al., "Cluster analysis of bone microarchitecture from high resolution peripheral quantitative computed tomography demonstrates two separate phenotypes associated with high fracture risk in men and women," *Bone*, vol. 88, pp. 131–137, 2016.
- [3] D. Liu, C. Wang, and Y. Jing, "Estimating the optimal number of communities by cluster analysis," *International Journal of Modern Physics B*, vol. 30, no. 8, 1650037, 10 pages, 2016.
- [4] L. Dong, L. Wang, S. F. Khahro, S. Gao, and X. Liao, "Wind power day-ahead prediction with cluster analysis of NWP," *Renewable and Sustainable Energy Reviews*, vol. 60, pp. 1206–1212, 2016.
- [5] A. Z. Arifin and A. Asano, "Image segmentation by histogram thresholding using hierarchical cluster analysis," *Pattern Recognition Letters*, vol. 27, no. 13, pp. 1515–1521, 2006.
- [6] J. Shi and J. Malik, "Normalized cuts and image segmentation," *IEEE Transactions on Pattern Analysis and Machine Intelligence*, vol. 22, no. 8, pp. 888–905, 2000.
- [7] M. B. Eisen, P. T. Spellman, P. O. Brown, and D. Botstein, "Cluster analysis and display of genome-wide expression patterns," *Proceedings of the National Academy of Sciences of the United States of America*, vol. 95, no. 25, pp. 14863–14868, 1998.
- [8] L. Kaufman and P. Rousseeuw, *Finding Groups in Data: An Introduction to Cluster Analysis*, John Wiley & Sons, New York, NY, USA, 1990.
- [9] C. Ding, X. He, H. Zha, M. Gu, and H. Simon, "A min-max cut algorithm for graph partitioning and data clustering," in *Proceedings of the IEEE International Conference on Data Mining (ICDM '01)*, pp. 107–114, San Jose, Calif, USA, 2001.
- [10] D. G. Corneil and C. C. Gotlieb, "An efficient algorithm for graph isomorphism," *Journal of the Association for Computing Machinery*, vol. 17, pp. 51–64, 1970.
- [11] M. E. J. Newman, "Modularity and community structure in networks," *Proceedings of the National Academy of Sciences of the United States of America*, vol. 103, no. 23, pp. 8577–8582, 2006.
- [12] F. R. Chung, *Spectral Graph Theory*, CBMS Regional Conference Series in Mathematics, American Mathematical Society, 1997.
- [13] S. M. von Dongen, *Graph clustering by flow simulation [Doctoral dissertation]*, University of Utrecht, 2000.
- [14] A. Arenas, A. Díaz-Guilera, and C. J. Pérez-Vicente, "Synchronization reveals topological scales in complex networks," *Physical Review Letters*, vol. 96, no. 11, Article ID 114102, 2006.
- [15] J. Yu and L. Wang, "Group consensus in multi-agent systems with switching topologies and communication delays," *Systems & Control Letters*, vol. 59, no. 6, pp. 340–348, 2010.
- [16] H.-X. Hu, L. Yu, W.-A. Zhang, and H. Song, "Group consensus in multi-agent systems with hybrid protocol," *Journal of the Franklin Institute. Engineering and Applied Mathematics*, vol. 350, no. 3, pp. 575–597, 2013.
- [17] H.-X. Hu, W. Yu, Q. Xuan, C.-G. Zhang, and G. Xie, "Group consensus for heterogeneous multi-agent systems with parametric uncertainties," *Neurocomputing*, vol. 142, pp. 383–392, 2014.
- [18] H. Su, Z. Rong, M. Z. Q. Chen, X. Wang, G. Chen, and H. Wang, "Decentralized adaptive pinning control for cluster synchronization of complex dynamical networks," *IEEE Transactions on Systems, Man, and Cybernetics B: Cybernetics*, vol. 43, no. 1, pp. 394–399, 2013.
- [19] H. Su, M. Z. Chen, X. Wang, H. Wang, and N. V. Valeyev, "Adaptive cluster synchronisation of coupled harmonic oscillators with multiple leaders," *IET Control Theory & Applications*, vol. 7, no. 5, pp. 765–772, 2013.
- [20] D. Xie, Q. Liu, L. Lv, and S. Li, "Necessary and sufficient condition for the group consensus of multi-agent systems," *Applied Mathematics and Computation*, vol. 243, pp. 870–878, 2014.
- [21] H. S. Son, J. B. Park, and Y. H. Joo, "Segmentalized FCM-based tracking algorithm for zigzag maneuvering target," *International Journal of Control, Automation and Systems*, vol. 13, no. 1, pp. 231–237, 2014.
- [22] N. Cai and L. Xue, "Clustering by group consensus of unstable dynamic linear high-order multi-agent systems," in *Proceedings of the 34th Chinese Control Conference (CCC '15)*, pp. 7212–7216, July 2015.
- [23] L. Guo, H. Pan, and X. Nian, "Adaptive pinning control of cluster synchronization in complex networks with Lurie-type nonlinear dynamics," *Neurocomputing*, vol. 182, pp. 294–303, 2016.
- [24] F. Xiao and L. Wang, "Consensus problems for high dimensional multi-agent systems," *IET Control Theory & Applications*, vol. 1, no. 3, pp. 830–837, 2007.
- [25] J. Wang, D. Cheng, and X. Hu, "Consensus of multi-agent linear dynamic systems," *Asian Journal of Control*, vol. 10, no. 2, pp. 144–155, 2008.
- [26] J. Xi, M. He, H. Liu, and J. Zheng, "Admissible output consensus control for singular multi-agent systems with time delays," *Journal of the Franklin Institute. Engineering and Applied Mathematics*, vol. 353, no. 16, pp. 4074–4090, 2016.
- [27] Z. Li, Z. Duan, G. Chen, and L. Huang, "Consensus of multiagent systems and synchronization of complex networks: a unified viewpoint," *IEEE Transactions on Circuits and Systems I: Regular Papers*, vol. 57, no. 1, pp. 213–224, 2010.
- [28] N. Cai, J.-X. Xi, and Y.-S. Zhong, "Swarm stability of high-order linear time-invariant swarm systems," *IET Control Theory & Applications*, vol. 5, no. 2, pp. 402–408, 2011.
- [29] W. Ren and R. W. Beard, "Consensus seeking in multiagent systems under dynamically changing interaction topologies," *IEEE Transactions on Automatic Control*, vol. 50, no. 5, pp. 655–661, 2005.
- [30] R. A. Horn and C. R. Johnson, *Matrix Analysis*, Cambridge University Press, Cambridge, UK, 1985.

Research Article

Stabilization of a Network of the FitzHugh–Nagumo Oscillators by Means of a Single Capacitor Based RC Filter Feedback Technique

Elena Adomaitienė,¹ Skaidra Bumelienė,¹ Gytis Mykolaitis,^{1,2} and Arūnas Tamaševičius¹

¹Department of Electronics, Center for Physical Sciences and Technology, Saulėtekio Av. 3, LT-10257 Vilnius, Lithuania

²Department of Physics, Vilnius Gediminas Technical University, Saulėtekio Av. 11, LT-10223 Vilnius, Lithuania

Correspondence should be addressed to Arūnas Tamaševičius; arunas.tamasevicius@ftmc.lt

Received 19 May 2017; Revised 24 July 2017; Accepted 3 August 2017; Published 5 September 2017

Academic Editor: Viet-Thanh Pham

Copyright © 2017 Elena Adomaitienė et al. This is an open access article distributed under the Creative Commons Attribution License, which permits unrestricted use, distribution, and reproduction in any medium, provided the original work is properly cited.

We suggest employing the first-order stable RC filters, based on a single capacitor, for control of unstable fixed points in an array of oscillators. A single capacitor is sufficient to stabilize an entire array, if the oscillators are coupled strongly enough. An array, composed of 24 to 30 mean-field coupled FitzHugh–Nagumo (FHN) type asymmetric oscillators, is considered as a case study. The investigation has been performed using analytical, numerical, and experimental methods. The analytical study is based on the mean-field approach, characteristic equation for finding the eigenvalue spectrum, and the Routh–Hurwitz stability criteria using low-rank Hurwitz matrix to calculate the threshold value of the coupling coefficient. Experiments have been performed with a hardware electronic analog, imitating dynamical behavior of an array of the FHN oscillators.

1. Introduction

A large number of adaptive control techniques have been developed so far to stabilize unstable fixed points (UFP) of dynamical systems. These include derivative control [1–3], tracking filter technique, based on either low-pass or high-pass first-order RC filters [4–9], and notch filter technique that employs two second-order Wien-bridge filters with the incommensurate resonance frequencies [10]. The delayed feedback technique, though originally designed to control chaos, that is, to stabilize unstable periodic orbits [11, 12], under appropriate setting of parameters can stabilize the UFP as well [5, 6, 13–19].

The above-mentioned techniques can stabilize unstable nodes (UFP with even number of real positive eigenvalues λ_i , e.g., $\lambda_{1,2} > 0$ and no imaginary parts of the eigenvalues, i.e., $\text{Im } \lambda_{1,2} = 0$) and unstable spirals (UFP with even number of complex eigenvalues with positive real parts, e.g., $\text{Re } \lambda_{1,2} > 0$). However, the methods fail to stabilize saddle-type UFP, more specifically, UFP with an odd number of real positive eigenvalues, for example, $\lambda_1 > 0$, $\lambda_2 < 0$. To solve

the problem of the odd number limitation, Pyragas and coauthors proposed to use an unstable first-order filter [20, 21]. It was an elegant idea to fight one instability by means of another instability. The method was demonstrated for a variety of mathematical models and experimental systems [20–23]. Later an unstable filter control was developed to stabilize saddle-type UFP in conservative and weakly damped systems [24–26] also under the influence of delay (inertia) in the feedback loop of the controller.

The first-order RC filters, based on a single capacitor, as well as other methods developed for stabilizing the UFP have been applied to single oscillators only. The question thus arises: can a single capacitor stabilize a network of oscillators? The answer depends on the properties of the network. Evidently, if the oscillators in the array are uncoupled or weakly coupled, a single capacitor is insufficient to control the entire network. Each individual oscillator should be provided with a separate controller. Such solution is impractical for applications. However, when the oscillators are coupled strongly enough, one could expect that it is possible to stabilize the entire network using a single controller.

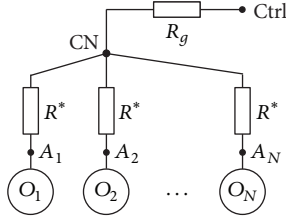


FIGURE 1: Network of mean-field coupled oscillators, O_1, O_2, \dots, O_N . A_1, A_2, \dots, A_N are the outputs of the corresponding oscillators and R^* are the coupling resistors. The CN is the coupling node, in general not accessible directly from outside, but via some passive resistive network, represented here by an effective buffer resistor R_g . The Ctrl is an accessible control node.

In this paper, we demonstrate the possibility of stabilizing the network analytically, numerically, and experimentally.

2. Mathematical Model and Its Analysis

To be specific we consider an array of FitzHugh–Nagumo (FHN) oscillators [27], also known in literature as Bonhoeffer–van der Pol (BVP) oscillators [28, 29]. The FHN (or BVP) oscillator actually is a simplified version of the Hodgkin–Huxley (HH) oscillator, imitating the dynamics of spiking neurons [30]. A set of the FHN oscillators is described by

$$\begin{aligned} \dot{x}_i &= ax_i - f(x_i) - y_i - c_i, \\ \dot{y}_i &= x_i - by_i, \quad i = 1, 2, \dots, N. \end{aligned} \quad (1)$$

Here $f(x_i)$ is a nonlinear function approximated by a three-segment piecewise linear function [31]

$$f(x_i) = \begin{cases} d(x_i + 1), & x_i < -1, \\ 0, & -1 \leq x_i \leq 1, \\ g(x_i - 1), & x_i > 1. \end{cases} \quad (2)$$

In (2) $d \gg g$. Therefore, $f(x)$ is an essentially asymmetric function, in contrast to common FHN or BVP cubic function x^3 [27–29]. The bias parameters c_i in (1) are intentionally set to be different for each individual oscillator thus making them nonidentical units.

An array of mean-field coupled (star coupling) oscillators is sketched in Figure 1.

The array in Figure 1 is given by the $2N$ -dimensional system

$$\begin{aligned} \dot{x}_i &= ax_i - f(x_i) - y_i - c_i + k(\langle x \rangle - x_i), \\ \dot{y}_i &= x_i - by_i, \quad i = 1, 2, \dots, N. \end{aligned} \quad (3)$$

Here $\langle x \rangle$ is the mean value of the variables x_i

$$\langle x \rangle = \frac{1}{N} \sum_{i=1}^N x_i. \quad (4)$$

When an RC tracking filter is applied to the Ctrl node (Figure 1) of the network the overall system becomes $(2N+1)$ -dimensional system

$$\begin{aligned} \dot{x}_i &= ax_i - f(x_i) - y_i - c_i + k(z - x_i), \\ \dot{y}_i &= x_i - by_i, \quad i = 1, 2, \dots, N, \\ \dot{z} &= \omega_f (\langle x \rangle - z). \end{aligned} \quad (5)$$

The cut-off frequency ω_f of the filter should be low ($\omega_f \ll 1$) to ensure tracking the state of the system under control. Note that, in comparison with (3), here in the first equation the mean $\langle x \rangle$ is replaced with its filtered variable z . The case of a single oscillator ($N = 1$, yielding the 3-dimensional system) has been investigated in [31]. Analysis of $2N$ -dimensional system (3) and $(2N + 1)$ -dimensional systems (5) is very complicated. Therefore, we consider a mean-field approach. The mean-field variables are obtained by directly averaging the variables x_i and y_i and the parameters c_i over all oscillators i in (3) and (5), respectively:

$$\langle \dot{x} \rangle = a \langle x \rangle - \langle f(x_i) \rangle - \langle y \rangle - \langle c \rangle, \quad (6a)$$

$$\langle \dot{y} \rangle = \langle x \rangle - b \langle y \rangle.$$

$$\begin{aligned} \langle \dot{x} \rangle &= a \langle x \rangle - \langle f(x_i) \rangle - \langle y \rangle - \langle c \rangle + k(z - \langle x \rangle), \\ \langle \dot{y} \rangle &= \langle x \rangle - b \langle y \rangle, \end{aligned} \quad (7a)$$

$$\dot{z} = \omega_f (\langle x \rangle - z).$$

Note that (6a) lacks the term $k(\dots)$, since $(\langle x \rangle - \langle x \rangle) = 0$.

For $ab < 1$ and $|c| < 1/(b-a)$ the steady-state solutions of (1), (6a), and (7a) are presented by the following fixed points:

$$\begin{aligned} x_{0i} &= -\frac{bc_i}{1-ab}, \\ y_{0i} &= -\frac{c_i}{1-ab}, \end{aligned} \quad (8)$$

$i = 1, 2, \dots, N$

$$\langle x \rangle_0 = -\frac{b \langle c \rangle}{1-ab}, \quad (9)$$

$$\langle y \rangle_0 = -\frac{\langle c \rangle}{1-ab}.$$

$$\langle x \rangle_0 = -\frac{b \langle c \rangle}{1-ab},$$

$$\langle y \rangle_0 = -\frac{\langle c \rangle}{1-ab}, \quad (10)$$

$$z_0 = -\frac{b \langle c \rangle}{1-ab}.$$

Note that the RC tracking filter in (7a) does not change the position of the fixed point: compare (10) with (9). The values given by (10) are independent on k , since $\langle x \rangle_0 = z_0$ and the

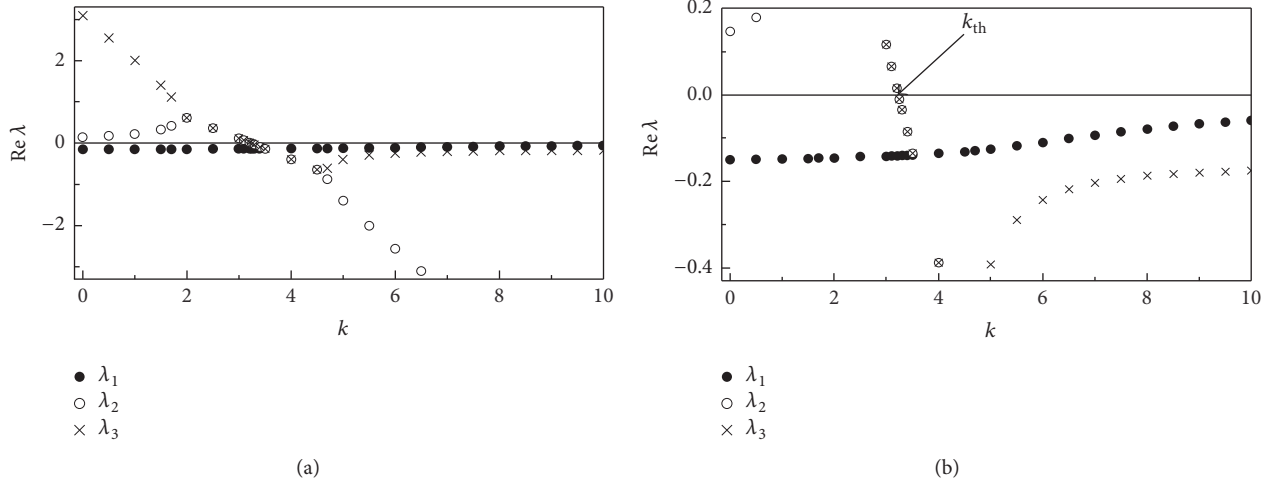


FIGURE 2: Real parts of the eigenvalues, $\text{Re } \lambda_{1,2,3}$ as functions of the coupling parameter k . (a) Full view and (b) vertically stretched view. $a = 3.4$, $b = 0.16$, and $\omega_f = 0.15$. The arrow in plot (b) indicates the coupling parameter $k_{\text{th}} = 3.23$, where the largest eigenvalues $\text{Re } \lambda_{2,3}$ cross zero axis.

coupling term $k(z - \langle x \rangle)$ in (7a) vanishes for the fixed point. The fixed points (9) and (10) are similar in form to fixed points of the individual uncoupled oscillators (8), except the fact that the fixed points (9) and (10) are single points, whereas (8) yields N points in the phase space.

System (7a), when linearized around the fixed point (10), reads

$$\begin{aligned} \dot{\langle x \rangle} &= a \langle x \rangle - \langle y \rangle + k(z - \langle x \rangle), \\ \dot{\langle y \rangle} &= \langle x \rangle - b \langle y \rangle, \\ \dot{z} &= \omega_f (\langle x \rangle - z). \end{aligned} \quad (11)$$

The corresponding characteristic equation, obtained from differential equation (11) using a standard procedure, has the following algebraic form:

$$\lambda^3 + h_2 \lambda^2 + h_1 \lambda + h_0 = 0, \quad (12)$$

where $h_2 = -a + b + k + \omega_f$, $h_1 = 1 - ab + bk - (a - b)\omega_f$, $h_0 = (1 - ab)\omega_f$.

The fixed point of the mean field is stable, if the real parts of all three eigenvalues $\text{Re } \lambda_{1,2,3}$ are negative. Equation (12) has been solved numerically for different values of coupling coefficient k (Figure 2) and the threshold value k_{th} , for which the largest $\text{Re } \lambda_{\text{max}} = 0$, is found.

In addition, the necessary and sufficient conditions of stability can be estimated analytically from the Hurwitz matrix

$$H = \begin{pmatrix} h_2 & h_0 & 0 \\ 1 & h_1 & 0 \\ 0 & h_2 & h_0 \end{pmatrix}. \quad (13)$$

According to the Routh–Hurwitz stability criterion $\text{Re } \lambda_{1,2,3} < 0$ if all diagonal minors of the H -matrix are positive

$$\begin{aligned} \Delta_1 &= h_2 > 0, \\ \Delta_2 &= h_2 h_1 - h_0 > 0, \\ \Delta_3 &= h_0 \Delta_2 > 0. \end{aligned} \quad (14)$$

We start the analysis with Δ_3 . Since Δ_2 should be positive according to the second inequality, the third inequality for Δ_3 can be simplified to $h_0 > 0$. This can be further simplified to $ab < 1$, because $\omega_f > 0$ by definition. The inequality $ab < 1$ is always satisfied, since it was used to derive the fixed points (8)–(10). Consequently, we are left with the first and the second inequalities in (14). We define the threshold k_{th} requiring that for $k > k_{\text{th}}$ the both minors, Δ_1 and Δ_2 are positive. The first minor $\Delta_1 = h_2$ is rather simple and $k_{\text{th}1}$ is readily obtained:

$$k_{\text{th}1} = a - b - \omega_f. \quad (15)$$

For the parameter values given in Figure 2, $k_{\text{th}1} = 3.09$. The second inequality in (14) is more cumbersome and yields quadratic equation with respect to $k_{\text{th}2}$.

$$p_2 k_{\text{th}2}^2 + p_1 k_{\text{th}2} + p_0 = 0, \quad (16)$$

where $p_2 = b$, $p_1 = 1 - 2ab + b^2 - (a - 2b)\omega$, $p_0 = -(a - b)[1 - ab - (a - b)\omega + \omega^2]$.

Analytical solution of (16)

$$k_{\text{th}} = \frac{(-p_1 \pm \sqrt{p_1^2 - 4p_2 p_0})}{2p_2} \quad (17)$$

gives two different values: $k'_{\text{th}2} = 3.23$ and $k''_{\text{th}2} = 0.047$. Finally, we obtain $k_{\text{th}} = \max(k_{\text{th}1}, k'_{\text{th}2}, k''_{\text{th}2}) = 3.23$, which is in an excellent agreement with the numerical result, derived from Figure 2(b), where $\text{Re } \lambda_{2,3}$ cross the abscissa axis at $k_{\text{th}} = 3.23$.

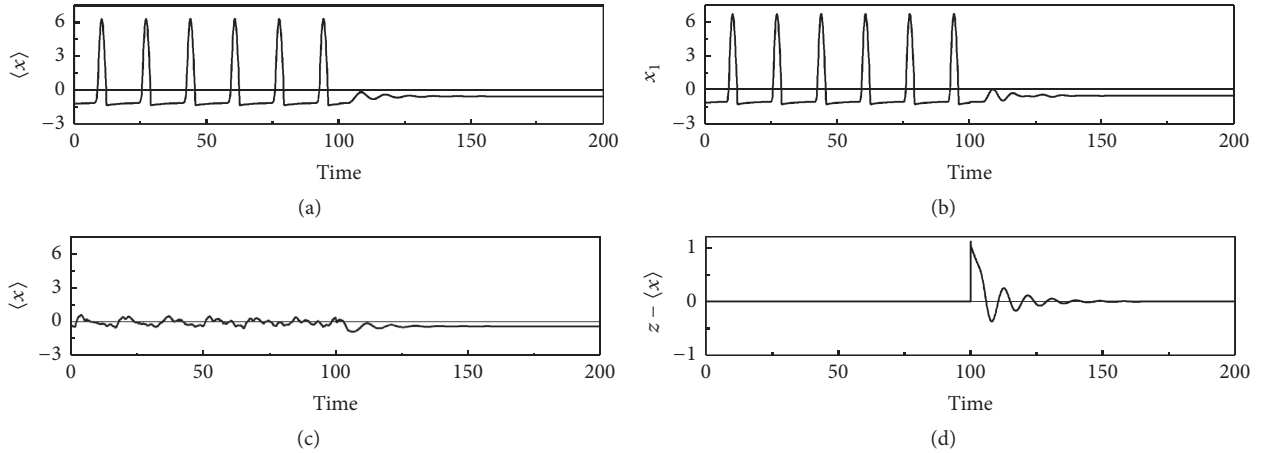


FIGURE 3: Waveforms from (5). (a) Mean-field variable $\langle x \rangle$ of the synchronized array, (b) dynamical variable x_1 of the first oscillator, (c) mean-field variable $\langle x \rangle$ of the unsynchronized (uncoupled) array, and (d) control term $z - \langle x \rangle$. $N = 24$, $k = 3.4$, $a = 3.4$, $b = 0.16$, and $c_i = 43.5/(24 + i)$, where $i = 1, 2, \dots, N$, $d = 60$, $g = 3.4$, and $\omega_f = 0.15$. Control is switched on at $t = 100$; in (a), (b), and (d) $\langle x \rangle$ in the coupling term is replaced with z ; in (c) the whole control term $k(z - x_i)$ is applied.

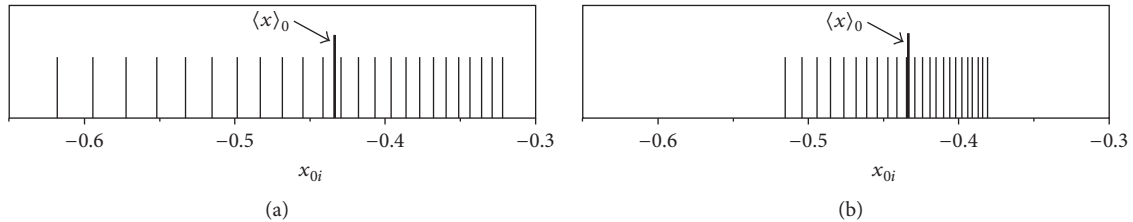


FIGURE 4: Fixed point spectra x_{0i} ($i = 1, 2, \dots, 24$). (a) Unsynchronized (uncoupled) oscillators from (8) and (b) stabilized oscillators from numerical solution of (5) at $t = 200$. Parameters are the same as in the caption of Figure 3. The higher and thicker lines in the spectra indicate the mean-field fixed points $\langle x \rangle_0$.

3. Numerical Results

System (5) have been solved numerically using MATHEMATICA, version 9.0 software package. The results are presented in Figure 3. The waveforms of the mean variable $\langle x \rangle(t)$ (Figure 3(a)) and of the individual oscillators, say $x_1(t)$ (Figure 3(b)), look nearly the same, since the array is synchronized. Other variables $x_i(t)$, not shown in Figure 3, have similar form with only small phase shifts, as expected for nonidentical elements. The main difference is in the UFP values x_{0i} due to different bias parameters c_i . The differences between the fixed points x_{0i} of the individual oscillators ($i = 1, 2, \dots, 24$) are brought out by the fixed point spectra, presented in Figure 4.

It is worth noting that stabilization of the UFP can be achieved in the unsynchronized (uncoupled) array (Figure 3(c)) applying the whole control term $k(z - x_i)$ in (5) at $t = 100$ with a sufficiently large coefficient $k > k_{th}$. However, this feature is important from a theoretical point of view only. The term $k(z - x_i)$ in (5) means that it controls every individual oscillator “ i .” It is easy to do in a mathematical model, but in practical (experimental) situations, it requires direct access to every neuronal oscillator. Moreover, from a practical point of view, especially for a possible application to neuronal systems there is no need to stabilize the UFP, if the

oscillators are not synchronized. Unsynchronized oscillators yield low mean field, as evidenced by the left hand part ($0 < t < 100$) of the plot in Figure 3(c). For larger arrays, say $N > 100$, the mean field becomes even lower. We recall that in this paper we consider the case of coupled and synchronized oscillators.

In Figure 4(a), $\langle x \rangle_0 = -0.434$ is in a good agreement with the value calculated from (9). In the case of coupled and stabilized array (Figure 3(b)) the spectrum is narrower in comparison with the case of uncoupled oscillators due to strong interaction between oscillators. In Figures 3(a), 3(c), and 4(b) $\langle x \rangle_0 = -0.434$. It well coincides with the value of $\langle x \rangle_0$ in Figure 4(a).

4. Experimental Setup

The experiments have been carried out using an electronic analog array, composed of 30 mean-field coupled FHN type oscillators and described in detail elsewhere [32]. This electronic array has been employed earlier to implement experimentally both the repulsive synchronization [33, 34] and the mean-field nullifying techniques [34, 35].

An individual FHN type oscillator is presented in Figure 5(a). Dimensionless variables x , y , z , and t , as well as the parameters a , b , c , d , g , and k introduced in (5), are related

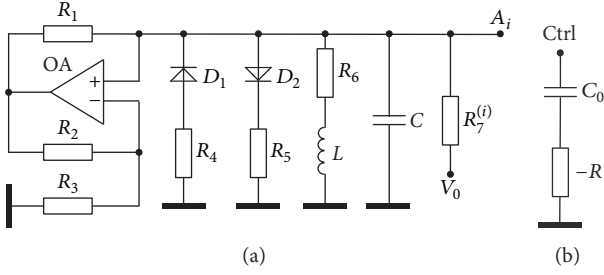


FIGURE 5: Circuit diagrams. (a) FHN asymmetric electronic oscillator. OA is an operational amplifier, for example, NE5534, D_1 and D_2 are the BAV99 type diodes, $V_D = 0.6$ V. $L = 10$ mH, $C = 3.3$ nF, $R_1 = R_2 = 1$ k Ω , $R_3 = 510$ Ω , $R_4 = 30$ Ω , $R_5 = 510$ Ω ($R_4 \ll R_5$), $R_6 = 275$ Ω (external resistor 220 Ω in series with the coil ohmic resistance 55 Ω), $R_7 = (24 + i)$ k Ω , $i = 1, 2, \dots, 30$, and $V_0 = -15$ V. (b) The first-order RC chain. Note the negative resistor “ $-R$,” used to compensate the positive buffer resistor R_g of the network (see Figure 1). The value of the capacitor C_0 is specified in the caption to Figure 7.

to the electrical values of the analog circuits (Figure 5) in the following way:

$$\begin{aligned}
 x_i &= \frac{V_C^{(i)}}{V_D}, \\
 y_i &= \frac{\rho I_L^{(i)}}{V_D}, \\
 z &= \frac{V_{C0}}{V_D}, \\
 t &\rightarrow \frac{t}{\sqrt{LC}}, \\
 \rho &= \sqrt{\frac{L}{C}}, \\
 \omega_f &= \frac{N\sqrt{LC}}{R^*C_0}, \\
 a &= \frac{\rho}{R_3}, \\
 b &= \frac{R_6}{\rho}, \\
 c_i &= \frac{\rho V_0}{R_7^{(i)}V_D}, \\
 d &= \frac{\rho}{R_4}, \\
 g &= \frac{\rho}{R_5}, \\
 k &= \frac{\rho}{R^*}.
 \end{aligned} \tag{18}$$

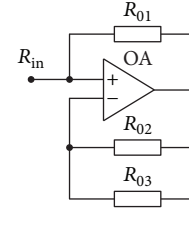


FIGURE 6: Negative impedance converter: active circuit implementation of the negative resistor “ $-R$ ” in Figure 5(b). OA is an operational amplifier, for example, NE5534. $R_{01} = R_{02} = 300$ Ω . For $R_{01} = R_{02}$, $R_{in} = -R_{03}$. The value of the resistor R_{03} is specified in the caption to Figure 7.

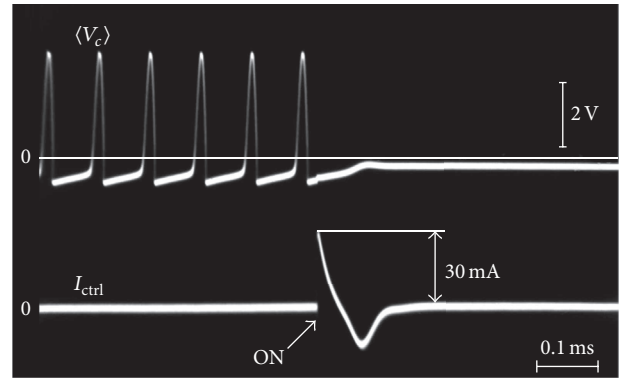


FIGURE 7: Experimental waveforms, the mean-field voltage $\langle V_C \rangle$, and the control current I_{ctrl} . The arrow indicates the time moment, when the RC chain (node Ctrl in Figure 5(b)) is connected to the node Ctrl in Figure 1 (the electronic switch, connecting the controller to the array and its driver is not shown in Figures 1 and 5 for simplicity). $N = 30$, $R^* = 510$ Ω , $R_g = 100$ Ω , and $R_{03} = 100$ Ω ($R_{in} = -100$ Ω ; $R_g + R_{in} = 0$). $C_0 = 2.2$ μ F.

Here V_D is the breakpoint voltage of the forward current-voltage characteristic of the diodes.

The negative resistor “ $-R$ ” in Figure 5(b) has been implemented by means of the negative impedance converter (Figure 6) [36]. The input resistance of the NIC $R_{in} < 0$. The capacitor C_0 with negative resistor “ $-R$ ” in series should not be confused with an unstable RC filter, employed to stabilize saddle-type UFP [25, 26]. Here “ $-R$ ” simply compensates the positive buffer resistor R_g of the network. The RC tracking filters are actually composed of the coupling resistors R^* (Figure 1) and the capacitor C_0 ; see also definition of the cut-off frequency ω_f in (18).

5. Experimental Results

Experimental waveforms have been taken by means of a digital camera from the screen of a multichannel analog oscilloscope and are shown in Figure 7.

Similarly to the numerical results (Figure 3) the experimental waveform in Figure 7 exhibits negative stabilized state (the nonzero value is due to the dc bias V_0 in Figure 5(a)). Whereas the control current I_{ctrl} in Figure 7 becomes vanishingly small after a relatively short transient process.

6. Discussion

The investigation performed here is not an end in itself. The purpose of the study is the search of practical techniques inhibiting activity of neuronal arrays. It is widely believed that strong synchrony of spiking neurons in the brain causes the symptoms of Parkinson's disease [37].

One of the simplest methods to damp spiking neurons is the external stimulation of certain brain areas with strong high frequency (about 100 to 150 Hz) periodic pulses. It is a conventional clinically approved therapy for patients with the Parkinson's symptoms, so-called deep brain stimulation (DBS) [38–40]. Unfortunately, the DBS treatment is often accompanied with undesirable side effects. In recent papers [41–43], it has been demonstrated that the high frequency forcing eventually stabilizes the UFP of the neuronal oscillators in case of HH, FHN, and other neuronal models. Two shortcomings of the DBS have been emphasized [43]. Firstly, though the spiking neurons are suppressed, relatively high amplitude (10 to 20%) high frequency artifact oscillations are observed. Secondly, the fixed points of the membrane voltages are essentially moved from their natural values because of the rectifying effect in the cells [43]. This can be a reason of the side effects.

A number of more sophisticated methods to avoid synchronization of interacting oscillators in general and more specifically with the possible application to neuronal arrays have been described in literature, for example [33, 37, 44–54].

Specifically, in [47] suppression of synchrony of coupled oscillators by means of a passive oscillator is described. The controller is a four-terminal third-order device with separate recording and field application electrodes. The feedback loop contains a second-order damped oscillator, an integrator, an adder, and two amplifiers. Our controller is much simpler. It is a two-terminal first-order device with the same voltage sensing and current application electrode. The controller contains a single capacitor and a negative impedance converter (NIC) based on a single operational amplifier. The NIC is not necessary, if the buffer resistance R_g is small.

In addition, a recently found phenomenon of oscillation quenching in the systems of coupled nonlinear oscillators is worth mentioning [55–58]. It can manifest via two different mechanisms, the so-called oscillation death and amplitude death. The effect, in particular the oscillation death, can be perspective for oscillation suppression in neuronal disorders, such as the Parkinson's disease and essential tremor. This type of oscillation quenching depends on the intrinsic parameters of the individual oscillators, but even more on the way and the strength of coupling. The parameters of the oscillators and the parameters of coupling can be easily controlled in the artificially made physical, chemical, electronic, and so on systems. However, these parameters are difficult to tune in natural, for example, biological, systems. Therefore, the techniques employing external feedback loops seem to be advantageous solutions.

7. Conclusions

An array of coupled neuronal type oscillators, specifically the FitzHugh–Nagumo cells, can be stabilized by means

of a single capacitor based RC filter feedback technique. The feedback signals become vanishingly small, when the UFP is stabilized, similarly to the feedback suppression of synchrony described in [47]. This can be an advantage over the nonfeedback techniques, for example, the DBS employing external high frequency periodic forcing.

Our future work will focus on the investigation of an array of weakly coupled FHN oscillators ($k < k_{th}$), when stabilization of the UFP is impossible. We hope that a single capacitor based RC filter can desynchronize oscillators in the array, somewhat likewise to the repulsive coupling [33, 34] and the mean-field nullifying [34, 35] techniques.

Conflicts of Interest

The authors declare that there are no conflicts of interest regarding the publication of this paper.

Acknowledgments

The authors thank Dr. Nikolai Rulkov for critical discussion of the results and especially for the suggestion of emphasizing the effect of control at the level of individual elements and also for drawing their attention to the fact that there is no reason for the array, given by (5), to oscillate synchronously before the control term is applied. The authors are also grateful to Professor Michael Rosenblum for drawing their attention to the fact that, in paper [47], along with the suppression of synchrony in an ensemble of interacting units, stabilization of an active oscillator by means of a passive oscillator, included in the feedback loop, is also described.

References

- [1] S. Bielawski, M. Bouazaoui, D. Derozier, and P. Glorieux, "Stabilization and characterization of unstable steady states in a laser," *Physical Review A*, vol. 47, no. 4, pp. 3276–3279, 1993.
- [2] G. A. Johnston and E. R. Hunt, "Derivative control of the steady state in chua's circuit driven in the chaotic region," *IEEE Transactions on Circuits and Systems I*, vol. 40, no. 11, pp. 833–835, 1993.
- [3] P. Parmananda, M. A. Rhode, G. A. Johnson, R. W. Rollins, H. D. Dewald, and A. J. Markworth, "Stabilization of unstable steady states in an electrochemical system using derivative control," *Physical Review E*, vol. 49, no. 6, pp. 5007–5011, 1994.
- [4] N. F. Rulkov, L. S. Tsimring, and H. D. I. Abarbanel, "Tracking unstable orbits in chaos using dissipative feedback control," *Physical Review E*, vol. 50, no. 1, pp. 314–324, 1994.
- [5] A. Namajūnas, K. Pyragas, and A. Tamaševičius, "Stabilization of an unstable steady state in a Mackey-Glass system," *Physics Letters A*, vol. 204, no. 3–4, pp. 255–262, 1995.
- [6] A. Namajūnas, K. Pyragas, and A. Tamaševičius, "Analog techniques for modeling and controlling the Mackey-Glass system," *International Journal of Bifurcation and Chaos in Applied Sciences and Engineering*, vol. 7, no. 4, pp. 957–962, 1997.
- [7] M. Ciofini, A. Labate, R. Meucci, and M. Galanti, "Stabilization of unstable fixed points in the dynamics of a laser with feedback," *Physical Review E*, vol. 60, no. 1, pp. 398–402, 1999.
- [8] A. S. Zu Schweinsberg and U. Dressler, "Characterization and stabilization of the unstable fixed points of a frequency doubled

- Nd: YAG laser," *Physical Review E*, vol. 63, no. 5, pp. 562101–5621012, 2001.
- [9] H. Huijberts, "Linear controllers for the stabilization of unknown steady states of chaotic systems," *IEEE Transactions on Circuits and Systems. I. Regular Papers*, vol. 53, no. 10, pp. 2246–2254, 2006.
- [10] A. Ahlborn and U. Parlitz, "Chaos control using notch filter feedback," *Physical Review Letters*, vol. 96, no. 3, article 034102, 2006.
- [11] K. Pyragas, "Continuous control of chaos by self-controlling feedback," *Physics Letters A*, vol. 170, no. 6, pp. 421–428, 1992.
- [12] K. Pyragas and A. Tamaševičius, "Experimental control of chaos by delayed self-controlling feedback," *Physics Letters A*, vol. 180, no. 1-2, pp. 99–102, 1993.
- [13] K. Pyragas, "Control of chaos via extended delay feedback," *Physics Letters. A*, vol. 206, no. 5-6, pp. 323–330, 1995.
- [14] A. Chang, J. C. Bienfang, G. M. Hall, J. R. Gardner, and D. J. Gauthier, "Stabilizing unstable steady states using extended time-delay autosynchronization," *Chaos*, vol. 8, no. 4, pp. 782–790, 1998.
- [15] P. Hövel and E. Schöll, "Control of unstable steady states by time-delayed feedback methods," *Physical Review E*, vol. 72, no. 4, article 046203, pp. 23–46, 2005.
- [16] S. Yanchuk, M. Wolfrum, P. Hövel, and E. Schöll, "Control of unstable steady states by long delay feedback," *Physical Review E*, vol. 74, no. 2, article 026201, 2006.
- [17] Y. Ding, W. Jiang, and H. Wang, "Delayed feedback control and bifurcation analysis of Rossler chaotic system," *Nonlinear Dynamics*, vol. 61, no. 4, pp. 707–715, 2010.
- [18] B. Rezaie and M.-R. Jahed Motlagh, "An adaptive delayed feedback control method for stabilizing chaotic time-delayed systems," *Nonlinear Dynamics*, vol. 64, no. 1-2, pp. 167–176, 2011.
- [19] A. Gjurchinovski, T. Jüngling, V. Urumov, and E. Schöll, "Delayed feedback control of unstable steady states with high-frequency modulation of the delay," *Physical Review E*, vol. 88, no. 3, article 032912, 2013.
- [20] K. Pyragas, V. Pyragas, I. Z. Kiss, and J. L. Hudson, "Stabilizing and tracking unknown steady states of dynamical systems," *Physical Review Letters*, vol. 89, no. 24, pp. 2441031–2441034, 2002.
- [21] K. Pyragas, V. Pyragas, I. Z. Kiss, and J. L. Hudson, "Adaptive control of unknown unstable steady states of dynamical systems," *Physical Review E*, vol. 70, no. 2, article 026215, 2004.
- [22] D. J. Braun, "Adaptive steady-state stabilization for nonlinear dynamical systems," *Physical Review E*, vol. 78, no. 1, article 016213, 2008.
- [23] A. Tamaševičius, E. Tamaševičiute, G. Mykolaitis, and S. Bumelienė, "Switching from stable to unknown unstable steady states of dynamical systems," *Physical Review E*, vol. 78, no. 2, article 026205, 2008.
- [24] A. Tamaševičius, E. Tamaševičiūtė, G. Mykolaitis, S. Bumelienė, and R. Kirvaitis, "Stabilization of saddle steady states of conservative and weakly damped dissipative dynamical systems," *Physical Review E*, vol. 82, no. 2, article 026205, 2010.
- [25] A. Tamaševičius, E. Tamaševičiute, G. Mykolaitis, and S. Bumelienė, "Enhanced control of saddle steady states of dynamical systems," *Physical Review E*, vol. 88, no. 3, article 032904, 2013.
- [26] E. Tamaševičiūtė, G. Mykolaitis, S. Bumelienė, and A. Tamaševičius, "Stabilizing saddles," *Physical Review E*, vol. 88, no. 6, article 060901 (R), 2013.
- [27] R. Fitzhugh, "Impulses and physiological states in theoretical models," *Biophysical Journal*, vol. 1, no. 6, pp. 445–466, 1961.
- [28] A. Rabinovitch, R. Thieberger, and M. Friedman, "Forced Bonhoeffer-van der Pol oscillator in its excited mode," *Physical Review E*, vol. 50, no. 2, pp. 1572–1578, 1994.
- [29] M. Sekikawa, K. Shimizu, N. Inaba et al., "Sudden change from chaos to oscillation death in the Bonhoeffer-van der Pol oscillator under weak periodic perturbation," *Physical Review E*, vol. 84, no. 5, article 056209, 2011.
- [30] W. Gerstner and W. M. Kistler, *Spiking Neuron Models: Single Neurons, Populations, Plasticity*, Cambridge University Press, Cambridge, UK, 2002.
- [31] A. Tamaševičius, E. Tamaševičiute, G. Mykolaitis, S. Bumelienė, R. Kirvaitis, and R. Stoop, "Neural spike suppression by adaptive control of an unknown steady state," *Lecture Notes in Computer Science*, vol. 5768, no. 1, pp. 618–627, 2009.
- [32] E. Tamaševičiūtė, G. Mykolaitis, and A. Tamaševičius, "Analogue modelling an array of the FitzHugh-Nagumo oscillators," *Nonlinear Analysis: Modelling and Control*, vol. 17, no. 1, pp. 118–125, 2012.
- [33] L. S. Tsimring, N. F. Rulkov, M. L. Larsen, and M. Gabbay, "Repulsive synchronization in an array of phase oscillators," *Physical Review Letters*, vol. 95, no. 1, article 014101, 2005.
- [34] A. Tamaševičius, E. Tamaševičiute, and G. Mykolaitis, "Feedback controller for destroying synchrony in an array of the FitzHugh-Nagumo oscillators," *Applied Physics Letters*, vol. 101, no. 22, article 223703, 2012.
- [35] A. Tamaševičius, G. Mykolaitis, E. Tamaševičiūtė, and S. Bumelienė, "Two-terminal feedback circuit for suppressing synchrony of the Fitz Hugh–Nagumo oscillators," *Nonlinear Dynamics*, vol. 81, no. 1-2, pp. 783–788, 2015.
- [36] P. Horowitz and W. Hill, *The Art of Electronics*, Cambridge University Press, Cambridge, UK, 1993.
- [37] M. G. Rosenblum and A. S. Pikovsky, "Controlling synchronization in an ensemble of globally coupled oscillators," *Physical Review Letters*, vol. 92, article 114102, 2004.
- [38] S. Breit, J. B. Schulz, and A.-L. Benabid, "Deep brain stimulation," *Cell and Tissue Research*, vol. 318, no. 1, pp. 275–288, 2004.
- [39] J. S. Perlmutter and J. W. Mink, "Deep brain stimulation," *Annual Review of Neuroscience*, vol. 29, pp. 229–257, 2006.
- [40] A. L. Benabid, S. Chabardes, J. Mitrofanis, and P. Pollak, "Deep brain stimulation of the subthalamic nucleus for the treatment of Parkinson's disease," *The Lancet Neurology*, vol. 8, no. 1, pp. 67–81, 2009.
- [41] K. Pyragas, V. Novičenko, and P. A. Tass, "Mechanism of suppression of sustained neuronal spiking under high-frequency stimulation," *Biological Cybernetics*, vol. 107, no. 6, pp. 669–684, 2013.
- [42] K. Pyragas and P. A. Tass, "Suppression of spontaneous oscillations in high-frequency stimulated neuron models," *Lithuanian Journal of Physics*, vol. 56, no. 4, pp. 223–238, 2016.
- [43] E. Adomaitienė, G. Mykolaitis, S. Bumelienė, and A. Tamaševičius, "Inhibition of spikes in an array of coupled Fitz-Hugh–Nagumo oscillators by external periodic forcing," *Nonlinear Analysis: Modelling and Control*, vol. 22, no. 3, pp. 421–429, 2017.
- [44] O. V. Popovych, C. Hauptmann, and P. A. Tass, "Effective desynchronization by nonlinear delayed feedback," *Physical Review Letters*, vol. 94, no. 16, article 164102, 2005.
- [45] O. V. Popovych, C. Hauptmann, and P. A. Tass, "Control of neuronal synchrony by nonlinear delayed feedback," *Biological Cybernetics*, vol. 95, no. 1, pp. 69–85, 2006.

- [46] P. A. Tass, *Phase Resetting in Medicine and Biology: Stochastic Modelling and Data Analysis*, Springer, Berlin, Germany, 2007.
- [47] N. Tikhlina, M. Rosenblum, A. Pikovsky, and J. Kurths, "Feedback suppression of neural synchrony by vanishing stimulation," *Physical Review E*, vol. 75, no. 1, article 011918, 2007.
- [48] K. Pyragas, O. V. Popovych, and P. A. Tass, "Controlling synchrony in oscillatory networks with a separate stimulation-registration setup," *Europhysics Letters*, vol. 80, no. 4, article 40002, 2007.
- [49] M. Luo and J. Xu, "Suppression of collective synchronization in a system of neural groups with washout-filter-aided feedback," *Neural Networks*, vol. 24, no. 6, pp. 538–543, 2011.
- [50] H. Hong and S. H. Strogatz, "Kuramoto model of coupled oscillators with positive and negative coupling parameters: an example of conformist and contrarian oscillators," *Physical Review Letters*, vol. 106, no. 5, article 054102, 2011.
- [51] A. Franci, A. Chaillet, E. Panteley, and F. Lamnabhi-Lagarrigue, "Desynchronization and inhibition of Kuramoto oscillators by scalar mean-field feedback," *Mathematics of Control, Signals, and Systems*, vol. 24, no. 1-2, pp. 169–217, 2012.
- [52] G. Montaseri, M. J. Yazdanpanah, A. Pikovsky, and M. Rosenblum, "Synchrony suppression in ensembles of coupled oscillators via adaptive vanishing feedback," *Chaos*, vol. 23, no. 3, article 033122, 2013.
- [53] I. Ratas and K. Pyragas, "Controlling synchrony in oscillatory networks via an act-and-wait algorithm," *Physical Review E*, vol. 90, no. 3, article 032914, 2014.
- [54] I. Ratas and K. Pyragas, "Eliminating synchronization in bistable networks," *Nonlinear Dynamics*, vol. 83, no. 3, pp. 1137–1151, 2016.
- [55] A. Koseska, E. Volkov, and J. Kurths, "Transition from amplitude to oscillation death via Turing bifurcation," *Physical Review Letters*, vol. 111, no. 2, article 024103, 2013.
- [56] A. Koseska, E. Volkov, and J. Kurths, "Oscillation quenching mechanisms: amplitude vs. oscillation death," *Physics Reports*, vol. 531, no. 4, pp. 173–199, 2013.
- [57] W. Zou, D. V. Senthilkumar, A. Koseska, and J. Kurths, "Generalizing the transition from amplitude to oscillation death in coupled oscillators," *Physical Review E*, vol. 88, no. 5, article 050901, 2013.
- [58] A. Gjurchinovski, A. Zakharova, and E. Schöll, "Amplitude death in oscillator networks with variable-delay coupling," *Physical Review E*, vol. 89, no. 3, article 032915, 2014.

Research Article

A New Nonlinear Chaotic Complex Model and Its Complex Antilag Synchronization

Emad E. Mahmoud^{1,2} and Fatimah S. Abood³

¹Department of Mathematics, College of Science, Sohag University, Sohag 82524, Egypt

²Department of Mathematics, College of Science, Taif University, Taif, Saudi Arabia

³Department of Mathematics, College of Science, King Khalid University, Abha, Saudi Arabia

Correspondence should be addressed to Emad E. Mahmoud; emad_eluan@yahoo.com

Received 4 April 2017; Revised 23 May 2017; Accepted 8 June 2017; Published 3 August 2017

Academic Editor: Olfa Boubaker

Copyright © 2017 Emad E. Mahmoud and Fatimah S. Abood. This is an open access article distributed under the Creative Commons Attribution License, which permits unrestricted use, distribution, and reproduction in any medium, provided the original work is properly cited.

Another chaotic nonlinear Lü model with complex factors is covered here. We can build this riotous complex system when we add a complex nonlinear term to the third condition of the complex Lü system and think of it as if every one of the factors is mind boggling or complex. This system in real adaptation is a 6-dimensional continuous autonomous chaotic system. Different types of chaotic complex Lü system are developed. Also, another sort of synchronization is presented by us which is simple for anybody to ponder for the chaotic complex nonlinear system. This sort might be called a complex antilag synchronization (CALS). There are irregular properties for CALS and they do not exist in the literature; for example, (i) the CALS contains or fused two sorts of synchronizations (antilag synchronization ALS and lag synchronization LS); (ii) in CALS the attractors of the main and slave systems are moving opposite or similar to each other with time lag; (iii) the state variable of the main system synchronizes with a different state variable of the slave system. A scheme is intended to accomplish CALS of chaotic complex systems in light of Lyapunov function. The acquired outcomes and effectiveness can be represented by a simulation case for our new model.

1. Introduction

The chaotic system is an extremely specific nonlinear dynamical system. This chaotic system has numerous properties like the sensibility to starting conditions and in addition a sporadic, unusual conduct. The “butterfly effect” is the well-known name of the sensibility of the introductory states of the chaotic systems [1]. Since the development of the first chaotic attractor in a three-dimensional (3D) self-governing chaotic system in 1963 by Lorenz [2], over the most recent 30 years chaos has been seriously explored [3–5]. Other chaotic systems were ordered in progression relying upon the arrangement of Lorenz, for example, Lü and Chen chaotic systems [6] and Liu chaotic system [7]. Each of the past chaotic systems has one positive Lyapunov exponent, and every one of them is three-dimensional chaotic system. Be that as it may, there are likewise many fascinating cases including complex factors which have not been effectively investigated. For instance, we say here the mind-boggling

Lorenz conditions which are utilized to depict and reproduce the physics of detuned laser and thermal convection of fluid flows [8] and some of its dynamical properties are contemplated in [9]. The electric field abundance and the nuclear polarization sufficiency are both complex; for details see [10] and reference therein. In secured communications, utilizing complex variable expands the substance security of the transmitted data [11]. Complex Lü and Chen systems are presented and contemplated as of late in [12].

In 2007, Mahmoud et al. [12] introduced the complex Lü system as follows:

$$\begin{aligned}\dot{x} &= \rho(y - x), \\ \dot{y} &= \nu y - xz, \\ \dot{z} &= \frac{1}{2}(\bar{x}y + x\bar{y}) - \mu z,\end{aligned}\tag{1}$$

where ρ , ν , and μ are positive parameters, $x = w_1 + jw_2$ and $y = w_3 + jw_4$ are complex components, $z = w_5$ is real variable,

$j = \sqrt{-1}$, $w_i = 1, 2, \dots, 5$, dots refer to derivatives according to time, and the meaning of overbar is complex conjugate variables.

Complex synchronization of chaotic (hyperchaotic) complex systems is a critical nonlinear occurrence [13–25]. Complex synchronization of chaotic complex systems considers a couple of complex chaotic systems called main and slave systems, and it means to accomplish asymptotic tracking of the conditions of the slave system to the conditions of the main system. In the quest for the higher ability for enhancing the security of communication systems, some efforts have been dedicated to synchronization with complex-esteemed scaling components between chaotic (hyperchaotic) complex-variable systems. Lately, complex complete synchronization (CCS) [13], complex lag synchronization (CLS) [14], complex projective synchronization (CPS) [15], and modified projective synchronization with complex scaling components (CMPS) [16, 17] are explored for coupled chaotic complex dynamical systems. Complex modified generalized projective synchronization (CMGPS) [18] and complex modified hybrid projective synchronization (CMHPS) [19] were executed between the same or different dimensional partial request complex chaotic (hyperchaotic). Complex generalized synchronization as for a mind-boggling vector map [20, 21] was presented for two indistinguishable or nonidentical chaotic (hyperchaotic) complex-variable systems. The complex modified projective synchronization of complex chaotic (hyperchaotic) systems with uncertain complex parameters was studied in [22, 23] while the complex modified function projective synchronization of complex chaotic systems is investigated in [24, 25].

As of late, a few sorts of synchronization with time lag were concentrated; for example, antilag synchronization (ALS), lag synchronization (LS), and modified projective lag synchronization (MPLS) of two riotous or hyperchaotic complex systems are investigated in [26–29]. In designing the applications, time delay always exists. For example, in the arrangement of telephone communication, the receiver hears the speaker voice at time t . This is the speaker voice or transmitter at time $t - \tau$ ($\tau \geq 0$ and it is the lag time). In chaos communication, the time lag is the transmit flag that transmits to the receiver's end [26, 27].

In this research, we introduce a modern chaotic model with complex components by embedding a complex nonlinear expression to the third equation of the complex Lü system (1) as

$$\begin{aligned} \dot{x} &= \rho(y - x), \\ \dot{y} &= \nu y - xz, \\ \dot{z} &= \frac{1}{2}(\bar{x}y + x\bar{y}) - \mu z + j \operatorname{Im}(x) \operatorname{Re}(y), \end{aligned} \quad (2)$$

where ρ, ν , and μ are positive parameters, $x = w_1 + jw_2$, $y = w_3 + jw_4$, and $z = w_5 + jw_6$ are complex functions, $\operatorname{Im}(x)$ is imaginary part of x equal to w_2 , and $\operatorname{Re}(y)$ is the real part of y equal to w_3 .

In addition, we present a novel sort of synchronization which we can name as complex antilag synchronization

(CALS). The term CALS can be dealt with as synchronizing among ALS and LS. ALS occurs between the real part of the main system and the imaginary part of a slave system, while LS occurs between a real part of the slave system and an imaginary part of the main system.

This paper is organized as follows: in the tracking section invariance, dissipation, fixed points, and their stability analysis of some points are contemplated. The complex comportment of system (2) can without much of a stretch be studied. As indicated by estimations of Lyapunov exponents, we can figure the scope of parameters qualities at the chaotic attractors numerically. We get the best classification of the progression of (2) by the signs of Lyapunov types. We get the Lyapunov dimension of (2). We develop different types of chaotic complex Lü systems in Section 3. In Section 4 a definition of CALS is acquainted and a scheme to achieve CALS of chaotic complex nonlinear systems is proposed. In Section 5, we study CALS of two indistinguishable chaotic complexes Lü systems (2) as a case of Section 4. Finally, we will find that the fundamental conclusions of our investigations are totalized in Section 6.

2. Basic Properties of System (2)

We study the basic dynamical analysis of our new system (2).

The real version of system (2) reads

$$\begin{aligned} \dot{w}_1 &= \rho(w_3 - w_1), \\ \dot{w}_2 &= \rho(w_4 - w_2), \\ \dot{w}_3 &= \nu w_3 - w_1 w_5 + w_2 w_6, \\ \dot{w}_4 &= \nu w_4 - w_1 w_6 - w_2 w_5, \\ \dot{w}_5 &= w_1 w_3 + w_2 w_4 - \mu w_5, \\ \dot{w}_6 &= -\mu w_6 + w_2 w_3. \end{aligned} \quad (3)$$

System (3) has many main dynamical qualities as tracking.

2.1. Symmetry and Invariance. In system (3), we notice that this system is invariant transformation: $(w_1, w_2, w_3, w_4, w_5, w_6) \Rightarrow (-w_1, -w_2, -w_3, -w_4, w_5, w_6)$; therefore if $(w_1, w_2, w_3, w_4, w_5, w_6)$ is the solution of system (3), then $(-w_1, -w_2, -w_3, -w_4, w_5, w_6)$ is known as the solution of the similar system.

2.2. Dissipation. It is clear to find $\nabla \cdot V = \sum_{i=1}^6 (\partial \dot{w}_i / \partial w_i) = \partial \dot{w}_1 / \partial w_1 + \partial \dot{w}_2 / \partial w_2 + \partial \dot{w}_3 / \partial w_3 + \partial \dot{w}_4 / \partial w_4 + \partial \dot{w}_5 / \partial w_5 + \partial \dot{w}_6 / \partial w_6 = -2\rho + 2\nu - 2\mu < 0$. When $\nu < (\rho + \mu)$, the system is dissipative and meets $dV/dt = e^{-(\nu - \rho - \mu)t}$ with type shape. It implies that the volume component V_0 contracts to the volume component $V_0 e^{-(\nu - \rho - \mu)t}$ at the time t . At the point when $t \rightarrow \infty$, each volume component which contains the system direction congregates to 0 with exponent rate form $\nu - \rho - \mu$. Thus, the majority of the system directions will finally be limited to zero volume subset, and the dynamic development is fixed on an attractor.

2.3. *Equilibria and Their Stability.* The equilibria of system (3) can be found by solving the tracking system of equations:

$$\begin{aligned}
0 &= \rho(w_3 - w_1), \\
0 &= \rho(w_4 - w_2), \\
0 &= v w_3 - w_1 w_5 + w_2 w_6, \\
0 &= v w_4 - w_1 w_6 - w_2 w_5, \\
0 &= w_1 w_3 + w_2 w_4 - \mu w_5, \\
0 &= -\mu w_6 + w_2 w_3.
\end{aligned} \tag{4}$$

Obviously, $F_0 = (0, 0, 0, 0, 0, 0)$ is trivial fixed point. Other nonzero equilibria are given by

$$\begin{aligned}
F_1 &= (0, \sqrt{\mu v}, 0, \sqrt{\mu v}, v, 0), \\
F_2 &= (0, -\sqrt{\mu v}, 0, -\sqrt{\mu v}, v, 0), \\
F_3 &= (\sqrt{\mu v}, 0, \sqrt{\mu v}, 0, v, 0), \\
F_4 &= (-\sqrt{\mu v}, 0, -\sqrt{\mu v}, 0, v, 0), \\
F_5 &= (\sqrt{\mu v}, j\sqrt{\mu v}, \sqrt{\mu v}, j\sqrt{\mu v}, 0, jv), \\
F_6 &= (\sqrt{\mu v}, -j\sqrt{\mu v}, \sqrt{\mu v}, -j\sqrt{\mu v}, 0, -jv), \\
F_7 &= (-\sqrt{\mu v}, j\sqrt{\mu v}, -\sqrt{\mu v}, j\sqrt{\mu v}, 0, -jv), \\
F_8 &= (-\sqrt{\mu v}, -j\sqrt{\mu v}, -\sqrt{\mu v}, -j\sqrt{\mu v}, 0, jv).
\end{aligned} \tag{5}$$

2.3.1. *Stability of F_0 .* To study the stability of F_0 the Jacobian matrix of system (3) at F_0 is

$$J_{F_0} = \begin{pmatrix} -\rho & 0 & \rho & 0 & 0 & 0 \\ 0 & -\rho & 0 & \rho & 0 & 0 \\ 0 & 0 & v & 0 & 0 & 0 \\ 0 & 0 & 0 & v & 0 & 0 \\ 0 & 0 & 0 & 0 & -\mu & 0 \\ 0 & 0 & 0 & 0 & 0 & -\mu \end{pmatrix}. \tag{6}$$

The characteristic polynomial equation is

$$(\lambda + \rho)^2 (\lambda + \mu)^2 (\lambda - v)^2 = 0. \tag{7}$$

Then the eigenvalues are $\lambda_1 = \lambda_2 = -\rho$, $\lambda_3 = \lambda_4 = -\mu$, and $\lambda_5 = \lambda_6 = v$. The trivial fixed point $(0, 0, 0, 0, 0, 0)$ is a stable point if v has negative values and ρ and μ are positive and else, it is not stable fixed point.

2.3.2. *Stability of $F_1, F_2, F_3,$ and F_4 .* $F_1, F_2, F_3,$ and F_4 have the same characteristic polynomial, which is

$$\begin{aligned}
&[\lambda^3 + \lambda^2(\mu - v + \rho) + \lambda\mu\rho + 2\mu v\rho] \\
&\cdot [\lambda^3 + \lambda^2(\mu - v + \rho) + \lambda\mu(\rho - v) + \mu v\rho] = 0.
\end{aligned} \tag{8}$$

According to the Routh-Hurwitz theorem [30] the necessary and sufficient conditions for all roots to have negative real parts are if and only if (stable fixed points)

$$\begin{aligned}
v &< \rho + \mu, \\
\mu v \rho &> 0, \\
3v &< \rho + \mu, \\
\mu \left(1 - \frac{v}{\rho}\right) + \rho + \frac{v^2}{\rho} &> 3v;
\end{aligned} \tag{9}$$

otherwise they are unstable fixed points.

Likewise we can study the stability of $F_5, F_6, F_7,$ and F_8 .

2.4. *Lyapunov Exponents.* System (3) in vector notation can be written as

$$\dot{w}(t) = g(w(t); M), \tag{10}$$

where $w(t) = (w_1(t), w_2(t), w_3(t), w_4(t), w_5(t), w_6(t))^T$ is the state space vector, $g = (g_1, g_2, g_3, g_4, g_5, g_6)^T$, M is the set of parameters, and $(\dots)^T$ indicates transpose. The equations for small deviations δw from the trajectory $w(t)$ are

$$\delta \dot{w}(t) = J_{kl}(w(t); M) \delta w, \quad k = I = 1, 2, 3, 4, 5, 6, \tag{11}$$

where $J_{kl} = \partial g_j / \partial w_l$ is the Jacobian matrix of the form

$$J_{kl} = \begin{pmatrix} -\rho & 0 & \rho & 0 & 0 & 0 \\ 0 & -\rho & 0 & \rho & 0 & 0 \\ -w_5 & w_6 & v & 0 & -w_1 & w_2 \\ -w_6 & -w_5 & 0 & v & -w_2 & -w_1 \\ w_3 & w_4 & w_1 & w_2 & -\mu & 0 \\ 0 & w_3 & w_2 & 0 & 0 & -\mu \end{pmatrix}. \tag{12}$$

The Lyapunov exponents l_I of the system are defined by [31]

$$l_I = \lim_{t \rightarrow \infty} \frac{1}{t} \log \frac{\|\partial w_I(t)\|}{\|\partial w_I(0)\|}. \tag{13}$$

To find l_I , (10) and (11) must be numerically determined simultaneously. Runge-Kutta method of order 4 is used to compute l_I .

For the case of $\rho = 21$, $v = 10$, and $\mu = 6$, the initial conditions are as follows: $t_0 = 0$, $w_1(0) = 1$, $w_2(0) = 2$, $w_3(0) = 3$, $w_4(0) = 4$, $w_5(0) = 5$, and $w_6(0) = 6$. We compute the Lyapunov exponents as $l_1 = 2.034$, $l_2 = 0$, $l_3 = -0.99$, $l_4 = -4.16$, $l_5 = -22.49$, and $l_6 = -2.45$.

This implies that our system (3) under this selection of ρ, v, μ is a chaotic system due to the fact that one of the Lyapunov exponents is positive.

The Lyapunov dimension of the attractors of (3) according to Kaplan-Yorke conjecture is defined as [32]

$$D = \Omega + \frac{\sum_{k=1}^{\Omega} l_k}{|l_{\Omega+1}|}, \tag{14}$$

such that Ω is the largest integer that $\sum_{k=1}^{\Omega} l_k > 0$ and $\sum_{k=1}^{\Omega+1} l_k < 0$. The Lyapunov dimension of this chaotic attractor using (14) with $\rho = 21$, $v = 10$, and $\mu = 6$ is $D = 3.2509$.

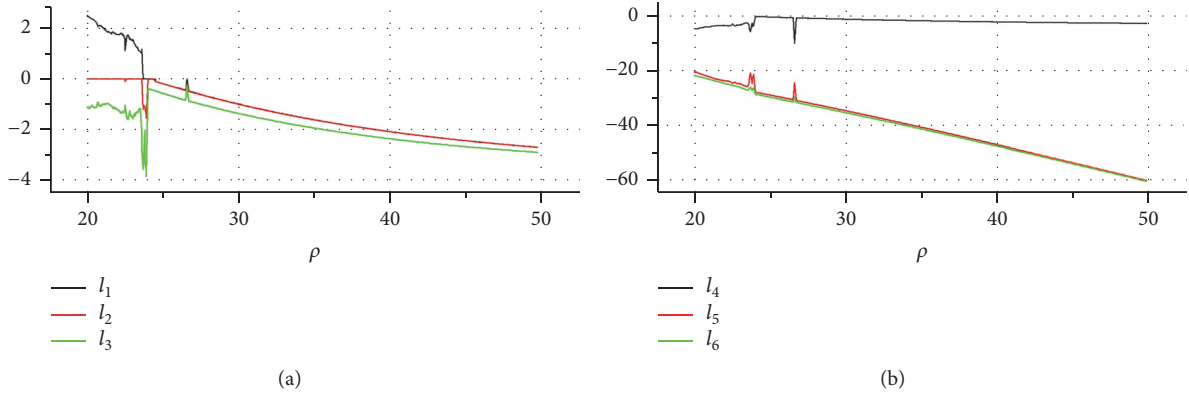


FIGURE 1: The Lyapunov exponents l_I , $I = 1, 2, \dots, 6$ of system (3) when we fix $v = 10$ and $\mu = 6$ and vary $\rho \in [20, 50]$.

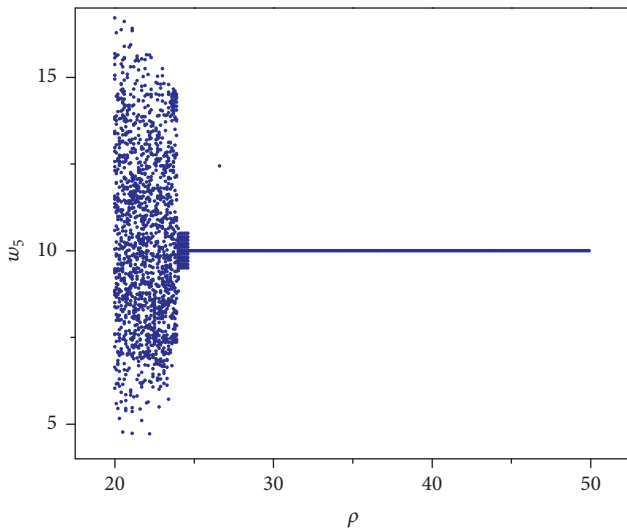


FIGURE 2: The bifurcation diagram of system (3) when the parameter ρ is varying $\rho \in [20, 50]$.

2.4.1. Fix $v = 10$ and $\mu = 6$ and Vary $\rho \in [20, 50]$. In light of Lyapunov exponents l_I (13) the system' parameter qualities were computed (3) at which chaotic attractors, periodic, quasiperiodic attractors and fixed points exist. The review modifies and differs one parameter and fixes the extra parameters as indicated by their states which fulfill the dissipative condition and the dependability state of the trifling fixed focuses.

Utilizing (13) we ascertain l_I , $I = 1, 2, \dots, 6$, and the estimations of l_1, l_2, \dots, l_6 versus ρ are plotted in Figure 1.

Obviously from Figure 1, when $\rho \in [20, 23.6]$ system (3) has chaotic attractors. The intermittent or periodic attractors of (3) exist for ρ which lies in the interims $(23.6, 24]$. The quasiperiodic conduct models up when $\rho \in (24.1, 24.6]$ while the arrangement is equilibrium point when $\rho \in (24.6, 50]$.

In Figure 2, we figure the bifurcation diagram of system (3) when the parameter ρ is varying or modifying to guarantee that our system is chaotic. A bifurcation diagram outlines

a system parameter on the horizontal axis and a report of the attractor's action on the vertical axis. So, bifurcation diagrams present a kind method to picture how a system's behavior varies according to the value of a parameter [33]. Figure 2 shows (ρ, w_5) bifurcation diagram for $\rho \in [20, 50]$. It can be discerned that when $\rho \in [20, 23.6]$, system (3) has solutions that approach chaotic attractors and when $\rho \in (23.6, 24.6]$ it has periodic and quasiperiodic behavior. The equilibrium points are shown when $\rho \in (24.6, 50]$. The dynamical behavior of Figure 2 is similar to this which is given in Figure 1.

Testing this numerically (utilizing, e.g., Mathematica 7 programming) in different sections and best notes is found and is agreeable with our outcomes. For instance, picking $v = 10$ and $\mu = 6$, with the underlying conditions $t_0 = 0$, $w_1(0) = 1$, $w_2(0) = 2$, $w_3(0) = 3$, $w_4(0) = 4$, $w_5(0) = 5$, and $w_6(0) = 6$, and when $\rho = 21$, the arrangement of system (3) has chaotic attractor (see Figure 3(a)). In Figure 3(b) the arrangement is periodic with $\rho = 23.9$. The quasiperiodic attractor is represented in Figure 3(c), $\rho = 24.2$. In Figure 3(d) the balance point is indicated when $\rho = 30$.

3. Different Forms of Chaotic Complex Lü Systems

In this section, we demonstrate that the complex Lü system (2) is not just the one that has chaotic attractors with all factors or variables being complex. In this way, we search for different systems that yield chaotic conduct. We can build these systems in light of system (1) by adding a complex nonlinear term to the third equation of (1) with thought, all factors are complex. We can build six different types of riotous complex Lü systems and compute their Lyapunov exponents as

$$\begin{aligned}
 \dot{x} &= \rho(y - x), \\
 \dot{y} &= \nu y - xz, \\
 \dot{z} &= \frac{1}{2}(\bar{x}y + x\bar{y}) - \mu z + j \operatorname{Re}(x) \operatorname{Re}(y),
 \end{aligned} \tag{15}$$

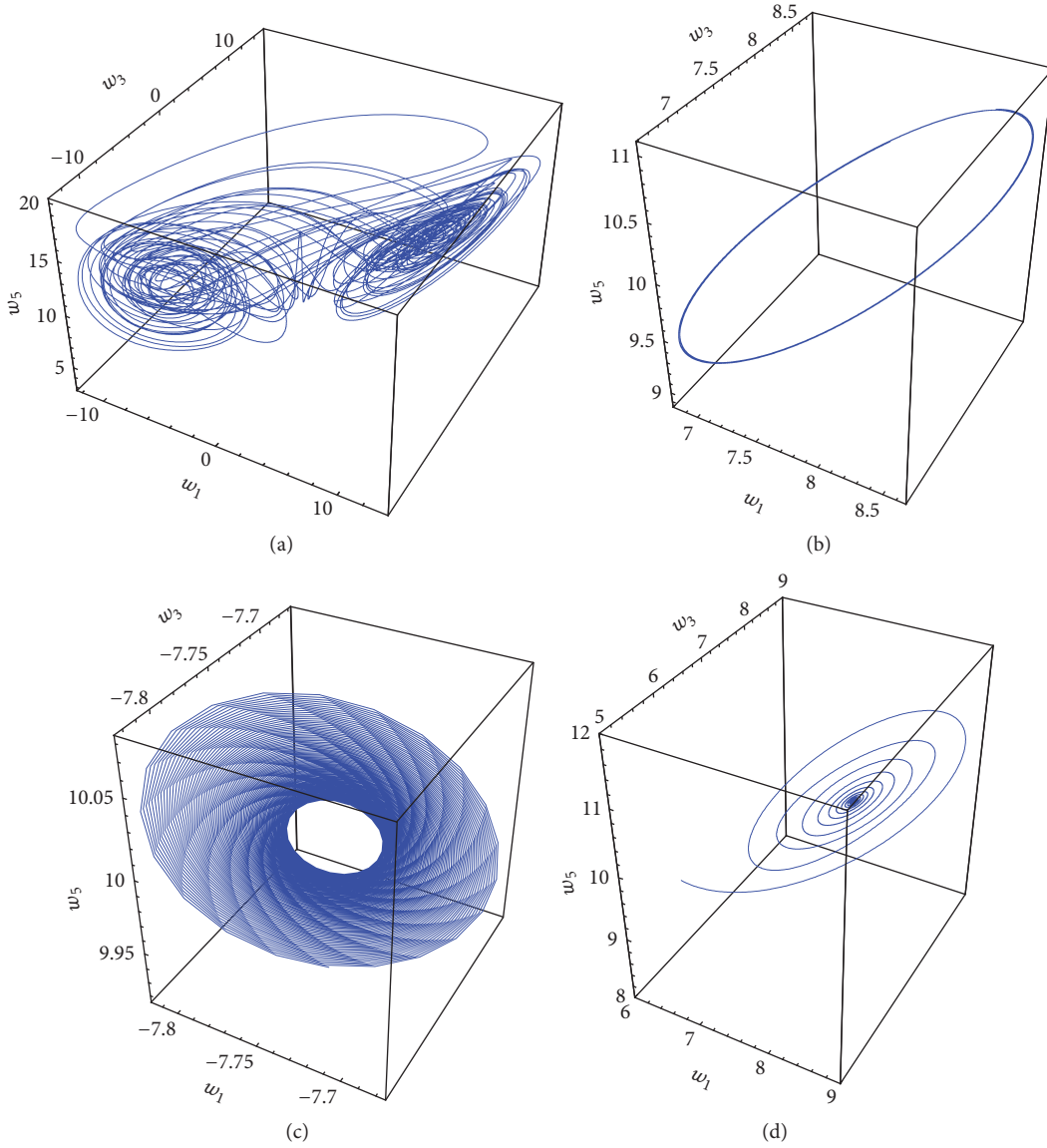


FIGURE 3: For $v = 10$ and $\mu = 6$, vary ρ . (a) Chaotic attractor, $\rho = 21$ in (w_1, w_3, w_5) . (b) Periodic attractor, $\rho = 23.9$ in (w_1, w_3, w_5) . (c) Quasiperiodic attractor, $\rho = 24.2$ in (w_1, w_3, w_5) . (d) Fixed point, $\rho = 30$ in (w_1, w_3, w_5) .

where $l_1 = 0.549$, $l_2 = 0$, $l_3 = 0$, $l_4 = -4.19$, $l_5 = -11.540$, $l_6 = -17.72$, $\rho = 20$, $\mu = 2.5$, and $v = 18$.

$$\begin{aligned} \dot{x} &= \rho(y - x), \\ \dot{y} &= \nu y - xz, \\ \dot{z} &= \frac{1}{2}(\bar{x}y + x\bar{y}) - \mu z + j \operatorname{Im}(x) \operatorname{Im}(y), \end{aligned} \quad (16)$$

where $l_1 = 1.31$, $l_2 = 0$, $l_3 = 0$, $l_4 = -5.804$, $l_5 = -17.201$, $l_6 = -22.013$, $\rho = 25$, $\mu = 3$, and $v = 12$.

$$\begin{aligned} \dot{x} &= \rho(y - x), \\ \dot{y} &= \nu y - xz, \\ \dot{z} &= \frac{1}{2}(\bar{x}y + x\bar{y}) - \mu z + j \operatorname{Im}(y) \operatorname{Re}(z), \end{aligned} \quad (17)$$

where $l_1 = 0.6$, $l_2 = 0$, $l_3 = 0$, $l_4 = -4.88$, $l_5 = -8.5$, $l_6 = -11.65$, $\rho = 19$, $\mu = 2.5$, and $v = 16$.

$$\begin{aligned} \dot{x} &= \rho(y - x), \\ \dot{y} &= \nu y - xz, \\ \dot{z} &= \frac{1}{2}(\bar{x}y + x\bar{y}) - \mu z + j \operatorname{Im}(z) \operatorname{Re}(y), \end{aligned} \quad (18)$$

where $l_1 = 0.957$, $l_2 = 0$, $l_3 = 0$, $l_4 = -0.98$, $l_5 = -7.86$, $l_6 = -13.7$, $\rho = 22$, $\mu = 4$, and $v = 18$.

$$\begin{aligned} \dot{x} &= \rho(y - x), \\ \dot{y} &= \nu y - xz, \\ \dot{z} &= \frac{1}{2}(\bar{x}y + x\bar{y}) - \mu z + j \operatorname{Re}(z) \operatorname{Re}(y), \end{aligned} \quad (19)$$

where $l_1 = 1.200, l_2 = 0.01, l_3 = 0, l_4 = -2.89, l_5 = -10.96, l_6 = -15.04, \rho = 27, \mu = 5, \text{ and } \nu = 14.6$.

$$\begin{aligned} \dot{x} &= \rho(y - x), \\ \dot{y} &= \nu y - xz, \\ \dot{z} &= \frac{1}{2}(\bar{x}y + x\bar{y}) - \mu z + j \operatorname{Im}(x) \operatorname{Re}(z), \end{aligned} \quad (20)$$

where $l_1 = 1.6, l_2 = 0, l_3 = 0, l_4 = -5.80, l_5 = -16.908, l_6 = -19.20, \rho = 20, \mu = 3, \text{ and } \nu = 11$.

All the above systems have one positive Lyapunov exponent. We ascertain these Lyapunov types as we accomplished in system (2) indistinguishable beginning conditions (Figure 1). The fundamental properties of these systems can be likewise examined as we have in Section 2.

4. A Definition and Achievement for CALS

Consider the chaotic complex nonlinear system as follows:

$$\dot{\mathbf{x}} = \Psi \mathbf{x} + \mathbf{F}(\mathbf{x}), \quad (21)$$

where $\mathbf{x} = (x_1, x_2, \dots, x_n)^T \in \mathbb{C}^n$ is a state complex vector, $\mathbf{x} = \mathbf{x}^{\operatorname{Re}} + j\mathbf{x}^{\operatorname{Im}}, \mathbf{x}^{\operatorname{Re}} = (w_1, w_3, \dots, w_{2n-1})^T, \mathbf{x}^{\operatorname{Im}} = (w_2, w_4, \dots, w_{2n})^T, j = \sqrt{-1}, T$ denotes transpose, $\Psi \in \mathbb{R}^{n \times n}$ is real (or complex) matrix of system parameters, $\mathbf{F} = (f_1, f_2, \dots, f_n)^T$ is a vector of nonlinear complex functions, and coordinating Re and Im symbolize the real and imaginary parts of the state complex vector \mathbf{x} .

In this work we present and study the definition of CALS of two systems of shape (21) (indistinguishable) with known parameters by scheming a control plot. We tried its rightness numerically.

We consider two indistinguishable chaotic complex nonlinear systems of shape (21): one is the main system (we indicate the main system with the subscript m) as

$$\dot{\mathbf{x}}_m = \dot{\mathbf{x}}_m^{\operatorname{Re}} + j\dot{\mathbf{x}}_m^{\operatorname{Im}} = \Psi \mathbf{x}_m + \mathbf{F}(\mathbf{x}_m), \quad (22)$$

and the second is the controlled slave system (with subscript s) as

$$\dot{\mathbf{x}}_s = \dot{\mathbf{x}}_s^{\operatorname{Re}} + j\dot{\mathbf{x}}_s^{\operatorname{Im}} = \Psi \mathbf{x}_s + \mathbf{F}(\mathbf{x}_s) + \mathbf{L}, \quad (23)$$

where the additive complex controllers are as follows: $\mathbf{L} = (\mathbf{L}_1, \mathbf{L}_2, \dots, \mathbf{L}_n)^T = \mathbf{L}^{\operatorname{Re}} + j\mathbf{L}^{\operatorname{Im}}, \mathbf{L}^{\operatorname{Re}} = (\zeta_1, \zeta_3, \dots, \zeta_{2n-1})^T, \text{ and } \mathbf{L}^{\operatorname{Im}} = (\zeta_2, \zeta_4, \dots, \zeta_{2n})^T$.

Definition 1. Two indistinguishable complex dynamical systems coupled in a main-slave configuration can exhibit CALS if there exists a vector of the complex error function \mathbf{e} defined as

$$\mathbf{e} = \mathbf{e}^{\operatorname{Re}} + j\mathbf{e}^{\operatorname{Im}} = \lim_{t \rightarrow \infty} \|\mathbf{x}_s(t) + j\mathbf{x}_m(t - \tau)\| = 0, \quad (24)$$

where $\mathbf{e} = (e_1, e_2, \dots, e_n)^T, \mathbf{x}_m$ and \mathbf{x}_s are the state complex vectors of the main and slave, respectively, $\mathbf{e}^{\operatorname{Re}} = \lim_{t \rightarrow \infty} \|\mathbf{x}_s^{\operatorname{Re}}(t) - \mathbf{x}_m^{\operatorname{Re}}(t - \tau)\| = 0, \mathbf{e}^{\operatorname{Im}} = \lim_{t \rightarrow \infty} \|\mathbf{x}_s^{\operatorname{Im}}(t) + \mathbf{x}_m^{\operatorname{Re}}(t - \tau)\| = 0, \mathbf{e}^{\operatorname{Re}} = (e_{w_1}, e_{w_3}, \dots, e_{w_{2n-1}})^T, \mathbf{e}^{\operatorname{Im}} = (e_{w_2}, e_{w_4}, \dots, e_{w_{2n}})^T, \text{ and } \tau$ is the positive time lag.

In CALS we define the error in simple case:

$$\begin{aligned} x_s(t) + jx_m(t - \tau) &= 0, \text{ as } t \rightarrow \infty, \text{ where } x = w_1 + jw_2 \\ [w_{1s}(t) + jw_{2s}(t)] + j[w_{1m}(t - \tau) + jw_{2m}(t - \tau)] &= 0, \\ [w_{1s}(t) + jw_{2s}(t)] + [-w_{2m}(t - \tau) + jw_{1m}(t - \tau)] &= 0, \\ [w_{1s}(t) - w_{2m}(t - \tau)] + j[w_{2s}(t) + w_{1m}(t - \tau)] &= 0, \\ \implies w_{1s}(t) - w_{2m}(t - \tau) = 0 &\implies (\text{LS}) \\ \implies w_{2s}(t) + w_{1m}(t - \tau) = 0 &\implies (\text{ALS}) \end{aligned} \left. \vphantom{\begin{aligned} x_s(t) + jx_m(t - \tau) = 0, \text{ as } t \rightarrow \infty, \text{ where } x = w_1 + jw_2 \right\} \implies (\text{CALS})$$

Box 1: Complex antilag synchronization (CALS).

In ALS the error in simple case:

$$\begin{aligned} x_s(t) + x_m(t - \tau) &= 0, \text{ as } t \rightarrow \infty, \text{ where } x = w_1 + jw_2 \\ [w_{1s}(t) + jw_{2s}(t)] + [w_{1m}(t - \tau) + jw_{2m}(t - \tau)] &= 0, \\ [w_{1s}(t) + jw_{2s}(t)] + [w_{1m}(t - \tau) + jw_{2m}(t - \tau)] &= 0, \\ [w_{1s}(t) + w_{1m}(t - \tau)] + j[w_{2s}(t) + w_{2m}(t - \tau)] &= 0, \\ \implies w_{1s}(t) + w_{1m}(t - \tau) = 0 &\implies (\text{ALS}) \\ \implies w_{2s}(t) + w_{2m}(t - \tau) = 0 &\implies (\text{ALS}) \end{aligned} \left. \vphantom{\begin{aligned} x_s(t) + x_m(t - \tau) = 0, \text{ as } t \rightarrow \infty, \text{ where } x = w_1 + jw_2 \right\} \implies (\text{ALS})$$

Box 2: Antilag synchronization (ALS) [27].

Remark 2. When $\tau = 0$ in (24) we define complex antisynchronization CAS between (22) and (23).

Remark 3. If we define $\mathbf{e} = \lim_{t \rightarrow \infty} \|\mathbf{x}_s(t) - j\mathbf{x}_m(t - \tau)\|$ and $\tau = 0$, we get CCS of systems (22) and (23) [13], while if $\tau > 0$, we obtain CLS of the same systems [14].

Remark 4. The complex state is as follows:

$$j = \rho(\cos \theta + j \sin \theta), \quad (25)$$

where $\rho = |j| = 1$ (ρ is the modulus of j) and $\theta = \pi/2$ (θ is the phase of j).

Remark 5. The sum of the imaginary part of slave system $\mathbf{x}_s^{\operatorname{Im}}(t)$ and the real part of main system $\mathbf{x}_m^{\operatorname{Re}}(t - \tau)$ is vanishing when $t \rightarrow \infty$ (ALS) [27].

Remark 6. The error between the real part of slave system $\mathbf{x}_s^{\operatorname{Re}}(t)$ and the imaginary part of main system $\mathbf{x}_m^{\operatorname{Im}}(t - \tau)$ goes to zero as $t \rightarrow \infty$ (LS) [26].

Remark 7. The difference between CALS and ALS [27] can be illustrated from Boxes 1 and 2.

Theorem 8. If nonlinear controller is designed as

$$\begin{aligned} \mathbf{L} &= \mathbf{L}^{\operatorname{Re}} + j\mathbf{L}^{\operatorname{Im}} = -\Psi \mathbf{x}_s(t) - \mathbf{F}(\mathbf{x}_s(t)) \\ &\quad - j[\Psi \mathbf{x}_m(t - \tau) + \mathbf{F}(\mathbf{x}_m(t - \tau))] - \xi \mathbf{e}, \\ &= -\Psi \mathbf{x}_s^{\operatorname{Re}}(t) - \mathbf{F}^{\operatorname{Re}}(\mathbf{x}_s(t)) + \Psi \mathbf{x}_m^{\operatorname{Im}}(t - \tau) \\ &\quad + \mathbf{F}^{\operatorname{Im}}(\mathbf{x}_m(t - \tau)) - \xi \mathbf{e}^{\operatorname{Re}} + j[-\Psi \mathbf{x}_s^{\operatorname{Im}}(t) \end{aligned}$$

$$\begin{aligned} & -\mathbf{F}^{\text{Im}}(\mathbf{x}_s(t)) - \Psi \mathbf{x}_m^{\text{Re}}(t-\tau) - \mathbf{F}^{\text{Re}}(\mathbf{x}_m(t-\tau)) \\ & - \xi \mathbf{e}^{\text{Im}} \Big], \end{aligned} \quad (26)$$

then the main system (22) and the slave system (23) are moving in CALS manner asymptotically, $\xi > 0$.

Proof. From the definition of CALS,

$$\mathbf{e} = \mathbf{e}^{\text{Re}} + j\mathbf{e}^{\text{Im}} = \mathbf{x}_s(t) + j\mathbf{x}_m(t-\tau). \quad (27)$$

So

$$\begin{aligned} \dot{\mathbf{e}} &= \dot{\mathbf{e}}^{\text{Re}} + j\dot{\mathbf{e}}^{\text{Im}} = \dot{\mathbf{x}}_s(t) + j\dot{\mathbf{x}}_m(t-\tau), \\ \dot{\mathbf{e}} &= \dot{\mathbf{e}}^{\text{Re}} + j\dot{\mathbf{e}}^{\text{Im}} \\ &= \dot{\mathbf{x}}_s^{\text{Re}}(t) - \dot{\mathbf{x}}_m^{\text{Im}}(t-\tau) + j[\dot{\mathbf{x}}_s^{\text{Im}}(t) + \dot{\mathbf{x}}_m^{\text{Re}}(t-\tau)], \end{aligned} \quad (28)$$

and from chaotic complex systems (22) and (23), we get the error complex dynamical system as follows:

$$\begin{aligned} \dot{\mathbf{e}} &= \dot{\mathbf{e}}^{\text{Re}} + j\dot{\mathbf{e}}^{\text{Im}} = \Psi \mathbf{x}_s^{\text{Re}}(t) + \mathbf{F}^{\text{Re}}(\mathbf{x}_s(t)) - \Psi \mathbf{x}_m^{\text{Im}}(t \\ & - \tau) - \mathbf{F}^{\text{Im}}(\mathbf{x}_m(t-\tau)) + \mathbf{L}^{\text{Re}} + j[\Psi \mathbf{x}_s^{\text{Im}}(t) \\ & + \mathbf{F}^{\text{Im}}(\mathbf{x}_s(t)) + \Psi \mathbf{x}_m^{\text{Re}}(t-\tau) + \mathbf{F}^{\text{Re}}(\mathbf{x}_m(t-\tau)) \\ & + \mathbf{L}^{\text{Im}} \Big]. \end{aligned} \quad (29)$$

By separating the real and the imaginary parts in (29), the error complex system is written as

$$\begin{aligned} \dot{\mathbf{e}}^{\text{Re}} &= \Psi \mathbf{x}_s^{\text{Re}}(t) + \mathbf{F}^{\text{Re}}(\mathbf{x}_s(t)) - \Psi \mathbf{x}_m^{\text{Im}}(t-\tau) \\ & - \mathbf{F}^{\text{Im}}(\mathbf{x}_m(t-\tau)) + \mathbf{L}^{\text{Re}}, \\ \dot{\mathbf{e}}^{\text{Im}} &= \Psi \mathbf{x}_s^{\text{Im}}(t) + \mathbf{F}^{\text{Im}}(\mathbf{x}_s(t)) + \Psi \mathbf{x}_m^{\text{Re}}(t-\tau) \\ & + \mathbf{F}^{\text{Re}}(\mathbf{x}_m(t-\tau)) + \mathbf{L}^{\text{Im}}. \end{aligned} \quad (30)$$

For positive parameters, we may now define a Lyapunov function for this system by the tracking positive definite quantity:

$$\begin{aligned} V(t) &= \frac{1}{2} \left[(\mathbf{e}^{\text{Re}})^T \mathbf{e}^{\text{Re}} + (\mathbf{e}^{\text{Im}})^T \mathbf{e}^{\text{Im}} \right], \\ &= \frac{1}{2} \left[(e_{w_1}^2 + e_{w_3}^2 + \cdots + e_{w_{2n-1}}^2) \right. \\ & \left. + (e_{w_2}^2 + e_{w_4}^2 + \cdots + e_{w_{2n}}^2) \right] = \frac{1}{2} \left(\sum_{h=1}^n e_{w_{2h-1}}^2 \right. \\ & \left. + \sum_{h=1}^n e_{w_{2h}}^2 \right). \end{aligned} \quad (31)$$

Note now that the total time derivative of $V(t)$ along the trajectory of error system (30) is as follows:

$$\begin{aligned} \dot{V}(t) &= (\dot{\mathbf{e}}^{\text{Re}})^T \mathbf{e}^{\text{Re}} + (\dot{\mathbf{e}}^{\text{Im}})^T \mathbf{e}^{\text{Im}}, \\ &= (\Psi \mathbf{x}_s^{\text{Re}}(t) + \mathbf{F}(\mathbf{x}_s^{\text{Re}}(t)) - \Psi \mathbf{x}_m^{\text{Im}}(t-\tau) \\ & - \mathbf{F}(\mathbf{x}_m^{\text{Im}}(t-\tau)) + \mathbf{L}^{\text{Re}})^T \mathbf{e}^{\text{Re}} + (\Psi \mathbf{x}_s^{\text{Im}}(t) \\ & + \mathbf{F}(\mathbf{x}_s^{\text{Im}}(t)) + \Psi \mathbf{x}_m^{\text{Re}}(t-\tau) + \mathbf{F}(\mathbf{x}_m^{\text{Re}}(t-\tau)) \\ & + \mathbf{L}^{\text{Im}})^T \mathbf{e}^{\text{Im}}. \end{aligned} \quad (32)$$

By substituting from (26) about \mathbf{L}^{Re} and \mathbf{L}^{Im} in (32) we obtain

$$\begin{aligned} \dot{V}(t) &= -\xi \left[(\mathbf{e}^{\text{Re}})^T \mathbf{e}^{\text{Re}} + (\mathbf{e}^{\text{Im}})^T \mathbf{e}^{\text{Im}} \right], \\ &= -\xi \left(\sum_{h=1}^n e_{w_{2h-1}}^2 + \sum_{h=1}^n e_{w_{2h}}^2 \right). \end{aligned} \quad (33)$$

Obviously, $V(t)$ is a positive definite capacity and its subordinate is negatively definite; therefore as per the Lyapunov hypothesis, intricate mistake system (29) is asymptotically steady, which implies that $e_{w_{2h}} \rightarrow 0$ and $e_{w_{2h-1}} \rightarrow 0$ as $t \rightarrow \infty$ and $h = 1, 2, \dots, n$. Along these lines, the CALS between systems (22) and (23) is accomplished. This supplements the confirmation. \square

At last, by applying it for two comparable riotous complexes Lü systems in Section 5, our composition is stated.

5. Example

5.1. Construction of the Controller. In the current subsection, we can demonstrate the likelihood and effectiveness of the proposed synchronization plot in the forward segment. We review the CALS of two indistinguishable chaotic complex Lü systems. The main and the slave systems are consequently defined, individually, as follows:

$$\begin{aligned} \dot{x}_m &= \rho(y_m - x_m), \\ \dot{y}_m &= \nu y_m - x_m z_m, \end{aligned} \quad (34)$$

$$\begin{aligned} \dot{z}_m &= \frac{1}{2}(\bar{x}_m y_m + x_m \bar{y}_m) - \mu z_m + j\omega_{2m} \omega_{3m}, \\ \dot{x}_s &= \rho(y_s - x_s) + L_1, \\ \dot{y}_s &= \nu y_s - x_s z_s + L_2, \end{aligned} \quad (35)$$

$$\dot{z}_s = \frac{1}{2}(\bar{x}_s y_s + x_s \bar{y}_s) - \mu z_s + j\omega_{2s} \omega_{3s} + L_3,$$

where $x_m = w_{1m} + jw_{2m}$, $y_m = w_{3m} + jw_{4m}$, $z_m = w_{5m} + jw_{6m}$, $x_s = w_{1s} + jw_{2s}$, $y_s = w_{3s} + jw_{4s}$, $z_s = w_{5s} + jw_{6s}$, $L_1 = \zeta_1 + j\zeta_2$,

$L_2 = \zeta_3 + j\zeta_4$, and $L_3 = \zeta_5 + j\zeta_6$ are complex control functions, respectively, which are to be determined.

Complex systems (34) and (35) can be formed, respectively, as

$$\begin{aligned} \begin{pmatrix} \dot{x}_m \\ \dot{y}_m \\ \dot{z}_m \end{pmatrix} &= \begin{pmatrix} -\rho & \rho & 0 \\ 0 & v & 0 \\ 0 & 0 & -\mu \end{pmatrix} \begin{pmatrix} x_m \\ y_m \\ z_m \end{pmatrix} \\ &+ \begin{pmatrix} 0 \\ -x_m z_m \\ \frac{1}{2}(\bar{x}_m y_m + x_m \bar{y}_m) + jw_{2m}w_{3m} \end{pmatrix}, \\ \begin{pmatrix} \dot{x}_s \\ \dot{y}_s \\ \dot{z}_s \end{pmatrix} &= \begin{pmatrix} -\rho & \rho & 0 \\ 0 & v & 0 \\ 0 & 0 & -\mu \end{pmatrix} \begin{pmatrix} x_s \\ y_s \\ z_s \end{pmatrix} \\ &+ \begin{pmatrix} 0 \\ -x_s z_s \\ \frac{1}{2}(\bar{x}_s y_s + x_s \bar{y}_s) + jw_{2s}w_{3s} \end{pmatrix} \end{aligned} \quad (36)$$

$$+ \begin{pmatrix} L_1 \\ L_2 \\ L_3 \end{pmatrix}.$$

(37)

So, by comparing complex systems (36) and (37) with the form of systems (22) and (23), respectively, we find

$$\begin{aligned} \Psi &= \begin{pmatrix} -\rho & \rho & 0 \\ 0 & v & 0 \\ 0 & 0 & -\mu \end{pmatrix}, \\ \mathbf{F}(\mathbf{x}_m) &= \begin{pmatrix} 0 \\ -x_m z_m \\ \frac{1}{2}(\bar{x}_m y_m + x_m \bar{y}_m) + jw_{2m}w_{3m} \end{pmatrix}, \\ \mathbf{F}(\mathbf{x}_s) &= \begin{pmatrix} 0 \\ -x_s z_s \\ \frac{1}{2}(\bar{x}_s y_s + x_s \bar{y}_s) + jw_{2s}w_{3s} \end{pmatrix}. \end{aligned} \quad (38)$$

According to Theorem 8, the controller is computed as

$$L = [-\Psi \mathbf{x}_s(t) - \mathbf{F}(\mathbf{x}_s(t))] - j[\Psi \mathbf{x}_m(t - \tau) + \mathbf{F}(\mathbf{x}_m(t - \tau))] - \xi \mathbf{e},$$

$$\begin{pmatrix} L_1 \\ L_2 \\ L_3 \end{pmatrix} = \begin{pmatrix} -\rho(y_s(t) - x_s(t)) - j\rho(y_m(t - \tau) - x_m(t - \tau)) - \xi e_1 \\ -vy_s(t) + \varphi_1 - j(vy_m(t - \tau) - \varphi_2) - \xi e_2 \\ -\varphi_3 + \mu z_s(t) - jw_{2s}(t)w_{3s}(t) - j(\varphi_4 - \mu z_m(t - \tau) + jw_{2m}(t - \tau)w_{3m}(t - \tau)) - \xi e_3 \end{pmatrix}, \quad (39)$$

where $\varphi_1 = x_s(t)z_s(t)$, $\varphi_2 = x_m(t - \tau)z_m(t - \tau)$, $\varphi_3 = 1/2(\bar{x}_s(t)y_s(t) + x_s(t)\bar{y}_s(t))$, and $\varphi_4 = 1/2(\bar{x}_m(t - \tau)y_m(t - \tau) + x_m(t - \tau)\bar{y}_m(t - \tau))$.

So, the controller in (39) can be written as

$$\begin{aligned} \begin{pmatrix} \zeta_1 + j\zeta_2 \\ \zeta_3 + j\zeta_4 \\ \zeta_5 + j\zeta_6 \end{pmatrix} &= \begin{pmatrix} -\rho(w_{3s}(t) - w_{1s}(t) - w_{4m}(t - \tau) + w_{2m}(t - \tau)) - \xi e_{w_1} \\ -v(w_{3s}(t) - w_{4m}(t - \tau)) + \varphi_5 - \xi e_{w_3} \\ -\varphi_7 + \mu(w_{5s}(t) - w_{6m}(t - \tau)) + w_{2m}(t - \tau)w_{3m}(t - \tau) - \xi e_{w_5} \end{pmatrix} \\ &+ j \begin{pmatrix} -\rho(w_{4s}(t) - w_{2s}(t) + w_{3m}(t - \tau) - w_{1m}(t - \tau)) - \xi e_{w_2} \\ -v(w_{4s}(t) + w_{3m}(t - \tau)) + \varphi_6 - \xi e_{w_4} \\ -\varphi_8 + \mu(w_{6s}(t) + w_{5m}(t - \tau)) - w_{2s}(t)w_{3s}(t) - \xi e_{w_6} \end{pmatrix}, \end{aligned} \quad (40)$$

where $\varphi_5 = w_{1s}(t)w_{5s}(t) - w_{2s}(t)w_{6s}(t) - w_{1m}(t - \tau)w_{6m}(t - \tau) - w_{2m}(t - \tau)w_{5m}(t - \tau)$, $\varphi_6 = w_{1s}(t)w_{6s}(t) + w_{2s}(t)w_{5s}(t) + w_{1m}(t - \tau)w_{5m}(t - \tau) - w_{2m}(t - \tau)w_{6m}(t - \tau)$, $\varphi_7 = w_{1s}(t)w_{3s}(t) + w_{2s}(t)w_{4s}(t)$, $\varphi_8 = w_{1m}(t - \tau)w_{3m}(t - \tau) + w_{2m}(t - \tau)w_{4m}(t - \tau)$.

5.2. Numerical Results. To demonstrate and confirm the value of the suggested plot, we clarify the recreation consequences of the CALS among two indistinguishable chaotic complex systems (34) and (35). Systems (34) and (35) with the

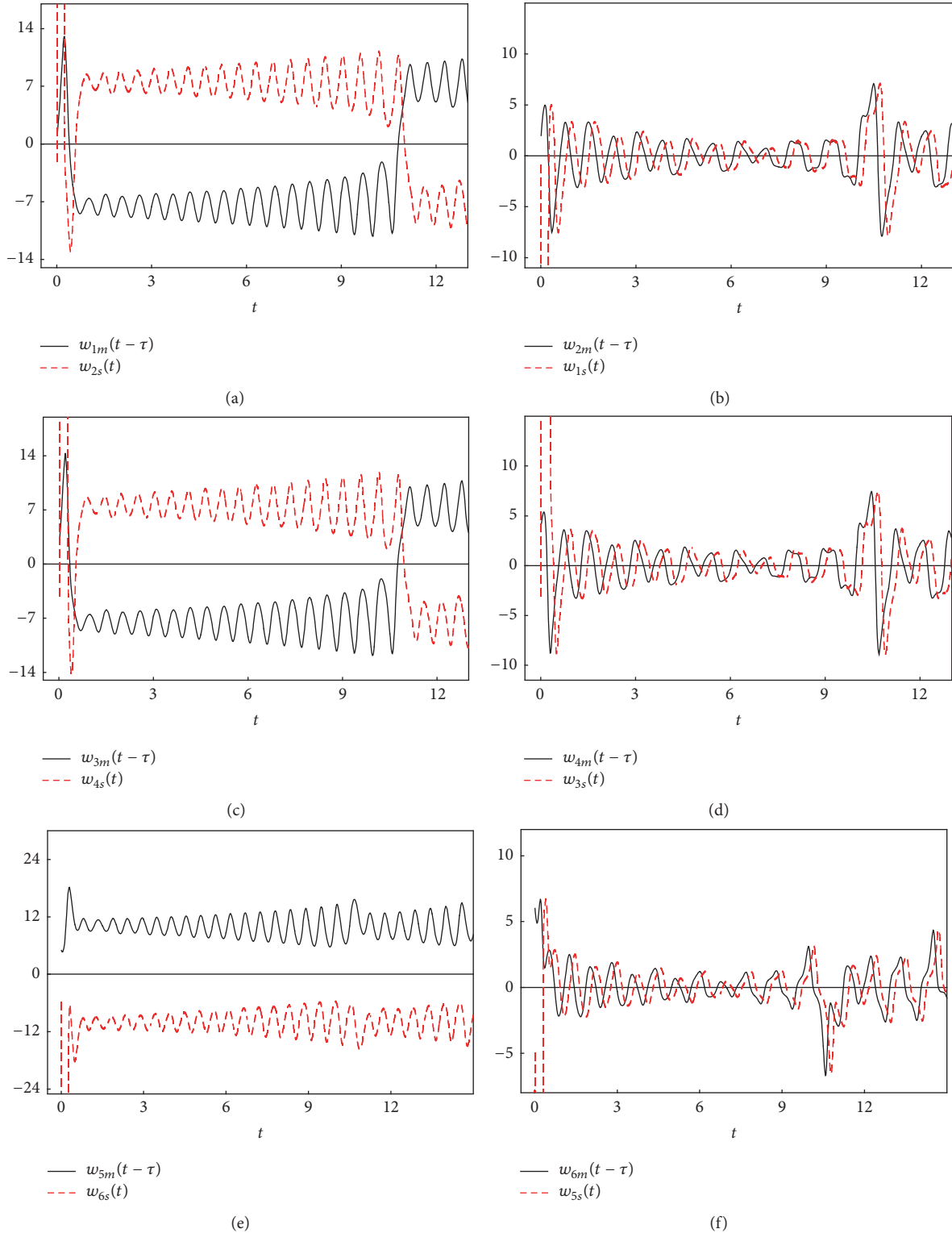


FIGURE 4: CALS between two identical systems (34) and (35) with the controller (40). (a) $w_{1m}(t-\tau)$ and $w_{2s}(t)$. (b) $w_{2m}(t-\tau)$ and $w_{1s}(t)$. (c) $w_{3m}(t-\tau)$ and $w_{4s}(t)$. (d) $w_{4m}(t-\tau)$ and $w_{3s}(t)$. (e) $w_{5m}(t-\tau)$ and $w_{6s}(t)$. (f) $w_{6m}(t-\tau)$ and $w_{5s}(t)$.

controller (40) are illuminated numerically, and the parameters are picked as $\rho = 23$, $\mu = 6$, and $\nu = 10$. The underlying necessity of the main model and the underlying state of the slave models ξ , τ are considered basically $(x_m(0), y_m(0),$

$$z_m(0))^T = (1 + 2j, 3 + 4j, 5 + 6j)^T, (x_s(0), y_s(0), z_s(0))^T = (-1 - 2j, -3 - 4j, -5 - 6j)^T, \xi = 10, \text{ and } \tau = 0.2.$$

In Figure 4 the arrangements of (34) and (35) are plotted which are subject to different beginning conditions and

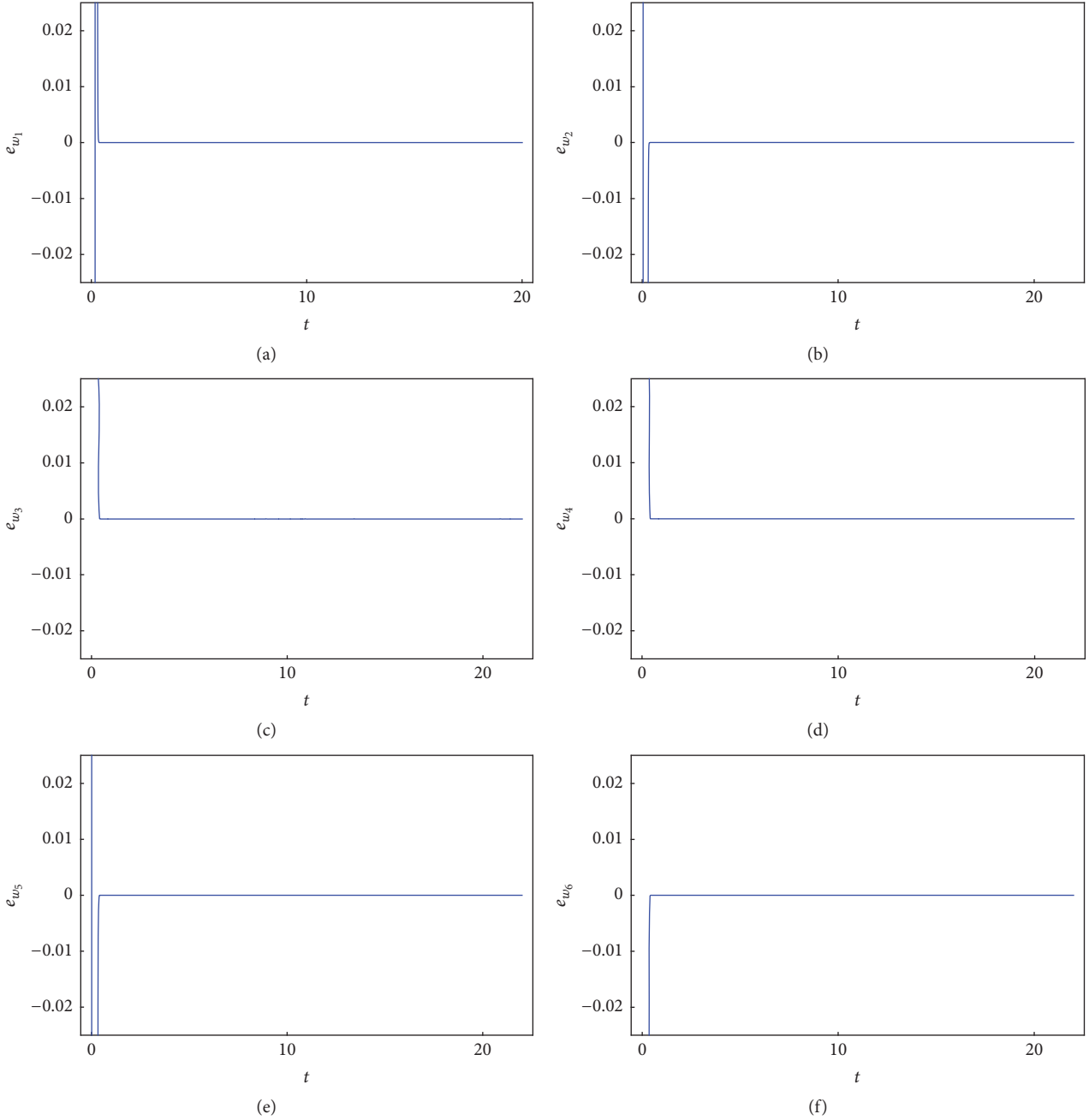


FIGURE 5: CALS errors between systems (34) and (35): (a) $w_{1s}(t) - w_{2m}(t - \tau)$. (b) $w_{2s}(t) + w_{1m}(t - \tau)$. (c) $w_{3s}(t) - w_{4m}(t - \tau)$. (d) $w_{4s}(t) + w_{3m}(t - \tau)$. (e) $w_{5s}(t) - w_{6m}(t - \tau)$. (f) $w_{6s}(t) + w_{5m}(t - \tau)$.

demonstrate that CALS is to be surely accomplished after a next to no time t . We can see that w_{1s} , w_{3s} , w_{5s} have a similar indication of w_{2m} , w_{4m} , w_{6m} with time lag, while w_{2s} , w_{4s} , w_{6s} have an inverse indication of w_{1m} , w_{3m} , w_{5m} with time lag. This implies that LS is accomplished between the imaginary part of system (34) and the real part of system (35) while ALS happens between the real part of slave system (34) and the fanciful part of the main system (35). It is clear from Figure 4 that the state variables of the main system synchronize with different state variables of the slave

system. In this way, the CALS gives more prominent security in secure communications. Figure 4 indicates that CALS is accomplished after little time interim. The CALS errors are plotted in Figure 5. Of course from the above exschematory contemplations the CALS errors $e_{w_{2h-1}}$ and $e_{w_{2h}}$ converge to zero as $t \rightarrow \infty$ and $h = 1, 2, 3$. In Figure 5 it can be seen that the errors will approach zero after little estimation of t . The development of the attractors of main and slave systems in the wake of accomplishing the CALS is shown in Figure 6. Another marvel is represented in Figure 6 and does not model

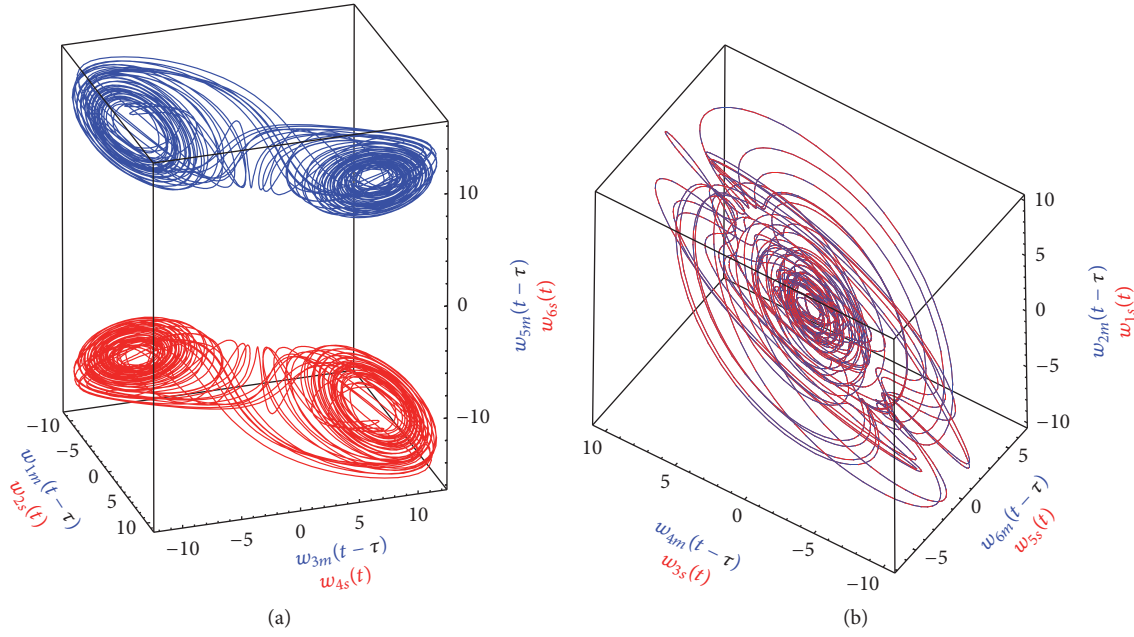


FIGURE 6: The attractors of systems (34) and (35). (a) Attractor of the main system has the opposite shape of the slave system. (b) Attractor of the main system has the similar shape of the slave system.

up in a wide range of synchronizations in the writing. The attractors of the main and slave systems in CALS are moving in opposite or similar shape to each other with different state variables and time lag as found in Figure 6. In Figure 6(a), the attractor of the main system in $(w_{1m}(t - \tau), w_{3m}(t - \tau), w_{5m}(t - \tau))$ has the opposite shape of the slave system in $(w_{2s}(t), w_{4s}(t), w_{6s}(t))$, while the attractor of the slave system in $(w_{1s}(t), w_{3s}(t), w_{5s}(t))$ has the similar shape of the main system with time lag in $(w_{2m}(t - \tau), w_{4m}(t - \tau), w_{6m}(t - \tau))$ as shown in Figure 6(b).

In the numerical reenactments, we register the module errors and phase errors of main and slave models, respectively. For every unpredictable number, the module and phase are resolved as follows:

$$\rho_x = \sqrt{(x^{\text{Re}})^2 + (x^{\text{Im}})^2}, \quad (41)$$

$$\theta_x = \begin{cases} \arctan\left(\frac{x^{\text{Im}}}{x^{\text{Re}}}\right), & x^{\text{Re}} > 0, x^{\text{Im}} \geq 0, \\ 2\pi + \arctan\left(\frac{x^{\text{Im}}}{x^{\text{Re}}}\right), & x^{\text{Re}} > 0, x^{\text{Im}} < 0, \\ \pi + \arctan\left(\frac{x^{\text{Im}}}{x^{\text{Re}}}\right), & x^{\text{Re}} < 0. \end{cases} \quad (42)$$

Figure 7 models the modules errors and phases errors of main system (34) and slave systems (35). It is clear from Figures 7(a), 7(b), and 7(c) that the modules errors $\rho_{x_m} - \rho_{x_s}, \rho_{y_m} - \rho_{y_s}$, and $\rho_{z_m} - \rho_{z_s}$ converge to zero as $t \rightarrow \infty$, while the phases errors $\theta_{x_m} - \theta_{x_s}, \theta_{y_m} - \theta_{y_s}$, and $\theta_{z_m} - \theta_{z_s}$ go to $\pi/2$ or $-\pi/2$ as $t \rightarrow \infty$; see Figures 7(d), 7(e), and 7(f).

6. Conclusions

In this paper, we have presented a cutting edge chaotic complex Lü system (2) and we concentrated the elements of it. By affixing an unpredictable expression of the third condition of the complex Lü system (1), we can develop this system. In this system all factors are intricate. Our system in real adaptation is six measurements or by different words system (2) are high measurements. In spite of this, our new system does not create hyperchaotic practices. Consequently, we close from these outcomes that the expansion in the measurements is the important and not sufficient condition for producing hyperchaotic practices. The steadiness investigations of the fixed purposes of system (2) are completed. We presented in Section 3 different types of chaotic complex Lü systems which can be comparatively explored as we accomplished for system (2) in Section 2. These new systems leave room for further investigations.

We present another kind of complex synchronization which is called complex antilag synchronization (CALS). A definition of CALS of two indistinguishable chaotic complex systems is given. We dissect and concentrate the CALS concerning two indistinguishable chaotic complex nonlinear systems. The CALS can be concentrated just in complex nonlinear systems. The CALS can be considered as syncretizing among ALS and LS (see Figure 4). LS occurs between a real part of the slave system and an imaginary part of the main system, while ALS occurs between the real part of the main system and the fanciful part of a slave system. In CALS, the state variables of the main system synchronize with different state variables of the slave system (see Figure 4). Thus, CALS gives more prominent security in secure interchanges. The

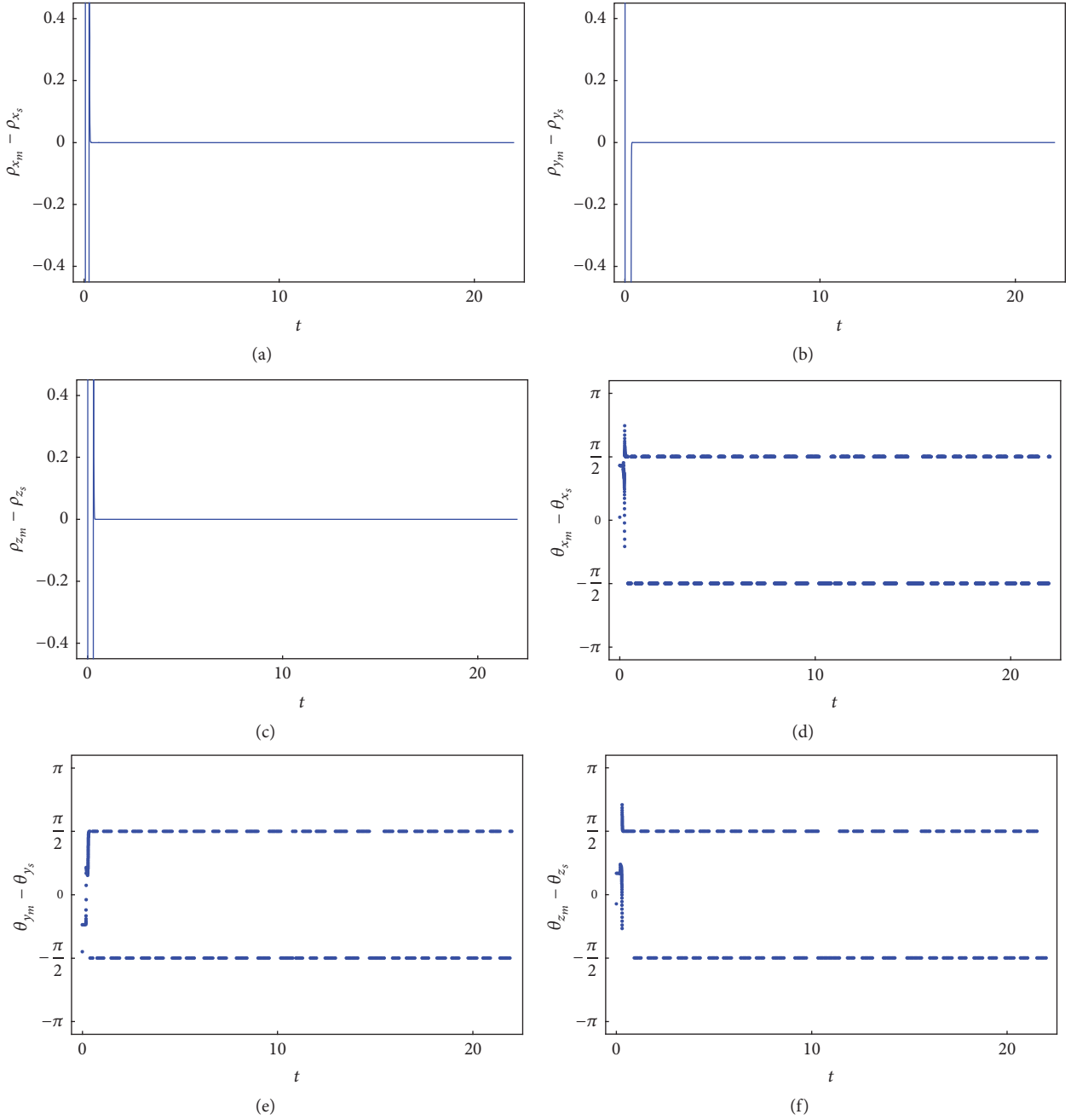


FIGURE 7: The modules errors and phases errors of systems (34) and (35): (a) $\rho_{x_m} - \rho_{x_s}$ versus t . (b) $\rho_{y_m} - \rho_{y_s}$ versus t . (c) $\rho_{z_m} - \rho_{z_s}$ versus t . (d) $\theta_{x_m} - \theta_{x_s}$ versus t . (e) $\theta_{y_m} - \theta_{y_s}$ versus t . (f) $\theta_{z_m} - \theta_{z_s}$ versus t .

most outstanding normal for the CALS is the attractors of the main and slave systems are moving in opposite or similar shape to each other with different state variables (see Figures 6(a) and 6(b)). These marvels did not come to pass and appear for any sorts of synchronization in the writing.

A scheme is laid out to acknowledge CALS of two indistinguishable chaotic complex nonlinear systems in view of Lyapunov capacities. Amid this scheme, we analytically concluded the control complex capacities to accomplish

CALS. It is simple and advantageous to utilize this scheme for chaotic and hyperchaotic complex systems. We apply our scheme, for instance, for two indistinguishable chaotic complex systems with different introductory qualities, main system (34) and slave systems (35). All the hypothetical outcomes are verified by numerical recreations of our case. A great assertion is found as shown in Figures 4, 5, and 6. In Figure 7 we register the modules errors and phase errors in light of the fact that, in the complex nonlinear

dynamical systems, the noticeable or quantifiable physical amounts more often than not are module and phase.

Conflicts of Interest

The authors declare that there are no conflicts of interest regarding the publication of this paper.

References

- [1] T. K. Alligood, T. Sauer, and J. A. Yorke, *An Introduction to Dynamical Systems*, Chaos, Springer, New York, NY, USA, 1997.
- [2] E. N. Lorenz, "Deterministic nonperiodic flow," *Journal of the Atmospheric Sciences*, vol. 20, no. 2, pp. 130–141, 1963.
- [3] F. J. Li, N. Li, Y. P. Liu, and Y. Gan, "Linear and nonlinear generalized synchronization of a class of chaotic systems by using a single driving variable," *Journal of Applied Physical Science*, vol. 58, pp. 779–784, 2009.
- [4] Y. X. Wang and M. J. Meng, "Chaotic control of the coupled logistic map," *Acta Physica Sinica*, vol. 57, pp. 726–773.
- [5] S. Liu, B. Liu, and P. M. Shi, "Nonlinear feedback control of Hopf bifurcation in a relative rotation dynamical system," *Acta Physica Sinica*, vol. 58, no. 7, pp. 4383–4389, 2009.
- [6] J. Lü and G. Chen, "A new chaotic attractor coined," *International Journal of Bifurcation and Chaos in Applied Sciences and Engineering*, vol. 12, no. 3, pp. 659–661, 2002.
- [7] C. Liu, T. Liu, L. Liu, and K. Liu, "A new chaotic attractor," *Chaos, Solitons & Fractals*, vol. 22, no. 5, pp. 1031–1038, 2004.
- [8] A. C. Fowler, J. D. Gibbon, and M. J. McGuinness, "The complex Lorenz equations," *Physica D*, vol. 4, no. 2, pp. 139–163, 1982.
- [9] G. M. Mahmoud, M. A. Al-Kashif, and S. A. Aly, "Basic properties and chaotic synchronization of complex Lorenz system," *International Journal of Modern Physics C*, vol. 18, no. 2, pp. 253–265, 2007.
- [10] A. Rauh, L. Hannibal, and N. B. Abraham, "Global stability properties of the complex Lorenz model," *Physica D*, vol. 99, no. 1, pp. 45–58, 1996.
- [11] J. H. Peng, E. J. Ding, M. Ding, and W. Yang, "Synchronizing hyperchaos with a scalar transmitted signal," *Physical Review Letters*, vol. 76, no. 6, pp. 904–907, 1996.
- [12] G. M. Mahmoud, T. Bountis, and E. E. Mahmoud, "Active control and global synchronization of the complex Chen and Lü systems," *International Journal of Bifurcation and Chaos in Applied Sciences and Engineering*, vol. 17, no. 12, pp. 4295–4308, 2007.
- [13] E. E. Mahmoud, "Complex complete synchronization of two nonidentical hyperchaotic complex nonlinear systems," *Mathematical Methods in the Applied Sciences*, vol. 37, no. 3, pp. 321–328, 2014.
- [14] E. E. Mahmoud and K. M. Abualnaja, "Complex lag synchronization of two identical chaotic complex nonlinear systems," *Central European Journal of Physics*, vol. 12, no. 1, pp. 63–69, 2014.
- [15] Z. Wu, J. Duan, and X. Fu, "Complex projective synchronization in coupled chaotic complex dynamical systems," *Nonlinear Dynamics*, vol. 69, no. 3, pp. 771–779, 2012.
- [16] G. M. Mahmoud and E. E. Mahmoud, "Complex modified projective synchronization of two chaotic complex nonlinear systems," *Nonlinear Dynamics*, vol. 73, no. 4, pp. 2231–2240, 2013.
- [17] F.-F. Zhang, S.-T. Liu, and W.-Y. Yu, "Modified projective synchronization with complex scaling factors of uncertain real chaos and complex chaos," *Chinese Physics B*, vol. 22, no. 12, article 120505, 2013.
- [18] J. Liu, S. Liu, and W. Li, "Complex modified generalized projective synchronization of fractional-order complex chaos and real chaos," *Advances in Difference Equations*, pp. 1–16, 2015.
- [19] J. Liu, "Complex modified hybrid projective synchronization of different dimensional fractional-order complex chaos and real hyper-chaos," *Entropy*, vol. 16, no. 12, pp. 6195–6211, 2014.
- [20] S. Wang, X. Wang, and B. Han, "Complex generalized synchronization and parameter identification of nonidentical nonlinear complex systems," *PLoS ONE*, vol. 11, no. 3, article e0152099, 2016.
- [21] S. Wang, X. Wang, Y. Zhou, and B. Han, "A memristor-based hyperchaotic complex Lü system and its adaptive complex generalized synchronization," *Entropy*, vol. 18, no. 2, article 58, 2016.
- [22] J. Liu, S. Liu, and C. Yuan, "Adaptive complex modified projective synchronization of complex chaotic (hyperchaotic) systems with uncertain complex parameters," *Nonlinear Dynamics*, vol. 79, no. 2, pp. 1035–1047, 2015.
- [23] J. Liu, S. Liu, and F. Zhang, "A novel four-wing hyperchaotic complex system and its complex modified hybrid projective synchronization with different dimensions," *Abstract and Applied Analysis*, pp. 1–16, 2014.
- [24] J. Liu and S. Liu, "Complex modified function projective synchronization of complex chaotic systems with known and unknown complex parameters," *Applied Mathematical Modelling*, vol. 48, pp. 440–450, 2017.
- [25] J. Liu, S. Liu, and J. C. Sprott, "Adaptive complex modified hybrid function projective synchronization of different dimensional complex chaos with uncertain complex parameters," *Nonlinear Dynamics*, vol. 83, no. 1-2, pp. 1109–1121, 2016.
- [26] G. M. Mahmoud and E. E. Mahmoud, "Lag synchronization of hyperchaotic complex nonlinear systems," *Nonlinear Dynamics*, vol. 67, no. 2, pp. 1613–1622, 2012.
- [27] E. E. Mahmoud, "Adaptive anti-lag synchronization of two identical or non-identical hyperchaotic complex nonlinear systems with uncertain parameters," *Journal of the Franklin Institute*, vol. 349, no. 3, pp. 1247–1266, 2012.
- [28] E. E. Mahmoud, "Lag synchronization of hyperchaotic complex nonlinear systems via passive control," *Applied Mathematics & Information Sciences*, vol. 7, no. 4, pp. 1429–1436, 2013.
- [29] G. M. Mahmoud and E. E. Mahmoud, "Modified projective lag synchronization of two nonidentical hyperchaotic complex nonlinear systems," *International Journal of Bifurcation and Chaos*, vol. 21, no. 8, pp. 2369–2379, 2011.
- [30] M. S. Klamkin and A. Liu, "Three more proofs of routh's theorem," *Crux Math*, vol. 7, pp. 199–203, 1981.
- [31] A. Wolf, J. B. Swift, H. L. Swinney, and J. A. Vastano, "Determining Lyapunov exponents from a time series," *Physica D*, vol. 16, no. 3, pp. 285–317, 1985.
- [32] P. Frederickson, J. L. Kaplan, E. D. Yorke, and J. A. Yorke, "The Liapunov dimension of strange attractors," *Journal of Differential Equations*, vol. 49, no. 2, pp. 185–207, 1983.
- [33] E. E. Mahmoud and M. A. Al-Adwani, "Dynamical behaviors, control and synchronization of a new chaotic model with complex variables and cubic nonlinear terms," *Results in Physics*, vol. 7, pp. 1346–1356, 2017.

Research Article

Study on Triopoly Dynamic Game Model Based on Different Demand Forecast Methods in the Market

Junhai Ma,¹ Lijian Sun,^{1,2} and Xueli Zhan³

¹College of Management and Economics, Tianjin University, Tianjin 300072, China

²College of Science, Tianjin University of Science and Technology, Tianjin 300457, China

³School of Economics, Beijing Wuzi University, Beijing 101149, China

Correspondence should be addressed to Junhai Ma; mjhtju@aliyun.com and Xueli Zhan; xuelz20163205@126.com

Received 11 February 2017; Revised 22 March 2017; Accepted 26 March 2017; Published 6 July 2017

Academic Editor: Christos Volos

Copyright © 2017 Junhai Ma et al. This is an open access article distributed under the Creative Commons Attribution License, which permits unrestricted use, distribution, and reproduction in any medium, provided the original work is properly cited.

The impact of inaccurate demand beliefs on dynamics of a Triopoly game is studied. We suppose that all the players make their own estimations on possible demand with errors. A dynamic Triopoly game with such demand belief is set up. Based on this model, existence and local stable region of the equilibriums are investigated by 3D stable regions of Nash equilibrium point. The complex dynamics, such as bifurcation scenarios and route to chaos, are displayed in 2D bifurcation diagrams, in which e_1 and α are negatively related to each other. Basins of attraction are investigated and we found that the attraction domain becomes smaller with the increase in price modification speed, which indicates that all the players' output must be kept within a certain range so as to keep the system stable. Feedback control method is used to keep the system at an equilibrium state.

1. Introduction

A Triopoly is a market structure dominated by three firms in the market. The market is known as Cournot game if firms choose quantities as their strategic variables to maximize their profits in an uncertain demand environment.

In conventional market games, players are supposed to have common accurate demand functions of market. The dynamics of such system with this assumption have been intensively investigated in literature [1–8].

Assuming cost function to be twice differentiable increasing, Elabbasy et al. [1] analyzed the dynamics of oligopoly games with three types of players: bounded rational, naive, and adaptive.

Ma and Liu [2] studied a generalized nonlinear Fokker-Planck diffusion equation with external force and absorption. They obtained the corresponding exact solution expressed by q -exponential function and the solutions can have a compact behavior or a long tailed behavior.

Yassen and Agiza [3] studied a repeated Cournot game model with delayed bounded rationality in the duopoly market and demonstrated that the lagged structure is helpful

to expand the stable region of the system via numerical simulations.

Ma and Ren [4] focused on the influence of parameters on the macroeconomics IS-LM model and improved the analysis capabilities of the traditional economic models to suit the actual macroeconomic environment. They found that the system order has an important influence on the running state of the system.

Tramontana and Elsadany [5] discussed a triopolistic market with heterogeneous firms when the demand function is isoelastic. He found that double routes lead to chaos, via period-doubling and Neimark–Sacker bifurcations.

Ma and Ji [6] built a Triopoly outputs game model in electric power market. They obtained that the Triopoly model is a chaotic system and it is better than the duopoly model in applications.

Ma and Wu [7] studied the complexity of a Triopoly price game model and influence of delayed decisions on the stability. All those approaches assume that there is one uniform and accurate market demand function available and shared by all player.

Ma and Pu [8] researched the Cournot-Bertrand duopoly model with the application of nonlinear dynamics theory. They analyzed the stability of the fixed points and gave the bifurcation diagram and Lyapunov exponent spectrum along with the corresponding chaotic attractor. The research results show that either the change of output modification speed or the change of price modification speed will lead the market to the chaotic state which is disadvantageous for both of the firms.

All those literatures assume that there is one accurate market demand function, which is shared by all players. In practice, demand functions may be influenced by lots of different factors and every player has to estimate his own market demand function on the basis of past experience.

Because it is impossible for the firms to get the whole information, they cannot know the accurate demand function, so all the players have to make an estimate for demand function. Compared to real market demand function, it is inevitable for all the players to make demand evaluation biases. Thus, it is important to study how dynamics of the Triopoly game will be influenced by those evaluation biases, in terms of equilibrium points, local stability, and system performance.

A few works have been done to investigate the system dynamics, equilibrium offset with inaccurate demand beliefs. Bischi et al. [9] studied a model of a quantity-setting duopoly market with misspecified demand, the global dynamics of this game was investigated, and the number of steady states and their welfare properties were characterized. The impact of misspecified demand on the steady state was also studied. However, the asymmetric system with heterogeneous players' behavior has not been considered.

Wang and Ma [10] considered a Cournot-Bertrand mixed duopoly game model with limited information about the market and opponent. They studied the local stability of the game model at the Nash equilibrium point and discussed the influences of the parameters on the system's performance.

Bischi et al. [11] considered a repeated oligopoly game in single product Cournot oligopolies and proposed a method to learn demand function in a repeated oligopoly game via a closed loop feedback of real market price, which adjusts the evaluated demand function.

Guo and Ma [12] built a collecting price game model for a close-loop supply chain system with a manufacturer and a retailer who have different rationalities. They analyzed the influences of parameters on complex dynamic phenomena, such as the bifurcation, chaos, and continuous power spectrum.

Qiu et al. [13] studied the impact of uncertain demand on dynamic output-setting market games. A dynamic game with uncertain demand for two heterogeneous players was built. Based on this model, the impact of uncertain demand on the game's complex dynamics was investigated. Sun and Ma [14] constructed the three-oligopoly game model and investigated the existence of the fixed points. The 3D stable regions were given. The complex dynamic behavior of the game model is studied and the chaos was successfully controlled.

In this paper, we analyze the complex dynamics of a Triopoly model with heterogeneous players and demand evaluation bias, focusing on the following perspectives:

- (1) Impact of demand estimate bias on equilibrium, stable region, and profits.
- (2) Impact of adjustment strategy on basins of attraction.

The paper is organized as follows. In Section 2, a Triopoly game model with inaccurate demand belief is established. In Section 3, the existence and local stability of equilibrium points are discussed. The effects of inaccurate demand on stable region, profit, and equilibriums are shown in Section 4. Dynamical behaviors of the game are investigated by numerical simulations using 2D bifurcation diagrams [15] in Section 5. Basins of attraction [16] of the model are given in Section 7. In Section 8, conclusions are drawn from our analysis.

2. The Cournot Triopoly Game Model

We consider a Cournot Triopoly game in which the price and the demand of firm i 's product are denoted by p_i and q_i , $i = 1, 2, 3$, and the demand functions for the three firms are as follows:

$$p = a - b(q_1 + q_2 + q_3) \quad (1)$$

in which a and b are both positive constants. Assume that all the three firms have nonlinear cost function considering that if q_i exceeds a certain level, the cost will increase quickly and the cost function of the i th firm has a quadratic form [3]:

$$C_i(q_i) = c_i q_i^2 \quad (i = 1, 2, 3). \quad (2)$$

While in practice, not all the firms can get the whole information, they may do not know demand function (1), so all the players have to make an estimate for demand function.

For each player, we assume that the actual demand function held by player i can be denoted by multiplying the demand function (1) with an error coefficient e_i . And it has the following form:

$$p = e_i(a - b(q_1 + q_2 + q_3)) \quad (3)$$

which is called its subjective demand function.

The error coefficient e_i which is between (0, 3) means the imperfection degree of player i about the market.

If $e_i = 1$, it indicates that the evaluated demand function is just the true demand function. If $e_i < 1$, it indicates that the demand is underestimated by player, while if $e_i > 1$, it indicates the case where the demand is overestimated.

So the firms can get their maximum profits according to the following profit functions:

$$\begin{aligned} \pi_1(t) &= e_1(a - b(q_1 + q_2 + q_3))q_1 - c_1 q_1^2 \\ \pi_2(t) &= e_2(a - b(q_1 + q_2 + q_3))q_2 - c_2 q_2^2 \\ \pi_3(t) &= e_3(a - b(q_1 + q_2 + q_3))q_3 - c_3 q_3^2 \end{aligned} \quad (4)$$

in which $\pi_i(t)$ is the profit of firm i . Hence, the marginal profit functions of firms in period t are given by

$$\begin{aligned}\frac{\partial \pi_1(t)}{\partial q_1(t)} &= e_1 (a - 2bq_1(t) - b(q_2(t) + q_3(t))) - 2c_1q_1 \\ \frac{\partial \pi_2(t)}{\partial q_2(t)} &= e_2 (a - 2bq_2(t) - b(q_1(t) + q_3(t))) - 2c_2q_2 \quad (5) \\ \frac{\partial \pi_3(t)}{\partial q_3(t)} &= e_3 (a - 2bq_3(t) - b(q_2(t) + q_1(t))) - 2c_3q_3,\end{aligned}$$

while in practice, firms usually cannot get the whole information. For example, they cannot know other firm's price in the next period in advance, for which they cannot compute the price by the marginal profit functions above. In this paper, we consider all the firms as bounded rational players and their next-period price decisions are made on the basis of the local estimate to their marginal profit in current period. So the players make their strategies as the following form:

$$q_i(t+1) = q_i(t) + k_i q_i(t) \frac{\partial \pi_i(t)}{\partial q_i(t)} \quad (k_i = \alpha, \beta, \gamma). \quad (6)$$

The equation means that if the marginal profit of the current period is positive, the firm will raise its price the next period; otherwise, it will reduce it. So the dynamical Triopoly system can be described as

$$\begin{aligned}q_1(t+1) &= q_1(t) + \alpha q_1(t) G_1(t) \\ q_2(t+1) &= q_2(t) + \beta q_2(t) G_2(t) \quad (7) \\ q_3(t+1) &= q_3(t) + \gamma q_3(t) G_3(t),\end{aligned}$$

where

$$\begin{aligned}G_1(t) &= e_1 (a - 2bq_1(t) - b(q_2(t) + q_3(t))) - 2c_1q_1 \\ G_2(t) &= e_2 (a - 2bq_2(t) - b(q_1(t) + q_3(t))) - 2c_2q_2 \quad (8) \\ G_3(t) &= e_3 (a - 2bq_3(t) - b(q_2(t) + q_1(t))) - 2c_3q_3.\end{aligned}$$

$0 < \alpha, \beta, \gamma < 1$ denote the players' adjustment speeds, respectively.

3. Equilibrium Points and Local Stability

3.1. Equilibrium Points. According to system (7), let $p_i(t+1) = p_i(t)$; then eight equilibrium points can be obtained:

$$\begin{aligned}E_1 &= (0, 0, 0) \\ E_2 &= \left(0, \frac{ae_2}{2(c_2 + be_2)}, 0\right) \\ E_3 &= \left(\frac{ae_1}{2(c_1 + be_1)}, 0, 0\right) \\ E_4 &= \left(0, 0, \frac{ae_3}{2(c_3 + be_3)}\right) \\ E_5 &= \left(0, \frac{ae_2(2c_3 + be_3)}{(4c_2c_3 + 4bc_2e_3 + 4bc_3e_2 + 3b^2e_2e_3)}, \frac{ae_3(2c_2 + be_2)}{(4c_2c_3 + 4bc_2e_3 + 4bc_3e_2 + 3b^2e_2e_3)}\right) \\ E_6 &= \left(\frac{ae_1(2c_2 + be_2)}{(4c_2c_1 + 4bc_1e_2 + 4bc_2e_1 + 3b^2e_2e_1)}, \frac{ae_2(2c_1 + be_1)}{(4c_2c_1 + 4bc_1e_2 + 4bc_2e_1 + 3b^2e_2e_1)}, 0\right) \\ E_7 &= \left(\frac{ae_1(2c_3 + be_3)}{(4c_3c_1 + 4bc_1e_3 + 4bc_3e_1 + 3b^2e_3e_1)}, 0, \frac{ae_3(2c_1 + be_1)}{(4c_3c_1 + 4bc_1e_3 + 4bc_3e_1 + 3b^2e_3e_1)}\right),\end{aligned} \quad (9)$$

and the Nash equilibrium point

$$E_8 = (q_1^*, q_2^*, q_3^*) \quad (10)$$

can be obtained, where

$$\begin{aligned}q_1^* &= \frac{(4ac_2c_3e_1 + 2abc_2e_1e_3 + 2abc_3e_1e_2 + ab^2e_1e_2e_3)}{(2(4c_1c_2c_3 + 3b^2c_1e_2e_3 + 3b^2c_2e_1e_3 + 3b^2c_3e_1e_2 + 2b^3e_1e_2e_3 + 4bc_1c_2e_3 + 4bc_1c_3e_2 + 4bc_2c_3e_1))} \\ q_2^* &= \frac{(ae_2(2c_1 + be_1)(2c_3 + be_3))}{(2(4c_1c_2c_3 + 3b^2c_1e_2e_3 + 3b^2c_2e_1e_3 + 3b^2c_3e_1e_2 + 2b^3e_1e_2e_3 + 4bc_1c_2e_3 + 4bc_1c_3e_2 + 4bc_2c_3e_1))} \\ q_3^* &= \frac{(ae_3(2c_1 + be_1)(2c_2 + be_2))}{(2(4c_1c_2c_3 + 3b^2c_1e_2e_3 + 3b^2c_2e_1e_3 + 3b^2c_3e_1e_2 + 2b^3e_1e_2e_3 + 4bc_1c_2e_3 + 4bc_1c_3e_2 + 4bc_2c_3e_1))}.\end{aligned} \quad (11)$$

It can be seen from above that E_8 is independent of the adjustment factors. From an economic point of view, that means

the value of the system local stability point in this dynamic game is independent of the players' adjustment speed, but just

determined by the characteristics of the system. We can find from (11) that if e_i of player i increases and e_j of other players remains the same, q_i^* will increase.

3.2. Nash Points in Error-Free System-Benchmark. If the players have perfect knowledge, their subjective demand functions totally coincide with the real ones. Setting $e_1 = e_2 = e_3 = 1$ in (11), we can get

$$\begin{aligned} q_1^* &= \frac{a(b+2c_2)(b+2c_3)}{(6b^2c_1+6b^2c_2+6b^2c_3+4b^3+8bc_1c_2+8bc_1c_3+8bc_2c_3+8c_1c_2c_3)} \\ q_2^* &= \frac{a(b+2c_1)(b+2c_3)}{(6b^2c_1+6b^2c_2+6b^2c_3+4b^3+8bc_1c_2+8bc_1c_3+8bc_2c_3+8c_1c_2c_3)} \\ q_3^* &= \frac{a(b+2c_1)(b+2c_2)}{(6b^2c_1+6b^2c_2+6b^2c_3+4b^3+8bc_1c_2+8bc_1c_3+8bc_2c_3+8c_1c_2c_3)}. \end{aligned} \quad (12)$$

Note that the denominator of q_1^* , q_2^* , and q_3^* is the same, the output depends on the cost of the players, and the greater the cost, the lower the yield. These results match the results in [17].

3.3. Local Stability of System Equilibriums. In order to analyze the stability of the preceding equilibrium points, the Jacobian matrix for discrete dynamic system (7) is found as follows:

$$J = \begin{pmatrix} J_1 & -\alpha be_1 q_1 & -\alpha be_1 q_1 \\ -\beta be_2 q_2 & J_2 & -\beta be_2 q_2 \\ -\gamma be_3 q_3 & -\gamma be_3 q_3 & J_3 \end{pmatrix} \quad (13)$$

in which

$$\begin{aligned} J_1 &= 1 - \alpha q_1 (2c_1 + 2be_1) \\ &\quad - \alpha (e_1 (b(q_2 + q_3) - a + 2bq_1) + 2c_1 q_1) \\ J_2 &= 1 - \beta q_2 (2c_2 + 2be_2) \\ &\quad - \beta (e_2 (b(q_1 + q_3) - a + 2bq_2) + 2c_2 q_2) \\ J_3 &= 1 - \gamma q_3 (2c_3 + 2be_3) \\ &\quad - \gamma (e_3 (b(q_1 + q_2) - a + 2bq_3) + 2c_3 q_3). \end{aligned} \quad (14)$$

According to Routh-Hurwitz condition, the necessary and sufficient conditions for equilibrium points to be asymptotically stable are that all roots of the characteristic equations have magnitudes of eigenvalues less than 1.

Remark 1. E_1, E_2, E_3, E_4 are unstable equilibrium points.

As for E_1 , $J_1 = 1 + \alpha a > 1$ is one eigenvalue which corresponds to E_1 , so E_1 is an unstable equilibrium point.

As for E_2 , $J_1 = 1 + \alpha e_1 a (1 - be_2 / (2c_2 + 2be_2)) > 1$ is one eigenvalue which corresponds to E_2 , so E_2 is an unstable equilibrium point. In the same way we can prove that E_3 and E_4 are unstable equilibrium points.

Remark 2. E_5, E_6 , and E_7 are unstable equilibrium points.

As for E_5 , $J_1 = 1 - \alpha (e_1 (b(q_2 + q_3) - a))$ is one eigenvalue which corresponds to E_1 ; set $q_2 = ae_2(2c_3 + be_3)/(4c_2c_3 +$

$4bc_2e_3 + 4bc_3e_2 + 3b^2e_2e_3)$, $q_3 = ae_3(2c_2 + be_2)/(4c_2c_3 + 4bc_2e_3 + 4bc_3e_2 + 3b^2e_2e_3)$, and then $b(q_2 + q_3) - a < 0$, so $J_1 = 1 - \alpha (e_1 (b(q_2 + q_3) - a)) > 1$.

So E_5 is an unstable equilibrium point. In the same way we can prove that E_6 and E_7 are unstable equilibrium points.

From an economic point of view, in the stable state of this dynamic game, no player is forced to withdraw from the market.

As for E_8 , the necessary and sufficient condition of asymptotic stability is that all the eigenvalues are inside the unit circle in complex plane. So a stable system must satisfy the following conditions:

$$\begin{aligned} f(1) &= 1 + A + B + C > 0 \\ -f(-1) &= 1 - A + B - C > 0 \\ C^2 - 1 &< 0 \end{aligned} \quad (15)$$

$$(1 - C^2)^2 - (B - AC)^2 > 0,$$

where $f(\lambda) = \lambda^3 + A\lambda^2 + B\lambda + C = 0$ is the characteristic polynomial at E_8 .

For convenience, we set the parameters as follows:

$$\begin{aligned} a &= 10, \\ b &= 0.2, \\ c_1 &= 0.1, \\ c_2 &= 0.1, \\ c_3 &= 0.1, \\ e_1 &= 0.9, \\ e_2 &= 1.0; \\ e_3 &= 1.1; \end{aligned} \quad (16)$$

and the initial values are chosen as $(1, 1, 1)$.

According to the parameters above,

$$E_8 = (9.4832, 10.0100, 10.4867). \quad (17)$$

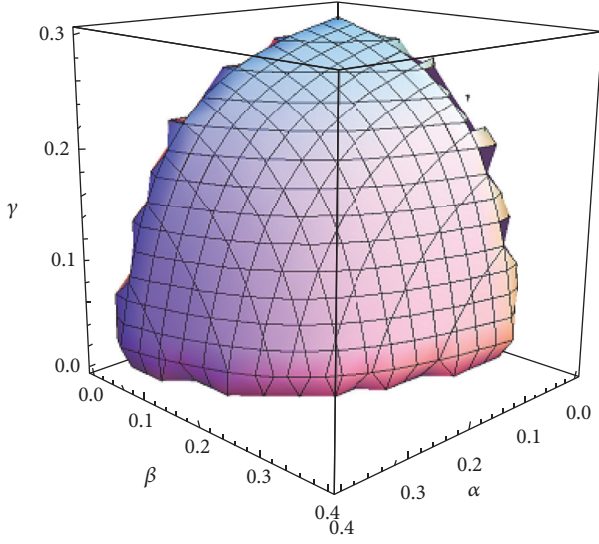


FIGURE 1: The stable region of Nash equilibrium point, $(e_1, e_2, e_3) = (0.9, 1.0, 1.1)$.

Its Jacobian matrix is

$$J(E_8) = \begin{pmatrix} 1.0 - 5.31\alpha & -1.71\alpha & -1.71\alpha \\ -2.0\beta & 1.0 - 6.01\beta & -2.0\beta \\ -2.31\gamma & -2.31\gamma & 1.0 - 6.71\gamma \end{pmatrix}. \quad (18)$$

The characteristic equation of Jacobian matrix (18) is

$$f(\lambda) = \lambda^3 + A_1\lambda^2 + B_1\lambda + C_1 = 0 \quad (19)$$

in which

$$\begin{aligned} A_1 &= (5.31\alpha + 6.01\beta + 6.71\gamma - 3.0) \\ B_1 &= ((6.71\gamma - 1.0)(5.31\alpha + 6.01\beta - 2.0) - 3.42\alpha\beta \\ &\quad - 3.94\alpha\gamma - 4.62\beta\gamma + (5.31\alpha - 1.0)(6.01\beta - 1.0)) \\ C_1 &= 2.31\gamma(3.42\alpha\beta + 1.71\alpha(5.31\alpha - 1.0)) - (3.94\alpha\gamma \\ &\quad + 4.62\beta\gamma)(5.31\alpha + 6.01\beta - 2.0) - (6.71\gamma - 1.0) \\ &\quad \cdot (3.42\alpha\beta - (5.31\alpha - 1.0)(6.01\beta - 1.0)) \\ &\quad + 2.31\gamma(2.0\beta(6.01\beta - 1.0) + 3.42\alpha\beta). \end{aligned} \quad (20)$$

As what can be shown in Figure 1, a stable region in the space of (α, β, γ) is determined by the above inequalities. In the stable region, the final prices of the three oligarchs will stay stable at E_8 after a number of games. From Figure 1, we can see that the market is stable when $\nu \in [0, 1]$, but the market may be unstable when α, β, γ increases. The economic meaning of the stable region is that if (α, β, γ) is in the stable region, prices of three firms will achieve the Nash equilibrium at last.

3.4. The Effects of Parameters e_i on Stable Region. In order to analyze the effects of parameter w on stable region, let

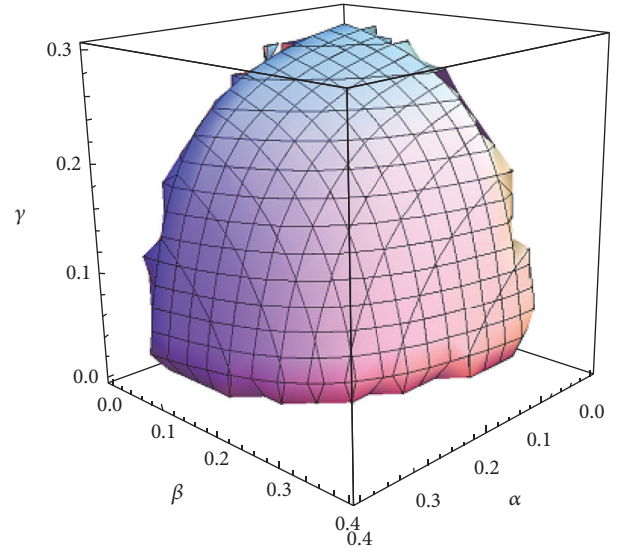


FIGURE 2: The stable region of Nash equilibrium point, $(e_1, e_2, e_3) = (1, 1.1, 1.2)$.

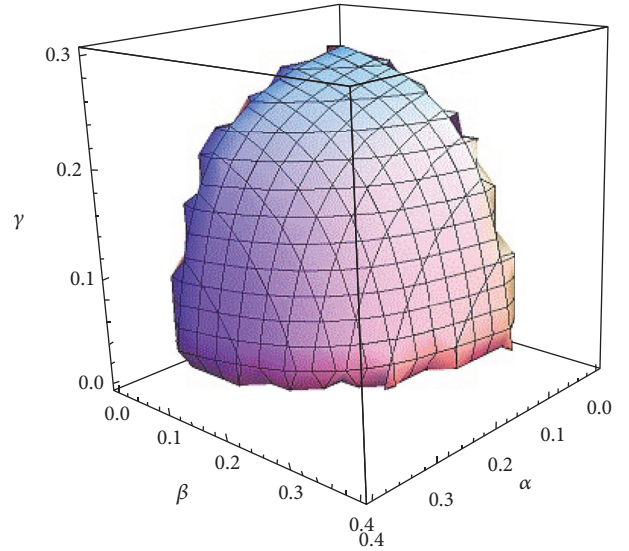


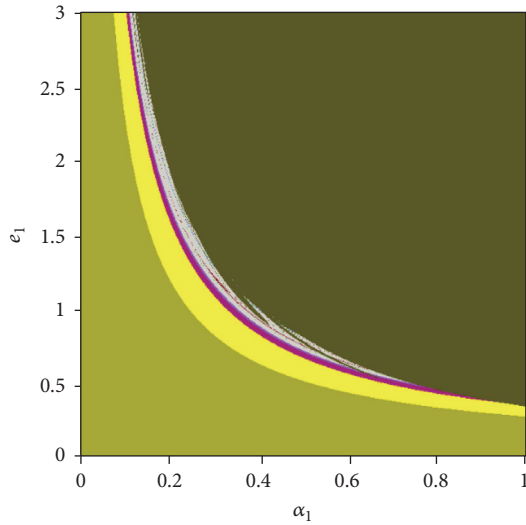
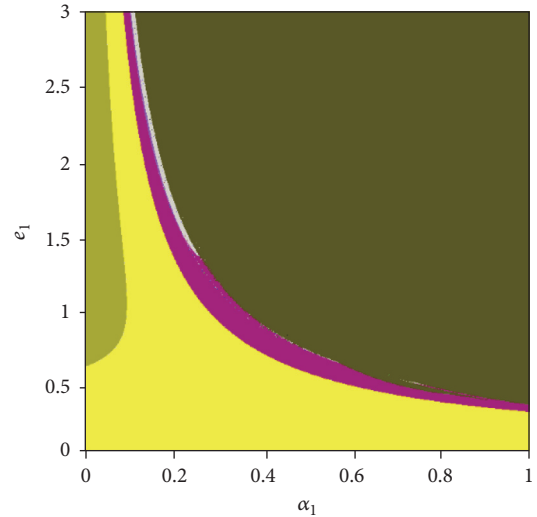
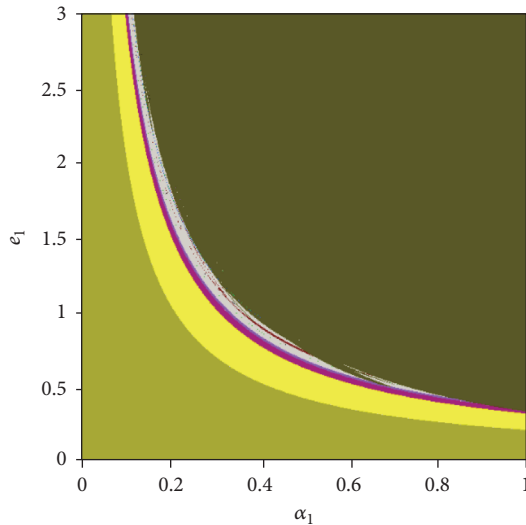
FIGURE 3: The stable region of Nash equilibrium point, $(e_1, e_2, e_3) = (0.8, 0.9, 1)$.

$(e_1, e_2, e_3) = (1, 1.1, 1.2)$ and $(0.8, 0.9, 1)$, respectively; then the corresponding stable region is shown in Figures 2 and 3. From the comparison we find that, with the increase of e_i , the stable region narrows.

From an economic point of view, if the players overestimate the demand, the range of price adjustment speed will be smaller; however if the players underestimate the demand, the range of price adjustment speed will be bigger.

4. Bifurcation Diagrams

4.1. 2D Bifurcation Diagrams and Interactive Relationships between e_1 and α, β , and γ . 2D bifurcation diagram is a more powerful tool in the numerical analysis of nonlinear

FIGURE 4: (e_1, α) -2D bifurcation diagram with $\beta = 0.2$ and $\gamma = 0.1$.FIGURE 6: (e_1, α) -2D bifurcation diagram with $\beta = 0.3$ and $\gamma = 0.1$.FIGURE 5: (e_1, α) -2D bifurcation diagram with $\beta = 0.25$ and $\gamma = 0.1$.

dynamics than a 1D bifurcation diagram. In the 2D bifurcation diagram, bifurcation scenarios and route to chaos can be displayed more clearly. In this section, the 2D bifurcation diagram will be used to analyze the effects of players' adjustment speeds and e_1 on system stability.

For convenience, we choose $e_2 = 1$ and $e_3 = 1.1$ and study the interactive relationships between e_1 and α by 2D bifurcation diagrams.

First let $\gamma = 0.1$ and $\beta = 0.2, 0.25, 0.3$, respectively; then three (α, e_1) 2D bifurcation diagrams are shown in Figures 4, 5, and 6.

In Figures 4–6, different colors are assigned to each region to show the particular behavior of system (7), that is, light green, stable states; yellow, period-2 stable cycles; purple, period-4; gray, chaotic state; dark green, escape.

In the 2D bifurcation diagrams, the system exhibits a sequence of flip bifurcations to chaos (which means that the

market will fall into chaos), then to divergence at last (which means the players will be out of the market).

As seen from Figure 4, if player 1's adjustment speed is relatively slow (in the brown area), the economic system will be in a stable state. Along with the increase in the adjustment speed parameters, the economic system will experience cyclical shocks, chaos, and even disappearance. Obviously, relatively large parameters are detrimental to the economic system.

We can find the following results from Figures 4, 5, and 6,

- (1) We find that, in the stable region in every figure, with the increase in α , the maximum of e_1 decreases; with the increase in e_1 , the maximum of α decreases.
- (2) We find that, with the increase in β , stable region reduces, while escape region does not expand obviously, but period-2 stable cycles expand obviously.

Secondly fix β at 0.1, let $\gamma = 0.2, 0.25, 0.3$, respectively, and then three (α, e_1) 2D bifurcation diagrams can be shown in Figures 7, 8, and 9. Comparing Figures 7, 8, and 9, we find that, with the increasing of γ , stable region reduces, while escape region does not expand obviously, but period-2 stable cycles and period-4 stable cycles expand obviously, from the comparison of Figures 7, 8, and 9, stable region of player 1 reduces when β and γ increase.

Let $\beta = 0.2$ and $\gamma = 0.2$, and then we can get Figure 10.

Comparing Figures 4 and 10, we can find that β and γ are nearly symmetrical and any parameter (β and γ) of changes will make stable region smaller.

4.2. 1D Bifurcation Diagrams and Interactive Attractors. We will display the consistency between 1D bifurcation diagrams and 2D bifurcation diagrams for Figure 10 and show the attractors.

In Figure 10, $\beta = 0.2$ and $\gamma = 0.2$; if e_1 is fixed at 0.9, then we can get the bifurcation diagrams with α in Figure 11, in which blue set of points denotes $p_1(t)$, red set of points

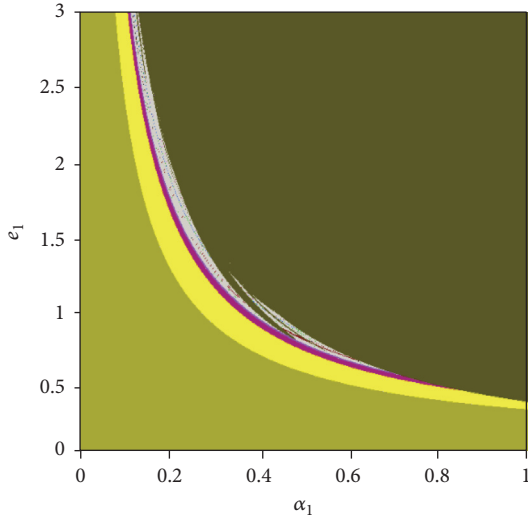


FIGURE 7: (e_1, α) -2D bifurcation diagram with $\beta = 0.1$ and $\gamma = 0.2$.

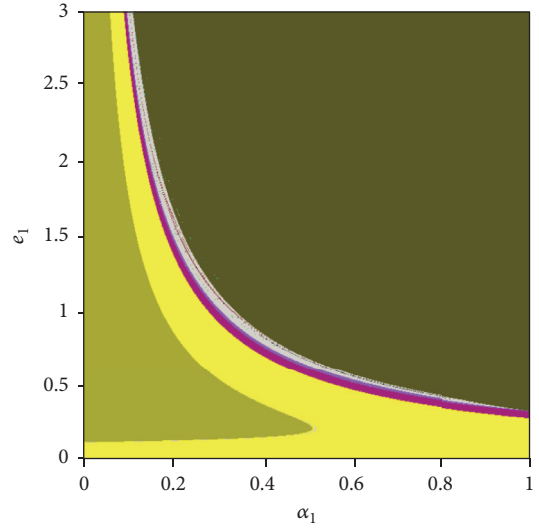


FIGURE 10: (e_1, α) -2D bifurcation diagram with $\beta = 0.2$ and $\gamma = 0.2$.

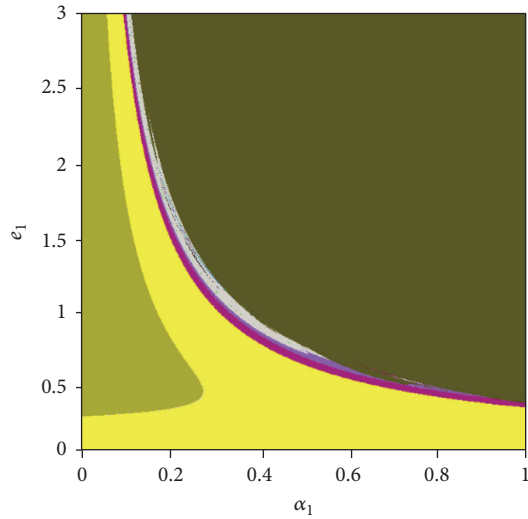


FIGURE 8: (e_1, α) -2D bifurcation diagram with $\beta = 0.1$ and $\gamma = 0.25$.

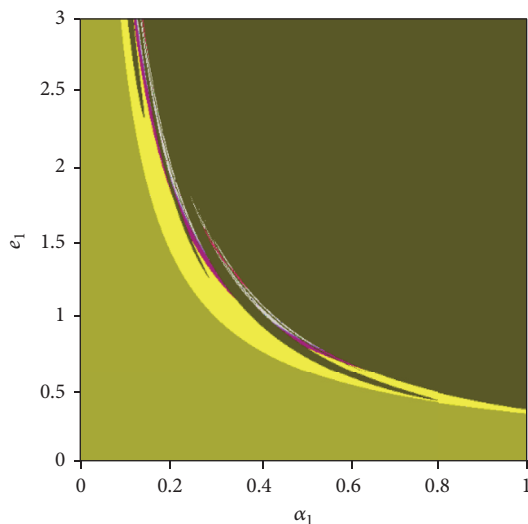


FIGURE 9: (e_1, α) -2D bifurcation diagram with $\beta = 0.1$ and $\gamma = 0.3$.

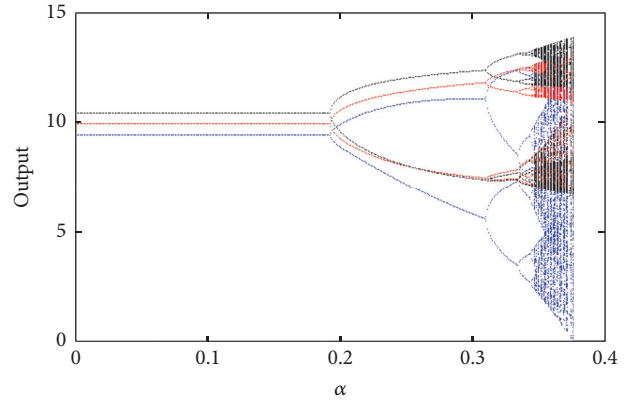


FIGURE 11: Bifurcation diagram with $\alpha, \beta = 0.2$ and $\gamma = 0.2$.

denotes $p_2(t)$, and black set of points denotes $p_3(t)$. As can be seen, system (7) loses its stability when $\alpha = 0.2$, and after a series of flip bifurcations, it falls into chaos when $\alpha = 0.36$, which is consistent with Figure 10. We can find that, with the same cost, the player i with bigger e_i has a higher equilibrium output, and player i with smaller e_i has a lower equilibrium output. We also give the corresponding largest Lyapunov exponent (LLE), which is consistent with Figure 12.

According to Figure 8, when $\alpha = 0.3$ and $\beta = 0.6$, LLE is positive, then system (7) is in chaos, and the chaotic attractor is shown in Figure 13.

From an economic point of view, the appearance of flip bifurcation means market gradually going into the chaotic state from the constant and violent fluctuations.

Under certain conditions, higher e_1 can improve the equilibrium result, as shown in Figure 11. However, it is not to say that the increase in e_1 will certainly increase the equilibrium output, if e_1 goes beyond the stability region. Increase in e_1 may lead to fluctuations in the system and not necessarily can play a role in improving production, which

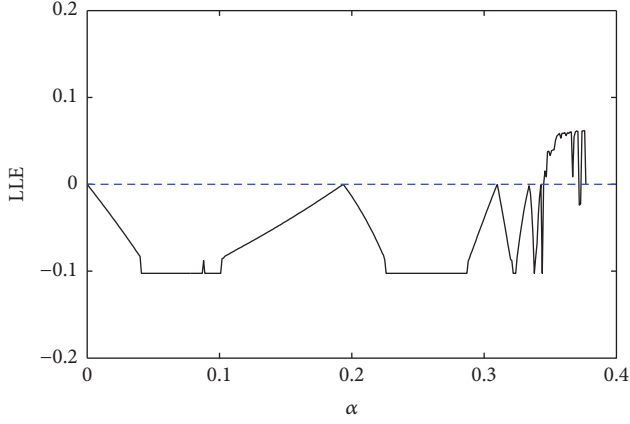


FIGURE 12: Largest Lyapunov exponent with $\alpha, \beta = 0.2$ and $\gamma = 0.2$.

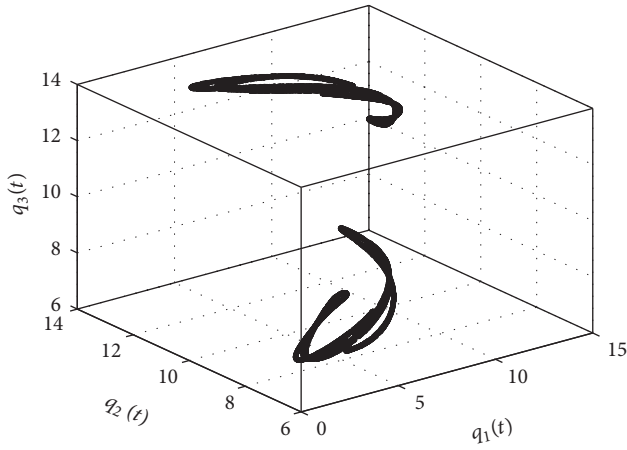


FIGURE 13: The chaotic attractor of system (7) with $\alpha = 0.36, \beta = 0.2$, and $\gamma = 0.2$.

can be seen in Figures 14, 15, and 16. We also find that the increase in e_1 will decrease output of other players.

5. The Effects of e_i on Profits

Next we will discuss the effects of e_i on profits; merge (4)–(7):

$$\begin{aligned}
 q_1(t+1) &= q_1(t) + \alpha q_1(t) \\
 [e_1(a - 2bq_1(t) - b(q_2(t) + q_3(t))) - 2c_1q_1] \\
 q_2(t+1) &= q_2(t) + \beta q_2(t) \\
 [e_2(a - 2bq_2(t) - b(q_1(t) + q_3(t))) - 2c_2q_2] \\
 q_3(t+1) &= q_3(t) + \gamma q_3(t) \\
 [e_3(a - 2bq_3(t) - b(q_2(t) + q_1(t))) - 2c_3q_3] \\
 \pi_1(t) &= e_1(a - b(q_1 + q_2 + q_3))q_1 - c_1q_1^2 \\
 \pi_2(t) &= e_2(a - b(q_1 + q_2 + q_3))q_2 - c_2q_2^2 \\
 \pi_3(t) &= e_3(a - b(q_1 + q_2 + q_3))q_3 - c_3q_3^2.
 \end{aligned} \tag{21}$$

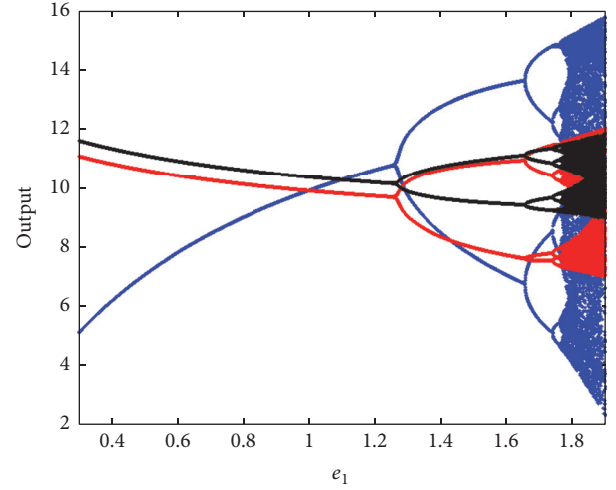


FIGURE 14: Bifurcation diagram with $e_1, \alpha = 0.2, \beta = 0.2$, and $\gamma = 0.1$.

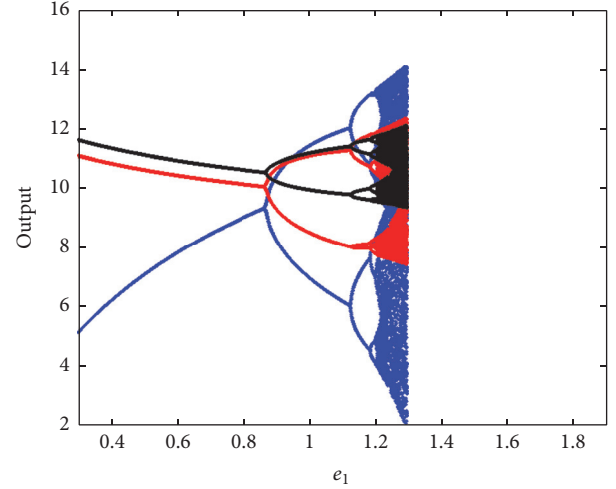


FIGURE 15: Bifurcation diagram with $e_1, \alpha = 0.3, \beta = 0.2$, and $\gamma = 0.1$.

The effects of e_1 on the three firms' profits can be shown in Figures 17–19.

The values of the parameters are the same as above, blue set of points denotes $\pi_1(t)$, red set of points denotes $\pi_2(t)$, and black set of points denotes $\pi_3(t)$.

We can conclude from Figure 17 that if $e_1 < 1.3$, with increase of e_1 , $\pi_1(t)$ increases, $\pi_2(t)$ and $\pi_3(t)$ decrease; when $e_1 > 1.3$, all the firms' profits will lose stability and even fall into chaos. Comparing Figures 15 and 16, we can get Figures 18 and 19.

When the speed of adjustment is accelerated, increase of e_1 may cause the system to lose stability, not necessarily to improve the profit.

An interesting phenomenon is that, compared with bifurcation diagram with e_1 , fluctuations in profits are smaller than fluctuations in output.

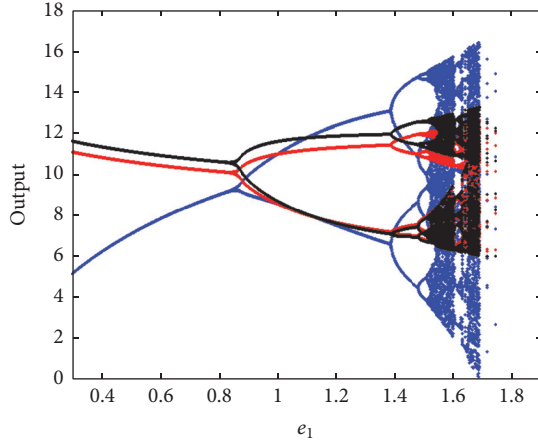


FIGURE 16: Bifurcation diagram with e_1 , $\alpha = 0.2$, $\beta = 0.2$, and $\gamma = 0.2$.

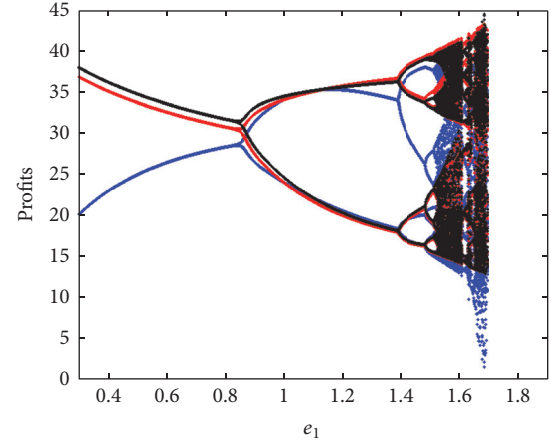


FIGURE 19: Effects of e_1 on profits, $\alpha = 0.2$, $\beta = 0.2$, and $\gamma = 0.2$.

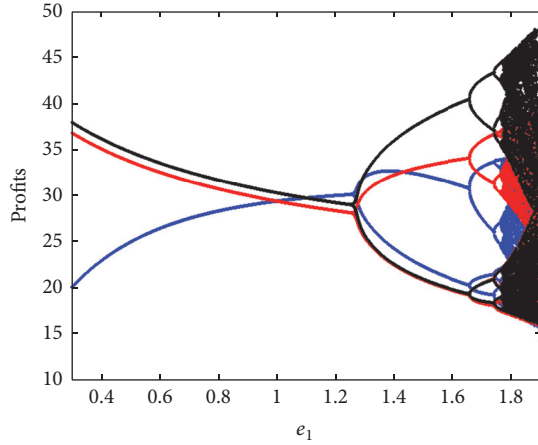


FIGURE 17: Effects of e_1 on profits, $\alpha = 0.2$, $\beta = 0.2$, and $\gamma = 0.1$.

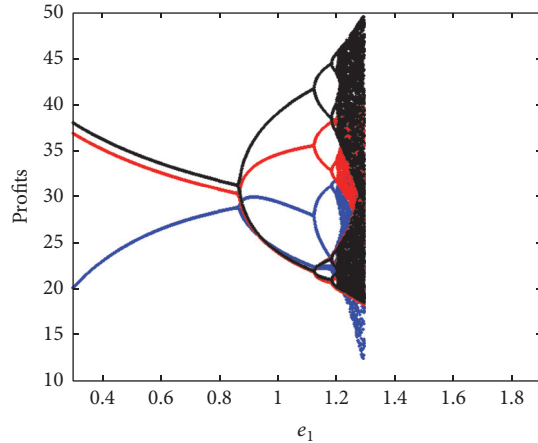


FIGURE 18: Effects of e_1 on profits, $\alpha = 0.3$, $\beta = 0.2$, and $\gamma = 0.1$.

6. Chaos Control

According to the above numerical simulation, we can see that if the firms' price adjustment speeds are beyond the stable region, the market will lose stability and even fall into chaos.

Chaos in the economic systems is harmful to all the firms. In order to avert the risk, it is expedient for prices chosen by Triopoly to maintain at Nash equilibrium.

Many methods for the chaos control have been proposed, such as time-delayed feedback method [18], modified straight-line stabilization method [19], OGY method [20], and pole placement method [21]. In this section, feedback control method proposed by Elabbasy et al. [1] is used, so the controlled system is given by

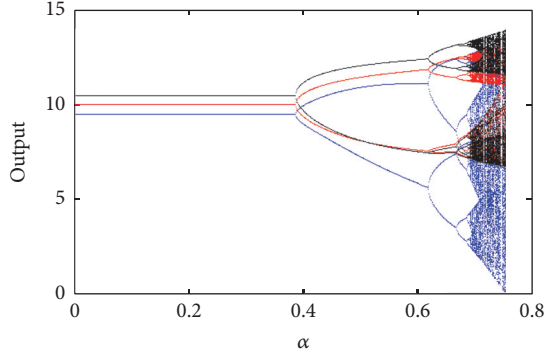
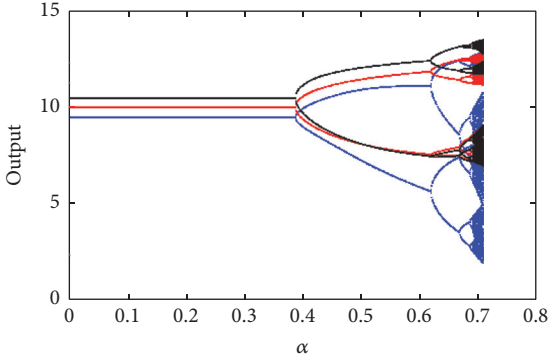
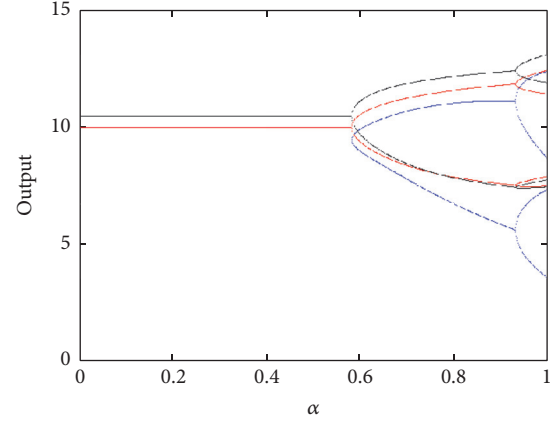
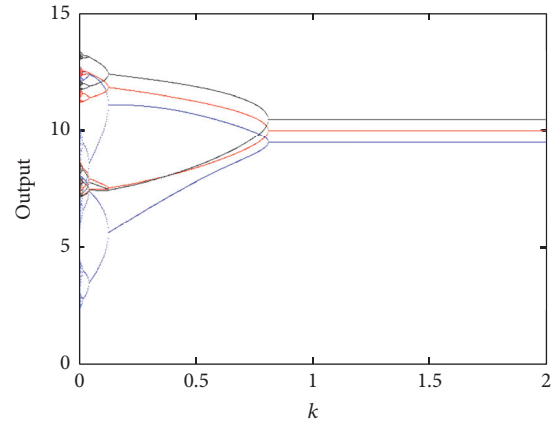
$$\begin{aligned}
 q_1(t+1) &= q_1(t) + \alpha q_1(t) \\
 [e_1(a - 2bq_1(t) - b(q_2(t) + q_3(t))) - 2c_1q_1] \\
 q_2(t+1) &= q_2(t) + \frac{\beta}{k+1}q_2(t) \\
 [e_2(a - 2bq_2(t) - b(q_1(t) + q_3(t))) - 2c_2q_2] \\
 q_3(t+1) &= q_3(t) + \gamma q_3(t) \\
 [e_3(a - 2bq_3(t) - b(q_2(t) + q_1(t))) - 2c_3q_3],
 \end{aligned} \tag{22}$$

where k is the controlling factor and the Jacobian matrix of (22) is given as

$$J = \begin{pmatrix} J_1 & -\alpha be_1q_1 & -\alpha be_1q_1 \\ -\frac{\beta}{k+1}be_2q_2 & \frac{J_2}{k+1} & -\frac{\beta}{k+1}be_2q_2 \\ -\gamma be_3q_3 & -\gamma be_3q_3 & J_3 \end{pmatrix}, \tag{23}$$

where

$$\begin{aligned}
 J_1 &= 1 - \alpha q_1(2c_1 + 2be_1) \\
 &\quad - \alpha(e_1(b(q_2 + q_3) - a + 2bq_1) + 2c_1q_1) \\
 J_2 &= 1 - \beta q_2(2c_2 + 2be_2) \\
 &\quad - \beta(e_2(b(q_1 + q_3) - a + 2bq_2) + 2c_2q_2) \\
 J_3 &= 1 - \gamma q_3(2c_3 + 2be_3) \\
 &\quad - \gamma(e_3(b(q_1 + q_2) - a + 2bq_3) + 2c_3q_3).
 \end{aligned} \tag{24}$$

FIGURE 20: Bifurcation diagram with α , $k = 0.5$.FIGURE 21: Bifurcation diagram with α , $k = 1$.FIGURE 22: Bifurcation diagram with α , $k = 2$.FIGURE 23: Bifurcation diagram with the controlling factor k , $\alpha = 0.35$, $\beta = 0.2$, and $\gamma = 0.2$.

In the practice market, k can be considered as the learning ability or adaptability of firm 2. For example, firm 2 analyzed the information in the past and adjusted the speed of price. As what can be seen from Figures 20, 21, and 22, the chaos can be delayed and even eliminated with proper k . As for Figure 11, set $k = 0.5, 1, 2$, respectively; we can get Figures 20–22.

As can be seen, with the increase of the control factor k , the emergence of bifurcation is delayed. So if the second bounded rational player adopts this adjustment method, the price game can reach equilibrium state finally.

Let $\alpha = 0.35$, $\beta = 0.2$, and $\gamma = 0.2$, according to Figure 11; the system is in chaos, if α , β , and γ are fixed, and player 2 changes the controlling factor k ; we can get the following bifurcation diagram with the controlling factor k . As can see from Figure 23, when $k < 0.028$, the system is in a chaotic state, when $0.029 \leq k \leq 0.030$, the system is in a 16-period cycle, when $0.031 \leq k \leq 0.037$, the system is in 8-period cycle, when $0.038 \leq k \leq 0.16$, the system is in a 4-period cycle, when $0.16 \leq k \leq 0.76$, the system is in a 2-period cycle state, and the system reaches equilibrium state when $k \leq 0.76$.

7. Global Stability of the System

In order to investigate the impact of price adjustment speed on the global stability, we introduced basins of attraction, which include attraction domain, attractor, and escaping area. Let $(e_1, e_2) = (1, 1)$, and fix q_3 at 10, 7, 5. We make basins of attraction with initial output q_1 and q_2 .

The attraction domain is the set of initial output where the same attractor will emerge after a series of iteration if the initial price is taken from the attraction domain. As for the attractor, if it is one equilibrium point, from an economic point of view, the corresponding attraction domain will be a safe region, which means that if the initial output of two sides is in the safe region, the system will remain stable after iteration. If the initial price is in the escape area, the system will fall into divergence at last.

By fixing the system parameters as mentioned above and setting $(\alpha, \beta) = (0.3, 0.1), (0.3, 0.25)$, respectively, six basins of attraction about (p_1, p_2) of the system are shown in Figures 24–29 in which the green region denotes attraction domain, the red set of points denotes attractor, and the blue set of points denotes escape area.

In Figure 24, when $\alpha = 0.3$, $\beta = 0.1$, and $q_3 = 10$, the system is in 2-period cycle, and we can see that the attraction domain is an irregular hexagon. In Figure 25, when $\alpha = 0.3$, $\beta = 0.25$, and $q_3 = 10$, the system is in period-2 state, which means that if the initial prices of two sides are in this attraction domain, then outputs will oscillate between two points at last. The attraction domain is also an irregular pentagon area and chaotic attractor appears. In Figure 26, when $\alpha = 0.3$, $\beta = 0.1$, and $q_3 = 7$, the system is in 2-period

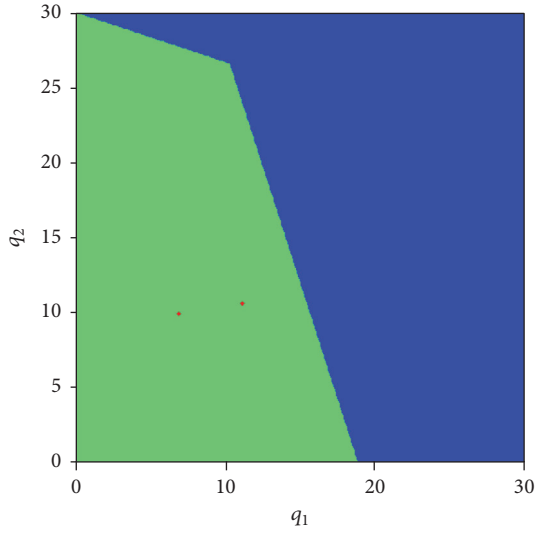


FIGURE 24: Basins of attraction, $\alpha = 0.3$, $\beta = 0.1$, and $q_3 = 10$.

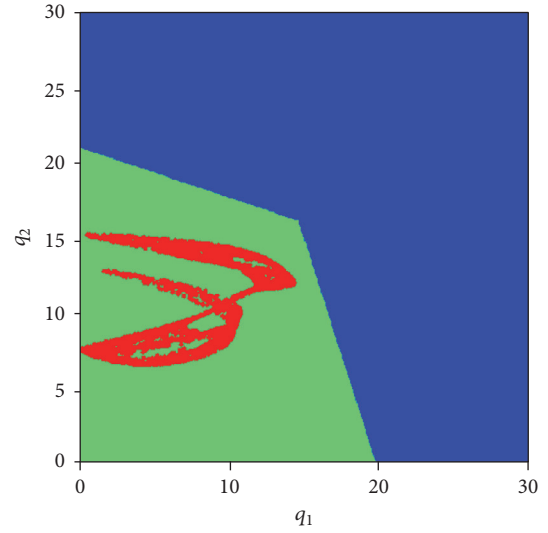


FIGURE 27: Basins of attraction, $\alpha = 0.3$, $\beta = 0.25$, and $q_3 = 7$.

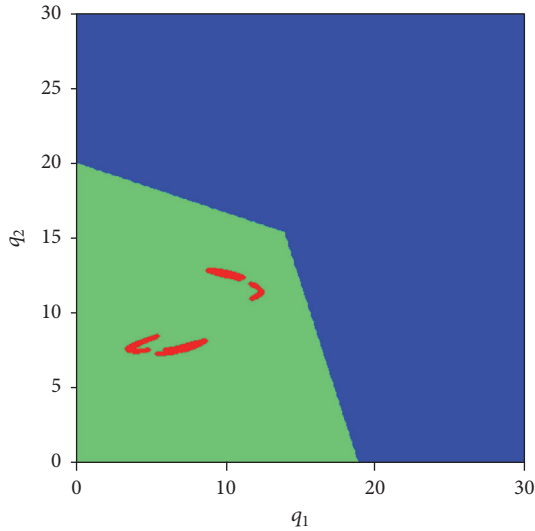


FIGURE 25: Basins of attraction, $\alpha = 0.3$, $\beta = 0.25$, and $q_3 = 10$.

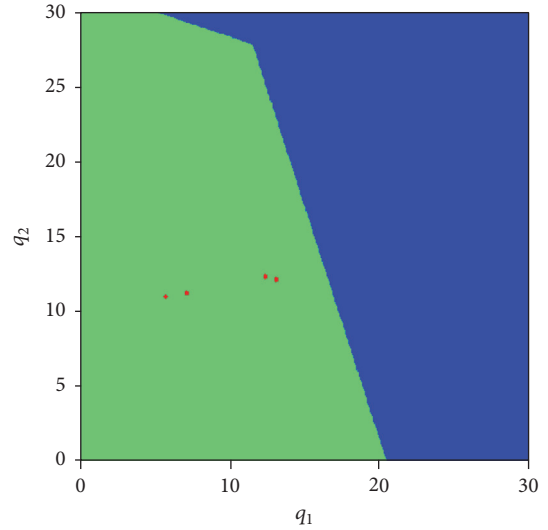


FIGURE 28: Basins of attraction, $\alpha = 0.3$, $\beta = 0.1$, and $q_3 = 5$.

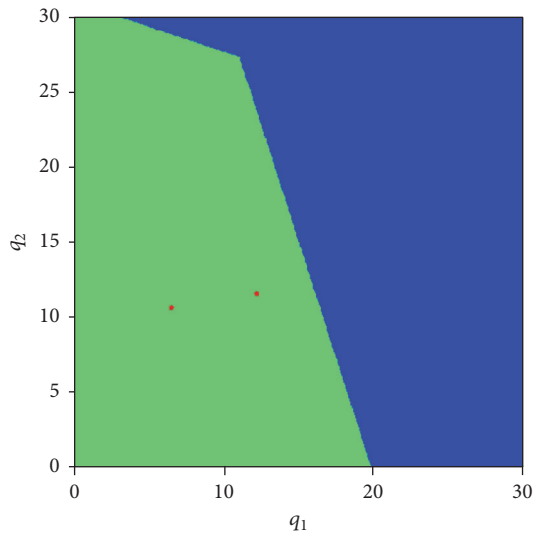


FIGURE 26: Basins of attraction, $\alpha = 0.3$, $\beta = 0.1$, and $q_3 = 7$.

cycle. In Figure 27, when $\alpha = 0.3$, $\beta = 0.25$, and $q_3 = 7$, the system is in chaos. In Figure 28, when $\alpha = 0.3$, $\beta = 0.1$, and $q_3 = 5$, the system is in 4-period cycle. In Figure 29, when $\alpha = 0.3$, $\beta = 0.25$, and $q_3 = 5$, the system is in chaos.

Comparing Figures 24–29, we find that the attraction domain reduces with the increase of price modification speed. Obviously, when β of player 2 increases, in the attraction domain, the range of q_2 reduces. We can also find that, with increase of q_3 , attraction domain reduces, although not so obvious.

From an economic perspective, the initial outputs of firm 1 and 2 should be lower in order to maintain market stability.

8. Conclusion

In this paper, Triopoly game with inaccurate demand beliefs is considered. Suppose all the firms as bounded rationally

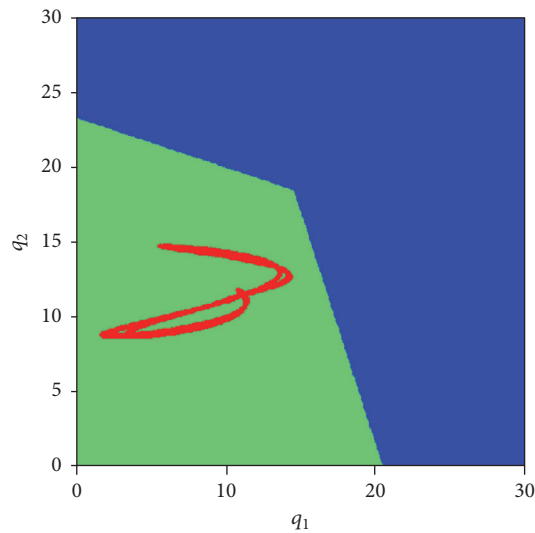


FIGURE 29: Basins of attraction, $\alpha = 0.3$, $\beta = 0.25$, and $q_3 = 5$.

players with demand evaluation bias. Equilibrium output is negatively related to players' costs; the value of e_i is negatively related to range of stability.

2D bifurcation diagram is introduced and we find that with the increase of output modification speed or e_i , the system will fall into chaos via period-doubling bifurcations. Increase in e_1 will increase equilibrium output q_1 while decreasing equilibrium output of other players.

Basins of attraction are investigated and results show that if a player speeds up his own output adjustment, the output of this player in the attraction domain will become smaller. In order to maintain market stability, a firm's output must be kept within a certain range. Feedback control method is used to help the system to keep at an equilibrium state.

Conflicts of Interest

The authors declare that they have no competing financial interests.

Acknowledgments

The research was supported by the National Natural Science Foundation of China (no. 71571131) and Tianjin University Innovation Fund.

References

- [1] E. M. Elabbasy, H. N. Agiza, and A. A. Elsadany, "Analysis of nonlinear triopoly game with heterogeneous players," *Computers & Mathematics with Applications*, vol. 57, no. 3, pp. 488–499, 2009.
- [2] J. Ma and Y. Liu, "Exact solutions for a generalized nonlinear fractional Fokker-Planck equation," *Nonlinear Analysis: Real World Applications*, vol. 11, no. 1, pp. 515–521, 2010.
- [3] M. T. Yassen and H. N. Agiza, "Analysis of a duopoly game with delayed bounded rationality," *Applied Mathematics and Computation*, vol. 138, no. 2-3, pp. 387–402, 2003.
- [4] J. Ma and W. Ren, "Complexity and Hopf bifurcation analysis on a kind of fractional-order IS-LM macroeconomic system," *International Journal of Bifurcation and Chaos*, vol. 26, no. 11, pp. 1–11, 2016.
- [5] F. Tramontana and A. E. Elsadany, "Heterogeneous triopoly game with isoelastic demand function," *Nonlinear Dynamics*, vol. 68, no. 1-2, pp. 187–193, 2011.
- [6] J.-H. Ma and W.-Z. Ji, "Complexity of repeated game model in electric power triopoly," *Chaos, Solitons and Fractals*, vol. 40, no. 4, pp. 1735–1740, 2009.
- [7] J. Ma and K. Wu, "Complex system and influence of delayed decision on the stability of a triopoly price game model," *Nonlinear Dynamics*, vol. 73, no. 3, pp. 1741–1751, 2013.
- [8] J. Ma and X. Pu, "The research on Cournot-Bertrand duopoly model with heterogeneous goods and its complex characteristics," *Nonlinear Dynamics*, vol. 72, no. 4, pp. 895–903, 2013.
- [9] G.-I. Bischi, C. Chiarella, and M. Kopel, "The long run outcomes and global dynamics of a duopoly game with misspecified demand functions," *International Game Theory Review*, vol. 6, no. 3, pp. 343–379, 2004.
- [10] H. Wang and J. Ma, "Complexity analysis of a cournot-bertrand duopoly game model with limited information," *Discrete Dynamics in Nature and Society*, vol. 2013, Article ID 287371, 6 pages, 2013.
- [11] G.-I. Bischi, L. Sbragia, and F. Szidarovszky, "Learning the demand function in a repeated cournot oligopoly game," *International Journal of Systems Science*, vol. 39, no. 4, pp. 403–419, 2008.
- [12] Y. Guo and J. Ma, "Research on game model and complexity of retailer collecting and selling in closed-loop supply chain," *Applied Mathematical Modelling*, vol. 37, no. 7, pp. 5047–5058, 2013.
- [13] Z. Qiu, N. Gui, and G. Deconinck, "Analysis of dynamic game played with inaccurate demand beliefs," *Applied Mathematics and Computation*, vol. 230, pp. 530–541, 2014.
- [14] L. Sun and J. Ma, "Study and simulation on discrete dynamics of Bertrand triopoly team-game," *Mathematical Problems in Engineering*, vol. 2015, Article ID 960380, 12 pages, 2015.
- [15] I. Manimehan and P. Philominathan, "Composite dynamical behaviors in a simple series-parallel LC circuit," *Chaos, Solitons & Fractals*, vol. 45, no. 12, pp. 1501–1509, 2012.
- [16] Z. Zhang, J. Wu, Y. Suo, and X. Song, "The domain of attraction for the endemic equilibrium of an SIRS epidemic model," *Mathematics and Computers in Simulation*, vol. 81, no. 9, pp. 1697–1706, 2011.
- [17] J. X. Zhang, Q. L. Da, and Y. H. Wang, "Analysis of nonlinear duopoly game with heterogeneous players," *Economic Modelling*, vol. 24, no. 1, pp. 138–148, 2007.
- [18] H. N. Agiza, "On the analysis of stability, bifurcation, chaos and chaos control of Kopel map," *Chaos, Solitons & Fractals*, vol. 10, no. 11, pp. 1909–1916, 1999.
- [19] J. Du, T. Huang, and Z. Sheng, "Analysis of decision-making in economic chaos control," *Nonlinear Analysis. Real World Applications*, vol. 10, no. 4, pp. 2493–2501, 2009.
- [20] J. A. Holyst and K. Urbanowicz, "Chaos control in economical model by time-delayed feedback method," *Physica A: Statistical Mechanics and its Applications*, vol. 287, no. 3-4, pp. 587–598, 2000.
- [21] A. Matsumoto, "Controlling the cournot-nash chaos," *Journal of Optimization Theory and Applications*, vol. 128, no. 2, pp. 379–392, 2006.

Research Article

Autaptic Modulation of Electrical Activity in a Network of Neuron-Coupled Astrocyte

Shengli Guo,¹ Jun Tang,² Jun Ma,^{1,3} and Chunni Wang¹

¹Department of Physics, Lanzhou University of Technology, Lanzhou 730050, China

²School of Physics, China University of Mining and Technology, Xuzhou 221116, China

³NAAM-Research Group, Department of Mathematics, Faculty of Science, King Abdulaziz University, P.O. Box 80203, Jeddah 21589, Saudi Arabia

Correspondence should be addressed to Jun Ma; hyperchaos@163.com

Received 10 April 2017; Accepted 9 May 2017; Published 5 June 2017

Academic Editor: Christos Volos

Copyright © 2017 Shengli Guo et al. This is an open access article distributed under the Creative Commons Attribution License, which permits unrestricted use, distribution, and reproduction in any medium, provided the original work is properly cited.

Autapse connection is considered on a biological neuron coupled by astrocyte, and the effect of autapse driving-induced response in electrical activities is investigated. In this paper, a simple network is developed on the Hodgkin-Huxley (HH) neuron coupled by astrocyte and the autapse effect is also considered. The modulation of autapse connected to HH neuron can change the membrane potential by applying time-delayed feedback along a close loop. It is found that the self-adaption of autapse driving can make the network of neuron-astrocyte generate different modes of electrical activities, and oscillating behavior of Ca^{2+} and IP_3 setting is controlled. This new network model can give potential understanding about self-adaption of neuron to external forcing when the coupling of astrocyte and autapse is considered.

1. Introduction

It is ever believed that neuron is the most important basic unit of nerve system, and many experimental evidences have confirmed that gliocyte, particularly, astrocyte, can play an important role in changing the fluctuation of membrane potential of neuron by adjusting the concentration of Ca^{2+} via IP_3 (inositol triphosphate) [1–3]. It is also found that astrocyte can format the inputting and activity of synapse [4, 5] and regulate the processing propagation of electrical signal in neurons [6–9]. Autapse [10–15] is often connected to some moderate neurons, and the feedback on membrane potential is realized by adding time-delayed forcing current on the membrane, where autapse is a specific synapse connected to the neuron via close loop. When autapse connection is triggered, the electrical activities and dynamical response will be changed [16–18]. Furthermore, autapse driving in the network can regulate the collective behaviors of network by generating continuous pulse or wave fronts, thus synchronization; pattern selection can be realized [19–22]. Readers can find brief survey for neurodynamics and dynamics in

neuronal network in [23] and references therein. The author of this paper ever explained the formation mechanism of autapse connection to neuron; it is argued that formation of autapse can be helpful to enhance signal propagation along an auxiliary loop; thus autapse is developed [24]; then time delay and feedback gain are used to describe the properties of this loop. On the other hand, the electrical activities of neurons can be changed when neurons or neuronal tissue are exposed to electromagnetic radiation; for example, failure in heart induced by electromagnetic radiation [25] is discussed. In fact, complex electromagnetic induction is triggered in neurons during the exchange of ions current across membrane because the distribution of charged ions is changed. Therefore, Lv et al. suggested that magnetic flux [26, 27] can be used to detect the effect of electromagnetic induction and further for the effect of electromagnetic radiation [28]. Furthermore, Xu et al. argued [29] that autaptic driving can be helpful for neuron to suppress the electromagnetic radiation. Therefore, it is important to further discuss the network connection of neurons that the self-adaption of autapse connection can be understood.

In fact, most of the previous works about neurodynamics have discussed the neuron-coupled astrocyte model [30–34] and some results could be helpful to understand the occurrence of seizure-like behavior [35]. Based on the well-known neuron models, networks with different topological connections have been set to investigate the synchronization stability [36, 37], pattern selection, and mode transition in collective behaviors [38–45]. Indeed, reliable and biophysical neuron model is critical and important for further investigation on neurodynamics and potential mechanism of some neuronal diseases [46]. Therefore, it is interesting to set a more reliable neuron model that the effect of autapse driving and astrocyte on electrical activities can be explored. In this paper, we propose an improved neuron model coupled by astrocyte and autapse connection is also considered. The modulation of autapse driving on electrical activities in astrocyte-coupled neuron will be discussed, and the exchange of signal between astrocyte and neurons can be detected and understood.

2. Model Setting and Description

For simplicity but biophysical meaning, Hodgkin-Huxley neuron model will be driven by autaptic current, and additive modulation from astrocyte will be considered; it reads as follows:

$$\begin{aligned}
 C_m \frac{dV}{dt} &= g_k n^4 (V_k - V) + g_{Na} m^3 h (V_{Na} - V) \\
 &\quad + g_L (V_L - V) + I_{ext} + I_{astro} + I_{aut} \\
 \frac{dm}{dt} &= \alpha_m (V) (1 - m) - \beta_m (V) m \\
 \frac{dh}{dt} &= \alpha_h (V) (1 - h) - \beta_h (V) h \\
 \frac{dn}{dt} &= \alpha_n (V) (1 - n) - \beta_n (V) n,
 \end{aligned} \tag{1}$$

where the coefficients [7] for (1) are defined by

$$\begin{aligned}
 \alpha_m &= 0.1 \frac{25 - V}{\exp [(25 - V) / 10] - 1}; \\
 \beta_m &= 4 \exp \left[\frac{-V}{18} \right]; \\
 \alpha_h &= 0.07 \exp \left[\frac{-V}{20} \right]; \\
 \beta_h &= \frac{1}{\exp [(30 - V) / 10] + 1}; \\
 \alpha_n &= 0.01 \frac{10 - V}{\exp [(10 - V) / 10] - 1}; \\
 \beta_n &= 0.125 \exp \left[\frac{-V}{80} \right],
 \end{aligned} \tag{2}$$

where V is the membrane potential, m, n, h are the gate variable, and I_{ext} denotes an external forcing current, respectively.

I_{aut} represents the autaptic current from autapse connection to the neuron, and in case of electric autapse driving, the autaptic current is calculated as follows:

$$I_{aut} = g_e (V(t - \tau) - V(t)), \tag{3}$$

where g_e and τ are the feedback gain and time delay, respectively. Positive feedback is triggered to excite and enhance the oscillating behavior by setting negative values for g_e , while positive value for g_e can generate negative feedback to suppress the excitability and bursting behaviors in neuron. I_{astro} defines the additive forcing current generated by astrocyte which changes the concentration of calcium and inositol triphosphate (IP_3) via adjusting the neurotransmitter such as ATP and glutamic acid. The modulation for concentration of IP_3 can be approached by

$$\begin{aligned}
 \frac{d [IP_3]}{dt} &= \frac{1}{\tau_{IP_3}} ([IP_3]^* - [IP_3]) \\
 &\quad + r_{IP_3} \Theta (V - 50.0 \text{ mV}),
 \end{aligned} \tag{4}$$

where $[IP_3]^*$ is the concentration of IP_3 under equilibrium state and the parameter r_{IP_3} represents the response efficiency of astrocyte to action potential, also called production ratio for IP_3 . That is, the larger r_{IP_3} , the larger density of distribution of mGluR on the membrane. $\Theta(*)$ is Heaviside function; as a result, the astrocyte can change the electrical activities of neuron and generate IP_3 when the action potential or membrane potential is beyond 50 mV. The fluctuation of IP_3 makes the receptor of IP_3 trigger release of calcium ion; thus concentration of calcium ion $[Ca^{2+}]$ began to oscillate. For simplicity, Li-Rinzel [47] model is used to describe the oscillating of $[Ca^{2+}]$; it is often calculated by

$$\begin{aligned}
 \frac{d [Ca^{2+}]}{dt} &= -J_{Channel}(q) - J_{Pump} - J_{Leak} \\
 \frac{dq}{dt} &= \alpha_q (1 - q) - \beta_q q,
 \end{aligned} \tag{5}$$

where $J_{Channel}(q)$ denote the calcium ion flux emitted from endoplasmic reticulum to cytoplasm via channels of IP_3 receptor and thus the concentration of calcium ion is increased. J_{Pump} is ATP-independent pump flux that calcium ion is pumped into calcium store. J_{Leak} is leakage current from endoplasmic reticulum to cytoplasm. Order parameter q is

the gate variable that calculates the open probability of ion channels. The calcium flux [34] is described by

$$\begin{aligned}
J_{\text{Channel}}(q) &= c_1 v_1 m_{\infty}^3 n_{\infty}^3 q^3 \left([\text{Ca}^{2+}] - [\text{Ca}^{2+}]_{\text{ER}} \right); \\
J_{\text{Pump}} &= \frac{v_3 [\text{Ca}^{2+}]^2}{k_3^2 + [\text{Ca}^{2+}]^2}; \\
J_{\text{Leak}} &= c_1 v_2 \left([\text{Ca}^{2+}] - [\text{Ca}^{2+}]_{\text{ER}} \right); \\
m_{\infty} &= \frac{[\text{IP}_3]}{[\text{IP}_3] + d_1}; \\
n_{\infty} &= \frac{[\text{Ca}^{2+}]}{[\text{Ca}^{2+}] + d_5}; \\
\alpha_q &= a_2 d_2 \frac{[\text{IP}_3] + d_1}{[\text{IP}_3] + d_3}; \\
\beta_q &= a_2 [\text{Ca}^{2+}].
\end{aligned} \tag{6}$$

And the forcing current from astrocyte is often approached by [30]

$$\begin{aligned}
I_{\text{astro}} &= 2.11 \Theta(\ln y) \ln y; \\
y &= [\text{Ca}^{2+}] / \text{nM} - 196.69.
\end{aligned} \tag{7}$$

As reported in [48–50], many chemical neurotransmitters are released to gaps of cells when the concentration of calcium ions is increased; for example, it is argued that the release of glutamic acid can trigger the release of calcium ions. However, blocking the transmission of glutamic acid between astrocytes seldom prevents the release of glutamic acid induced by increase of calcium ion concentration; it could account that glutamic acid comes from the interior of cells. It is believed that concentration increase in calcium ions is necessary setting to trigger the release of glutamic acid. When glutamic acid is released to gaps of cells, it is used as neurotransmitter to act on the ionophilic receptors (NMDA, AMPA), and depolarization of neuron occurs to trigger an action potential; as a result, signal propagation from synapse is regulated. It is found in [50] that slow introverted currents (SICs) via NMDA receptor can connect to thalamus neurons when pulse induced by Ca^{2+} oscillating in concentration was released and propagated to gaps between cells. For simplicity, the forcing current associated with astrocyte dependence on calcium concentration is approached in (7) described as above. The physical unit in astrocyte for calcium ions is $\mu\text{mol/L}$, pA is used for current, and the cell or neuron is described as a sphere with a radius about $25 \mu\text{m}$, and the density of current of I_{astro} is $\mu\text{mol/L}\cdot\text{cm}^2$ to be consistent with the physical units in Hodgkin-Huxley neuron model. For detailed description, Table 1 gives the parameter setting and physical units.

TABLE 1: Parameter values setting.

Parameter	Value and meaning
C_m	$1 \mu\text{F}/\text{cm}^2$
g_K	$36.0 \text{ ms}/\text{cm}^2$
g_{Na}	$120.0 \text{ ms}/\text{cm}^2$
g_L	$0.3 \text{ ms}/\text{cm}^2$
V_K	-12.0 mV
V_{Na}	115.0 mV
V_L	10.6 mV
$[\text{IP}_3]^*$	160.0 nmol/L
$1/\tau_{\text{IP}_3}$	0.00014 (m/s)
c_0	$2.0 \mu\text{mol/L}$
c_1	0.185
v_1	6 s^{-1}
v_2	0.11 s^{-1}
v_3	$0.9 \mu\text{mol/L}\cdot\text{s}$
k_3	$0.1 \mu\text{mol/L}$
d_1	$0.13 \mu\text{mol/L}$
d_2	$1.049 \mu\text{mol/L}$
d_3	$0.9434 \mu\text{mol/L}$
d_5	$0.08234 \mu\text{mol/L}$
a_2	$0.2 \mu\text{mol/L}\cdot\text{s}$
r_{IP_3}	Response efficiency of astrocyte to action potential
g_e	Feedback gain in autapse
τ	Time delay in autapse

3. Numerical Results and Discussion

The fourth-order Runge-Kutta algorithm is presented to find numerical solution of membrane potential with time step 0.001. The parameter r_{IP_3} is set to change different values, and the electric autapse driving is considered. Then the dynamical response in action potential is investigated to explore the possible biological function of autapse connection in the astrocyte-coupled neuron network. At first, the autapse connection is switched off, the external forcing is imposed on neuron as $I_{\text{ext}} = 10.0 \mu\text{mol/L}\cdot\text{cm}^2$ at $t < 40 \text{ s}$, the calcium concentration of astrocyte and IP_3 is calculated at $r_{\text{IP}_3} = 0.2$, and the results are plotted in Figure 1.

It is found that the membrane potential is decreased to quiescent state when the external forcing current is removed and the oscillating in Ca^{2+} is also stabilized, the mechanism is that astrocyte and neuron are coupled with weak intensity, insufficient IP_3 is not effective to trigger continuous oscillation in calcium concentration, and the exchange of transmembrane current is suppressed. Now, the effect of autapse connection and driving is considered by activating the autapse connection; for example, time delay in electric autapse is set $\tau = 2$, and positive feedback is investigated in Figure 2 by setting different feedback gains in the autapse.

It is found that the membrane potentials of neuron begin to fluctuate when the feedback gain in the electric autapse is increased beyond the threshold ($g_e = -0.48$); furthermore, the IP_3 and Ca^{2+} follow its oscillating behavior to modulate the membrane potential greatly. The potential

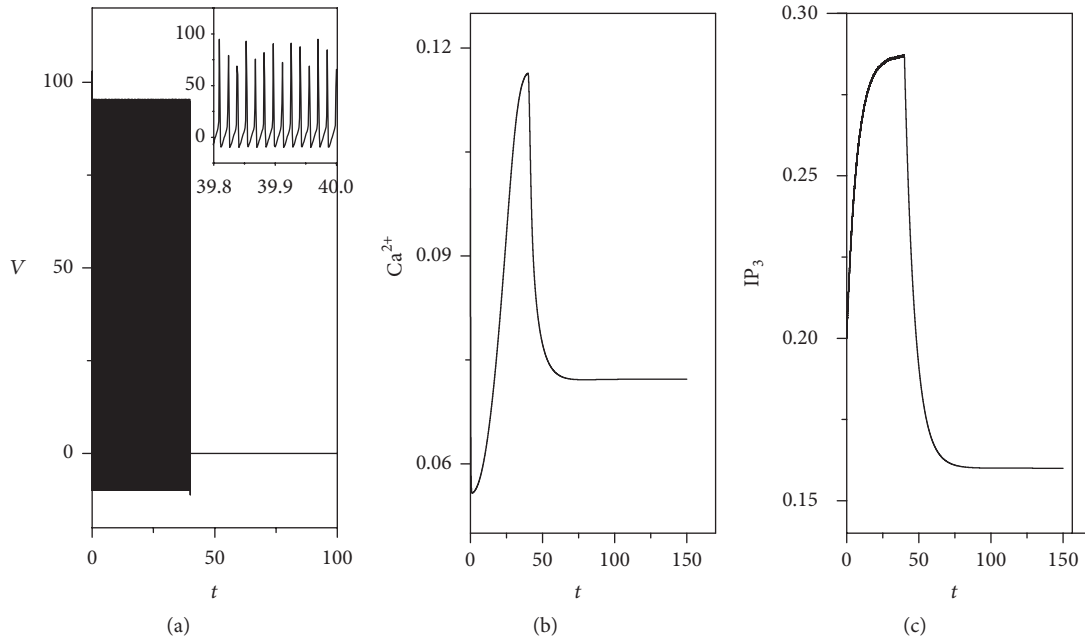


FIGURE 1: Sampled time series for membrane potential (a), calcium concentration in astrocyte (b), and IP_3 in astrocyte (c), $r_{IP_3} = 0.2$, and the external forcing current regulates the neuronal activities by setting $I_{ext} = 10.0 \mu\text{mol/L}\cdot\text{cm}^2$ at $t < 40$ s; the autaptic current is set as zero.

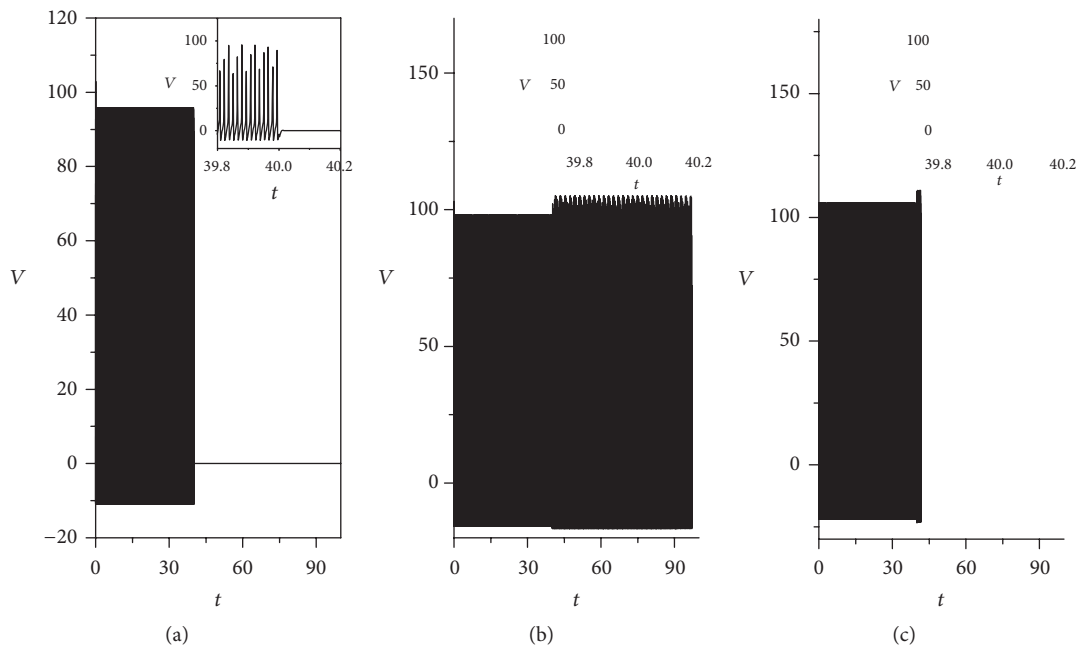


FIGURE 2: Sampled time series for membrane potential of neuron coupled by astrocyte when autapse driving is considered at $\tau = 2$, for (a) $g_e = -0.1$, (b) $g_e = -0.5$, and (c) $g_e = -1.0$. The parameter is set as $r_{IP_3} = 0.2$, and inserted figures are enlarged ones. And the external forcing current regulates the neuron by $I_{ext} = 10.0 \mu\text{mol/L}\cdot\text{cm}^2$ at $t < 40$ s.

mechanism is that positive feedback in autapse connection to neuron remembers the previous stimuli and continuous stimuli imposed on neuron can be effective to enhance the excitability of neuron, and then the neuron is excited. Furthermore, the oscillation of Ca^{2+} and changes of IP_3 are calculated in Figure 3.

The results in Figure 3 confirmed that enough high concentration in IP_3 is critical to trigger and enhance continuous oscillation of Ca^{2+} when electric autapse is set with strong feedback gain being applied. When the external forcing current is removed, the concentration of IP_3 is decreased quickly because continuous release of neurotransmitter occurs in

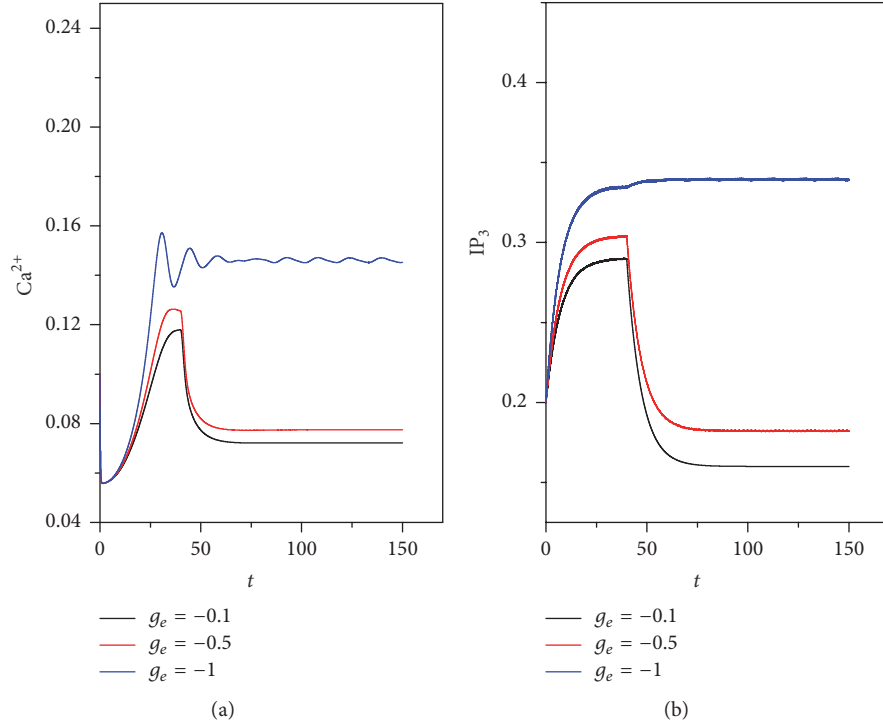


FIGURE 3: Fluctuation in Ca^{2+} concentration and IP_3 concentration is calculated by applying different feedback gains g_e in electric autapse with time delay $\tau = 2$. The parameter is set as $r_{\text{IP}_3} = 0.2$. And the external forcing current regulates the neuron by setting $I_{\text{ext}} = 10.0 \mu\text{mol/L}\cdot\text{cm}^2$ at $t < 40$ s.

presence of external stimuli beyond threshold. The interaction between neurotransmitter and metabolic receptor of astrocyte (mGluRs) can produce more IP_3 ; as a result, IP_3 -independent Ca^{2+} can induce rapid release of Ca^{2+} from endoplasmic reticulum. On the other hand, positive feedback in electric autapse can also increase the IP_3 concentration; thus the concentration of Ca^{2+} can be enhanced; for example, $g_e = -1.0$. Furthermore, the case of negative feedback is considered by setting positive feedback gain in the electric autapse; the results are plotted in Figure 4.

It is found that the fluctuation of membrane potential can be suppressed, and the neuronal activities are changed to become quiescent state when autapse driving imposed negative feedback on the neuron. Furthermore, the Ca^{2+} and IP_3 concentration are calculated in Figure 5.

That is, negative feedback in electric autapse can suppress the fluctuation of membrane potential and then the ion current of Ca^{2+} ; as a result, the concentration of IP_3 is also decreased completely. Indeed, neuron can be induced to trigger hyperexcitability when neuron is coupled by astrocyte with stronger intensity (e.g., larger value setting for r_{IP_3}). In case of smaller r_{IP_3} , the positive feedback in electric autapse becomes dominant and very important to enhance the excitability of neuron and also the oscillation in Ca^{2+} concentration. Furthermore, larger r_{IP_3} ($=0.8$) is used to investigate the same problem by applying external forcing current $I_{\text{ext}} = 10.0 \mu\text{mol/L}\cdot\text{cm}^2$ with a transient period $t = 40$ s from beginning, and the results are plotted in Figure 6.

It is confirmed that oscillating behavior of Ca^{2+} concentration and increase in IP_3 concentration can also be detected by setting larger coupling intensity between neuron and astrocyte (larger r_{IP_3}) when autapse connection is removed or the autaptic current is set as zero. In case of large value setting for r_{IP_3} , Ca^{2+} and IP_3 show slight oscillation in concentration when external forcing current is removed. It is interesting to detect the inhibition effect on Ca^{2+} and IP_3 oscillation in concentration by applying negative feedback in electric autapse, and the results are calculated in Figures 7 and 8.

It is found in Figure 7 that the spiking behavior of neuron can be suppressed by electric autapse with negative feedback; even the coupling between neuron and astrocyte is enhanced by setting larger r_{IP_3} . Furthermore, the changes of Ca^{2+} and IP_3 are calculated in Figure 8.

It is consistent with the previous prediction that Ca^{2+} keeps oscillating and IP_3 holds large concentration when autaptic modulation on membrane potential under negative feedback is weak because the astrocyte contributes more in regulating the membrane potential than electric autapse in this case. By further increasing in the negative feedback in electric autapse, the oscillating behavior in Ca^{2+} and IP_3 will be suppressed completely due to the modulation of electric autapse. It is important to detect and discuss whether positive feedback in autapse can enhance the oscillating behaviors of Ca^{2+} and IP_3 in case of larger value setting for r_{IP_3} , and the results are shown in Figures 9 and 10.

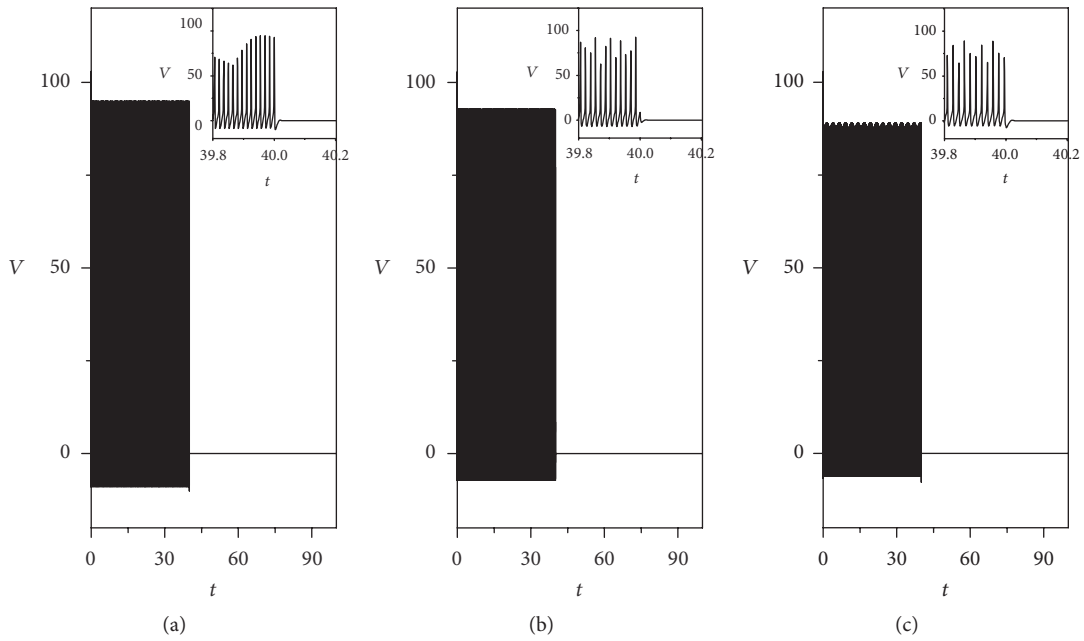


FIGURE 4: Sampled time series for membrane potential of neuron are calculated when neuron is coupled by astrocyte and autapse driving with negative feedback is considered at $\tau = 2$, for (a) $g_e = 0.1$, (b) $g_e = 0.5$, and (c) $g_e = 1.0$. The parameter is set as $r_{IP_3} = 0.2$, and inserted figures are enlarged ones. And the external forcing current regulates the neuron by $I_{\text{ext}} = 10.0 \mu\text{mol/L}\cdot\text{cm}^2$ at $t < 40$ s. The inserted figures are enlarged to show the sampled time series for membrane potential from $t = 39.8$ to 40.2 ms.

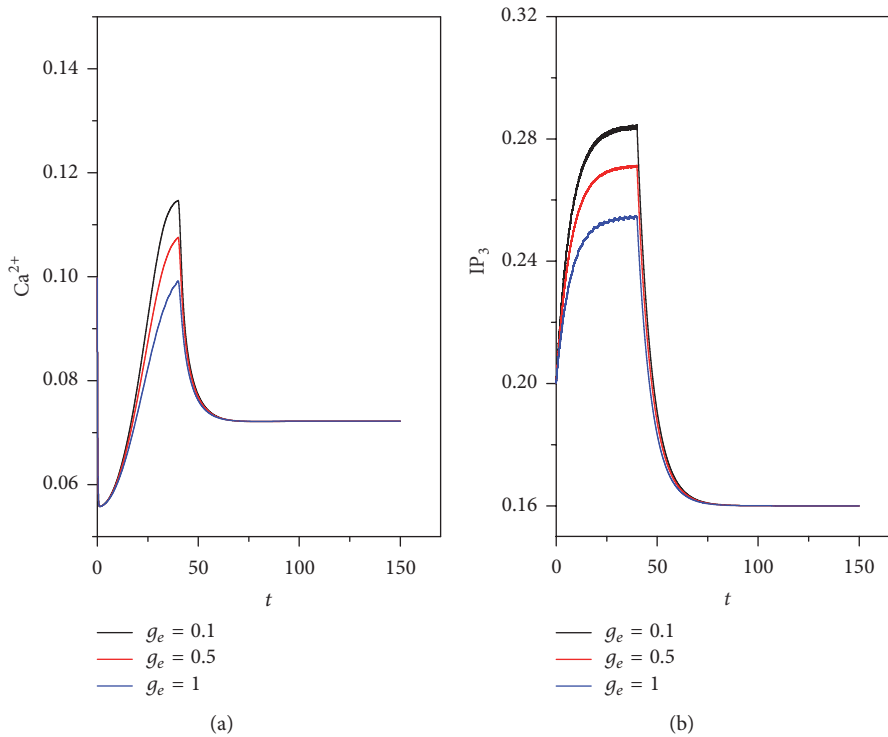


FIGURE 5: Fluctuation in Ca^{2+} concentration and IP_3 concentration is calculated by applying different feedback gains g_e in autapse with time delay $\tau = 2$. The parameter is set as $r_{IP_3} = 0.2$. And the external forcing current regulates the neuron by setting $I_{\text{ext}} = 10.0 \mu\text{mol/L}\cdot\text{cm}^2$ at $t < 40$ s.

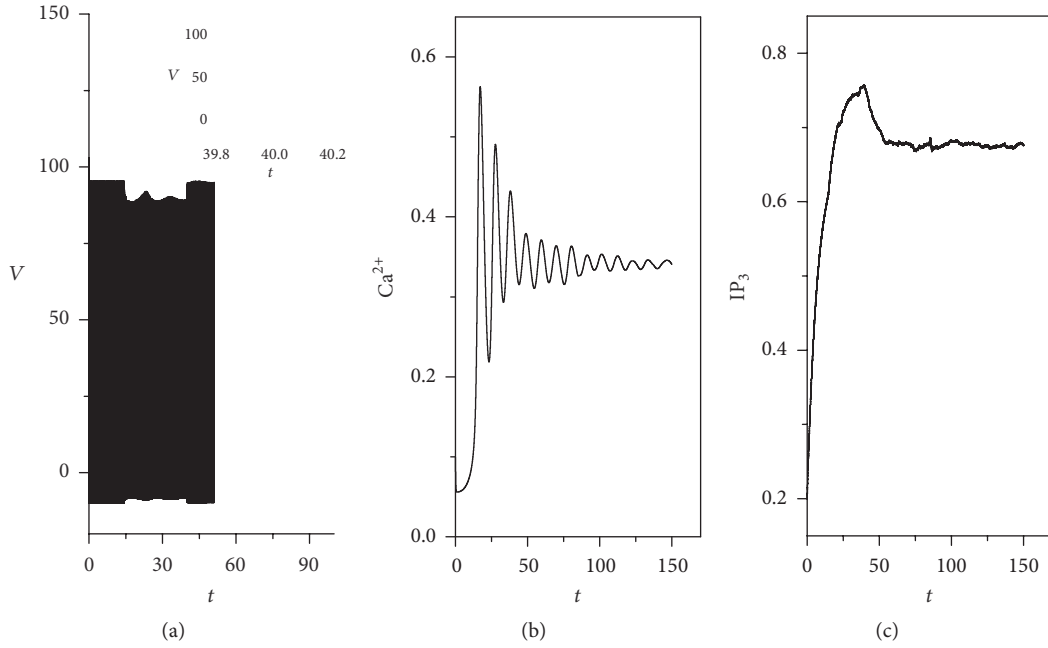


FIGURE 6: Sampled time series for membrane potential (a), calcium concentration in astrocyte (b), and IP_3 in astrocyte (c), $r_{IP_3} = 0.8$, and the external forcing current regulates the neuron by $I_{ext} = 10.0 \mu\text{mol/L}\cdot\text{cm}^2$ at $t < 40$ s. The autaptic current is set as zero, and the inserted figure is enlarged to show the sampled time series for membrane potential from $t = 39.8$ to 40.2 ms.

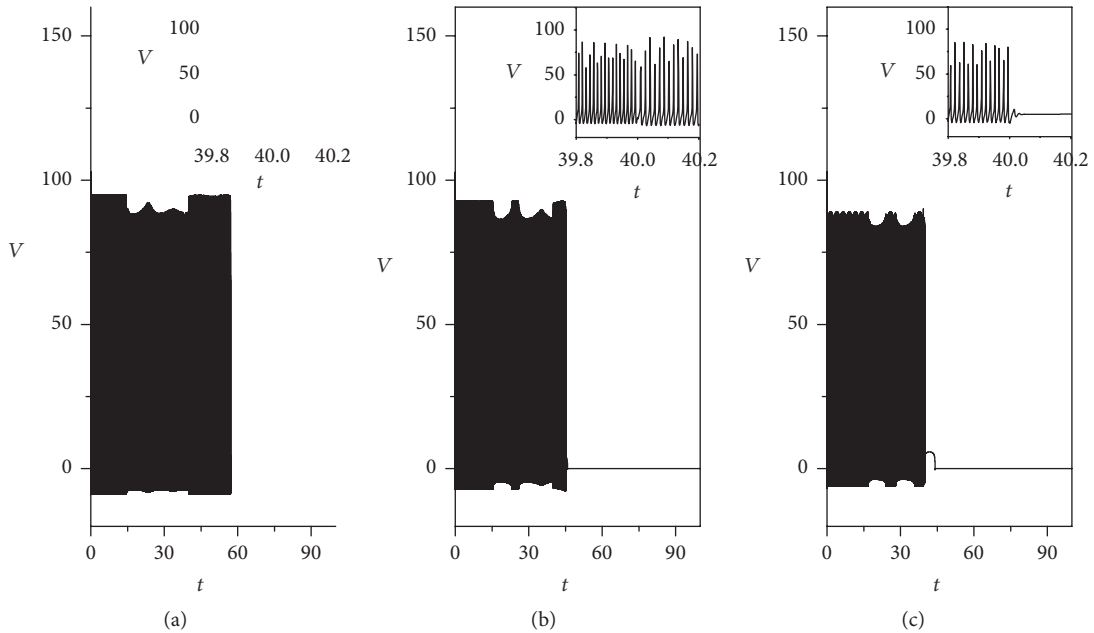


FIGURE 7: Sampled time series for membrane potential of neuron coupled by astrocyte when autapse driving is considered at $\tau = 2$, for (a) $g_e = 0.1$, (b) $g_e = 0.5$, and (c) $g_e = 1.0$. The parameter is set as $r_{IP_3} = 0.8$, and inserted figures are enlarged ones. And the external forcing current regulates the neuron by $I_{ext} = 10.0 \mu\text{mol/L}\cdot\text{cm}^2$ at $t < 40$ s. The inserted figure is enlarged to show the sampled time series for membrane potential from $t = 39.8$ to 40.2 ms.

It is confirmed that positive feedback in electric autapse can further enhance the oscillating behavior of Ca^{2+} and IP_3 and also the excitability of neuron when the coupling intensity between neuron and astrocyte is set as higher value. As it is known, the autaptic modulation in autapse

also depends on the value setting for time delay, which is dependent on the close loop. As a result, different time delays in electric autapse are selected to check the response of electrical activities and the oscillating behaviors of Ca^{2+} and IP_3 , and the results are plotted in Figures 11 and 12.

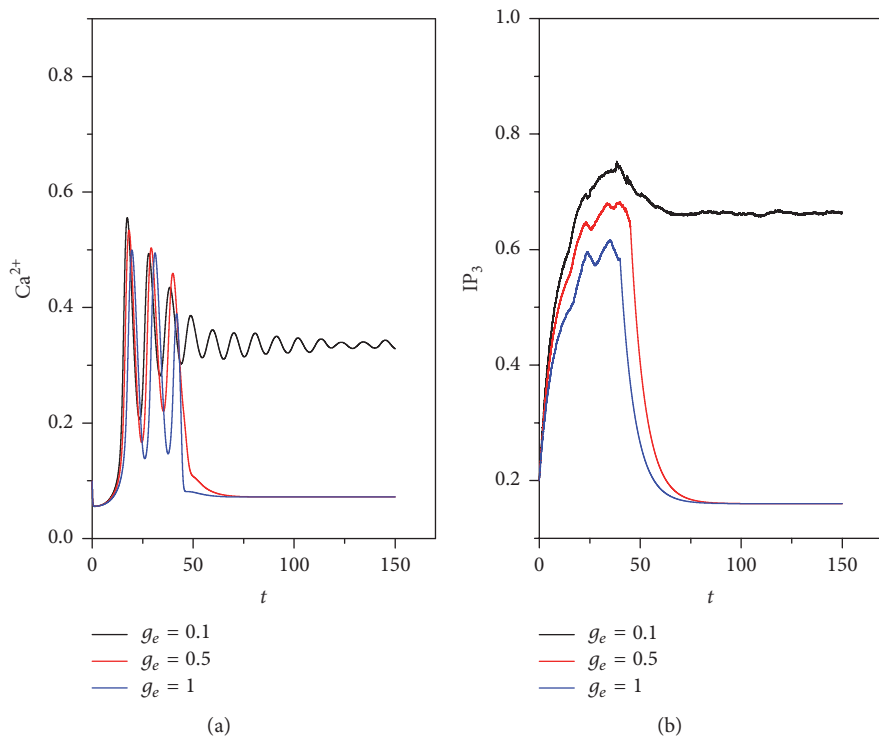


FIGURE 8: Fluctuation in Ca^{2+} concentration and IP_3 concentration is calculated by applying different feedback gains g_e in autapse with time delay $\tau = 2$. The parameter is set as $r_{\text{IP}_3} = 0.8$. And the external forcing current regulates the neuron by $I_{\text{ext}} = 10.0 \mu\text{mol/L}\cdot\text{cm}^2$ at $t < 40$ s.

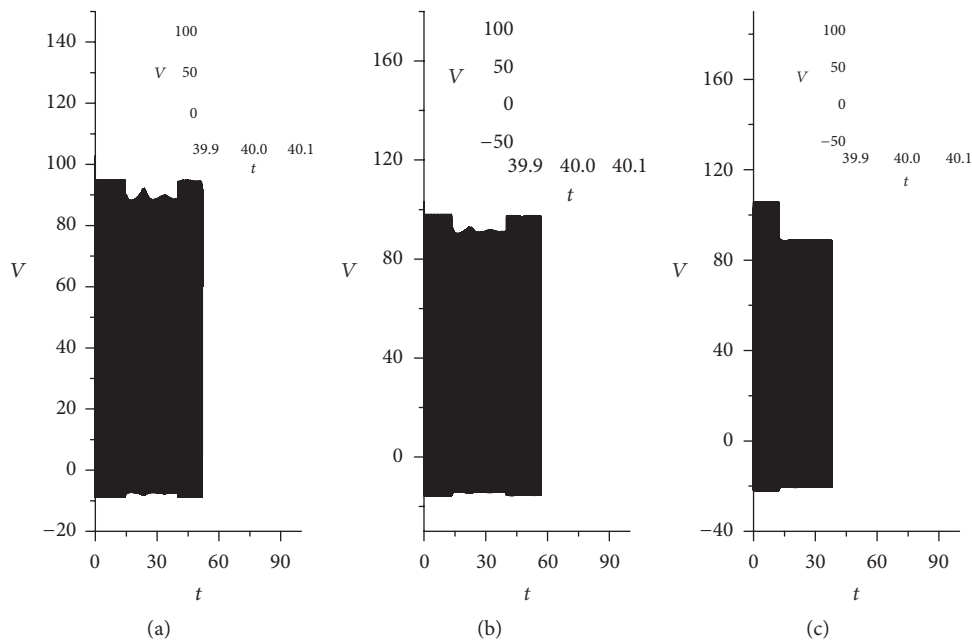


FIGURE 9: Sampled time series for membrane potential of neuron coupled by astrocyte when autapse driving is considered at $\tau = 2$, for (a) $g_e = -0.1$, (b) $g_e = -0.5$, and (c) $g_e = -1.0$. The parameter is set as $r_{\text{IP}_3} = 0.8$, and inserted figures are enlarged ones. And the external forcing current regulates the neuron by $I_{\text{ext}} = 10.0 \mu\text{mol/L}\cdot\text{cm}^2$ at $t < 40$ s. The inserted figure is enlarged to show the sampled time series for membrane potential from $t = 39.8$ to 40.2 ms.

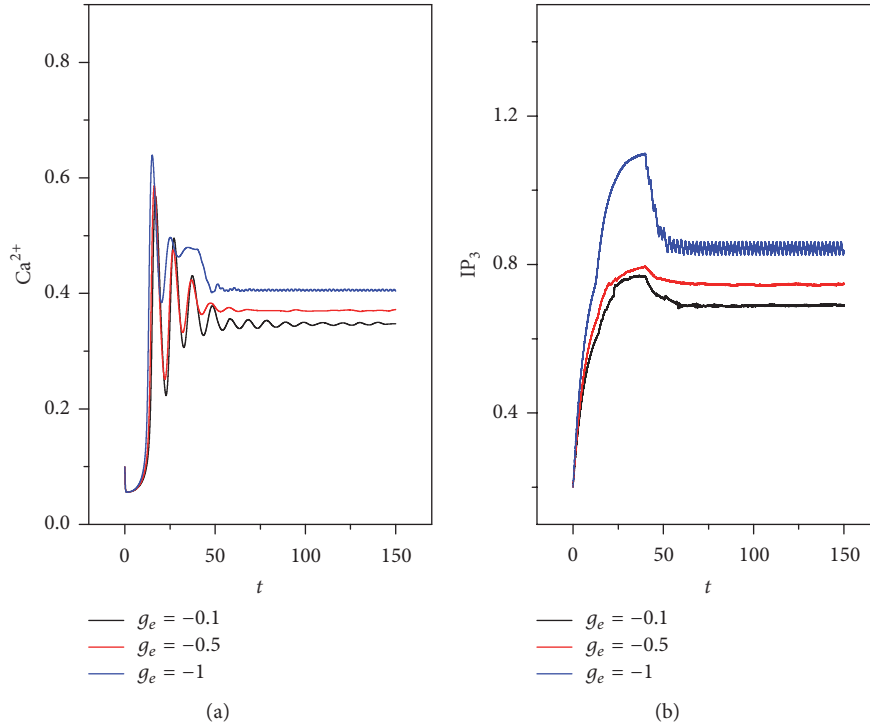


FIGURE 10: Fluctuation in Ca^{2+} concentration and IP_3 concentration is calculated by applying different feedback gains g_e in autapse with time delay $\tau = 2$. The parameter is set as $r_{\text{IP}_3} = 0.8$. And the external forcing current regulates the neuron by setting $I_{\text{ext}} = 10.0 \mu\text{mol/L}\cdot\text{cm}^2$ at $t < 40$ s.

It is found in Figure 11 that the spiking behavior is enhanced and began to show bursting behavior with increasing the time delay in electric autapse; even the coupling intensity between neuron and astrocyte is set as small value for $r_{\text{IP}_3} = 0.2$. Furthermore, the oscillating behavior of Ca^{2+} and changes of IP_3 concentration are calculated in Figure 12.

It is confirmed in Figure 12 that the concentration of IP_3 is decreased and the oscillating behavior in Ca^{2+} is also suppressed when the time delay in autapse is small. By further increasing the time delay in autapse, the memory effect makes neuron remember the action potential and oscillating behavior for Ca^{2+} though the intrinsic time delay in electric autapse is finite. Finally, the bifurcation analysis is carried out and the dependence of Ca^{2+} , IP_3 , and ISI on parameters r_{IP_3} and g_e is discussed in Figure 13, respectively.

It is confirmed that the consistent oscillating behaviors of Ca^{2+} and IP_3 are dependent on the selection of r_{IP_3} , and positive feedback in autapse is effective to enhance the oscillating behaviors and bursting firing in electrical activities. In fact, the Ca^{2+} oscillating in astrocyte is much complex when uncertain perturbation such as noise and time delay is considered [51–53]. Different disturbances on excitable media are often described by applying different types of noise (additive or multiplicative) on the media and possible statistical properties are discussed [54]. Mutual coupling between astrocyte and neuron driven by autapse

can trigger complex stimuli for neuron, astrocyte by setting different external forcing currents, and time delay and feedback gain in autapse; as a result, the response of electrical activities becomes more complex. That is, both of autaptic modulation and astrocyte can cooperate and contribute the mode selection of electrical activities in neurons; thus the self-adaption of neurons can be enhanced.

In summary, autapse connection and driving, external forcing, and also the coupling between neuron and astrocyte all contribute the oscillating behavior for Ca^{2+} by increasing the IP_3 concentration beyond the threshold to keep continuous oscillating in Ca^{2+} concentration. As a result, continuous action potential is triggered to propagate the electric signal between neurons. As mentioned in [24], formation and development of autapse can be associated with the self-adaption of neuron to external stimuli; particularly, it could be associated with injury in the neuron loop of circuit because only a few of neurons are found to be connected with autapse. Extensive evidences also confirmed that external setting of electric field can be effect to bridge the injured parts of axon; thus blocked signal can be propagated [55]. In this way, it could give guidance to further understand the formation mechanism of autapse; in the case of astrocyte modulation, the autaptic driving still plays an important role in regulating the signal exchange between neurons and astrocyte; these results could be helpful for further investigation on collective neuronal network composed of a large number of neurons coupled by astrocytes.

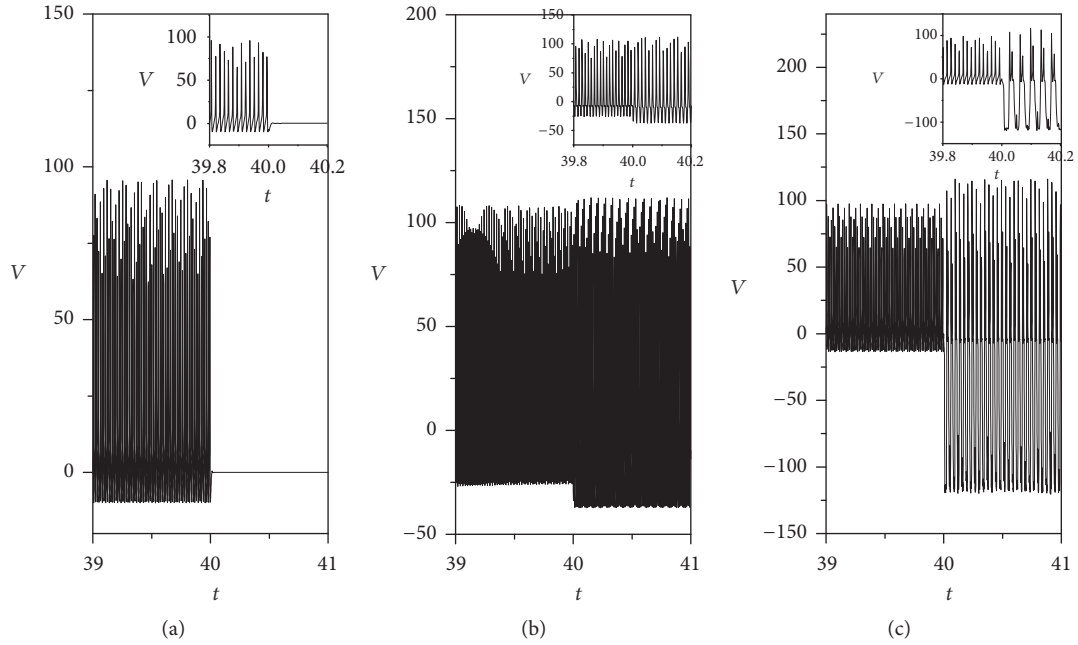


FIGURE 11: Sampled time series for membrane potential of neuron coupled by astrocyte when autapse driving is considered different time delays at $g_e = -0.5$, for (a) $\tau = 0.1$, (b) $\tau = 6$, and (c) $\tau = 15$. The parameter is set as $r_{IP_3} = 0.2$, and inserted figures are enlarged ones. And the external forcing current regulates the neuron by setting $I_{ext} = 10.0 \mu\text{mol/L}\cdot\text{cm}^2$ at $t < 40$ s. The inserted figure is enlarged to show the sampled time series for membrane potential from $t = 39.8$ to 40.2 ms.

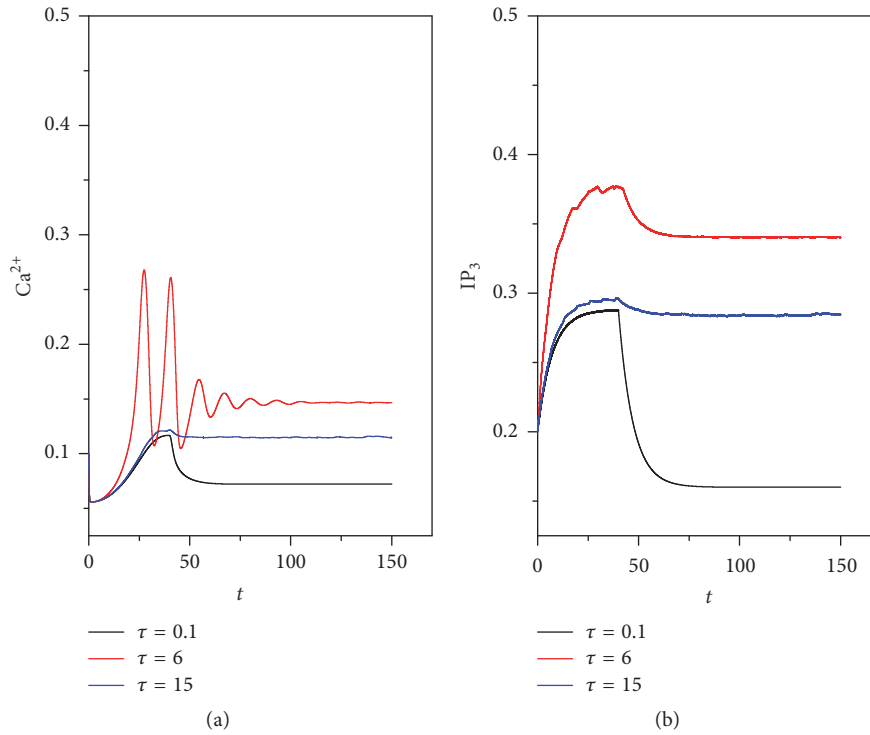


FIGURE 12: Fluctuation in Ca^{2+} concentration (a) and IP_3 concentration (b) is calculated by applying different time delays in autapse with feedback gain $g_e = -0.5$. The parameter is set as $r_{IP_3} = 0.2$. And the external forcing current regulates the neuron by setting $I_{ext} = 10.0 \mu\text{mol/L}\cdot\text{cm}^2$ at $t < 40$ s.

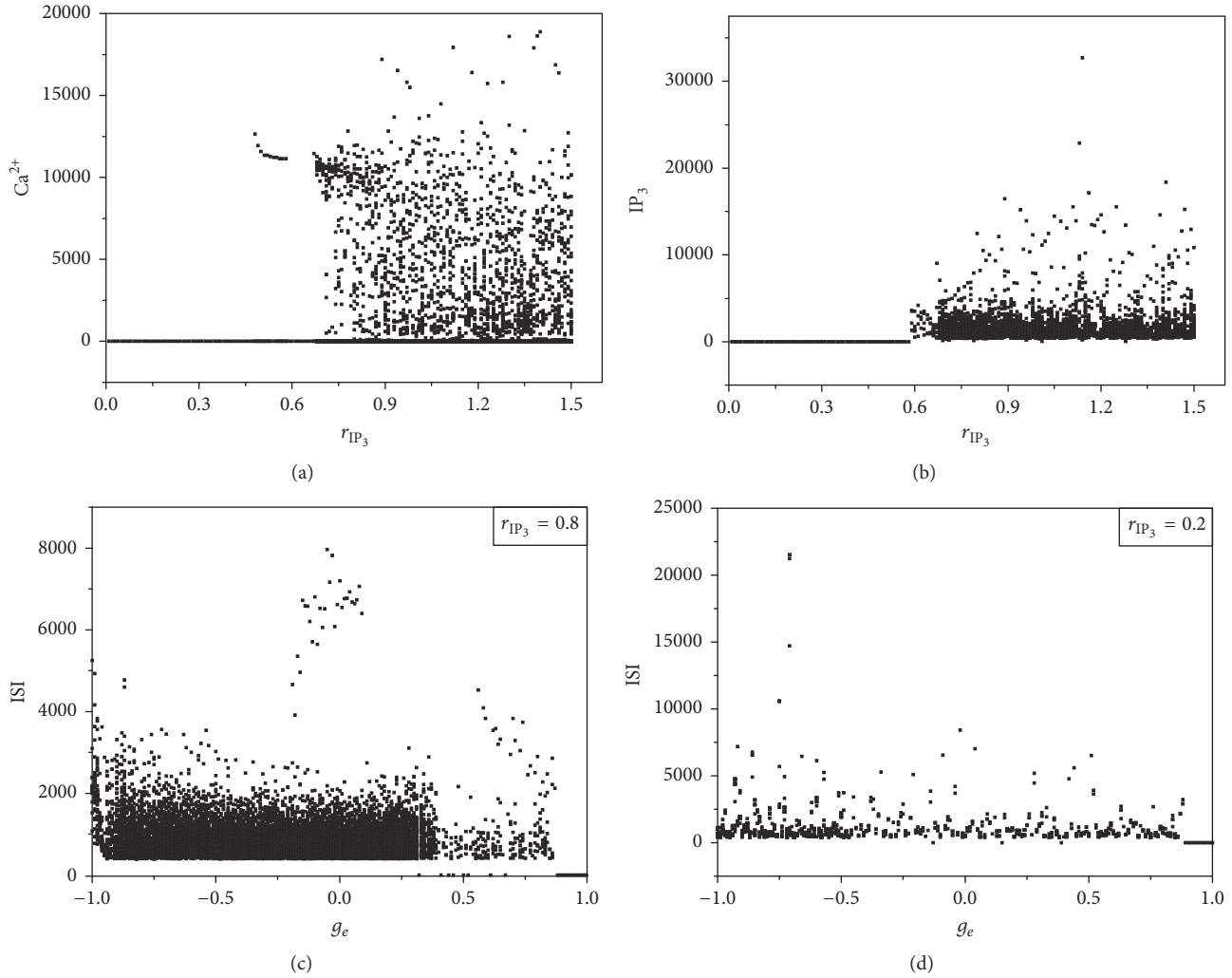


FIGURE 13: Bifurcation diagram for Ca^{2+} , IP_3 , and ISI is calculated by setting different r_{IP_3} and g_e , respectively.

4. Conclusions

Based on the Hodgkin-Huxley neuron model, the effects of astrocyte modulation and autapse connection are considered to set an improved neuron-astrocyte-autapse network model so that the biological function of autapse can be discussed. For the isolate neuron models, the dynamical properties in electrical activities have been extensively investigated to be consistent with the experimental series. The biological role of astrocyte is confirmed on the mode transition of electrical activities in neuron coupled by astrocyte, and action potential is controlled by Ca^{2+} oscillation and changes of IP_3 via release of neurotransmitter. Autapse connection to neuron has confirmed that autaptic modulation could be helpful to enhance excitability of neuron under positive feedback while spiking and bursting behaviors can be suppressed by negative feedback in autapse. As a result, it is important to set a complete neuron model so that the biological function of astrocyte and autapse connection can be estimated

completely. Based on our proposed new neuron model, it is found that autapse connection can also be helpful to change the oscillating behaviors for Ca^{2+} and also the changes of IP_3 ; as a result, electric response to external forcing and mode selection in neuron can be self-adaptive.

The main contribution of this submission could be that we proposed a new neuronal network model developed from the biological HH model with the biological effect of astrocyte and autapse connection being considered. It explains the biological function of autapse connection and intrinsic exchange of signal in neuron from molecular level. It could be helpful to investigate the collective behavior of neuronal network composed of large number neurons.

Conflicts of Interest

The authors declare that there are no conflicts of interest regarding the publication of this paper.

Acknowledgments

This work is partially supported by the National Natural Science of Foundation of China under the Grant nos. 11672122, 11365014, and 11372122.

References

- [1] E. A. Newman, "New roles for astrocytes: regulation of synaptic transmission," *Trends in Neurosci*, vol. 26, pp. 536–542, 2003.
- [2] R. D. Fields and B. Stevens-Graham, "Neuroscience: new insights into neuron-glia communication," *Science*, vol. 298, no. 5593, pp. 556–562, 2002.
- [3] G. Bonvento, C. Giaume, and J. Lorenceau, "Neuron-glia interactions: from physiology to behavior," *Journal of Physiology Paris*, vol. 96, no. 3, pp. 167–168, 2002.
- [4] V. Parpura and P. G. Haydon, "Physiological astrocytic calcium levels stimulate glutamate release to modulate adjacent neurons," *Proceedings of the National Academy of Sciences of the United States of America*, vol. 97, no. 15, pp. 8629–8634, 2000.
- [5] S. J. Smith, "Neural signalling: neuromodulatory astrocytes," *Current Biology*, vol. 4, no. 9, pp. 807–810, 1994.
- [6] T. Fellin, "Communication between neurons and astrocytes: relevance to the modulation of synaptic and network activity," *Journal of Neurochemistry*, vol. 108, no. 3, pp. 533–544, 2009.
- [7] A. C. Charles, J. E. Merrill, E. R. Dirksen, and M. J. Sanderson, "Intercellular signaling in glial cells: calcium waves and oscillations in response to mechanical stimulation and glutamate," *Neuron*, vol. 6, no. 6, pp. 983–992, 1991.
- [8] A. H. Cornell-Bell, S. M. Finkbeiner, M. S. Cooper, and S. J. Smith, "Glutamate induces calcium waves in cultured astrocytes: long-range glial signaling," *Science*, vol. 247, no. 4941, pp. 470–473, 1990.
- [9] J. W. Dani, A. Chernjavsky, and S. J. Smith, "Neuronal activity triggers calcium waves in hippocampal astrocyte networks," *Neuron*, vol. 8, no. 3, pp. 429–440, 1992.
- [10] H. Van Der Loos and E. M. Glaser, "Autapses in neocortex cerebri: synapses between a pyramidal cell's axon and its own dendrites," *Brain Research*, vol. 48, pp. 355–360, 1972.
- [11] A. B. Karabelas and D. P. Purpura, "Evidence for autapses in the substantia nigra," *Brain Research*, vol. 200, no. 2, pp. 467–473, 1980.
- [12] J. M. Bekkers and C. F. Stevens, "Excitatory and inhibitory autaptic currents in isolated hippocampal neurons maintained in cell culture," *Proceedings of the National Academy of Sciences of the United States of America*, vol. 88, no. 17, pp. 7834–7838, 1991.
- [13] J. M. Bekkers, "Synaptic transmission: functional autapses in the cortex," *Current Biology*, vol. 13, no. 11, pp. R433–R435, 2003.
- [14] C. S. Herrmann and A. Klaus, "Autapse turns neuron into oscillator," *International Journal of Bifurcation and Chaos in Applied Sciences and Engineering*, vol. 14, no. 2, pp. 623–633, 2004.
- [15] R. Saada, N. Miller, I. Hurwitz, and A. J. Susswein, "Autaptic excitation elicits persistent activity and a plateau potential in a neuron of known behavioral function," *Current Biology*, vol. 19, no. 6, pp. 479–484, 2009.
- [16] K. Suga, "Isoproterenol facilitates GABAergic autapses in fast-spiking cells of rat insular cortex," *Journal of Oral Science*, vol. 56, no. 1, pp. 41–47, 2014.
- [17] H. Wang, L. Wang, Y. Chen, and Y. Chen, "Effect of autaptic activity on the response of a Hodgkin-Huxley neuron," *Chaos. An Interdisciplinary Journal of Nonlinear Science*, vol. 24, no. 3, Article ID 033122, 13 pages, 2014.
- [18] X. L. Song, C. N. Wang, J. Ma, and J. Tang, "Transition of electric activity of neurons induced by chemical and electric autapses," *Science China Technological Sciences*, vol. 58, no. 6, pp. 1007–1014, 2015.
- [19] D. Guo, M. Chen, M. Perc et al., "Firing regulation of fast-spiking interneurons by autaptic inhibition," *EPL*, vol. 114, no. 3, Article ID 30001, 2016.
- [20] J. Ma, X. Song, J. Tang, and C. Wang, "Wave emitting and propagation induced by autapse in a forward feedback neuronal network," *Neurocomputing*, vol. 167, pp. 378–389, 2015.
- [21] J. Ma, H. Qin, X. Song, and R. Chu, "Pattern selection in neuronal network driven by electric autapses with diversity in time delays," *International Journal of Modern Physics B*, vol. 29, no. 1, Article ID 1450239, 2015.
- [22] E. Yilmaz, V. Baysal, M. Ozer, and M. z. Perc, "Autaptic pacemaker mediated propagation of weak rhythmic activity across small-world neuronal networks," *Physica A. Statistical Mechanics and its Applications*, vol. 444, pp. 538–546, 2016.
- [23] J. Ma and J. Tang, "A review for dynamics of collective behaviors of network of neurons," *Science China Technological Sciences*, vol. 58, no. 12, pp. 2038–2045, 2015.
- [24] C. Wang, S. Guo, Y. Xu et al., "Formation of autapse connected to neuron and its biological function," *Complexity*, vol. 2017, Article ID 5436737, 9 pages, 2017.
- [25] F. Wu, C. Wang, Y. Xu et al., "Model of electrical activity in cardiac tissue under electromagnetic induction," *Scientific Reports*, vol. 6, Article ID 28, 2016.
- [26] M. Lv and J. Ma, "Multiple modes of electrical activities in a new neuron model under electromagnetic radiation," *Neurocomputing*, vol. 205, pp. 375–381, 2016.
- [27] M. Lv, C. Wang, G. Ren, J. Ma, and X. Song, "Model of electrical activity in a neuron under magnetic flow effect," *Nonlinear Dynamics*, vol. 85, no. 3, pp. 1479–1490, 2016.
- [28] Y. Wang, J. Ma, Y. Xu, F. Wu, and P. Zhou, "The electrical activity of neurons subject to electromagnetic induction and Gaussian white noise," *International Journal of Bifurcation and Chaos*, vol. 27, no. 2, Article ID 1750030, 12 pages, 2017.
- [29] Y. Xu, H. Ying, Y. Jia et al., "Autaptic regulation of electrical activities in neuron under electromagnetic induction," *Scientific Reports*, vol. 7, Article ID 43452, 2017.
- [30] S. Nadkarni and P. Jung, "Spontaneous oscillations of dressed neurons: a new mechanism for epilepsy?" *Physical Review Letters*, vol. 91, no. 26, Article ID 268101, 2003.
- [31] D. E. Postnov, L. S. Ryazanova, N. A. Brazhe et al., "Giant glial cell: new insight through mechanism-based modeling," *Journal of Biological Physics*, vol. 34, no. 3, pp. 441–457, 2008.
- [32] P. Allegrini, L. Fronzoni, and D. Pirino, "The influence of the astrocyte field on neuronal dynamics and synchronization," *Journal of Biological Physics*, vol. 35, no. 4, pp. 413–423, 2009.
- [33] M. Amiri, N. Hosseinmardi, F. Bahrami et al., "Astrocyte-neuron interaction as a mechanism responsible for generation of neural synchrony: a study based on modeling and experiments," *Journal of Computational Neuroscience*, vol. 34, no. 3, pp. 489–504, 2013.
- [34] J. Tang, J. M. Luo, and J. Ma, "Information transmission in a neuron-astrocyte coupled model," *PLoS ONE*, vol. 8, no. 11, Article ID e80324, 2013.

- [35] J. Tang, J. Zhang, J. Ma et al., "Astrocyte calcium wave induces seizure-like behavior in neuron network," *Science China Technological Sciences*, pp. 1–8, 2016.
- [36] X. Song, C. Wang, J. Ma, and G. Ren, "Collapse of ordered spatial pattern in neuronal network," *Physica A: Statistical Mechanics and its Applications*, vol. 451, pp. 95–112, 2016.
- [37] J. Ma, Y. Xu, G. Ren, and C. Wang, "Prediction for breakup of spiral wave in a regular neuronal network," *Nonlinear Dynamics. An International Journal of Nonlinear Dynamics and Chaos in Engineering Systems*, vol. 84, no. 2, pp. 497–509, 2016.
- [38] W.-T. Yu, J. Tang, J. Ma et al., "Heterogeneous delay-induced asynchrony and resonance in a small-world neuronal network system," *EPL*, vol. 114, no. 5, Article ID 50006, 2016.
- [39] E. Yilmaz, M. Ozer, V. Baysal, and M. Perc, "Autapse-induced multiple coherence resonance in single neurons and neuronal networks," *Scientific Reports*, vol. 6, Article ID 30914, 2016.
- [40] H. G. Gu, B. B. Pan, and Y. Y. Li, "The dependence of synchronization transition processes of coupled neurons with coexisting spiking and bursting on the control parameter, initial value, and attraction domain," *Nonlinear Dynamics*, vol. 82, no. 3, pp. 1191–1210, 2015.
- [41] R. Uzun, M. Ozer, and M. Perc, "Can scale-freeness offset delayed signal detection in neuronal networks?" *EPL*, vol. 105, no. 6, Article ID 60002, 2014.
- [42] Q. Wang, H. Zhang, M. z. Perc, and G. Chen, "Multiple firing coherence resonances in excitatory and inhibitory coupled neurons," *Communications in Nonlinear Science and Numerical Simulation*, vol. 17, no. 10, pp. 3979–3988, 2012.
- [43] X. Sun, J. Lei, M. Perc et al., "Burst synchronization transitions in a neuronal network of subnetworks," *Chaos*, vol. 21, no. 1, Article ID 016110, 2011.
- [44] Q. Wang, G. Chen, and M. Perc, "Synchronous bursts on scale-free neuronal networks with attractive and repulsive coupling," *PLoS ONE*, vol. 6, no. 1, Article ID e15851, 2011.
- [45] H. Gu and Z. Zhao, "Dynamics of time delay-induced multiple synchronous behaviors in inhibitory coupled neurons," *PLoS ONE*, vol. 10, no. 9, Article ID e0138593, 2015.
- [46] D. Fan, Q. Wang, and M. Perc, "Disinhibition-induced transitions between absence and tonic-clonic epileptic seizures," *Scientific Reports*, vol. 5, Article ID 12618, 2015.
- [47] Y.-X. Li and J. Rinzel, "Equations for InsP_3 receptor-mediated $[\text{Ca}^{2+}]_i$ oscillations derived from a detailed kinetic model: a Hodgkin-Huxley like formalism," *Journal of Theoretical Biology*, vol. 166, no. 4, pp. 461–473, 1994.
- [48] P. Bezzi, G. Carmignoto, L. Pasti et al., "Prostaglandins stimulate calcium-dependent glutamate release in astrocytes," *Nature*, vol. 391, no. 6664, pp. 281–285, 1998.
- [49] L. Pasti, A. Volterra, T. Pozzan, and G. Carmignoto, "Intracellular calcium oscillations in astrocytes: a highly plastic, bidirectional form of communication between neurons and astrocytes in situ," *The Journal of Neuroscience*, vol. 17, no. 20, pp. 7817–7830, 1997.
- [50] H. R. Parri, T. M. Gould, and V. Crunelli, "Spontaneous astrocytic Ca^{2+} oscillations in situ drive NMDAR-mediated neuronal excitation," *Nature Neuroscience*, vol. 4, no. 8, pp. 803–812, 2001.
- [51] W.-L. Duan and C. Zeng, "Statistics for anti-synchronization of intracellular calcium dynamics," *Applied Mathematics and Computation*, vol. 293, pp. 611–616, 2017.
- [52] W.-L. Duan and C. Zeng, "Signal power amplification of intracellular calcium dynamics with non-Gaussian noises and time delay," *Applied Mathematics and Computation*, vol. 292, pp. 400–405, 2017.
- [53] W.-L. Duan and C. Zeng, "Role of time delay on intracellular calcium dynamics driven by non-Gaussian noises," *Scientific Reports*, vol. 6, Article ID 25067, 2016.
- [54] C. Zeng, C. Zeng, A. Gong, and L. Nie, "Effect of time delay in FitzHugh-Nagumo neural model with correlations between multiplicative and additive noises," *Physica A: Statistical Mechanics and its Applications*, vol. 389, no. 22, pp. 5117–5127, 2010.
- [55] S. Guo, C. Wang, J. Ma, W. Jin et al., "Transmission of blocked electric pulses in a cable neuron model by using an electric field," *Neurocomputing*, vol. 215, pp. 627–637, 2016.

Research Article

Chaos Control in Fractional Order Smart Grid with Adaptive Sliding Mode Control and Genetically Optimized PID Control and Its FPGA Implementation

Anitha Karthikeyan and Karthikeyan Rajagopal

Centre for Non-Linear Dynamics, Defense University, Bishoftu, Ethiopia

Correspondence should be addressed to Karthikeyan Rajagopal; rkarthikeyan@gmail.com

Received 16 January 2017; Revised 1 March 2017; Accepted 9 March 2017; Published 13 April 2017

Academic Editor: Viet-Thanh Pham

Copyright © 2017 Anitha Karthikeyan and Karthikeyan Rajagopal. This is an open access article distributed under the Creative Commons Attribution License, which permits unrestricted use, distribution, and reproduction in any medium, provided the original work is properly cited.

We investigate a specific smart grid system and its nonlinear properties. Lyapunov exponents are derived to prove the existence of chaos and bifurcation and bicoherence contours are investigated to show the parameter dependence and existence of quadratic nonlinearities, respectively. A fractional order model of the smart grid system (FOSG) is then derived and bifurcation of the FOSG system with variation in the commensurate fractional order of the system is investigated to show that largest Lyapunov exponent of the system exists in fractional order. Hence we proposed two different control methods to suppress the chaotic oscillations. In the first method we derive fractional order adaptive sliding mode control (FOASMC) algorithm to control chaotic oscillations and in the second method we used genetically optimized fractional order PID controllers (GAFOPID) for chaos control. Numerical simulations are conducted to show the effectiveness of the controllers and also to prove that GAFOPID controllers are more effective than FOASMC controllers for fractional order systems. The GAFOPID controllers are then realized in FPGA to show that the proposed methodology is hardware realizable.

1. Introduction

Smart grid holds the promise that the power sector can go “green” by taking more aggressive measures to lower the carbon dioxide (CO₂) emissions through efficient integration of renewable energy sources [1, 2]. Smart grids and its technologies modernize our electric grids ensure safe, secure, cost effective, and reliable power transmission [3, 4]. Nonlinear phenomenon in power systems such as voltage collapse and oscillatory phenomenon can be analyzed using chaos theory [5]. Unpredictability and high sensitivity to initial conditions are the important characters of chaotic systems which led to severe blackouts and power system failures [6].

Control of chaotic systems in science and engineering is an important research area in the control literature [7]. Particularly chaos control methodologies have been of greater use in nonlinearity suppression of electrical systems such as in brushless DC motor [8], bifurcation and chaos control in a permanent magnet synchronous motor [9, 10], and PI

controlled induction motor [11]. Uncertainty plays an important role in controlling nonlinearity in power systems. As discussed in literatures, the uncertainty caused by the state changes because of parallel distribution and generation in smart grids are not investigated [12, 13].

Recently many researchers have shown interest in the study of fractional order nonlinear systems [14–16]. Methods for simulating fractional order chaotic system were presented by Petras [17] and Matlab solutions for numerical analysis of fractional order chaotic systems were discussed by Trzaska [18]. In chaos control of electrical systems fractional order controllers play an important role as larger Lyapunov exponents occur when fractional orders are close to “1” [19–21]. Chaos suppression in fractional order brushless DC motor using sliding mode controllers [19] and fractional order permanent magnet synchronous motor, pi controlled induction motor by extended back stepping control [20], and fractional order PMSM motors with adaptive nonlinear controllers [21] is earlier investigated in the literatures. The

stability of fractional order systems using Lyapunov stability theory has been investigated in the literature [22, 23]. A fractional order controller to stabilize the unstable fixed points of an unstable open-loop system was proposed by Tavazoei and Haeri [24]. A delayed feedback control (DFC) based on the act-and-wait concept for nonlinear dynamical systems was proposed by Konishi et al. [25], which reduces the dynamics of DFC systems to that of discrete-time systems. The control and synchronization of an induction motor system were investigated by Jin et al. [26]. Fractional order controller design for brushless DC motors and induction motors were investigated in the literature [19, 20]. FPGA implementation of fractional order systems is first discussed by Rajagopal et al. [27, 28].

Recently many digital implementations of chaotic systems have been proposed and implemented in field programmable gate arrays (FPGA) [29–31]. Image crypto systems using chaotic random number generators are implemented in FPGA and are of greater interest because of the robustness and complexity of the chaos encryption systems [32]. FPGA based weak signal detectors using a Duffing oscillator were proposed by Rashtchi and Nourazar [33]. Multiscroll attractors and their digital implementation using FPGA are extensively investigated in recent years [29, 34]. Memristor based chaotic system and its FPGA circuits were proposed by Xu et al. [35].

Motivated by the above discussions, in this paper we propose a chaos control scheme for a fractional order smart grid model with fractional order adaptive sliding mode controllers (FOASMC) and genetically optimized fractional order PID controllers (FOGAPID). Dynamic analyses of the specific smart grid integer order dimensionless model [36] like Lyapunov exponents and bifurcation and bicoherence plots are derived to prove that chaos exists for selective values of the parameters. The fractional order smart grid (FOSG) model is then derived from the integer order smart grid model [36]. Bifurcation analysis of the FOSG system for variations fractional orders is investigated to prove that the largest Lyapunov exponent exists when fractional order is close to “1.” Hence fractional order adaptive sliding mode (FOASM) controllers and genetically optimized fractional order PID controllers are proposed to suppress the chaotic oscillations. By numerical simulations GAFOPID controllers are proven effective compared to the FOASM controllers. The proposed GAFOPID controllers are then implemented in FPGA to show that the proposed control scheme is hardware realizable.

2. Chaotic Dynamics of Smart Grid

In this section we investigate the chaotic dynamics of the specific smart grid system [36]. The dynamics of the system depends on rotor angle δ_t , load voltage angle δ_L , load voltage V_L , angular rotation ω , and inverter current i_0 . To analyze the chaotic behavior of the smart grid parameters $[\delta_t, \omega, \delta_L, V_L]^T$ are taken as fixed parameters and i_0 is taken as the variable parameter. For simplicity the parameters are

assumed as $x = [x_1, x_2, x_3, x_4]^T = [\delta_t, \omega, \delta_L, V_L]^T$. The dimensionless model of the smart grid system is as given in

$$\begin{aligned}
 \dot{x}_1 &= x_2, \\
 \dot{x}_2 &= 0.573 - 0.167x_2 + 20x_4 \cos(x_1 - x_3 + 1.483) \\
 &\quad + 11.667x_4 \cos(x_1 + 1.483), \\
 \dot{x}_3 &= 69 - 93.33x_4 - 179.05x_4^2 - 50i_0x_4 \sin x_3 \\
 &\quad - 300x_4 \sin x_3 \cos(x_1 - 1.483), \\
 \dot{x}_4 &= 25.322x_4^2 + 13.054x_4 + 3.529x_4 \cos(x_1 - 1.483) \\
 &\quad - 3.529x_4 \cos x_3 \cos(x_3 - 1.483) \\
 &\quad + 42.353x_4 \sin x_3 \cos(x_1 - 1.483) \\
 &\quad + 7.059i_0x_4 \sin x_3 \\
 &\quad - 42.353x_4 \sin x_3 \cos(x_3 - 1.483) \\
 &\quad - 35.294x_4 \sin(x_3 + 1.483) \\
 &\quad + 0.588i_0x_4 \cos x_3 + 2.941x_4 \cos(x_3 - 1.483) \\
 &\quad + 1.31778.
 \end{aligned} \tag{1}$$

System (1) shows chaotic behavior for the selected initial conditions $[0.3, 0.2, 0.1, 0.97]$ and $i_0 = 0.01$. Figure 1 shows the 3D phase portrait of the smart grid system (1).

3. Dynamic Analysis of the Smart Grid System

In this section we investigate the properties of the smart grid system discussed in Section 2. The initial conditions for the analysis are taken as in Section 2.

3.1. Equilibrium Points and Jacobian Matrix. The smart grid system (1) has one unstable equilibrium point $E_1 = 0.7336, 0, 0.8731, 0.2278$. The characteristic equation of system (1) is given as $\lambda^4 + 32.4\lambda^3 + 530.9\lambda^2 + 444.29\lambda - 4541$ and the eigenvalues are $\lambda_{1,2} = -15.46 \pm 15.98i$, $\lambda_3 = -3.85$, $\lambda_4 = 2.38$ and λ_4 is the unstable focus.

The Jacobian matrix of the smart grid system (1) at any point $X \in R^4$ is found as

$$J(X) = \begin{bmatrix} 0 & 1 & 0 & 0 \\ f_5(x) & 0.167 & f_9(x) & f_6(x) \\ f_{10}(x) & 0 & f_8(x) & f_3(x) \\ f_4(x) & 0 & f_1(x) & f_2(x) \end{bmatrix} \tag{2}$$

and the elements of matrix are the functions defined as

$$\begin{aligned}
 f_1(x) &= 3.529x_4 \sin x_3 \cos(x_3 - 1.483) \\
 &\quad + 3.529x_4 \cos x_3 \sin(x_3 - 1.483)
 \end{aligned}$$

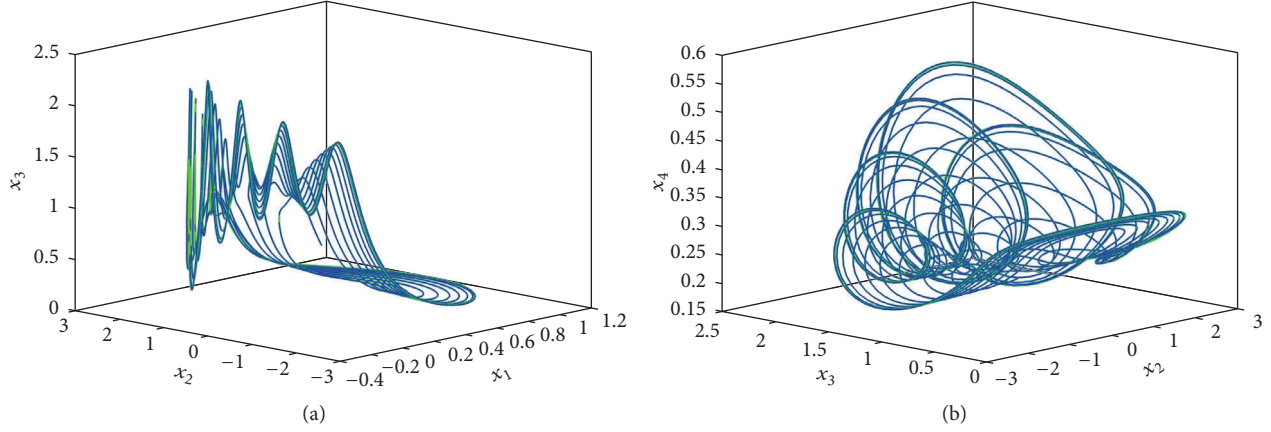


FIGURE 1: 3D phase portraits of the smart grid system (1).

$$\begin{aligned}
& + 42.353x_4 \cos x_3 \cos(x_1 - 1.483) \\
& + 7.059i_0 x_4 \cos x_3 \\
& - 42.353x_4 \cos x_3 \cos(x_3 - 1.483) \\
& + 42.353x_4 \sin x_3 \sin(x_3 - 1.483) \\
& - 35.294x_4 \cos(x_3 + 1.483) \\
& - 0.588i_0 x_4 \sin x_3 \\
& - 2.941x_4 \sin(x_3 - 1.483), \\
f_2(x) = & 50.644x_4 + 13.054 + 3.529 \cos(x_1 - 1.483) \\
& - 3.529 \cos x_3 \cos(x_3 - 1.483) \\
& + 42.353 \sin x_3 \cos(x_1 - 1.483) \\
& + 7.059i_0 \sin x_3 \\
& - 42.353 \sin x_3 \cos(x_3 - 1.483) \\
& - 35.294 \sin(x_3 + 1.483) + 0.588i_0 \cos x_3 \\
& + 2.941 \cos(x_3 - 1.483), \\
f_3(x) = & -93.33 - 358.1x_4 - 50i_0 \sin x_3 \\
& - 300 \sin x_3 \cos(x_1 - 1.483), \\
f_4(x) = & -3.529x_4 \sin(x_1 - 1.483) \\
& - 42.353x_4 \sin x_3 \sin(x_1 - 1.483), \\
f_5(x) = & -20x_4 \sin(x_1 - x_3 + 1.483) \\
& - 11.667x_4 \sin(x_1 + 1.483), \\
f_6(x) = & 20 \cos(x_1 - x_3 + 1.483) \\
& + 11.667 \cos(x_1 + 1.483),
\end{aligned}$$

$$\begin{aligned}
f_7(x) = & -50i_0 x_4 \cos x_3 \\
& + 300x_4 \cos x_3 \cos(x_1 - 1.483), \\
f_9(x) = & 20x_4 \sin(x_1 - x_3 + 1.483), \\
f_{10}(x) = & 300x_4 \sin x_3 \sin(x_1 - 1.483).
\end{aligned} \tag{3}$$

3.2. Lyapunov Exponents and Kaplan-Yorke Dimension. Lyapunov exponents of a nonlinear system define the convergence and divergence of the states. The existence of positive Lyapunov exponents confirms the chaotic behavior of the system [37, 38]. We take the parameters of the smart grid system (1) with initial conditions and parameters as in Section 2; then the Lyapunov exponents of the smart grid system (1) are numerically found as

$$\begin{aligned}
L_1 = & 0.270809, \\
L_2 = & -1.408465, \\
L_3 = & -7.882472, \\
L_4 = & -25.888492.
\end{aligned} \tag{4}$$

Since there are positive Lyapunov exponents in (4), it is clear that the smart grid system (1) is chaotic. Figure 2 shows the Lyapunov exponents of the smart grid system. We note that the sum of the Lyapunov exponents of system (1) is negative. In fact,

$$L_1 + L_2 + L_3 + L_4 = -34.908 < 0. \tag{5}$$

This shows that the smart grid system (1) is dissipative.

Also, the Kaplan-Yorke dimension of the smart grid system (1) is derived as

$$D_{KY} = 3 + \frac{L_1 + L_2 + L_3}{L_4} = 3.3484. \tag{6}$$

3.3. Bifurcation. In order to understand the parameter dependence of the smart grid system, we fix all the other

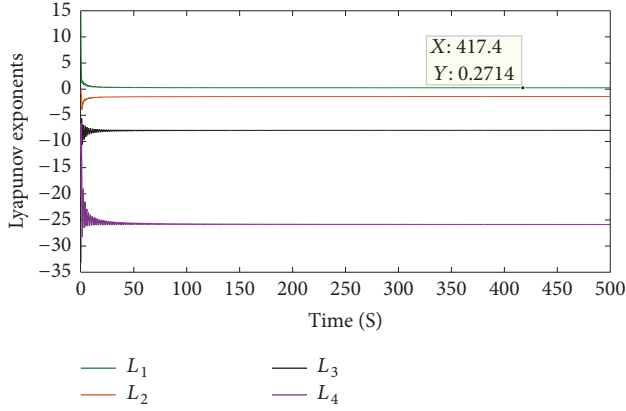


FIGURE 2: Lyapunov exponents of the smart grid system (1).

parameters $([x_1, x_2, x_3, x_4]^T = [\delta, \omega, \delta_L, V_L]^T)$, i_0 is varied, and the behavior of the integer order smart grid system (1) is investigated. The bifurcation plot for various states versus the inverter current i_0 is given by Figures 3(a), 3(b), 4(a), and 4(b). From the figures, it is clear that, for the values $0 \leq i_0 \leq 2.78$, the system shows denser points confirming the existence of system's largest positive Lyapunov exponent. Therefore, from the Lyapunov exponents and bifurcation diagrams in these figures, a conclusion can be obtained that chaos exists in smart grid system (1) for a certain range of parameters.

3.4. Bicoherence. The bicoherence or the normalized bispectrum is a measure of the amount of phase coupling that occurs in a signal or between two signals. Both bicoherence and bispectrum are used to find the influence of a nonlinear system on the joint probability distribution of the system input. Phase coupling is the estimate of the proportion of energy in every possible pair of frequency components (f_j, f_k) . Bicoherence analysis is able to detect coherent signals in extremely noisy data, provided that the coherency remains constant for sufficiently long times, since the noise contribution falls off rapidly with increasing number of segments N .

The autobispectrum of a chaotic system is given by Pezeshki [39]. He derived the autobispectrum with the Fourier coefficients

$$B(\omega_1, \omega_2) = E[A(\omega_1)A(\omega_2)A^*(\omega_1 + \omega_2)], \quad (7)$$

where ω_n is the radian frequency and A is the Fourier coefficients of the time series. The normalized magnitude spectrum of the bispectrum known as the squared bicoherence is given by

$$b(\omega_1, \omega_2) = \frac{|B(\omega_1, \omega_2)|^2}{P(\omega_1)P(\omega_2)P(\omega_1 + \omega_2)}, \quad (8)$$

where $P(\omega_1)$ and $P(\omega_2)$ are the power spectrums at f_1 and f_2 .

The motivation to study the bicoherence is twofold. First, the bicoherence can be used to extract information due to deviations from Gaussianity and suppress additive (colored) Gaussian noise. Second, the bicoherence can be used to detect and characterize asymmetric nonlinearity in signals via

quadratic phase coupling or identify systems with quadratic nonlinearity. The bicoherence is the third-order spectrum. Whereas the power spectrum is a second-order statistics, formed from $X'(f) * X(f)$, where $X(f)$ is the Fourier transform of $x(t)$, the bispectrum is third-order statistics formed from $X(f_j) * X(f_k) * X'(f_j + f_k)$. The bispectrum is therefore a function of a pair of frequencies (f_j, f_k) . It is also a complex-valued function. The (normalized) square amplitude is called the bicoherence (by analogy with the coherence from the cross-spectrum). The bispectrum is calculated by dividing the time series into M segments of length N_{seg} , calculating their Fourier transforms and biperiodogram, then averaging over the ensemble. Although the bicoherence is a function of two frequencies the default output of this function is a one-dimensional output, with the bicoherence refined as a function of only the sum of the two frequencies.

Figures 5 and 6 depict the contours of the bicoherence of the states x and y for the smart grid system (1). Figure 7 shows the bicoherence contours of all the states together. Shades in yellow represent the multifrequency components contributing to the power spectrum. From Figures 5, 6, and 7, the cross-bicoherence is significantly nonzero, and nonconstant, indicating a nonlinear relationship between the states. In Figures 5 and 6 (autobicoherence) the yellow shades indicate that the nonlinear relationship of the states x and y is not narrowband processes. The yellow shades and nonsharpness of the peaks, as well as the presence of structure around the origin in Figure 7 (cross-bicoherence), indicate that the nonlinearity between the states x, y, z, w is not of the quadratic nonlinearity and hence may be because of nonlinearity of higher dimensions. The most two dominant frequencies (f_1, f_2) are taken for deriving the contour of bicoherence. The sampling frequency (f_s) is taken as the reference frequency. Direct FFT is used to derive the power spectrum for individual frequencies and Hankel operator is used as the frequency mask. Hanning window is used as the FIR filter to separate the frequencies.

4. Fractional Order Current Driven Induction Motor

In this section we will derive the dimensionless fractional order model of the induction motor. The dimensionless integer order model of a PI speed regulated current driven induction motor is given by [36] as follows:

$$D^{q_1} x_1 = x_2,$$

$$D^{q_2} x_2 = 0.573 - 0.167x_2 + 20x_4 \cos(x_1 - x_3 + 1.483) + 11.667x_4 \cos(x_1 + 1.483),$$

$$D^{q_3} x_3 = 69 - 93.33x_4 - 179.05x_4^2 - 50i_0x_4 \sin x_3 - 300x_4 \sin x_3 \cos(x_1 - 1.483),$$

$$D^{q_4} x_4 = 25.322x_4^2 + 13.054x_4 + 3.529x_4 \cos(x_1 - 1.483)$$

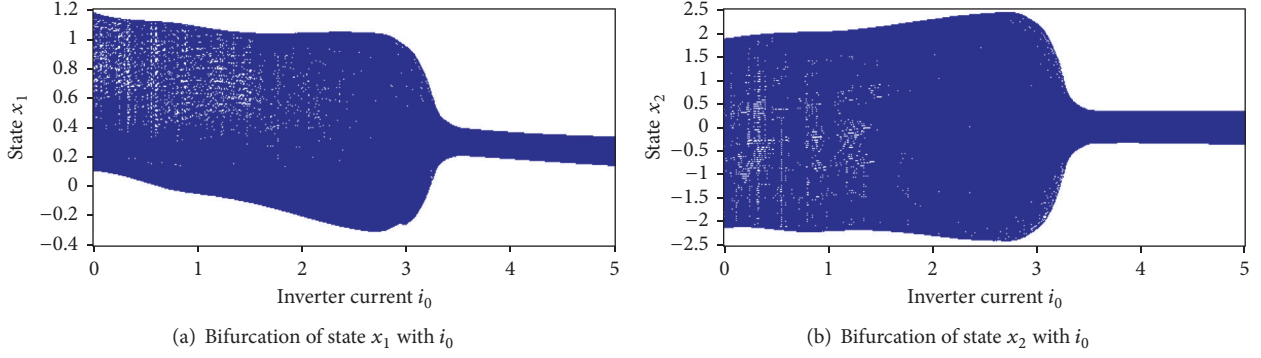


FIGURE 3

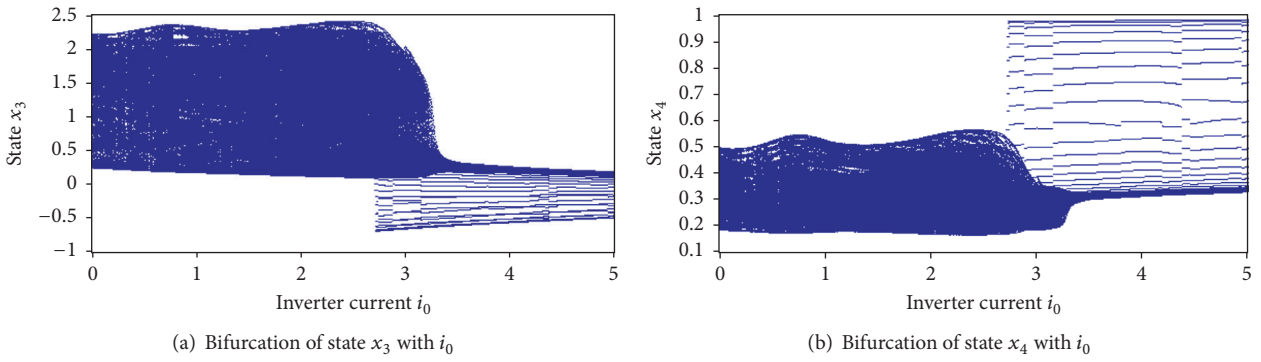
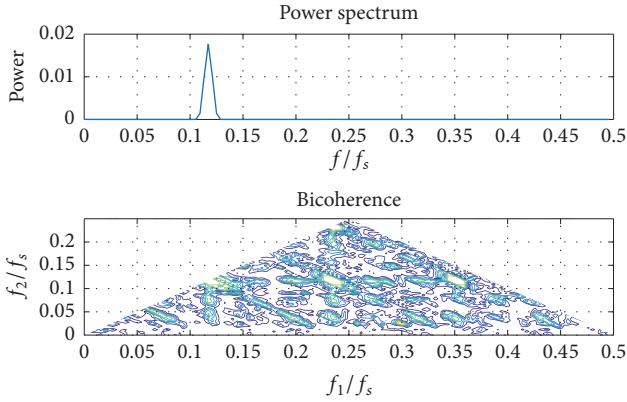
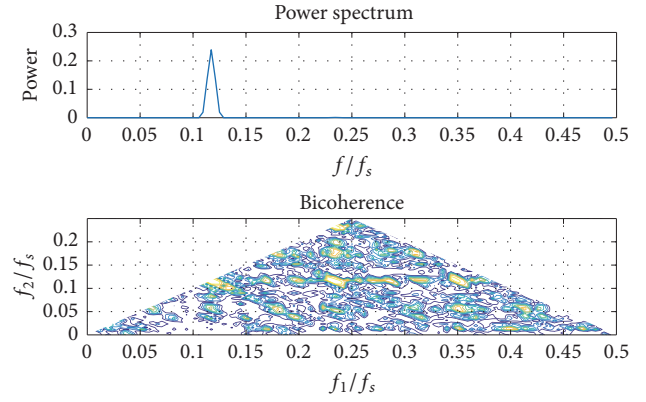


FIGURE 4

FIGURE 5: Contour of bicoherence of state x for the smart grid system.FIGURE 6: Contour of bicoherence of state y for the smart grid system.

$$\begin{aligned}
 & - 3.529x_4 \cos x_3 \cos(x_3 - 1.483) \\
 & + 42.353x_4 \sin x_3 \cos(x_1 - 1.483) \\
 & + 7.059i_0x_4 \sin x_3 \\
 & - 42.353x_4 \sin x_3 \cos(x_3 - 1.483) \\
 & - 35.294x_4 \sin(x_3 + 1.483) \\
 & + 0.588i_0x_4 \cos x_3 \\
 & + 2.941x_4 \cos(x_3 - 1.483) + 1.31778.
 \end{aligned} \tag{9}$$

The initial conditions and the parameters are the same as discussed for the integer order model in Section 2. The fractional orders q_i with $i = 1, 2, 3, 4$ are kept close to “1” to get

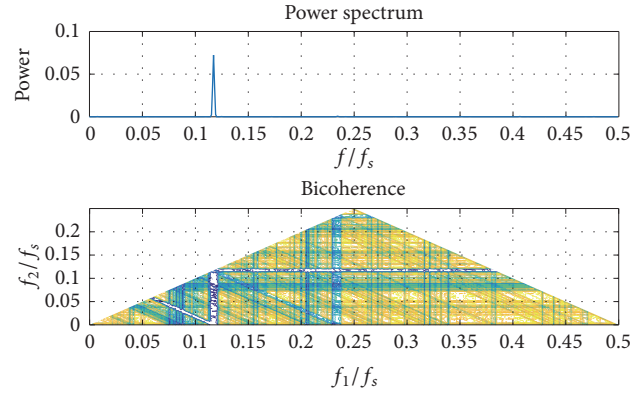


FIGURE 7: Contour of bicoherence of all the states of the smart grid system.

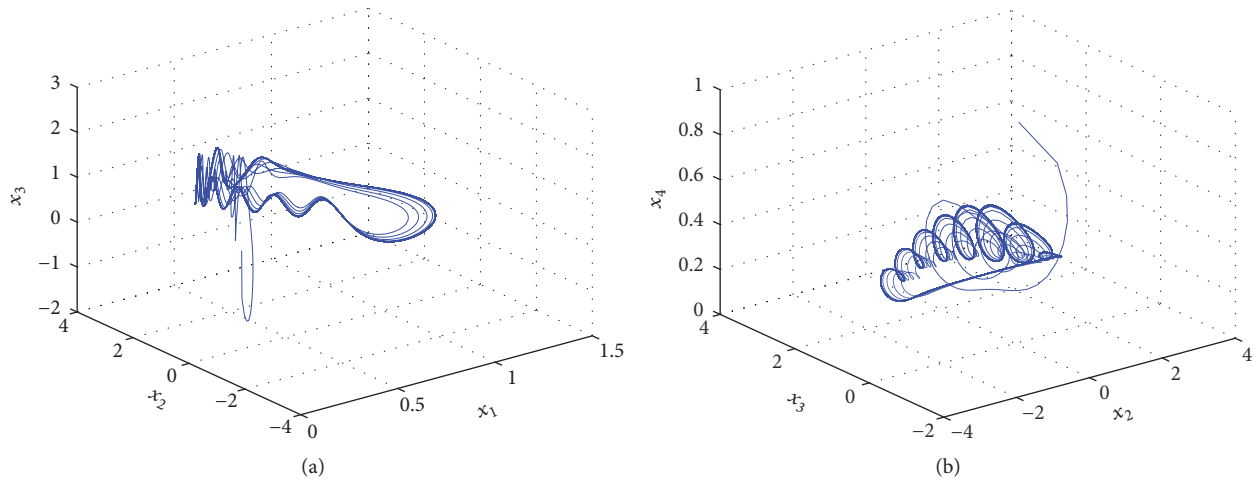


FIGURE 8: 3D phase portraits of the fractional order smart grid system.

the largest Lyapunov exponents. Figure 8 shows the 3D phase portraits of the fractional order smart grid (FOSG) system for $q_i = 992$.

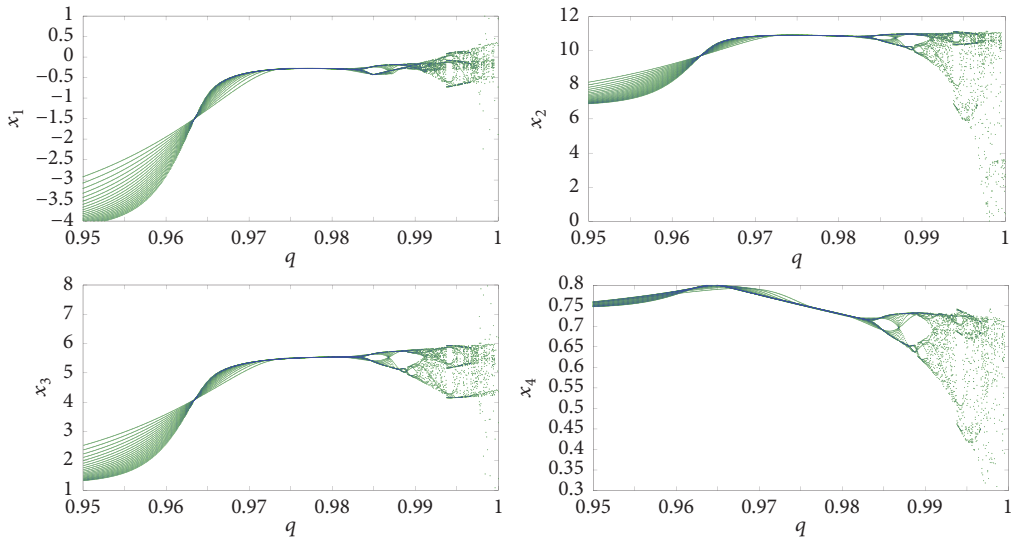
5. Dynamic Analysis of the FOSG System

5.1. Bifurcation with Fractional Order. Most of the dynamic properties of the integer order system (1) like the Lyapunov exponents and bifurcation with parameters are preserved in the fractional order if $q_i > 0.985$, where $i = 1, 2, 3, 4$. The most important analysis of interest when investigating a fractional order system is the bifurcation with fractional orders. Figure 9(a) shows the bifurcation of the FOSG system with commensurate fractional order $q_1 = q_2 = q_3 = q_4 = q$ and Figure 9(b) shows the 3D state portrait (x_2, x_3, x_4 plane) of the FOSG system for various commensurate fractional orders $q_1 = q_2 = q_3 = q_4 = q$. The largest positive Lyapunov exponent ($L_1 = 0.271921$) of the FOSG system appears when $q = 0.992$ against its largest integer order Lyapunov exponent ($L_1 = 0.270809$). Hence fractional order chaos suppression/control proves efficient compared to the integer order controls as the systems show the largest positive

Lyapunov exponent in fractional order close to “1.” It can also be seen that, as the fractional order q decreases, the FOSG system starts losing its largest positive Lyapunov exponent. When $q \leq 0.98$ the only positive Lyapunov exponent of the system becomes negative and thus the chaotic oscillations in the system disappear.

5.2. Stability Analysis of FOSG System

Commensurate Order. For commensurate FOSG system of order q , the system is stable and exhibits chaotic oscillations if $|\arg(\text{eig}(J_E))| = |\arg(\lambda_i)| > q\pi/2$, where J_E is the Jacobian matrix at the equilibrium E and λ_i are the eigenvalues of the FOSG system, where $i = 1, 2, 3, 4$. As seen from the FOSG system, the eigenvalues should remain in the unstable region and the necessary condition for the FOSG system to be stable is $q > (2/\pi)\tan^{-1}(|\text{Im } \lambda|/\text{Re } \lambda)$. As we know, the eigenvalues of the system are $\lambda_{1,2} = -15.46 \pm 15.98i$, $\lambda_3 = -3.85$, $\lambda_4 = 2.38$ and it is clearly seen that λ_4 is an unstable focus and hence λ_4 contributes to the existence of chaotic oscillations in FOSG system.



(a) Bifurcation with fractional orders for FPSG system

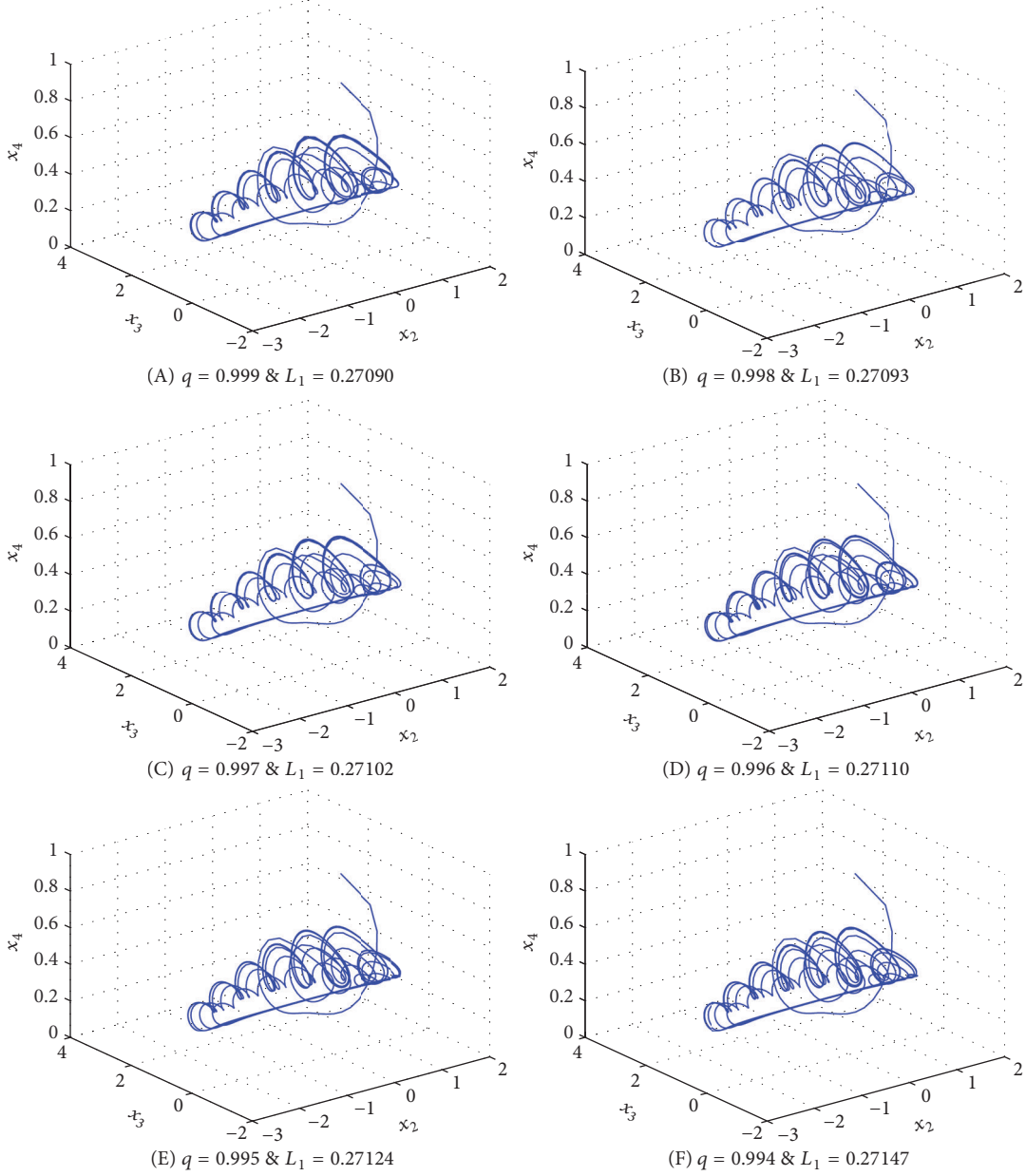


FIGURE 9: Continued.

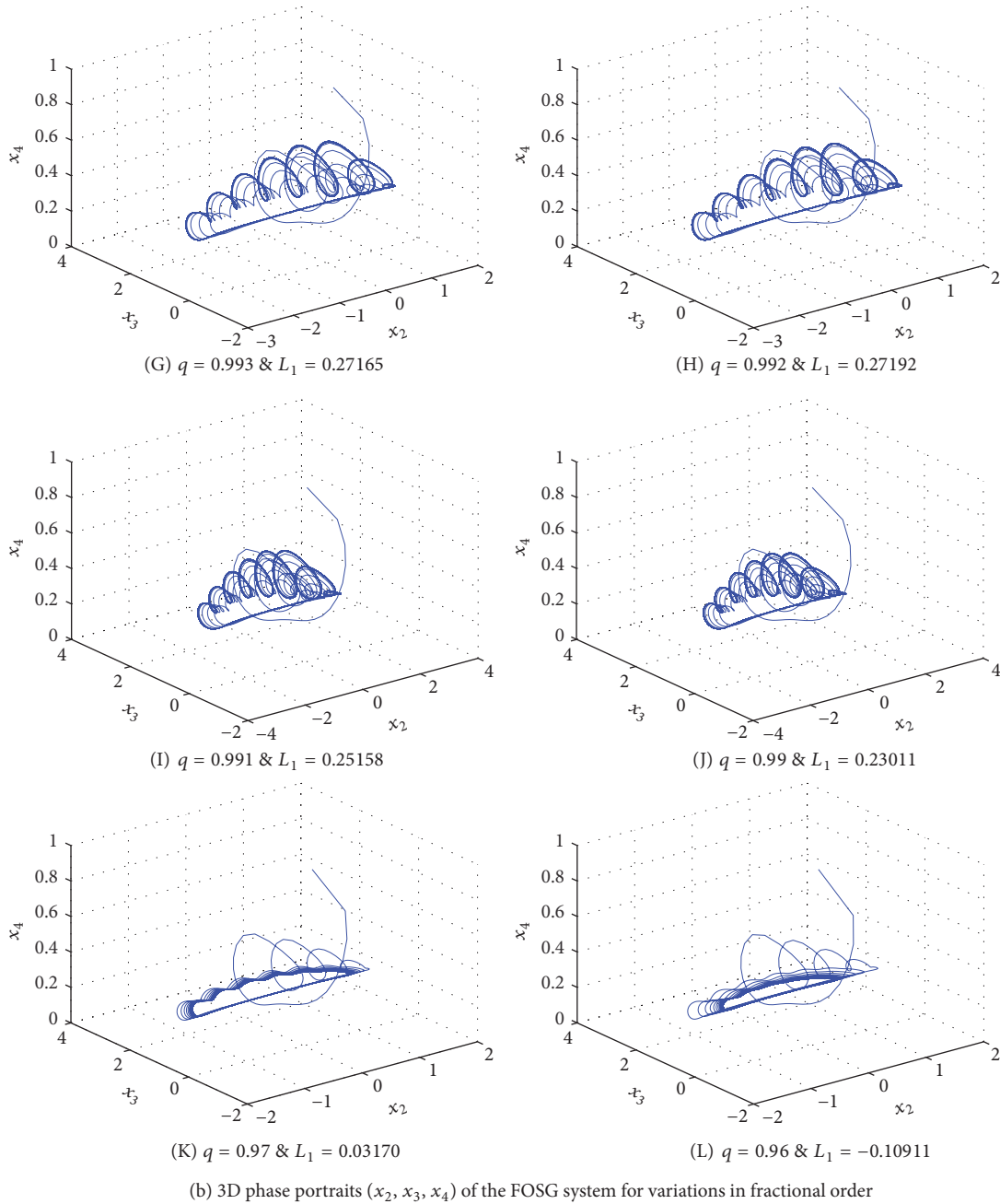


FIGURE 9

Incommensurate Order. The necessary condition for the FOSG system to exhibit chaotic oscillations in the incommensurate case is $\pi/2M - \min_i(|\arg(\lambda_i)|) > 0$, where M is the LCM of the fractional orders. If $q_x = 0.99$, $q_y = 0.98$, $q_z = 0.97$, and $q_w = 0.96$, then $M = 100$. The characteristic equation of the system evaluated at the equilibrium is $\det(\text{diag}[\lambda^{Mq_x}, \lambda^{Mq_y}, \lambda^{Mq_z}, \lambda^{Mq_w}] - J_E) = 0$ and by substituting the values of M and the fractional orders, $\det(\text{diag}[\lambda^{99}, \lambda^{98}, \lambda^{97}, \lambda^{96}] - J_E) = 0$, the characteristic equation for the equilibrium point E_1 is $\lambda^{390} + \lambda^{295} + \lambda^{294} + 33.21\lambda^{293} + 1.17\lambda^{292} + \lambda^{199} + 33.23\lambda^{198} + 521.14\lambda^{197} + 33.40\lambda^{196} + 38.59\lambda^{195} + 0.167\lambda^{194} + 6.56\lambda^{193}$

$+ \lambda^{102} + 33.40\lambda^{101} + 557.57\lambda^{100} + 606.81\lambda^{99} + 38.94\lambda^{98} - 0.18\lambda^{97} - 369.75\lambda^{96} + \lambda^4 + 32.4\lambda^3 + 530.9\lambda^2 + 444.29\lambda - 4541$. The approximated solution of the characteristic equation is $\lambda_{390} = 0.72$, whose argument is zero, which is the minimum argument, and hence the stability necessary condition becomes $\pi/200 - 0 > 0$ which solves for $0.01571 > 0$. Hence, the FOSG system is stable and chaos exists in the incommensurate system.

5.3. Bicoherence of FOSG System. In Section 3.4, we have discussed the bicoherence of integer order smart grid. In this section we will investigate the bicoherence of FOSG

system. The commensurate fractional order of the FOSG system is taken as 0.992. As can be seen from Figures 10(a) and 10(b), compared to the integer order bicoherence contours (Figures 5 and 6), the bicoherence of FOSG systems shows multifrequency components contributing to the power spectrum. The multifrequency components can be seen denser in FOSG bicoherence confirming the existence of higher dimension spectrums. Also the same can be observed when investigating the bicoherence contours of all states together as seen from Figure 10(c). When compared with the integer order all state bicoherence (Figure 7), we can see that the fractional order bicoherence shows more yellow shades confirming the cross-bicoherence is significantly nonzero, and nonconstant, indicating a nonlinear relationship between the states. Hence by the above investigations we conclude that the nonlinearities occurring in the fractional order model of the smart grid system are more of the multifrequency nature and thus contributing to greater power spectrums compared to the integer order bicoherence.

6. Adaptive Sliding Mode Control of Nonlinearity in FOSG

The control goal of this paper is to design a suitable adaptive sliding mode controller for suppression of chaotic oscillations in the fractional order smart grid (FOSG) system (9). For deriving the robust ASMC controller for system (9), let us redefine the fractional order system with an adaptive sliding mode controller $u_i(t)$, $i = 1, 2, 3, 4$,

$$D^{q_1} x_1 = x_2 + u_1,$$

$$D^{q_2} x_2 = 0.573 - 0.167x_2 + 20x_4 \cos(x_1 - x_3 + 1.483) + 11.667x_4 \cos(x_1 + 1.483) + u_2,$$

$$D^{q_3} x_3 = 69 - 93.33x_4 - 179.05x_4^2 - 50\hat{i}_0 x_4 \sin x_3 - 300x_4 \sin x_3 \cos(x_1 - 1.483) + u_3,$$

$$D^{q_4} x_4 = 25.322x_4^2 + 13.054x_4 + 3.529x_4 \cos(x_1 - 1.483) - 3.529x_4 \cos x_3 \cos(x_3 - 1.483) + 42.353x_4 \sin x_3 \cos(x_1 - 1.483) + 7.059\hat{i}_0 x_4 \sin x_3 - 42.353x_4 \sin x_3 \cos(x_3 - 1.483) - 35.294x_4 \sin(x_3 + 1.483) + 0.588\hat{i}_0 x_4 \cos x_3$$

$$+ 2.941x_4 \cos(x_3 - 1.483) + 1.31778 + u_4. \quad (10)$$

The initial conditions are the same as in Section 2 and the parameter value i_0 is assumed unknown and is estimated with a parameter estimate \hat{i}_0 .

6.1. Controller Design

6.1.1. Problem Statement. In this section we investigate the adaptive fractional order sliding mode control (FOASMC) of a fractional order system. Let us define a generalized fractional order system with FOASMC as

$$D^q x = f(x) + F(x)a + u(t), \quad (11)$$

where q is the fractional order of the system and where $u(t)$ is the adaptive controller for controlling the chaotic oscillations in the slave system.

Let us define the control error as

$$e = 0 - x. \quad (12)$$

The sliding surface for the fractional order integral sliding mode control [40, 41] is defined as

$$s(e) = e + k \int e(\tau) d\tau. \quad (13)$$

The fractional first derivative of the sliding surface is derived as

$$D^q s = D^q e + ke. \quad (14)$$

The fractional order error dynamics is defined as

$$D^q e = -D^q x. \quad (15)$$

Using (11) and (12) in (15)

$$D^q e = -f(x) - F(x)a + u(t). \quad (16)$$

Let us define the adaptive controller as

$$u(t) = f(x) + F(x)\hat{a} - ke - \eta \operatorname{sgn}(s) - \rho s, \quad (17)$$

where k, η, ρ are positive gain values, \hat{a} is parameter estimate fractional order system, and s is the sliding surface.

Using (17) in (16), the error dynamics simplifies to

$$D^q e = -F(x)[a - \hat{a}] - \eta \operatorname{sgn}(s) - \rho s. \quad (18)$$

The Lyapunov candidate function to analyze the stability of the controller is defined as

$$V = \frac{1}{2}s^2 + \frac{1}{2}(a - \hat{a})^2. \quad (19)$$

The Lyapunov first derivate is derived as

$$\dot{V} = s \cdot \dot{s} + (a - \hat{a}) \left(-\dot{\hat{a}} \right). \quad (20)$$

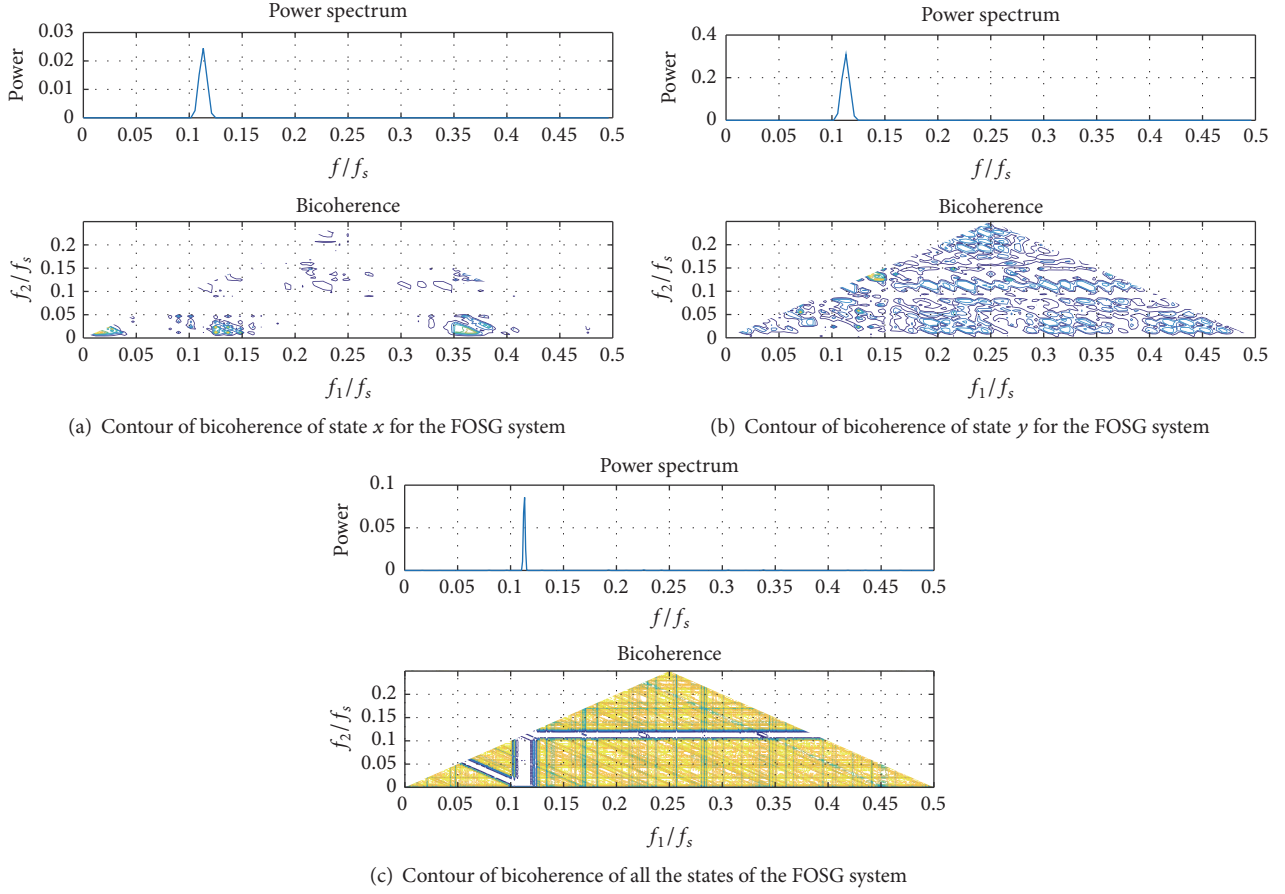


FIGURE 10: Bicoherence of FOSG system.

By definition of fractional calculus [42–44],

$$\dot{x}(t) = D_t^{1-q} \cdot D_t^q x(t). \quad (21)$$

Using (21) in (20),

$$\dot{V} = s \cdot D_t^{1-q} \cdot D_t^q s - (a - \hat{a}) (D_t^{1-q} \cdot D_t^q \hat{a}). \quad (22)$$

Finding the sign of the Lyapunov first derivative using (22) seems difficult and hence we use the modified fractional order Lyapunov method defined by Rajagopal et al. [19] as

$$\frac{1}{2} D_t^q x^2(t) \leq x(t) \frac{1}{2} D_t^q x(t), \quad q \in (0, 1). \quad (23)$$

Using (23), (18), and (17) in (20),

$$\begin{aligned} \dot{V} \leq ks [-F(x)(a - \hat{a}) - \eta \operatorname{sgn}(s) - \rho s] \\ - (a - \hat{a}) (D^q \hat{a}). \end{aligned} \quad (24)$$

Let us define the parameter estimate laws as

$$D^q \hat{a} = ks \cdot F(x). \quad (25)$$

Using (25) in (24)

$$\dot{V} = -\eta |s_w| - \rho s^2 \quad (26)$$

as η and ρ are all positive and \dot{V} is negative definite. Using Barbalat's lemma [45], we conclude that $e(t) \rightarrow 0$ as $t \rightarrow \infty$.

6.1.2. Adaptive Sliding Mode Control of FOSG System. The main control objective of this paper is to design adaptive sliding mode controllers (u_1, u_2, u_3, u_4) such that the chaotic oscillations in the FOSG system are controlled. Sliding mode control methodology is a simple approach to robust control and good at dealing with dynamic uncertainty [40]. The control design procedure consists of two steps: first constructing a sliding surface which presents the desired dynamics [41, 46] and second selecting a switching control law so as to verify sliding condition.

Let us define the integral sliding surface as

$$s_i = x_i + k_i \int_0^t x_i(\tau) d\tau, \quad i = 1, 2, 3, 4. \quad (27)$$

The fractional derivate of the sliding surface is given by

$$D^{q_i} s_i = D^{q_i} x_i + k_i x_i, \quad i = 1, 2, 3, 4. \quad (28)$$

For any initial conditions, the problem control of chaotic oscillations in FOSG system is equivalent to that of the states of the FOSG system remaining on the surface s_i for all $t > 0$. When the system operates in the sliding surface, it satisfies $s = 0$ and $D^{q_i} s = 0$ for $i = 1, 2, 3, 4$.

The parameter estimation errors are given by

$$e_{i_0} = \hat{i}_0 - i_0. \quad (29)$$

The fractional derivative of the parameter estimation errors is

$$D^q e_{i_0} = D^q \hat{i}_0 - i_0. \quad (30)$$

Let us define the adaptive sliding mode controllers as

$$\begin{aligned} u_1 &= -x_2 - k_1 x_1 - \eta_1 \operatorname{sgn}(s_1) - \rho_1 s_1, \\ u_2 &= -0.573 + 0.167x_2 - 20x_4 \cos(x_1 - x_3 + 1.483) \\ &\quad - 11.667x_4 \cos(x_1 + 1.483) - k_2 x_2 \\ &\quad - \eta_2 \operatorname{sgn}(s_2) - \rho_2 s_2, \\ u_3 &= -69 + 93.33x_4 + 179.05x_4^2 + 50\hat{i}_0 x_4 \sin x_3 \\ &\quad + 300x_4 \sin x_3 \cos(x_1 - 1.483) - k_3 x_3 \\ &\quad - \eta_3 \operatorname{sgn}(s_3) - \rho_3 s_3, \\ u_4 &= -25.322x_4^2 - 13.054x_4 \\ &\quad - 3.529x_4 \cos(x_1 - 1.483) \\ &\quad + 3.529x_4 \cos x_3 \cos(x_3 - 1.483) \\ &\quad - 42.353x_4 \sin x_3 \cos(x_1 - 1.483) \\ &\quad - 7.059\hat{i}_0 x_4 \sin x_3 \\ &\quad + 42.353x_4 \sin x_3 \cos(x_3 - 1.483) \\ &\quad + 35.294x_4 \sin(x_3 + 1.483) \\ &\quad - 0.588\hat{i}_0 x_4 \cos x_3 \\ &\quad - 2.941x_4 \cos(x_3 - 1.483) - 1.31778 - k_4 x_4 \\ &\quad - \eta_4 \operatorname{sgn}(s_4) - \rho_4 s_4, \end{aligned} \quad (31)$$

where k_i , ρ_i , η_i for $i = 1, 2, 3, 4$ are positive constants and the parameter estimate of i_0 is

$$\begin{aligned} D^q \hat{i}_0 &= -50s_3 x_4 \sin x_3 + 7.059s_4 x_4 \sin x_3 \\ &\quad + 0.588s_4 x_4 \cos x_3 - k e_{i_0}, \end{aligned} \quad (32)$$

where k is the estimation gain and is always positive.

6.2. Stability Analysis of the Controller

Theorem 1. *Considering that adaptive sliding mode control input law in (15) is used to control the FOSG system in (10) with parameter estimate in (32), then the controller (31) is globally asymptotically stable.*

Proof. To check the stability of the controlled system, let us consider the following Lyapunov candidate function:

$$V = \frac{1}{2} [s_1^2 + s_2^2 + s_3^2 + s_4^2 + e_{i_0}^2]. \quad (33)$$

The first derivative of the Lyapunov candidate function is

$$\dot{V} = s_1 \dot{s}_1 + s_2 \dot{s}_2 + s_3 \dot{s}_3 + s_4 \dot{s}_4 + e_{i_0} \dot{e}_{i_0}. \quad (34)$$

By definition of fractional calculus [42–44], we obtain

$$\dot{x}(t) = D_t^{1-q} \cdot D_t^q x(t). \quad (35)$$

Applying (35) in (34)

$$\begin{aligned} \dot{V} &= s_1 D_t^{1-q_1} \cdot D_t^{q_1} s_1 + s_2 D_t^{1-q_2} \cdot D_t^{q_2} s_2 + s_3 D_t^{1-q_3} \\ &\quad \cdot D_t^{q_3} s_3 + s_4 D_t^{1-q_4} \cdot D_t^{q_4} s_4 + e_{i_0} D_t^{1-q} \cdot D_t^q e_{i_0}. \end{aligned} \quad (36)$$

Thus, it is clear that stability calculations with (36) are very difficult. So, we use modified Lyapunov stability theory as given in [19].

Let $x(t)$ be a time continuous and derivable function. As proved in [19], for any time instant $t \geq t_0$, we have

$$\frac{1}{2} D_t^q x^2(t) \leq x(t) \cdot D_t^q x(t) \quad \forall q \in (0, 1). \quad (37)$$

Using (37) in (34)

$$\begin{aligned} \dot{V} &\leq s_1 [D^{q_1} x_1 + k_1 x_1] + s_2 [D^{q_2} x_2 + k_2 x_2] \\ &\quad + s_3 [D^{q_3} x_3 + k_3 x_3] + s_4 [D^{q_4} x_4 + k_4 x_4] \\ &\quad + e_{i_0} D^q \hat{i}_0. \end{aligned} \quad (38)$$

Using the ASM controllers (31) and parameter estimate (32) in (38),

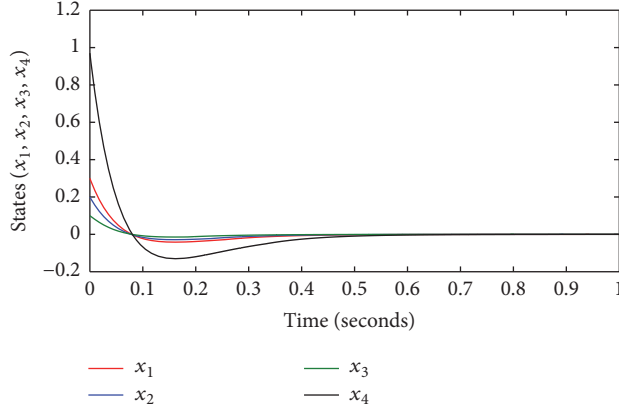
$$\begin{aligned} \dot{V} &\leq -\eta_1 |s_1| - \eta_2 |s_2| - \eta_3 |s_3| - \eta_4 |s_4| - \rho_1 s_1^2 - \rho_2 s_2^2 \\ &\quad - \rho_3 s_3^2 - \rho_4 s_4^2. \end{aligned} \quad (39)$$

As ρ_i and η_i are positive for $i = 1, 2, 3, 4$, using Barbalat's lemma [45], the Lyapunov first derivative (39) is a negative definite function which infers that the controller is stable and is valid for any bounded initial conditions. \square

7. Numerical Simulations

The FOSG system (10) with the robust adaptive sliding mode controller (31) and parameter estimate (32) with initial conditions as in Section 2 and initial condition for the parameter estimate $i_0(0) = 0.1$ are numerically analyzed using Matlab. The fractional orders of the FOSG system are chosen as commensurate order $q = 0.992$. The controller gains are taken as $k_i = 10$ and sliding surface gains are taken as $\rho_i = 25$ and $\eta_i = 0.1$ with $i = 1, 2, 3, 4$.

The state trajectories of the controlled fractional order induction chaotic system (10) are shown in Figure 11(a). Figure 11(b) shows the parameter estimate with controller in action. It can be clearly observed that the state trajectories converge to zero as soon as the controller is introduced which clearly shows that the fractional order system (9) is well-controlled by the adaptive controller with the uncertainty in the inverter current i_0 .



(a) Time history of the controlled states of FOSG system

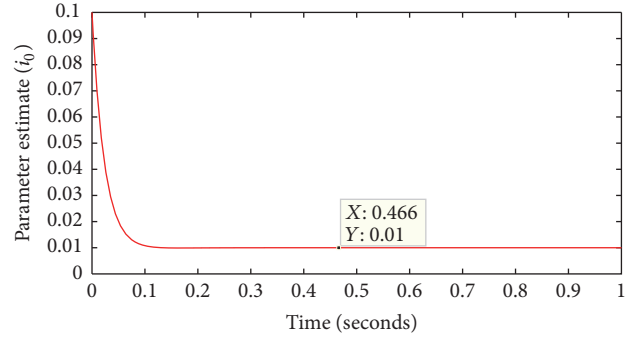
(b) Time history of parameter estimate \hat{i}_0

FIGURE 11

8. Chaos Control with Genetically Optimized Fractional Order PID Controllers (GAFOPID)

Fractional order PID (FOPID) controllers described by using fractional calculus are the most common and useful algorithm in control systems engineering. In most cases, feedback loops are controlled using PID algorithms; they are designed to correct error(s) between instant value(s) in a system and chosen set point values. Design of FOPID controller using genetic algorithms (GA) which is a stochastic global search method uses the process of natural evolution. It is one of the methods used for optimization and successfully applied in [47, 48]. GA have to be initialized before the algorithm can proceed. The initialization of the population size, variable bounds, and the evaluation objective functions are required, to evaluate the best gain values of FOPID controller for the system. An objective function could be created to find a FOPID controller that gives a minimal error. The error functions such as sum absolute error (SAE) are used as objective functions in this work.

Let us define the fractional order PID controllers as

$$u_i = K_P e_i + K_I \int_0^t e_i d\tau^\beta + K_D \frac{d^\delta e_i}{dt^\delta}, \quad i = 1, 2, 3, 4, \quad (40)$$

where u_i is the fractional order PID action control, δ, β are the fractional order differential and integral operators [42–44], e_i is the error signal given by $e_i = 0 - x_i$, and K_P, K_I, K_D are the proportional, integral, and the derivative gains to suppress the nonlinearity in the FOSG system.

Matlab optimization tool box is used for numerical simulation with the following options:

Variable bounds matrix of the proportional, integral, and the derivative gains = $[-0.001, 0.001]$, but for the states x_3, x_4 the values are multiplied to hundred and ten for the difference of variation range.

Population size = 100, GA. Generally the bigger the population size, the better the final approximation.

Number of generations = 100.

TABLE 1: FOPID controller gain values optimized with GA.

FOPID controller	K_P	K_I	K_D
u_1	0.0601	0.0975	0.2522
u_2	0.0830	0.1151	0.1719
u_3	0.0081	0.3316	0.0417
u_4	-0.0365	0.2448	0.2107

Selection function = stochastic uniform.

Crossover fraction = 0.8.

Mutation function = Gaussian.

Stopping criteria = error performance criterion.

Length of the chromosome = 12, decimal coding.

The objective function is written based on error performance criterion sum absolute error as

$$\text{fitness} = \frac{1}{\sum (e_i)}, \quad i = 1, 2, 3, 4. \quad (41)$$

Table 1 shows the FOPID gain values after running the GA solver from the optimization tool with the options cited above, we get the best solutions tracked over generations for the complete chaos suppression of the FOSG system via fractional order PID controllers using gains values genetically optimized; Figure 12 shows the time history of the FOSG states (x_1, x_2, x_3, x_4) and Figure 13 shows the time history of parameter estimate.

As seen from Figures 10 and 12, in the fractional order adaptive sliding mode controller (FOASMC) method of control the states converge at $t = 0.462$ s whereas in the GAFOPID based control, the states converge at $t = 0.22$ s. The states control in Figures 10 and 12 and the parameter estimation plots shown in Figures 11 and 13 clearly indicate that GAFOPID controllers are efficient compared to the FOASMC controllers. As can be seen from Figures 11 and 13, FOASMC based parameter estimation ($t = 0.2521$ s) is slower than the GAFOPID controllers ($t = 0.1746$ s). This proves that the optimized controllers are better in performance

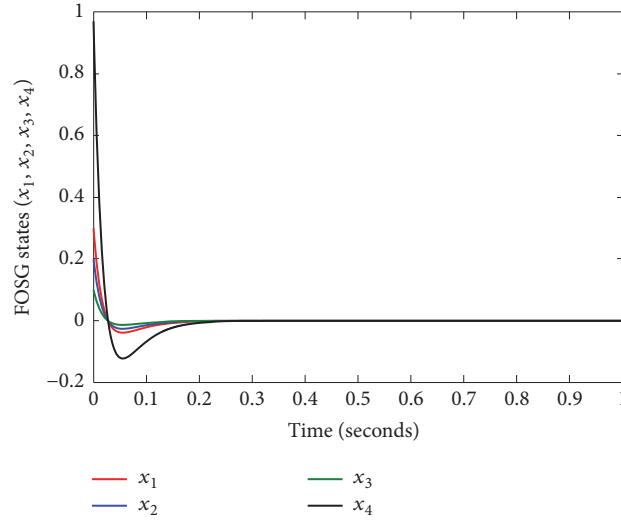


FIGURE 12: Time history of GAFOPID controlled FOSG system states.

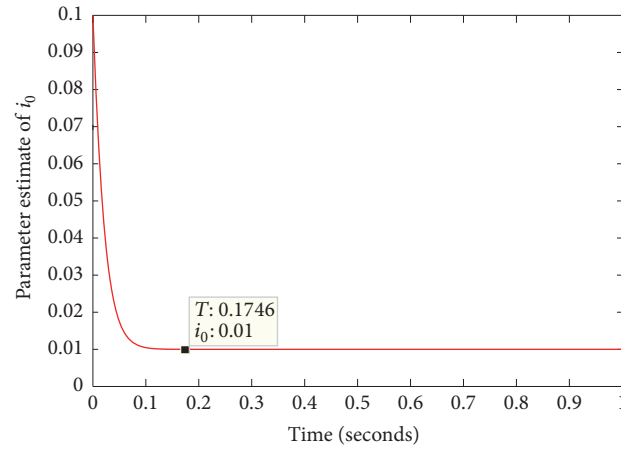


FIGURE 13: Time history of GAFOPID controlled parameter estimates.

than sliding mode controllers in the case of nonlinearity suppression in fractional order systems.

9. FPGA Implementation of the FOSG System and GAFOPID Controllers

9.1. FPGA Implementation of the FOSG System. In this section we discuss the implementation of the proposed fractional order smart grid system in FPGA [49–54] using the Xilinx (Vivado) System Generator toolbox in Simulink. Firstly we configure the available built-in blocks of the System Generator toolbox. The Add/Sub blocks are configured with zero latency and 32/16-bit fixed point settings. The output of the block is configured to rounded quantization in order to reduce the bit latency. For the multiplier block a latency of 3 is configured and the other settings are the same as in Add/Sub block. Next we will have to design the fractional order integrator which is not a readily available block in the System Generator [49]. Hence we implement the integrators using the mathematical relation discussed in [50] and the

value of h is taken as 0.001 and the initial conditions are fed into the forward register with fractional order taken as $q = 0.992$ for FOSG system. The sinusoidal functions are implemented using the CORDIC 6.0 blocks and Figures 14, 15, 16(a), and 16(b) show the Xilinx RTL schematics of the FOSG system implemented in Kintex 7 (device = 7k160t; package = fbg484 S) and 3D phase portraits of the FPGA implemented FOSG system, power utilized by the system and power utilized for various fractional orders, respectively. Table 2 shows the resources utilized by the FOSG system including the clock frequency. Increasing the sampling time period in some implementations may lead to a clock frequency mismatch and hence plays a critical role in implementation. Also negative time slack may also create problems while implementing the design and hence choosing constraints may also be critical in cases where the number of logical operations is more. Also avoiding DDR clocks helps in reducing the route delays. For analyzing the power consumed by the controllers, we use the approximation methodology discussed in [53, 54]. It confirms that larger

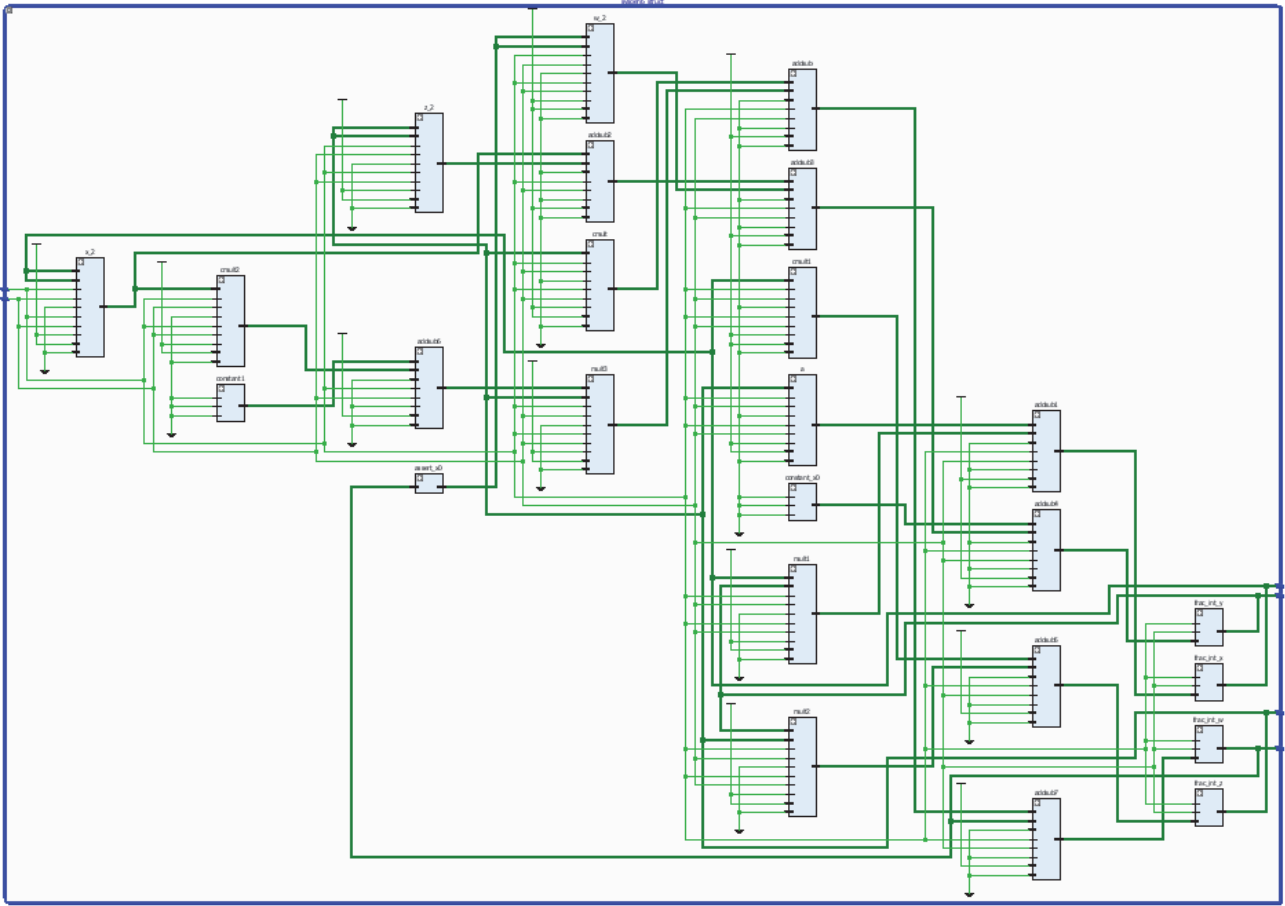


FIGURE 14: Xilinx schematics of the FOSG system implemented in Kintex 7 (device = 7k160t; package = fbg484 S).

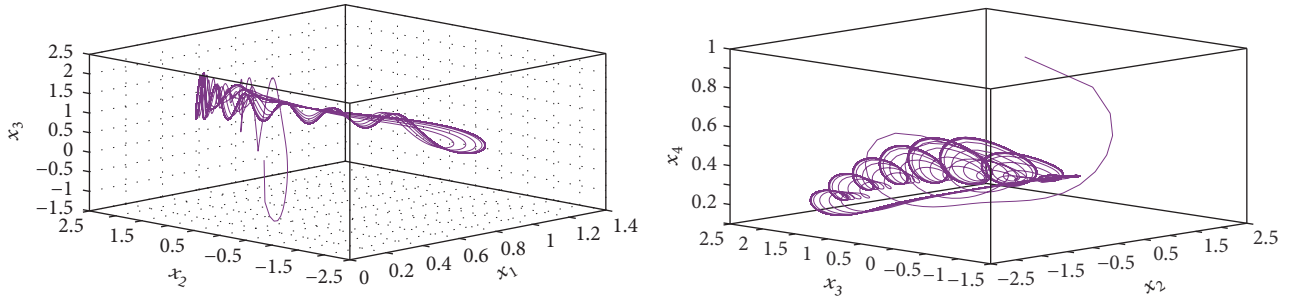


FIGURE 15: 3D phase portraits of the FPGA implemented FOSG system.

TABLE 2: Resources utilized by the FOSG system.

Kintex 7 k160t	Utilization	Available	Utilization%	Clock frequency	
				f_{max}	Used
LUT	1027	101400	1.01	500 Mhz	311 Mhz
FF	954	202800	0.47	300 Mhz	160 Mhz
DSP	51	600	8.5	500 Mhz	352 Mhz
IO	132	285	46.3	250 Mhz	161 Mhz
BUFG	3	32	9.37	300 Mhz	127 Mhz

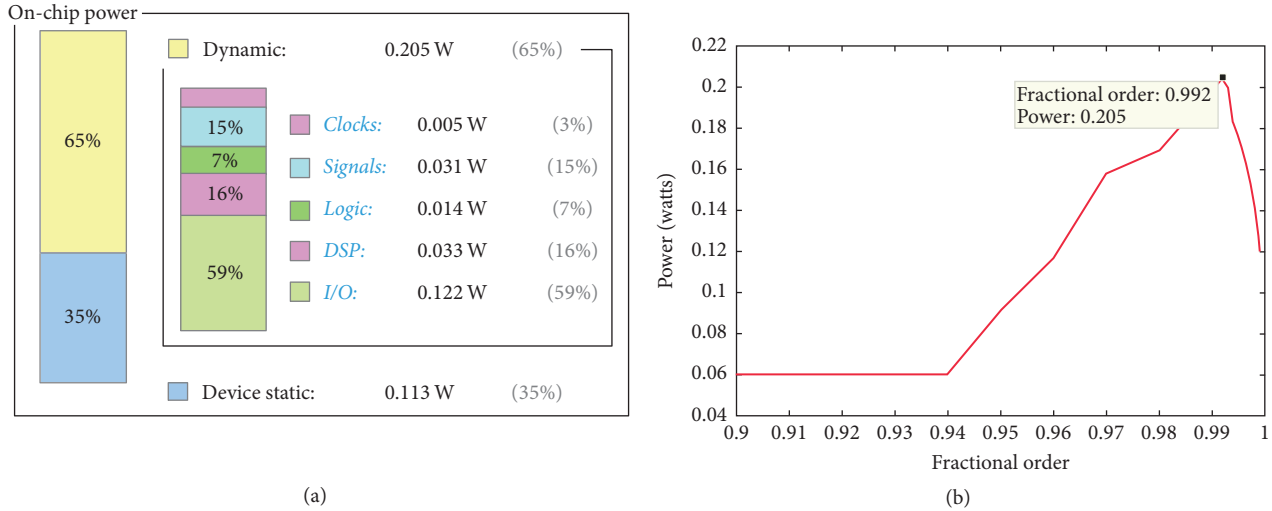


FIGURE 16: (a) Power utilized by FOSG system. (b) Power utilized for various fractional orders.

TABLE 3: Resource utilization of GAFOPID controllers.

Kintex 7 k160t	Utilization	Available	Utilization%	Clock frequency	
				f_{\max}	Used
LUT	1124	101400	1.11	500 Mhz	339 Mhz
FF	850	202800	0.42	300 Mhz	140 Mhz
DSP	36	600	6.00	500 Mhz	344 Mhz
IO	129	285	45.26	250 Mhz	129 Mhz
BUFG	1	32	3.13	300 Mhz	112 Mhz

power will be consumed by the system when the FOSG system shows largest Lyapunov exponents ($q = 0.992$). To utilize the power of FPGA, the computation needs to be divided into several independent blocks of threads that can be executed simultaneously [51]. The performance on FPGA is directly related to the number of threads and its performances decrease when number of branching instructions increases. Hence we designed the system and the GAFOPID controllers as four parallel threads each as shown in Figures 18 and 19. The fractional order operators are implemented as building blocks and the so-called frame delay is not noticeable in the FPGA hardware implementation due to its parallel data structure, unlike a microprocessor-based implementation. While FPGA implementations have a reputation for being difficult to design, with the help of systematic methodology, a system can be put together with less work than is required for more traditional software-based realizations [52].

9.2. FPGA Implementation of GAFOPID Controllers. In this section we implement the proposed fractional order genetically optimized PID controllers (GAFOPID) derived in (15) along with the fractional parameter update law (16). For implementation of the entire control scheme we use Kintex 7 (device = 7k160t; package = fbg484 S). The fractional order of the FOSG system and GAFOPID controllers are kept as $q = 0.992$. For analyzing the power consumed by the controllers, we use the approximation methodology discussed in [54]. It confirms that larger power will be consumed

by the controller when the FOSG system shows the largest Lyapunov exponent. Figure 17 shows the RTL schematics of the GAFOPID controllers implemented in Kintex 7 (device = 7k160t; package = fbg484 S). Figures 18(a) and 18(b) show the power utilization of the controller and power utilization with change in fractional orders, respectively. Table 3 shows the resources utilized by the GAFOPID controllers. Figure 19 shows the time history of the FOSG states controlled with FPGA implemented GAFOPID controllers. Figure 20 shows the time history of parameter estimates. The initial conditions for the numerical analysis are taken as in Section 7.

10. Conclusion

In this work we investigated the nonlinearity in a specific smart grid system. We showed the existence of chaotic oscillations for specific initial conditions and inverter current value. Fractional order smart grid dimensionless model of the smart grid is derived and investigated. Bifurcation of the system with fractional orders is investigated and it is shown that the largest Lyapunov exponent of the system exists in the fractional order. Hence fractional order control schemes for suppression of chaotic oscillations with fractional order adaptive sliding mode control (FOASMC) and genetically optimized fractional order PID control (GAFOPID) are derived. Numerical simulations prove that GAFOPID controllers are effective compared to FOASMC for chaos control

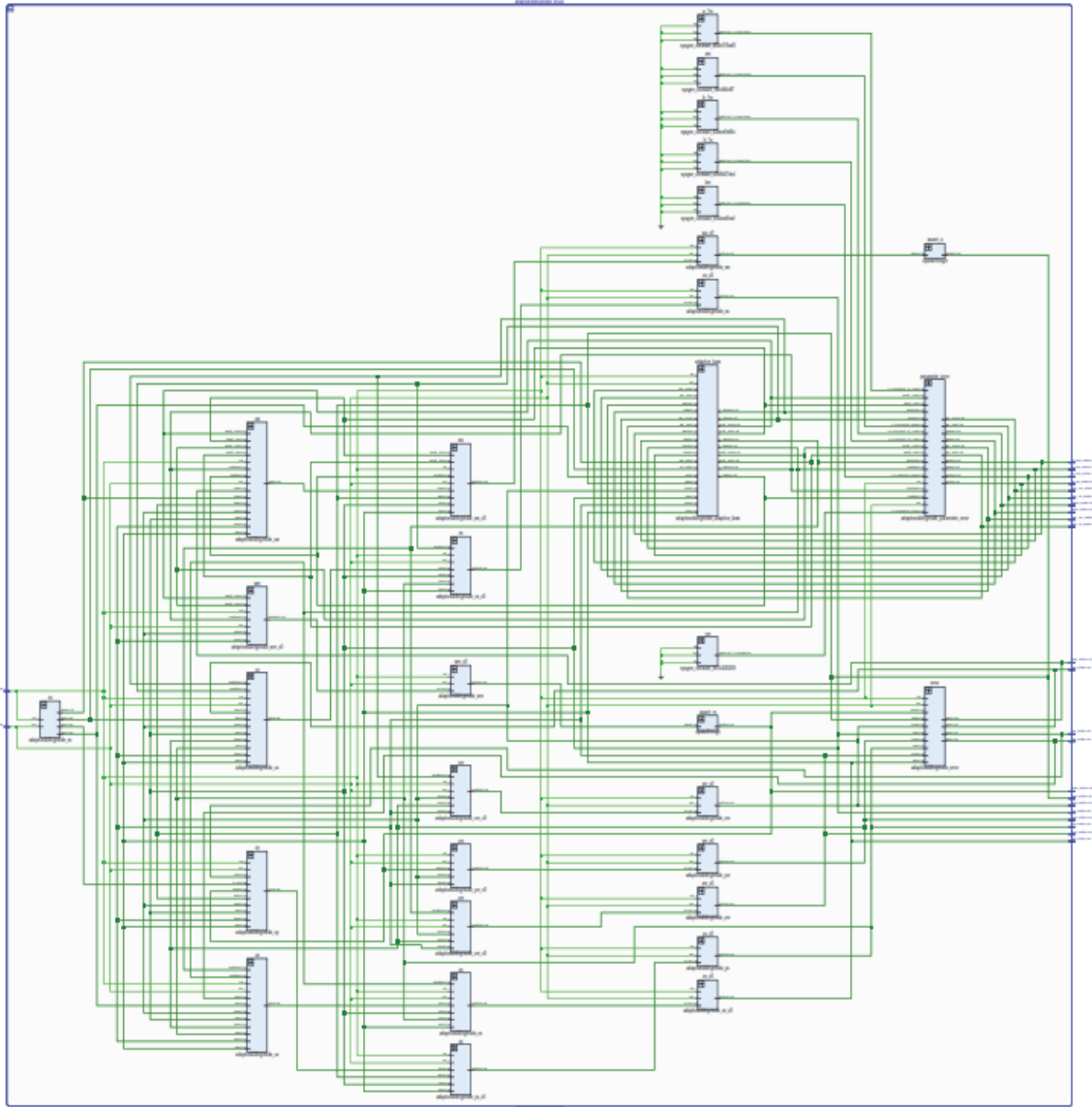
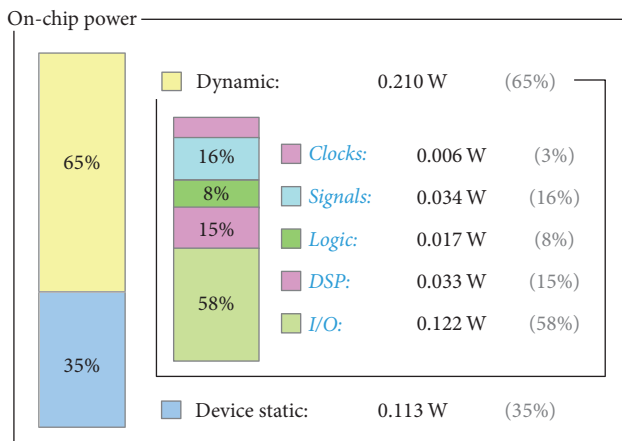
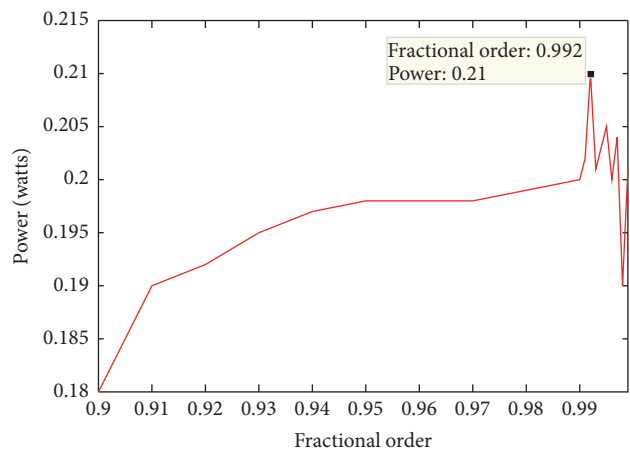


FIGURE 17: Xilinx schematics of the GAFOPID controllers implemented in Kintex 7 (device = 7k160t; package = fbg484 S).



(a)



(b)

FIGURE 18: (a) Power utilized and (b) power utilization versus fractional order of GAFOPID controllers.

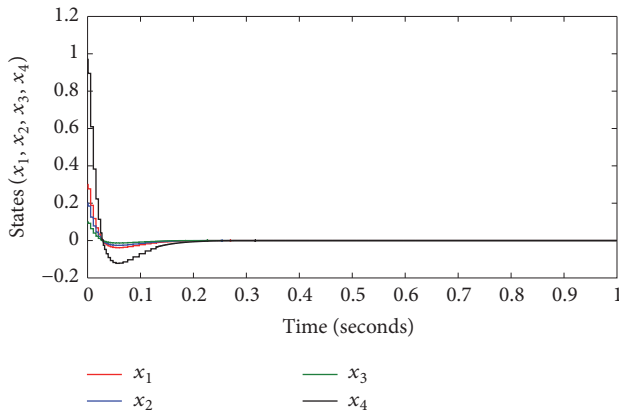


FIGURE 19: Time history of FOSG states controlled with FPGA implemented GAFOPID controllers.

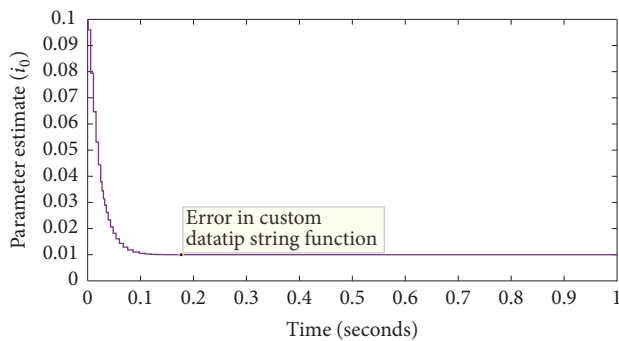


FIGURE 20: Time history of parameter estimates.

in fractional order systems. The proposed GAFOPID controllers are implemented in FPGA to show that the control scheme is hardware realizable. Power utilization for various fractional orders is presented and it is shown that the system uses maximum power when the FOSG system exhibits its largest Lyapunov exponent.

Conflicts of Interest

The authors declare that there are no conflicts of interest regarding the publication of this paper.

References

- [1] R. Tongia, "Ph.D. Smart Grids White Paper: WH-1:14.8," <https://cstep.in/node/47>.
- [2] K. Moslehi and R. Kumar, "A reliability perspective of the smart grid," *IEEE Transactions on Smart Grid*, vol. 1, no. 1, pp. 57–64, 2010.
- [3] US Department of Energy, *How the Smart Grid Promotes a Greener Future*, 2010, <http://energy.gov/oe/downloads/how-smart-grid-promotes-greener-future>.
- [4] J. Xia and Y. Wang, "Secure key distribution for the smart grid," *IEEE Transactions on Smart Grid*, vol. 3, no. 3, pp. 1437–1443, 2012.
- [5] C. Canizares, "Voltage stability assessment, procedures and guides," IEEE/PES Power System Stability Subcommittee Special Publication, 2001.
- [6] W. Qiao, G. K. Venayagamoorthy, and R. G. Harley, "Missing-sensor-fault-tolerant control for SSSC FACTS device with real-time implementation," *IEEE Transactions on Power Delivery*, vol. 24, no. 2, pp. 740–750, 2009.
- [7] S. Vaidyanathan and C. Volos, *Advances and Applications of Chaotic Systems*, Springer, Berlin, Germany, 2016.
- [8] N. Hemati and M. C. Leu, "A complete model characterization of brushless DC motors," *IEEE Transactions on Industry Applications*, vol. 28, no. 1, pp. 172–180, 1992.
- [9] Z. Li, J. B. Park, Y. H. Joo, B. Zhang, and G. Chen, "Bifurcations and chaos in a permanent-magnet synchronous motor," *IEEE Transactions on Circuits and Systems I: Fundamental Theory and Applications*, vol. 49, no. 3, pp. 383–387, 2002.
- [10] Z. Jing, C. Yu, and G. Chen, "Complex dynamics in a permanent-magnet synchronous motor model," *Chaos, Solitons & Fractals*, vol. 22, no. 4, pp. 831–848, 2004.
- [11] N. Jabli, H. Khammari, M. F. Mimouni, and R. Dhifaoui, "Bifurcation and chaos phenomena appearing in induction motor under variation of PI controller parameters," *WSEAS Transactions on Systems*, vol. 9, no. 7, pp. 784–793, 2010.
- [12] H. Gholizadeh, A. Hassannia, and A. Azarfar, "Chaos detection and control in a typical power system," *Chinese Physics B*, vol. 22, no. 1, Article ID 010503, 2013.
- [13] H.-K. Chen, T.-N. Lin, and J.-H. Chen, "Dynamic analysis, controlling chaos and chaotification of a SMIB power system," *Chaos, Solitons and Fractals*, vol. 24, no. 5, pp. 1307–1315, 2005.
- [14] M. P. Aghababa, "Robust finite-time stabilization of fractional-order chaotic systems based on fractional Lyapunov stability theory," *Journal of Computational and Nonlinear Dynamics*, vol. 7, no. 2, pp. 21–31, 2012.
- [15] E. A. Boroujeni and H. R. Momeni, "Non-fragile nonlinear fractional order observer design for a class of nonlinear fractional order systems," *Signal Processing*, vol. 92, no. 10, pp. 2365–2370, 2012.
- [16] R. Zhang and J. Gong, "Synchronization of the fractional-order chaotic system via adaptive observer," *Systems Science & Control Engineering*, vol. 2, no. 1, pp. 751–754, 2014.
- [17] I. Petras, "Method for simulation of the fractional order chaotic systems," *Acta Montanistica Slovaca*, vol. 11, no. 4, pp. 273–277, 2006.
- [18] Z. W. Trzaska, *Matlab Solutions of Chaotic Fractional Order Circuits*, InTech, Rijeka, Croatia, 2013, <https://cdn.intechopen.com/pdfs-wm/21404.pdf>.
- [19] K. Rajagopal, S. Vaidyanathan, A. Karthikeyan, and P. Duraisamy, "Dynamic analysis and chaos suppression in a fractional order brushless DC motor," *Electrical Engineering*, 2016.
- [20] K. Rajagopal, A. Karthikeyan, and P. Duraisamy, "Chaos suppression in fractional order permanent magnet synchronous motor and PI controlled induction motor by extended back stepping control," *Nonlinear Engineering*, vol. 5, no. 4, 2016.
- [21] C.-L. Li, S.-M. Yu, and X.-S. Luo, "Fractional-order permanent magnet synchronous motor and its adaptive chaotic control," *Chinese Physics B*, vol. 21, no. 10, Article ID 100506, 2012.
- [22] Y. Li, Y. Chen, and I. Podlubny, "Stability of fractional-order nonlinear dynamic systems: Lyapunov direct method and generalized Mittag-Leffler stability," *Computers & Mathematics with Applications*, vol. 59, no. 5, pp. 1810–1821, 2010.

- [23] J. A. Gallegos and M. A. Duarte-Mermoud, "On the Lyapunov theory for fractional order systems," *Applied Mathematics and Computation*, vol. 287–288, pp. 161–170, 2016.
- [24] M. S. Tavazoei and M. Haeri, "Chaos control via a simple fractional-order controller," *Physics Letters A*, vol. 372, no. 6, pp. 798–807, 2008.
- [25] K. Konishi, H. Kokame, and N. Hara, "Delayed feedback control based on the act-and-wait concept," *Nonlinear Dynamics*, vol. 63, no. 3, pp. 513–519, 2011.
- [26] Y. Jin, Y.-Q. Chen, and D. Xue, "Time-constant robust analysis of a fractional order [proportional derivative] controller," *IET Control Theory and Applications*, vol. 5, no. 1, pp. 164–172, 2011.
- [27] K. Rajagopal, L. Guessas, S. Vaidyanathan, A. Karthikeyan, and A. Srinivasan, "Dynamical analysis and FPGA implementation of a novel hyperchaotic system and its synchronization using adaptive sliding mode control and genetically optimized PID Control," *Mathematical Problems in Engineering*, vol. 2017, Article ID 7307452, 14 pages, 2017.
- [28] K. Rajagopal, A. Karthikeyan, and A. K. Srinivasan, "FPGA implementation of novel fractional-order chaotic systems with two equilibriums and no equilibrium and its adaptive sliding mode synchronization," *Nonlinear Dynamics*, vol. 87, no. 4, pp. 2281–2304, 2017.
- [29] E. Tlelo-Cuautle, A. D. Pano-Azucena, J. J. Rangel-Magdaleno, V. H. Carbajal-Gomez, and G. Rodriguez-Gomez, "Generating a 50-scroll chaotic attractor at 66 MHz by using FPGAs," *Nonlinear Dynamics*, vol. 85, no. 4, pp. 2143–2157, 2016.
- [30] Q. Wang, S. Yu, C. Li et al., "Theoretical design and FPGA-based implementation of higher-dimensional digital chaotic systems," *IEEE Transactions on Circuits and Systems. I. Regular Papers*, vol. 63, no. 3, pp. 401–412, 2016.
- [31] E. Dong, Z. Liang, S. Du, and Z. Chen, "Topological horseshoe analysis on a four-wing chaotic attractor and its FPGA implementation," *Nonlinear Dynamics*, vol. 83, no. 1–2, pp. 623–630, 2016.
- [32] E. Tlelo-Cuautle, V. H. Carbajal-Gomez, P. J. Obeso-Rodelo, J. J. Rangel-Magdaleno, and J. C. Nunez-Perez, "FPGA realization of a chaotic communication system applied to image processing," *Nonlinear Dynamics*, vol. 82, no. 4, pp. 1879–1892, 2015.
- [33] V. Rashtchi and M. Nourazar, "FPGA implementation of a real-time weak signal detector using a duffing oscillator," *Circuits, Systems, and Signal Processing*, vol. 34, no. 10, pp. 3101–3119, 2015.
- [34] E. Tlelo-Cuautle, J. J. Rangel-Magdaleno, A. D. Pano-Azucena, P. J. Obeso-Rodelo, and J. C. Nunez-Perez, "FPGA realization of multi-scroll chaotic oscillators," *Communications in Nonlinear Science and Numerical Simulation*, vol. 27, no. 1–3, pp. 66–80, 2015.
- [35] Y.-M. Xu, L.-D. Wang, and S.-K. Duan, "A memristor-based chaotic system and its field programmable gate array implementation," *Acta Physica Sinica*, vol. 65, no. 12, Article ID 120503, 2016.
- [36] Q. Sun, Y. Wang, J. Yang, Y. Qiu, and H. Zhang, "Chaotic dynamics in smart grid and suppression scheme via generalized fuzzy hyperbolic model," *Mathematical Problems in Engineering*, vol. 2014, Article ID 761271, 2014.
- [37] J. M. Munoz-Pacheco, L. d. Gómez-Pavón, O. G. Félix-Beltrán, and A. Luis-Ramos, "Determining the Lyapunov spectrum of continuous-time 1D and 2D multiscroll chaotic oscillators via the solution of m-PWL variational equations," *Abstract and Applied Analysis*, vol. 2013, Article ID 851970, 11 pages, 2013.
- [38] A. Wolf, J. B. Swift, H. L. Swinney, and J. A. Vastano, "Determining Lyapunov exponents from a time series," *Physica D: Nonlinear Phenomena*, vol. 16, no. 3, pp. 285–317, 1985.
- [39] C. Pezeshki, "Bispectral analysis of [systems] possessing chaotic motion," *Journal of Sound and Vibration*, vol. 137, no. 3, pp. 357–368, 1990.
- [40] K. Rajagopal and A. Karthikeyan, "Chaos suppression of fractional order willamowski-rössler chemical system and its synchronization using sliding mode control," *Nonlinear Engineering*, vol. 5, no. 3, 2016.
- [41] E. F. E. Mehmet Onder, "Fractional order sliding mode control with reaching law approach," *Turkish Journal of Electrical Engineering and Computer Sciences*, vol. 18, no. 5, p. 731, 2010.
- [42] D. Baleanu, K. Diethelm, E. Scalas, and J. J. Trujillo, *Fractional Calculus: Models and Numerical Methods*, World Scientific, Singapore, 2014.
- [43] Y. Zhou, *Basic Theory of Fractional Differential Equations*, World Scientific, Singapore, 2014.
- [44] K. Diethelm, *The Analysis of Fractional Differential Equations*, vol. 2004 of *Lecture Notes in Mathematics*, Springer, Berlin, Germany, 2010.
- [45] H. K. Khalil, *Nonlinear Systems*, Prentice Hall, New York, NY, USA, 2002.
- [46] J. Slotine and W. Li, *Applied Nonlinear Control*, Prentice Hall, Upper Saddle River, NJ, USA, 1991.
- [47] Z. Chen, X. Yuan, B. Ji, P. Wang, and H. Tian, "Design of a fractional order PID controller for hydraulic turbine regulating system using chaotic non-dominated sorting genetic algorithm II," *Energy Conversion and Management*, vol. 84, pp. 390–404, 2014.
- [48] A. Ahuja and S. K. Aggarwal, "Design of fractional order pid controller for DC motor using evolutionary optimization techniques," *WSEAS Transactions on Systems and Control*, vol. 9, pp. 171–182, 2014.
- [49] A. Charef, "Analogue realisation of fractional-order integrator, differentiator and fractional PID μ controller," *IEE Proceedings-Control Theory and Applications*, vol. 153, no. 6, pp. 714–720, 2006.
- [50] Y. Q. Chen, B. M. Vinagre, and I. Podlubny, "Continued fraction expansion approaches to discretizing fractional order derivatives—an expository review," *Nonlinear Dynamics*, vol. 38, no. 1–4, pp. 155–170, 2004.
- [51] Q. Wang, S. Yu, C. Li et al., "Theoretical design and FPGA-based implementation of higher-dimensional digital chaotic systems," *IEEE Transactions on Circuits and Systems. I. Regular Papers*, vol. 63, no. 3, pp. 401–412, 2016.
- [52] X. Jiang, *A systematic approach for digital hardware realization of fractional-order operators and systems [Ph.D. thesis]*, 2013, Ohiolink Database Accession Number: 1386649994.
- [53] E. Tlelo-Cuautle, J. Rangel-Magdaleno, and L. G. de la Fraga, *Engineering Applications of FPGAs—Chaotic Systems, Artificial Neural Networks, Random Number Generators, and Secure Communication Systems*, Springer, 2016.
- [54] C. Wang, R. Chu, and J. Ma, "Controlling a chaotic resonator by means of dynamic track control," *Complexity*, vol. 21, no. 1, pp. 370–378, 2015.

Research Article

Leader-Follower Fixed-Time Group Consensus Control of Multiagent Systems under Directed Topology

Yilun Shang and Yamei Ye

School of Mathematical Sciences, Tongji University, Shanghai 200092, China

Correspondence should be addressed to Yilun Shang; shylmath@hotmail.com

Received 19 January 2017; Accepted 1 March 2017; Published 16 March 2017

Academic Editor: Jinde Cao

Copyright © 2017 Yilun Shang and Yamei Ye. This is an open access article distributed under the Creative Commons Attribution License, which permits unrestricted use, distribution, and reproduction in any medium, provided the original work is properly cited.

This paper investigates the fixed-time group consensus problem for a leader-follower network of integrators with directed topology. A nonlinear distributed control protocol, based on local information, is proposed such that the follower agents in each subgroup are able to track their corresponding leaders in a prescribed convergence time regardless of the initial conditions. Simulation examples are presented to demonstrate the availability of our theoretical results.

1. Introduction

The past decade has witnessed an increasing attention on cooperative control of multiagent systems due to its broad applications in diverse fields including distributed computation, formation of unmanned vehicles, data fusion of sensor networks, synchronization of coupled chaotic oscillators, flocking, and swarming. A fundamental issue in coordination of multiagent systems is the consensus problem, which requires that all the agents should reach an agreement using the local information of their neighbors, which is determined by the underlying communication topology. Toward this aim, an essential step is to design proper distributed control laws such that as time goes on, all the agents converge to a consistent value asymptotically; see, e.g., [1–3] for some representative works on this topic. More backgrounds and applications of consensus problems can be found in the survey papers [4, 5] and references therein.

Most of the existing work focuses on complete consensus in the sense that all agents ultimately achieve a common group decision value [4]. However, in many real-world circumstances in cooperative control, a group of agents should be able to split into multiple subgroups and different consistent states are desired with the changes of environments, situations, and tasks. Examples include pattern formation of bacteria colonies, predator evasion and separated foraging for animal herds, cooperative task searching for

autonomous vehicles, and coordinated military operations. As a generalization of complete consensus problems, group consensus has been studied intensively in recent years [6–11], where the agents in a network are divided into multiple subgroups and the states of agents in each subgroup can reach an individual consistent state asymptotically. For example, a group consensus protocol is proposed in [6] for the first-order continuous-time multiagent systems with switching topology by using double-tree-form transformation, which converts the group consensus problem into the stability of a corresponding reduced system. A combinatorial necessary and sufficient condition for discrete-time group consensus problem is proposed in [11]. Moreover, many applications in cooperative control require dynamic leaders, which can be virtual for their followers [1, 12]. The leader-follower consensus problems are more challenging than their leaderless counterparts because these controllers not only ensure the consensus of the followers but also determine the final consensus value, which is defined by the dynamic leader. Recently, a leader-follower group consensus protocol has been proposed for second-order multiagent systems in [13]. An event-triggered control protocol has been introduced in [14] to achieve leader-follower group consensus for nonlinear multiagent systems.

It is worth noting that, for the aforementioned works, the (group) consensus can only be reached in an asymptotic manner; namely, the settling time is infinite. In many

applications, a high speed convergence characterized by a finite-time control law is essential. Finite-time consensus can lead to better disturbance rejection and more robustness against uncertainties [15]. Numerous finite-time controllers have been designed for both complete consensus problems (e.g., [16–20]) and group consensus problems (e.g., [21, 22]). Recently, a new concept, called fixed-time stability, has been proposed in [23], which guarantees a finite settling time independent of initial conditions. This fixed-time approach is promising since the knowledge of initial conditions is usually not available in advance in distributed systems. Based on the fixed-time stability notion, many new results are reported. For example, in the leaderless cases, the fixed-time average consensus has been investigated in [24–26] for the first-order integrator systems over undirected topologies. Several fixed-time group consensus protocols are analyzed in [27] over undirected topologies. Fixed-time leader-follower consensus for second-order multiagent systems with bounded input uncertainties is studied in [28], while unknown nonlinear inherent dynamics are considered in [29] for first-order leader-follower multiagent systems. The fixed-time master-slave synchronization control problems for the delayed Cohen-Grossberg neural networks and delayed memristor-based recurrent neural networks are studied in [30, 31], respectively. Two fixed-time distributed control strategies are proposed in [32] such that leaderless and leader-follower consensus can be reached over directed communication topology. It is worth noting that previous works heavily rely on the symmetry property of the network topology, and [32] is the only one dealing with general asymmetric topology concerning fixed-time consensus problems to our knowledge.

In this paper, we aim to move a further step along this line of research by studying leader-follower fixed-time group consensus for multiagent systems under directed topology. The contribution of this paper is twofold. First, a generalization of the fixed-time leader-follower consensus protocol is proposed to accommodate both directed topology and multiple leaders. Second, an explicit estimation of the settling time is presented regardless of initial conditions.

The rest of the paper is organized as follows. Section 2 provides some preliminaries and formulates the leader-follower group consensus problem. Section 3 is devoted to the analysis of our proposed fixed-time control strategy. Some numerical examples are given in Section 4 to illustrate the correctness of the obtained theoretical results. A conclusion is drawn in Section 5.

2. Background and Preliminaries

To start with, we fix some standard notations that will be used throughout the paper. The cardinality of a set S and the absolute value of a number $s \in \mathbb{R}$ are denoted by $|S|$ and $|s|$, respectively. Let \mathbb{R}_+ represent the set of nonnegative real numbers. Denote by M^T the transpose of a matrix M . The maximum and minimum eigenvalues of a symmetric matrix M are denoted by $\lambda_{\max}(M)$ and $\lambda_{\min}(M)$, respectively. $\mathbf{1}_N \in \mathbb{R}^N$ is a vector with all the entries being 1, and $\text{diag}(a_1, \dots, a_N) \in \mathbb{R}^{N \times N}$ is a diagonal matrix with diagonal entries a_1, \dots, a_N . Similar notations will be adopted for block

diagonal matrices. For a vector $x = (x_1, \dots, x_N)^T \in \mathbb{R}^N$ and $a \geq 0$, we define $|x|^a = (\text{sgn}(x_1)|x_1|^a, \dots, \text{sgn}(x_N)|x_N|^a)^T$, where $\text{sgn}(\cdot)$ is the signum function. For $p > 0$, the p -norm $\|\cdot\|_p$ is defined as $\|x\|_p = (\sum_{i=1}^N |x_i|^p)^{1/p}$ for a vector $x \in \mathbb{R}^N$. The following lemma relating different norms is often used in the analysis of fixed-time consensus problems, a proof of which can be found in [33].

Lemma 1. *Let $x \in \mathbb{R}^N$ and $p > q > 0$. Then*

$$\|x\|_p \leq \|x\|_q \leq N^{1/q-1/p} \|x\|_p. \quad (1)$$

2.1. Graph Theory. The communication network of a multiagent system can often be described by a directed graph [34]. Let $G = (V, E, A)$ be a weighted directed graph, where the node set $V = \{1, 2, \dots, N\}$ represents N follower agents and the edge set $E \subseteq V \times V$ describes the information exchange among the followers. Here, $A = (a_{ij}) \in \mathbb{R}^{N \times N}$ is the associated weighted adjacency matrix of the graph, where $a_{ji} \neq 0$ if $(i, j) \in E$ and $a_{ji} = 0$ otherwise. A path in G from i_1 to i_k is a sequence of distinct nodes (i_1, \dots, i_k) such that $(i_j, i_{j+1}) \in E$ for $j = 1, \dots, k-1$. G is said to have a spanning tree if there exists a node, called root, which has a path to any other nodes in the graph G . The (in-degree) Laplacian matrix of G is defined as $L = (l_{ij}) \in \mathbb{R}^{N \times N}$ with $l_{ii} = \sum_{j \neq i} a_{ij}$ and $l_{ij} = -a_{ij}$ for $i \neq j$. It is well-known that L is positive semidefinite and zero is an eigenvalue of L with the eigenvector $\mathbf{1}_N$. Moreover, if G contains a spanning tree, then zero is algebraically simple and all other eigenvalues of L are with positive real parts [3]. Let \bar{G} be the directed graph with node set $V \cup \{0\}$ and edge set having the form $E \cup \{(0, i) \mid \text{for some } i \in V\}$. Assume that $B = \text{diag}(b_1, \dots, b_N)$ is a nonnegative diagonal matrix with $b_i > 0$ if and only if $(0, i)$ is an edge in \bar{G} . Some properties of $H := L + B$ are characterized by the following lemma.

Lemma 2 (see [35]). *If \bar{G} has a spanning tree with 0 being the root, then H is nonsingular. Let*

$$\begin{aligned} (p_1, \dots, p_N)^T &= H^{-T} \mathbf{1}_N, \\ P &= \text{diag}(p_1, \dots, p_N), \\ Q &= PH + H^T P. \end{aligned} \quad (2)$$

Then both matrices P and Q are positive definite.

To explore the group consensus, a *grouping* $\mathcal{G} = \{\mathcal{G}_1, \dots, \mathcal{G}_K\}$ of the graph G is defined by dividing its node set into disjoint subgroups $\{\mathcal{G}_k\}_{k=1}^K$. In other words, \mathcal{G} satisfies $\bigcup_{k=1}^K \mathcal{G}_k = V$ and $\mathcal{G}_k \cap \mathcal{G}_{k'} = \emptyset$ for $k \neq k'$. We write $\mathcal{G}_1 = \{1, \dots, r_1\}$, $\mathcal{G}_2 = \{r_1 + 1, \dots, r_2\}$, \dots , $\mathcal{G}_K = \{r_{K-1} + 1, \dots, N\}$ and let $r_0 = 0$ and $r_K = N$. We assume that the interactions between agents in the same subgroup are cooperative; namely, $a_{ij} \geq 0$ if $i, j \in \mathcal{G}_k$ for some k . Each subgroup \mathcal{G}_k ($1 \leq k \leq K$) inherits the structure of G naturally in the sense of induced subgraph [34]. For each $1 \leq k \leq K$, the (in-degree) Laplacian matrix of \mathcal{G}_k is similarly defined as $L_k = (l_{ij}) \in \mathbb{R}^{|\mathcal{G}_k| \times |\mathcal{G}_k|}$ with $l_{ii} = \sum_{j \in \mathcal{G}_k, j \neq i} a_{ij}$ and $l_{ij} = -a_{ij}$ for $i \neq j$.

Let $\Theta = \{\theta_1, \theta_2, \dots, \theta_K\}$ be the set of K virtual leader agents. We make the following assumption.

Assumption 3. Fix any $k \in \{1, \dots, K\}$. For each $i \in \mathcal{G}_k$, there is a path from θ_k to i . Moreover, there is no edge from θ_k to $j \in \mathcal{G}_{k'}$ for $k' \neq k$.

Assumption 3 indicates that the follower agents in each subgroup \mathcal{G}_k have access to the information of their own leader θ_k but not to that of the other leaders directly. This assumption eases analysis for multiple leaders, which is also adopted in [13, 14]. We assume that the weight $a_{i\theta_k} \geq 0$ for $i \in \mathcal{G}_k$ and denote $B_k = \text{diag}(a_{r_{k-1}+1, \theta_k}, \dots, a_{r_k, \theta_k}) \in \mathbb{R}^{|\mathcal{G}_k| \times |\mathcal{G}_k|}$ for $1 \leq k \leq K$. Note that, under Assumption 3, the matrix $H_k := L_k + B_k$ is nonsingular by Lemma 2. Moreover,

$$\begin{aligned} P_k &= \text{diag}(p_{k, r_{k-1}+1}, \dots, p_{k, r_k}), \\ Q_k &= P_k H_k + H_k^T P_k \end{aligned} \quad (3)$$

are positive definite, where $(p_{k, r_{k-1}+1}, \dots, p_{k, r_k})^T = H_k^{-T} \mathbf{1}_{|\mathcal{G}_k|}$. Define the block diagonal matrix Q by $Q = \text{diag}(Q_1, \dots, Q_K) \in \mathbb{R}^{N \times N}$, which is also positive definite.

Assumption 4. Fix any $k \in \{1, \dots, K\}$. For each $i \in \mathcal{G}_k$ and $k' \neq k$, $\sum_{j \in \mathcal{G}_{k'}} a_{ij} = 0$. Moreover, for each $i \in \mathcal{G}_k$, $\sum_{k' \neq k} \sum_{j \in \mathcal{G}_{k'}} |a_{ij}| \leq a_{i\theta_k}$. These inequalities hold strictly for at least one $i \in V$.

The first part of Assumption 4, commonly known as the intergroup balance condition, indicates a balance of influence between an agent in a subgroup and all agents in any other subgroup and is typically required for group consensus problems in the existing literature; see, e.g., [6–11, 13, 14, 27, 36]. The second part of Assumption 4 suggests that, for each follower agent i , the accumulated influence stemming from agents in other subgroups should be dominated by that from the agent's leader. In bird flight formation, for example, it has been observed that the flock leaders often have strong influence while the groups of followers are evolved to interact with proximal 6–7 birds only with minimal information exchange rate [37, 38]. This assumption plays a key role in our analysis of fixed-time consensus over directed network topology.

2.2. Fixed-Time Stability. Consider the general differential equation

$$\begin{aligned} \dot{x}(t) &= f(t, x(t)), \\ x(0) &= x_0, \end{aligned} \quad (4)$$

where $x \in \mathbb{R}^n$ and $f: \mathbb{R}_+ \times \mathbb{R}^n \rightarrow \mathbb{R}^n$ is a nonlinear function. The solutions of (4) are understood in the sense of Filippov [39]. Suppose that the origin is an equilibrium of (4).

Definition 5 (see [15]). The origin of system (4) is a globally finite-time equilibrium if there is a function $T: \mathbb{R}_+ \rightarrow \mathbb{R}_+$, called settling time function, such that, for all $x_0 \in \mathbb{R}^n$, the

solution $x(t, x_0)$ of system (4) is defined and $x(t, x_0) \in \mathbb{R}^n$ for $t \in [0, T(x_0))$ and $\lim_{t \rightarrow T(x_0)} x(t, x_0) = 0$.

Definition 6 (see [23]). The origin of system (4) is said to be globally fixed-time stable if it is globally finite-time stable and the settling time function $T(x_0)$ is bounded; namely, there is some $T_{\max} > 0$ such that $T(x_0) \leq T_{\max}$ for any $x_0 \in \mathbb{R}^n$.

For example, the origin of the simple scalar system $\dot{x} = -x^{1/3}$ is a globally finite-time equilibrium with $T(x_0) = (3/2)\sqrt[3]{|x_0|^2}$. The origin of $\dot{x} = -|x|^{1/3} - |x|^2$ is a globally fixed-time equilibrium because $T(x_0) \leq \pi$ for any $x_0 \in \mathbb{R}$.

Lemma 7 (see [24, 32]). Suppose that there is a continuous radially unbounded function $V: \mathbb{R}^n \rightarrow \mathbb{R}_+$ such that (i) $V(x) = 0 \Leftrightarrow x = 0$ and (ii) any solution $x(t)$ of (4) satisfies the inequality $\dot{V}(x(t)) \leq -aV^p(x(t)) - bV^q(x(t))$ for some $a, b > 0$, $p = 1 - 1/(2\mu)$, $q = 1 + 1/(2\mu)$, and $\mu > 1/2$. Then the origin is globally fixed-time stable and the following estimate of the settling time holds:

$$T(x_0) \leq T_{\max} = \frac{\pi\mu}{\sqrt{ab}}, \quad \forall x_0 \in \mathbb{R}^n. \quad (5)$$

This lemma provides a good estimate of the settling time independent of the initial conditions.

2.3. Problem Formulation. We consider the following multi-agent system with N follower agents and K virtual leaders governed by

$$\begin{aligned} \dot{x}_i &= u_i, \quad i \in V, \\ \dot{x}_{\theta_k} &= u_{\theta_k}, \quad k \in \{1, \dots, K\}, \end{aligned} \quad (6)$$

where $x_i \in \mathbb{R}^m$ (resp., $x_{\theta_k} \in \mathbb{R}^m$) is the state of agent i (resp., leader θ_k) and $u_i \in \mathbb{R}^m$ (resp., $u_{\theta_k} \in \mathbb{R}^m$) is the control input of agent i (resp., leader θ_k). The unknown input u_{θ_k} is assumed to be bounded by a known constant ω ; that is, $\|u_{\theta_k}\|_{\infty} \leq \omega$ for all $1 \leq k \leq K$.

In this paper, we extend the notion of fixed-time equilibrium in Definition 6 to the setting of coordination control of multiagent systems and define the leader-follower fixed-time group consensus as follows.

Definition 8. The multiagent system (6) is said to achieve leader-follower fixed-time group consensus if, for some appropriately designed distributed inputs $\{u_i\}_{i \in V}$, there exists a constant $T_{\max} > 0$ so that, for any initial condition of the agents and the bounded inputs $\{u_{\theta_k}\}_{k=1}^K$, it holds that $x_i(t) = x_{\theta_k}(t)$ for all $i \in \mathcal{G}_k$, $k = 1, \dots, K$, and $t \geq T_{\max}$.

For simplicity, we assume $m = 1$ in the following. However, the analysis is valid for $m > 1$ by using the properties of the Kronecker product.

3. Fixed-Time Group Consensus Analysis under Directed Topology

In this section, motivated by the fixed-time control techniques used in [24, 27, 32], we design the following distributed controller for follower agents in order to realize leader-follower fixed-time group consensus:

$$\begin{aligned} u_i = & \alpha \left[\sum_{j \in \mathcal{G}_k \cup \theta_k} a_{ij} (x_j - x_i) + \sum_{k' \neq k} \sum_{j \in \mathcal{G}_{k'}} a_{ij} x_j \right]^p \\ & + \beta \left[\sum_{j \in \mathcal{G}_k \cup \theta_k} a_{ij} (x_j - x_i) + \sum_{k' \neq k} \sum_{j \in \mathcal{G}_{k'}} a_{ij} x_j \right]^q \\ & + \gamma \operatorname{sgn} \left(\sum_{j \in \mathcal{G}_k \cup \theta_k} a_{ij} (x_j - x_i) + \sum_{k' \neq k} \sum_{j \in \mathcal{G}_{k'}} a_{ij} x_j \right), \end{aligned} \quad (7)$$

for $i \in \mathcal{G}_k, k = 1, \dots, K$, where $\alpha, \beta > 0, \gamma \geq \omega$ are positive control gains, $p \in (0, 1)$, and $q = 1/p$. Note that only local information between neighboring agents is needed.

Assumption 9. Denote $\rho = \max_{1 \leq k \leq K, i \in \mathcal{G}_k} \sum_{k' \neq k} \sum_{j \in \mathcal{G}_{k'}} p_{ki} |a_{ij}|$, where $\{p_{ki}\}$ are defined in (3). Assume that $\lambda_{\min}(Q) > \rho$.

Note that Assumption 9 is feasible since ρ will tend to zero when $|a_{ij}|$ tends to zero for $i \in \mathcal{G}_k, j \in \mathcal{G}_{k'},$ and $k' \neq k$. On the other hand, Q is a positive definite matrix, which does not rely on these intergroup weights $\{a_{ij}\}$. Assumption 9, together with Assumption 4, implies intuitively that the coupling strengths within each subgroup and among the leader and its followers are strong enough while the coupling strengths between different subgroups should be weak. Assumptions 3, 4, and 9 are the usual standard ones when considering the problems of group consensus or cluster synchronization.

Theorem 10. *Under Assumptions 3, 4, and 9, the multiagent system (6) with protocol (7) achieves leader-follower fixed-time group consensus, and the convergence time is bounded by*

$$T_{\max} = \frac{c_1 \pi (1+p)}{c_2 (\lambda_{\min}(Q) - \rho) (1-p)}, \quad (8)$$

where

$$\begin{aligned} c_1 = & \left(\frac{\bar{p}\alpha}{p+1} \right)^{2p/(p+1)} + \left(\frac{\bar{p}\beta}{q+1} \right)^{2p/(p+1)} \\ & + 2^{(q-1)/(q+1)} \left(\frac{\bar{p}\alpha}{p+1} \right)^{2q/(q+1)} \\ & + 2^{(q-1)/(q+1)} \left(\frac{\bar{p}\beta}{q+1} \right)^{2q/(q+1)}, \end{aligned}$$

$$c_2 = \begin{cases} \min \{ \beta^2 N^{1-2q}, \alpha^2 \}, & \text{if } 0 < p \leq \frac{1}{2}; \\ \min \{ \beta^2 N^{1-2q}, \alpha^2 N^{1-2p} \}, & \text{if } \frac{1}{2} \leq p < 1, \end{cases} \quad (9)$$

and $\bar{p} = \max_{1 \leq k \leq K, i \in \mathcal{G}_k} p_{ki}$.

Proof. Let $\tilde{x}_i = x_i - x_{\theta_k}$ for $i \in \mathcal{G}_k, 1 \leq k \leq K$, and $\tilde{y}_i = \sum_{j \in \mathcal{G}_k \cup \theta_k} a_{ij} (x_j - x_i) + \sum_{k' \neq k} \sum_{j \in \mathcal{G}_{k'}} a_{ij} x_j$ for $i = 1, \dots, N$. Denote $\tilde{x} = (\tilde{x}_1, \dots, \tilde{x}_N)^T$ and $\tilde{y} = (\tilde{y}_1, \dots, \tilde{y}_N)^T$. Therefore, we obtain

$$\dot{\tilde{y}} = -H\tilde{x} = (\operatorname{diag}(-H_1, \dots, -H_K) + \tilde{A})\tilde{x}, \quad (10)$$

where H_1, \dots, H_K are defined in (3) and

$$\tilde{A} = \begin{pmatrix} 0 & A_{12} & \cdots & A_{1K} \\ A_{21} & 0 & \cdots & A_{2K} \\ \vdots & \vdots & \ddots & \vdots \\ A_{K1} & A_{K2} & \cdots & 0 \end{pmatrix} \in \mathbb{R}^{N \times N}. \quad (11)$$

Here, each block $A_{kk'} = (a_{ij}) \in \mathbb{R}^{|\mathcal{G}_k| \times |\mathcal{G}_{k'}|}$ (inheriting from the weighted adjacency matrix A) characterizes the weights between agents in subgroups \mathcal{G}_k and $\mathcal{G}_{k'}$ for $k' \neq k$. It follows from Assumption 4 that H is strictly diagonally dominant and hence invertible [40]. Therefore, $\tilde{x} = 0$ if and only if $\tilde{y} = 0$, meaning that the leader-follower fixed-time group consensus is achieved if only if \tilde{y} converges to zero in fixed time.

In view of (6) and (10), we have $\dot{\tilde{y}}_i = \sum_{j \in \mathcal{G}_k} a_{ij} (u_j - u_i) + a_{i\theta_k} (u_{\theta_k} - u_i) + \sum_{k' \neq k} \sum_{j \in \mathcal{G}_{k'}} a_{ij} u_j$. Consider the Lyapunov function

$$V(t) = \sum_{k=1}^K \sum_{i \in \mathcal{G}_k} p_{ki} \left(\frac{\alpha |\tilde{y}_i|^{p+1}}{p+1} + \frac{\beta |\tilde{y}_i|^{q+1}}{q+1} \right). \quad (12)$$

For each $i \in \mathcal{G}_k, 1 \leq k \leq K$, we write $u_i = u_{i1} + u_{i2}$, where

$$\begin{aligned} u_{i1} = & \alpha \left[\sum_{j \in \mathcal{G}_k \cup \theta_k} a_{ij} (x_j - x_i) + \sum_{k' \neq k} \sum_{j \in \mathcal{G}_{k'}} a_{ij} x_j \right]^p \\ & + \beta \left[\sum_{j \in \mathcal{G}_k \cup \theta_k} a_{ij} (x_j - x_i) + \sum_{k' \neq k} \sum_{j \in \mathcal{G}_{k'}} a_{ij} x_j \right]^q \end{aligned} \quad (13)$$

and $u_{i2} = \gamma \operatorname{sgn}(\sum_{j \in \mathcal{G}_k \cup \theta_k} a_{ij} (x_j - x_i) + \sum_{k' \neq k} \sum_{j \in \mathcal{G}_{k'}} a_{ij} x_j)$. The time derivative of (12) along the solution of (6) satisfies

$$\begin{aligned}
\dot{V}(t) &= \sum_{k=1}^K \sum_{i \in \mathcal{E}_k} \left[p_{ki} (\alpha |\tilde{y}_i|^p + \beta |\tilde{y}_i|^q) \cdot \left(\sum_{j \in \mathcal{E}_k} a_{ij} (u_j - u_i) + a_{i\theta_k} (u_{\theta_k} - u_i) + \sum_{k' \neq k} \sum_{j \in \mathcal{E}_{k'}} a_{ij} u_j \right) \right] \\
&= \sum_{k=1}^K \sum_{i \in \mathcal{E}_k} \left[p_{ki} (\alpha |\tilde{y}_i|^p + \beta |\tilde{y}_i|^q) \cdot \left(\sum_{j \in \mathcal{E}_k} a_{ij} (u_{j1} - u_{i1}) - a_{i\theta_k} u_{i1} + \sum_{k' \neq k} \sum_{j \in \mathcal{E}_{k'}} a_{ij} u_{j1} \right) \right] \\
&\quad + \sum_{k=1}^K \sum_{i \in \mathcal{E}_k} \left[p_{ki} (\alpha |\tilde{y}_i|^p + \beta |\tilde{y}_i|^q) \cdot \left(\sum_{j \in \mathcal{E}_k} a_{ij} (u_{j2} - u_{i2}) + a_{i\theta_k} (u_{\theta_k} - u_{i2}) + \sum_{k' \neq k} \sum_{j \in \mathcal{E}_{k'}} a_{ij} (u_{j2} - u_{i2}) \right) \right],
\end{aligned} \tag{14}$$

where we exploited Assumption 4 in the last term on the righthand side of (14). By observing that $u_{j2} - u_{i2} \leq \gamma - \gamma \operatorname{sgn}(\tilde{y}_i)$, $u_{\theta_k} - u_{i2} \leq \omega - \gamma \operatorname{sgn}(\tilde{y}_i) \leq \gamma - \gamma \operatorname{sgn}(\tilde{y}_i)$, and $u_{j2} - u_{i2} \leq \gamma - \gamma \operatorname{sgn}(\tilde{y}_i)$, we obtain from (14) that

$$\begin{aligned}
\dot{V}(t) &\leq \sum_{k=1}^K \sum_{i \in \mathcal{E}_k} \left[p_{ki} (\alpha |\tilde{y}_i|^p + \beta |\tilde{y}_i|^q) \right. \\
&\quad \cdot \left. \left(\sum_{j \in \mathcal{E}_k} a_{ij} (u_{j1} - u_{i1}) - a_{i\theta_k} u_{i1} + \sum_{k' \neq k} \sum_{j \in \mathcal{E}_{k'}} a_{ij} u_{j1} \right) \right] \\
&= -\frac{1}{2} (\alpha |\tilde{y}|^p + \beta |\tilde{y}|^q)^T Q (\alpha |\tilde{y}|^p + \beta |\tilde{y}|^q) \\
&\quad + \frac{1}{2} (\alpha |\tilde{y}|^p + \beta |\tilde{y}|^q)^T [\operatorname{diag}(P_1, \dots, P_K) \bar{A} \\
&\quad + \bar{A}^T \operatorname{diag}(P_1, \dots, P_K)] \cdot (\alpha |\tilde{y}|^p + \beta |\tilde{y}|^q).
\end{aligned} \tag{15}$$

Recall the definition of ρ in Assumption 9, and it follows from the Geršgorin disc theorem [40] that the eigenvalues of the matrix $\operatorname{diag}(P_1, \dots, P_K) \bar{A} + \bar{A}^T \operatorname{diag}(P_1, \dots, P_K)$ lie within the interval $[-\rho, \rho]$. Hence, we have

$$\begin{aligned}
\dot{V}(t) &\leq -\frac{1}{2} (\lambda_{\min}(Q) - \rho) (\alpha |\tilde{y}|^p + \beta |\tilde{y}|^q)^T \\
&\quad \cdot (\alpha |\tilde{y}|^p + \beta |\tilde{y}|^q)
\end{aligned} \tag{16}$$

by using the Rayleigh-Ritz theorem [40].

Next, we will estimate the righthand side of (16). Following [32], we set $h_1(\tilde{y}) = (\alpha |\tilde{y}|^p + \beta |\tilde{y}|^q)^T (\alpha |\tilde{y}|^p + \beta |\tilde{y}|^q) = \alpha^2 \sum_{i=1}^N |\tilde{y}_i|^{2p} + 2\alpha\beta \sum_{i=1}^N |\tilde{y}_i|^{p+q} + \beta^2 \sum_{i=1}^N |\tilde{y}_i|^{2q}$, $h_2(\tilde{y}) = \sqrt{2p/(p+1)}(t)$, and $h_3(\tilde{y}) = \sqrt{2q/(q+1)}(t)$. It follows from (12) and Lemma 1 that

$$\begin{aligned}
h_2(\tilde{y}) &\leq \left(\frac{\bar{p}\alpha}{p+1} \left(\sum_{i=1}^N |\tilde{y}_i| \right)^{p+1} \right. \\
&\quad \left. + \frac{\bar{p}\beta}{q+1} \left(\sum_{i=1}^N |\tilde{y}_i| \right)^{q+1} \right)^{2p/(p+1)} \leq \left(\frac{\bar{p}\alpha}{p+1} \right)^{2p/(p+1)}
\end{aligned}$$

$$\begin{aligned}
&\cdot \left(\sum_{i=1}^N |\tilde{y}_i| \right)^{2p} + \left(\frac{\bar{p}\beta}{q+1} \right)^{2p/(p+1)} \\
&\cdot \left(\sum_{i=1}^N |\tilde{y}_i| \right)^{2p(q+1)/(p+1)}
\end{aligned} \tag{17}$$

since $p, q > 0$ and $0 < 2p/(p+1) < 1$. Similarly, since $2q/(q+1) > 1$, we obtain

$$\begin{aligned}
h_3(\tilde{y}) &\leq \left(\frac{\bar{p}\alpha}{p+1} \left(\sum_{i=1}^N |\tilde{y}_i| \right)^{p+1} \right. \\
&\quad \left. + \frac{\bar{p}\beta}{q+1} \left(\sum_{i=1}^N |\tilde{y}_i| \right)^{q+1} \right)^{2q/(q+1)} \\
&\leq 2^{(q-1)/(q+1)} \left(\frac{\bar{p}\alpha}{p+1} \right)^{2q/(q+1)} \left(\sum_{i=1}^N |\tilde{y}_i| \right)^{2q(p+1)/(q+1)} \\
&\quad + 2^{(q-1)/(q+1)} \left(\frac{\bar{p}\beta}{q+1} \right)^{2q/(q+1)} \left(\sum_{i=1}^N |\tilde{y}_i| \right)^{2q}.
\end{aligned} \tag{18}$$

We consider two cases according to the value of p .

Case 1 ($0 < p \leq 1/2$). In this case, we have

$$\begin{aligned}
h_1(\tilde{y}) &\geq \alpha^2 \left(\sum_{i=1}^N |\tilde{y}_i| \right)^{2p} + 2\alpha\beta N^{1-p-q} \left(\sum_{i=1}^N |\tilde{y}_i| \right)^{p+q} \\
&\quad + \beta^2 N^{1-2q} \left(\sum_{i=1}^N |\tilde{y}_i| \right)^{2q}
\end{aligned} \tag{19}$$

by Lemma 1. If $\sum_{i=1}^N |\tilde{y}_i| \geq 1$, then $h_1(\tilde{y}) \geq \beta^2 N^{1-2q} (\sum_{i=1}^N |\tilde{y}_i|)^{2q}$ by (19), and moreover, $(\sum_{i=1}^N |\tilde{y}_i|)^{2p} \leq (\sum_{i=1}^N |\tilde{y}_i|)^{2q}$, $(\sum_{i=1}^N |\tilde{y}_i|)^{2p(q+1)/(p+1)} \leq (\sum_{i=1}^N |\tilde{y}_i|)^{2q}$, and $(\sum_{i=1}^N |\tilde{y}_i|)^{2q(p+1)/(q+1)} \leq (\sum_{i=1}^N |\tilde{y}_i|)^{2q}$. Recalling the definition of c_1 , we have

$$h_1(\tilde{y}) \geq \frac{\beta^2 N^{1-2q}}{c_1} (h_2(\tilde{y}) + h_3(\tilde{y})) \tag{20}$$

by using (17) and (18). If $\sum_{i=1}^N |\tilde{y}_i| \leq 1$, then $h_1(\tilde{y}) \geq \alpha^2 (\sum_{i=1}^N |\tilde{y}_i|)^{2p}$ by (19), and moreover, $(\sum_{i=1}^N |\tilde{y}_i|)^{2q} \leq (\sum_{i=1}^N |\tilde{y}_i|)^{2p}$, $(\sum_{i=1}^N |\tilde{y}_i|)^{2p(q+1)/(p+1)} \leq (\sum_{i=1}^N |\tilde{y}_i|)^{2p}$, and $(\sum_{i=1}^N |\tilde{y}_i|)^{2q(p+1)/(q+1)} \leq (\sum_{i=1}^N |\tilde{y}_i|)^{2p}$. Analogously, it follows from (17) and (18) that

$$h_1(\tilde{y}) \geq \frac{\alpha^2}{c_1} (h_2(\tilde{y}) + h_3(\tilde{y})). \quad (21)$$

Case 2 ($1/2 \leq p < 1$). In this case, we have

$$\begin{aligned} h_1(\tilde{y}) &\geq \alpha^2 N^{1-2p} \left(\sum_{i=1}^N |\tilde{y}_i| \right)^{2p} \\ &\quad + 2\alpha\beta N^{1-p-q} \left(\sum_{i=1}^N |\tilde{y}_i| \right)^{p+q} \\ &\quad + \beta^2 N^{1-2q} \left(\sum_{i=1}^N |\tilde{y}_i| \right)^{2q} \end{aligned} \quad (22)$$

by Lemma 1. If $\sum_{i=1}^N |\tilde{y}_i| \geq 1$, we recover (20) similarly. If $\sum_{i=1}^N |\tilde{y}_i| \leq 1$, it follows again from (17) and (18) that

$$h_1(\tilde{y}) \geq \frac{\alpha^2 N^{1-2p}}{c_1} (h_2(\tilde{y}) + h_3(\tilde{y})). \quad (23)$$

Combining (20), (21), and (23) with (16), we are led to the conclusion that

$$\begin{aligned} \dot{V}(t) &\leq -\frac{c_2}{2c_1} (\lambda_{\min}(Q) - \rho) (h_2(\tilde{y}) + h_3(\tilde{y})) \\ &\leq -\frac{c_2}{2c_1} (\lambda_{\min}(Q) - \rho) \left(\sqrt{2p/(p+1)}(t) + \sqrt{2q/(q+1)}(t) \right). \end{aligned} \quad (24)$$

Recall that $q = 1/p$, and Lemma 7 yields that the convergence time is bounded by $T_{\max} = c_1 \pi(1+p)/c_2(\lambda_{\min}(Q) - \rho)(1-p)$ regardless of initial conditions by taking $a = b = (c_2/2c_1)(\lambda_{\min}(Q) - \rho)$ and $\mu = (1+p)/2(1-p) > 1/2$. Based on the comments above, the leader-follower fixed-time group consensus is achieved and the proof is complete. \square

Remark 11. Notice that the convergence time upper bound T_{\max} is fixed regardless of the initial conditions of the agents. Moreover, it is easy to check that T_{\max} decreases with respect to α and β , but independent of γ . When $K = 1$, that is, there exists only one leader, the problem reduces to the fixed-time leader-follower consensus, which has been solved in [32].

Remark 12. It is worth noting that the fixed-time group consensus tracking method studied in [27] essentially relies on the symmetry of the communication topology of each subgroup, which is not applicable here. Without the symmetry condition, a more careful analysis with two cases regarding the range of parameter p is needed. The parameter $0 < p < 1$ contributes to the fixed-time stability [23, 24], and the division of the two cases is due to technical reasons. Note that

the dependence of upper bound of the settling time, T_{\max} , on p is involved and nonmonotone (recall that $q = 1/p$). Thus, the convergence time for the two cases $p < 1/2$ and $p > 1/2$ is not comparable in general.

Remark 13. In controller (7), the third term $\gamma \operatorname{sgn}(\sum_{j \in \mathcal{G}_k \cup \theta_k} a_{ij}(x_j - x_i) + \sum_{k' \neq k} \sum_{j \in \mathcal{G}_{k'}} a_{ij}x_j)$ aims to deal with the dynamic leaders. If $\omega = 0$, that is, the leaders are static, one can choose the parameter $\gamma = 0$. In this case, the control protocol becomes

$$\begin{aligned} u_i &= \alpha \left[\sum_{j \in \mathcal{G}_k \cup \theta_k} a_{ij}(x_j - x_i) + \sum_{k' \neq k} \sum_{j \in \mathcal{G}_{k'}} a_{ij}x_j \right]^p \\ &\quad + \beta \left[\sum_{j \in \mathcal{G}_k \cup \theta_k} a_{ij}(x_j - x_i) + \sum_{k' \neq k} \sum_{j \in \mathcal{G}_{k'}} a_{ij}x_j \right]^q \end{aligned} \quad (25)$$

for $i \in \mathcal{G}_k$, $k = 1, \dots, K$, which is consistent with the protocol in [24] in the special case of $K = 1$ and $A = A^T$.

4. Numerical Examples

In this section, we present some numerical examples to illustrate our theoretical results. Consider a multiagent system (6)-(7) with $K = 3$ leader agents and $N = 9$ follower agents having $\mathcal{G}_1 = \{1, 2, 3, 4\}$, $\mathcal{G}_2 = \{5, 6\}$, and $\mathcal{G}_3 = \{7, 8, 9\}$. The network topology G together with its associated edge weights is shown in Figure 1. The control inputs for the three leaders are taken as $u_{\theta_1} = -1$, $u_{\theta_2} = 1 + \cos(t)$, and $u_{\theta_3} = 2 \cos(t)$; they are bounded by $\omega = 2$. By direct calculations, we have $\rho = 1.2$ and $\lambda_{\min}(Q) = 1.5$. It is then easy to check that Assumptions 3, 4, and 9 are true. It is noteworthy that some negative weights between different subgroups are present. They indicate that the interactions between nodes in different subgroup can be competitive [27, 36], which play a crucial role in the analysis of bipartite consensus over signed graphs [41].

Example 1 ($p = 1/3$ and $q = 3$). In this example, we consider the case of $p = 1/3 < 1/2$. By taking $\alpha = \beta = 1$ and $\gamma = 2$, we obtain from Theorem 10 an explicit estimation of the settling time as $T_{\max} \approx 4.5 \times 10^6$ s, which is independent of the initial conditions of the multiagent system. With the initial conditions $(x_{\theta_1}(0), x_{\theta_2}(0), x_{\theta_3}(0), x_1(0), x_2(0), x_3(0), x_4(0), x_5(0), x_6(0), x_7(0), x_8(0), x_9(0)) = (-3, 1, 6, -2, 4, -1, 3, 4, -6, 4, 3, -5)$ and $(x_{\theta_1}(0), x_{\theta_2}(0), x_{\theta_3}(0), x_1(0), x_2(0), x_3(0), x_4(0), x_5(0), x_6(0), x_7(0), x_8(0), x_9(0)) = (150, 100, -200, -130, 200, -150, 300, 250, -125, 300, -250, -100)$, the simulation results are shown in Figures 2(a) and 2(b), respectively. We observe that, for all the initial conditions, the follower agents are able to track their corresponding leaders quite rapidly. In view of the conservativeness of our theoretical estimation, a more practical settling time could be derived by simulating the dynamical system for the followers with sufficiently large initial conditions. This is viable since the fixed-time convergence is theoretically guaranteed and thus the convergence time will tend to a finite limit as the initial conditions increase. As

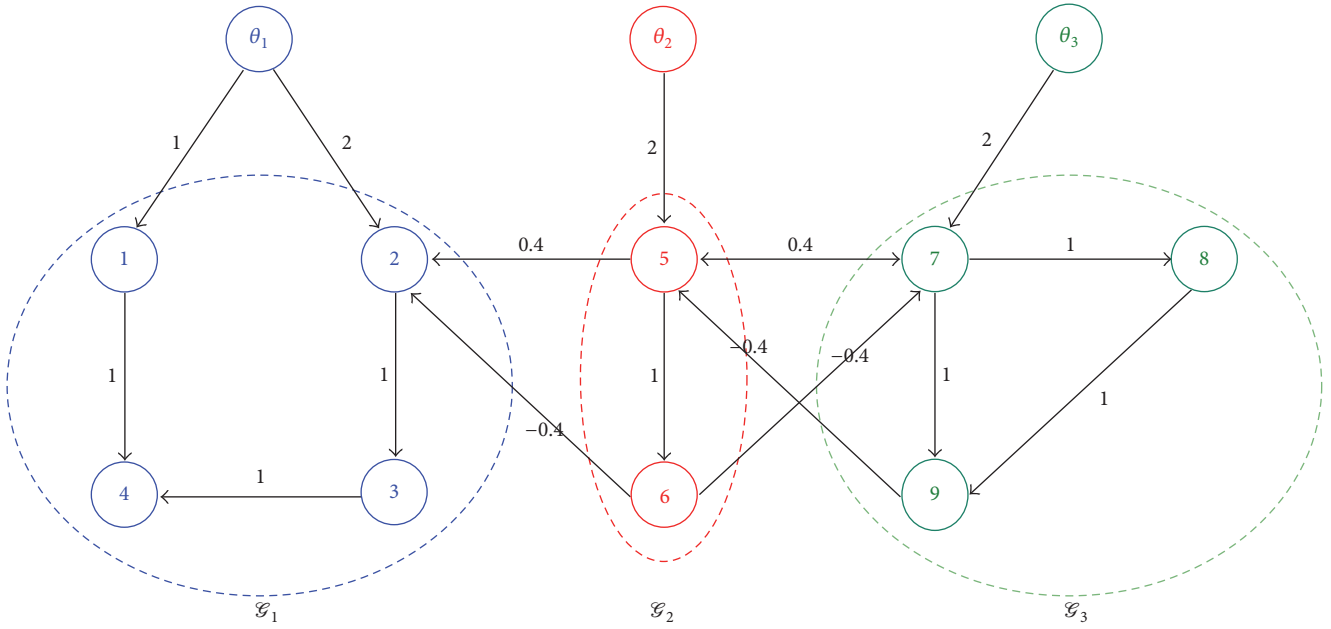


FIGURE 1: Communication topology.

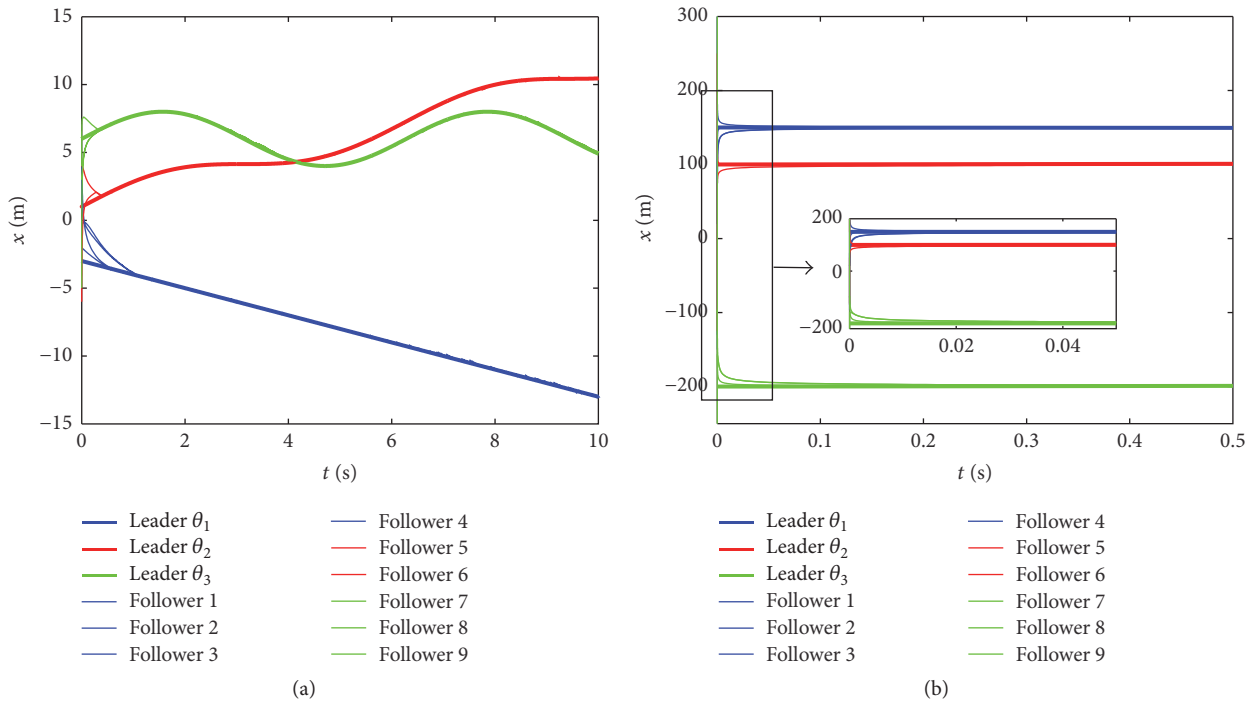


FIGURE 2: Leader-follower fixed-time group consensus for the multiagent system (6)-(7) in Example 1. (a) is for $(x_{\theta_1}(0), x_{\theta_2}(0), x_{\theta_3}(0), x_1(0), x_2(0), x_3(0), x_4(0), x_5(0), x_6(0), x_7(0), x_8(0), x_9(0)) = (-3, 1, 6, -2, 4, -1, 3, 4, -6, 4, 3, -5)$; and (b) is for $(x_{\theta_1}(0), x_{\theta_2}(0), x_{\theta_3}(0), x_1(0), x_2(0), x_3(0), x_4(0), x_5(0), x_6(0), x_7(0), x_8(0), x_9(0)) = (150, 100, -200, -130, 200, -150, 300, 250, -125, 300, -250, -100)$.

such, we estimate the convergence time as about 10 s through simulations over sufficiently large initial conditions.

Example 2 ($p = 2/3$ and $q = 3/2$). In this example, we consider the case of $p = 2/3 > 1/2$. By taking $\alpha = \beta = 1$ and $\gamma = 2$ again, we obtain from Theorem 10 an

explicit estimation of the settling time as $T_{\max} \approx 1.3 \times 10^4$ s, which is independent of the initial conditions of the multiagent system. With the same initial conditions as in Example 1, the simulation results are shown in Figures 3(a) and 3(b), respectively. Similarly, the estimated settling time upper bound is very conservative. By simulating the system

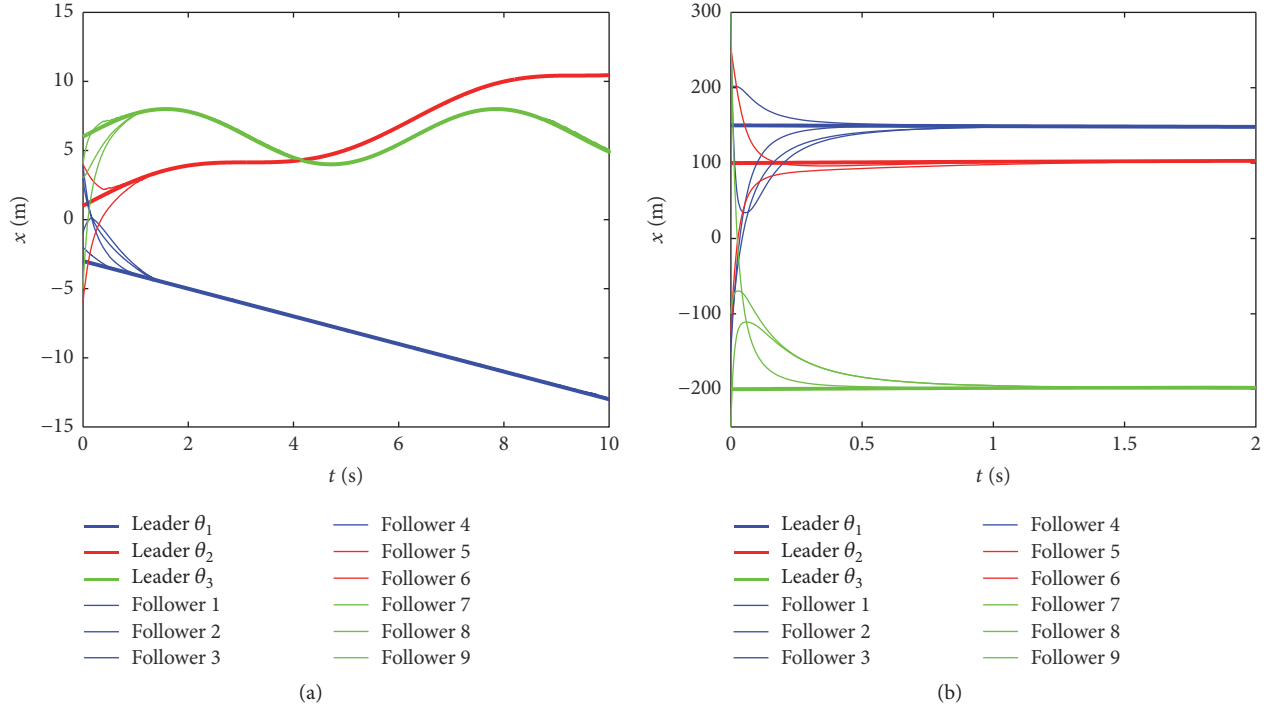


FIGURE 3: Leader-follower fixed-time group consensus for the multiagent system (6)-(7) in Example 2. (a) is for $(x_{\theta_1}(0), x_{\theta_2}(0), x_{\theta_3}(0), x_1(0), x_2(0), x_3(0), x_4(0), x_5(0), x_6(0), x_7(0), x_8(0), x_9(0)) = (-3, 1, 6, -2, 4, -1, 3, 4, -6, 4, 3, -5)$; and (b) is for $(x_{\theta_1}(0), x_{\theta_2}(0), x_{\theta_3}(0), x_1(0), x_2(0), x_3(0), x_4(0), x_5(0), x_6(0), x_7(0), x_8(0), x_9(0)) = (150, 100, -200, -130, 200, -150, 300, 250, -125, 300, -250, -100)$.

with sufficiently large initial conditions, the convergence time can be determined as about 10 s.

5. Conclusions

In this paper, the fixed-time consensus problem is generalized to the group tracking control of multiagent systems with multiple leaders and the underlying communication topology is composed of a directed network. A new distributed controller is proposed which solves the leader-follower fixed-time group consensus problem. An explicit estimation of the settling time is provided regardless of the initial conditions. As future works, we will consider how to obtain sharper estimation of the settling time over directed networks and study the effect of communication delays as well as robustness against disturbances.

Conflicts of Interest

The authors declare that there are no conflicts of interest regarding the publication of this paper.

Acknowledgments

This work was funded by the National Natural Science Foundation of China (11505127) and the Shanghai Pujiang Program (15PJ1408300).

References

- [1] A. Jadbabaie, J. Lin, and A. S. Morse, "Coordination of groups of mobile autonomous agents using nearest neighbor rules," *IEEE Transactions on Automatic Control*, vol. 48, no. 6, pp. 988–1001, 2003.
- [2] R. Olfati-Saber and R. M. Murray, "Consensus problems in networks of agents with switching topology and time-delays," *IEEE Transactions on Automatic Control*, vol. 49, no. 9, pp. 1520–1533, 2004.
- [3] W. Ren and R. W. Beard, "Consensus seeking in multiagent systems under dynamically changing interaction topologies," *IEEE Transactions on Automatic Control*, vol. 50, no. 5, pp. 655–661, 2005.
- [4] R. Olfati-Saber, J. A. Fax, and R. M. Murray, "Consensus and cooperation in networked multi-agent systems," *Proceedings of the IEEE*, vol. 95, no. 1, pp. 215–233, 2007.
- [5] Y. Cao, W. Yu, W. Ren, and G. Chen, "An overview of recent progress in the study of distributed multi-agent coordination," *IEEE Transactions on Industrial Informatics*, vol. 9, no. 1, pp. 427–438, 2013.
- [6] J. Yu and L. Wang, "Group consensus in multi-agent systems with switching topologies and communication delays," *Systems & Control Letters*, vol. 59, no. 6, pp. 340–348, 2010.
- [7] J. Yu and L. Wang, "Group consensus of multi-agent systems with directed information exchange," *International Journal of Systems Science*, vol. 43, no. 2, pp. 334–348, 2012.
- [8] Y. Han, W. Lu, and T. Chen, "Achieving cluster consensus in continuous-time networks of multi-agents with inter-cluster non-identical inputs," *IEEE Transactions on Automatic Control*, vol. 60, no. 3, pp. 793–798, 2015.

- [9] Y. Wang, Z. Ma, J. Cao, A. Alsaedi, and F. E. Alsaadi, "Adaptive cluster synchronization in directed networks with nonidentical nonlinear dynamics," *Complexity*, vol. 21, no. S2, pp. 380–387, 2016.
- [10] Y. Shang, " L^1 group consensus of multi-agent systems with switching topologies and stochastic inputs," *Physics Letters. A*, vol. 377, no. 25–27, pp. 1582–1586, 2013.
- [11] Y. Shang, "A combinatorial necessary and sufficient condition for cluster consensus," *Neurocomputing*, vol. 216, pp. 611–616, 2016.
- [12] T. H. Lee, J. H. Park, D. H. Ji, and H. Y. Jung, "Leader-following consensus problem of heterogeneous multi-agent systems with nonlinear dynamics using fuzzy disturbance observer," *Complexity*, vol. 19, no. 4, pp. 20–31, 2014.
- [13] Q. Cui, D. Xie, and F. Jiang, "Group consensus tracking control of second-order multi-agent systems with directed fixed topology," *Neurocomputing*, vol. 218, pp. 286–295, 2016.
- [14] Z. Tu, D. Zhang, X. Xia, and H. Yu, "Event-triggered group consensus of leader-following multi-agent systems with nonlinear dynamics," in *Proceedings of the 35th Chinese Control Conference (CCC '16)*, pp. 7885–7890, Chengdu, China, July 2016.
- [15] S. P. Bhat and D. S. Bernstein, "Finite-time stability of continuous autonomous systems," *SIAM Journal on Control and Optimization*, vol. 38, no. 3, pp. 751–766, 2000.
- [16] L. Wang and F. Xiao, "Finite-time consensus problems for networks of dynamic agents," *IEEE Transactions on Automatic Control*, vol. 55, no. 4, pp. 950–955, 2010.
- [17] Y. Cao and W. Ren, "Finite-time consensus for multi-agent networks with unknown inherent nonlinear dynamics," *Automatica*, vol. 50, no. 10, pp. 2648–2656, 2014.
- [18] X. Liu, J. Lam, W. Yu, and G. Chen, "Finite-time consensus of multiagent systems with a switching protocol," *IEEE Transactions on Neural Networks and Learning Systems*, vol. 27, no. 4, pp. 853–862, 2016.
- [19] Y. Han, D. Zhao, and Y. Sun, "Finite-time flocking problem of a Cucker-smale-type self-propelled particle model," *Complexity*, vol. 21, pp. 354–361, 2016.
- [20] G. Mei, X. Wu, D. Ning, and J.-A. Lu, "Finite-time stabilization of complex dynamical networks via optimal control," *Complexity*, vol. 21, pp. 417–425, 2016.
- [21] W. Cui, J.-a. Fang, W. Zhang, and X. Wang, "Finite-time cluster synchronization of Markovian switching complex networks with stochastic perturbations," *IET Control Theory & Applications*, vol. 8, no. 1, pp. 30–41, 2014.
- [22] Y. Shang, "Finite-time cluster average consensus for networks via distributed iterations," *International Journal of Control, Automation and Systems*, 2017.
- [23] A. Polyakov, "Nonlinear feedback design for fixed-time stabilization of linear control systems," *IEEE Transactions on Automatic Control*, vol. 57, no. 8, pp. 2106–2110, 2012.
- [24] S. Parsegov, A. Polyakov, and P. Shcherbakov, "Fixed-time consensus algorithm for multi-agent systems with integrator dynamics," in *Proceedings of the 4th IFAC Workshop on Distributed Estimation and Control in Networked Systems*, pp. 110–115, Koblenz, Germany, September, 2013.
- [25] Z. Zuo and L. Tie, "A new class of finite-time nonlinear consensus protocols for multi-agent systems," *International Journal of Control*, vol. 87, no. 2, pp. 363–370, 2014.
- [26] Z. Zuo and L. Tie, "Distributed robust finite-time nonlinear consensus protocols for multi-agent systems," *International Journal of Systems Science*, vol. 47, no. 6, pp. 1366–1375, 2016.
- [27] X. Liu and T. Chen, "Fixed-time cluster synchronization for complex networks via pinning control," <https://arxiv.org/abs/1509.03350>.
- [28] J. Fu and J. Wang, "Fixed-time coordinated tracking for second-order multi-agent systems with bounded input uncertainties," *Systems & Control Letters*, vol. 93, pp. 1–12, 2016.
- [29] M. Defoort, A. Polyakov, G. Demesure, M. Djemai, and K. Veluvolu, "Leader-follower fixed-time consensus for multi-agent systems with unknown non-linear inherent dynamics," *IET Control Theory & Applications*, vol. 9, no. 14, pp. 2165–2170, 2015.
- [30] Y. Wan, J. Cao, G. Wen, and W. Yu, "Robust fixed-time synchronization of delayed Cohen-Grossberg neural networks," *Neural Networks*, vol. 73, pp. 86–94, 2016.
- [31] J. Cao and R. Li, "Fixed-time synchronization of delayed memristor-based recurrent neural networks," *Science China Information Sciences*, vol. 60, no. 3, Article ID 032201, 2017.
- [32] J. Fu and J. Wang, "Finite-time consensus for multi-agent systems with globally bounded convergence time under directed communication graphs," *International Journal of Control*, 2016.
- [33] G. H. Hardy, J. E. Littlewood, and G. Pólya, *Inequalities*, vol. 2nd, Cambridge, at the University Press, 1952.
- [34] M. Mesbahi and M. Egerstedt, *Graph Theoretic Methods in Multiagent Networks*, Princeton University Press, New Jersey, NJ, USA, 2010.
- [35] H. Zhang, Z. Li, Z. Qu, and F. L. Lewis, "On constructing Lyapunov functions for multi-agent systems," *Automatica*, vol. 58, pp. 39–42, 2015.
- [36] Y. Shang, "Couple-group consensus of continuous-time multi-agent systems under Markovian switching topologies," *Journal of the Franklin Institute*, vol. 352, no. 11, pp. 4826–4844, 2015.
- [37] M. Nagy, Z. Ákos, D. Biro, and T. Vicsek, "Hierarchical group dynamics in pigeon flocks," *Nature*, vol. 464, no. 7290, pp. 890–893, 2010.
- [38] Y. Shang and R. Bouffanais, "Influence of the number of topologically interacting neighbors on swarm dynamics," *Scientific Reports*, vol. 4, article 4184, 2014.
- [39] A. F. Filippov, *Differential Equations with Discontinuous Right-Hand Side*, Kluwer Academic Publishers, Dordrecht, The Netherlands, 1988.
- [40] R. A. Horn and C. R. Johnson, *Matrix analysis*, Cambridge University Press, New York, NY, USA, 1985.
- [41] C. Altafini, "Consensus problems on networks with antagonistic interactions," *IEEE Transactions on Automatic Control*, vol. 58, no. 4, pp. 935–946, 2013.

Research Article

Centralized and Decentralized Data-Sampling Principles for Outer-Synchronization of Fractional-Order Neural Networks

Jin-E Zhang

Hubei Normal University, Hubei 435002, China

Correspondence should be addressed to Jin-E Zhang; zhang86021205@163.com

Received 24 December 2016; Revised 6 February 2017; Accepted 21 February 2017; Published 8 March 2017

Academic Editor: Olfa Boubaker

Copyright © 2017 Jin-E Zhang. This is an open access article distributed under the Creative Commons Attribution License, which permits unrestricted use, distribution, and reproduction in any medium, provided the original work is properly cited.

This paper aims to investigate the outer-synchronization of fractional-order neural networks. Using centralized and decentralized data-sampling principles and the theory of fractional differential equations, sufficient criteria about outer-synchronization of the controlled fractional-order neural networks are derived for structure-dependent centralized data-sampling, state-dependent centralized data-sampling, and state-dependent decentralized data-sampling, respectively. A numerical example is also given to illustrate the superiority of theoretical results.

1. Introduction

Fractional operator has become visible in application domains [1–15]. As the demanding performance expectations with uncertainty, fractional operator offers more degrees of freedom to designers to meet some predefined performance indexes. After gradually recognizing the importance of fractional operator, it is found that the description of fractional-order model is more accurate and totally different from that of the corresponding integer-order model. As a direct application, the characteristic of fractional-order model can be used to identify possible behavior of electrical signals from neurons. In physical implementation of neurodynamic systems, arbitrary order analog fractance circuit is most appropriate, which reveals profoundly the relationships among neural circuit elements [9–11]. In that way, real neurodynamic systems should be addressed by fractional-order models. Fractional-order neurodynamic systems can better describe how action potentials in neurons are launched and spread. In addition, fractional-order neurodynamic systems possess infinite memory, and yet, integer-order neurodynamic systems are not of such feature [3–8, 12–15]. Therefore, fractional-order neurodynamic systems have the potential to accomplish what integer-order ones can not do. More feasible analysis methods and

easy-to-use techniques to be deal with fractional-order neurodynamic systems are worth looking into.

As a coherent behavior within nonlinear systems, synchronization of nonlinear systems has attracted phenomenal worldwide attention. Many studies have shown that synchronization mechanism is a universal phenomenon and has a wide range of applications in engineering systems. Generally, two schemes for synchronization are frequently used: inner-synchronization and outer-synchronization. For inner-synchronization, all nodes within a network will achieve a coherent behavior. However, for outer-synchronization, all individuals in two networks will achieve identical behaviors. In many application fields, outer-synchronization may seem practical [16–23]. For example, in heuristic computational intelligence, it is known that outer-synchronization is rooted in brain-inspired computing from evolutionary strategies to cognitive tasks. Nevertheless, results focusing on outer-synchronization of complex control systems have seldom been reported [19]. Control strategy for outer-synchronization deserves more investigation.

Sampled-data control through only using the local information has recently generated significant research interest [24–38]. Unlike continuous-time control, which requires the continuous communication data, sampled-data control is more appropriate under networked environment. For

control systems, once we can give effective sampling policies and schedule, then the sampled-data control will reduce communication data and save energy dramatically. Thus, how to develop high-efficiency, heuristic information-based sampled-data control with the ultimate aim of maximizing the data collected is worth studying [38]. However, relevant studies of the data-sampling strategy for control systems are still in early stage.

Motivated by the above discussions, in this paper, we introduce the centralized and decentralized data-sampling principles to achieve outer-synchronization between coupled fractional-order neural networks. The efficient allocation of the limited energy resources of centralized and decentralized data-sampling principles that maximizes the information value of the data collected is clearly a step forward. Meanwhile, to more efficiently design the sampling method, we merge the structure and state clusters through centralized and decentralized data-sampling principles and then select the best sampling time. On the basis of some analytical tools of fractional differential equations, a series of criteria on outer-synchronization are derived. It should be noted that such criteria capture the information on sampling pattern and may have much wider application range.

The rest of the paper is organized as follows. In Section 2, we present the preliminaries and problem formulation. In Section 3, we state main results in detail. In Section 4, simulation example is illustrated. Finally, Section 5 concludes the paper.

2. Preliminaries and Problem Formulation

First, some preliminaries of fractional operator are given.

Fractional integral $I^q(\cdot)$ for $\mathcal{H}(t)$ with order $q > 0$ is described as

$$I^q \mathcal{H}(t) = \frac{1}{\Gamma(q)} \int_{t_0}^t (t-s)^{q-1} \mathcal{H}(s) ds, \quad t \geq t_0, \quad (1)$$

where $\Gamma(\cdot)$ is Gamma function and t_0 is the initial time.

Caputo fractional derivative ${}^C D_{t_0}^q(\cdot)$ for $\mathcal{H}(t) \in \mathcal{C}^{m+1}([t_0, +\infty), \mathfrak{R})$ with order $q > 0$ is described as

$${}^C D_{t_0}^q \mathcal{H}(t) = \frac{1}{\Gamma(m-q)} \int_{t_0}^t \frac{\mathcal{H}^{(m)}(s)}{(t-s)^{q-m+1}} ds, \quad t \geq t_0, \quad (2)$$

where $\Gamma(\cdot)$ is Gamma function, $m-1 < q < m$, m is a positive integer, and t_0 is the initial time.

One-parameter Mittag-Leffler function $E_q(\cdot)$ is described as

$$E_q(s) = \sum_{k=0}^{+\infty} \frac{s^k}{\Gamma(kq+1)}, \quad (3)$$

where $\Gamma(\cdot)$ is Gamma function, $q > 0$, and s is a complex number.

Consider a class of fractional-order neural networks

$${}^C D_{t_0}^q x_i(t) = -a_i(t) x_i(t) + \sum_{j=1}^n b_{ij}(t) f_j(x_j(t)) + u_i(t), \quad i = 1, 2, \dots, n, \quad (4)$$

where $0 < q < 1$, $a_i(t) > 0$, $b_{ij}(t)$ and $u_i(t)$ are piecewise continuous and bounded, and feedback function $f_j(\cdot)$ satisfies

$$0 \leq \frac{f_j(\mathcal{U}_1) - f_j(\mathcal{U}_2)}{\mathcal{U}_1 - \mathcal{U}_2} \leq F_j, \quad (5)$$

$$\forall \mathcal{U}_1, \mathcal{U}_2 \in \mathfrak{R}, \mathcal{U}_1 \neq \mathcal{U}_2,$$

in which $F_j > 0$, $j = 1, 2, \dots, n$.

For the centralized data-sampling principle, (4) is rewritten as

$${}^C D_{t_0}^q x_i(t) = -a_i(t) x_i(t_k) + \sum_{j=1}^n b_{ij}(t) f_j(x_j(t_k)) + u_i(t), \quad i = 1, 2, \dots, n, \quad (6)$$

where t_k is simple notion of $t_{k(t)}$ with $k(t) = \max\{\mathcal{K} : t_{\mathcal{K}} \leq t\}$ and $0 = t_0 < t_1 < \dots < t_k < \dots$ is uniform for all the system states. Every neuron intersperses its state to its out-neighbors and receives the state information from its in-neighbors at the same time point t_k .

For the decentralized data-sampling principle, (4) is rewritten as

$${}^C D_{t_0}^q x_i(t) = -a_i(t) x_i(t_k^i) + \sum_{j=1}^n b_{ij}(t) f_j(x_j(t_k^j)) + u_i(t), \quad i = 1, 2, \dots, n, \quad (7)$$

where t_k^i is simple notion of $t_{k(t)}^i$ with $k(t) = \max\{\mathcal{K} : t_{\mathcal{K}}^i \leq t\}$ and $0 = t_0^i < t_1^i < \dots < t_k^i < \dots$ is distributed for $i \in \{1, 2, \dots, n\}$. Each neuron i pushes its state information to its out-neighbors at time t_k^i when it updates its state. It receives the information of in-neighbor state at time t_k^j when the neighbor neuron j updates its state.

Now, we state definition and problem formulation.

Definition 1 (see [19]). For any two trajectories $w(t) = (w_1(t), w_2(t), \dots, w_n(t))^T$ and $\bar{w}(t) = (\bar{w}_1(t), \bar{w}_2(t), \dots, \bar{w}_n(t))^T$ of (4) starting from different initial values $w(0)$ and $\bar{w}(0)$, if there exists some control scheme such that

$$\lim_{t \rightarrow +\infty} \|w(t) - \bar{w}(t)\| = 0, \quad (8)$$

then we call system (4) can achieve outer-synchronization, where $\|\cdot\|$ denotes norm.

Let $u(t) = (u_1(t), u_2(t), \dots, u_n(t))^T$ and $v(t) = (v_1(t), v_2(t), \dots, v_n(t))^T$ be two trajectories of (6) starting from different initial values $u(0)$ and $v(0)$. Defining $z_i(t) = u_i(t) - v_i(t)$, $i = 1, 2, \dots, n$, it follows that

$${}^C D_{t_0}^q z_i(t) = -a_i(t) z_i(t_k) + \sum_{j=1}^n b_{ij}(t) h_j(t_k), \quad i = 1, 2, \dots, n, \quad (9)$$

where $h_j(t) = f_j(u_j(t)) - f_j(v_j(t))$, $j = 1, 2, \dots, n$, for all $t \in [t_k, t_{k+1})$, $k = 0, 1, 2, \dots$

When we adopt the centralized data-sampling principle via structure to achieve outer-synchronization of (6), according to Definition 1, we need to design control strategy based on system structure of (9) such that

$$\lim_{t \rightarrow +\infty} \|z(t)\| = 0, \quad (10)$$

where $\|\cdot\|$ denotes norm, $z(t) = (z_1(t), z_2(t), \dots, z_n(t))^T$.

When we adopt the centralized data-sampling principle via state to achieve outer-synchronization of (6), in this case, consider state measurement error

$$e_i(t) = z_i(t_k) - z_i(t), \quad i = 1, 2, \dots, n, \quad (11)$$

where $t \in [t_k, t_{k+1})$, $k = 0, 1, 2, \dots$. According to Definition 1, we need to design control strategy based on state measurement error (11) such that

$$\lim_{t \rightarrow +\infty} \|z(t)\| = 0, \quad (12)$$

where $\|\cdot\|$ denotes norm, $z(t) = (z_1(t), z_2(t), \dots, z_n(t))^T$.

Let $u(t) = (u_1(t), u_2(t), \dots, u_n(t))^T$ and $v(t) = (v_1(t), v_2(t), \dots, v_n(t))^T$ be two trajectories of (7) starting from different initial values $u(0)$ and $v(0)$. Defining $z_i(t) = u_i(t) - v_i(t)$, $i = 1, 2, \dots, n$, it follows that

$${}^C D_{t_0}^q z_i(t) = -a_i(t) z_i(t_k) + \sum_{j=1}^n b_{ij}(t) h_j(t_k^j), \quad (13)$$

$$i = 1, 2, \dots, n,$$

where $h_j(t) = f_j(u_j(t)) - f_j(v_j(t))$, $j = 1, 2, \dots, n$, for all $t \in [t_k^j, t_{k+1}^j)$, $k = 0, 1, 2, \dots$

When we adopt the decentralized data-sampling principle via state to achieve outer-synchronization of (7), in this case, consider state measurement error

$$e_i(t) = z_i(t_k^i) - z_i(t), \quad i = 1, 2, \dots, n, \quad (14)$$

where $t \in [t_k^i, t_{k+1}^i)$, $k = 0, 1, 2, \dots$. According to Definition 1, we need to design control strategy based on state measurement error (14) such that

$$\lim_{t \rightarrow +\infty} \|z(t)\| = 0, \quad (15)$$

where $\|\cdot\|$ denotes norm, $z(t) = (z_1(t), z_2(t), \dots, z_n(t))^T$.

Next, we present relevant lemmas.

Lemma 2 (see [1]). *Let $0 < q < 1$. If $\mathcal{H}(t) \in \mathcal{C}^1[t_0, +\infty]$, then*

$${}^C D_{t_0}^q |\mathcal{H}(t)| \leq \text{sgn}(\mathcal{H}(t)) {}^C D_{t_0}^q \mathcal{H}(t), \quad t \geq t_0, \quad (16)$$

where

$${}^C D_{t_0}^q |\mathcal{H}(t)| = \frac{1}{\Gamma(1-q)} \int_{t_0}^t \frac{(d/ds)|\mathcal{H}(s)|}{(t-s)^q} ds. \quad (17)$$

Lemma 3 (see [39]). *Given $q > 0$, let $\mathcal{A}(t)$ be nonnegative and locally integrable on $[a, b]$; let $\mathcal{G}(t)$ be continuous, bounded, nonnegative, and nondecreasing on $[a, b]$. Assuming $\mathcal{Y}(t)$ to be nonnegative and locally integrable on $[a, b]$ with*

$$\mathcal{Y}(t) \leq \mathcal{A}(t) + \mathcal{G}(t) \int_0^t (t-s)^{q-1} \mathcal{Y}(s) ds, \quad (18)$$

$$t \in [a, b],$$

then

$$\begin{aligned} \mathcal{Y}(t) &\leq \mathcal{A}(t) \\ &+ \int_0^t \sum_{k=1}^{+\infty} \left[\frac{[\mathcal{G}(t) \Gamma(q)]^k}{\Gamma(kq)} (t-s)^{kq-1} \mathcal{A}(s) \right] ds, \end{aligned} \quad (19)$$

$$t \in [a, b].$$

Moreover, if $\mathcal{A}(t)$ is nondecreasing on $[a, b]$, then

$$\mathcal{Y}(t) \leq \mathcal{A}(t) E_q(\mathcal{G}(t) \Gamma(q) t^q), \quad t \in [a, b], \quad (20)$$

where $\Gamma(\cdot)$ is Gamma function and $E_q(\cdot)$ is one-parameter Mittag-Leffler function.

In the following, we end this section with some notations that are needed later.

Let $\beta_i > 0$ ($i = 1, 2, \dots, n$) be positive constants, throughout this paper; denote

$$\theta_i(t) = a_i(t) - F_i b_{ii}^+(t),$$

$$\lambda_j(\beta, t) = \theta_j(t) - F_j \sum_{j=1, j \neq i}^n \frac{\beta_i}{\beta_j} |b_{ij}(t)|, \quad (21)$$

$$\rho(t) = \max_{1 \leq i \leq n} \{a_i(t) - F_i b_{ii}^-(t)\},$$

$$M = \max_{1 \leq j \leq n} \sup_{t \geq t_0} \left\{ a_j(t) + \sum_{i=1}^n \frac{\beta_i}{\beta_j} |b_{ij}(t)| F_j \right\}, \quad (22)$$

where $b_{ii}^+(t) = \max\{0, b_{ii}(t)\}$, $b_{ii}^-(t) = \min\{0, b_{ii}(t)\}$. For vector $\mathcal{V} = (\mathcal{V}_1, \mathcal{V}_2, \dots, \mathcal{V}_n)^T$, vector norm $\|\mathcal{V}\| = \sum_{i=1}^n \beta_i |\mathcal{V}_i|$. In addition, by the boundedness of $a_i(t)$ and $b_{ij}(t)$, there exist positive constants B and C such that

$$\sup_{t \geq t_0} \rho(t) \leq B, \quad (23)$$

$$\max_{1 \leq j \leq n} \sup_{t \geq t_0} \lambda_j(\beta, t) \leq C.$$

3. Main Results

For problem formulation in preceding section, in this section, we propose the corresponding control schemes for centralized data-sampling principle and decentralized data-sampling principle, respectively.

To facilitate the narrative, we first address the control designs, then review, and analyze the theoretical results.

3.1. Centralized Data-Sampling Principle

Theorem 4. Let $0 < \varepsilon < 1$ and $\iota > 0$ be positive constants with $B\varepsilon \leq \iota$ and $C\varepsilon \leq \iota(2 - \varepsilon)$. Assume that there exist positive constants $\beta_i > 0$ ($i = 1, 2, \dots, n$) such that $\lambda_j(\beta, t) \geq \iota$ for all $j = 1, 2, \dots, n$ and $t \in [t_0, +\infty)$. Set t_{k+1} as a time point such that

$$\begin{aligned} & t_{k+1} \\ &= \sup_{\tau \geq t_k} \left\{ \tau : \min_{1 \leq j \leq n} \left(\frac{1}{\Gamma(q)} \int_{t_k}^{\tau} (t-s)^{q-1} \lambda_j(\beta, s) ds \right) \right. \\ & \left. \leq \varepsilon, \forall t \in (t_k, \tau) \right\} \end{aligned} \quad (24)$$

for $k = 0, 1, 2, \dots$. Then system (6) reaches outer-synchronization.

Proof. From $\lambda_j(\beta, t) \geq \iota$ for all $j = 1, 2, \dots, n$ and $t \in [t_0, +\infty)$, together with (23), it follows that

$$\begin{aligned} & \frac{\iota}{\Gamma(q)} \int_{t_k}^t (t-s)^{q-1} ds \\ & \leq \frac{1}{\Gamma(q)} \int_{t_k}^t (t-s)^{q-1} \lambda_j(\beta, s) ds \\ & \leq \frac{C}{\Gamma(q)} \int_{t_k}^t (t-s)^{q-1} ds; \end{aligned} \quad (25)$$

then

$$\begin{aligned} \frac{\iota(t-t_k)^q}{\Gamma(q+1)} & \leq \frac{1}{\Gamma(q)} \int_{t_k}^t (t-s)^{q-1} \lambda_j(\beta, s) ds \\ & \leq \frac{C(t-t_k)^q}{\Gamma(q+1)}, \end{aligned} \quad (26)$$

for all $j = 1, 2, \dots, n$ and any $t \in [t_k, t_{k+1})$. According to (9), $z(t) = (z_1(t), z_2(t), \dots, z_n(t))^T$ will not update until

$$\min_{1 \leq j \leq n} \left(\frac{1}{\Gamma(q)} \int_{t_k}^t (t-s)^{q-1} \lambda_j(\beta, s) ds \right) = \varepsilon \quad (27)$$

at time point $t = t_{k+1}$. Thus, we get $\iota(t_{k+1} - t_k)^q / \Gamma(q+1) \leq \varepsilon \leq C(t_{k+1} - t_k)^q / \Gamma(q+1)$, which implies

$$\frac{\varepsilon}{C} \leq \frac{(t_{k+1} - t_k)^q}{\Gamma(q+1)} \leq \frac{\varepsilon}{\iota}, \quad (28)$$

for $k = 0, 1, 2, \dots$. Then

$$t_k \geq t_0 + k \left(\frac{\Gamma(q+1)\varepsilon}{C} \right)^{1/q}; \quad (29)$$

therefore, the Zeno behavior can be excluded. Combining with (24) and (28),

$$\begin{aligned} & \frac{1}{\Gamma(q)} \int_{t_k}^{t_{k+1}} (t_{k+1} - s)^{q-1} \lambda_j(\beta, s) ds \leq \frac{C\varepsilon}{\iota} \leq 2 - \varepsilon, \\ & \frac{1}{\Gamma(q)} \int_{t_k}^{t_{k+1}} (t_{k+1} - s)^{q-1} \lambda_j(\beta, s) ds \\ & \geq \min_{1 \leq j \leq n} \frac{1}{\Gamma(q)} \int_{t_k}^{t_{k+1}} (t_{k+1} - s)^{q-1} \lambda_j(\beta, s) ds = \varepsilon, \end{aligned} \quad (30)$$

so

$$\varepsilon \leq \frac{1}{\Gamma(q)} \int_{t_k}^{t_{k+1}} (t_{k+1} - s)^{q-1} \lambda_j(\beta, s) ds \leq 2 - \varepsilon, \quad (31)$$

for $k = 0, 1, 2, \dots$. By the definition of vector norm in this paper, from (9), now let us consider $z_i(t)$ ($i = 1, 2, \dots, n$) at time $t = t_{k+1}$,

$$\begin{aligned} \|z(t_{k+1})\| &= \sum_{i=1}^n \beta_i |z_i(t_{k+1})| = \sum_{i=1}^n \beta_i \left| z_i(t_k) + \frac{1}{\Gamma(q)} \right. \\ & \cdot \int_{t_k}^{t_{k+1}} (t_{k+1} - s)^{q-1} \\ & \cdot \left[-a_i(s) z_i(t_k) + \sum_{j=1}^n b_{ij}(s) h_j(t_k) \right] ds \Big| = \sum_{i=1}^n \beta_i \\ & \cdot \left| z_i(t_k) + \frac{1}{\Gamma(q)} \int_{t_k}^{t_{k+1}} (t_{k+1} - s)^{q-1} \right. \\ & \cdot \left[-a_i(s) z_i(t_k) \right. \\ & \left. \left. + b_{ii}(s) m_i(t_k) z_i(t_k) \right. \right. \\ & \left. \left. + \sum_{j=1, j \neq i}^n b_{ij}(s) m_j(t_k) z_j(t_k) \right] ds \right| = \sum_{i=1}^n \beta_i \\ & \cdot \left| z_i(t_k) \left\{ 1 - \frac{1}{\Gamma(q)} \int_{t_k}^{t_{k+1}} (t_{k+1} - s)^{q-1} \right. \right. \\ & \cdot [a_i(s) - b_{ii}(s) m_i(t_k)] ds \Big\} + \frac{1}{\Gamma(q)} \\ & \cdot \sum_{j=1, j \neq i}^n \int_{t_k}^{t_{k+1}} (t_{k+1} - s)^{q-1} \\ & \cdot [b_{ij}(s) m_j(t_k) z_j(t_k)] ds \Big|, \end{aligned} \quad (32)$$

where

$$m_i(t) = \begin{cases} \frac{h_i(t)}{z_i(t)}, & z_i(t) \neq 0, \\ 0, & z_i(t) = 0. \end{cases} \quad (33)$$

According to (5), obviously, $0 \leq m_i(t) \leq F_i$ for all $i = 1, 2, \dots, n$, $t > t_0$, and

$$b_{ii}^-(s) F_i \leq b_{ii}^-(s) m_i(t_k) \leq b_{ii}^+(s) F_i. \quad (34)$$

Notice that $B\varepsilon \leq \iota$; then for any $t \in [t_k, t_{k+1}]$,

$$\begin{aligned} & \frac{1}{\Gamma(q)} \int_{t_k}^{t_{k+1}} (t_{k+1} - s)^{q-1} [a_i(s) - b_{ii}^-(s) m_i(t_k)] ds \\ & \leq \frac{1}{\Gamma(q)} \int_{t_k}^{t_{k+1}} (t_{k+1} - s)^{q-1} [a_i(s) - b_{ii}^-(s) F_i] ds \\ & \leq \frac{B}{\Gamma(q)} \int_{t_k}^{t_{k+1}} (t_{k+1} - s)^{q-1} ds = \frac{B(t_{k+1} - t_k)^q}{\Gamma(q+1)} \\ & \leq \frac{B\varepsilon}{\iota} \leq 1; \end{aligned} \quad (35)$$

thus

$$1 - \frac{1}{\Gamma(q)} \int_{t_k}^{t_{k+1}} (t_{k+1} - s)^{q-1} [a_i(s) - b_{ii}^-(s) m_i(t_k)] ds \geq 0. \quad (36)$$

By (32) and (36),

$$\begin{aligned} \|z(t_{k+1})\| &= \sum_{i=1}^n \beta_i |z_i(t_{k+1})| \leq \sum_{i=1}^n \beta_i z_i(t_k) \left\{ 1 - \frac{1}{\Gamma(q)} \right. \\ & \cdot \left. \int_{t_k}^{t_{k+1}} (t_{k+1} - s)^{q-1} [a_i(s) - b_{ii}^-(s) m_i(t_k)] ds \right\} \\ & + \frac{1}{\Gamma(q)} \sum_{i=1}^n \beta_i \\ & \cdot \sum_{j=1, j \neq i}^n \int_{t_k}^{t_{k+1}} (t_{k+1} - s)^{q-1} b_{ij}(s) m_j(t_k) z_j(t_k) ds \\ & \leq \sum_{j=1}^n \beta_j |z_j(t_k)| \left\{ 1 - \frac{1}{\Gamma(q)} \right. \\ & \cdot \left. \int_{t_k}^{t_{k+1}} (t_{k+1} - s)^{q-1} [a_j(s) - b_{jj}^+(s) F_j] ds \right\} + \frac{1}{\Gamma(q)} \\ & \cdot \sum_{i=1}^n \sum_{j=1, j \neq i}^n \beta_j |z_j(t_k)| \\ & \cdot \int_{t_k}^{t_{k+1}} \left[(t_{k+1} - s)^{q-1} \frac{\beta_i}{\beta_j} |b_{ij}(s)| F_j \right] ds \\ & \leq \sum_{j=1}^n \beta_j |z_j(t_k)| \left\{ 1 - \frac{1}{\Gamma(q)} \right. \\ & \cdot \left. \int_{t_k}^{t_{k+1}} (t_{k+1} - s)^{q-1} \lambda_j(\beta, s) ds \right\} \leq (1 - \varepsilon) \\ & \cdot \sum_{j=1}^n \beta_j |z_j(t_k)| = (1 - \varepsilon) \|z(t_k)\|, \end{aligned} \quad (37)$$

which leads to

$$\|z(t_k)\| = o(t_k^{-q-1}), \quad t_k \rightarrow +\infty, \quad (38)$$

hence

$$\lim_{t_k \rightarrow +\infty} \|z(t_k)\| = 0. \quad (39)$$

Recalling system (9), we have

$$\begin{aligned} \lim_{t \rightarrow +\infty} \|z(t)\| &= \lim_{t \rightarrow +\infty} \sum_{i=1}^n \beta_i |z_i(t) - z_i(t_k) + z_i(t_k)| \\ &= \lim_{t \rightarrow +\infty} \|z(t_k)\| + \lim_{t \rightarrow +\infty} \sum_{i=1}^n \beta_i \left| \frac{1}{\Gamma(q)} \int_{t_k}^{t_{k+1}} (t-s)^{q-1} \right. \\ & \cdot \left. \left[-a_i(s) z_i(t_k) + \sum_{j=1}^n b_{ij}(s) h_j(t_k) \right] ds \right| \\ & \leq \lim_{k \rightarrow +\infty} \|z(t_k)\| + \lim_{t \rightarrow +\infty} M \sum_{j=1}^n \beta_j |z_j(t_k)| \frac{1}{\Gamma(q)} \int_{t_k}^t (t-s)^{q-1} ds \\ & \leq \lim_{k \rightarrow +\infty} \|z(t_k)\| + M \\ & \cdot \lim_{t \rightarrow +\infty} \frac{(t_{k+1} - t_k)^q}{\Gamma(q+1)} \|z(t_k)\| = 0; \end{aligned} \quad (40)$$

where M is defined in (22). It can be concluded that outer-synchronization of system (6) is proved. \square

Remark 5. From inequality (28), we can see

$$\left[\frac{\Gamma(q+1)\varepsilon}{C} \right]^{1/q} \leq t_{k+1} - t_k \leq \left[\frac{\Gamma(q+1)\varepsilon}{\iota} \right]^{1/q} \quad (41)$$

for all $k = 0, 1, 2, \dots$, which excludes the Zeno behavior for rule (24).

Theorem 6. Let $\varphi(t)$ be a positive and continuous function on $[t_0, +\infty)$. Set t_{k+1} as a time point such that

$$t_{k+1} = \sup_{\tau \geq t_k} \{ \tau : \|e(t)\| \leq \varphi(t), \forall t \in (t_k, \tau) \} \quad (42)$$

for all $k = 0, 1, 2, \dots$, where $e(t) = (e_1(t), e_2(t), \dots, e_n(t))^T$ is defined in (11). If there exist positive constants $\beta_i > 0$ ($i = 1, 2, \dots, n$) such that $\min_{1 \leq j \leq n} \lambda_j(\beta, t) \geq N$ for some $N > 0$ and all $t \geq t_0$, $\sup_{t \geq t_0} (1/\Gamma(q)) \int_{t_0}^t (t-s)^{q-1} \varphi(s) ds < +\infty$, then system (6) reaches outer-synchronization.

Proof. According to Lemma 2, from (9) and (42),

$$\begin{aligned}
{}^C D_{t_k}^q \|z(t)\| &= \sum_{i=1}^n \beta_i {}^C D_{t_k}^q |z_i(t)| \leq \sum_{i=1}^n \operatorname{sgn}(z_i(t)) \\
&\cdot \beta_i {}^C D_{t_k}^q z_i(t) = \sum_{i=1}^n \operatorname{sgn}(z_i(t)) \beta_i \left\{ -a_i(t) z_i(t_k) \right. \\
&+ \left. \sum_{j=1}^n b_{ij}(t) h_j(t_k) \right\} = \sum_{i=1}^n \operatorname{sgn}(z_i(t)) \beta_i \left\{ -a_i(t) \right. \\
&\cdot [z_i(t_k) - z_i(t) + z_i(t)] + \sum_{j=1}^n b_{ij}(t) \\
&\cdot \left. [m_j(t_k) z_j(t_k) - m_j(t) z_j(t) + m_j(t) z_j(t)] \right\} \\
&= \sum_{i=1}^n \operatorname{sgn}(z_i(t)) \beta_i \left\{ -a_i(t) e_i(t) + \sum_{j=1}^n b_{ij}(t) m_j(t_k) \right. \\
&\cdot e_j(t) - a_i(t) z_i(t) + b_{ii}(t) m_i(t_k) z_i(t) \\
&+ \left. \sum_{j=1, j \neq i}^n b_{ij}(t) m_j(t_k) z_j(t) \right\} \leq \sum_{j=1}^n \left\{ a_j(t) \right. \\
&+ \sum_{i=1}^n \frac{\beta_i}{\beta_j} |b_{ij}(t)| F_j \left. \right\} \beta_j |e_j(t)| \\
&- \sum_{j=1}^n \left\{ a_j(t) - b_{jj}^+(t) F_j - \sum_{i=1, i \neq j}^n \frac{\beta_i}{\beta_j} |b_{ij}(t)| F_j \right\} \\
&\cdot \beta_j |z_j(t)| \leq -N \|z(t)\| + M \|e(t)\| \leq -N \|z(t)\| \\
&+ M \varphi(t),
\end{aligned} \tag{43}$$

where M is defined in (22), and

$$m_i(t) = \begin{cases} \frac{h_i(t)}{z_i(t)}, & z_i(t) \neq 0, \\ 0, & z_i(t) = 0. \end{cases} \tag{44}$$

On the other hand, by (43),

$$\begin{aligned}
\|z(t)\| &\leq \|z(t_0)\| \\
&+ \frac{1}{\Gamma(q)} \int_{t_0}^t (t-s)^{q-1} [-N \|z(s)\| + M \varphi(s)] ds
\end{aligned}$$

$$\begin{aligned}
&= \|z(t_0)\| - \frac{1}{\Gamma(q)} \int_{t_0}^t (t-s)^{q-1} N \|z(s)\| ds \\
&+ \frac{1}{\Gamma(q)} \int_{t_0}^t (t-s)^{q-1} M \varphi(s) ds \\
&\leq \|z(t_0)\| - \frac{1}{\Gamma(q)} \int_{t_0}^t (t-s)^{q-1} N \|z(s)\| ds + M \delta,
\end{aligned} \tag{45}$$

for $s \in [t_k, t)$, $t \in [t_k, t_{k+1})$, where $(1/\Gamma(q)) \int_{t_0}^t (t-s)^{q-1} \varphi(s) ds \leq \delta < +\infty$.

Using Lemma 3, from (45), it follows

$$\lim_{t \rightarrow +\infty} \|z(t)\| \leq \lim_{t \rightarrow +\infty} \Theta E_q(-N(t-t_0)^q) = 0, \tag{46}$$

$t \geq t_0,$

where $\Theta = \|z(t_0)\| + M \delta$, which implies that $\|z(t)\|$ converges to 0 by the sampling time sequence $\{t_k\}_{k=0}^{+\infty}$. Therefore, system (6) reaches out-synchronization. \square

3.2. Decentralized Data-Sampling Principle

Theorem 7. Let $\phi(t) = (\phi_1(t), \phi_2(t), \dots, \phi_n(t))^T$ be positive and continuous on $[t_0, +\infty)$. Set t_{k+1} as a time point such that

$$t_{k+1} = \sup_{\tau \geq t_k} \left\{ \tau : |e_i(t)| \leq \phi_i(t), \forall t \in (t_k^i, \tau] \right\} \tag{47}$$

for $i = 1, 2, \dots, n$ and all $k = 0, 1, 2, \dots$, where $e(t) = (e_1(t), e_2(t), \dots, e_n(t))^T$ is defined in (14). If there exist positive constants $\beta_i > 0$ ($i = 1, 2, \dots, n$) such that $\min_{1 \leq j \leq n} \lambda_j(\beta, t) \geq K$ for some $K > 0$ and all $t \geq t_0$, and $\sup_{t \geq t_0} (1/\Gamma(q)) \int_{t_0}^t (t-s)^{q-1} \|\phi(s)\| ds < +\infty$, then system (7) reaches outer-synchronization.

Proof. According to Lemma 2, from (13) and (47),

$$\begin{aligned}
{}^C D_{t_k}^q \|z(t)\| &= \sum_{i=1}^n \beta_i {}^C D_{t_k}^q |z_i(t)| \leq \sum_{i=1}^n \operatorname{sgn}(z_i(t)) \\
&\cdot \beta_i {}^C D_{t_k}^q z_i(t) = \sum_{i=1}^n \operatorname{sgn}(z_i(t)) \beta_i \left\{ -a_i(t) z_i(t_k^i) \right. \\
&+ \left. \sum_{j=1}^n b_{ij}(t) h_j(t_k^j) \right\} = \sum_{i=1}^n \operatorname{sgn}(z_i(t)) \beta_i \left\{ -a_i(t) \right. \\
&\cdot \left. [z_i(t_k^i) - z_i(t) + z_i(t)] + \sum_{j=1}^n b_{ij}(t) \right.
\end{aligned}$$

$$\begin{aligned}
& \cdot \left[m_j(t_k^j) z_j(t_k^j) - m_j(t_k^j) z_j(t) \right. \\
& \left. + m_j(t_k^j) z_j(t) \right] = \sum_{i=1}^n \operatorname{sgn}(z_i(t)) \beta_i \left\{ -a_i(t) \right. \\
& \cdot e_i(t) - a_i(t) z_i(t) + b_{ii}(t) m_i(t_k^i) z_i(t) \\
& \left. + \sum_{j=1}^n b_{ij}(t) m_j(t_k^j) e_j(t) \right. \\
& \left. + \sum_{j=1, j \neq i}^n b_{ij}(t) m_j(t_k^j) z_j(t) \right\} \leq \sum_{j=1}^n \left\{ a_j(t) \right. \\
& \left. + \sum_{i=1}^n \frac{\beta_i}{\beta_j} |b_{ij}(t)| F_j \right\} \beta_j |e_j(t)| - \sum_{j=1}^n \left\{ a_j(t) \right. \\
& \left. - b_{jj}^+(t) F_j - \sum_{i=1, i \neq j}^n \frac{\beta_i}{\beta_j} |b_{ij}(t)| F_j \right\} \beta_j |z_j(t)| \\
& \leq -K \|z(t)\| + M \|e(t)\| \leq -K \|z(t)\| + M \|\phi(t)\|, \tag{48}
\end{aligned}$$

where M is defined in (22), and

$$m_j(t_k^j) = \begin{cases} h_j(t_k^j), & z_j(t_k^j) \neq 0, \\ z_j(t_k^j), & z_j(t_k^j) = 0. \end{cases} \tag{49}$$

On the other hand, by (48),

$$\begin{aligned}
& \|z(t)\| \\
& \leq \|z(t_0)\| \\
& \quad + \frac{1}{\Gamma(q)} \int_{t_0}^t (t-s)^{q-1} [-K \|z(s)\| + M \|\phi(s)\|] ds \\
& = \|z(t_0)\| - \frac{1}{\Gamma(q)} \int_{t_0}^t (t-s)^{q-1} K \|z(s)\| ds \\
& \quad + \frac{1}{\Gamma(q)} \int_{t_0}^t (t-s)^{q-1} M \|\phi(s)\| ds \\
& \leq \|z(t_0)\| - \frac{1}{\Gamma(q)} \int_{t_0}^t (t-s)^{q-1} K \|z(s)\| ds + M\rho, \tag{50}
\end{aligned}$$

for $s \in [t_k^i, t)$, $t \in [t_k^i, t_{k+1}^i)$, where $(1/\Gamma(q)) \int_{t_0}^t (t-s)^{q-1} \|\phi(s)\| ds \leq \rho < +\infty$.

Using Lemma 3, from (50), it follows

$$\lim_{t \rightarrow +\infty} \|z(t)\| \leq \lim_{t \rightarrow +\infty} \Pi E_q (-K(t-t_0)^q) = 0, \quad t \geq t_0, \tag{51}$$

where $\Pi = \|z(t_0)\| + M\rho$, which implies that $\|z(t)\|$ converges to 0 by the sampling time sequence $\{t_k^i\}_{k=0}^{+\infty}$, $i = 1, 2, \dots, n$. Therefore, system (7) reaches out-synchronization. \square

Remark 8. As Theorem 5 in [19], under the data-sampling rule in Theorem 6 or Theorem 7, the interevent interval of each system state is strictly positive and possesses a common positive lower bound. Furthermore, the Zeno behavior is excluded.

Remark 9. For the sampled-data control, how to choose the proper scheme with the ultimate aim of maximizing the data collected to control the system is challenging. For example, as revealed in [9, 10], it is extremely difficult to design the sampling time point inherited from the sampled-data control strategy. However, according to Theorems 4–7, this situation can be effectively solved if the centralized and decentralized data-sampling principles are cleverly utilized.

Remark 10. For three control schemes in Theorems 4–7, these are just the type and level of points, not the merits of good points of difference. Theorem 4 is entirely focused around the centralized data-sampling principle via structure. Theorem 6 is concerned with the centralized data-sampling principle via state. Theorem 7 is to place emphasis on the decentralized data-sampling principle via state.

Remark 11. Note that the sampled-data control in Theorems 4–7 exerts only at the sampling time point, that is, every system state employs only its neighbors' information at t_k or t_k^i . Thus, compared with the continuous-time control strategy, the control schemes in Theorems 4–7 can effectively save the bandwidth and reduce the communication cost. Moreover, the results obtained here are the first ones on centralized and decentralized data-sampling principles for outer-synchronization of fractional-order neural networks.

Remark 12. The key features of outer-synchronization in Theorems 4–7 are follows. (1) Each outer-synchronization scheme is closely related to the sampling time point. Once the sampling time point is given, the states of the controlled fractional-order neural networks will achieve outer-synchronization. (2) Centralized data-sampling principle via structure makes full use of the characteristic of system itself, while centralized or decentralized data-sampling principle via state skillfully combines the feature of state measurement error.

Remark 13. The analytical methods for outer-synchronization in Theorems 4–7 are quite different from conventional complete synchronization, projective synchronization, phase synchronization, distributed synchronization, pinning synchronization, and cluster synchronization.

4. A Numerical Example

In this section, a numerical example is utilized to show the effectiveness of the results obtained.

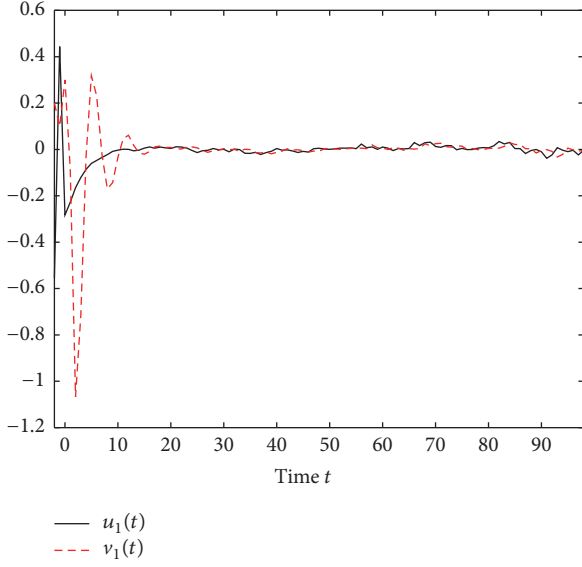


FIGURE 1: Dynamics of $u_1(t)$ and $v_1(t)$ in the triggering mechanism as Theorem 4.

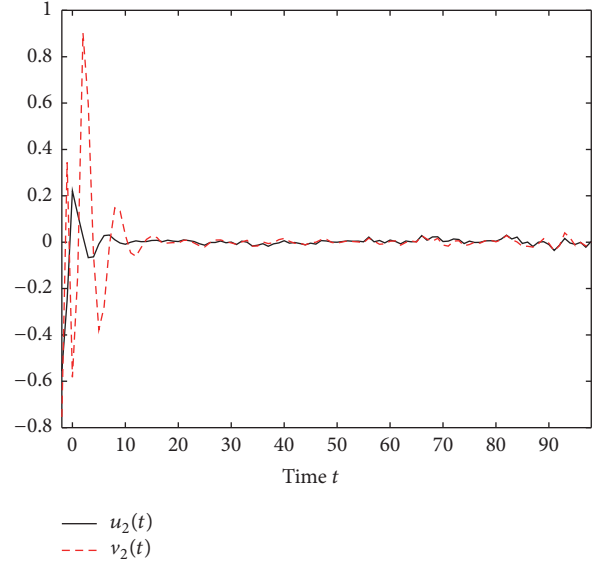


FIGURE 2: Dynamics of $u_2(t)$ and $v_2(t)$ in the triggering mechanism as Theorem 4.

Consider a class of fractional-order neural networks as follows:

$$\begin{aligned} {}^C D_{t_0}^q x_1(t) &= -a_1(t)x_1(t) + b_{11}(t)f_1(x_1(t)) \\ &\quad + b_{12}(t)f_2(x_2(t)) + u_1(t), \\ {}^C D_{t_0}^q x_2(t) &= -a_2(t)x_2(t) + b_{21}(t)f_1(x_1(t)) \\ &\quad + b_{22}(t)f_2(x_2(t)) + u_2(t), \end{aligned} \quad (52)$$

where $q = 1/2$, $t_0 = 0$, $A = \begin{pmatrix} a_1(t) & 0 \\ 0 & a_2(t) \end{pmatrix} = \begin{pmatrix} 1.5 & 0 \\ 0 & 1.5 \end{pmatrix}$, $B = \begin{pmatrix} b_{11}(t) & b_{12}(t) \\ b_{21}(t) & b_{22}(t) \end{pmatrix} = \begin{pmatrix} 0.3 & -0.7 \\ -1.2 & -0.1 \end{pmatrix}$, $u = \begin{pmatrix} u_1(t) \\ u_2(t) \end{pmatrix} = \begin{pmatrix} 0.1 \\ 0.1 \end{pmatrix}$, $f_1(\mathbb{X}) = f_2(\mathbb{X}) = 1/(1 + e^{-\mathbb{X}})$.

By direct calculation, we can obtain

$$\begin{aligned} \lambda_1(\beta, t) &= a_1(t) - F_1 b_{11}^+(t) - \frac{F_1 \beta_2}{\beta_1} |b_{21}(t)|, \\ \lambda_2(\beta, t) &= a_2(t) - F_2 b_{22}^+(t) - \frac{F_2 \beta_1}{\beta_2} |b_{12}(t)|. \end{aligned} \quad (53)$$

To choose $\varepsilon = 0.2$, $\iota = 0.8$, $\beta_1 = \beta_2 = 1$, then it follows that $B = 1.6$, $C = 1.05$. Hence the following inequalities hold:

$$\begin{aligned} B\varepsilon - \iota &\leq 0, \\ C\varepsilon - \iota(2 - \varepsilon) &\leq 0. \end{aligned} \quad (54)$$

According to Theorem 4, system (52) reaches outer-synchronization. Figures 1 and 2 depict the dynamics of $u_1(t)$ and $v_1(t)$, $u_2(t)$ and $v_2(t)$ in the triggering time points as Theorem 4, respectively. Figure 3 describes the release time points and release intervals.

To select $\varphi(t) = 1/(t+1)^{1/2}$, together with

$$\sup_{t \geq 0} \frac{1}{\Gamma(1/2)} \int_0^t (t-s)^{q-1} \frac{1}{(s+1)^{1/2}} ds < +\infty, \quad (55)$$

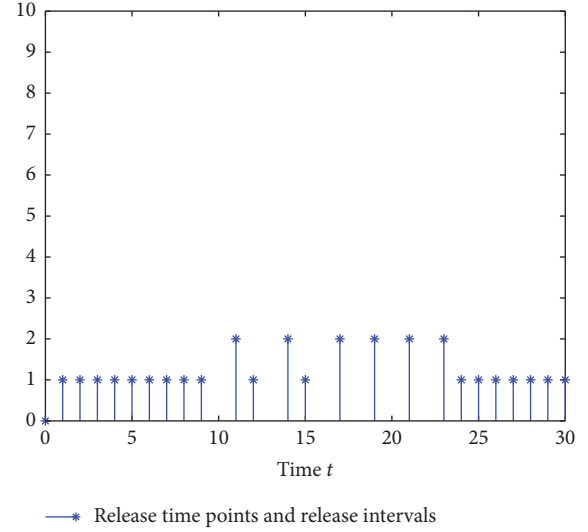


FIGURE 3: The release time points and release intervals in the triggering mechanism as Theorem 4.

according to Theorem 6, system (52) reaches outer-synchronization. Figures 4 and 5 depict the dynamics of $u_1(t)$ and $v_1(t)$, $u_2(t)$ and $v_2(t)$ in the triggering time points as Theorem 6, respectively. Figure 6 describes the release time points and release intervals.

To select $\phi_1(t) = 1/(t+1)^{1/2}$, $\phi_2(t) = 1/(t+2)^{1/2}$, together with

$$\begin{aligned} \sup_{t \geq 0} \frac{1}{\Gamma(1/2)} \int_0^t (t-s)^{q-1} \frac{1}{(s+1)^{1/2}} ds < +\infty, \\ \sup_{t \geq 0} \frac{1}{\Gamma(1/2)} \int_0^t (t-s)^{q-1} \frac{1}{(s+2)^{1/2}} ds < +\infty, \end{aligned} \quad (56)$$

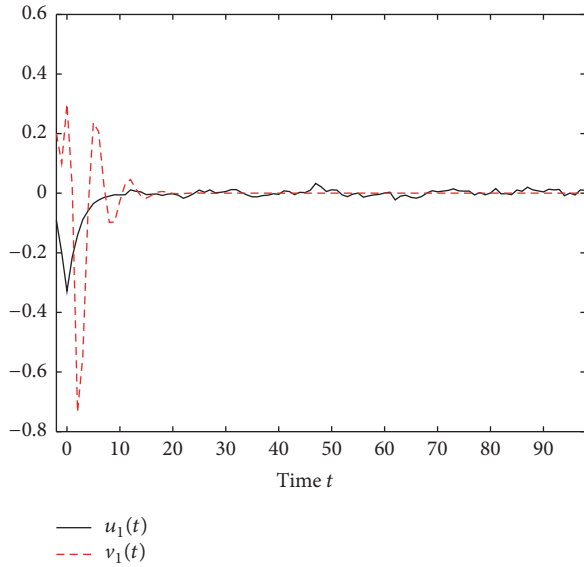


FIGURE 4: Dynamics of $u_1(t)$ and $v_1(t)$ in the triggering mechanism as Theorem 6.

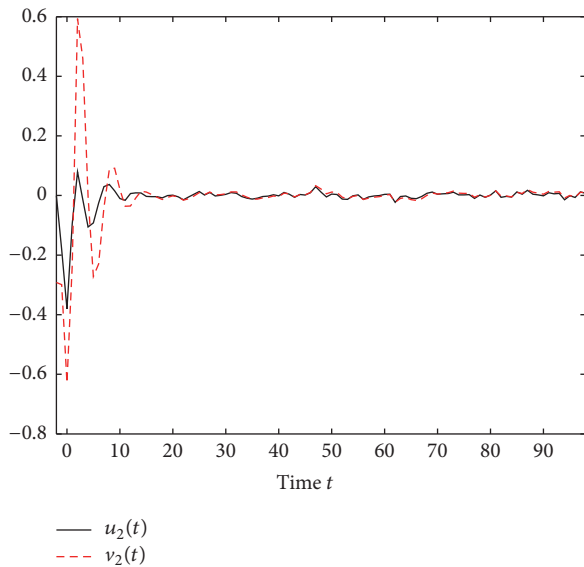


FIGURE 5: Dynamics of $u_2(t)$ and $v_2(t)$ in the triggering mechanism as Theorem 6.

according to Theorem 7, system (52) reaches outer-synchronization. Figures 7 and 8 depict the dynamics of $u_1(t)$ and $v_1(t)$, $u_2(t)$ and $v_2(t)$ in the triggering time points as Theorem 7, respectively. Figure 9 describes the release time points and release intervals.

Remark 14. In existing publications, there has been no theoretic criterion to achieve outer-synchronization of (52). In addition, using centralized or decentralized data-sampling principle to analyze and control fractional-order systems is also rare.

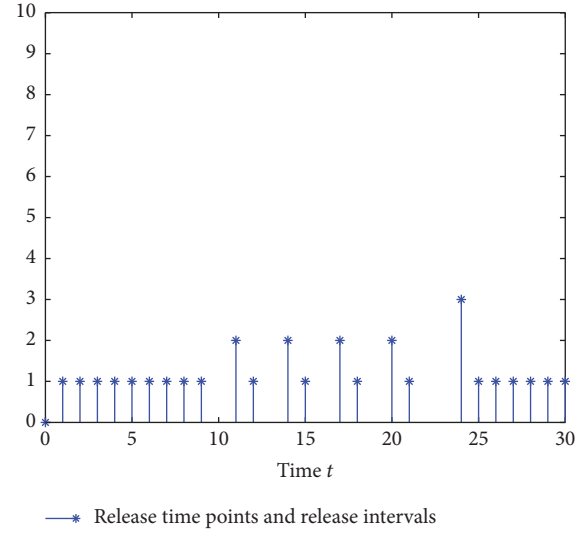


FIGURE 6: The release time points and release intervals in the triggering mechanism as Theorem 6.

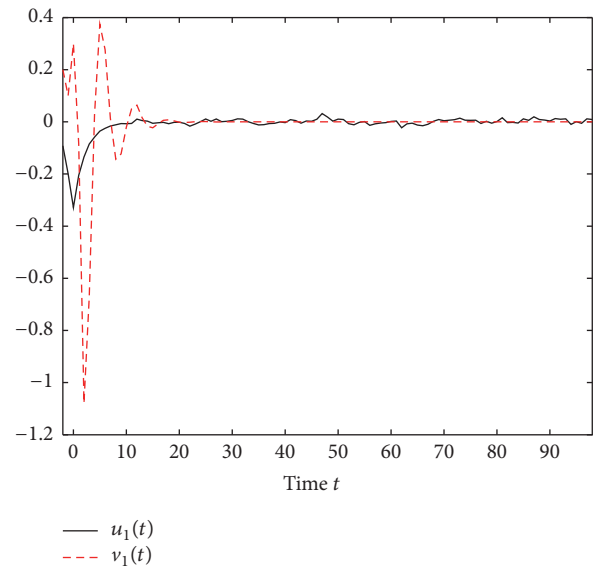


FIGURE 7: Dynamics of $u_1(t)$ and $v_1(t)$ in the triggering mechanism as Theorem 7.

Remark 15. According to simulation analysis in Figures 1–9, there is no essential difference regarding outer-synchronization performance in three control schemes as Theorems 4–7. By comparative analysis of Figures 3, 6, and 9, the release intervals via control scheme as Theorem 4 are relatively minor, and the triggering time points via control scheme as Theorem 7 are spread more thinly.

5. Concluding Remarks

In this paper, we show that outer-synchronization of fractional-order neural networks can be achieved by applying appropriate centralized and decentralized data-sampling

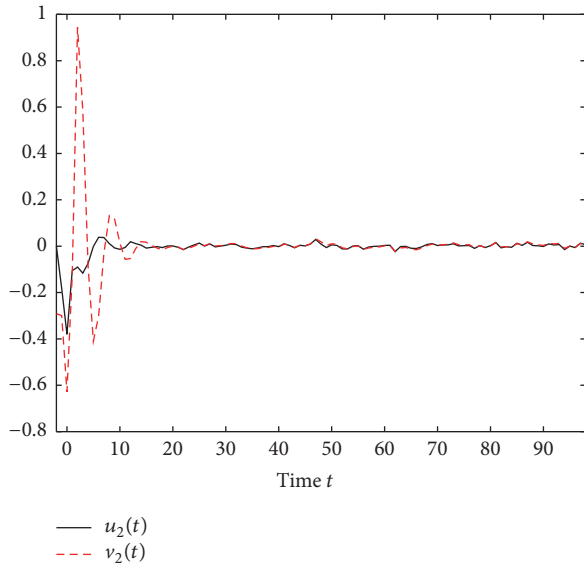


FIGURE 8: Dynamics of $u_2(t)$ and $v_2(t)$ in the triggering mechanism as Theorem 7.

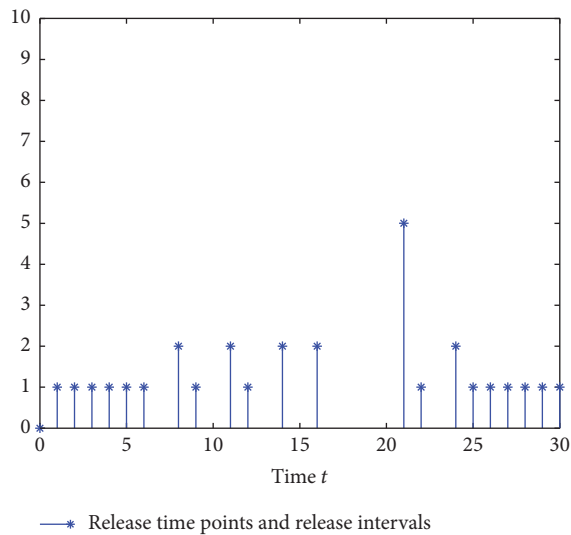


FIGURE 9: The release time points and release intervals in the triggering mechanism as Theorem 7.

principles. Such theoretical results improve and supplement some existing related results. The results obtained here are sufficient conditions for outer-synchronization of fractional-order neural networks and may remain room for improvement. Further extensions would be welcome: (1) outer-synchronization of fractional-order neural networks considering both conservativeness and complexity; (2) analyzing the outer-synchronization of fractional-order neural networks subject to time-delay; (3) analyzing the outer-synchronization of fractional-order neural networks subject to stochastic disturbance.

Conflicts of Interest

The author declares that there are no conflicts of interest regarding the publication of this paper.

Acknowledgments

The work is supported by the Research Project of Hubei Provincial Department of Education of China under Grant T201412.

References

- [1] B. Chen and J. Chen, "Global asymptotical ω -periodicity of a fractional-order non-autonomous neural networks," *Neural Networks*, vol. 68, pp. 78–88, 2015.
- [2] I. Pan and S. Das, "Fractional order AGC for distributed energy resources using robust optimization," *IEEE Transactions on Smart Grid*, vol. 7, no. 5, pp. 2175–2186, 2015.
- [3] J. Shen and J. Lam, "Stability and performance analysis for positive fractional-order systems with time-varying delays," *IEEE Transactions on Automatic Control*, vol. 61, no. 9, pp. 2676–2681, 2016.
- [4] L. P. Chen, R. C. Wu, J. Cao, and J.-B. Liu, "Stability and synchronization of memristor-based fractional-order delayed neural networks," *Neural Networks*, vol. 71, pp. 37–44, 2015.
- [5] C. Huang, J. Cao, M. Xiao, A. Alsaedi, and T. Hayat, "Bifurcations in a delayed fractional complex-valued neural network," *Applied Mathematics and Computation*, vol. 292, pp. 210–227, 2017.
- [6] S. Liang, R. Wu, and L. Chen, "Comparison principles and stability of nonlinear fractional-order cellular neural networks with multiple time delays," *Neurocomputing*, vol. 168, pp. 618–625, 2015.
- [7] M. B. Delghavi, S. Shoja-Majidabad, and A. Yazdani, "Fractional-order sliding-mode control of islanded distributed energy resource systems," *IEEE Transactions on Sustainable Energy*, vol. 7, no. 4, pp. 1482–1491, 2016.
- [8] R. Rakkiyappan, G. Velmurugan, and J. Cao, "Stability analysis of fractional-order complex-valued neural networks with time delays," *Chaos, Solitons and Fractals*, vol. 78, pp. 297–316, 2015.
- [9] A. Wu, L. Liu, T. Huang, and Z. Zeng, "Mittag-Leffler stability of fractional-order neural networks in the presence of generalized piecewise constant arguments," *Neural Networks*, vol. 85, pp. 118–127, 2017.
- [10] A. Wu and Z. Zeng, "Boundedness, Mittag-Leffler stability and asymptotical ω -periodicity of fractional-order fuzzy neural networks," *Neural Networks*, vol. 74, pp. 73–84, 2016.
- [11] A. L. Wu and Z. G. Zeng, "Global Mittag-Leffler stabilization of fractional-order memristive neural networks," *IEEE Transactions on Neural Networks and Learning Systems*, vol. 28, no. 1, pp. 206–217, 2017.
- [12] X. Yang, C. Li, Q. Song, T. Huang, and X. Chen, "Mittag-Leffler stability analysis on variable-time impulsive fractional-order neural networks," *Neurocomputing*, vol. 207, pp. 276–286, 2015.
- [13] N. Ullah, M. Asghar Ali, R. Ahmad, and A. Khattak, "Fractional order control of static series synchronous compensator with parametric uncertainty," *IET Generation, Transmission & Distribution*, vol. 11, no. 1, pp. 289–302, 2017.

- [14] S. Zhang, Y. G. Yu, and H. Wang, "Mittag-Leffler stability of fractional-order Hopfield neural networks," *Nonlinear Analysis: Hybrid Systems*, vol. 16, pp. 104–121, 2015.
- [15] A. Azami, S. V. Naghavi, R. Dadkhah Tehrani, M. H. Khooban, and F. Shabaninia, "State estimation strategy for fractional order systems with noises and multiple time delayed measurements," *IET Science, Measurement & Technology*, vol. 11, no. 1, pp. 9–17, 2017.
- [16] T. Jing, F. Chen, and Q. Li, "Finite-time mixed outer synchronization of complex networks with time-varying delay and unknown parameters," *Applied Mathematical Modelling*, vol. 39, no. 23–24, pp. 7734–7743, 2015.
- [17] S. Li, "Linear generalized outer synchronization between two complex dynamical networks with time-varying coupling delay," *Optik*, vol. 127, no. 22, pp. 10467–10477, 2016.
- [18] J. Lu, C. Ding, J. Lou, and J. Cao, "Outer synchronization of partially coupled dynamical networks via pinning impulsive controllers," *Journal of the Franklin Institute. Engineering and Applied Mathematics*, vol. 352, no. 11, pp. 5024–5041, 2015.
- [19] W. Lu, R. Zheng, and T. Chen, "Centralized and decentralized global outer-synchronization of asymmetric recurrent time-varying neural network by data-sampling," *Neural Networks*, vol. 75, pp. 22–31, 2016.
- [20] W. G. Sun, Y. Q. Wu, J. Y. Zhang, and S. Qin, "Inner and outer synchronization between two coupled networks with interactions," *Journal of the Franklin Institute*, vol. 352, no. 8, pp. 3166–3177, 2015.
- [21] Y. Sun, W. Li, and J. Ruan, "Generalized outer synchronization between complex dynamical networks with time delay and noise perturbation," *Communications in Nonlinear Science and Numerical Simulation*, vol. 18, no. 4, pp. 989–998, 2013.
- [22] Z. Wu, G. Chen, and X. Fu, "Outer synchronization of drive-response dynamical networks via adaptive impulsive pinning control," *Journal of the Franklin Institute*, vol. 352, no. 10, pp. 4297–4308, 2015.
- [23] Y. Yang, Y. Wang, and T. Li, "Outer synchronization of fractional-order complex dynamical networks," *Optik*, vol. 127, no. 19, pp. 7395–7407, 2016.
- [24] W.-H. Chen, Z. Wang, and X. Lu, "On sampled-data control for master-slave synchronization of chaotic Lurè systems," *IEEE Transactions on Circuits and Systems II: Express Briefs*, vol. 59, no. 8, pp. 515–519, 2012.
- [25] W.-H. Chen and W. X. Zheng, "An improved stabilization method for sampled-data control systems with control packet loss," *IEEE Transactions on Automatic Control*, vol. 57, no. 9, pp. 2378–2384, 2012.
- [26] D. Ding, Z. Wang, G. Wei, and F. E. Alsaadi, "Event-based security control for discrete-time stochastic systems," *IET Control Theory & Applications*, vol. 10, no. 15, pp. 1808–1815, 2016.
- [27] H. Li, X. Liao, T. Huang, and W. Zhu, "Event-triggering sampling based leader-following consensus in second-order multi-agent systems," *IEEE Transactions on Automatic Control*, vol. 60, no. 7, pp. 1998–2003, 2015.
- [28] D. Wang, D. R. Liu, Q. C. Zhang, and D. B. Zhao, "Data-based adaptive critic designs for nonlinear robust optimal control with uncertain dynamics," *IEEE Transactions on Systems, Man, and Cybernetics: Systems*, vol. 46, no. 11, pp. 1544–1555, 2016.
- [29] J. Wang, X.-M. Zhang, and Q.-L. Han, "Event-triggered generalized dissipativity filtering for neural networks with time-varying delays," *IEEE Transactions on Neural Networks and Learning Systems*, vol. 27, no. 1, pp. 77–88, 2015.
- [30] L. C. Wang, Z. D. Wang, T. W. Huang, and G. L. Wei, "An event-triggered approach to state estimation for a class of complex networks with mixed time delays and nonlinearities," *IEEE Transactions on Cybernetics*, vol. 46, no. 11, pp. 2497–2508, 2016.
- [31] Z. Wang and D. Liu, "A data-based state feedback control method for a class of nonlinear systems," *IEEE Transactions on Industrial Informatics*, vol. 9, no. 4, pp. 2284–2292, 2013.
- [32] S. Wen, T. Huang, X. Yu, M. Z. Chen, and Z. Zeng, "Aperiodic sampled-data sliding-mode control of fuzzy systems with communication delays via the event-triggered method," *IEEE Transactions on Fuzzy Systems*, vol. 24, no. 5, pp. 1048–1057, 2016.
- [33] H.-Q. Xiao, Y. He, M. Wu, S.-P. Xiao, and J. She, "New results on H_∞ tracking control based on the T-S fuzzy model for sampled-data networked control system," *IEEE Transactions on Fuzzy Systems*, vol. 23, no. 6, pp. 2439–2448, 2015.
- [34] C.-K. Zhang, Y. He, and M. Wu, "Improved global asymptotical synchronization of chaotic lurè systems with sampled-data control," *IEEE Transactions on Circuits and Systems II: Express Briefs*, vol. 56, no. 4, pp. 320–324, 2009.
- [35] H. Zhang, J. Liu, D. Ma, and Z. Wang, "Data-core-based fuzzy min-max neural network for pattern classification," *IEEE Transactions on Neural Networks*, vol. 22, no. 12, pp. 2339–2352, 2011.
- [36] X. X. Yin, D. Yue, S. L. Hu, C. Peng, and Y. S. Xue, "Model-based event-triggered predictive control for networked systems with data dropout," *SIAM Journal on Control and Optimization*, vol. 54, no. 2, pp. 567–586, 2016.
- [37] X.-M. Zhang and Q.-L. Han, "Event-triggered dynamic output feedback control for networked control systems," *IET Control Theory & Applications*, vol. 8, no. 4, pp. 226–234, 2014.
- [38] R. Zheng, X. Yi, W. Lu, and T. Chen, "Stability of analytic neural networks with event-triggered synaptic feedbacks," *IEEE Transactions on Neural Networks and Learning Systems*, vol. 27, no. 2, pp. 483–494, 2016.
- [39] H. Ye, J. Gao, and Y. Ding, "A generalized Gronwall inequality and its application to a fractional differential equation," *Journal of Mathematical Analysis and Applications*, vol. 328, no. 2, pp. 1075–1081, 2007.